Triggers for the Pierre Auger Observatory, the current status and plans for the future

Zbigniew Szadkowski

Wydawnictwo Politechniki Warszawskiej, 2009

To Ann, Gregory and Lucas

From the Author

The Pierre Auger Observatory is a multi-national organization for research on ultra-high energy cosmic rays. The Southern Auger Observatory (*Auger-South*) in the province of Mendoza, Argentina, has been completed in 2008. First results on the energy spectrum, mass composition and distribution of arrival directions on the southern sky are really impressive. The planned Northern Auger Observatory in Colorado, USA, (*Auger-North*) will open a new window into the universe and establish charged particle astronomy to determine the origin and nature of ultra-high energy cosmic rays. These cosmic particles carry information complementary to neutrinos and photons and to gravitational waves. They also provide an extremely energetic beam for the study of particle interactions at energies that thirty times higher than those reached in terrestrial accelerators.

The Auger Observatory is a hybrid detector consisting of a **S**urface **D**etector (SD) and an atmospheric **F**luorescence **D**etector (FD). The hybrid data set obtained when both detectors are working together will be especially important for evaluating the systematics of both detectors. It will also provide an energy spectrum with small energy uncertainties. The hybrid data set will also provide the best evaluation of the primary particle composition utilizing all of the known parameters sensitive to the primary particle type.

The book describes the crucial components for the Pierre Auger Observatory: triggers - necessary in order to detect a very rare cosmic rays stream, estimated as a single particle per km^2 per steradian per century. A reasonable statistics requires a huge detection area, in Auger South 3000 km^2, in Auger North planned up to 22000 km^2. The very rare stream of ultra-energetic particles is deeply hidden in a huge background of lower-energy particles. The main goal of triggers is recognition and selection of interesting, high-energy events and a rejection of the background. The author is the designer of the Second Level Trigger for the Fluorescence Detector and also the designer of four generations of the First Level Trigger for the Surface Detector. The author's trigger designs have been successively implemented in the real Pierre Auger detectors and they have been working in both types of detectors since 2000.

Extensive Air Showers initiated in the atmosphere by a single cosmic ray particle (proton or a nucleus) with a macroscopic energy of ~50 joules (equivalent to the kinetic energy of a tennis ball at 160 km/h) and spread on the large area of tens km^2 are registered by the two independent detectors. They measure the fluorescence light emitted by nitrogen in the air (FD) and Cherenkov light in super–pure water, emitted by shower particles, in 1600 surface detectors spread on 3000 km^2. To improve the signal to noise ratio each detector contains a hierarchical trigger. The book presents the concept and technical details of triggers developed by the author in 1998–2009.

Although the "standard" (more than 1600 SD and 24 FD telescopes) Auger South has been completed, new techniques: underground muon counters (AMIGA), detection of the geo-synchrotron radiation (AREA), measurements of EAS in an early stage of their development (HEAT) are being implemented on the Infill Array (dedicated test area in Auger South).

Since 2008, the author develops the underground trigger system for AMIGA (Auger Muons and Infill for the Ground Array) synchronized with the standard Auger surface

detector, trigger system for AERA, new spectral triggers for the Auger North as well as new electronics with much higher sampling than in the standard Auger surface detectors.

The author would like to thank

- My wife Ann for a big endurance, forbearance and continuing support,
- Michigan Technological University for the access to the laboratory, where the author was working on the ASIC design within July 1999 – March 2000 and was developing APEX and ACEX designs within January 2000 – June 2002,
- Collége de France, where the author was optimizing the ACEX AHDL codes within July 2002 – March 2003 during the integration of FEB with Unified Boards (UB) and started to develop the Cyclone design within December 2002 – June 2003,
- Bergische Universität Wuppertal, where the author was developing the Cyclone design within July 2003 – December 2005,
- The Polish Committee of Scientific Researches for the financial support,
- Colleagues from the Pierre Auger Collaboration for their support.

1 Introduction

In 1938 Pierre Auger showed that energetic cosmic rays produce in the atmosphere **E**xtensive **A**ir **S**howers (EAS) that can be recorded by particle detectors separated by large distances at ground level. He demonstrated the existence of cosmic rays with energies up to at least 10^{15} eV [1]. This was a phenomenal energy at a time when energies of particles produced in laboratories did not exceed 10^{7} eV. In 1962 Linsley at Volcano Ranch recorded an air shower from a cosmic ray with apparent energy in excess of 10^{20} eV [2]. That extraordinary particle received less attention than it deserved because it predated the discovery of the **C**osmic **M**icrowave **B**ackground (CMB) radiation by Penzias and Wilson in 1965 [3]. Immediately after the CMB discovery, **G**reisen, **Z**atsepin, and **K**uzmin (GZK) [4] noted that photo–pion production by the CMB photons limits the path length for protons of such high energy. In the rest frame of a high–energy cosmic ray proton, the microwave radiation is a beam of energetic gamma rays. The GZK threshold is the cosmic ray energy at which a Lorentz–boosted CMB photon has energy equal to the pion rest energy. The Planck distribution of CMB photons causes pion photo-production energy loss for protons with energies above approximately 7×10^{19} eV.

The effect predicts that the spectrum from sources distributed homogeneously in the universe is suppressed above the GZK threshold at least one order of magnitude compared to the flux without the GZK energy attenuation. This is a robust consequence of special relativity and the physics of the pion photo-production. In the context of the limited exposures of cosmic ray experiments to date, that suppression makes super–GZK cosmic ray detection highly improbable, so the effect is widely known as the "expected GZK cut-off."

Photons at super–GZK energies are attenuated even faster than protons by pair production in collisions with diffuse radio photons, however nuclei a little bit slower by photodisintegration. Candidate air shower primary particles all suffer severe propagation losses that should produce an effective cut-off at $\leq 10^{20}$ eV in experiments so far, assuming only that high energy cosmic rays are normal particles that are produced in sources throughout the universe.

Similarly, there is dispute about possible deviations from an isotropy. Analyses of AGASA data have indicated clusters of arrival directions that significantly exceed what is expected by chance [5], while HiRes data do not support the existence of clustering [6] and alternative analyses of the AGASA arrival direction data question the statistical significance of the clustering in AGASA arrival directions [7].

At the moment, the topic of the highest energy cosmic rays remains a puzzle. Controversy surrounds measurements of the energy spectrum, composition, and anisotropy and the proposed models cannot be tested without a significant improvement in the observations. Studying the sources of the universe's highest energy cosmic particles is in any case a vital discipline that justifies a sensitive full–sky exposure in a large area detector.

The Pierre Auger Observatory is an international effort to make a high statistics study of cosmic rays at the highest energies. A cosmic ray with energy 10^{20} eV is 10^{8} times more energetic than that achieved in the highest energy terrestrial accelerators. A cosmic ray produces an extensive air shower of particles through its interactions in the atmosphere. The largest showers consist of about 10^{11} charged particles spread over a diameter of 5 km or more at an elevation of 1500 m.

Ultra high–energy cosmic rays with energies reported beyond 10^{20} eV have been investigated by several experiments, but their origin is still unknown, imposing upon us a

great challenge, while providing a unique opportunity to explore new physics, astronomy and cosmology. The largest exposure experiments to date, AGASA and HiRes (both located in the Northern hemisphere), report intriguing disagreement in the energy spectrum and clustering of cosmic ray arrival directions near the GZK energy threshold. This very fact indicates that we do need more accurate and larger–scale experiments to investigate this question unambiguously.

The statistics of registered events with energy about 10^{20} eV is insufficient due to extremely low flux estimated less than 0.5 per km^2 per century per steradian. So that only detectors of immense size will be able to observe a significant number of these extraordinary cosmic ray events.

To obtain full sky coverage, the construction of two nearly identical air shower detectors have been planned, one in the Southern Hemisphere (Malargüe, Argentina, Mendoza province, nearly completed) and another in the Northern Hemisphere (Colorado). Each installation will have an array of about 1600 detectors spread over 3000 km^2. Atmospheric fluorescence telescopes placed on the boundaries of the surface array will record showers that strike the array. The two air shower detector techniques working together form a powerful instrument for these studies.

To achieve the scientific goals in the Pierre Auger experiment: it should be explained:

- What is an origin and nature of the cosmic rays, which have been observed with the highest energies ($E > 10^{20}$ eV), that is most perplexing. How and where do they acquire such enormous energies?
- Mass spectrum: we have virtually no information as to their fundamental nature. Are they protons? Nuclei? Or perhaps something exotic?
- Sources: Are the highest CR coming from particularly energetic astrophysical objects? Do they exhibit any directional anisotropy?
- GZK cut-off: has Galactic or extragalactic origin?
- Can we go beyond the current physics?

1.1 High Energy Cosmic Rays

Cosmic rays are high–speed particles traveling throughout our Galaxy, including the Solar System. Some of these particles originate from the Sun, but most come from sources outside the Solar System and are known as **G**alactic **C**osmic **R**ays (GCR). The origin of the highest energy cosmic rays is expected to be extragalactic. Simple considerations about the confinement of particles in the Galaxy and Galactic halo strongly suggest that most of the highest-energy CR must have an extragalactic origin (unless their charge is unexpectedly large, which is also not favored by the observations). CR particles arriving at the top of the Earth's atmosphere are called primaries; their collisions with atmospheric nuclei give rise to secondaries.

At 10^{15} eV GCR consist mostly from protons (nuclei of hydrogen atoms) and alpha particles (helium nuclei). The remainders are electrons and nuclei of heavier atoms. The composition changes with energy. At present, high–energy cosmic rays are believed to consist mostly of charged nuclei. Gamma rays have been observed with energies as high as ~10^{12} eV. In the case of a gamma–ray primary particle, the particle shower produced would be almost purely electromagnetic. Generically, both types of cascades are called as **E**xtensive **A**ir **S**howers (EAS) – discovered in 1938 by the French physicist Pierre Auger.

Because most cosmic–ray primaries are strongly influenced by the solar magnetic field, most of those detected near the Earth have kinetic energies in excess of about 0.1 GeV. The

number of particles drops rapidly with increasing energy, but individual particles with the estimated energies as high as 10^{20} eV have also been detected.

Because of their deflection by magnetic fields, primary GCR follow convoluted paths and arrive at the top of the Earth's atmosphere nearly uniformly from all directions. Consequently, identification of cosmic–ray sources cannot be based on arrival directions but must be rather deduced by other ways like i.e. the charge spectrum compared to spectroscopy data of stars and interstellar regions. The abundances of different elements have been well studied for particles with energies from roughly 100 MeV to several hundreds of GeV.

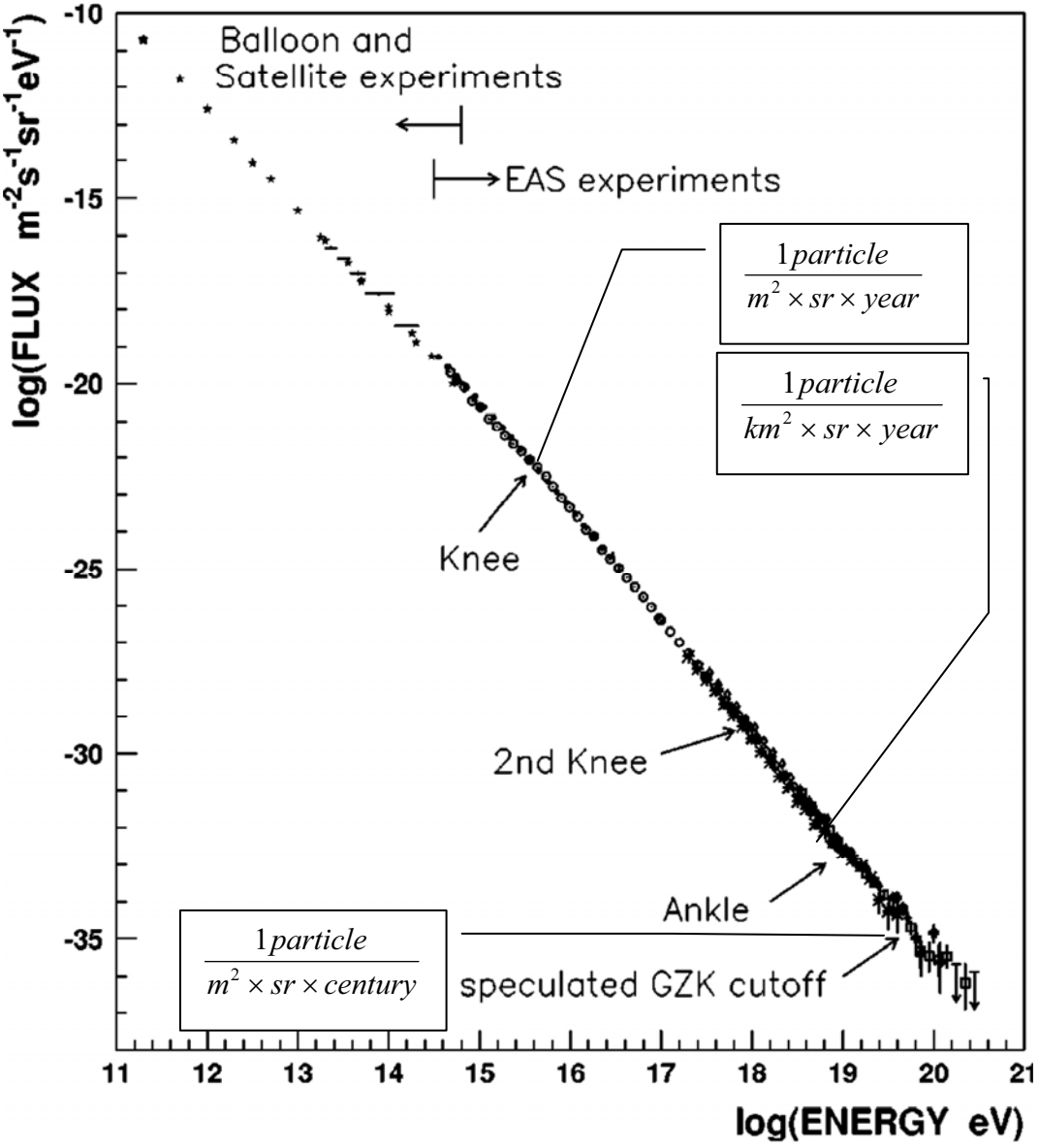

Figure 1 – Observed energy spectrum of primary cosmic rays. The spectrum is expressed by a power law from 10^{11} to 10^{20} eV with a slight change of slopes around $10^{15.5}$ eV (knee), $10^{17.8}$ eV (second knee), and 10^{19} eV (ankle) [8].

Cosmic rays have been observed with energies from 10^{9} eV to above 10^{20} eV. Over this range, the flux of cosmic rays (the number of arriving particles per unit area, per solid angle,

per unit time and unit energy) appears to follow an approximate single power law $\sim E^{-2.7}$, with sharper steepness $\sim E^{-3.0}$ between so–called knee and ankle (see Figure 1) corresponding to 10^{15} eV and 10^{18} eV respectively.

Cosmic Rays with energies above $\sim 10^{19}$ eV, known as **U**ltra–**H**igh **E**nergy **C**osmic **R**ays (UHECR) are microscopic particles with a macroscopic amount of energy about a joule or more. The existence of such energetic particles, the mechanism of the acceleration to such extreme energies, the regions of their creation and the composition remains still a mystery.

To study the acceleration mechanism, one must make careful measurements of the energy spectrum of UHECR to compare to the predictions from different acceleration models. To understand where the UHECR come from, one needs to make a careful survey of the arrival directions, and search for both small– and large–scale anisotropies in their distribution. Composition is one of the most difficult measurements because UHECR cannot be detected directly using conventional particle detectors. Consequently, the composition as well as energy spectrum and arrival directions must be inferred from auxiliary measurements.

1.2 Extensive Air Showers

The cosmic rays with energies greater than 10^{14} eV have been investigated by using the Earth's atmosphere itself as part of the detection equipment. The interaction between high–energy cosmic rays and the air produces a correlated cascade of secondary particles.

The process begins with the collision of the primary cosmic ray with a nucleus near the top of the atmosphere. This first collision produces typically several tens of secondary particles (depending on initial energy), mainly pions. The charged pions, as relatively long–lived, collide with another nucleus. The subsequent collisions are similar in nature to the primary collision. This process then leads to a cascade of particles, known as hadronic shower.

One third of the pions, created in collisions, are neutral. They are very short–lived and decay almost immediately into a pair of photons before interacting with nuclei in the atmosphere. Next, photons interacting with the nuclei in the air create electron–positron pairs, which in turn produce bremstrahlung photons. This cascading process leads to the formation of an electromagnetic cascade. The hadronic shower itself is continuously producing neutral pions and thus initiating secondary electromagnetic cascades along its path.

With an EAS development into the atmosphere, the number of generated particles successively increases (Figure 2). However, the process of multiplication is continued until the average energy of the shower particles is insufficient to produce more particles in subsequent collisions. Some part of energy is also leaking to the atmosphere due to ionization processes. Finally, the number of the particles traveling in the shower starts to decrease. This point of the EAS development is known as shower maximum. Beyond the maximum, the shower particles are gradually absorbed with an attenuation length of ~200 g/cm^2. The depth of shower maximum ($\boldsymbol{X_{max}}$) is a function of energy. With a value of about 500 g/cm^2 at 10^{15} eV, the average X_{max} for showers increases by 60–70 g/cm^2 for every decade of energy [9]. The measured value of X_{max} can also be used as a measure of the composition of the primary cosmic ray. Hadronic interaction length in air for protons is about 70 g/cm^2, and shorter for heavier nuclei. This means EAS induced by heavier elements tends to suffer its first interaction higher in the atmosphere, and hence have smaller X_{max} than showers of the same energy initiated by a lighter element.

Heavy primary particles tend to produce more muons and fewer electro-magnetic particles than do lighter primaries, of the same primary energy. Iron and proton showers can

be differentiated using surface detector data alone through the analysis of the ratio of muons to electromagnetic particles, as well as through the arrival time distribution of particles in the shower front.

Particles scatter from the region of the shower axis throughout their development. The shower core effectively acts as a moving point source of both fluorescence photons and particles, which make their way to detectors far from the core. The plane tangent to the shower front at the axis is the shower plane. The shower front itself is slightly curved, resembling a cone. Particles far from the core will arrive behind the shower plane due to simple geometry. Electromagnetic component diffuses away from the shower axis throughout the shower development. It is wider in comparison to the hadronic one. Thus, far from the core particles are spread in time, with the time spread roughly proportional to the distance from the axis. This time spread helps to distinguish distant large showers from nearby small showers, and is thus useful in triggering the surface array. The time spread becomes greater as the depth of shower maximum increases.

Fluctuations in shower development distinguish detected signals. One of the most important sources of fluctuations is the depth and characteristics of the first few interactions. Fluctuations in later interactions are averaged over a large number of particles and are not important.

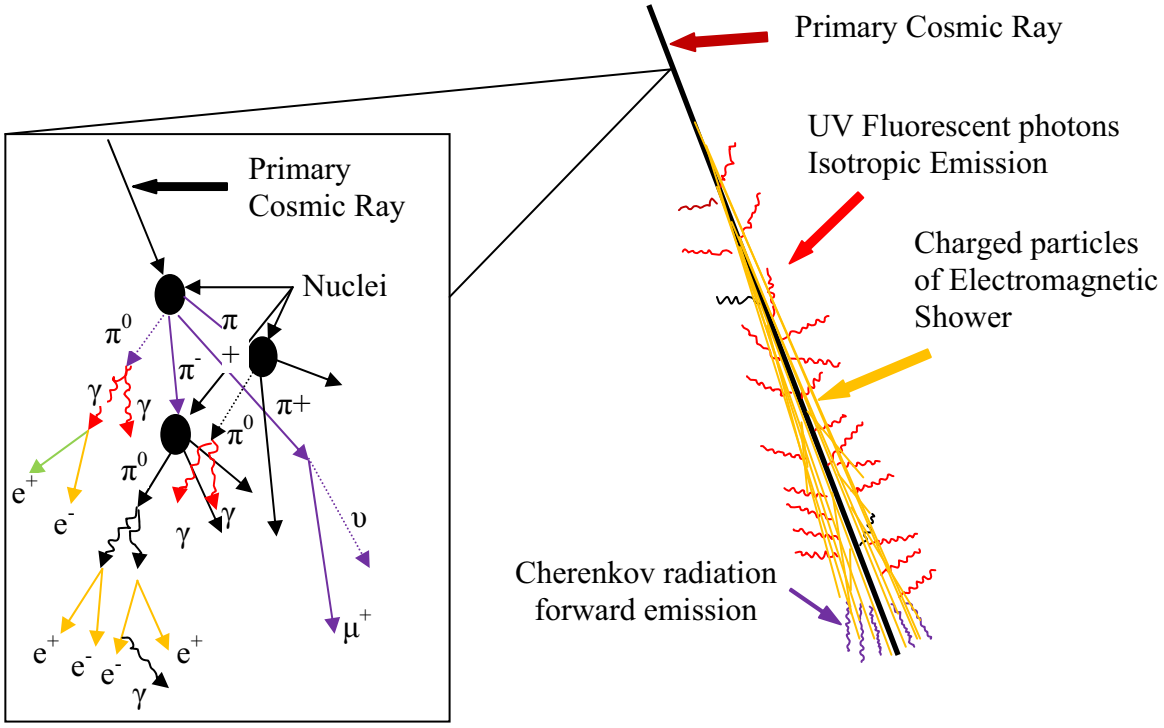

Figure 2 – The schematic of the hadronic and electromagnetic components generation in the EAS development.

1.3 The GZK cut-off

We do not know the composition of the UHECR. However, the set of stable particles as candidates for the UHECR, which can propagate over cosmological distances without losing most of their energy, is quite limited: heavy or light atomic nuclei, photons and neutrinos. Photons and neutrinos (as neutral) cannot be accelerated by any standard, electromagnetic mechanism. They can only be produced as secondary products in the interaction of a still

higher energy charged particle. Therefore, in the framework of conventional astrophysics, we believe that light and heavy nuclei are probably the best candidates for the UHECR.

There is experimental evidence that the Universe was created some ~14 billion years ago from some singularity in a giant explosion known as the "Big Bang". Perhaps the most conclusive evidence for the Big Bang is the existence of the isotropic, with Planck distribution T = 2.73 K radiation permeating the entire Universe known as the **C**osmic **M**icrowave **B**ackground (CMB). Shortly after the CMB discovery, Greisen and independently Zatsepin and Kuzmin predicted that at very high energies, the universe should become opaque to light or heavy nuclei due to the following reactions.

$$\begin{aligned} &p + \gamma_{CMB} \rightarrow N + \pi \qquad && E_p \geq 1.1 \times 10^{20}\ \text{eV} \\ &p + \gamma_{CMB} \rightarrow \Delta \rightarrow N + \pi \qquad && E_N \geq 2.5 \times 10^{20}\ \text{eV}, \end{aligned} \tag{1}$$

where : E_N – energy of nucleon being disintegrated.

The energy budget in the center–mass–frame, for an average CMB energy 6.34×10^{-4} eV and protons with energy above 110 EeV is sufficient for pion–production, during inelastic collisions with CMB photons.

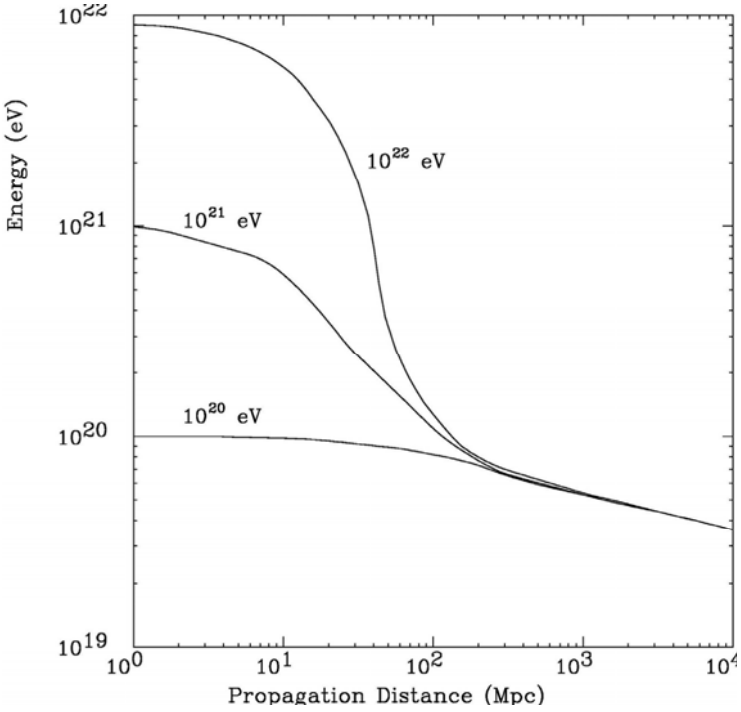

Figure 3 – Energy degradation for nucleons as a function of distance to the observer for 3 different injection energies [10].

Since in each such inelastic collision, protons leave a large part of their energy (of the order of 13% on average), their energy goes below 10 EeV (EeV=10^{18} eV) after a few tens of Mpc, whatever it was at the source. As an example, if the largest energy cosmic ray ever detected 320 EeV (it is more than 50 J) were a proton produced with an initial energy of 10 ZeV (ZeV = 10^{21} eV), the distance of its source should be less than 50 Mpc (Figure 3). The same effect is expected for heavy nuclei. Nucleons will be stripped off from the nucleus due to inelastic collisions with most of all infrared background and also with CMB. Thus, the highest energy cosmic rays cannot originate at distances larger than a few tens of Mpc.

1.3.1 "Bottom–up" production

In order to accelerate charge particles to energies above 10^{20} eV, extremely powerful electromagnetic fields should exist. However, we did not register any stable region with so large potential, which could assure such an extremely energy in a single shot process. One of the earliest theories on the acceleration of cosmic rays proposed was the second order Fermi mechanism [11], where plasma clouds roughly play the role of a magnetic mirror. A particle penetrating such a cloud from the front can be kicked back, like a tennis ball hit by a racket, with energy larger than its initial value. In this model, particles collide stochastically with magnetic clouds in the interstellar medium. Those particles involved in head-on collisions will gain energy ($\Delta E > 0$) (similar to a sling-shot process used to accelerate spacecrafts around planets), and those involved in tail-end collisions will lose energy ($\Delta E < 0$). On average however, head-on collisions are more probable. In this way, particles gain energy over many collisions. However, this mechanism is also too slow and too inefficient to account for the observed UHECR.

A more efficient and faster process is acceleration by crossing shock fronts generated in explosive phenomena (1^{st} order Fermi mechanism - $\Delta E > 0$) [12]. However that approach meets difficulties. Let us consider some hypothetical cosmic accelerator. The energy of accelerating particles depends on the value and the size of the magnetic field and is limited by the Larmor radius related to their confinement. If the Larmor radius of the particle exceeds the size of the "accelerator" then the particles escape from it. Candidates of astrophysical object, which possesses so large BR factor are given on the Hillas plot [13].

$$E_{max} = qBRc \tag{2}$$

where : E_{max} – maximal energy of particles confined in the magnetic field (J), q – electric charge (C) , B – induction of the magnetic field (T), R – radius of the confined trajectory (m), c - speed of light (m/s).

Many theories and models propose either sophisticated explanations or require some new physics. One of the models explores ultra relativistic shock acceleration such as in hot spots of powerful radio galaxies and **G**amma **R**ay **B**ursts (GRB) [14]. In the first case, relativistic jets are produced perpendicular to the accretion disk around a super–massive black hole in the central part of an active galactic nucleus. The shock on a jet, several hundreds kpc from the central engine, due to collision with the intergalactic medium is considered as being able to accelerate particles up to the highest energies. This hypothesis needs, however, to be completed by some further and necessary ingredients since such powerful galaxies are rare objects and should be clearly visible in the 50 Mpc distance authorized by propagation arguments.

The second fashionable model relates the UHECR to another long–lasting astrophysical puzzle: the Gamma Ray Bursts. These are characterized by the emission of huge amounts of energies (typically a non–negligible fraction of the mass energy of the Sun) over a very short time (minutes), observed as gamma rays but with, in some cases, X–ray and optical counterparts. Their distribution is cosmological and uniform over the sky. GRB happen at a rate of 2–3 per day. However, their distribution within the "GZK sphere" does not seem to agree with the UHECR observations. Other objects were proposed as putative sources of UHECR, such as rapidly rotating compact objects (young black holes, neutron stars or "magnetars"), which possibly are the sources of the most intense magnetic fields in the universe (field values up to the peta–gauss have been envisaged). The capability of such systems to reach the required 10^{21} eV energies is rather controversial.

1.3.2 "Top–down" production

If we have difficulties to imagine reliable mechanism accelerating particles from low to high energies, let us inverse the situation. Many theories propose top–down mechanism, decay of super–heavy, super–symmetric or **G**rand **U**nified **T**heories (GUT) particles [15]. The only problem is a justification of their existence or their surviving after the Big Bang. They could have survived up to now by some yet unknown mechanism (a very weakly violated quantum number, particles trapped inside huge potential walls called topological defects and released via spontaneous symmetry breaking mechanism...). They would have accumulated by gravitational attraction in the halo of galaxies (therefore escaping the GZK cut-off). Their decay into some ~10^4 secondary particles (mainly pions) by hadronization of quark – antiquark pairs would easily produce the ZeV energies we need and their decay products would then be dominated by photons (coming from the decay of neutral pions) and neutrinos (decay of charged pions). Indeed this scenario needs a series of hypotheses to work all together, but none of them calls for any extravagant model or theory. The important point is that there are a few experimental consequences of this model, which constitute, if observed, a unique and irrefutable signature of the existence of the Grand Unification, a horizon toward which all the modern quantum field theories are supposed to converge, i.e. heavy nuclei would rather exclude the top-down mechanism.

1.4 HiRes vs. AGASA discrepancy

The important energy loss mechanism above 6×10^{19} eV due to the pion production from interactions of UHECR on CMB would suggest the absence of particles in the UHECR flux above this energy. However, some experiments like **A**keno **G**iant **A**ir **S**hower **A**rray (AGASA) have registered EAS with energy, which is estimated as much higher than the GZK cut–off. Such super energetic events are known as super–GZK. On the other hand the HiRes results are rather consistent with the GZK limit (Figure 4).

Japanese experiment AGASA is an array of plastic scintillator covering 100 km^2 areas to detect EAS initiated by extremely high energy CR particles.

The HiRes observatory consists of two fluorescence detector (Chapter 1.5) sites separated by 12.6 km and located in Utah. Cosmic rays interacting in the upper atmosphere initiate EAS. Passage of charged particles excites nitrogen molecules causing emission of ultraviolet light (Figure 2).

Generally, there is a significant discrepancy between results registered in both experiments (it is not excluded that the bias is due to different techniques). The energy spectrum observed by AGASA with zenith angle smaller than 45º up until the end of 2002 encloses 11 events above 10^{20} eV, while according GZK cut–off the expected event number is ~1.8 [16]. This corresponds to 4.5 σ deviations from the GZK cut–off.

The HiRes energy spectrum contains two events with energies greater than 10^{20} eV, measured at 1.0× and 1.5×10^{20} eV. Assuming a purely molecular atmosphere, the energy limit is 0.9× and 1.2×10^{20} eV respectively. A power law fit to HiRes data from the ankle to the pion production threshold ($10^{18.7}$–$10^{19.8}$ eV) yields an index of (–2.82 ± 0.06). The AGASA data suggest rather that this power law should continue unchanged above the pion production threshold. The HiRes data are not consistent with that interpretation.

40 years after a GZK prediction it is still not clear if that effect really exists. Data from the above mentioned experiments show divergence in the measured CR flux in the GZK

region. The statistics in both experiments is insufficient to definitively conclude, whether the GZK effect has been confirmed or not. Additionally, it seems to be some systematic errors in an energy determination in the range of ($10^{18.5}$ – $10^{19.8}$) eV. AGASA flux is ~30 % higher. Even if we assume some systematic error in both experiments [17-18] namely that two experiments have a 15% shift in the energy determination (in a opposite directions) [19], the discrepancy in super–GZK region still remains.

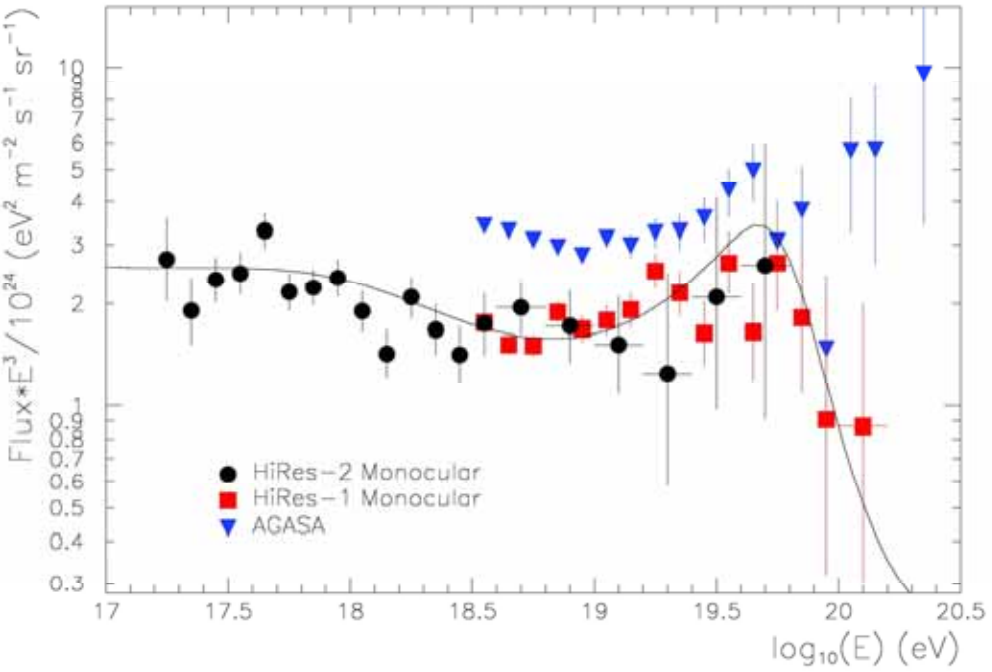

Figure 4 – HiRes monocular spectra, along with the AGASA spectra [20].

Nevertheless, below E_{GZK}, there were detected enough events to make measurements reliable. Experiments predict compatible fluxes, although some systematic uncertainties have to be still clarified. However at energies above E_{GZK} the fluxes measured in both experiments differ significantly from each other independently of measurement corrections.

The Pierre Auger Observatory may fix the GZK paradox as well as allows on identification of the cosmic ray sources and determination of the UHECR composition. Answers on these questions would provide only a partial resolution of the puzzle. A major challenge will remain in understanding the physics, maybe far beyond that what we can imagine today.

1.5 Overview of the Fluorescence Detection

Because of their very low flux, cosmic rays at the highest energies (above PeV = 10^{15} eV range) cannot be detected directly before they interact with the Earth's atmosphere (i.e. with balloon or satellite detectors). The detectors must have huge aperture and therefore are ground based. They must reconstruct the properties of the primary cosmic ray (nature, energy, direction) indirectly by measuring the secondary particles created in EAS by the chain reaction, which results from the interaction of the cosmic ray with atmospheric atoms. The successful results from the Fly's Eye and HiRes experiments, based on the fluorescence technique, determined to choose the same, well–known and fully confirmed technique for one of the type of detectors in the Auger project.

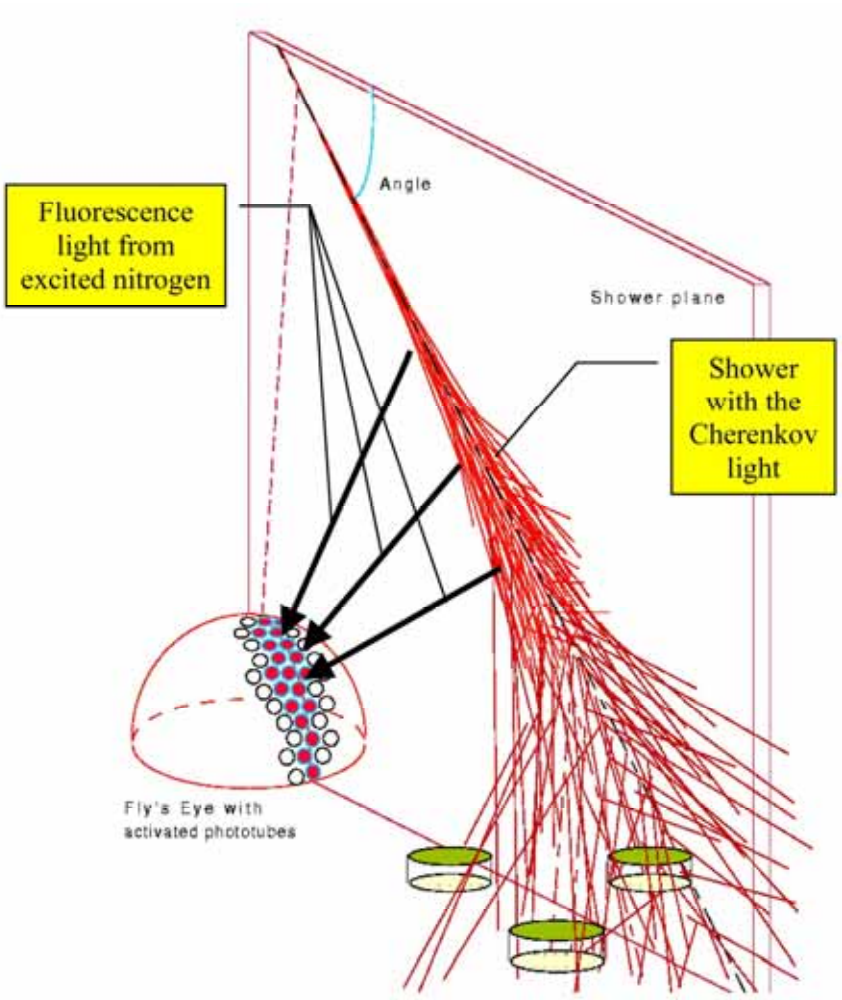

Figure 5 – Development of the shower in the atmosphere. Fluorescence light from excited nitrogen is emitted with an isotropic angular distribution from each point of the shower track and received by the photo-detectors. Cherenkov light associated with the shower is emitted mostly forward, however scattered Cherenkov light may be not negligible (Figure 7).

The avalanche of charged particles in the EAS propagating through the atmosphere results in excitation of nitrogen molecules to N_2^+ ions. If some other concurrent processes like collisions with the other molecules do not suppress the excitation, the excited nitrogen molecules generate fluorescence light in several bands mostly in the ultraviolet (UV) range (300 – 400 nm). About 88% of the total emission is concentrated in three bands: 337, 357 and 391nm respectively. Fluorescence from other molecules in this range is negligible. However, the molecular oxygen significantly quenches the nitrogen excitation. The competition between emission and collision de–excitation establishes some kind of equilibrium making the fluorescence efficiency relatively little dependent on temperature and pressure.

The fluorescence light generated by a shower and observed from a distance of hundred meters is too weak to be detected directly even by sensitive sensors. It has to be preliminary collected by some additional optics like lenses or spherical mirrors. Lenses have the significant advantage, they allow building more compact detector, however costs and long–term stability (especially plastic lenses) recommend using the mirror solution (like in

Figure 6) in similar as in the Fly's Eye and HiRes experiment (Figure 5 does not show mirrors, but only a final image of the shower on the **P**hoto–**M**ultiplier **T**ubes (PMT) matrix).

In the Pierre Auger Observatory, the fluorescence light generated by the high-energy showers is registered by optical/electronic multi-channel system with sufficient angular resolution both: vertically and horizontally (for relatively close showers). It allows investigating the longitudinal shower development as well as the lateral distributions of particles.

The light collected by the optics is next converted into electric signals by UV sensitive sensors located in the focal plane. At present, PMT are the only detectors assuring sufficient sensitivity, a large dynamic range, low noise, proper spectral characteristics and linearity. In order to achieve required accuracy of the EAS geometrical reconstruction the detector needs an abundance of PMT, typically built as a matrix with a sufficient size and a small grid.

Shower developing longwise its axis produces fluorescence light emitted from each point isotropic, visible on the PMT matrix after optical focusing as a small "traveling" spot. The size of the spot is finite and depends on the quality of the optical system. If each pixel will cover a 1.5° view from the sky (see Chapter 1.5.1), the spot size has to be smaller or equal to the pixel size. This requirement is necessary for good resolution purposes. To achieve this, the Schmidt Camera has been used. This camera has a simple spherical mirror with an aperture diaphragm on the mirror's curvature center plane (Figure 6). The optical collector has the advantage of producing homogeneous images in the entire field of view. The typical aberrations, which are presented off axis, principally the comma aberration, are eliminated.

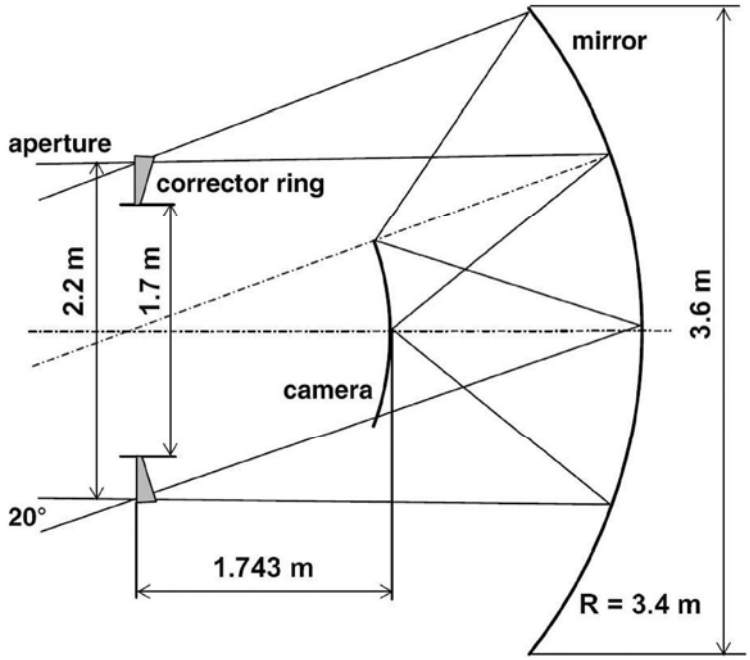

Figure 6 – The Schmidt's camera [21].

In the Schmidt optic each pixel on the PMT-matrix sees the light only from a very narrow angular range. The angular ranges corresponding to the neighboring pixels do not overlap. It means the "traveling" source of light (i.e. shower front) producing light with relatively small geometrical size will create a "traveling" light spot on the PMT-matrix. Each PMT-pixel will see the light coming from the shower track from the different angle. Electronics associated with each pixel (equipped with sufficiently fast FADC) allows on geometrical reconstruction of the track as well as analyses of receiving light stream, necessary for shower energy estimation.

Any distortions of the spot (i.e. due to mirror aberrations) "traveling" through the PMT pixels may contaminate the trigger decision taken by the electronics (compare Chapter 1.7.1 and Figure 17). For relatively long tracks, where the number of fired pixels is abundant, determination of the shower detector plane (SDP – defined in the space as the plane corresponded to a line representing the shower and the point representing the detector – see Figure 5) is pretty good. However, for short tracks, where there is no redundant information, uncertainty of the SDP determination may cause significant error in the estimation of the shower energy.

The shower longitudinal profile measured by the fluorescence detector provides model–independent characteristics of the electromagnetic shower energy, because

$$N_{\text{fluorescence}} \sim dE/dx \tag{3}$$

The FD requirements are driven by the required resolution in measurements of the atmospheric depth where the shower reaches its maximum size, X_{max}. Reasonable resolution is needed to evaluate the composition of the cosmic ray primaries. The resolution should be high compared to the (approximately 100 g/cm^2) difference expected between the depth of maximum for a proton shower and for an iron shower of the same energy. Moreover, the experimental resolution should not significantly increase the spread of values for any one component of the composition by itself. The width of the expected X_{max} distribution for any nuclear type decreases with mass *A*, and the distribution of iron depth of maximum values has an rms spread of approximately 30 g/cm^2. We will therefore require that the experimental X_{max} resolution should be no smaller than 20 g/cm^2.

The fluorescence light propagated through the atmosphere is attenuated due to the relatively weak in that range of (300 – 400 nm) absorption mostly by ozone and due to several types of scatterings, which the most significant are Rayleigh and Mie processes.

Rayleigh scattering refers to the scattering of light off the air molecules and can be extended to scattering from particles up to about a tenth of the wavelength of the light. It is Rayleigh scattering off the molecules of the air, which gives us the blue sky (due to λ^{-4} cross section dependence).

The angular distribution ~$(1 + \cos^2(\theta))$ gives the forward and backward lobes. Rayleigh scattering can be considered to be elastic scattering since the photon energies of the scattered photons are not changed. Scattering, in which the scattered photons have either a higher or lower photon energy is called Raman scattering. Usually this kind of scattering involves exciting some vibration mode of the molecules, giving a lower scattered photon energy, or scattering off an excited vibration state of a molecule which adds its vibration energy to the incident photon. In the horizontal direction at the sea level, the Rayleigh scattering attenuation is ~ 22 km at 400 nm and ~7 km at 300 nm.

The scattering from molecules and very tiny particles (<1/10 wavelength) is predominantly Rayleigh scattering. For particle sizes larger than the wavelength, Mie scattering predominates. This scattering produces a pattern like an antenna lobe, with a sharper and more intense forward lobe for larger particles. Mie (also called Aerosol) scattering depends significantly on the density of both natural and industry–made aerosols, size distribution and composition of the aerosol particles as well as vertical density profile. The scattering cross–section depends weekly on the wavelength (~1/λ). On the clear day in a desert for a relatively low altitude, the Mie contribution for the total scattering is on the level of 20 %, however it may rapidly increase when aerosol admixture in the clean air appears.

In addition to fluorescence light, showers produce prodigious numbers of Cherenkov photons, which are primarily beamed in the forward direction. (The Cherenkov emission

angle in the atmosphere is of the order of 1°, varying with altitude). The amount of Cherenkov light at a given point along the shower track depends upon the previous history of shower, and is thus not strictly proportional to the local shower size as is the fluorescent light. It is therefore necessary to estimate the amount of Cherenkov light in order to subtract its contribution to the observed signal. When a shower is viewed at small emission angles (less than 25°) with respect to the shower axis the Cherenkov signal can be many times larger than the fluorescence signal. The presence of this directly beamed Cherenkov light often impedes the proper observation of the first stages of shower development. In addition, as the Cherenkov component builds up with the propagating shower–front, the resultant intense beam can generate enough scattered light at low altitudes such that it competes with the locally produced fluorescence light. This effect complicates the observations of the later stages of shower development.

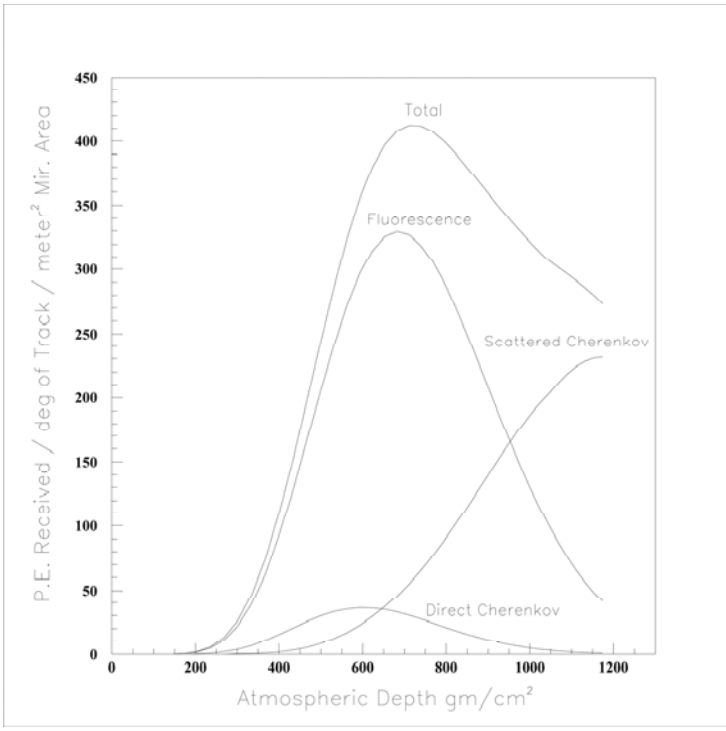

Figure 7 – Estimated signal vs. atmospheric depth of light production for a 10^{19} eV proton shower with zenith angle $\theta = 45°$ and azimuth with respect to $\varphi = 0°$ hitting the ground 10 km from the detector. The simulation included filters passing (300 – 400 nm) lights. The orientation and position of the shower has been chosen so that the contributions due to scattered and direct Cherenkov light are enhanced [22].

Both fluorescence and Cherenkov light are affected by the scattering properties of the atmosphere. The effects of scattering must be understood if one is to accurately estimate the shower size by light received from a distant section of air shower. With fluorescence light one is most concerned with the attenuation due to scattering as the light travels from the air shower to the detector. In the case of the (accumulated) Cherenkov beam, one is more concerned with the light scattered toward the detector. In both cases there are two scattering mechanisms: Rayleigh and Mie scattering.

The amount of molecular (Rayleigh) scattering at a given wavelength is proportional to the density of the air through which the beam is passing. The effect therefore tracks with the exponential density profile of the atmosphere with a scale height of 7.3 km. In general the

atmospheric density is well known and changes little over time. On the other hand, the degree of aerosol scattering depends on both the density and size distribution of particulate matter suspended in the air. These distributions are highly variable with time and location. The vertical density distribution varies depending on weather conditions between an exponential form, similar to the molecular scattering situation and a distribution in which uniform scattering occurs beneath a fixed–height mixing.

Many worst–case situations for events, which might be seen by the Auger Observatory near its energy threshold, were simulated. The difference in the heights of peak emission of the fluorescence light and of the total light suggests that an error in energy may be of about 30 % if the Cherenkov light contribution were ignored. This gives a significant shift of 50 g/cm^2 in X_{max}. Especially, for more inclined showers, directed at the eye, both direct and scattered Cherenkov cannot be neglected (Figure 7).

1.5.1 Fluorescence Detector in the Pierre Auger Observatory

The FD consists of 24 wide–angle telescopes grouped in four stations. Each telescope has a 30º field of view in azimuth and vertical angle. The four stations at the perimeter of the surface array consist of six telescopes each with an 180º field of view inward over the array. Each spherical mirror is segmented so as to obtain a total surface of 12 m^2 on a radius of curvature of 3.4 m. The aperture has a diameter of 2.2 m and is equipped with optical filters and a corrector lens. In the focal surface a PMT camera detects the light on 20×22 pixels. Each pixel covers about 1.5º by 1.5º field of view and the total number of PMTs in the FD system is 10 560. The number, distribution and resolution of the fluorescence telescopes was determined by the requirement that showers should be visible over the entire surface array at energies above 10^{19} eV.

Its primary purpose is to measure the longitudinal profile of showers recorded by the surface detector whenever it is dark and clear enough to make reliable measurements of atmospheric fluorescence from air showers. To obtain the performance goals shown above at minimum cost we have endeavored to optimize the integration of a large area surface array with an array of air fluorescence telescopes. The objective was to match the operational apertures of the two detectors so that the instantaneous fluorescence detector aperture matches the surface detector aperture. Telescopes are located on the edge of the surface array detector and are expected to operate always in conjunction with the surface detector layer.

An accurate longitudinal profile (achieving 20 g/cm^2 depth of maximum resolution) requires good geometric reconstruction of the shower axis. At large zenith angles, a small error in zenith angle causes a significant error in atmospheric slant depth. Averaging over the range of zenith angles (0 – 60^o) for showers detected in both FD and SD detectors (hybrid showers) leads to an estimation that an error of 1^o in zenith angle leads to an error of 20 g/cm^2 in X_{max}. The angular resolution of the hybrid showers must therefore be significantly better than 1°, since other uncertainties also contribute to the depth of maximum uncertainty [23].

If the final angular resolution of the detector is to be smaller than 1°, the design should be planned with an angular resolution of 0.5°. There are two aspects of the angular resolution: the shower–detector plane determination and the angle of the shower axis within that plane. The shower–detector plane is determined by the set of pixels that see the shower axis. The need to resolve the shower–detector plane to better than 0.5° has led to the constraint that the pixel size cannot be larger than 1.5° in effective diameter. Determining the shower axis within the track–detector plane is done exclusively with timing information. The angular

velocity of the shower front image moving through the FD field of view does not uniquely determine the shower axis. It does reduce the 2–parameter family of lines in the shower detector plane to a 1–parameter family of possible axes. Each hypothetical axis makes a specific prediction for the arrival time of the shower front at each surface detector. The measured arrival times, at one or more surface detectors thereby determine the correct shower axis. The need for good timing information is a primary reason for using sampling **A**nalog to **D**igital **C**onverters (ADC) rather than simply recording a charge integral for triggering pixels. The ADC trace in each pixel allows an accurate determination of the time at which the shower front passed the center of the pixel. Analytic arguments and simulations show that time slices of 100 ns will yield the necessary timing accuracy to achieve the required angular resolution.

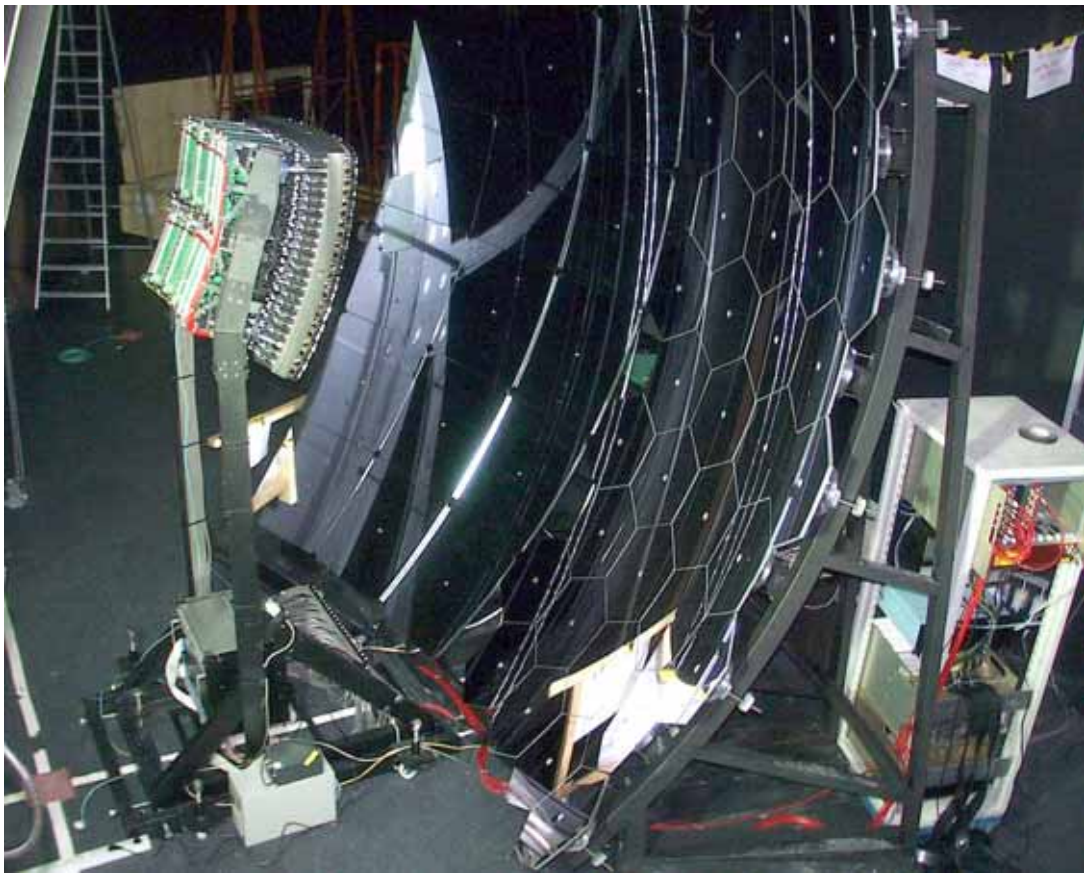

Figure 8 – A view to the Fluorescence Detector camera with mirrors.

The detailed design of the optics contains a large spherical mirror with radius of curvature R = 3.4 m (Figure 8), having a field of view of $30^{o}\times30^{o}$ with a diaphragm at the center of curvature whose outer radius is 0.85 m. These parameters are the result of signal/noise calculations for extensive air shower events at the experimental threshold, taking into account the amount of night sky background at the Southern site of the Auger project and the obscuration by the PMT camera and its support structures.

The diaphragm will eliminate coma aberration while guaranteeing an almost uniform spot size (circle of least confusion) over a large field of view. With the above configuration the spot diameter (containing 90% of the mirror–reflected light) is kept under 0.5^{o}. The

(curved) focal surface is at approximately half that distance from the center of curvature. The camera size and shape is therefore about 0.81 m^2.

Each pixel in the light detector should have a field of view small enough to measure accurately the light trajectory on the detector surface but large compared to the spot size. A diameter of about 1.5^o (26.2 mrad) is a good compromise. It corresponds to a size on the detector surface of about 0.0262×170 cm = 4.5 cm, easily matched to commercially available PMT (Figure 9). The image on the camera surface has finite dimensions due to two effects: spherical aberration and blurring due to mirror imperfections or alignment inaccuracy. Blurring and additional light from the outer diaphragm area with the corrector annulus do not increase the spot size as determined primarily by spherical aberration (see Figure 20 showing the shower tracks on the camera).

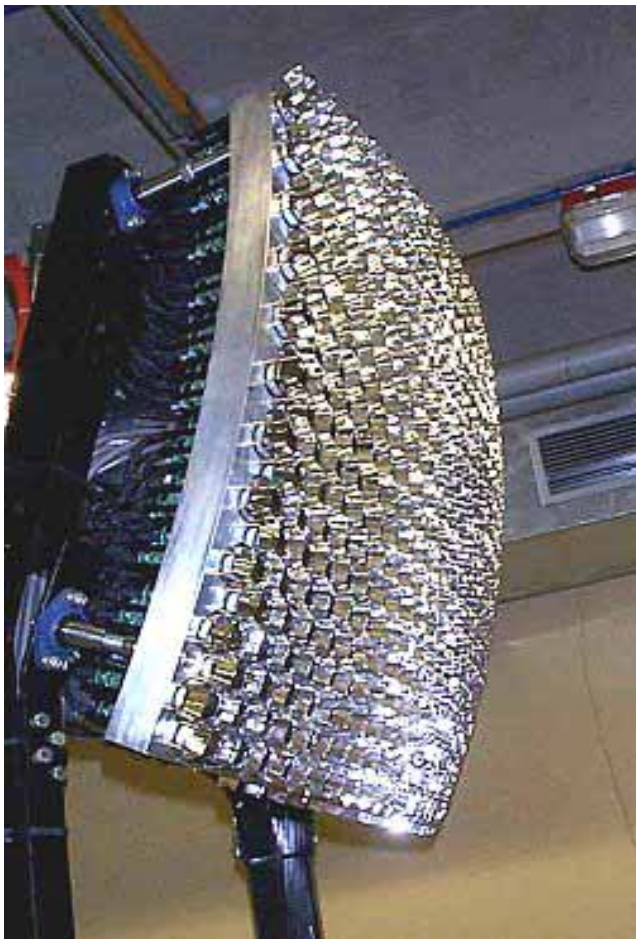

Figure 9 – A view to a Fluorescence Detector camera with 440 hexagonal PMT.

The observatory eye with a large angular investigation range, a sufficient angular resolution and supported by high–speed electronics assuring a precise timing measurements allows reconstructing geometrical parameters of the shower as well as inferring energy of the primary particle.

Analog signals from PMTs are digitized in **F**lash **A**nalog to **D**igital **C**onverters (FADC). Digital representation of the track is next taken for the trigger decision. A requirement of the timing accuracy imposes a high sampling rate. However (independently of

higher realization of faster solution), too short sampling interval decreases the signal to noise ratio.

The shower development profile needed for the shower energy estimation and the depth of the maximum is reconstructed from the FADC traces. The quality of the optics, electronics, understanding of all corrections and possible contaminations are crucial to achieve the reliable physical results. A lot of often, antagonistic parameters had to be optimized, tuned or sacrificed to get stable, reasonable compromise allowing getting high quality measurement system.

1.6 Overview of the Surface Detection techniques

Apart from the FD technique, one of the most frequently used detection techniques is a ground array of water Cherenkov tanks, scintillator, calorimeters etc., utilizing water, liquid or solid plastics and lead as radiators. The parameters of such a ground array (altitude, surface area, spacing between the detector stations) must be adapted to the energy range aimed for.

The water Cherenkov tanks is filled by de–ionized water. Ultra–relativistic secondaries from EAS passing through the water emit Cherenkov light. The light is converted by the PMTs into an electric signal for further processing. The tank is lined with the high-performance DuPont™ Tyvec® protective material (usually used as in a weather-resistant barrier) as a diffuse reflector on the walls.

The reflector and high transparency of the super–pure water, with large attenuation length, assure multiple photon reflections and in consequence long electric signal as a response to the light excitation.

EAS on the ground level hit usually several tanks. The number of hit tanks depends on the energy of the shower and the angle of arrival. The response of the surface detectors to EAS allows an estimation of the energy of the primary cosmic ray. This is obtained through the calculation of the integrated signal at the given distance from the shower axis. The distance is usually chosen to minimize shower-to-shower fluctuations (1000 m in the Pierre Auger Observatory). This signal, called hereafter S(1000) and expressed in **V**ertical **E**quivalent **M**uon (VEM) units, is interpolated after a fit of a lateral distribution function to the observed signals in a given event (see Chapter 5). Simulations show that it does not depend much on the choice of the lateral distribution function. Calculation of the primary energy from S(1000) by simulation is an advanced topic and may depend on the modeling. The estimation of the primary energy from S(1000) by comparison with simulations is not a sufficient technique. The energy of showers is calculated from the SD data but calibrated from the FD data (see Chapter 7.1).

One of the crucial measured parameters allowing inferring characteristics of EAS is the timing of registered signals. “Time shape” of a signal tells about the size of EAS and on a distance from the core, sharpness of rising edge enriches information on the muon composition, relative timing between neighboring detectors determines the geometrical configuration and arrival direction of the shower. Time resolution should be good enough not to lose important time–dependent structure.

Muons tend to arrive earlier than electrons and photons and to create shower with relatively flat front, because they suffer much less scattering and so have more direct paths to the ground. Signal differences between muon and electron/photon components of EAS increases with the showers age. Inclined and deeply penetrating showers are muon–rich. Muon flat front gives in PMTs a short, sharp response (electric spike). Electrons and photons

give much smooth PMT signal profiles, spread over longer interval. “Rise–time” measurements are the most robust diagnostics of composition for the surface array. Iron showers, which are both muon–rich and develop higher in the atmosphere relative to proton showers, have a signal, arriving in a shorter time than that from a proton shower with the same total energy.

A practical realization of very high time resolution system meets significant difficulties. Digitalization of very wide range of signals with high speed requires not only expensive FADC, but also very high speed processing electronics. The measurement system should fetch a reasonable compromise between a speed and performance needed from the physics point of view and the costs, a level of complication, power consumption, longevity and reliability from the point of view of the practical implementation. The current technology provides a sampling of the analog signals with the speed 40–100 Msps, with reasonable costs, high component integrity and expected reliability in long–term operation.

1.6.1 Surface Detectors in the Pierre Auger Observatory

For the surface detector, it is important to cover as much area as possible at the least cost while retaining the crucial knowledge of lateral distribution of the shower particles. The optimization process led to a detector spacing of 1.5 km. The total area of the array (3000 km^2) was chosen based on the statistics goal as well as an overall self–imposed cost constraint of about 50 M$ (per each of the two sites).

The Southern site of the Auger Observatory is located in western Argentina in the Province of Mendoza (Figure 11). The area covered by the array is an ancient lakebed sufficiently flat to accommodate line of sight radio communications between each detector station and one of four antenna towers located at the fluorescence detector buildings. On the boundary of the surface array, elevated surface features have been selected for the fluorescence buildings that elevate them above possible ground fog.

The surface detector is made of water–filled tanks that have 3.6 m diameters and 1.2 m heights. A tank contains 12 m^3 of clean water viewed by three 9–inch PMTs. A solar panel and a buffer battery provide electric power for the local intelligent electronics, **G**lobal **P**ositioning **S**ystem (GPS) synchronization system and wireless **L**ocal-**A**rea **N**etwork (LAN) communication (Figure 13). The signals from each PMT are continuously digitized by FADC with 15-bit dynamic range at 40 MHz sampling rate and temporarily stored in local memory. The time structure of PMT pulses carries rich information related to the mass of the primary particle.

The abundance of Cherenkov light produced in a water tank varies significantly as a function of its distance from the shower core. Based on simulations for the following PMTs: Hamamatsu R5912, ETL 9353 and Photonis XP1802, the maximum signal at the photo–cathode may reach 250 nA [24]. A linear PMT response up to this value requires a relatively low operating gain, on the level 2×10^5. To analyze precisely signals coming both from far and close showers, the analyzing system should have sufficient high resolution. Weak signals from far showers are on the level of 10 pA. It gives a required 14–16 bit dynamic range.

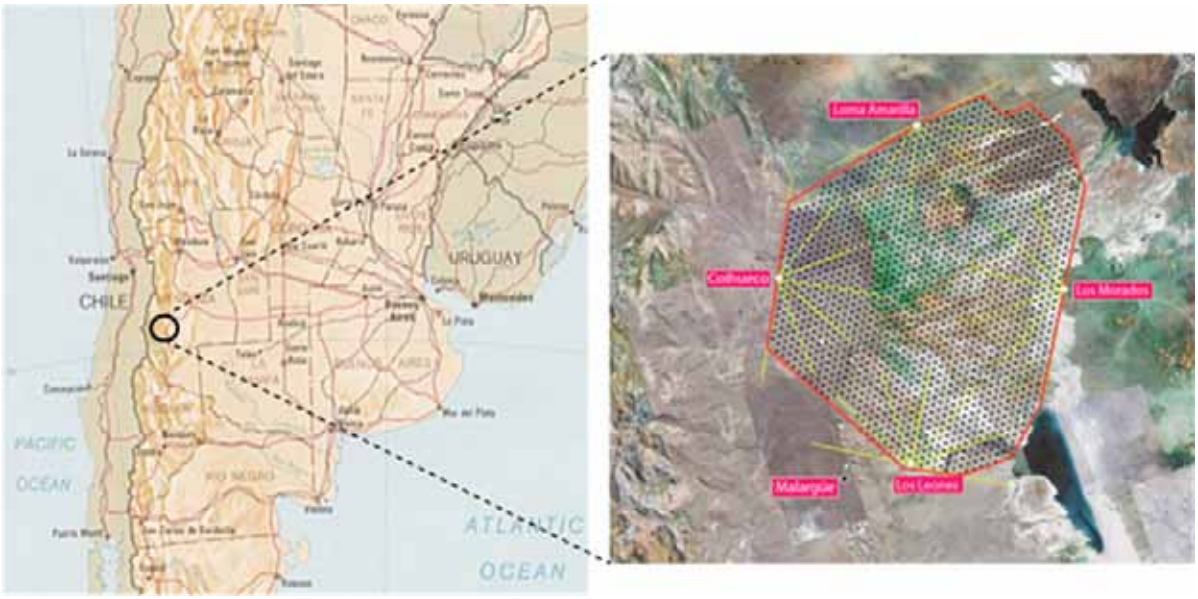

Figure 10 – Location of the Southern part of the Pierre Auger Observatory.

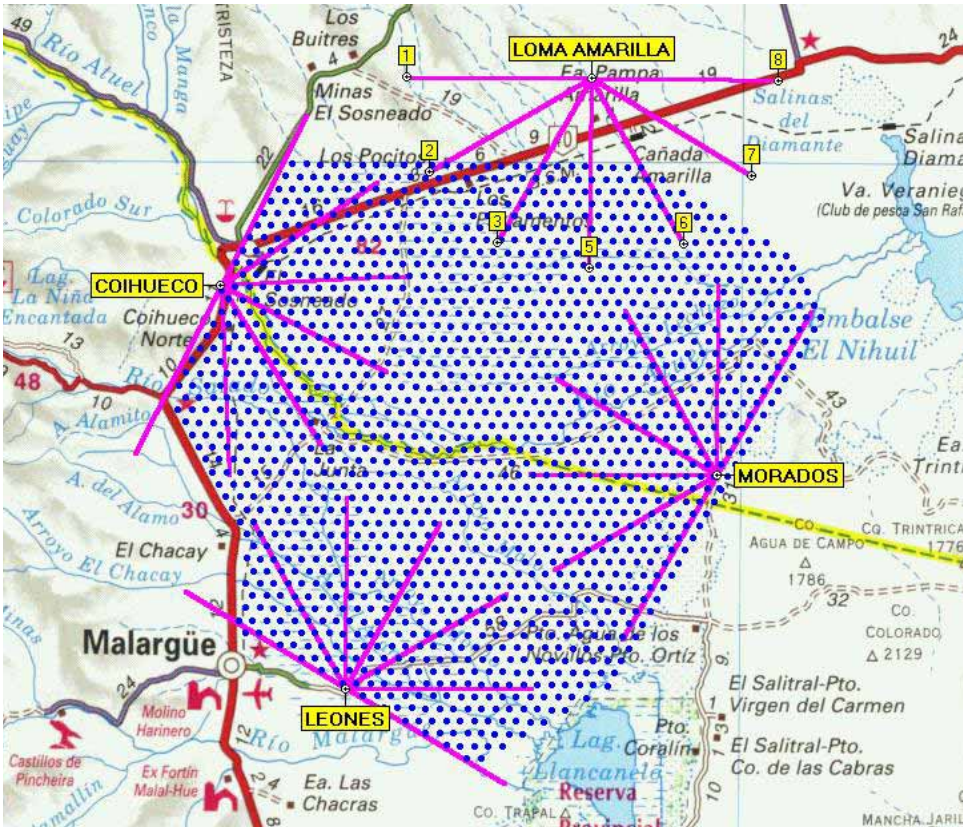

Figure 11 – A location of the 4 Fluorescence Detectors Stations and 1600 surface detectors (tanks) in the Southern Hemisphere of the Auger Observatory (Malargüe, Argentina). All 1600 tanks have been deployed. Each Fluorescence Detector Station consists of 6 telescope eyes. Lines outgoing from the Stations: Los Leones, Coiheco, Morados and Loma Amarilla mark the observation range [25].

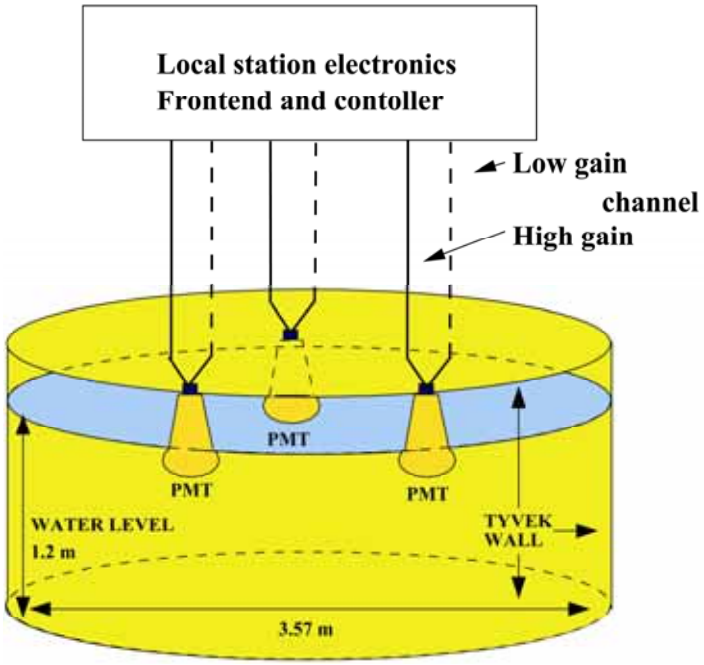

Figure 12 – Water Cherenkov tank schematics. Each tank contains 12 tons of water as a radiator. The light is detected by three PMT, each connected to a high- and a low-gain channel in the local station electronics [26].

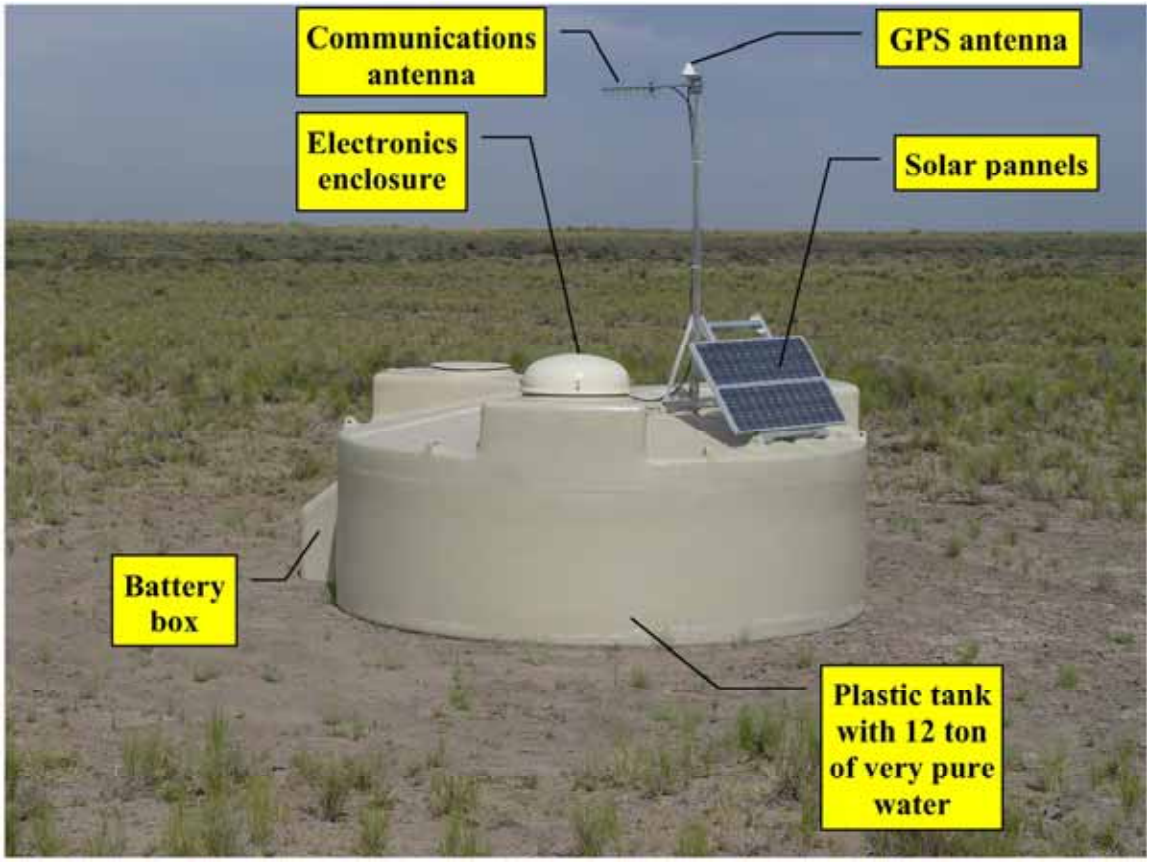

Figure 13 – A surface detector tank located in Argentinean Pampa Amarilla.

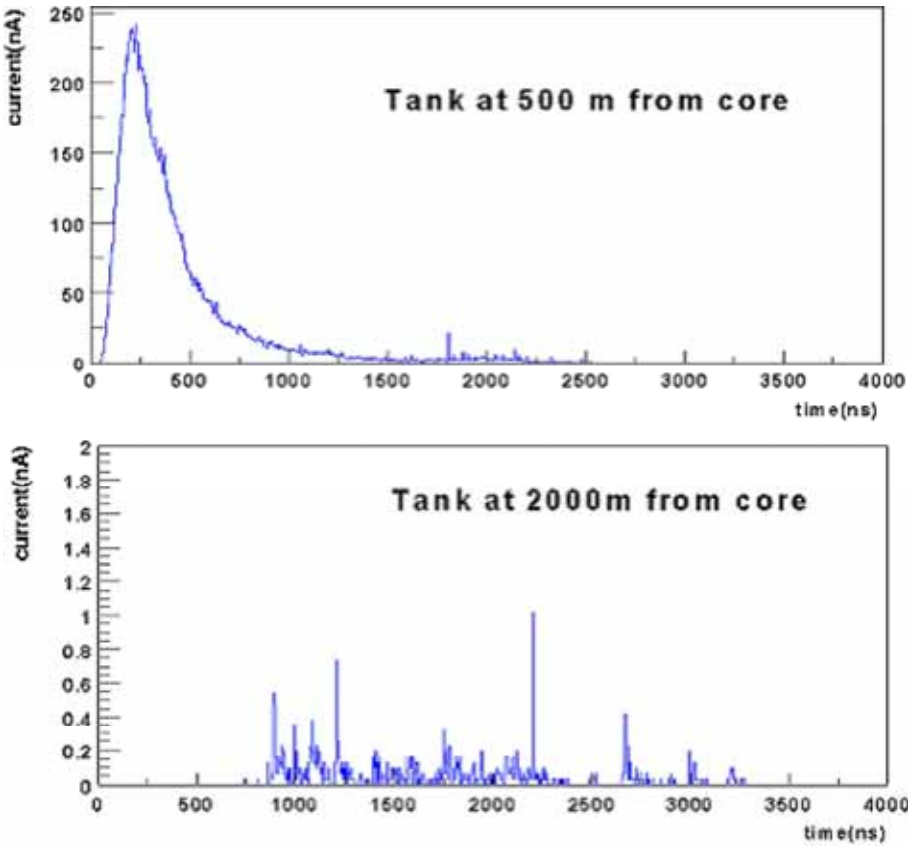

Figure 14 – Simulations for a 30° at 5×10^{20} eV proton shower, shower particles are detected in the Cherenkov tanks at 500 m and 2000 m from the shower core [22].

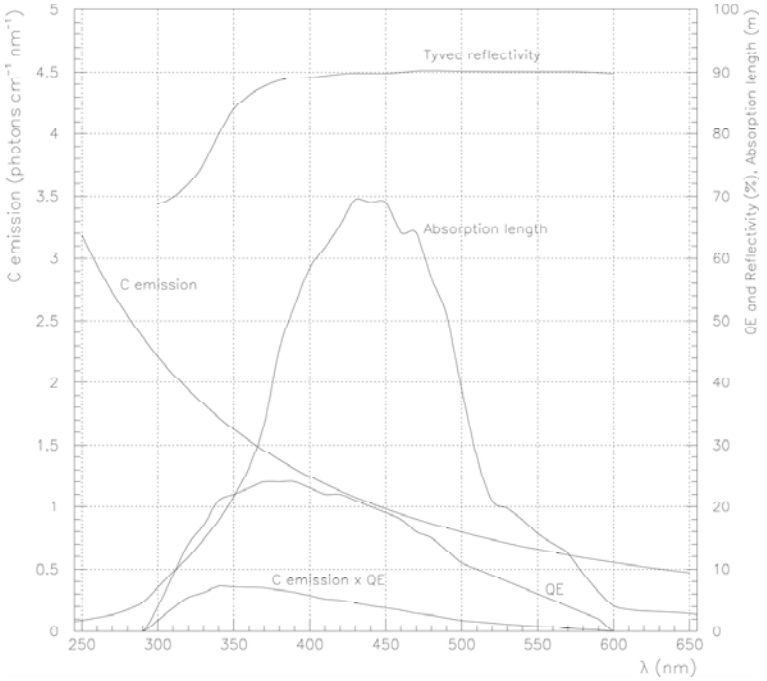

Figure 15 – Important spectral characteristics for a water Cherenkov detector. The quantum efficiency shown is for a bi–alkali photo cathode. Absorption length is for ultra–pure water [22].

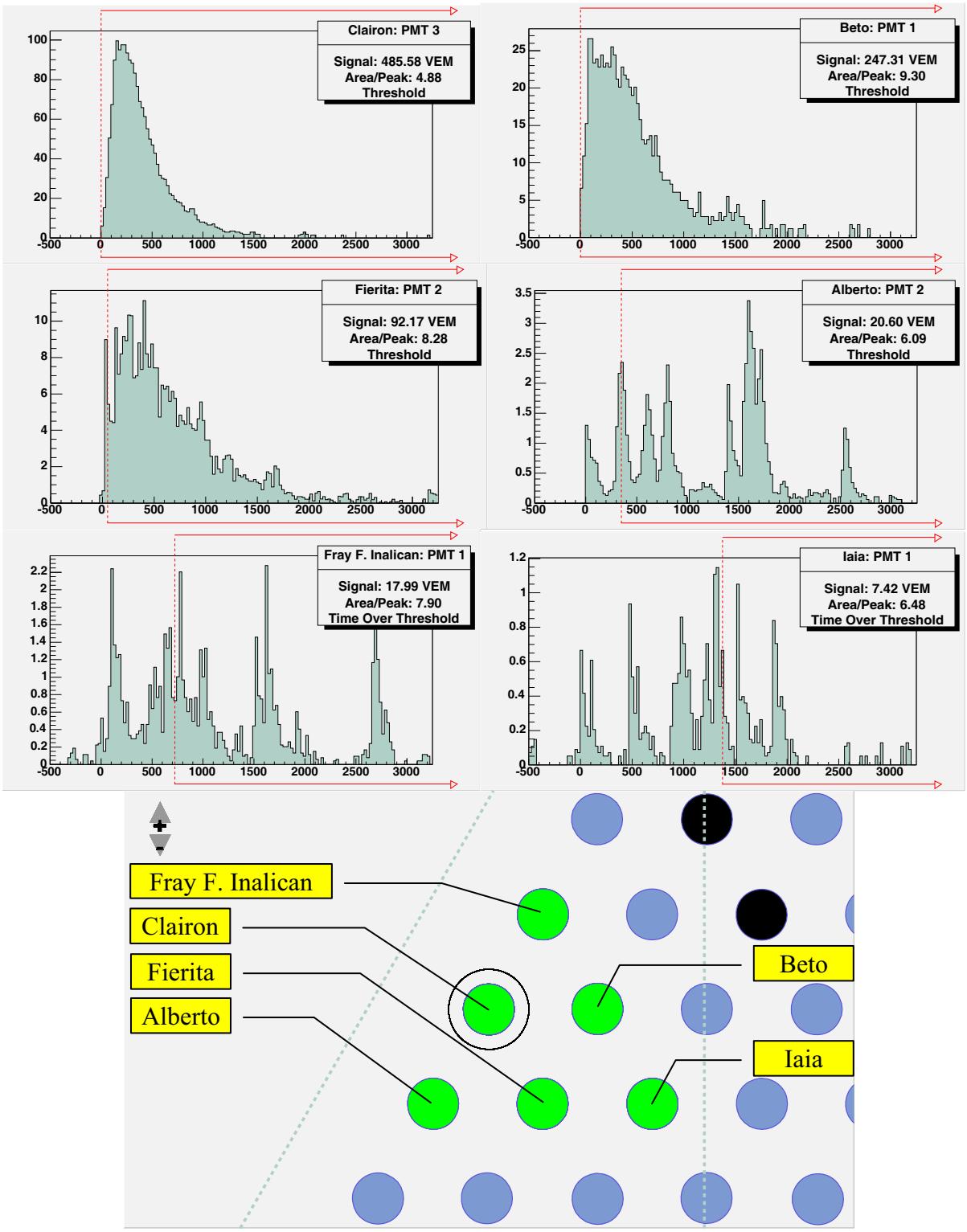

Figure 16 – Sample of signals from the same event (#01307007) registered in 6 tanks. Signals from Clairon, Beto and Fierita suggest that the shower core passed very close to these tanks. Signals from Iaia and Fray F. Inalican relatively weak and spread in time suggest far distance of these tanks from the shower core [27]. However, tanks triggered by the ToT are relatively close to the core (as neighbors of tanks with strongest signals). Geometrical reconstruction gives only 4.5º ± 0.5º of the zenith angle (almost vertical shower) and the energy of 21.45 EeV ± 4%.

Figure 14 shows an example of signals detected from the close and far showers. Figure 16 shows real measurements for similar distances from the core. Let us notice, that in simulations the ratio of amplitudes for close to far showers reaches the factor more than 100. Real measurements fully confirm a necessity of a very wide dynamic range implementation.

Digitalization of signals spread on such wide range with a sufficient speed is a real problem. There are available commercial ADCs with 16–bit resolution, however usually working with dual–slope integration or successive approximation algorithms, much too slow for the above system. Only flash ADCs provide sufficient speed on the level 40 MHz at 10–bit up to 100 MHz at 6–8 bits. In order to match the dynamic range, the PMT base has two outputs: one from the anode (low gain channel) and the other one from an amplifier connected to the last dynode (high gain channel). The charge ratio between the two outputs is 32. Such splitting of analog signals allows using 10–bit FADC with 5–bit overlapping to cover 15–bit dynamic range at reasonable costs.

The quality of a final converted signal strongly depends on PMT parameters like: quantum efficiency of the photo–cathode, single photoelectron spectra, gain and dark current, dark pulse rate, linearity, after–pulse ratio and others, as well as on the water transparency (as a consequence of its purity) and Tyvec spectral diffuse reflectivity.

Optimization of a photo–cathode material provides a sufficient convolution of quantum efficiency and the Cherenkov emission. Advanced water purification process allows exceeding 10 m absorption length of ultra–pure water across the wavelength range of interest (between 300 and 500 nm). Figure 15 shows the measured parameters matching the requirements for high–precision water Cherenkov detector.

1.7 Overview of triggers in the Pierre Auger Observatory

1.7.1 FD triggers

Each FD telescope consists of the matrix of 440 PMT and 440 1st level triggers controlling each PMT as well as a single 2nd level trigger investigating the structure of active PMT on the entire matrix.

The light coming from the fluorescence nitrogen excited by the EAS forms "tracks" of "fired" pixels on the PMT matrices.

The signal produced by each PMT (pixel) has a trapezoidal shape, with durations varying from a few hundreds of nanoseconds to several microseconds. Its intensity depends both on the shower size (i.e. number of electrons) at that particular point being observed and on the distance of observation, as r^{-2} dependence as well as atmospheric light scattering contribute to attenuation of the signal. Simulations show that the dynamic range for showers in the range 10^{19} to 10^{21} eV seen from a distance of 7 to 30 km will be of about 15 bits.

The track is more/less the straight line (sometimes with gap, if the traveling spot of light does not reach sufficiently the center of the PMT – see Figure 17). The 2nd level trigger investigates the "fired" PMT and creates the trigger, if the set of "fired" pixels matches with the topological pattern corresponding to the real EAS. This approach significantly reduces a background, because most of the configurations of the "fired" pixels correspond to the accidental coincidences (compare Figure 18).

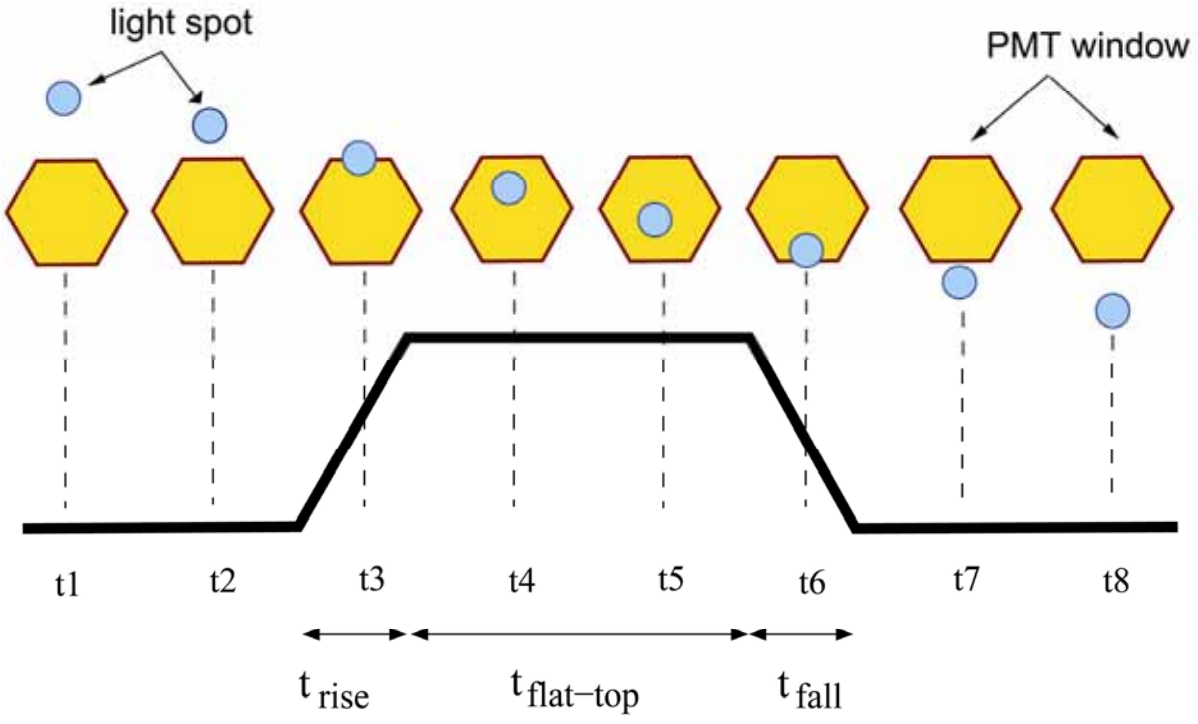

Figure 17 – Signal formation in the PMT. The light spot traveling through a center of the PMT gives strong signal, close to the edge signal decreases and may be below the threshold. Although the light spot "touches" the PMT, the pixel is not fired. There is a gap in a formed track [28].

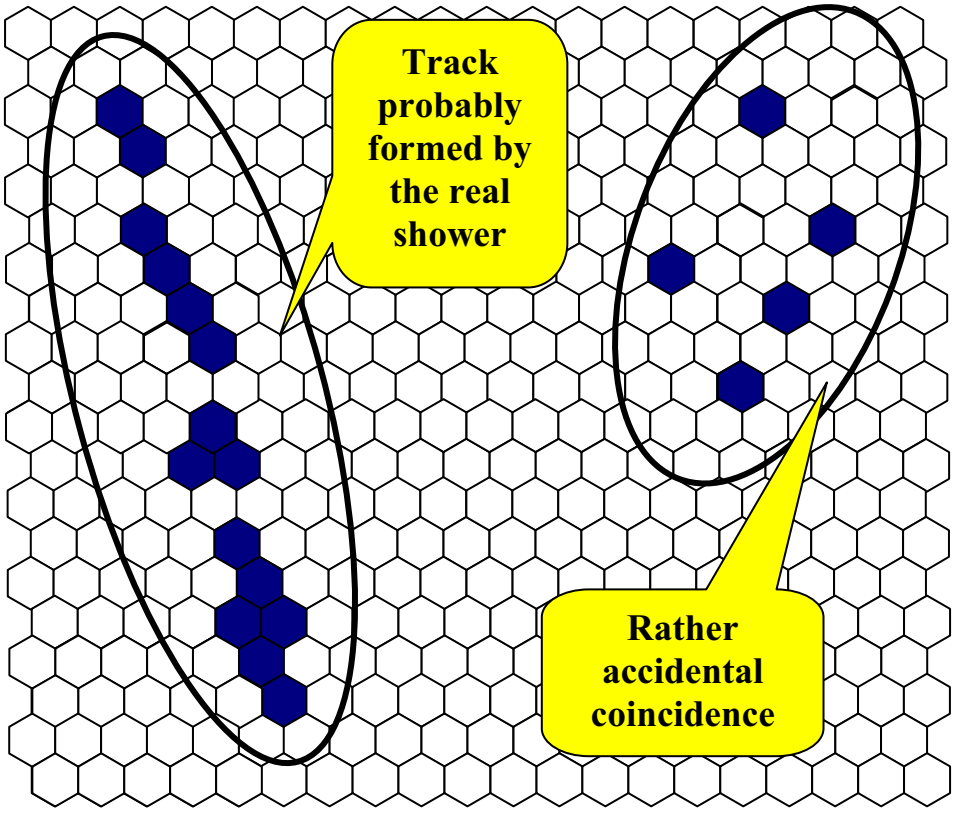

Figure 18 – Samples of configurations originated from the real EAS as well as from some accidental coincidence.

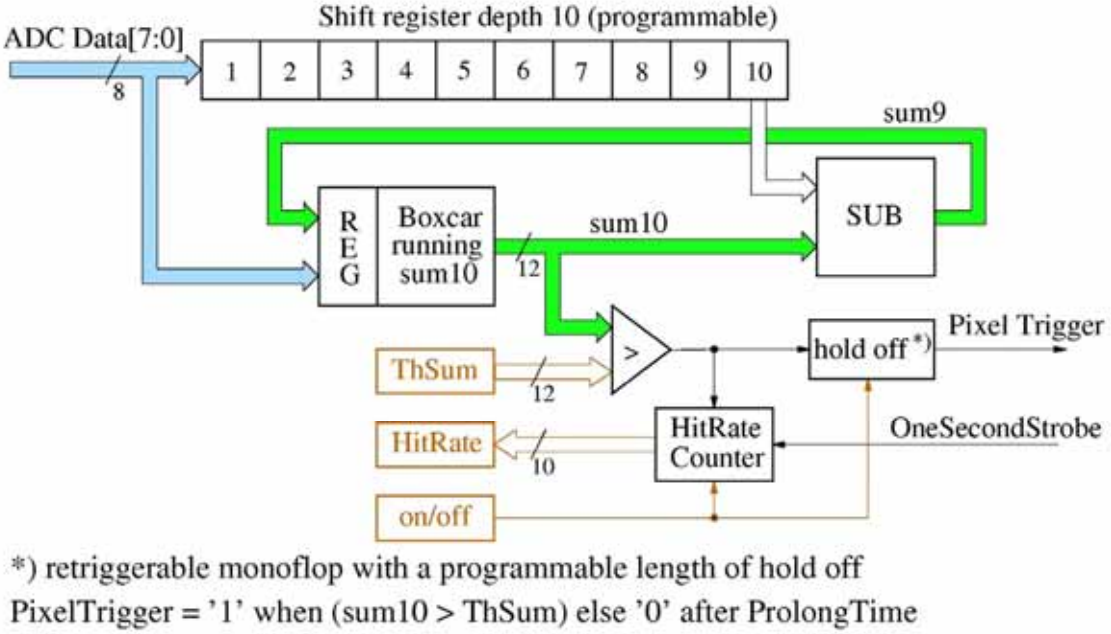

Figure 19 – First Level Trigger with boxcar integration and the rate control [36].

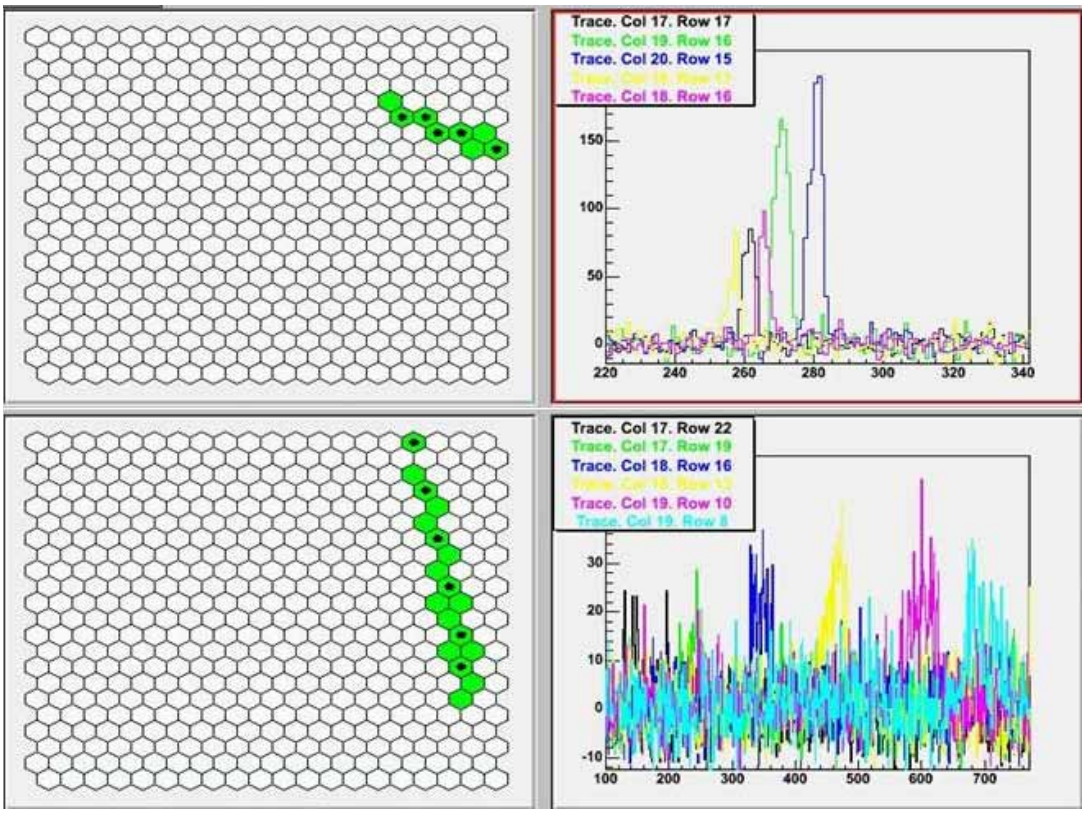

Figure 20 – Tracks of a shower on two PMT matrices as a stereo event (registered simultaneously by two eyes). The left graphs show a shower track on the PMT matrix created by "fired" PMT; right graphs show FADC traces of "fired" PMT [27].

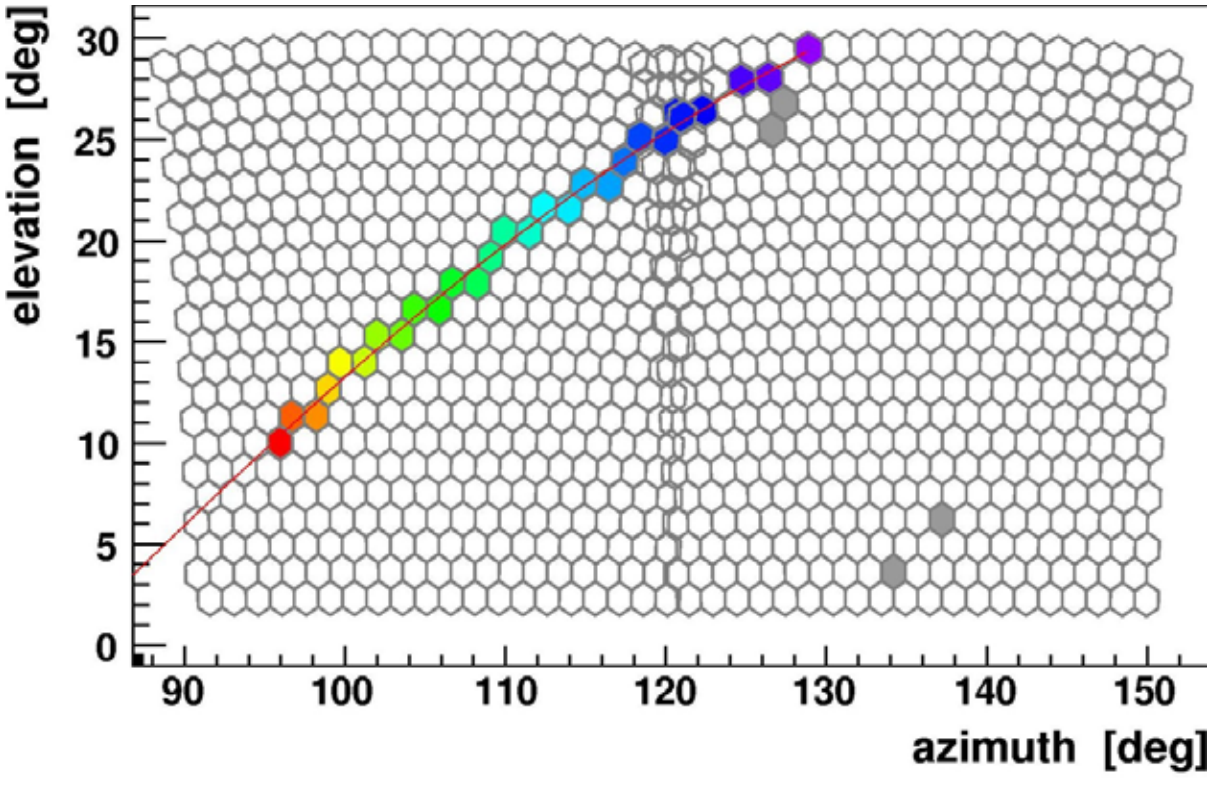

Figure 21 – Track view on two neighboring cameras for Coihueco.

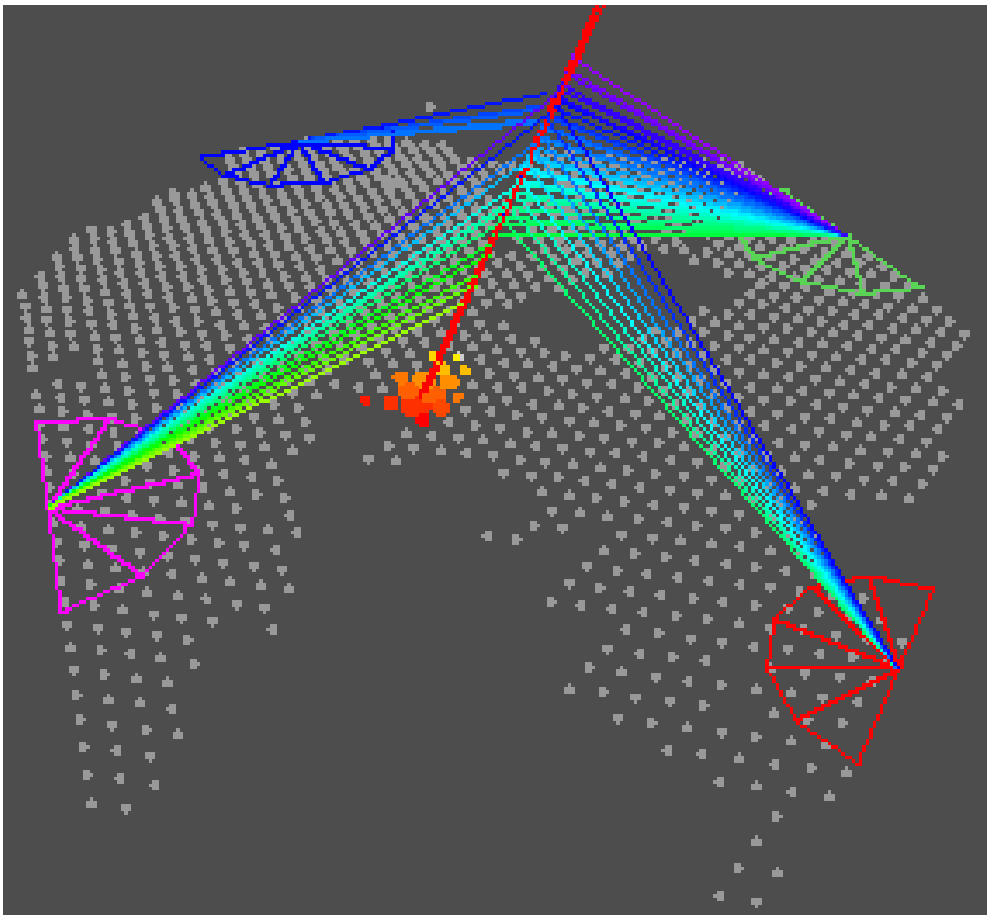

Figure 22 – First quadruple FD event registered in the Auger South [29]. The array is viewed from the Northeast corner. The bottom right FD is Loma Amarilla.

The 1st level trigger averages the signals from the last 10 samples to improve the signal to noise ratio and decides on the status of a particular PMT in the matrix.

The pure data rate in the FD detector is 10 Msps and corresponds to 10 MHz digitizing of analog PMT signals by FADC. A circuit averaging the last 10 samples integrates the FADC values. This improves the signal to noise ratio by a factor of $\sqrt{10}$. Further improvements can be achieved with longer integration times of up to 20 samples if necessary. The 1st level trigger is generated if integrated 10 FADC samples are above a defined threshold. The threshold is tuned in the calibration process to achieve ~200 pps per pixel. This value has been chosen as a compromise between accuracy and a density of data stream. The pixel trigger signal is generated for a programmable coincidence time (hold–off time, ~10 μs) whenever the Boxcar running sum10 (Figure 19) exceeds an adjustable threshold (ThSum). The hit rate of each channel is measured over a 5 s interval using the synchronization signal of the GPS clock. Larger deviations of this rate from the demand value of 200 pps will modify the threshold to maintain a constant rate and to compensate varying light intensities.

The task of the 2nd level trigger is a generation of a trigger on the pure geometrical criteria (programmed several topologically different patterns). Patterns of 4 or 5 adjacent pixels overlapping during the hold off time are accepted as valid trigger provided the overlap persists no longer than a programmed time. 4–fold pattern events rate is estimated on the level 0.2 pps per matrix.

The algorithm of the 2nd Level Trigger allows recognition of a probable track coming from the EAS and significantly suppresses noise from random firing pixels spread over a large matrix as well as allows investigation track registered on two neighboring cameras (Figure 20). The algorithm and a practical implementation in the FPGA will be described in details in the Chapter 2.

Contrary to the off-line investigation of huge database of possible events to select tracks really coming from the showers, on-line recognition of EAS tracks significantly improves a quality and performance of the system. It allows on-line synchronization of data acquisition from the surface detector in order to freeze data in selected water Cherenkov tanks to get data as hybrid events.

A practical implementation of the SLT with suitable flexibility, performance, speed and costs became possible with an appearance on the market powerful programmable logic devices. A construction of the hardware–equivalent net by software programming significantly speeded up a development of ideas, verification and optimization of possible variants as well as assured risk–free approach, impossible to achieve in previously developed strictly hardware or ASIC implementations.

1.7.2 SD triggers

The large background coming from small air showers, electronic noise etc. as well as random coincidences imposes special constraints on triggers, which have to select EAS. Triggers have been accomplished in a hierarchical way both in hardware and software to select possible interesting events and verify their structure in the consecutive levels. A splitting of triggers on hardware and software implementation is a consequence of the compromise between the speed (the processing of high rate signals possible by hardware only) and the performance of relatively complicated algorithms investigating timing and relationships between neighboring detectors (a software realization, possible due to much lower event rate and not necessarily too complicated for a hardware implementation).

The cosmic ray particle flux generates ~2.5 kpps event rate in the water Cherenkov tank (Figure 12). PMT noise adds next few kpps rate. The total background rate (single muons + small showers + PMT dark noise) is estimated on the level ~5 kpps per station.

The 1st Level Trigger (T1 in trigger/memory circuit in Figure 23) selects potentially interesting data from an uncorrelated background of several kpps to ~100 pps. The main tasks of the 1st level trigger are clipping muon signals to reduce both: the trigger sensitivity to the primary composition and bias from small showers close to the detector, from which the signal is spread over relatively short time. The first function is motivated by the strong dependence of the muon content on the primary species, the muon content of the shower providing the best handles of the primary composition. The second function is motivated by the increase in the time duration of the signal farther from the shower core. The first level trigger reduces the contribution of muons to the trigger sum by truncating the pulse height at the programmable threshold and integrating the signal below the clip level. The integration of the truncated signal biases the trigger against nearby small showers, with energy deposit over short time interval. The parallel implementation accepts events with large energy deposition and neglecting their time structure, coming from close to the core of large showers.

The 100 pps restrictions come from the compromise of the limited speed of the electronics and dead time of the system. Higher events rate requires more complicated and more expensive electronics and causes an increasing dead time due to processing more data

in the same time. The data transfer from a trigger circuit to the station controller with the save mode (1 wait state) takes ~100 μs. 100 pps limit gives ~1% dead time.

The 100 pps data rate from T1 is still too high for the communication system due to a limited bandwidth. The station controller analyses FADC traces from the 1st level trigger and in order to select by software more interesting events and to reduce the trigger rate as well as to generate the 2nd level trigger (T2, called also as local station trigger – implemented in the Station Controller – see Figure 23). The current rate is ~20 pps for events with large energy deposition without regard to the time structure and ~2 pps for time structured events. The 3rd (T3 – Central trigger) and next off-line levels (T4 - Physics trigger and T5 – Quality trigger) (see Chapter 3.1.2) have been evaluated and their algorithms are permanently being optimized to reduce any biases.

The 1st level trigger mentioned above is implemented in the main investigating channel focused on the signal profile recording. There is also the dedicated, adjacent channel used for calibrations (called as the "slow" one).

The trigger/memory circuit (Figure 24) registers and analyses the set of FADC samples in 6 channels corresponding to the profile of showers. The only high-gain sub-channel generates the trigger. The low-gain channel provides additional information, if the high-gain channel is saturated. The gain tuning of both sub-channels assures 15-bit dynamic range (each channel provides 10-bit dynamic range, with 5-bit overlapping).

The calibration channel calculates effective signals (see Chapter 1.7.3) in VEM units in order to remove pedestal dependence as well as to suppress a background signals. Nevertheless, trigger logic is still working with the ADC count levels and calibration signals are converted to the new thresholds expressed again in ADC counts. Signals calculated in the Station Controller (in VEM units) are real variable. ADC counts are always integer. An approximation of real to integer is potentially a source of uncertainties.

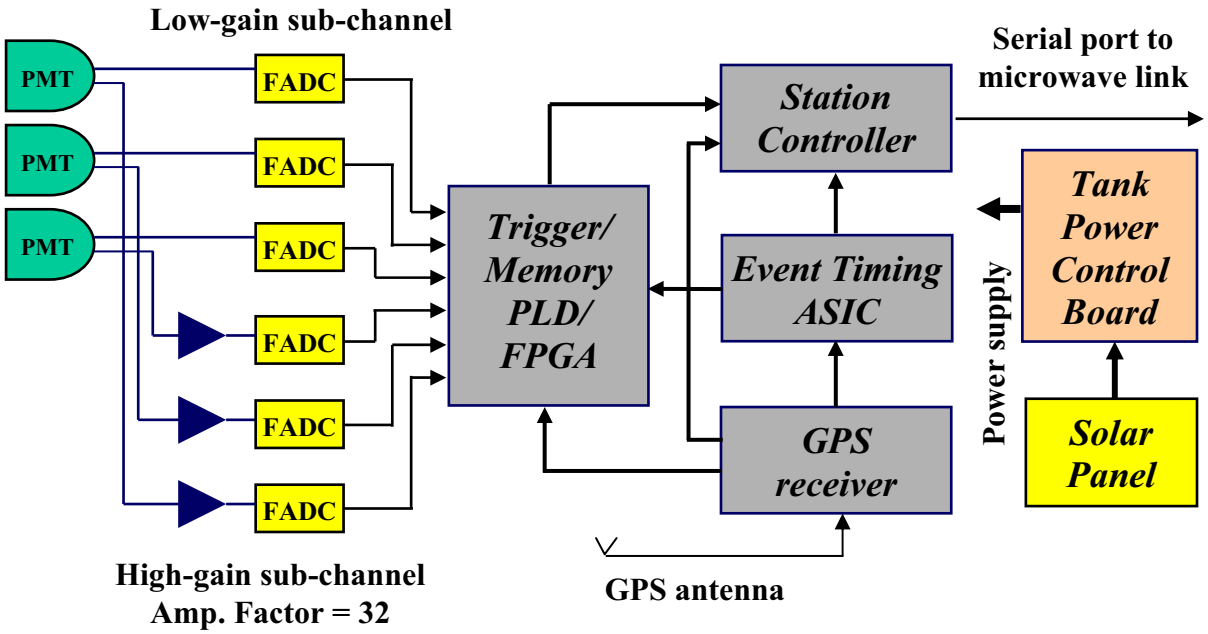

Figure 23 – Schematics of SD electronics in the tank.

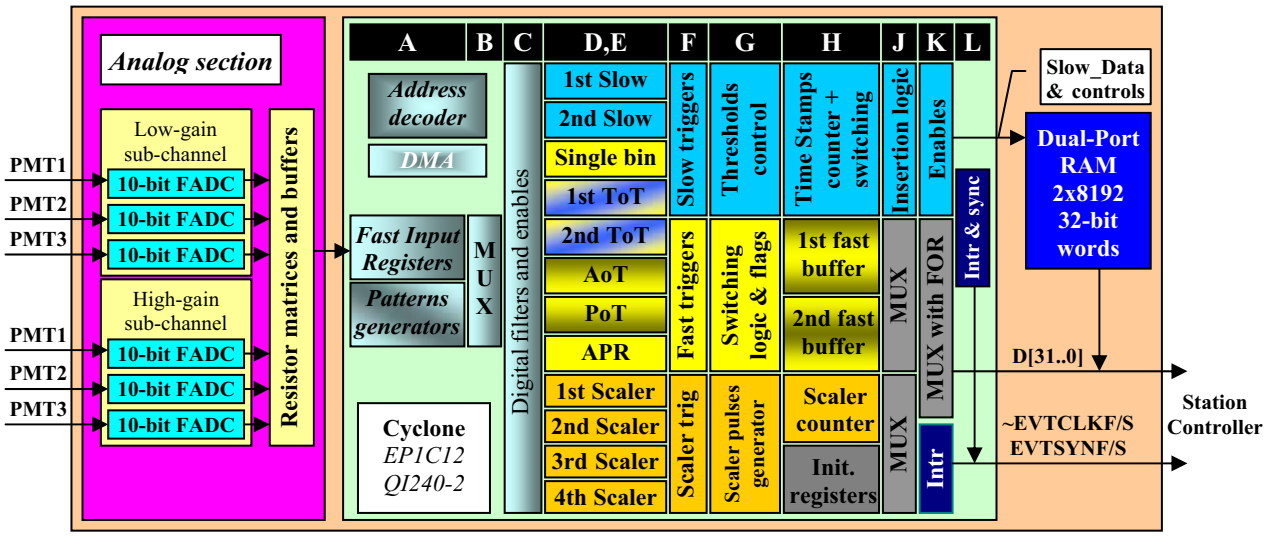

Figure 24 – Internal structure of the trigger/memory circuit.

1.7.3 Muon flux for an absolute energy calibration

Atmospheric muons, as result of low energy CR, are used as a simple way to calibrate the absolute signal scale of Auger surface detectors. This method does not require detailed knowledge of the detector parameters like: the absolute PMT gain, quantum efficiency, transparency of water, Tyvec reflectivity, transparency of the dome etc., as long as we can measure and monitor the charge converted from the Cherenkov light from a through going muons. The accuracy of measurements of parameters mentioned above is estimated as not better than 10%. FD is not supported by such natural calibration and has to measure and monitor all the detector parameters absolutely.

The natural unit of charge calibration in Auger surface detectors is the VEM (Vertical Equivalent Muon). This is the charge produced by the PMTs when a vertical muon, traveling along the axis of the cylindrical detectors, traverses the entire depth of water. The signal from showers particles in a given detector is expressed in terms of VEM. The majority of the muons cross the tank and stay relativistic all the way, emitting a constant amount of Cherenkov light throughout the tank. A fraction of the muons, those with momentum below 300 MeV/c, can stop and decay inside the tank.

Direct measurements of VEM in an individual detector would require additional triggers (usually two layer scintillator working with 2–fold coincidences) to select really through–going muons and to suppress stopped muons and/or the resulting decay into electron, as well as the soft component of the cosmic rays small showers. However, such a supporting trigger is absolutely too expensive to equip all detectors. Nevertheless, even without additional circuitry, the VEM unit can be calculated from indirect measurements of the charge distribution produced by the 3–fold coincidences of the PMTs in a given detector at a sufficiently low threshold [30].

Preliminary sample of data given below predicts the structure of test events, which could be used therefore for a calibration process. The length of FADC traces equals ~25 time-bins should be enough to analyze muon events necessary for calibration. To capture a full profile, especially with time bins referring the rising edges, the FADC trace should contain

couple of time bins before a trigger. Practically, 3 time bins before a trigger are sufficient. The charge histogram from the internal trigger is not a simple Gaussian. It has two humps: the hump at the higher value of the X–axis results from the crossing muons, and the hump at the lower value of the X–axis results from a combination of stopped muons, the decay electrons, and the soft component of the cosmic ray showers (see Figure 26). VEM unit has to be calculated by a de–convolution of a background.

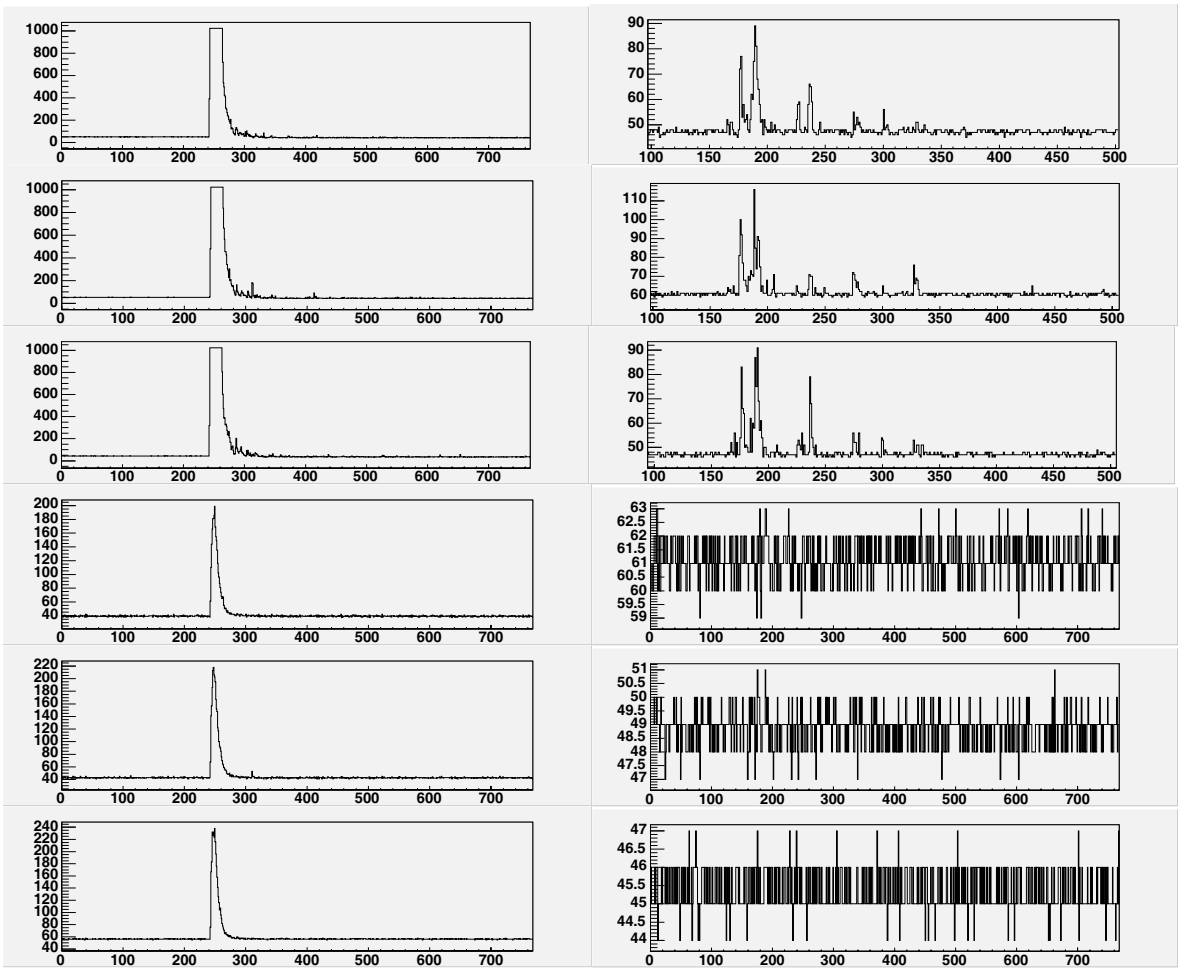

Figure 25 – Samples of FADC traces registered in the trigger/memory circuit. The event on left comes from the near shower (a saturation in the high-gain sub-channel), the event on right originates from far shower; signals are weaker and more spread in time [27].

A requirement of a stable, long–term operation imposes a necessity of a continuous monitoring of vital parameters (i.e. high voltages of the PMTs) and of tuning them, if necessary. As a consequence, a verification of the detector calibration has to be performed continuously. Because of lower muon flux necessary for calibration in comparison to the "normal" expected flux of EAS, an application of "regular" data may result an increase of a dead time of the system. A dedicated channel has been established for that task only. For this, the "muon triggers" could be taken all the time to verify the absolute calibration and the gain matching of the gains of the PMTs. Some of the normal event data will be used to re–compute the relative gain of the low– and high–gain channels.

An additional feature of the muon calibration is a verification of the water purity. If some water contamination occurs, the value for 1 VEM is reduced and simultaneously pulses are shorter due to the extra absorption of photons traveling longer distances in the tank [31].

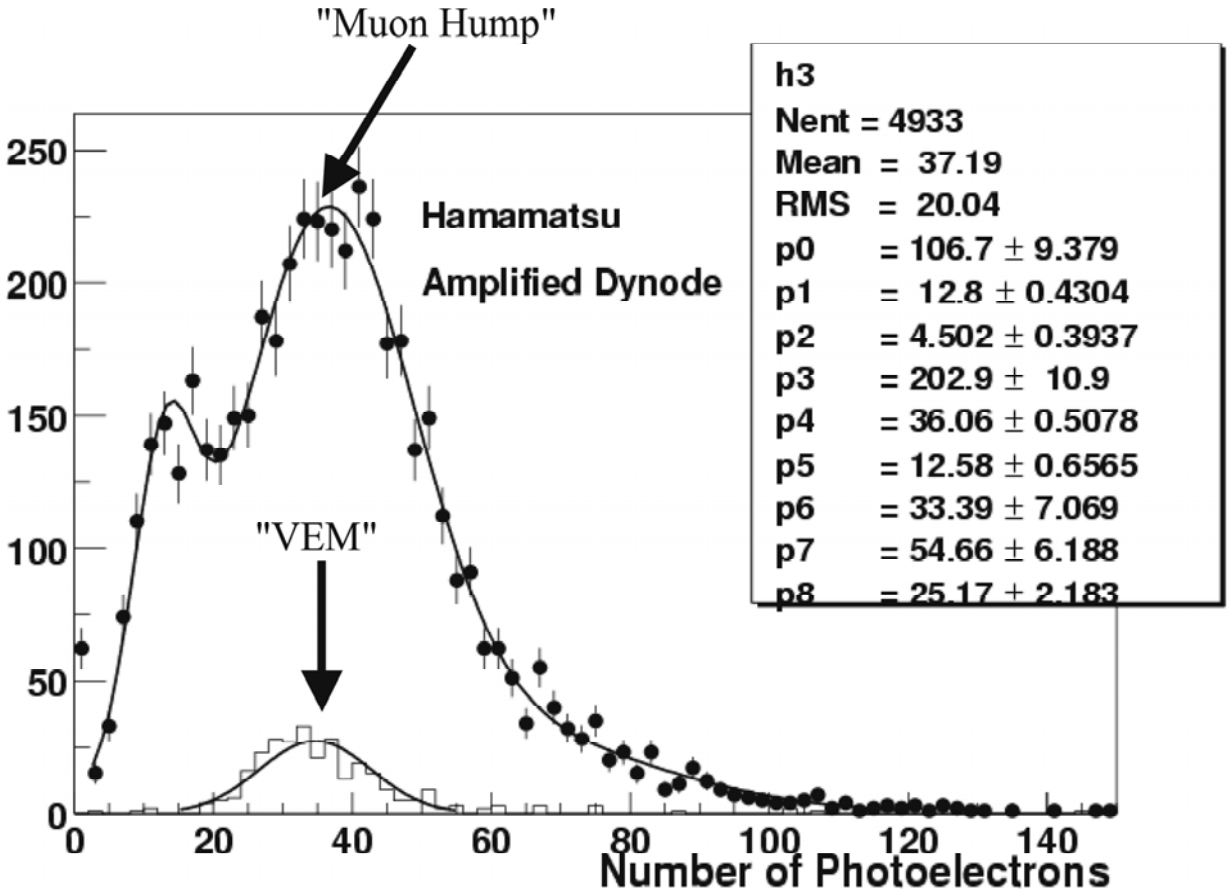

Figure 26 – Typical charge distributions resulting from vertical muons crossing through the tank (solid line histogram) using muon trigger paddles, and from the "internal trigger" requiring three–fold coincidence of the three PMTs in a tank (solid circles) [32]. The charge histogram from the internal trigger is not a simple Gaussian. It has two humps: the hump at the higher value of the X-axis results from the crossing muons, and the hump at the lower value of the X-axis results from a combination of stopped muons, the decay electrons, and the soft component of the cosmic ray showers. Also superimposed on the same plot is the VEM signal, obtained by placing trigger paddles on the top and bottom (the solid line histogram, indicated by the arrow as VEM).

2 The 2nd Level Trigger in the Pierre Auger Fluorescence Detector

2.1 Overview

The main tasks of the telescope electronics are to shape the PMT signals from FD cameras, digitize and store them, generate a trigger based on the camera image and initiate the readout of the stored data. A computer network compresses the data, refines the trigger decision, gathers data of the same event from different telescopes and transfers it to the **C**entral **D**ata **A**cquisition **S**ystem (CDAS).

The organization of the **F**ront–**E**nd (FE) electronics follows the structure of the telescopes in the FD buildings. Each of the 24 telescopes is readout by one FE sub–rack through its associated Mirror PC. Each sub–rack covers 22×20 pixels of the camera. Analog signals from each column of 22 PMT (photo–sensors of each pixel) are processed in the analog Front End Board, where signals are amplified, formed by anti–aliasing filter and next digitized by FADC. The First Level Trigger next analyzes digital representation of signals on the next board. Each sub–rack contains 20 analog FEB, 20 First Level Trigger (FLT) boards and a single Second Level Trigger (SLT) board, which performs an analysis of entire PMT matrix searching for specified patterns corresponding to possible tracks of showers.

The concept for the front–end electronics, the data flow and the data processing rests upon the system requirements. The design uses re–programmable FPGA to obtain a cost–effective and flexible solution whenever possible. The large–scale integration of modern FPGA allowed a massive parallel solution for recognition of tracks and suppression of background. Using this concept we are able to fulfill our main design goals – low price and flexibility.

Table 1 – The minimal size of the chips (Altera® FLEX® 10K family) with the number of terms and utilized logic cells needed to implement 2nd level trigger with "continuous" 4–fold coincidences for rectangular and hexagonal matrices.

Size	Nr of terms	**Rectangular**	Logic cells	Nr of terms	**Hexagonal**	Logic cells
10x12	2456	30AQC208	1458 (84%)	1703	30AQC208	969 (56%)
12x12	3086	50VRC240	1913 (66%)	2132	30AQC208	1260 (72%)
14x14	4474	50VBC356	2799 (97%)	3065	50VBC356	1911 (66%)
16x16	6118	100ABC356	3842 (76%)	4166	50VBC356	2585 (89%)
18x18	8018	130VGC599	5455 (81%)	5435	70VGC503	3503 (93%)
20x20	10174	250ABC600	6488 (53%)	6872	130VBC600	4559 (68%)
22x20	11316	250ABC600	7201 (59%)	7628	130VBC600	5013 (75%)

The Fluorescence Detector built from a set of cameras with a matrix of PMT allows analyzing light tracks of fluorescence of nitrogen from ultra relativistic showers. Each camera of FD contains 440 hexagonal PMTs. The field of view of each PMT is relatively narrow, only 1.5º. Such a big angular resolution allows obtaining a narrow image of a track on the PMT surface, often below a transversal size of PMT. "Fired" PMTs, above the threshold of the First Level Trigger (FLT), derived from real track correspond to collinear patterns only. The main trigger will be generated on the base of the set of collinear patterns,

however even such patterns may be generated by sky background, point sources like aircrafts as well as statistically by electronic noise. Nevertheless a probability of accidental coincidences is small and such a coincidence technique reasonably improves the signal to noise ratio. The general calculation shows that the 4–fold coincidence is sufficient. The trigger and readout system have been implemented into PLD chips to achieve high flexibility, high reliability and a possibility to change the algorithm on line. The Altera® FLEX®10K family grants all above criteria as well as cost effectiveness. The internal structure of these chips allows building sophisticated electronic systems with sufficient registered performance. In order to estimate the capacity and flexibility of the 10 K family, the configuration files for triggers of a 4–fold "collinear" coincidences have been prepared for rectangular and hexagonal matrices of various sizes. Results collected in the Table 1 show that the 2nd level trigger for the entire array could be implemented in a single chip only for the biggest one [33-34]. However, the cost of the chip above 1 k$ is a significant limitation for multi-board productions. For 22×20 matrix simultaneous connection of all 440 I/O pins to First Level Triggers is difficult due to a huge number of needed lines. So for real Second Level Trigger the multiplexing technique has been chosen. It allows also a significant reduction of the total cost due to the choice of smaller and much cheaper PLD chips. The entire matrix will be scanned by shifted "scanning window".

2.2 Topology of patterns

If the light falling on a PMT is close to the threshold, a gap or missing end point may occur on the track. As a consequence, the requirement of a 5–fold coincidence would result in unacceptable efficiency for the showers of interest. However, since 4–fold coincidences reduce sufficiently the noise, they will be incorporated in the trigger. Such 4–fold patterns created by removal of one PMT from 5–fold patterns will be processed by the 4–fold logic chosen. In all cases a pattern is characterized by the horizontal and vertical indices of the pixels whose signals are sensed above threshold. The first step in specifying the trigger is a determination of the complete set of indices that are to be presented to 4–fold coincidence logic (4 pairs).

The five topologically different 5–fold patterns (Figure 27) are:

- 5 PMTs in a single row (5),
- The one PMT deflected from the main direction (4–1),
- Two PMTs deflected from the main direction from both ends (1–3–1),
- PMTs lying on the one row and the next two on the neighboring one (3–2),
- PMTs lying on three neighboring rows 2+2+1 respectively (2–2–1)

All patterns can be obtained from the basic patterns either by horizontal or vertical translation or by mirror reflection and by rotation, taking into consideration the 60–degree symmetry (compare Figure 28). In this geometry the indices of PMTs lying in the odd and even rows cannot be obtained directly by vertical shifting. The patterns for even and odd vertical indices have to taken into consideration separately. Thus the basic pattern count (called classes) increases to 2×39 = 78.

Finally a list of all 4–pixel indices (the numbers that defined the inputs to the coincidence circuit) that result from patterns and location is generated. This list of 4–fold coincidence indices contains duplicates when the remaining 4 tubes from 2 distinct patterns are the same after one tube is removed. These duplicate coincidences are then removed. 78

basic patterns (classes) expand to 390 4–fold coincidences (Figure 29) which, in turn, are reduced to 271 when duplicates have been removed (Figure 30).

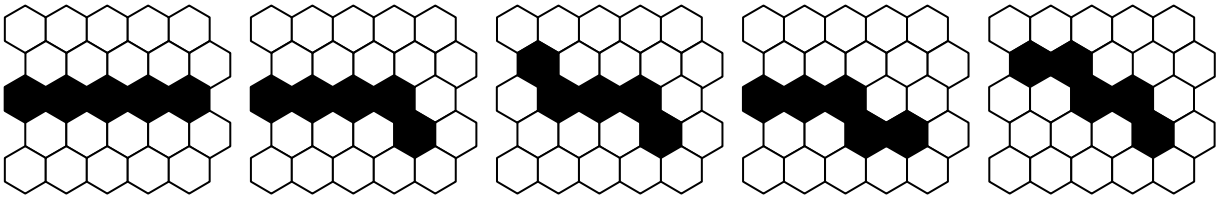

5	4_1	1_3_1	3_2	2_2_1

Figure 27 – Types of topologically different 5–fold patterns.

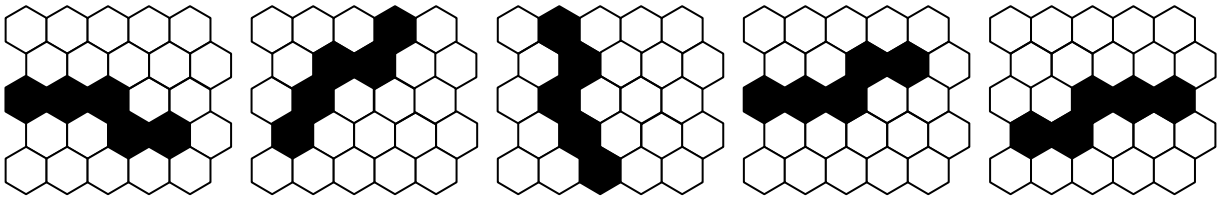

Basic pattern	60º rotated	120º rotated	X-axis mirrored	Y-axis mirrored

Figure 28 – Symmetry transformation of the basic pattern.

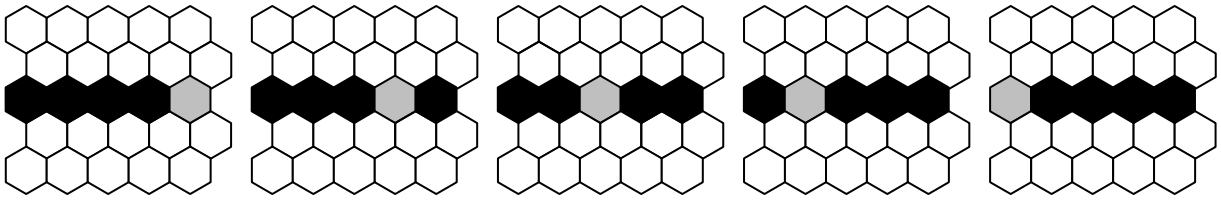

Figure 29 – A construction of patterns with the gap.

A direct implementation of all patterns into a single PLD is rather ineffective. Such an approach for 440 channels would require the largest chip from the FLEX® 10K or FLEX® 10KE family. Numbers of I/O pins as well as resources are sufficient, however a price on a level 1 k$ per chip was one of the most important criteria to look for a cheaper solution. The pixel trigger generated for each channel by the front–end boards is read via a 44–bit wide pixel trigger bus into the second level trigger board. The decision of the second level trigger is based purely on geometrical criteria. Pattern of 4 or 5 adjacent pixels overlapping during the hold off time are accepted as valid trigger provided the overlap persists no longer than a programmed time.

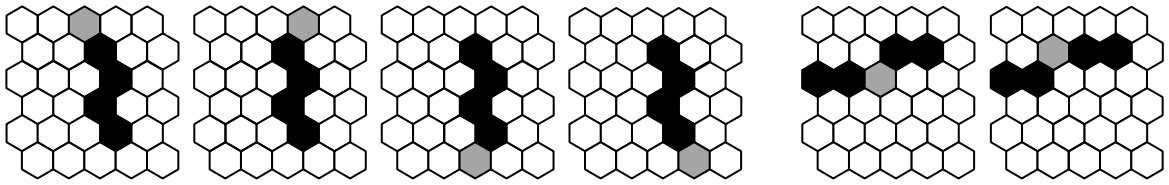

Figure 30 – Samples of patterns with the same set of indices, however coming from different parents.

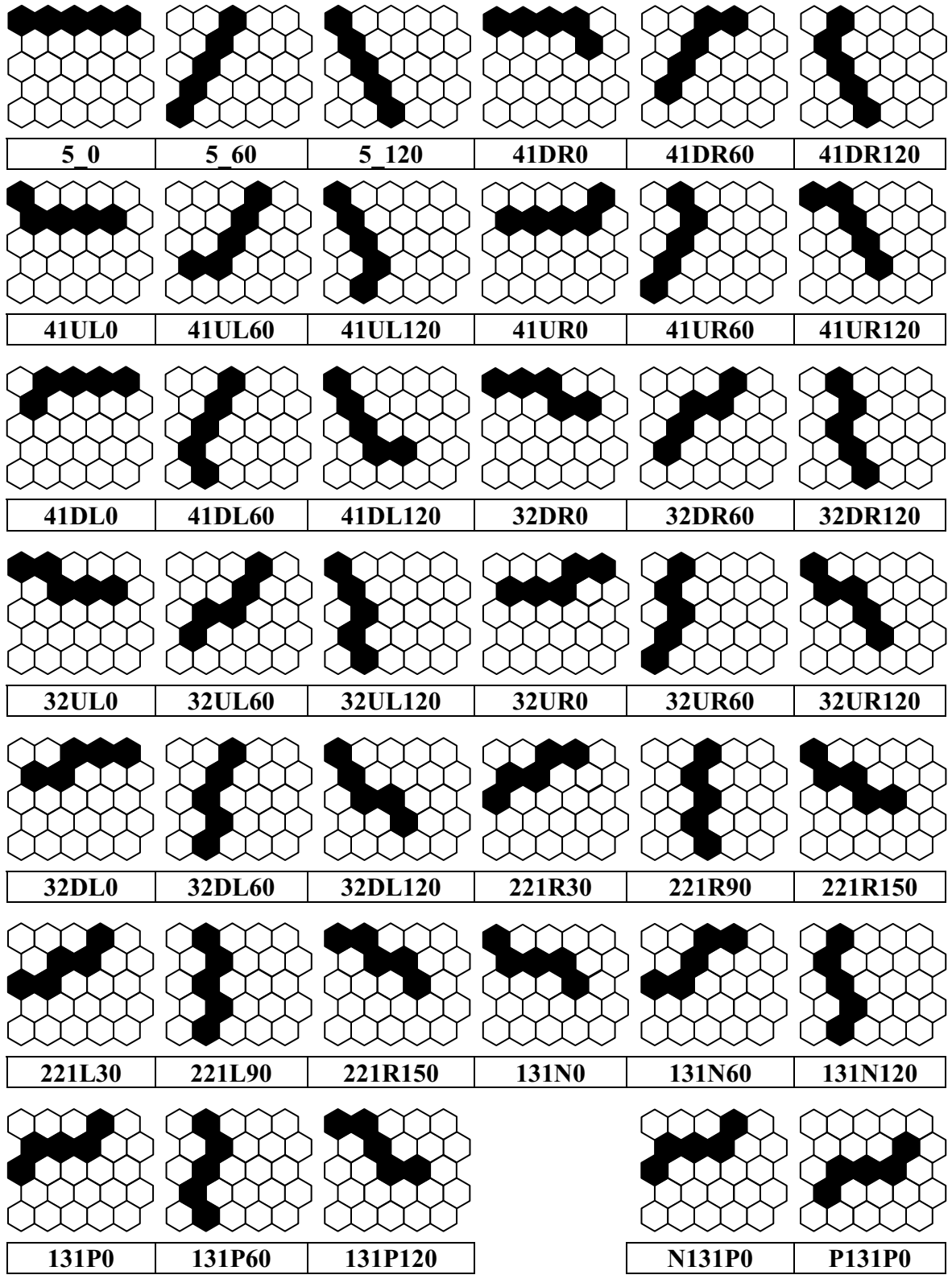

Figure 31 – 39 basic patterns after rotation and mirror reflection. The next 39 patterns are obtained by the vertical shift down. Indices for P – type patterns are not direct increment of X, Y, N – type pattern indices due to a hexagon matrix structure. The last two matrices show N and P sub–types for the same basic pattern.

A minimal width of the scanning window is 5 columns and corresponds to the 5–fold coincidence. For a scanning window, the total number of patterns is **7392**. Nevertheless, not all are independent. Some of patterns come from different parents, but have the same set of indices. Such repeated patterns are removed. Number of non–repeated patterns decreases to **5633**. Some of the classes consist entirely of removed patterns, causing the number of classes to be reduced. Only **216** classes survived [35].

2.3 Scanning of the matrix

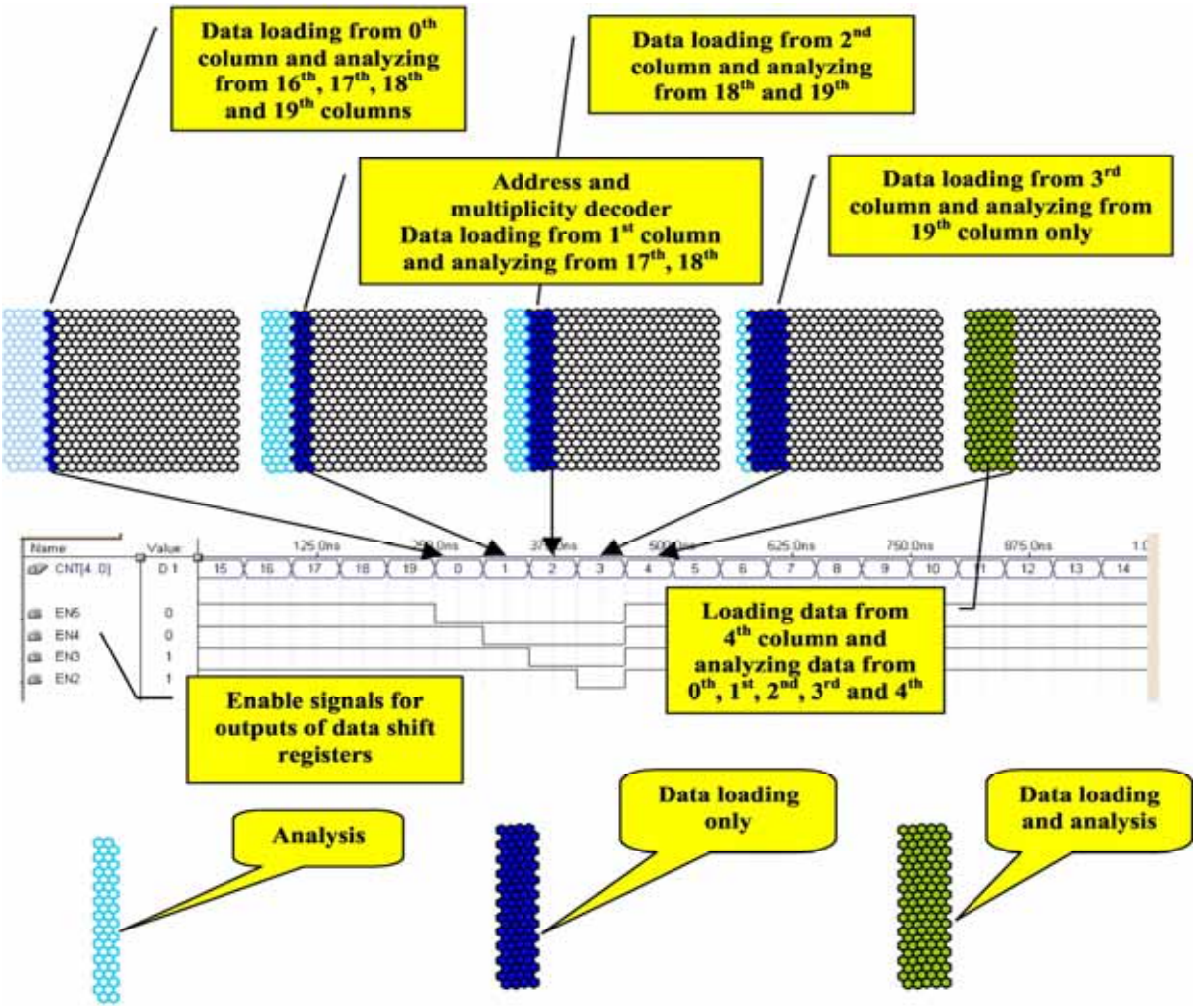

Figure 32 – The scheme of data analysis when the scanning window starts the new scans [35].

The 22×20 matrix is scanned in ten steps (see Figure 32 – The scheme of data analysis when the scanning window starts the new scans). In each step, two columns of 44 pixel triggers are read every 100 ns. Previously read columns are shifted in shift registers. For 10–step scanning, the minimal width of a scanning window should be 6 columns. A simultaneous analysis of whole patterns in the scanning window (22×6) would correspond to **7735** non–repeated ones. However, it is sufficient to take into consideration patterns starting from 1st and 2nd columns only. Patterns starting from next columns will be analyzed in the next scan. This reduces the number of simultaneous analyzing patterns to **4204** only. The transfer

frequency from pixel trigger to 2nd level trigger is set to 10 MHz. However, to reduce the number of simultaneous analyzing patterns, the scan frequency can be increased internally to 20 MHz (loading of data as previously 10 MHz, but with internal buffer added) then the analysis can be limited to the patterns starting from 1st column only (scanning window 22×5). The number of simultaneously considered patterns can be reduced to **2102**. Such an approach allows the use of a smaller and cheaper chip.

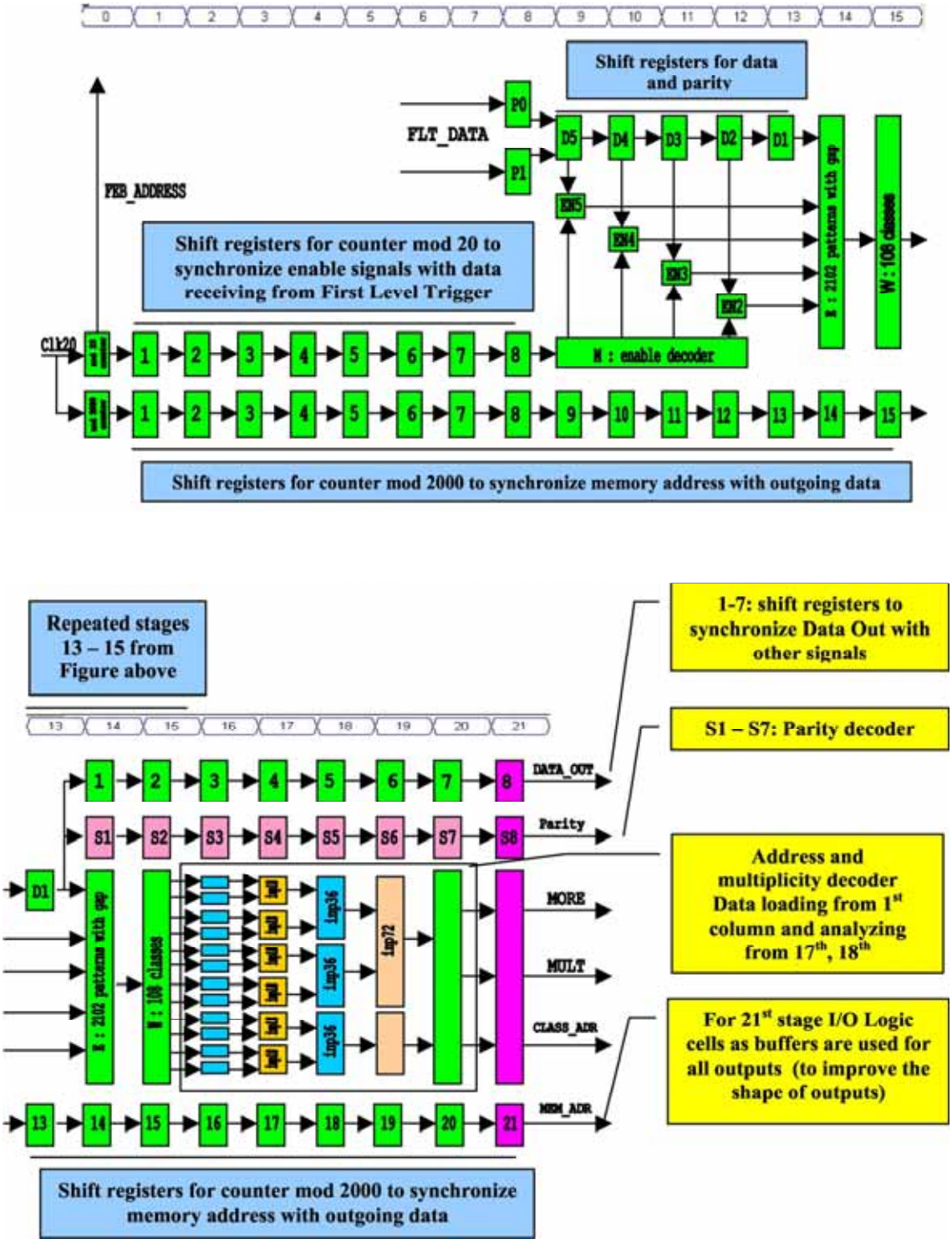

Figure 33 – Design of the internal structure of the 2nd level trigger [35].

Data from pixel triggers are loaded (at 10 MHz) to local storage registers (P0 and P1) and multiplexed at 20 MHz to 5–stage shift registers (D5–D1). If the 22×5 window scans columns from 4^{th} to 19^{th} data from outputs of all shift registers are given onto the matrix recognizing **2102** patterns (E block). When the scanning window reaches the end of PMT matrix and starts the new scanning cycle, data from 0^{th} column are only loaded, but data from previous cycle (from 16^{th} to 19^{th} column) are still being analyzed. In the next steps, data from FLT are progressively loaded but the columns 1^{st}, 2^{nd} and 3^{rd} are progressively disabled to prevent an analysis from columns 17^{th}–19^{th}, 18^{th}–19^{th} and finally 19^{th} only respectively. Possible patterns combined partially from the beginning and the end of the matrix do not correspond to the real track and have to be rejected by disabling the appropriate output of shift registers according to Figure 32.

2.4 "Angle" classes

Each of the surviving classes corresponds to a specific range of track angles. Additional nodes inside the chip are used to indicate the angular region of registered patterns. Patterns are first grouped (as a logical sum) into **216** surviving classes and next into classes corresponding to the angle of fitted line of the fired PMTs. The patterns in two surviving classes which can be covered themselves by vertical shift have the same angular origin. Hence, the number of independent angular classes reduces twice to **108** only.

Let us to find the angle of the line, which fits the geometrical centers of "fired" PMTs. Although the signals over the thresholds in each PMT may be different, this corresponds to a different light energy being transferred into PMTs and different angle of a real track, the best fit for "fired" pattern will be fixed. Therefore, we only can obtain approximate angular region but by hardware very fast. A distribution of fitted angles is not continuous.

The angles given by the hardware should be treated as the first estimate only. Not all angles are represented. The angle gaps correspond to the quantified pattern structures. The next step in angle analysis takes into consideration weights from FADC. After such fitting, the distribution of angles will be continuous. The equation of the straight line is given as follows

$$\left| y\cos\alpha - x\sin\alpha \right| - q = 0 \tag{4}$$

where α is the angle between line and X–axis and q is the distance from the line to the beginning of coordinate system and x, y are points on line. Showers generate on the PMTs matrix tracks, which can be fitted by lines with rather big angle α. It is more convenient to fit a line to the set of "fired" PMTs in the representation of the line related to the perpendicular to the previous one. For the 1^{st} quarter we get

$$x\cos\alpha + y\sin\alpha - p = 0 \tag{5}$$

where p is the distance from the line to the point (0, 0). Hence, small angles correspond to almost vertical lines (shower tracks). The distance of the point (x_i,y_i) from the line given by (5) is

$$d = x\cos\alpha + y\sin\alpha - p \tag{6}$$

Let us minimize the sum of the square distance of PMT centers from the fitting line:

$$\sigma = \sum_{i=1}^{n} (x_i \cos\alpha + y_i \sin\alpha - p)^2 \tag{7}$$

Minimum of σ provides the best fit of the line to the "fired" PMTs. The angle between line and X–axis is given as follows

$$\tan 2\alpha = 2 \times \frac{\frac{1}{n} S_x S_y - S_{xy}}{S_{yy} - S_{xx} + \frac{1}{n}(S_x^2 - S_y^2)} \tag{8}$$

where: n - number of fitted points and

$$S_{xx} = \sum_{i=1}^{n} x_i^2 \quad \mathrm{S_{yy}} = \sum_{i=1}^{n} y_i^2 \quad \mathrm{S_{xy}} = \sum_{i=1}^{n} x_i y_i \quad \mathrm{S_x} = \sum_{i=1}^{n} x_i \quad \mathrm{S_y} = \sum_{i=1}^{n} y_i \tag{9}$$

The scheme of the 2nd level trigger implemented in an Altera® chip is given on the Figure 33. Each 4–fold coincidence defines an angle "class" based on the average angle of tracks producing the pattern in addition to generating a trigger signal, MULT. This overall trigger signal initiates the reading of the entire 22×20 PMTs matrix. To improve the processing speed, the design includes pipeline stages. This approach helps to eliminate glitches at the expense of a modest increase in component resources within the chip. An additional output, MORE, indicates an event where more than two or more angle classes are active at the same time. In this case, the unique angular class number cannot be generated.

2nd Level Trigger sends the address to Front End Boards (10 channels per 44 pixel triggers) and after 6 clock cycles (20 MHz) receives data. To synchronize data written to the external memory, the FEB address is shifted in the shift register chain The reduction of patterns to **2102** only allowed simplifying the structure of **L**ook **U**p **T**able (LUT) cascade connections and decreasing the propagation time below 1 clock cycle (50 ns). Therefore, the 14th step corresponds to parallel 2102 four–input AND gates. A generation of "angle" classes from 2102 patterns to 108 ones requires relatively simple logic, which can be implemented in one time bin (15th). However, obtaining binary address from the set of 108 outputs of "angle" classes requires much more complicated logic, which have been developed in cascade chain (16th to 20th time bins) in several parallel blocks. Coder blocks are the same in 16th to 18th time bins respectively. In 19th and 20th time bin 3 combinational decoders work generating binary "angle" class address, when only one output in W block is active (1 from 108). Additionally S1–S7 blocks form the pipelined parity decoder indicating possible data deformation.

All electronics described above has been implemented into one Altera® chip EPF10K100QEC240 (quad flat package). The timing analyzer shows that the registered performance for this version is sufficient to run the trigger at 40 MHz internally. At this speed data from the FLT could be loaded with 20 MHz and a full scan could be decreased from 1000 ns to 500 ns [36].

3 The 1st Level Trigger in the Pierre Auger Surface Detector

3.1 APEX design

Originally, the trigger for the surface detector has been planned as an ASIC (**A**pplication **S**pecified **I**ntegrated **C**ircuit) [37]. The integration of the full trigger logic into one specialized chip has at least two advantages: the only a single low power chip in full trigger system is needed, so the reliability of such a solution is very high, especially for long–term operation, as well as the cost of ASIC per one chip is low for large production (~2000 chips). ASIC has also disadvantages: the fixed algorithm does not allow any modification in the future, even if the absolutely necessary function would have to be added and does not allow repairing the internal structure, if some bug were found. A dynamical development of programmable chips assuring the large flexibility for internal code and its functionality induced the Auger Collaboration to use new philosophy in electronic designs.

In May 2000 the new Altera® APEX™ 20K family appeared on market. The fully synchronous approach confirmed in the 2nd Level Trigger of the Fluorescence Detector implemented into the one of the fastest chip from the Altera® APEX™ 20K family allowed getting the register performance on the level of 147 MHz, by requested global clock of only 40 MHz.

All processes have been divided into maximally simplest sub–processes performed as possible in the single clock cycle. The design used only the single, global clock connected to the clock inputs of registers only. All sub–processes related to the same clock cycle were grouped in the time–bin routine. Even if the times needed to process of signals in various functions in the same routine were significantly different (but still smaller than a global clock period), processed signals were registered in the output registers and were available for the next time–bin routine simultaneously with the next rising clock edge. If some processes were relatively long (even if still shorter than a global clock period, but retaining too narrow safety margin), they were implemented as pipelined (two clock cycles) processes with additional registers delaying the adjacent signals to assure full synchronization of all signals.

The design assumed an independent signal performance in two channels to get profiles of showers (the fast channel) as well as calibration data (the slow channel). Both channels had to be supported by a memory to store temporarily data before sending them to the micro–controller. Also both channels were double buffered to reduce a dead time. If an event appeared and data have been written to the first buffer, the second buffer remained empty and ready to receive the next data. In the mean time data from the first buffer could be transferred to the micro–controller as an independent process. Just emptied buffer after a data transfer became ready for next data receiving. Dynamically switching of buffers assured significant reduction of dead time, if of course the data rate was on relatively low level guaranteeing not fulfilling both buffers in the same time.

Originally for the ASIC the fast channel was planned to investigate a profile of the showers (FADC traces) with a length of 1024 words from all 8-bit FADC (TLC5540). In order to increase a data resolution 8–bit FADC have been replaced by 10–bit FADC (AD9023), because the PLD chips were powerful enough to process wider data bus without any lost of speed or functionality. Three PMTs read out the Cherenkov light from the water tanks. Phototube signals from anodes (low–gain channel) and dynodes (high–gain channel) are transported on equal–length shielded cables to a Front End Board (Figure 12). Splitting of

signals allows extending a measured energy range to 15 bits with 5 bits overlapping. The system digitizes all analog signals (filtered by the anti–aliasing 5–pole Bessel filter with a cut–off 20 MHz frequency) at 40 MHz in AD9203 Flash ADC. Data on six 10–bit busses are to be next processed by PLD Altera® chip (300 MB/s).

Experiences collected by the ASIC development as well as a compromise between the performance and a cost of chips allowed selecting the industrial version, middle speed grade chip EP20K200RI240–2 (Table 2). The density level of elementary gates was the same as in the test FLEX® 10K chip EPF10K200SBC600–1 (200000 gates), however the price (still much too high for the final design – 440 $ per chip) was significantly lower than for the FLEX® 10K chip – 890 $. Additionally RQFP APEX™ 20K package assured significantly less expenses for assembling in comparison with 600–pins BGA package for EPF10K200SBC600–1 chip from FLEX® 10K family [38].

APEX™ 20K chips contain an internal memory grouped in the **E**mbedded **S**ystem **B**locks (ESB), which can implement various types of memory, including dual–port RAM, ROM, FIFO, and CAM blocks. The ESB includes input and output registers; the input registers synchronize writes, and the output registers can pipeline designs to improve system performance. The ESB offers a dual–port mode, which supports simultaneous reads and writes at two different clock frequencies. Each ESB can be configured in any of the following sizes: 128×16, 256×8, 512×4, 1,024×2, or 2,048×1. By combining multiple ESB, the Quartus® II software implements larger memory blocks automatically. Memory performance does not degrade for memory blocks up to 2,048 words deep. Each ESB can implement a 2,048–word–deep memory; the ESB are used in parallel, eliminating the need for any external control logic and its associated delays.

Table 2 – APEX™ 20K device features [39].

Table 1. APEX 20K Device Features *Note (1)*

Feature	EP20K30E	EP20K60E	EP20K100	EP20K100E	EP20K160E	EP20K200	EP20K200E
Maximum system gates	113,000	162,000	263,000	263,000	404,000	526,000	526,000
Typical gates	30,000	60,000	100,000	100,000	160,000	200,000	200,000
LEs	1,200	2,560	4,160	4,160	6,400	8,320	8,320
ESBs	12	16	26	26	40	52	52
Maximum RAM bits	24,576	32,768	53,248	53,248	81,920	106,496	106,496
Maximum macrocells	192	256	416	416	640	832	832
Maximum user I/O pins	128	196	252	246	316	382	376

Two buffers each 64–bit (2×30 bits for FADC traces and additional 2×2 bits as indicators of buffers type) and 1024–words length in the fast channel required 131 072 RAM bits (64 ESB). EP20K200RI240-2 contained 52 ESB only (Table 2). The next larger available chip EP20K400 with 104 ESB was too expensive for potential application even in the Engineering Array only. The series EP20KE was at that time not yet available. Preliminary analysis of required profile length showed that 1024–word long profiles are not absolutely

necessary and reduced, 768–word size is sufficient. Shortened fast buffers required totally 98304 RAM bits (48 ESB) and could be fully implemented into a single EP20K200 chip. The slow channel required an additional external memory.

An opportunity of an internal memory implementation as a dual–port RAM significantly simplified a data flow and allowed separating writing and reading processes. Both ports were however driven by the same global clock.

In the slow channel data were written together with time stamps (a single stamp per each 4–word data block). The ASIC design reserved independent memories for data and stamps with different lengths. An implementation of two different memories additionally to the PLD seemed to be ineffective. The author proposed to use a single external memory capable enough to store both stamps and data. Time stamps were inserted by a switch to the data stream on the beginning of each a slow data block and denoted as a "Time Stamps" by an additional data bit. Because the slow channel used data from high–gain sub–channel only (30 bits), typical 32–bit memories could be used utilizing 31st bit as a time stamp indicator. To simplify data exchange the author selected as the external memory: 3.3V 16K×36 synchronous pipelined Dual-Port static RAM IDT70V3569S6DRI.

3.1.1 Chronological sequence of output data in the fast channel

A profile describing a shower FADC traces should show its most significant structure as precisely as possible. It should present not only data, since a trigger appears, but also data before a trigger to have a complete view of timing/amplitude dependence. The 768–word buffer has been divided into two different–task sub–buffers. The 1st sub–buffer is a circulating one, it permanently monitors incoming data and freezes them, when a trigger appears. The 2nd sub-buffer next receives data after a trigger and allows completing a full profile.

256 + 512–word long of the 1st and 2nd buffer respectively were chosen. The 1st buffer is working as a ring one and when trigger appears and data became frozen, the older data has to be recovered from additional logic. A circulating buffer implemented as a 256–word long dual–port RAM written via the left port is controlled by an address counter, which address after a freezing is transferred as a starting address for a chronological data transfer to a micro–controller. Data transferred from the 1st buffer are next followed by the data from the 2nd one giving all data for an entire profile in a chronological way.

The communication with a 32-bit micro–controller is via 32-bit bus, however PLD receives 60-bit data. Data temporarily stored in buffers had to be additionally converted into 32-bit structure. They were transferred in an interlaced mode. 64-bit word related to a single time bin (60 bits of data + 4 bits of buffers stamps) was transmitted in two steps: data from the high–gain channel and next from the low–gain channel. Because of the same clock frequency for writing and reading the reading speed is twice slower than writing. It causes a potential dead time if the incoming data rate is too high.

3.1.2 Hierarchical triggers

Selection of the physical events is performed in a hierarchical way:

- **T1**: Hardware local trigger (station level) = Threshold trigger (rate ~ 100 Hz) or Time over Threshold (ToT) trigger (rate is ~1 Hz) (see next chapters),
- **T2**: Software local trigger (station level) = Threshold trigger (reduced rate to ~20 Hz) or ToT trigger with the same rate as in **T1**,
- **T3**: Central trigger (array level),
- **T4**: Physics trigger (off-line),
- **T5**: Quality trigger (off-line).

The **T3** trigger requires the coincidence of 3 tanks, which have passed the ToT conditions and meeting the requirement of a minimum of compactness (one of the tanks must have one of its closest neighbors and one of its second closest neighbors triggered). Since the ToT as a local trigger has already very low background (mainly double muons), this so-called 3ToT trigger selects mostly physical events. The rate of this T3 with the present number of working detectors in the array is around 600 events per day, or 1.3 events per triangle of 3 neighboring working stations. This trigger is relevant since 90% of the selected events are showers and is mostly efficient for vertical showers. Another implemented trigger is more permissive. It requires a four-fold coincidence of any T2 with a moderate compactness requirement (among the 4 "fired" tanks, one can be as far as 6 km away from others within appropriate time window). Such a trigger is absolutely needed to allow for the detection of horizontal showers that generate fast signals and have widely spread topological patterns. This trigger selects about 400 events per day, but only 2% are real showers.

A physical trigger (**T4**) is needed to select only showers from the set of stored T3 data. An official physical trigger is applied off-line to select events for zenith angles below 60°. The chosen criteria use two main characteristics of vertical showers. The 1st one is the compactness of the triggered tanks, the 2nd one is the fact that most FADC traces are spread enough in time to satisfy a ToT condition. It was shown that requiring a 3 ToT compact configuration in an event ensures that more than 99% are showers. The present physics trigger is dual and requires either a compact 3 ToT or a compact configuration of any local trigger called 4C1 (at least one" fired" station has 3 triggered tanks out of its 6 first neighbors). The tanks satisfying the 3 ToT or 4C1 condition must have their trigger time compatible with the speed of light (with a tolerance of 200 ns to keep very horizontal rare events). With the 3 ToT **T4** trigger, less than 5 % of showers below 60° are lost. The 4C1 trigger, whose event rate is about 2 % of the previous one, ensures to keep the 5% of the showers below 60° lost by the other T4 and also selects low energy events above 60°.

Among the events having passed the T4 trigger, we use only those that can be reconstructed with a known energy and angular accuracy. This is the task of the **T5** quality trigger. However, if an event is close to the border of the array, a part of the shower is probably missing and the real core could be outside of the existing array, whereas the reconstructed core will be by construction inside the array, in particular for low multiplicity events. Such events will have wrong core positions, so wrong energies and typically should not pass the quality trigger. The adopted T5 requires that the tank with highest signal must have at least 5 working tanks among its 6 closest neighbors at the time of the event and moreover, the reconstructed core must be inside an equilateral triangle of working stations. This represents an efficient quality cut by guaranteeing that no crucial information is missed for the shower reconstruction. The maximum systematic uncertainty in the reconstructed S(1000) due to event sampling into the array or to the effect of a missing internal tank is around 8%.

Events from the surface detector had to pass the 3-fold or the 4-fold data acquisition triggers and satisfy the high level physics trigger (T4) and the quality trigger (T5) [40]. The T5 selection is independent of energy and ensures a better quality for the event reconstruction. An estimated angular resolution is better than 2.2° for all of the 3-fold events (neglecting the zenith angle) and better than 1.7° for all events with multiplicities > 3 SD stations [41].

3.1.3 Triggers in the fast channel

Four types of trigger for **T1** level are implemented:

- Single-bin trigger (threshold trigger),
- Time over threshold trigger (ToT),
- External trigger. It can be configured as positive or negative active level. It is sent to the system immediately, when appeared on the input.
- Random trigger. It is generated after N clock cycles, after Random trigger is enabled. *N* is 30–bit data written into register. Delayed trigger is useful to check the system after some other operation has been completed.

The single-bin trigger (see Figure 34 and Figure 36) is a 3-fold coincidence of a simple 1.75 I_{VEM}^{est} threshold. The estimated current for a Vertical Equivalent Muon (I_{VEM}^{est}) is the reference unit for the calibration of FADC traces signals [42]. This trigger is relatively noisy, with a rate of about 100 Hz, it is used mainly to detect fast signals (in an interval < 200 ns) i.e. corresponding to the muonic component generated by horizontal showers. The single bin trigger is generated, when the input signal is above the fixed threshold, calculated in the Unified Board (UB) during the calibration process. It is the simplest trigger useful rather for high–level signals. A configuration register may select dynamically a type of a coincidence or the sum.

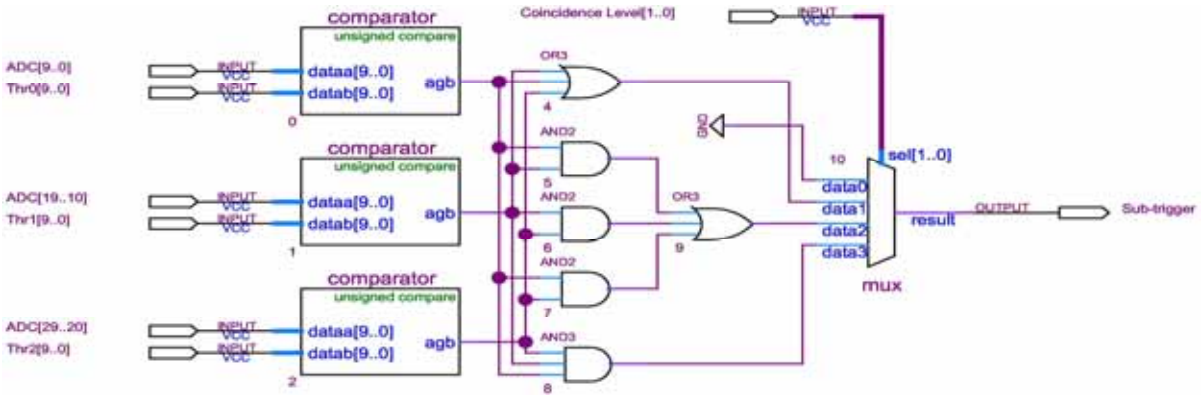

Figure 34 – The implementation of the single bin trigger with the selection of the coincidence level.

The Time over Threshold (ToT) trigger requires at least 13 “fired” time bins in a 120 bins sliding window with above a threshold of 0.2 I_{VEM} in coincidence on any two PMT. A pre-trigger (“fired” time bin) is generated if the signal is above the threshold of 0.2 I_{VEM} simultaneously in any two channels (two-fold coincidence). The amount of pre-triggers is analyzed in the interval of 120 time-bins (sliding window). If the number of pre-triggers

exceeds the occupancy threshold (= 13) the final ToT trigger is generated. This trigger has a relatively low rate of about 1.6 Hz, which is the expected rate for double muons for an Auger tank. It is relatively efficient for selecting small but spread in time signals, typical for high energy distant EAS or for low energy showers, while ignoring single muons background.

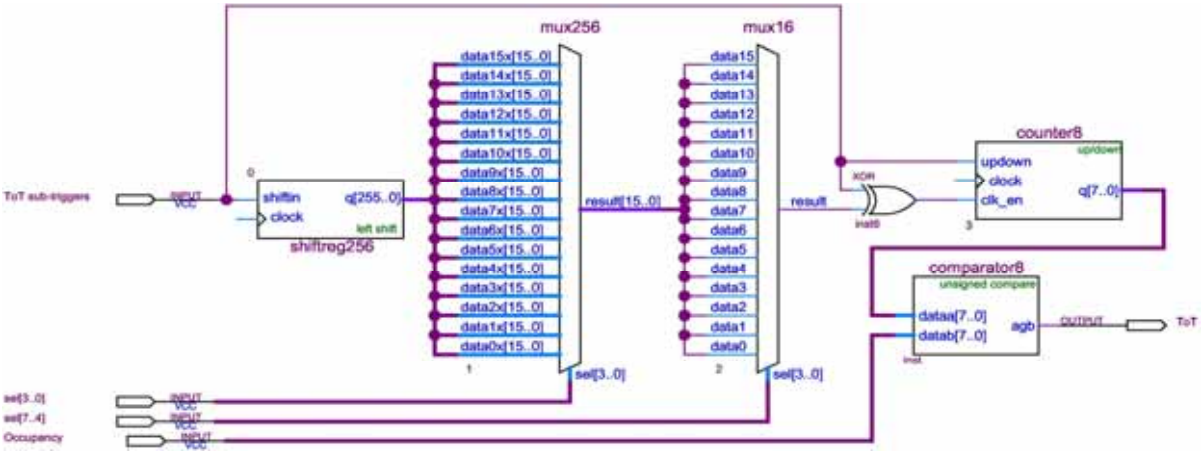

Figure 35 – The implementation of the Time over Threshold trigger. ToT pre-triggers are propagated in 256-bin shift register (shiftreg256). The width of the scanning window is selected by the multiplexer cascade mux256 and mux16. The number of pre-triggers ("fired" time bins) is calculated in up-down counter (counter8). If the number of pre-triggers counted in counter8 exceeds the chosen Occupancy (an input from the initialization register), the circuit generates the final ToT.

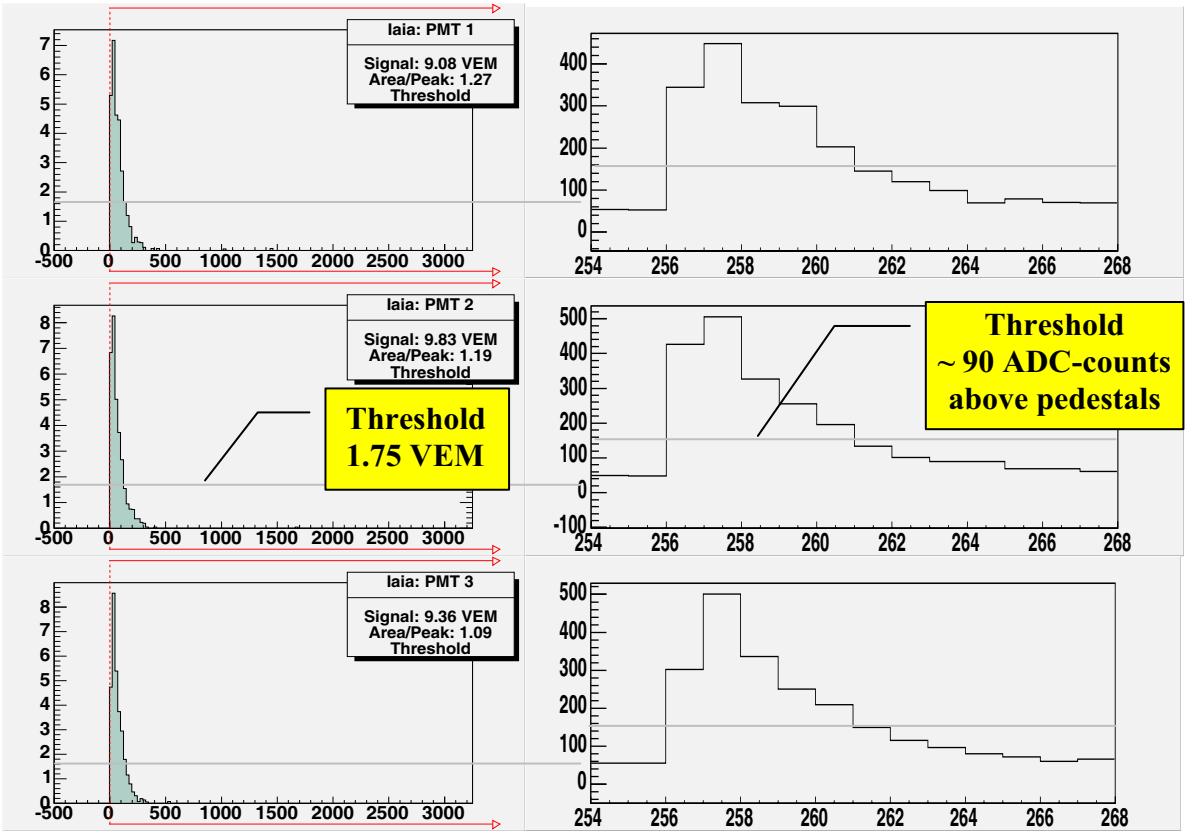

Figure 36 – An example of the event (#02898756 – Iaia) triggered by a threshold trigger [27].

The ToT trigger (Figure 35 and Figure 37) is generated as follows: input signals (with the same structure as for the single bin trigger) are compared with the threshold (separate set for ToT trigger, but with the same structure as for single bin trigger). If pre-triggers are generated, they are put into 256-bit shift register. The number of pre-triggers moving through the shift register is compared in the "Occupancy" comparator with the fixed value written in a register. If the number of pre-triggers is above the "Occupancy" threshold, the ToT trigger is generated. The window (the length of the shift registers) tracking the pre-triggers can be tuned by the selection of an output from the 256 inputs MUX.

If the pre-triggers are moving in the shift register, but the "distances" between them are too big, their number "seen" in the window maybe not enough to be above the "Occupancy" threshold and to generate the trigger. A discussion on advantages and disadvantages of ToT trigger and a proposal of its improvement will be presented by the 3rd generation of the 1st Level Trigger based on the Cyclone™ chip.

3.1.4 Pipelined internal routines structure

The structure of internal electronics has been designed fully pipelined. Only the functionality of the previous ASIC design has been assumed as an input. New concepts of data flow, memory management, read out system, DMA transfer, additional diagnostic routines, a slow data structure as well as a slow channel triggering and data storage have been implemented. Timing of all single-clock cycle routines were immediately verified and optimized, if some process did not provide a sufficient time safety margin. The APEX™ 20K capacity allowed implementing fully the fast channel as well as the logical pipeline. Insufficient memory size forced an adding an external memory for the slow channel.

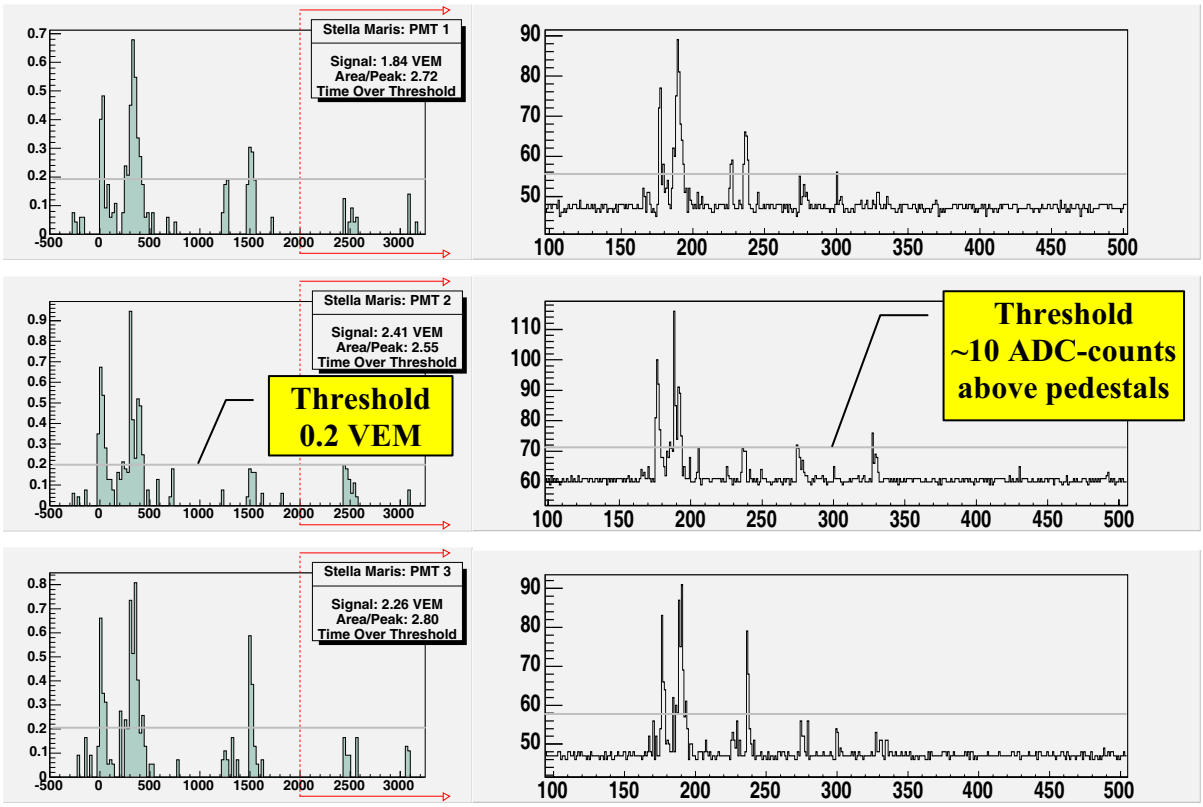

Figure 37 – Real data (#02840621 – Stella Maris), tank triggered by ToT [27].

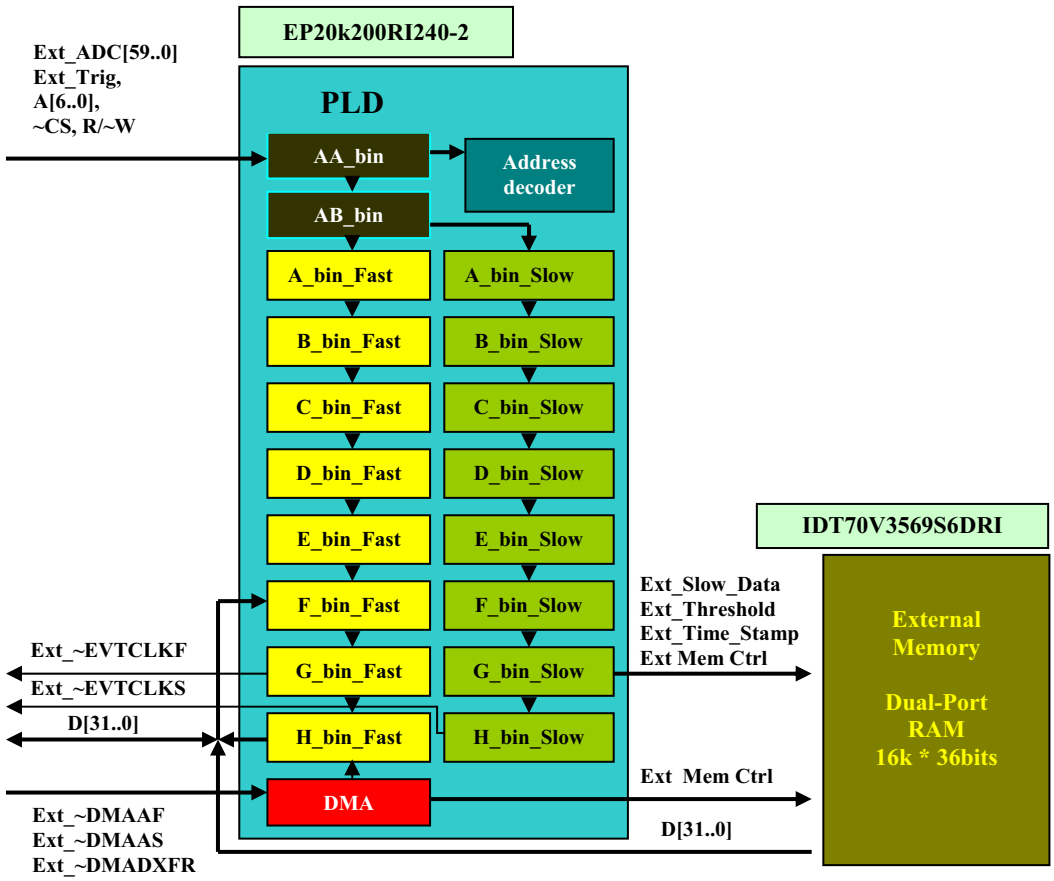

Figure 38 – Pipeline structure of internal routines in the APEX design.

In Figure 38 a pipeline structure of internal routines in the APEX design is shown. Two first AA_bin and AB_bin routines have been added later and contained internal pattern generators very convenient for diagnostics. Patterns could drive both channels and test them simultaneously. Next generations of the First Level trigger unify the names of routines and nodes to show its origin and a location in the pipeline chain as well as more precisely their function.

3.1.5 The memory structure in the fast channel

The dynamic range of analyzed data has been set on 15 bits. The simplest way would to be convert data from the analog to digital form by 15–bit ADC. In 1998–99, when the analog part was planned 15–bit analog to digital converters working with 40 Msps were not available. However, even at present (2008) their cost exceeds far the planned budget. But the main limitation is the power consumption. 16-bit FADC sampling data with 40 MHz consumes several Watts, far from the accepted power budget limited by solar panel supply system. To cover a full 15–bit dynamic range data are converted by two 10–bit FADC with 5–bit overlapping. Data from three PMTs are sent to 6 FADC. Three of them (ADC[29..20], ADC[19..10] ADC[9..0]) work as the high gain channel, the other three ADCs (ADC[59..50], ADC[49..40], ADC[39..0]) as the low gain channel. Only data from the high gain channel may generate the trigger. Data from low gain channel are converted and transferred to Local Station parallel with high gain channel data.

Data for the fast channel from both high and low gain sub–channels have to be recorded in the following way:

- 256 words before trigger,
- 512 words after trigger

To reduce a dead time data are recorded in 2 independent buffers. When trigger occurs and data are waiting to be transferred into the Local Station, the second adjacent buffer should be ready to receive next data, when the next trigger occurs and before transfer of data from the 1st buffer is finished. Such a solution requires 2×768 words×64 bits = 12288 Bytes of the buffer memory.

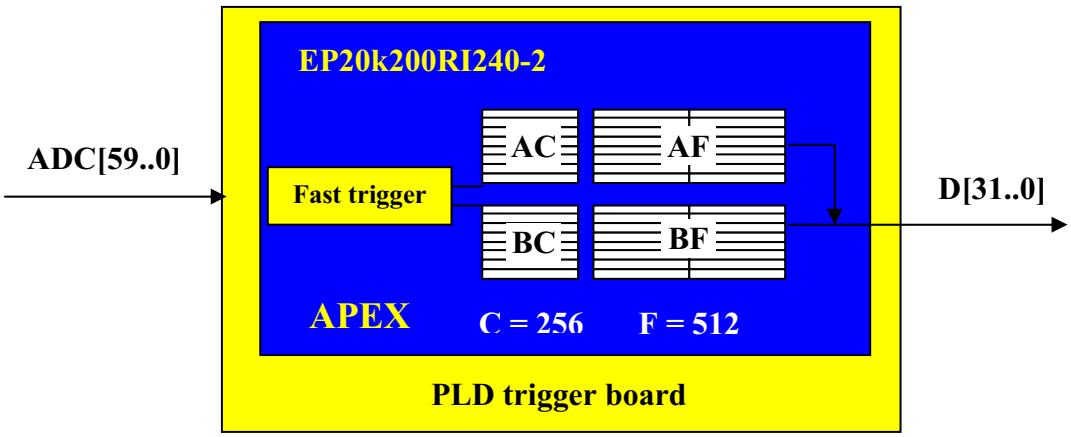

Figure 39 – The internal memory structure.

Altera® PLD chip EP20k200RI240–2 from the APEX™ 20K family contains 52 **E**mbedded **S**ystem **B**locks (ESB), ¼kB each (256 words×8 bits). 48 ESB are organized in 2 buffers (A and B) with 2 blocks (256 + 512 words) each. The width of the word is 64–bits related to the 6 ADC 10–bits channels. 4 bits are used as flags to indicate the type of buffer.
Fast[63..62]–11: (AF or BF), … Fast[61..32]–ADC[59..30], 3 low gain channels,
Fast[31..30]–00: (AC or BC),…Fast[29..0] –ADC[29..0], 3 high gain channels.

The internal memory (see Figure 39) is implemented as Dual–Port RAM with all registered inputs and outputs. Data temporarily written into internal memory are next transferred to Local Station via DMA mode.

3.1.6 Readout system in the fast channel

In the ASIC I/O readout system, the outputs of the configuration registers as well as the output from the memory were connected to the final bus via tri–state buffers. An implementation into PLD of such a configuration caused overloading an internal bus and producing of glitches on the output bus (Figure 40). Additionally significantly different propagation times for particular bits caused relatively large unstable area in the output data. All 32 bits were not switched simultaneously and setup and hold time of the output data were significantly reduced often below the limit allowing the system for a work. For DRAM used in the system, t_{setup} = 8 ns, t_{hold} = 10 ns.

A readout concept taken from the ASIC design did not give satisfactory results and has been replaced by pipelined multiplexer chain as presented in Figure 41. Such a solution

allowed on use of dedicated Fast Output Registers in I/O cells to assure simultaneous switching all output bits and remove unstable areas in output data. Times t_{setup} and t_{hold} became big enough to assure safety DMA transfer even for 0 wait state. A reduction of additional wait states speeds up data transfer from PLD to **U**nified **B**oard (UB – board containing micro-controller and controlling all electronics in the tank) and reduces dead time of the system. Propagation times for controlling lines have been additionally reduced by using dedicated inputs.

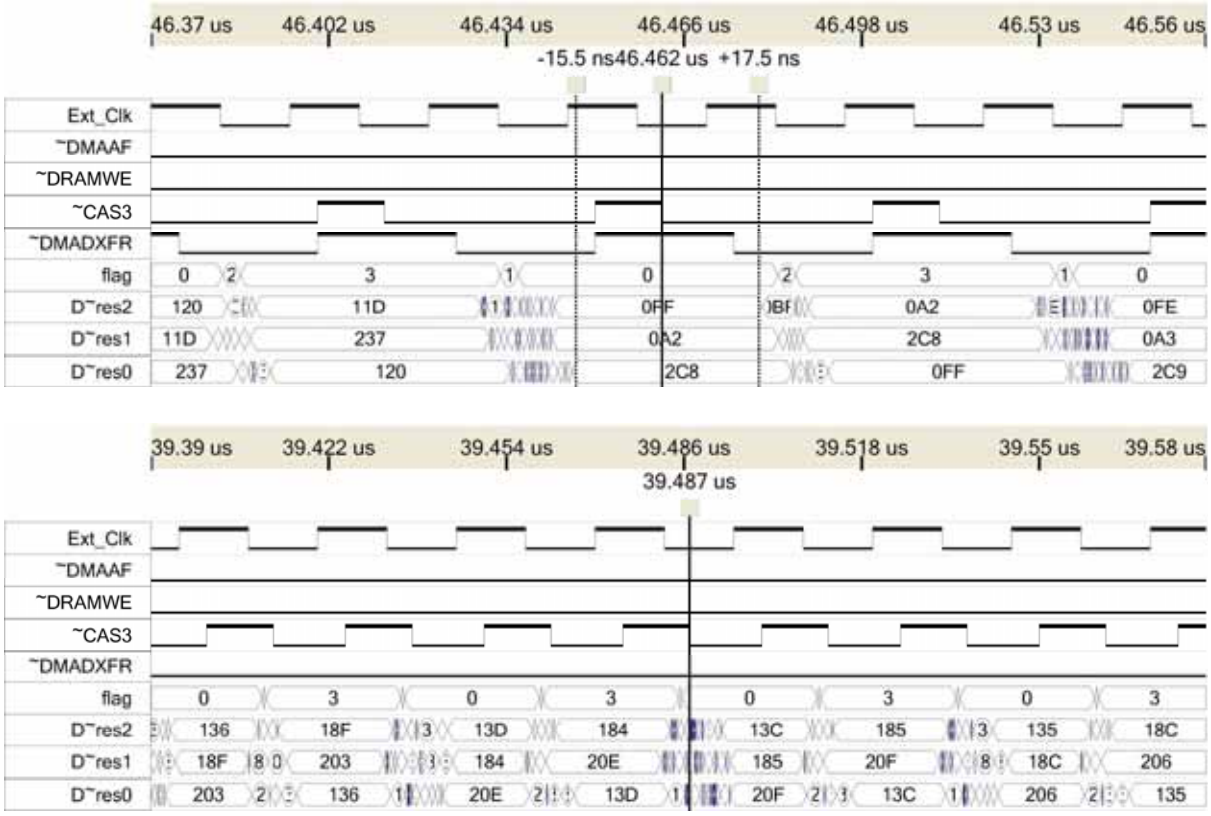

Figure 40 – Internal memories connected to the output bus via tri–state buffers (1WS above and 0WS below). Propagation delays cause that sometimes outputs from two memories are connected simultaneously. Theoretically both t_{setup} and t_{hold} are enough, however visible unstable areas strongly suggest an improvement necessity. 0WS mode is not available. Data are unstable for a falling ~CAS3 edge responsible for a data transfer.

Figure 42 shows, that timing is satisfactory in both 1WS and 0WS modes. Logic analyzer investigations confirmed a full reliability of the solution (Figure 43). The DMA transfer (independently of the mode) is interrupted due to refreshing of the dynamic memories in UB. PLD readout system has also taken into account all possible configuration of interruption in order either not to lose valid data or not to produce spurious states.

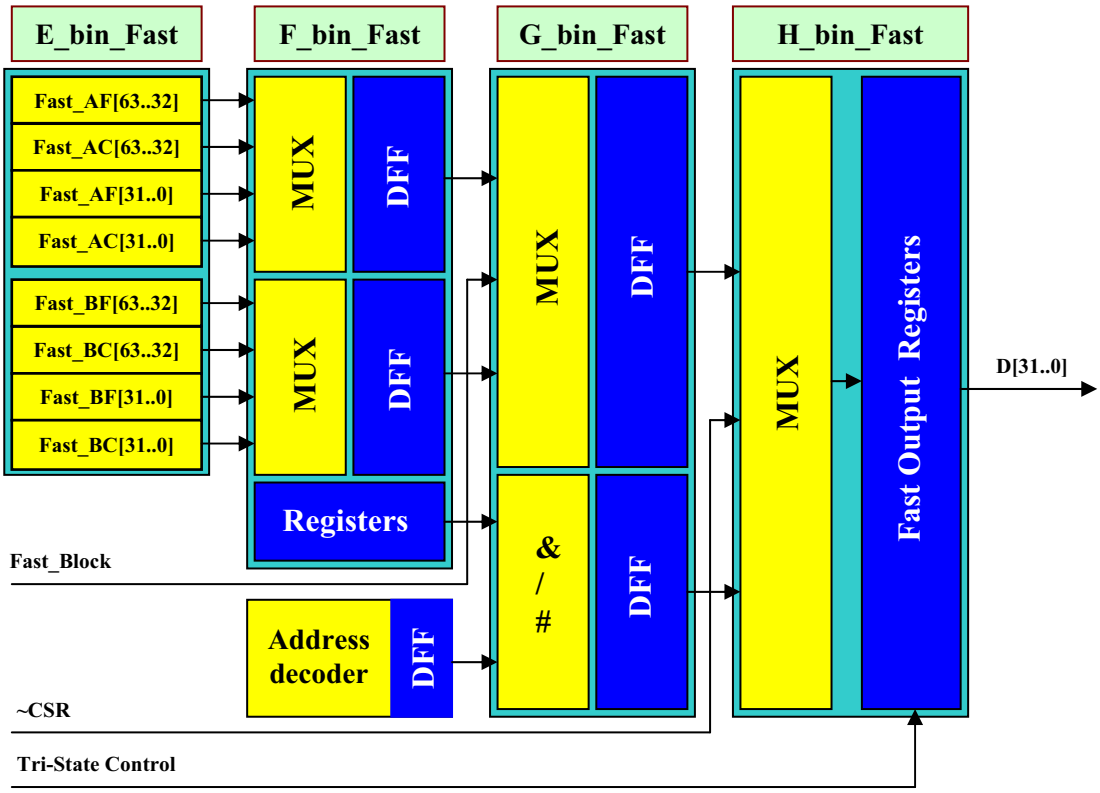

Figure 41 – The structure of the pipeline I/O system.

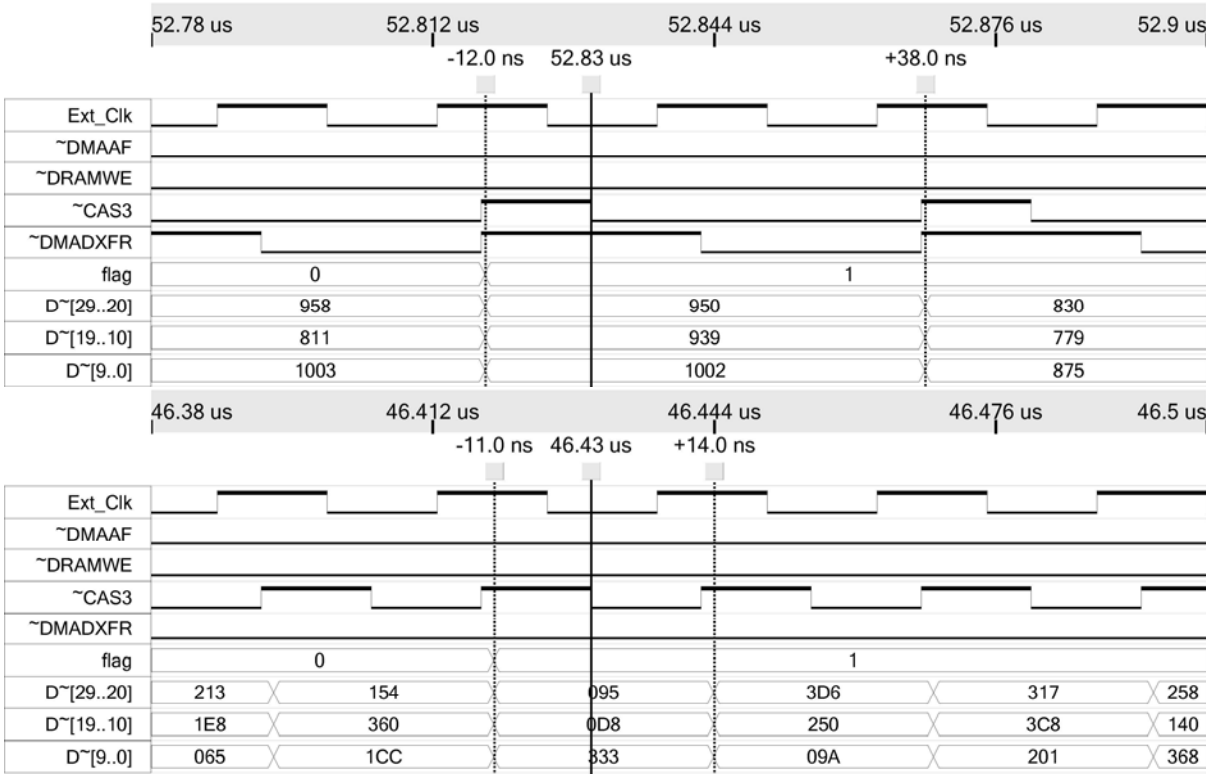

Figure 42 – Simultaneous switching of all 32 bits in the Fast Output Registers for 1 WS and 0 WS modes respectively.

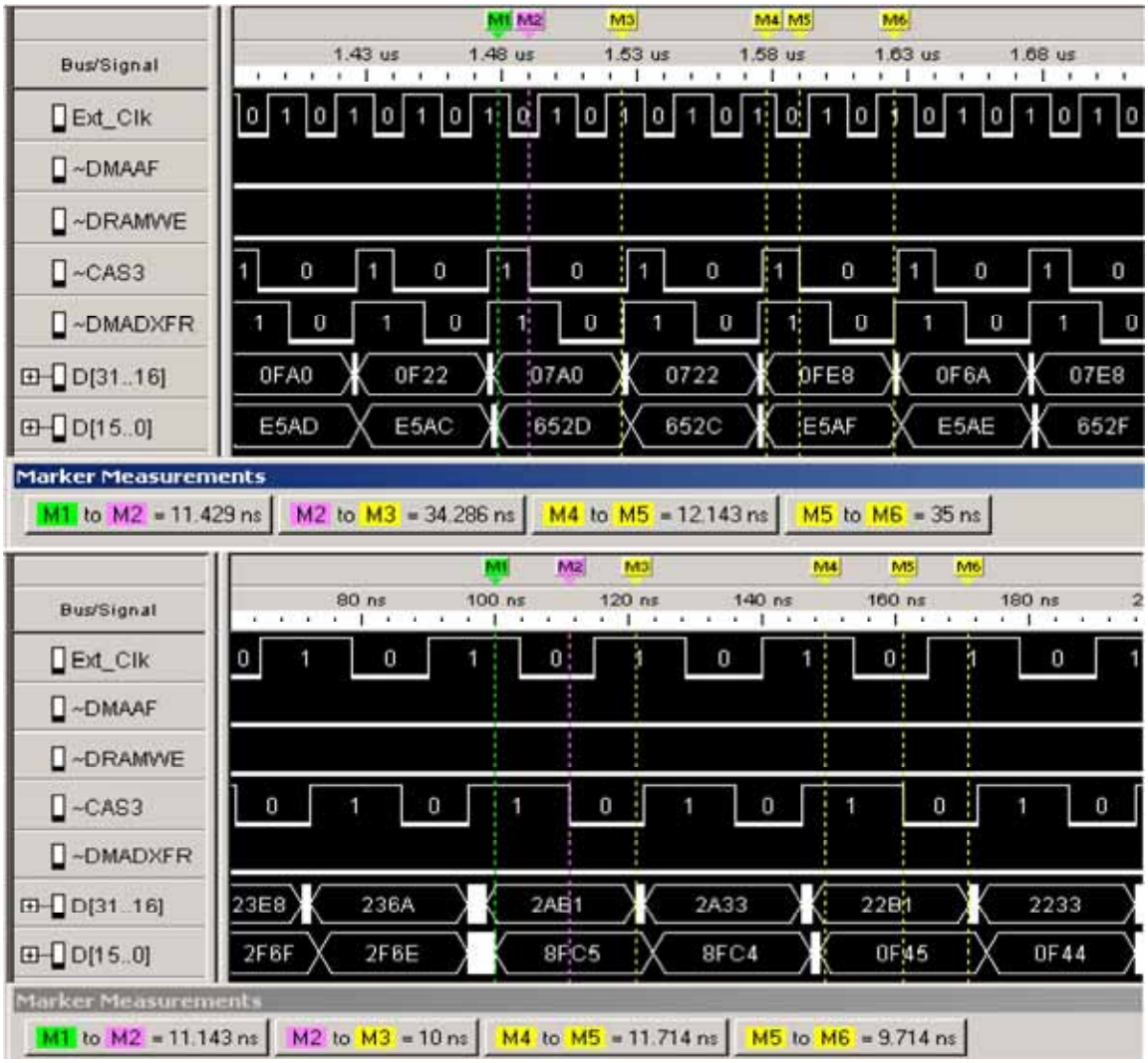

Figure 43 – View with logical analyzer for 1WS mode, 32 bits are switched simultaneously, some short unstable areas is a consequence of limited logic analyzer resolution (above) and view with logical analyzer for 0 WS mode (below).

3.1.7 Timing for triggers in the fast channel

The rate of recorded events depends on a type of trigger as well as on the trigger thresholds. Too low thresholds cause high trigger rate, which may be too high to be handled by the trigger/memory system. Due to the dead time some events may be ignored (not recorded). Timing for the two parallel buffers (temporarily registering events profiles) will be discussed below (see Figure 44 – Figure 54).

After an initialization of the whole system both buffers are empty and are waiting for a trigger. AC memory block starts working as a circulating buffer. When trigger (denoted on graphs by vertical arrows) appears, data in AC buffer has been frozen (256 words before a trigger) and next data are recorded in AF buffer (512 words). When the 1st 256 words in AF buffer have been written, the adjacent B buffer is activated and already can record data. For the 256 words recorded in the 2nd part of AF, BC buffer works as a circulating ring collecting 256 words before possible next trigger processed next by B buffers.

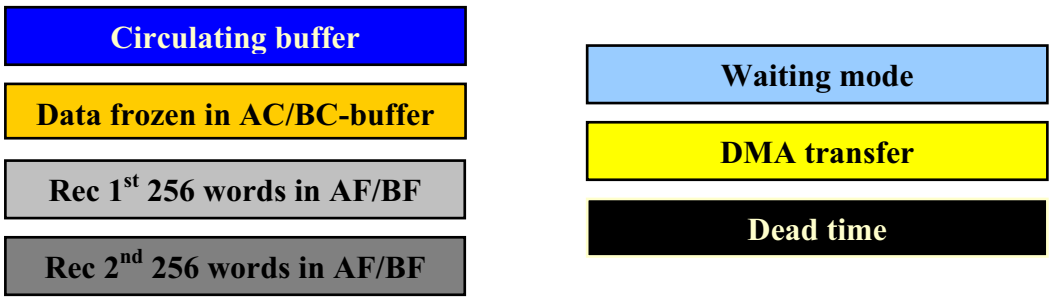

Figure 44 – A description of data flow modes in the fast channel.

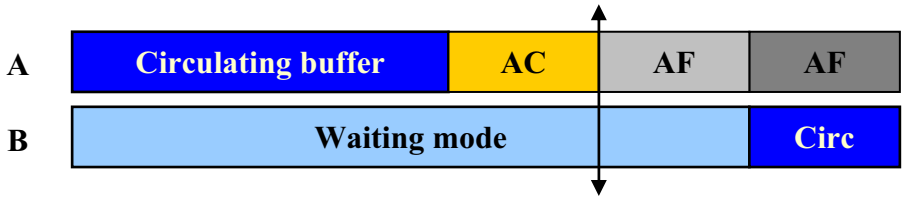

Figure 45 – An initialization mode: Data circulation into BC–buffer simultaneously with the data recording in the 2nd part of AF–buffer.

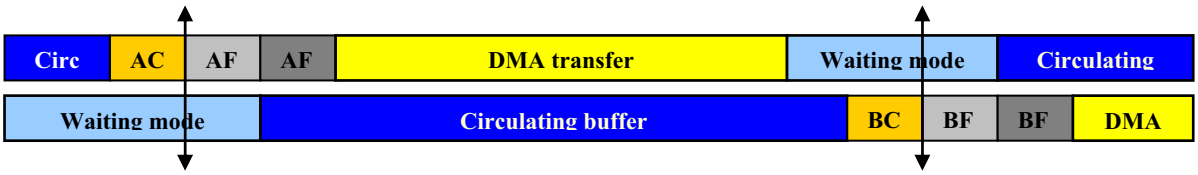

Figure 46 – Triggers separated, enough time to complete DMA transfer.

The graph in

Figure 46 presents a typical case, when two consecutive triggers appear rarely and it is enough time to transfer collected data from PLD to UB. When one of the buffer is fulfilled by event data, PLD notifies a transfer request via ~EVTCLKF interrupt. Data from PLD are next transferred to µC via DMA mode. The adjacent buffer is ready to receive next event, if appeared. Such a solution of two parallel buffers significantly reduces a dead time.

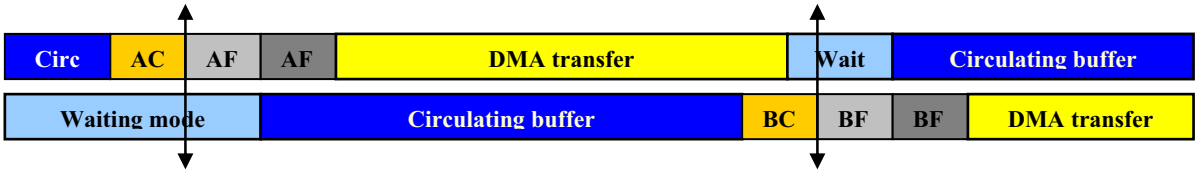

Figure47 – The next trigger just after DMA completed, data frozen in BC buffer, while DMA in progress.

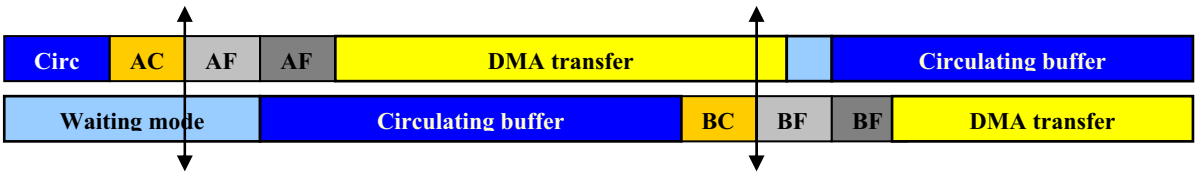

Figure 48 – The next trigger, when DMA in progress, still waiting mode in A–channel for BF.

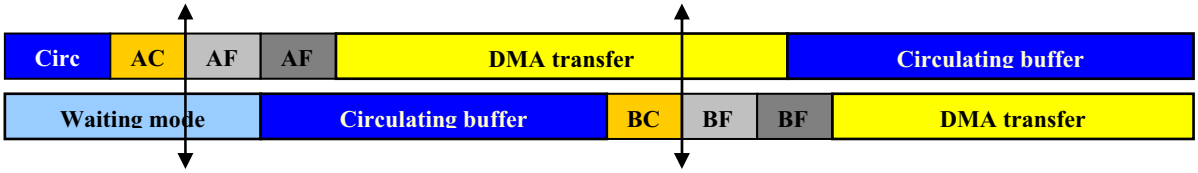

Figure 49 – Trigger, when DMA in progress, no waiting mode, but still no dead time.

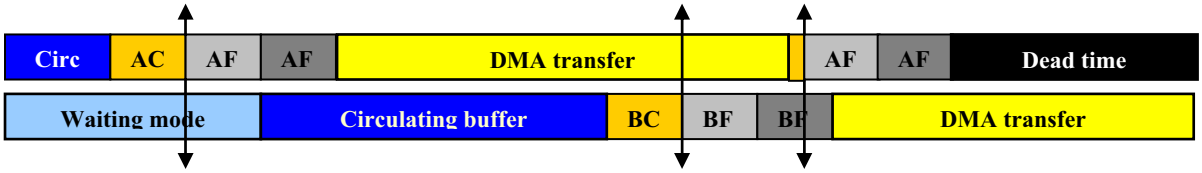

Figure 50 – For the 3rd trigger AC data can be recovered from BF–buffer of a previous cycle, a dead time in A channel.

The graphs in Figure 48 - Figure 50 describe cases when all data are recorded and no one word is lost. However, when the 3rd trigger appeared relatively close to the 2nd one, both buffers are full and the trigger/memory system becomes inactive due to a dead time.

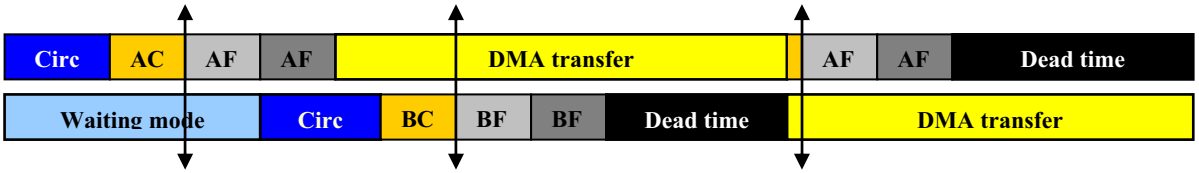

Figure 51 – AC data cannot be recovered, data partially lost, dead time in both channel

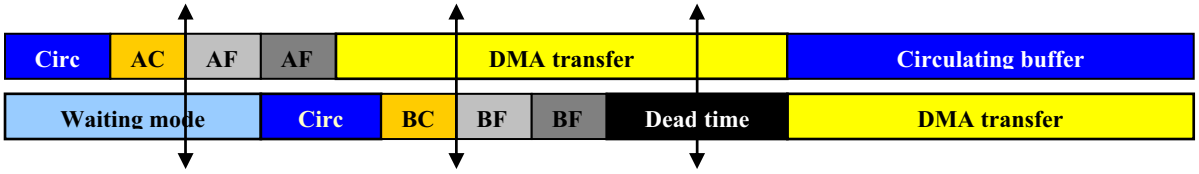

Figure 52 – Data related to the 3rd triggers totally lost, a dead time in B channel.

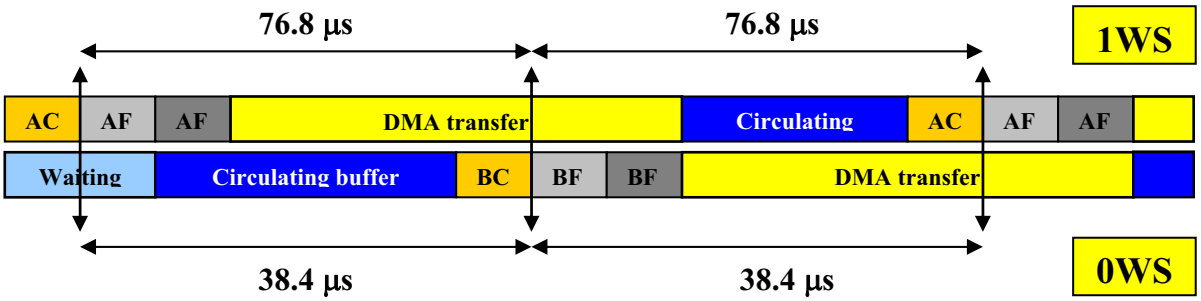

Figure 53 – Permanently allowed interval between consecutive triggers.

A trigger/memory system with no dead time would require additional adjacent buffers, switching logic etc. The construction is possible however not absolutely necessary. If the thresholds would be so adjusted to get relatively low event rate, a probability of three consecutive triggers (as presented in Figure 52) would be relatively small and we could agree

to reduce a little bit an efficiency of a trigger system not complicating the rest of the electronics. Such an approach (relatively high registration thresholds) is justified, because Pierre Auger Observatory focuses rather on highest energy events (which appear very rarely). Events related to the graph shown in the Figure 52 would correspond to relatively low energy, where a little bit lower efficiency is acceptable. However the trigger/memory system should reduce a dead time as possible.

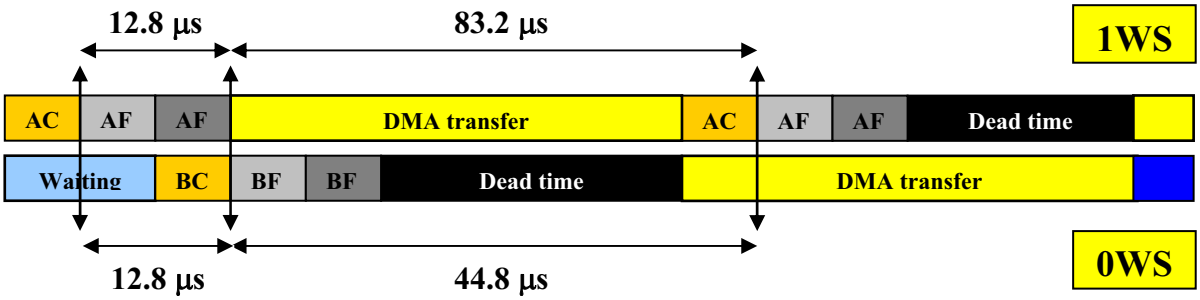

Figure 54 – The 2nd trigger allowed just after buffers switching (12.8 µs after the 1st one), but the 3rd trigger should not appear earlier than 83.2 µs (44.8 µs – 0 WS) after the 2nd one.

Preliminary analysis shows that data from PLD should be transferred to µC via 0 WS DMA mode. 1 WS mode inserting additional wait state increases hold time from ~10 ns (see Figure 43 (bottom) – interval between M2 and M3 or M5 and M6 time stamps) to ~35 ns (see Figure 43 (top) – interval between M2 and M3 or M5 and M6 time stamps). Required value for stable work is 10 ns only. Even for 0 WS there is a sufficient safety margin. APEX™ 20K contains **P**hase **L**ooked **L**oop generator (PLL), however does not support a clock shift feature in order to tune the stable area of data. Precisely time shift adjustment is in APEX™ 20K not possible. That feature will be used further in the Cyclone™ device.

3.1.8 Data integrity

Let us analyse the timing from the Figure 50.

If trigger occurs just after DMA transfer is completed (less than 6.4 µs = interval needed to fill the circulating buffer – i.e. as the 3rd trigger in Figure 55) and the adjacent buffer is still full, the AC/BC buffer has not enough time to be filled and will contain old data from the previous cycle.

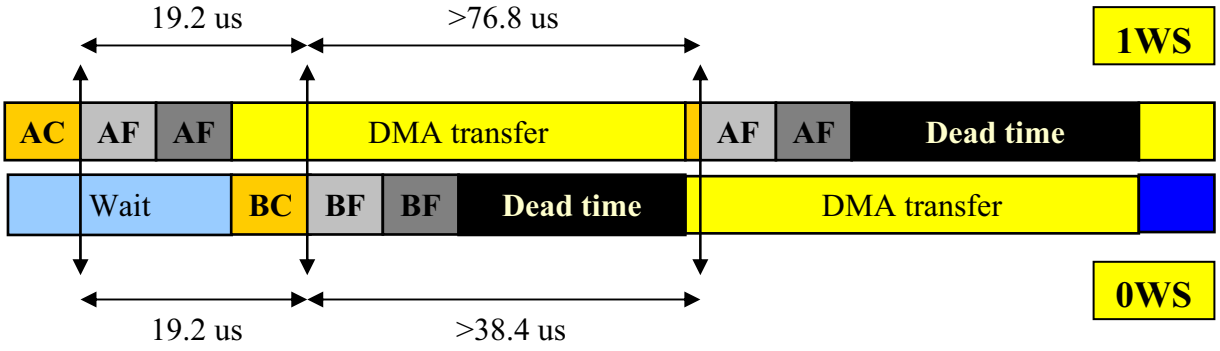

Figure 55 – Timing for triggers, when data integrity is violated.

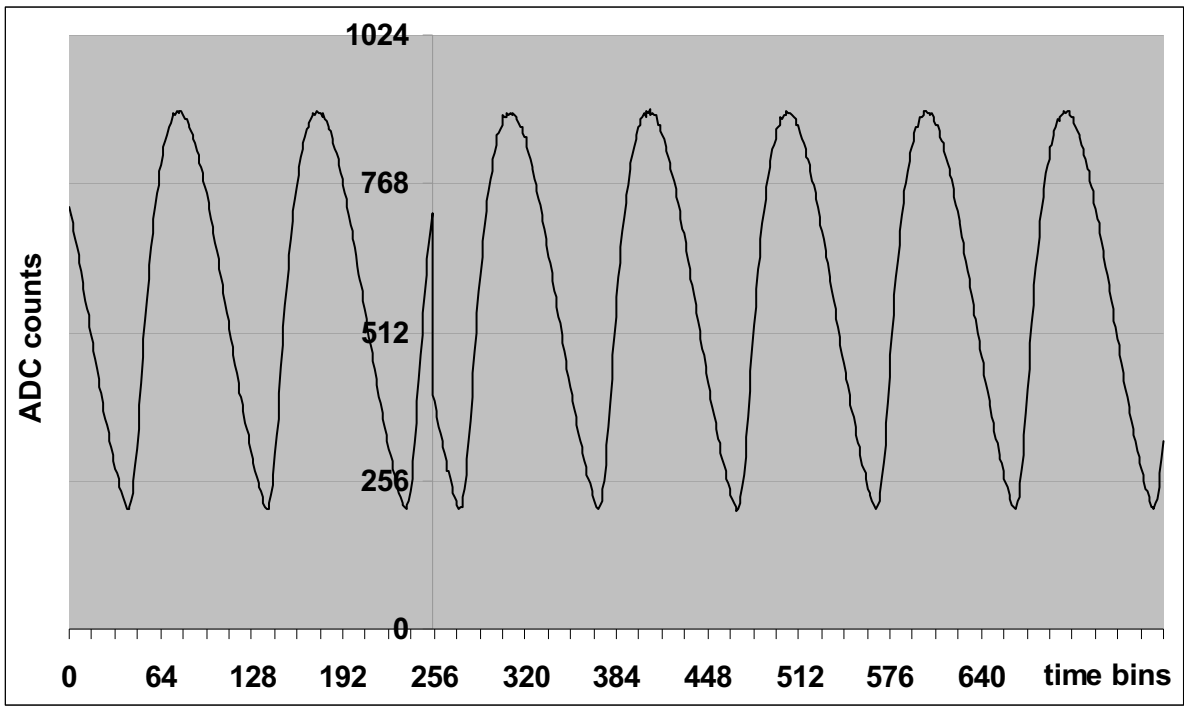

Figure 56 – Channel 1 of the PLD trigger board supplied by sin–wave generators with offset. Frequency = 400 kHz, minimal interval between triggers 12.8 μs, trigger allowed just after DMA transfer. Data in 0 – 255 time bins from the previous event. Data integrity is violated.

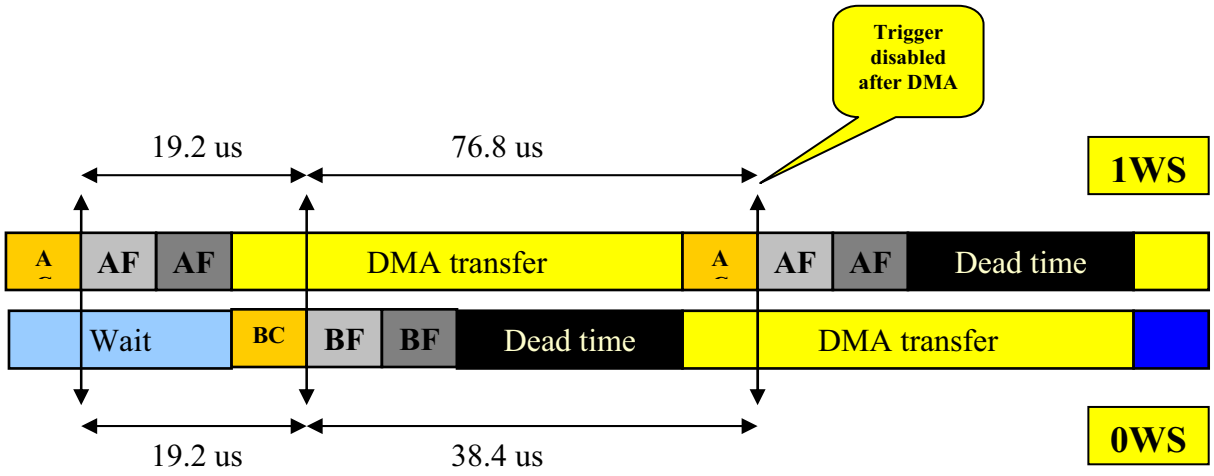

Figure 57 – Timing for triggers, when data integrity is not violated.

Figure 56 shows that the 1st 256 words are not consistent with the next 512. They correspond to the previous reading cycle. The sin-wave is not continuous. Trigger appeared just after DMA transfer without sufficient interval to fulfill the circulating buffer by a new data. To avoid problems with data integrity, triggers should be disabled for 6.4 μs after DMA transfer in order to fill the adjacent buffer by data related to the same event as data in AF/BF buffer as shown in Figure 57.

The minimal allowed interval between triggers should be set on 19.2 μs as shown in Figure 57. Disabling triggers till circulating buffer is filled is preferred in real measurements in order to avoid problems with data integrity violation. It provides continuous data structure as shown in Figure 58.

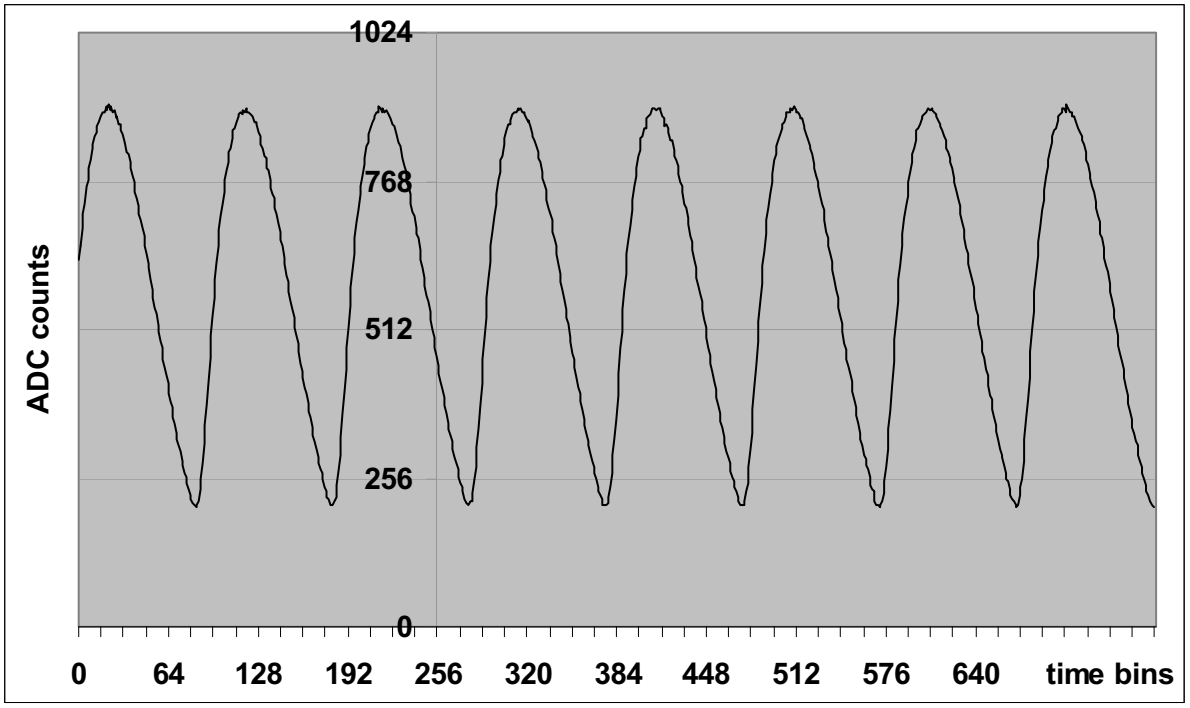

Figure 58 – Minimal interval between triggers 19.2 μs, trigger allowed 6.4 μs after DMA transfer.

3.1.9 Triggers in the slow channel

The structure of trigger logic in the slow channel is the same as for the single-bin trigger in the fast channel. In the slow mode, when the trigger appears, the threshold changes (decreases). Recording data with lower threshold allows investigating more detailed structure of weak signals, normally cut by high threshold. The main difference in recording of data in comparison with the fast channel is as follows: in the fast channel if trigger appeared, 256 words before and 512 words after trigger have been recorded independently of current values. So, always after trigger one of the fast buffers was filled. In the slow channel the length of recorded data depends on their values above the thresholds and cannot be anticipated. The length of the slow buffer is relatively long – 8192 words (32–bits). If one of the buffers is full, ~EVTCLKS signal is sent to the μC as an interrupt requiring a transfer of data from the external memory. However the priority of the transfer is lower than for the fast channel and the slow transfer may be interrupted by the fast DMA. Data may be written to the memory via left port independently and simultaneously with the data reading via right port. From available 36 bits, only 32 bits are used: 30 for high gain ADC data and two as indicators of threshold and time stamps. To synchronize data with the fast channel, time stamps are inserted into the same stream of data and are written together with real data in the external memory. The system of time stamps has been solved in other way than in original ASIC project. No additional special memory for time stamps only is used. Time stamps are inserted at the beginning of real data blocks (sometimes may be skipped, if inserting of stamps would violate data integration and lose data) and are indicated by the 31st bit treated as the flag [43].

To simplify the communication between PLD and the final recipient UB, the dual–port SRAM has been chosen. IDT70V3569S6DRI has been found as the cheapest chip (industrial temperature version, with the max. internal frequency 83 MHz) with the sufficient size. The full surface detector trigger contains only two VLSI chips.

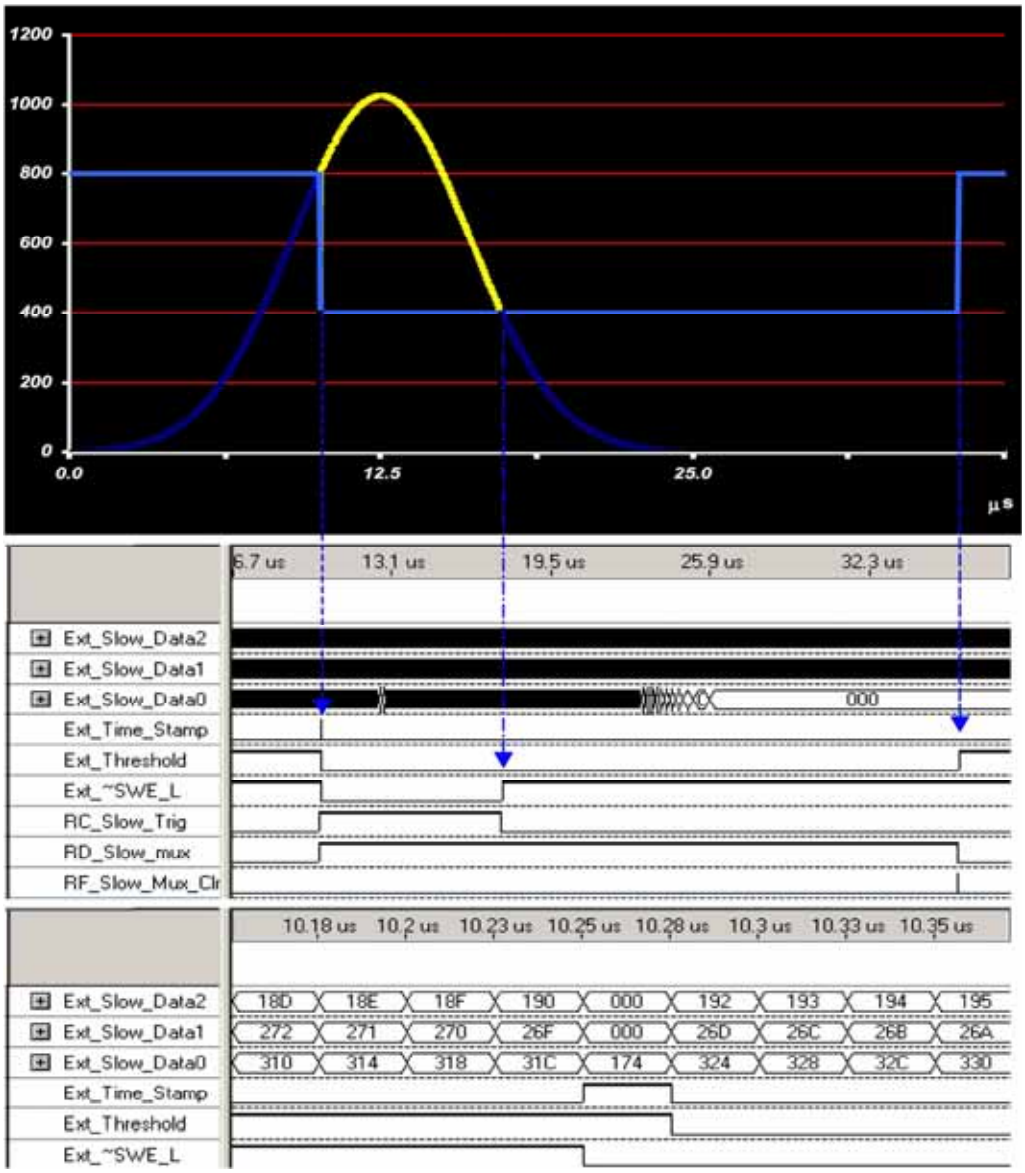

Figure 59 – An event, when only one pulse is recorded after the threshold decreased. The length of the "low" threshold is long enough to record the full shape of a pulse after the trigger. Only one time stamp is inserted before the real data. The 1st upper graph shows the shape of the signal with corresponding thresholds, the middle graph the simulation of signals, the lower graph is the zoom of simulation in the beginning of data, where Time Stamp is inserted. The signal Ext_~SWE_L (**E**xternal **S**low **W**rite **E**nable to the **L**eft port) enables to write data into the external Dual-Port RAM.

The initialization 10–bit register controls the interval length (max = 25.6 µs) of the low threshold. The low threshold can be extended if data are above the high threshold, when the low threshold interval expired (as shown on the graphs below).

Figure 59 - Figure 63 show various modes for triggering data in the slow channel.

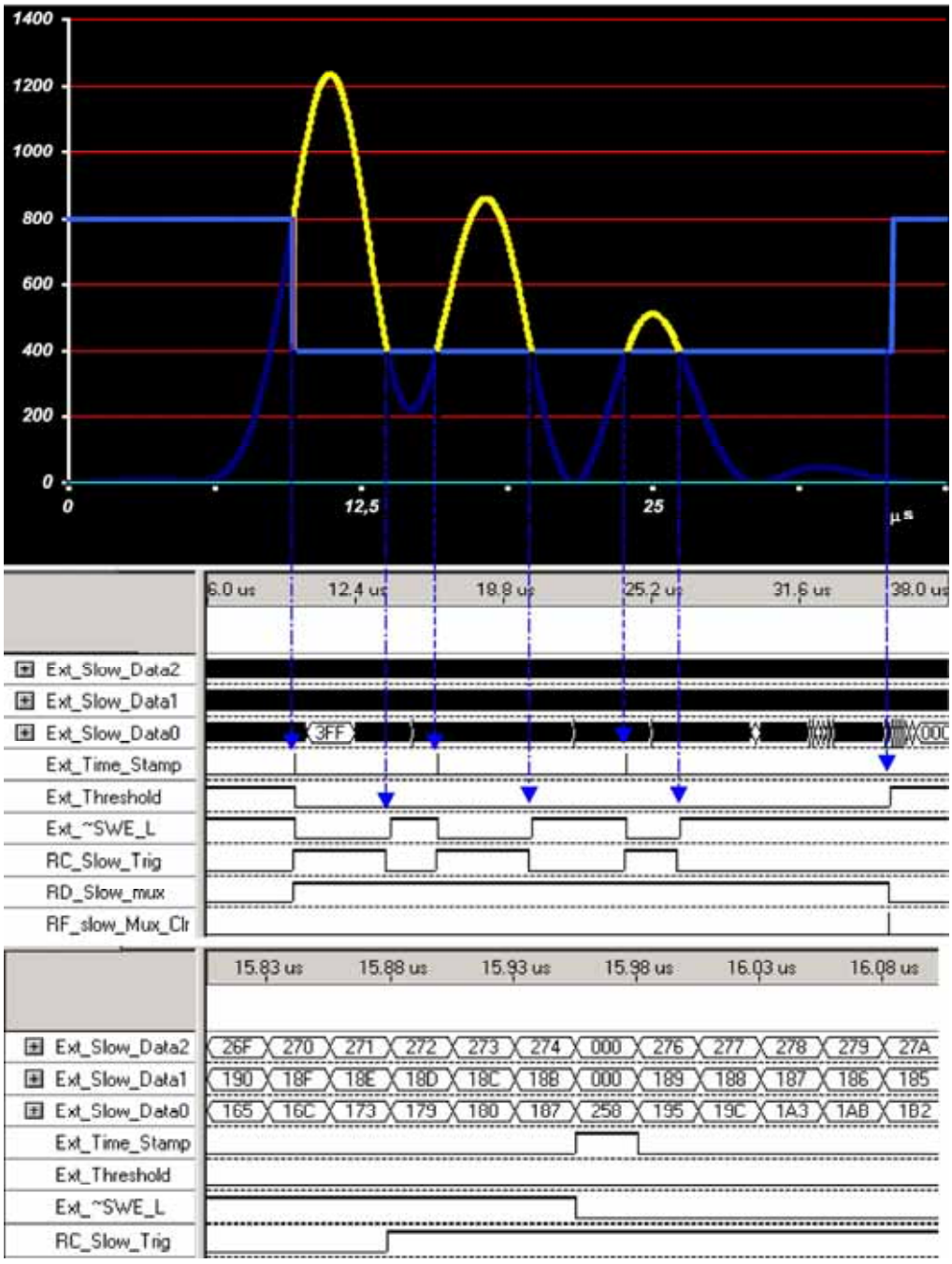

Figure 60 – An event, when many pulses are recorded after the threshold decreased. Each data section starts from the time stamp.

Figure 59 shows a simplest event, when only one pulse is recorded after the threshold decreased. The length of the “low” threshold is long enough to record the full shape of a pulse after the trigger. Only one time stamp is inserted before the real data.

Figure 60 shows the event, when many pulses are recorded after the threshold decreased. The length of the “low” threshold is long enough to record all pulses after the trigger. Each data section starts from the time stamp.

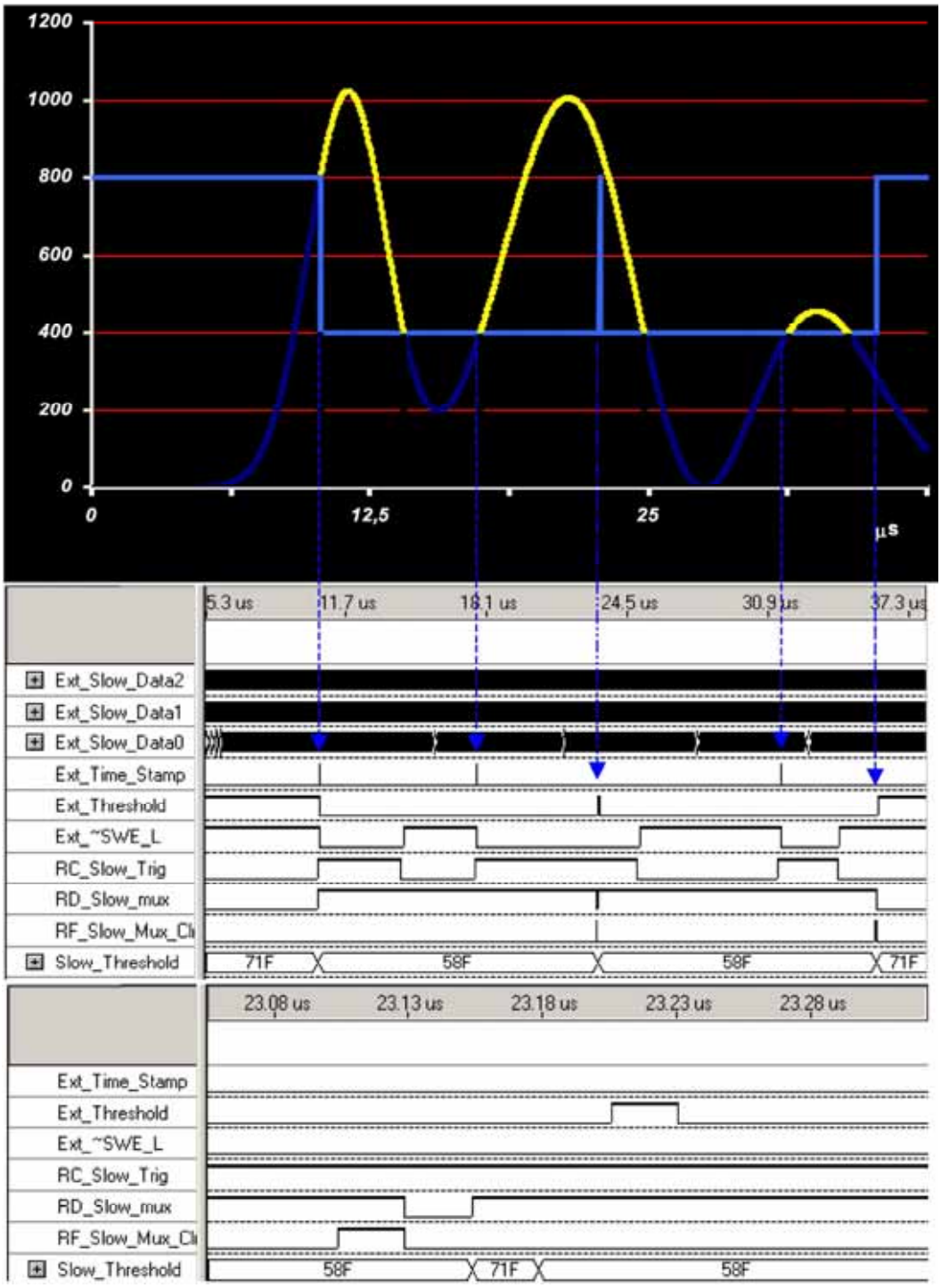

Figure 61 – An event longer than the “low” window. When “low” threshold expired and data are still over the “high” threshold, the time stamp is not inserted in order not to lose real data, however change of the threshold is indicated.

Figure 61 shows an event longer than the “low” window. When “low” threshold expired and data are still above the “high” threshold, the time stamp is not inserted in order not to lose the real data, however change of the threshold is indicated by Ext_Threshold signal..

Figure 62 - Figure 63 show the structure of the "slow" data. After the Time Stamp data from at least 4 time bins are recorded. When the input signal is longer above the threshold, the blocks of 1 Time Stamp + data in 4 · *n* time bins are recorded, where *n* – natural number.

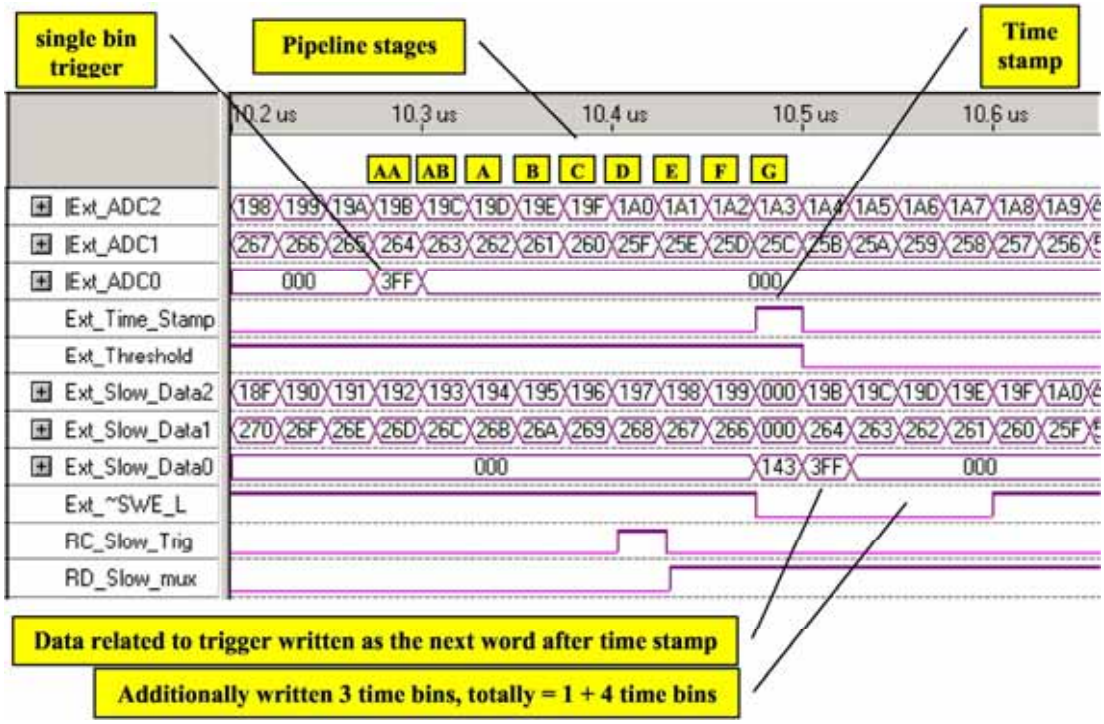

Figure 62 – The single bin trigger is generated on the output of G_bin_Slow nine clock cycles after a trigger condition appears on FADC inputs. The output is opened one clock cycle earlier to insert a time stamp before the 1st data. The additional data in the next 3 time bins are also recorded.

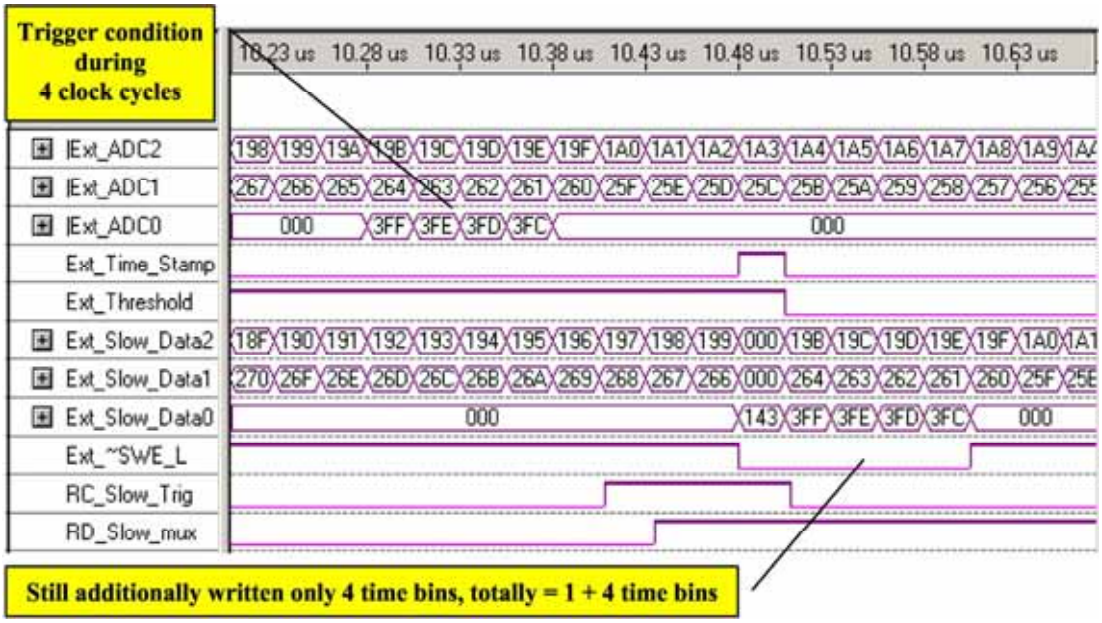

Figure 63 – For a trigger condition valid for four clock cycles, the structure of recorded data remains the same as for the single clock cycle condition.

Data sent from PLD are recorded into the external memory, when Ext_~SWE_L (**Ext**ernal **S**low **W**rite **E**nable **L**eft port) is low (Figure 59 - Figure 63). The memory is working with internal address generation. The address is not sent from PLD, due to lack of pins. The external memory is fully controlled by PLD. Some of the control lines are stuck to VCC because of one–way flow.

3.1.10 Conclusions from the Engineering Array phase

The trigger/memory circuitry described above successfully operated in the Auger EA (Figure 64). The successful operation in the EA demonstrated the suitability of a PLD based trigger logic in the Auger surface detectors, and provided the solid practical experience for the subsequent production design.

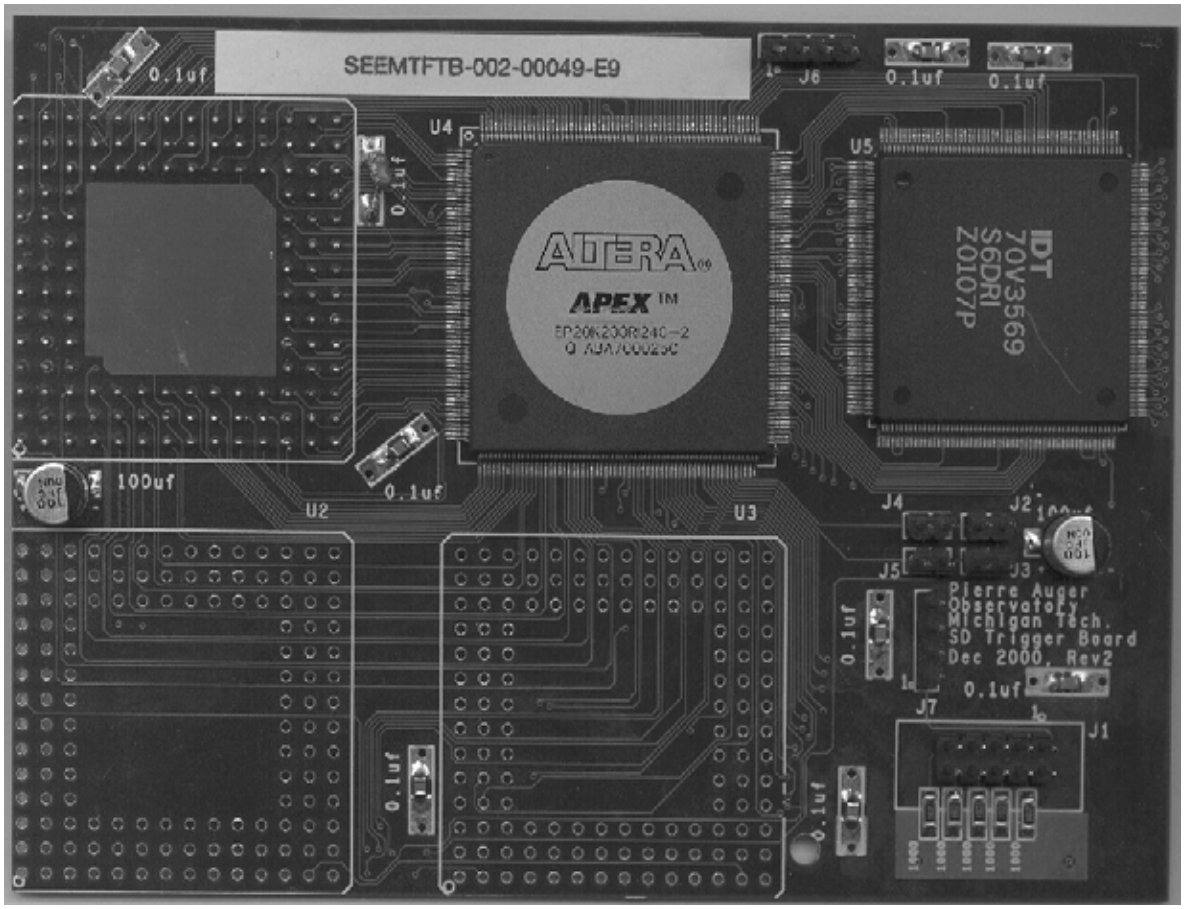

Figure 64 – The view of the APEX trigger board. In the upper left corner there is a plug in to connect "daughter" trigger board with the Front End board via PGA132 socket. On two empty places for PGA132 packages may have been assembled ASICs. A connector to the PLD external programmer is located on right down corner.

The basic concept of the following ideas of the author implemented into EA design is still valid and has been implemented also in the next generations of the trigger/memory circuits [44], [45], [46].

- The pipeline code structure,
- Chronological ordering of output data,
- An implementation of EAB as Dual–Port RAM for buffers,
- The full automatic fast buffers management to reduce as possible a dead time,
- The flag system informing, which trigger occurred,
- The zero–wait state DMA transfer mode,
- Triggers inhibition to avoid problems with the data integrity violation,
- The pipelined multiplexer structure of the readout system with the Fast Output Registers implementation to assure simultaneous switching of all bits on the data bus (solution based on classical tri–state buffers produced glitches due to overloading on the internal bus),
- Inserting Time Stamps into the same slow data stream, indication by 31st bit,
- The external Dual–Port RAM for the slow buffer working in the advanced address mode (addresses are not sent from PLD),
- Redundancy of reset network significantly improving registered performance,
- The PLD control of the right port of the external DPRAM.

3.2 ACEX design

3.2.1 The general concept

The APEX™ 20K or APEX™ 20KE chips would be the good solution for a surface detector trigger (big capacity of resources, fast register performance), but because of high price, the other cost–effective designs were investigated. The Altera® ACEX® 1K family gave a possibility to reduce significantly total price, not reducing any functionality. The slow channel remained the same. It required, as previously, an external memory. The biggest ACEX® 1K chip contains only 48 kbit internal RAM in Embedded Array Blocks (EAB). It allows implementing only 2×32 bit×768 words, exactly two fast buffers, but for 32–bit length only. To implement full-length (64–bit) bus, two chips were required. The fast channel was split into two high–gain and low–gain sub–channels. 10 additional lines between both chips were used for data exchange [47-48].

Trigger prepared in the high–gain sub–channel was transferred synchronously (by the 1st exchange line) to the 2nd chip (see Figure 65). The 2nd line used in the ACEX design was responsible for enabling/disabling tri–state buffers during DMA transfers, to prevent possible conflicts, if tri–state buffers in both were opened simultaneously. ADC[59..30] bus was connected to the ACEX_B only (low–gain channel, writing only), however ADC[29..0] was connected to both chips.

Some processes in the cost-effective ACEX chips are relative slow. To speed up the global register performance, adders have been implemented, as pipelined routines required 2 clock cycles (see CD_ and EF_ routines in Figure 65). The analyses of a lot of variants suggest, that the optimization of the design done by the compiler is not perfect and it is rather recommended to optimize the internal structure manually as much as possible. If processes related to the same clock cycle are spread in whole chip, the optimization is poor. The logic elements related to the same clock cycle should be located as close as possible to reduce to minimum propagation times. Grouping processes only in functional blocks reduces significantly register performance of the system.

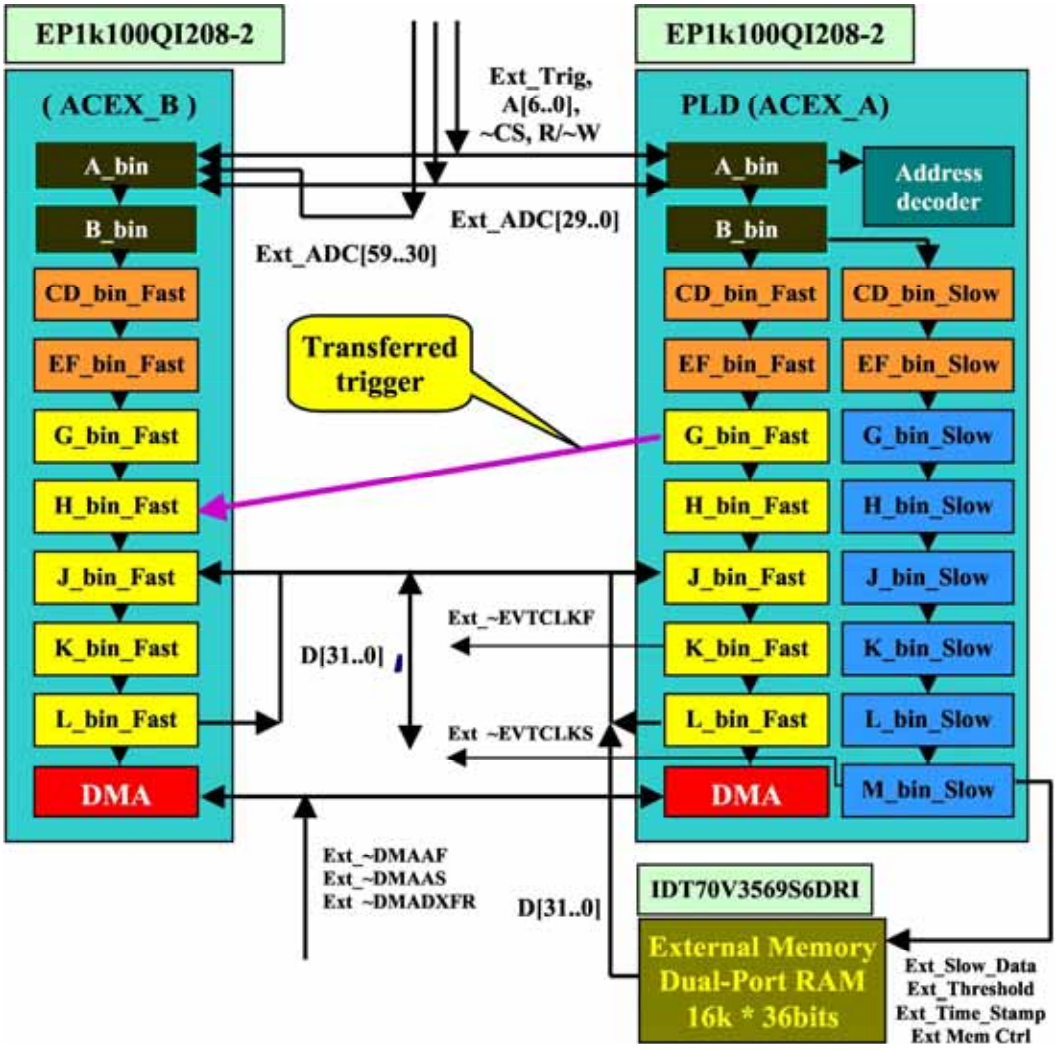

Figure 65 – Global pipeline internal structure of both chips. Routines CD and EF contain processes performed in two clock cycles (speed optimization).

In comparison with the APEX design:

- New functions have been implemented,
- DMA transfer mode has been changed into more natural for two chips – non–interlaced,
- Register structures and read–out system changed to 32–bits,
- The internal structure has been extended to more hierarchical one to encapsulate processes related to single time bins,

The structure of internal routines is fully pipelined. All processes are related to some time bins. Results of processes in each time bin are registered on the outputs. To simplify the navigation, the following convention is used: the 1st letter of output name node is R, if node is registered, otherwise is neglected, the next letter is related to the time bin. Nodes connected directly to external chip pins have prefix Ext_.

3.2.2 Synchronization of sub–channels

The trigger from ACEX_A is transferred into ACEX_B to write synchronously data in low–gain sub–channel. ACEX_A trigger is generated inside the 1st chip and it can be connected either:

- Directly between internal logic cells of both chips or
- With buffered Fast Input/Output Registers located in dedicated Input/Output Cells (IOC).

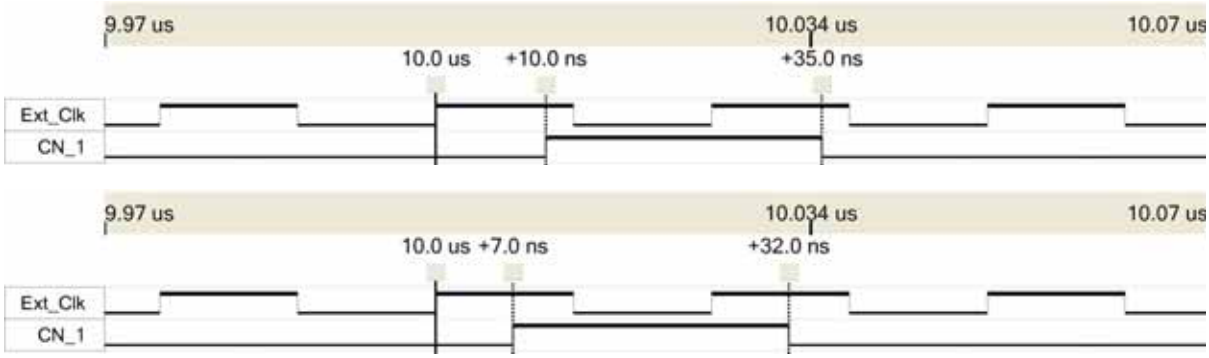

Figure 66 – Propagation time of the trigger to the pin from an internal logic cell (above) and from the Fast Output Register (below). Duplicated logic located directly in IOC allows reducing propagation time to the output pin on ~3 ns.

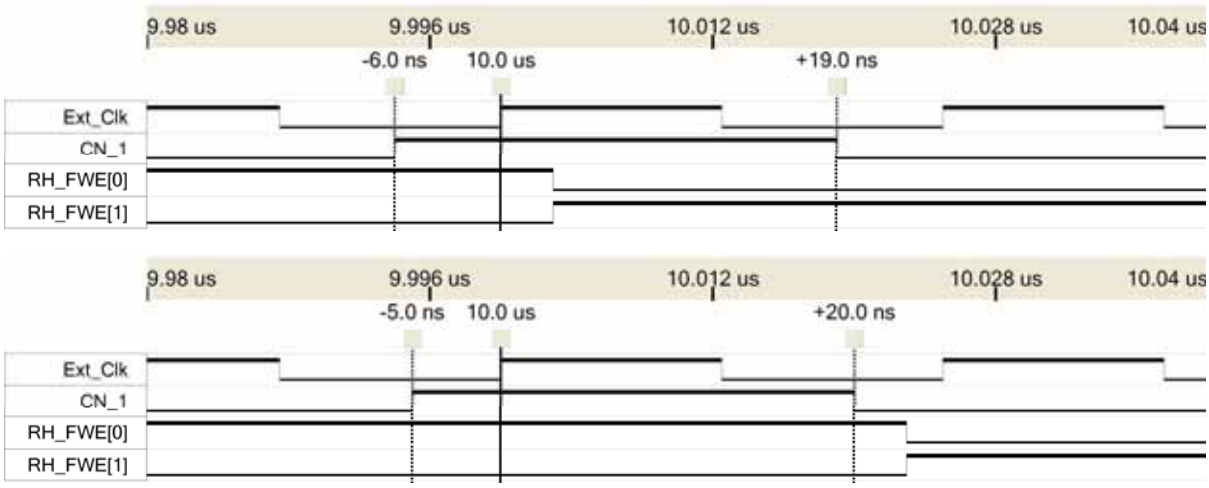

Figure 67 – Analysis of a setup time for CN_1 connected directly to internal logic cell. If the setup time is too short, registers will be switched in the next clock cycle. Data structure will be seriously violated. t_{setup} should be greater than 6 ns.

Direct connection between internal logic cells of both chips correspond to relatively long paths and propagation times. Duplicated logic located directly in IOC allows reducing propagation time to the output pin on ~3 ns (Figure 66). The shorter propagation time from the master ACEX_A chip to the slave ACEX_B chip extends a safety margin of synchronization of chips. If the setup time of a transferred trigger (interval between rising edge of the CN_1 and the rising edge of the clock) is too short, the slave chip maybe switched not by the proper clock cycle (compare Figure 67 – violation for t_{setup} = 5 ns and Figure 68 – violation for t_{setup} = 3 ns).

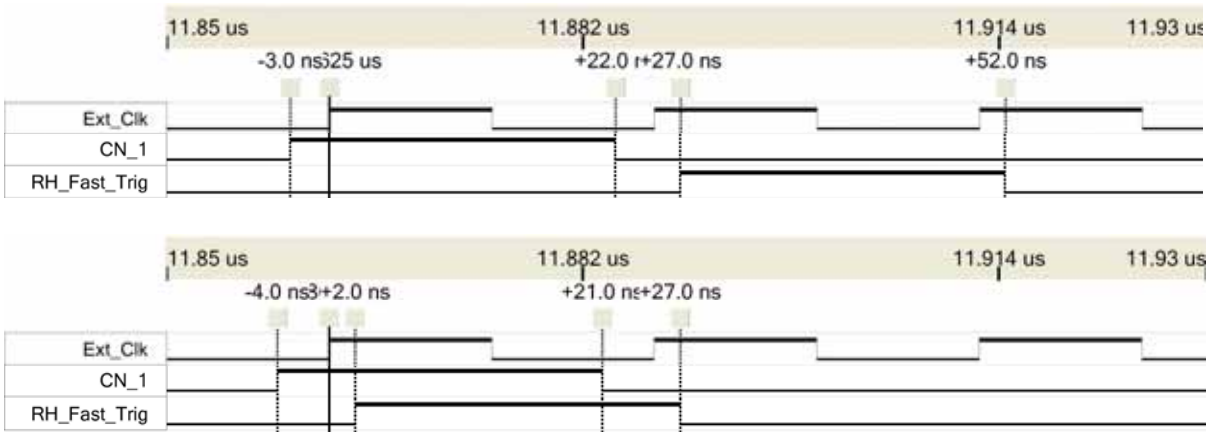

Figure 68 – The analysis of t_{setup} for CN_1 connected via Fast Input Register, t_{setup} > 4ns.

For 25 ns clock cycle, the 1st variant of direct connections gives relatively small safety margin of synchronization; only (25–10–6) ns = 9 ns, the 2nd one significantly improves safety to (25–7–4) ns = 14 ns. That time (for propagation of the trigger between pins of chips) is enough. That configuration has been also practically verified in the full temperature range (–20°C… +70°C).

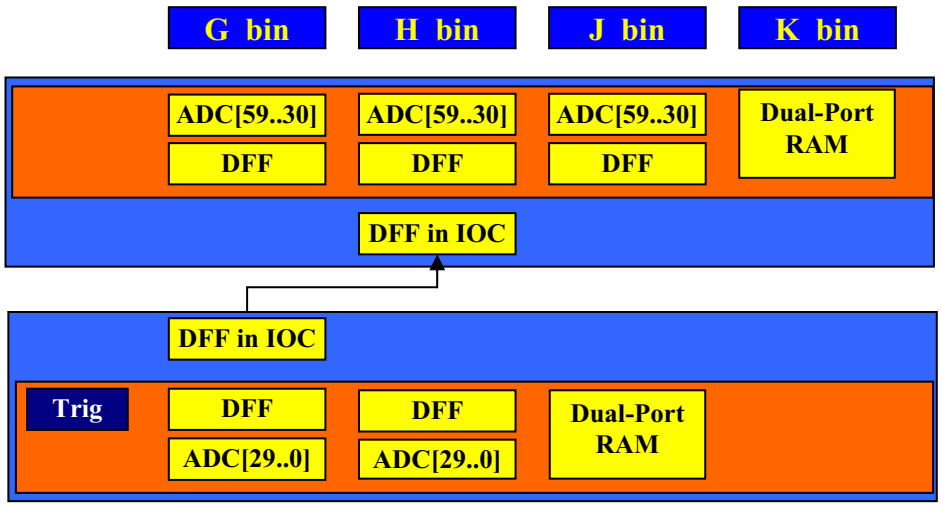

Figure 69 – Synchronization of chips. Trigger from ACEX_A transferred via two fast output–input registers located in I/O cells. Inserted H_bin routine in ACEX_B causes one clock cycle delay of ADC[59..30] data writing into the internal memory.

The variant shown in Figure 69 has been implemented into the ACEX design. Redundant DFF in IOC in the ACEX_A shorten the propagation time on 3 ns, the DFF in IOC in the ACEX_B extends the safety margin for the setup time on 2 ns. Finally, the synchronization range is bigger on 5 ns = 20% of the clock period.

3.2.3 Readout system.

On the contrary to the APEX design, data from both chips are transferred in non–interlaced mode, at first all data from ACEX_A, next from ACEX_B. Shorter multiplexer (MUX) chain (Figure 70) requires only 4 pulses for data pre–fetch (data to be available for DMA transfer).

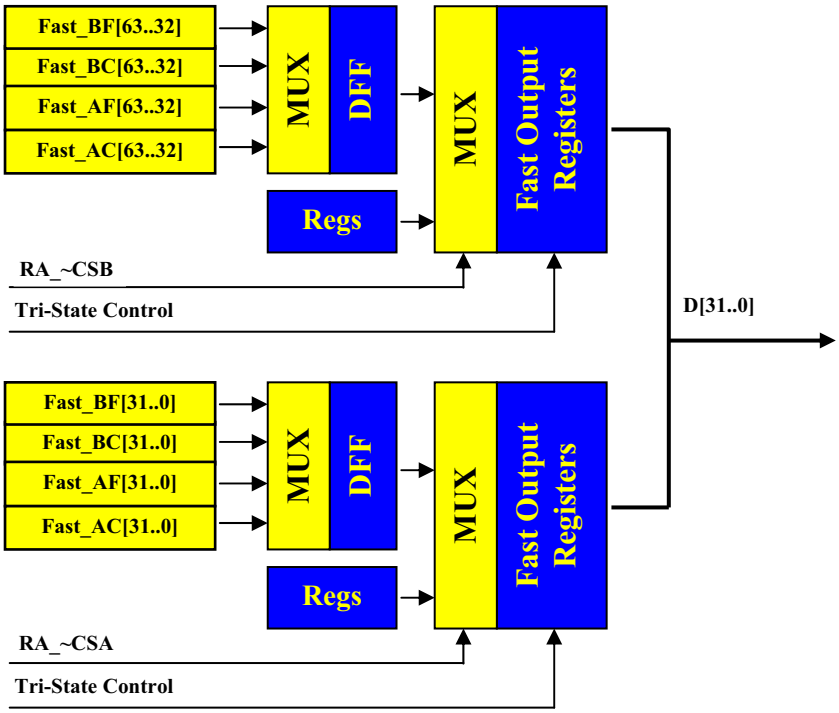

Figure 70 – Readout schematics for the ACEX design.

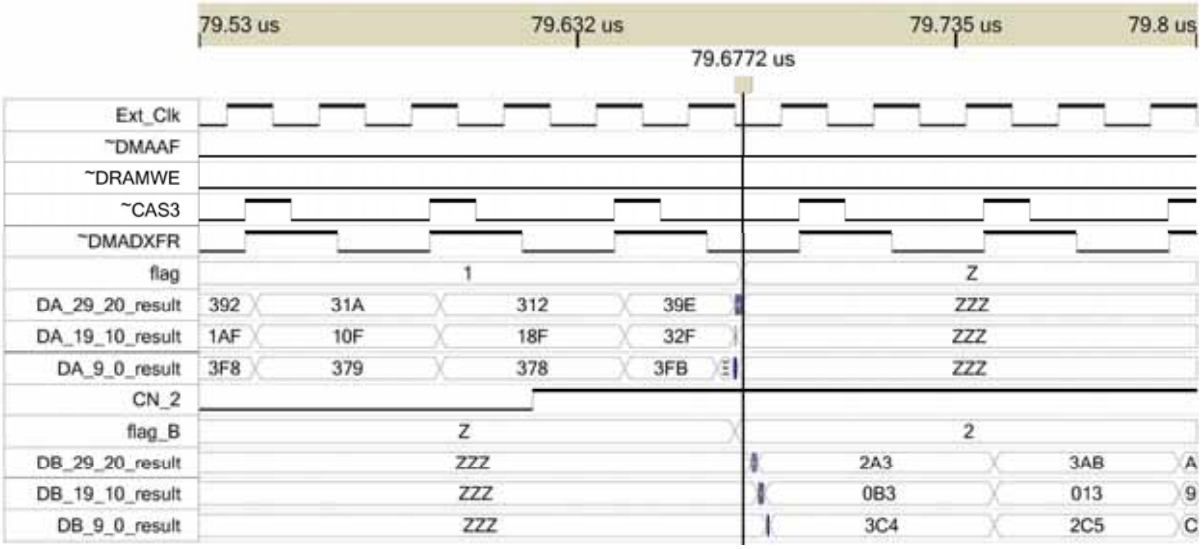

Figure 71 – Simulation of the DMA transfer with “on the fly” buffers switching. The last word from the ACEX_A is shorten and corresponds to the 0WS mode. The margin, when all busses are in the tri-state mode, is very narrow ~ 2 ns only. But, real measurements confirmed reliability of that “on the fly” buffer switching and continuous DMA transfer.

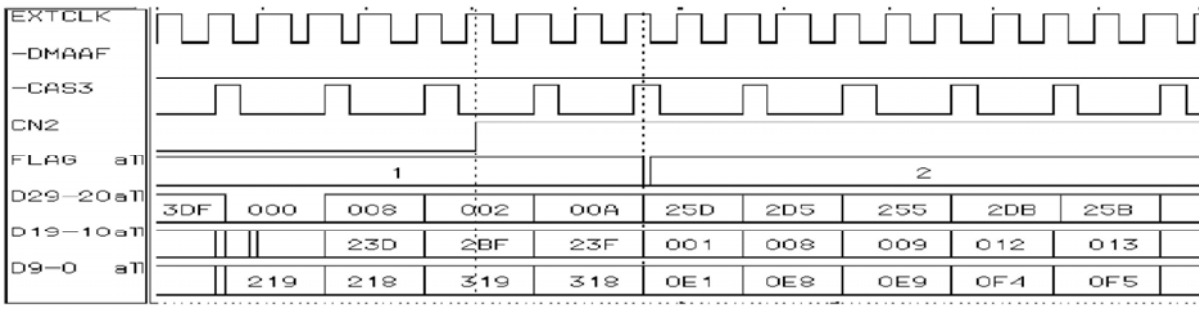

Figure 72 – View with logical analyzer of the "on the fly" buffer switching.

The readout system has been designed to allow continuous data transfer from both buffers, without intermediate state for buffers switching. Buffers are switched on the fly during the DMA transfer (as shown on the simulation in Figure 71).

This automatic mode has been fully confirmed (Figure 72) even in the 0WS mode. The PLD100 design has been preliminary approved as the baseline for the surface detector trigger on the Pierre Auger Collaboration Meeting in April 2002 [49]. Simultaneously, before the final decision, advanced tests of the trigger in a full temperature range (–20°C…. +70°C), as well as for much higher frequency 62.5 MHz (in comparison with the system clock 40 MHz) have been proposed. All tests have been performed in June 2002 [50]. Results confirmed that the internal structure of the PLD chip perfectly works in full temperature range, also for 62.5 MHz. Several variants of DMA transfers for fast and slow channels have been tested. Fast DMA for 1WS works perfectly, DMA transfer for the slow channel however needed additional measurements and an optimization of the algorithm.

The ACEX design has been approved by the Collaboration for the Auger South. 800 ACEX Front-End Boards (Figure 73) have been fabricated and installed in the pampas.

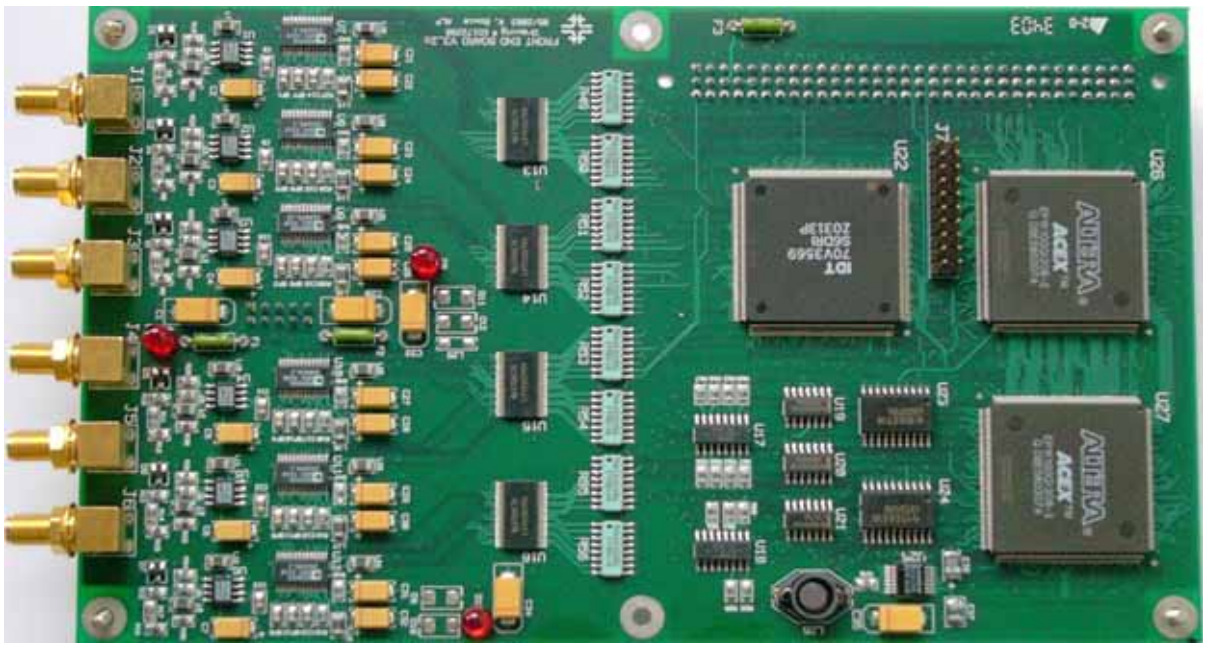

Figure 73 – The ACEX Front End Board.

3.3 Cyclone design

3.3.1 Introduction

A permanent progress in electronics was an inspiration to develop the 3rd generation of the FLT. In May 2003 the new Altera® FPGA family Cyclone™ appeared on the market. New chips allowed significantly simplifying the construction of the surface detector trigger as well as decreases the total costs and improves parameters. In comparison with ACEX® 1K chips, Cyclone™ chips contain much larger internal memory (it makes possible an implementation of the slow memory inside the PLD chip or an extension of the fast buffers). The core of Cyclone™ is supplied by 1.5 V, which reduces power consumption in comparison to the ACEX® 1K chips supplying by 2.5 V. The single chip allows implementing interlaced DMA mode and avoiding problems with chips synchronization [51-52].

Table 3 – Cyclone™ chips features [39].

Table 1–1. Cyclone Device Features

Feature	EP1C3	EP1C4	EP1C6	EP1C12	EP1C20
LEs	2,910	4,000	5,980	12,060	20,060
M4K RAM blocks (128 × 36 bits)	13	17	20	52	64
Total RAM bits	59,904	78,336	92,160	239,616	294,912
PLLs	1	2	2	2	2
Maximum user I/O pins *(1)*	104	301	185	249	301

For Auger code adapted to Cyclone™ chip the Quartus® compiler showed the registered performance on the level of 130 MHz. Such a high internal speed allows increasing the sampling frequency, which could improve a time resolution of the trigger. More resources allow implementing either new kind of triggers or merging slow buffers (as FIFO) to the PLD chip as a single chip solution. Such an approach has not been however accepted, due to too short internal slow memory buffer (however preliminary estimation accepted only 3584 words length) and no more room for other trigger implementation. Analysis and discussions concluded that it does not make sense to use a remaining internal memory for a slow buffer only; its utilization for new kind of triggers seems to be much more justified [53].

As the reasonable compromise between a price and a performance, EP1C12Q240I7 industrial temperature version chip in the PFQP package has been chosen. EP1C6 family contains too few logic elements (LE). The amount of LE should be on the level at least 8000 as in the previous designs (compare designs in Table 4). EP1C20 family is too expensive (see Table 3). Preliminary considered FBGA package has been rejected due to relatively high expenses for an assembling and Roentgen inspection.

Table 4 – A comparison of resources in the consecutives designs.

Family	Chip	LE	Mem bits	PLD chips	Mem chips	Applied
ASIC				1	0	Terminated in May 2002
APEX	EP20k200RI240-2	8 320	106 496	1	1	Used in 40 tanks in EA
ACEX	2×EP1k100QI208-2	9 984	98 304	2	1	Pre-production 800 tanks
Cyclone	EP1C12Q240I7	12 060	239 616	1	1	Production – next 800 tanks
Cyclone III	EP3C40F324C7	39 600	1 134 k	1	0	Prototypes in 2009

3.3.2 Internal routines

Generally the algorithm used in the Cyclone design is the same as in the ACEX design. This was the fundamental condition in order to approve the trigger/memory circuitry of the next generation based on the other family. After the Critical Design Review in 2003 the Pierre Auger management planned to cover the entire array homogenously by the approved ACEX design. However if the electronics on the entire array is not fully homogenous, any discrepancies in successive design generations have to be reduced to minimum.

The ACEX design had to use two parallel working chips due to limited internal memories. The selected Cyclone™ chip contains sufficient resources (both logic elements and internal memory bits) in order to implement algorithm from the master and slave ACEX® 1K chips respectively to a single chip only. An implementation of entire algorithm to a single chip has a big advantage; no synchronization between chips is needed. An additional logic for a synchronization of master and slave chips used in the ACEX design can be now totally removed. It frees additionally some logic elements. Also some logic, which has to be duplicated in the slave chip, (like address decoders) can be now removed also.

The registered performance of Cyclone™ chips is much higher in comparison to ACEX® 1K. It is a consequence of a new architecture of internal connections and new production technologies. Relatively slow routines (like adders) implemented in ACEX® 1K chips in pipeline chain and requiring two clock cycles can be implemented in Cyclone™ chips as a single clock cycle process. It allows reduction of resources utilized previously for parallel delaying of signals for their synchronization.

Lower resources occupancy (~40–50%) in Cyclone™ in comparison to ACEX® 1K (~70–80%) allows also much better optimisation of internal connections.

The requirement of implementation of the same functional algorithm into Cyclone™ does not exclude utilization of all advantages of the new family features. The selected Cyclone™ chip contains two internal PLL routines providing up to 6 independent clocks. A relative shifts between clocks can optimise processes, where phase relations between signals are crucial, i.e. DMA transfer.

Still free resources can be used in the future for new algorithms implementations. It is especially important for some specific type of showers, for which the current triggers seems to be not optimised. The resources occupancy in ACEX® 1K on the level 70–80% does not allow on adding any new significant routines. 100% occupancy of internal memories limits seriously any possible even small improvement of algorithms, i.e. implementation in logic elements of full bus shift registers is extreme spendthrift vs. an implementation in the internal memory.

The global routine schematics are similar as for the previous designs and they will not be shown in details. The slow channel remains exactly the same. The fast channel is simplified in comparison to the ACEX design by removing glue/synchronization logic.

The single chip design is similar to the 1st design based on the APEX™ 20K chip, where the interlaced mode for the DMA transfer has been used. However, in order not to change the UB software, the system still utilizes the non–interlaced mode of the DMA transfer.

3.3.3 PLL and DMA transfer optimization

ACEX® 1K industrial version chips used in the 2nd generation design support neither PLL 40 MHz clock with the multiplication factor ×2 nor any precision shift tuning. In the ACEX design PLL was not used at all. Cyclone™ chips offer phase locked loops and a global clock network for clock management solutions. Cyclone™ PLL offers clock multiplication and division, phase shifting, programmable duty cycle and external clock outputs, allowing system–level clock management and skew control. The Altera® Quartus® II software enables Cyclone™ PLL and their features without using any external devices. That feature was used for an optimization of the DMA transfer.

Both fast and slow channel are double buffered to reduce a dead time. However, if two consecutive events appear in short intervals, which cause fulfilling both adjacent buffers, triggers would be disabled till at least one of the buffers will get empty. A dead time depends on the data transfer speed (from FPGA to μC). 0 WS modes provide a maximum speed. Laboratory temperature tests confirmed a reliability of that mode, however to extend a safety margin in a real temperature extremes inherent in an uncontrolled environment, 1 WS mode has been chosen for DMA transfer in both channels. However, the additional wait state without a possibility of the internal clock shift can extend either setup or hold time of data transferred in DMA. Cyclone™ provides a precise internal clock tuning with a 10 ps grid. Precise shift of PLL clock in comparison to the external global clock assures optimal stable data position related to the falling edge of ~CAS3 edge responsible for the DMA data transfer.

Two Cyclone Front End Boards with the codes optimized for 0 WS and for 1 WS were tested in the climate chamber in the same conditions as the ACEX Front End Boards. Results show that temperature deviations for setup and hold times are not big and the safety margins for both 0 WS and 1 WS transfers are still sufficient for the entire temperature range.

Data are transferring from the FPGA to the μC by the falling edge of the ~CAS3. For the 1 WS DMA transfer for the ACEX design only for the 1st word ~CAS3 occurs in the middle on the stable data. For next transferred words the setup time (an interval between the beginning of a stable data area and the falling ~CAS3 edge) is much shorter than the hold time (an interval between the falling ~CAS3 edge and the end of the stable data area) (see Figure 74).

For the Cyclone™ chips the positions of the stable data for the DMA transfer can be tuned by the PLL. The safety margin for setup times is much larger than for the ACEX design, for the hold times is still sufficient (compare Figure 75).

The dynamic memories refreshment can interrupt the DMA transfer. PLL parameters are optimized for the fast channel as more critical. For the slow channel ~CAS3 occurs not in the middle of the stable data, however the hold time on the level 20 ns is still much higher than a required 10 ns (see Figure 76).

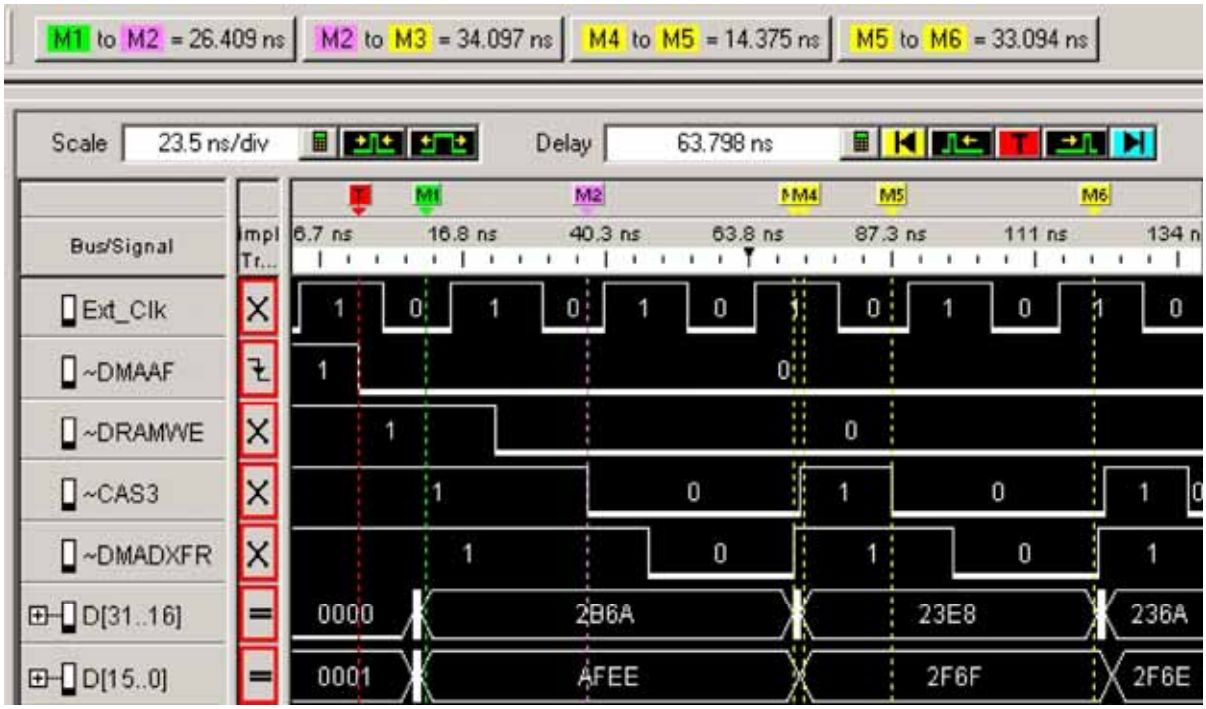

Figure 74 – View with logical analyzer of the beginning of the fast 1WS DMA transfer for ACEX® 1K. Data are transferring from FPGA to the UB by the falling edge of the ~CAS3. Only for the 1st word ~CAS3 occurs in the middle on the stable data. For next transferred words t_{setup} is much shorter than t_{hold}.

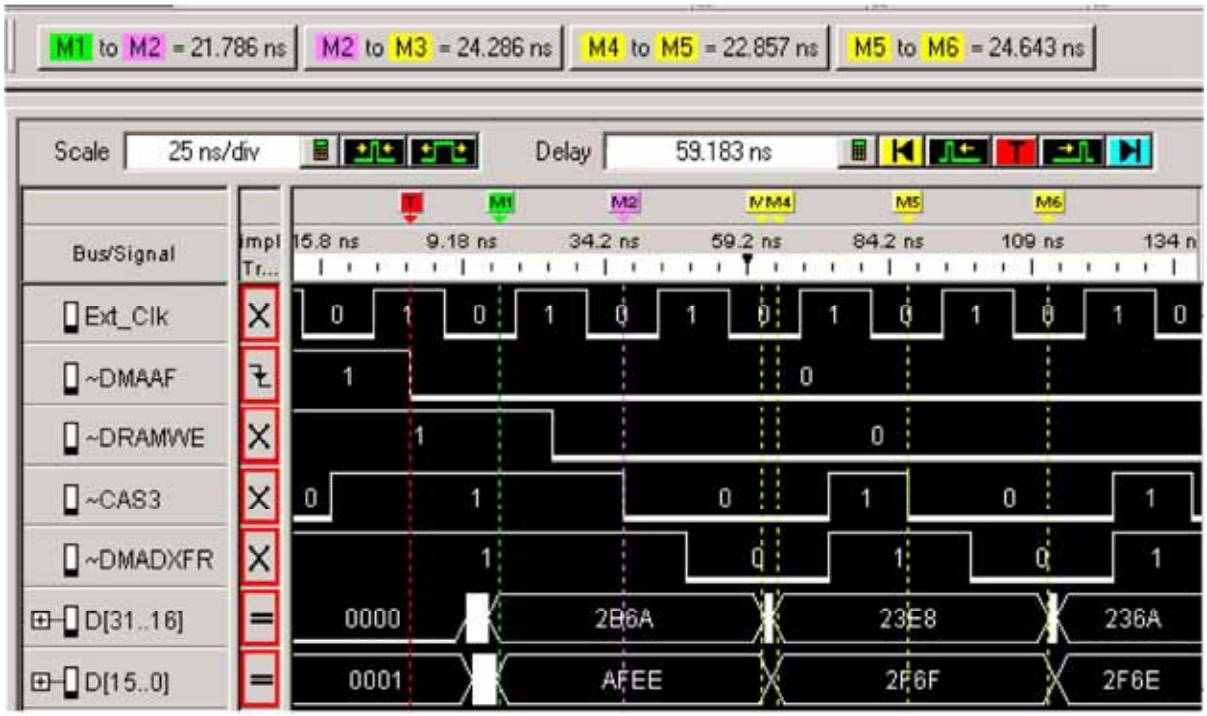

Figure 75 – View with logical analyzer of the beginning of the fast 1WS DMA transfer for Cyclone™. The positions of the stable data for transferring are tuned by the PLL. The safety margin for setup times is much larger than for the ACEX design, for the hold times is still sufficient.

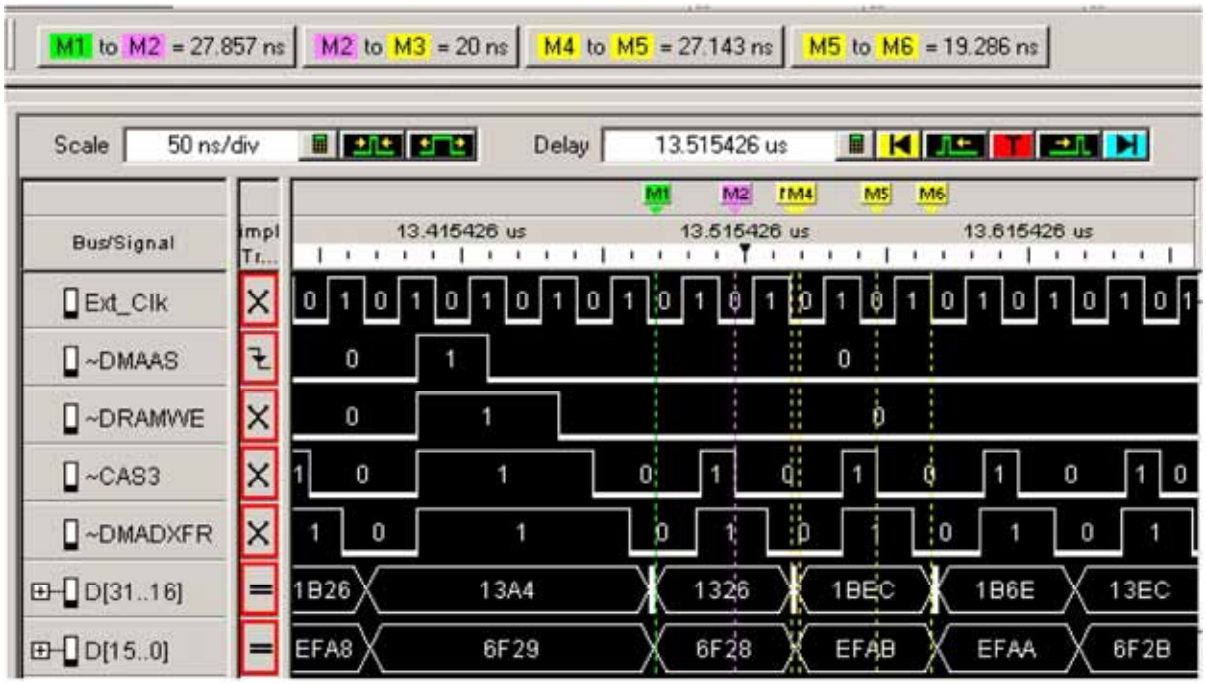

Figure 76 – The logic analyzer view of the slow 1WS DMA transfer for Cyclone™ (an short interruption for dynamic memory refreshment). PLL parameters are optimized for the fast channel as more critical. For the slow channel ~CAS3 occurs not in the middle of the stable data, however the hold time on the level 20 ns is still much higher than a required 10 ns.

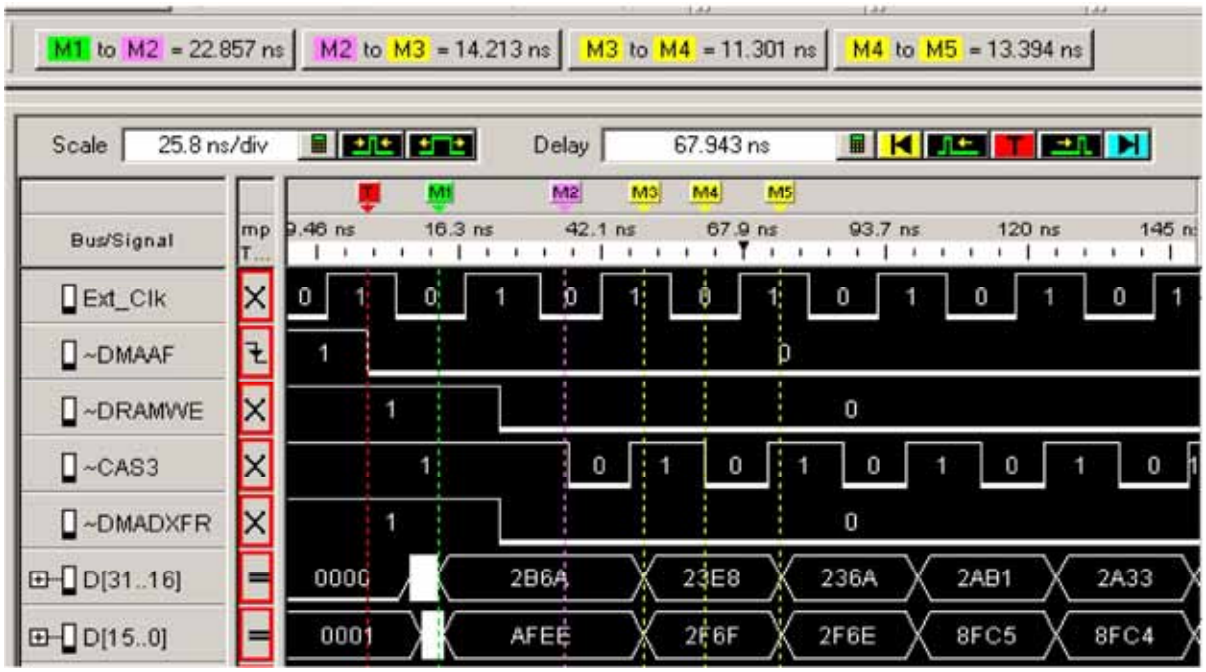

Figure 77 – 0WS DMA fast mode assures still a safety transfer.

0 WS mode offers a satisfactory timing (see Figure 77), however due to for a safety reasons related to the heavy environmental condition on pampas the 1WS mode has been

selected. 10 prototype Cyclone boards have been produced in March 2005 and have been tested in the same condition as for ACEX one. As previously for 120 hours of continuous data comparison with the temperature variation in the full –20 ºC up to +70 ºC range no one bit has been distorted for a transfer of totally 48 GB. It gives the final error rate is less than 2.5×10^{-12}.

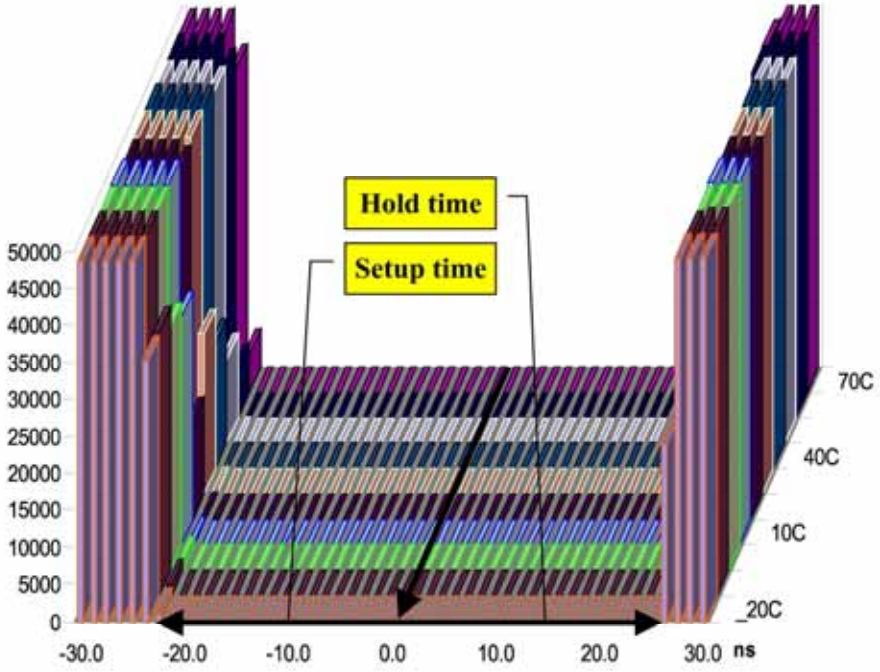

Figure 78 – Errors between a reference pattern at 0.0 ns and the data at shifted interval for the Cyclone™ 1WS mode.

Patterns generated in the internal pattern generator, processed in the fast channel, transferred via DMA are next compared in the μC with expected patterns obtained from simulations. The setup time is calculated as the time, where the received data still agrees with expected patterns starting from the falling ~CAS3 edge towards the earlier time with 1.25 ns grid related to the 800 MHz logic analyzer sampling. The hold time is calculated similarly, starting from the falling ~CAS3 edge towards later time. If received data stops agreeing with the expected pattern, errors started to be put on the vertical axis. Figure 78 shows that disagreement between received data and expected patterns appears ~20 ns before the falling edge of the ~CAS3 (it corresponds to the setup time) and ~25 ns after the falling ~CAS3 edge (it corresponds to the hold time). Dependence vs. temperature is weak.

3.3.4 Tests of the FEB and performance in the field

Prior to production of the full batch of 900 FEBs at Intratec-Elbau (Berlin, Germany) [54], 10 units were manufactured in a pre-production batch to verify the new design. The boards were tested intensively in the lab and in the climate chamber and no malfunctioning was observed. In order to perform the acceptance tests of the full batch within a time period of about half a year, a highly automized test bench has been developed and installed in the laboratories at the Wuppertal and Siegen Universities [55].

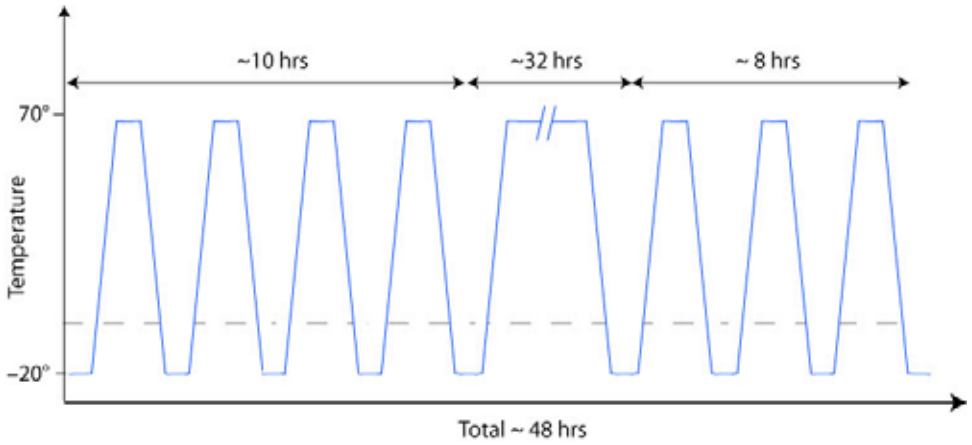

Figure 79 – Temperature profile for burn-inn test.

First, the boards were powered up and the current in the digital and analog part was verified to be in the specified range. All manufactured boards passed these initial tests. Next, groups of up to 22 boards were placed into a climate chamber (Figure 80) and a burn-in was performed under full current for 55 hours (Figure 79). It started with 4 thermal cycles between +70 °C and -20 °C over a period of 10 hours, followed by a 35 hours burn-in period at +70 °C followed again by 10 hours with 4 cycles between +70 °C and -20 °C. Formation of dew during temperature cycling was avoided by enriching the atmosphere in the climate chamber with Nitrogen.

A sketch of the hardware test configuration is depicted in Figure 81. A waveform generator provided pulses of various forms to a high quality 3×6 channel multiplexer. The 18 outputs were fed into three FEBs for simultaneous testing. Each of the multiplexer outputs could be switched on/off individually via a GPIB interface so that selected groups of FEB channels could be tested and cross-talk tests be performed. Data readout of the FEBs was performed via the Pierre Auger surface detector UB. Different from the operation in the field, data transmission was not done via a microwave link but via an extra RS232 interface integrated on the SC for diagnostic purposes when working on the station in the field. The RS232 interface could also be used for uploading the firmware into the UB after powering up. The FEBs were controlled via custom made synchronous opto-coupled links using the parallel-port interface of the PC and the I^2C protocol for data exchange. The PC also controlled the waveform generator, multiplexer, and climate chamber, so that the full sequence of acceptance tests could be programmed and run in an automized way.

The full sequence of tests at -20 °C, +25 °C and +70 °C and with data storage on the PC lasted about 4 hours for three simultaneously tested boards. Most of the time was actually needed for changing the temperature in the climate chamber. In this way, up to 9 boards could be tested per day.

If the FPGA chip is programmed correctly, the communication with all registers is verified by writing and next reading several tens random numbers per address. A comparison between uploaded and downloaded data must be perfect. No any distortion is tolerated. For diagnostics, several test routines have been implemented additionally into the FPGA code. The 1st pipeline stage in the data flow chain, which in DAQ mode is buffering ADCs and addresses busses, ~CS, R/~W, etc. signals contains also “events” and “noise” pattern generators.

Figure 80 – Up to 22 FEBs were placed in a climate chamber for burn-in under electric power.

The “events” generator is sending 10 pulses (on ADC[29..20] the sequence is #3FF, 0, #3FFh,... , 0, #3FF) and afterwards a pulse (#3FF) each Div1×Div2 (μs). The bus ADC[9..0] is increasing/decreasing continuously with the clock cycle; bus ADC[19..10] is decreasing/increasing respectively. The sum of both busses ADC[19..10] + ADC[9..0] is constant = #3FF. The “events” generator is controlled by two 12-bit words treated as dividers of the main clock. Preliminary the global clock is divided by 40 to 1MHz, afterwards divided again by a product of Div[23..12]×Div[11..0]. With that frequency ADC[29.20] bus is toggled on/off from the zero to saturation state. This generator was used to measure the current consumption for the I/O and the core of the FPGA vs. a trigger rate.

“Noise” generator generates pseudo-random signal useful to verify a behavior of system, when no any correlation between busses is expected and when any regularity in the following DMA transfers may hide some distortions. In the “noise” generator all bits in two 10-bit up and down counters are mixed together and additionally Ex-ORed with 30-bit pattern register. Patterns in consecutive DMA transfers were changed by additional mixing of bits with counter of DMA transfers independently for the fast and slow channels. “Noise-like” patterns obtained in simulations are next used for comparison online with patterns generated in the real, internal generator inside the FPGA. Due to limited memory space in the UB, the patterns for fast and slow channels were limited to 768 kB and 512 kB respectively. It corresponds to 128 and 64 DMA transfers for fast (6 kB = 768 words of 60 bits) and slow (8 kB = 2048 words of 30 bits) channels respectively. Data from the pattern generator are given on the regular data flow chain instead of ADC data. They pass through all trigger/memory processes and finally are sent to the UB, where are compared with patterns obtained from simulations. Internal counters are synchronized with the DMA transfers to provide proper patterns for comparisons. These tests were performed as the 1st one in each temperature before checking analog section of the Front-End.

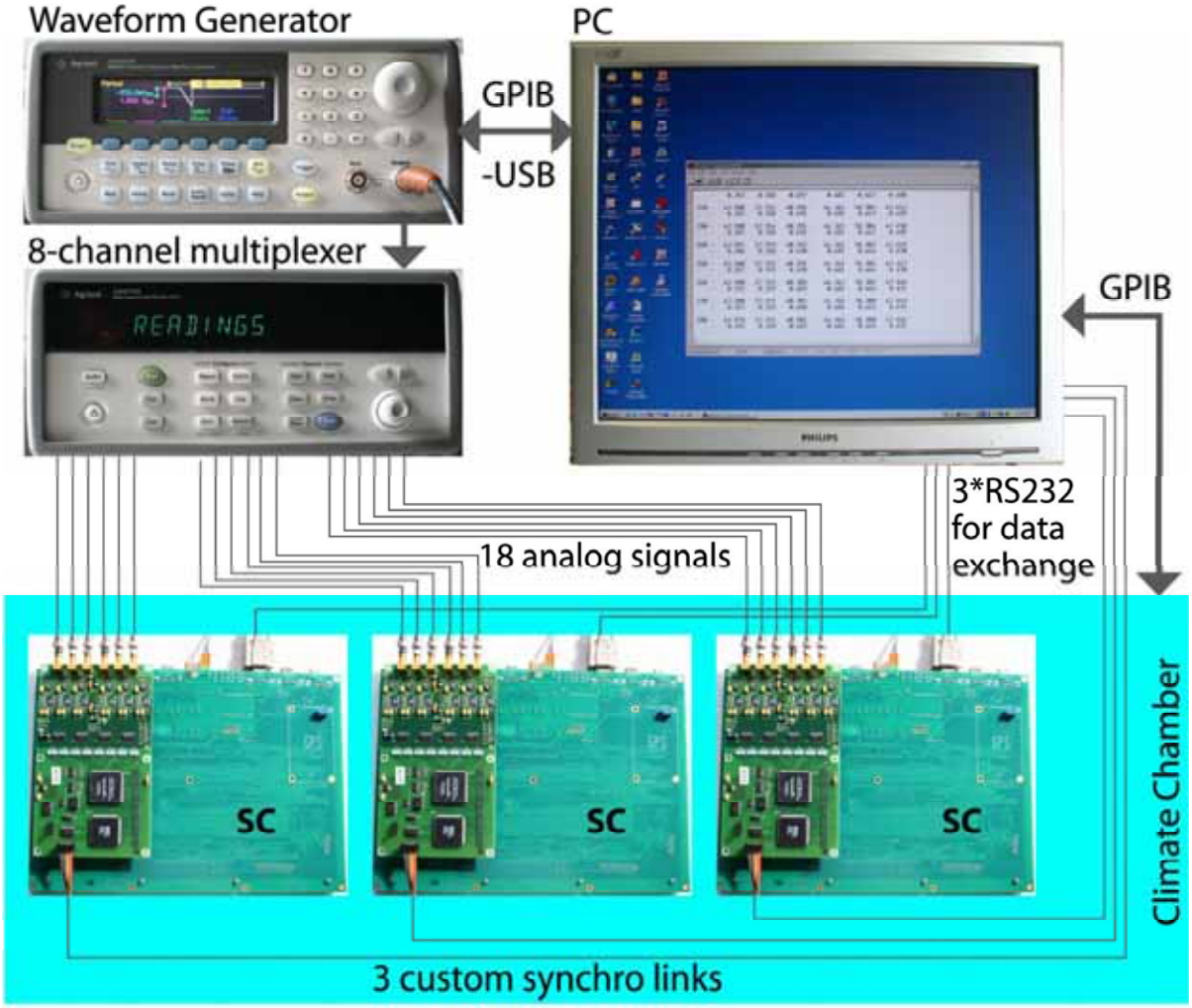

Figure 81 – Sketch of the automized test system.

3.3.5 Apparent differential non-linearity

The global and differential non-linearity was tested by ramping up the input signals using a saw tooth waveform and analyzing the digitized signals as a function of time (sample number). The rising edge of the analog signal was 19.2 μs corresponding to the 768 words length of the fast buffer registering the shower profile. For the global linearity the correlation coefficients (*CC*) were calculated for all 768 words. The values of (1 - *CC*) typically were at a level of a few times 10^{-6}, slightly above the minimal value originating from the quantization of ADC-counts. The correlation between ADC-counts relating to consecutive time-bins allowed also finding suspicious transitions corresponding to differential non-linearity.

For this purpose, 64 measurements with ramped up signals were repeated and the deviation of the measured and expected ADC value in each of the 768 samples was filled into a histogram. In case the standard deviation integrated over the full ADC range exceeded 0.95 ADC channels, the board has been rejected.

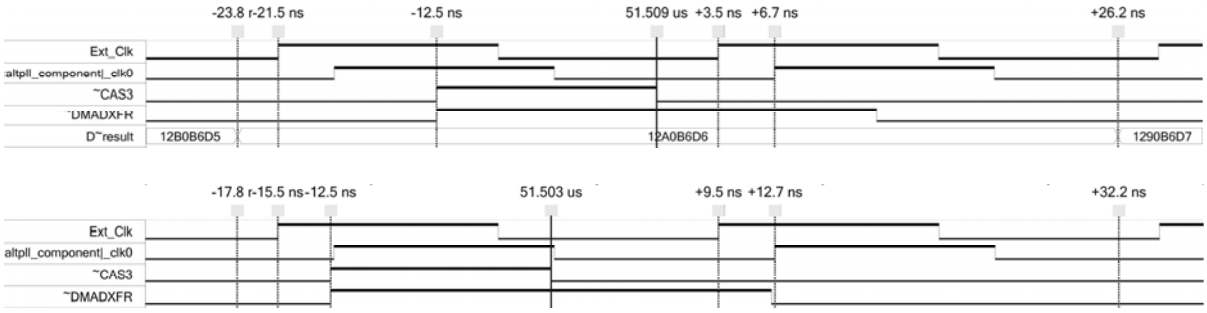

Figure 82 – Estimation of a stable area for the DMA transfer. Data are transferred for the falling edge of ~CAS3 (here at 51.509 μs). The position of ~CAS3 varies in the range of (15.5 ... 21.5) ns after the rising edge of the external clock [6]. For the effective PLL shift (6.5 - 3.5) ns = +3 ns the ranges of the setup and hold times are (18.0 ... 24.0) ns and (26.0 ... 32.0) ns respectively.

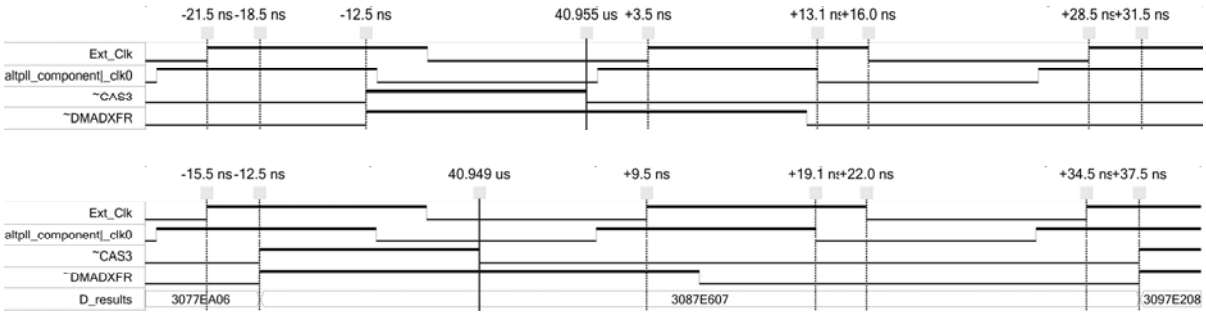

Figure 83 – Estimation of a stable area for the DMA transfer and FADC data latched in the 1st pipeline stage simultaneously. For the effective PLL shift (13.1 - 16.0) ns = -2.9 ns the ranges of the setup and hold times are (12.5 ... 18.5 ns) and (31.5 ... 37.5 ns) respectively. The selected mode of the DMA transfer is 1WS. Tests in laboratory conditions confirmed error-free transfer also with 0WS, however in order to enlarge a safety margin, 1WS has been selected at the expenses of an additional 38.4 μs dead time. Taking into account that the trigger rate is on the level of 100 Hz, the total dead time related to the 1WS DMA transfer increases on ~1% only.

Preliminary tests showed ca. 10% of channels in FEBs with suspicious structures in the linearity graphs (see Figure 4), but only in a temperature –20 °C. This apparent, differential non-linearity in fact was a result of a violation of FADC data latching in the first stage of the FPGA pipeline. Originally the DMA transfer has been optimized to reach a maximal stable area for transmitted data. Data are transferred from the FPGA into the DRAM in the UB by falling edge of the ~CAS3 edge. The required setup and hold times for the DRAM used in the UB are 0 ns and 8 ns respectively. In order to get a maximal stable area the setup time for the DMA transfer should be (50 - 8)/2 = 21 ns. The jitter of ~CAS3 is 6 ns (the time from rising edge of the clock to the falling edge of ~CAS3 varies from 15.5 till 21.5 ns [6]). Taking it into accounts the setup and hold times should be in the following ranges (18...24 ns) and (20...26 ns) respectively. This requires to set the PLL internal clock with the phase shift of 6.5 - 3.5 = 3 ns (Figure 82).

According to Altera note an internal clock in a normal mode is phase-aligned to the input clock pin. However, the simulator shows additional, unexpected shift -1.8 ns vs. the expected rising edge of the internal PLL. Taking it into account the phase shift in the PLL

Quartus® wizard has been selected to 4.8 ns. According to the spec of the AD9203, the output FADC data are stable ca. (4 ... 7) ns after the rising edge of the clock (external from the view of the FPGA). +3.0 ns shift of the internal clock is however close to the minimal value of FADC data stable area = 4 ns.

Although the temperature -20 °C is supposed not to be reached in any time, the PLL condition has been modified to enlarge the stability region of data latched in the 1st pipeline stage at the expenses of shorter setup time in the DMA transfer. The PLL shift in the Quartus® wizard has been chosen as -1.04 ns, which gives effectively a shift (19.1 – 22) ns = -2.9 ns (Figure 83).

The required setup and hold times for the DRAM K4E660812E are 0 ns and 8 ns respectively. By the optimized parameters the safety margin is still sufficiently wide. Tuning the internal PLL clocks to the stable DMA region allowed to fully fixing the virtual problem. In total, 6 only of the 900 tested FEBs were rejected by the acceptance tests because of their real differential non-linearity.

3.3.6 Noise vs. locations of the FPGA and the Dual-Port RAM

The layout of the ACEX board has not been well optimized (see Figure 73). ACEX® chips are located very far from the FADCs, connections are long and make half-loops. 60-bit bus from FADC is squeezed. Distances between lines are small. It may cause cross talks.

10 Prototype Cyclone FEB have been fabricated with only small modification of the PCB in comparison to the ACEX design. However, swapping positions of the FPGA (Cyclone™) and DPRAM on the PCB board in the 3rd generation simplifies the layout and in consequence reduces a danger of cross talks (compare Figure 84 and Figure 85). Additionally, the Cyclone core is powered by the 1.5 V, the DPRAM by 3.3 V. Preliminary measurements showed that the noise level generated by Cyclone is lower than the noise level of DPRAM. For mass production the PCB of the new FEB has been designed. Inputs/Outputs in Cyclone have been assigned to appropriate pins in order to reduce as possible connections length on the board, avoid loops and simplify the data flow as possible.

The noise in the prototype Cyclone boards was on the same level as in the 2nd generation design equipped with ACEX® chips. Optimization of the analog section allowed reduction of the noise level below 1 ADC-count in the high-gain channels and below 0.6 ADC-count in low-gain channel. Lower noise level in the high-gain channel (responsible for a trigger generation) allows improvement of the signal/noise ratio and reduction of spurious events triggered due to a noise contribution.

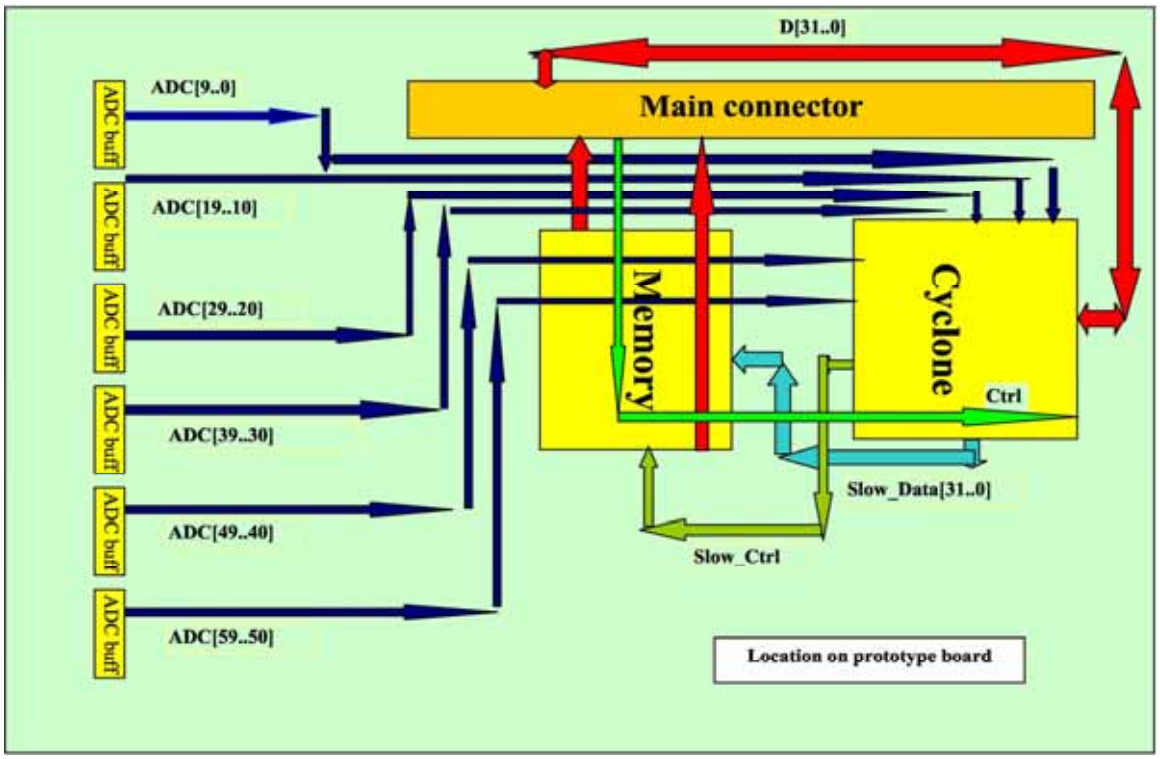

Figure 84 – The real connections on the prototype PCB Cyclone board (a prototype design).

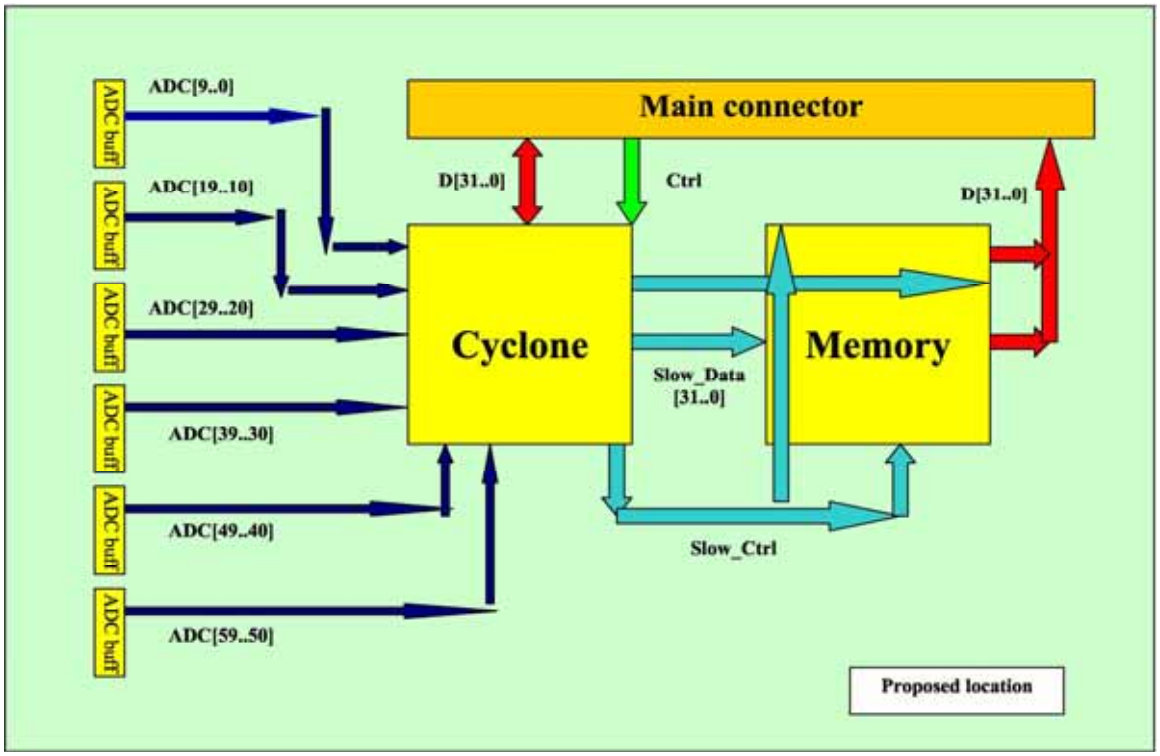

Figure 85 – Proposed connections on the PCB Cyclone FEB for the mass production.

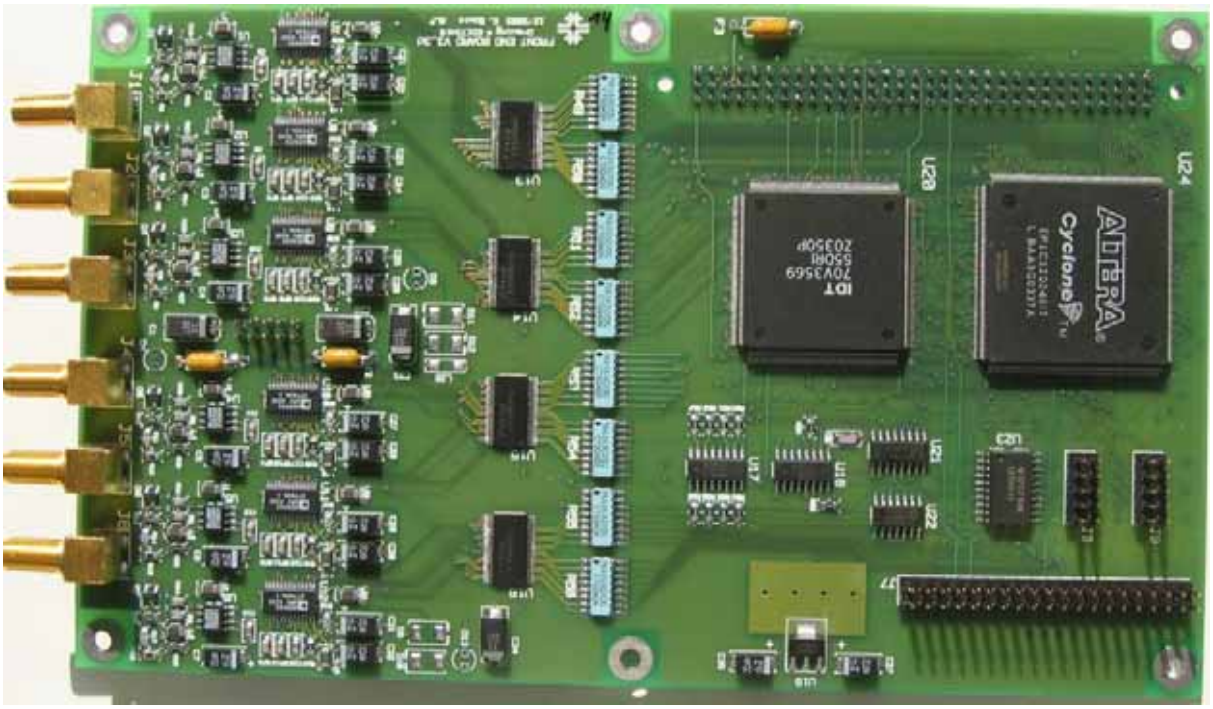

Figure 86 – Cyclone prototype board.

Figure 87 – Production Cyclone board.

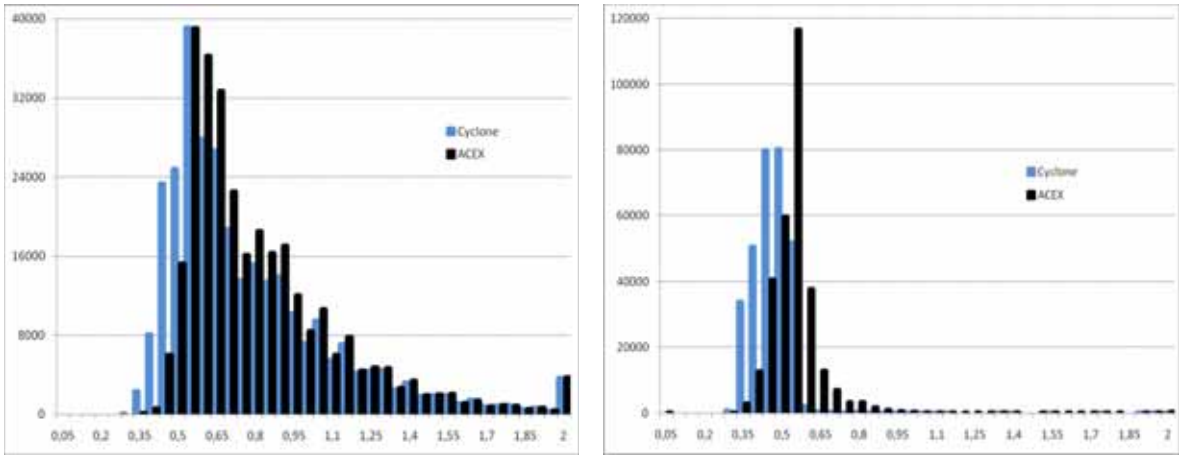

Figure 88 – Comparison of noise levels for the high-gain channel (left) and low-gain channel (right) for the Cyclone and ACEX FEBs measured in April 2008 for 175386 events registered in Cyclone FEBs and 324035 events registered in ACEX FEBs. RMS equal $\sigma_{Cyclone}^{high-gain} = 0.739$, $\sigma_{\text{Acex}}^{\text{high-gain}} = 0.780$, $\sigma_{Acex}^{high-gain} = 0.410$, $\sigma_{Acex}^{low-gain} = 0.497$ respectively. For ACEX® the noise is higher on 5.6 % for the high-gain channel and 21 % for the low-gain one in comparison to Cyclone boards. Graphs normalized to the same amount of events.

3.3.7 Custom monitoring

The standard Auger FPGA firmware does not provide a verification of the internal registers during a normal work. An access to the registers is possible, however only by specific commands from the UB level. Even the monitoring system (collecting data every 10 minutes) does not check the status of internal registers. The system works in dynamically changing conditions and the monitoring of some registers (especially controlling thresholds) seems to be crucial. In order not to modify the UB code and the CDAS package structure, the simplest way is to insert on the tail of FADC trace additional information on registers. The last words in the FADC trace correspond mostly to the noise. Replacing last 8 words by data from selected registers does not reduce real physics data.

Figure 89 shows the structure of modified traces with inserted registers on their tails. The width of all inserted registers is maximum 30 bits, because two most significant bits are neglected in FADC traces processing. FSThr, FWThr, FTThr are thresholds for the Threshold trigger, ToT trigger and 2nd ToT trigger respectively (the fast channel). SThrC, SThrD are thresholds for the slow channel. 30-bit thresholds actually merge three 10-bit thresholds for three channels : Thr[29..0] = (Thr_{ch3}[9..0], Thr_{ch2}[9..0], Thr_{ch1}[9..0]). ID registers identify a version of the firmware, date of the implementation and additional configuration info (ID_SUB). The rest of registers correspond to Enable, Status, Control registers etc. The reboot[51..22] is the register latching highest bits of continuously working counter starting its job after rebooting of the UB system. This mode with inserted registers is called a diagnostic one. The event showed in Figure 90 has been registered just in this diagnostic mode.

Large values on the tail of traces theoretically may cause a misinterpretation. However, some peaks very far after the trigger are rejected by the CDAS algorithms as uncompleted for an estimation of shower parameters. Nevertheless, the diagnostic mode provides additional information inaccessible in the standard monitoring.

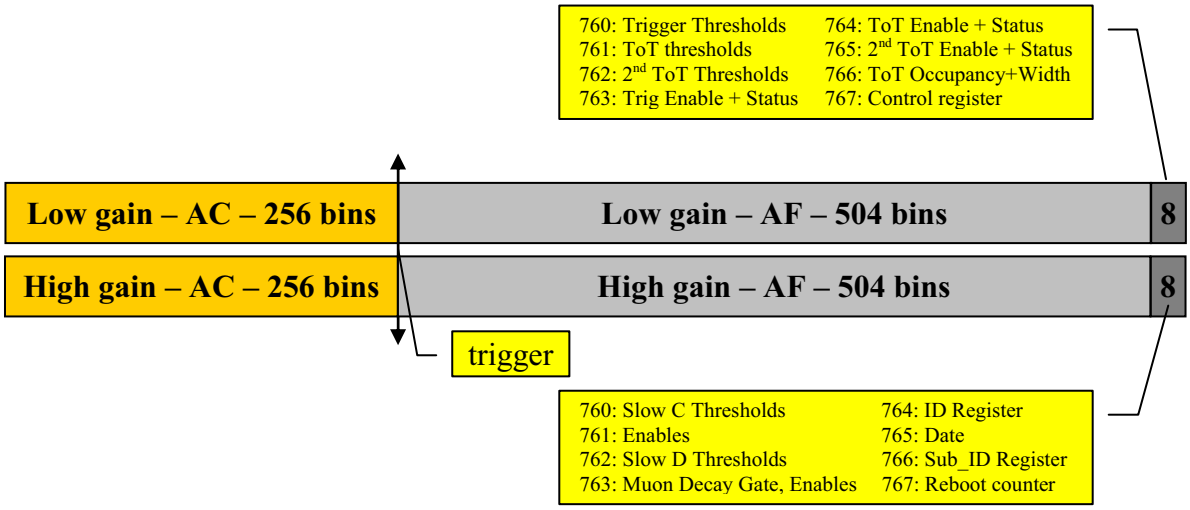

Figure 89 – The structure of modified FADC traces with inserted registers.

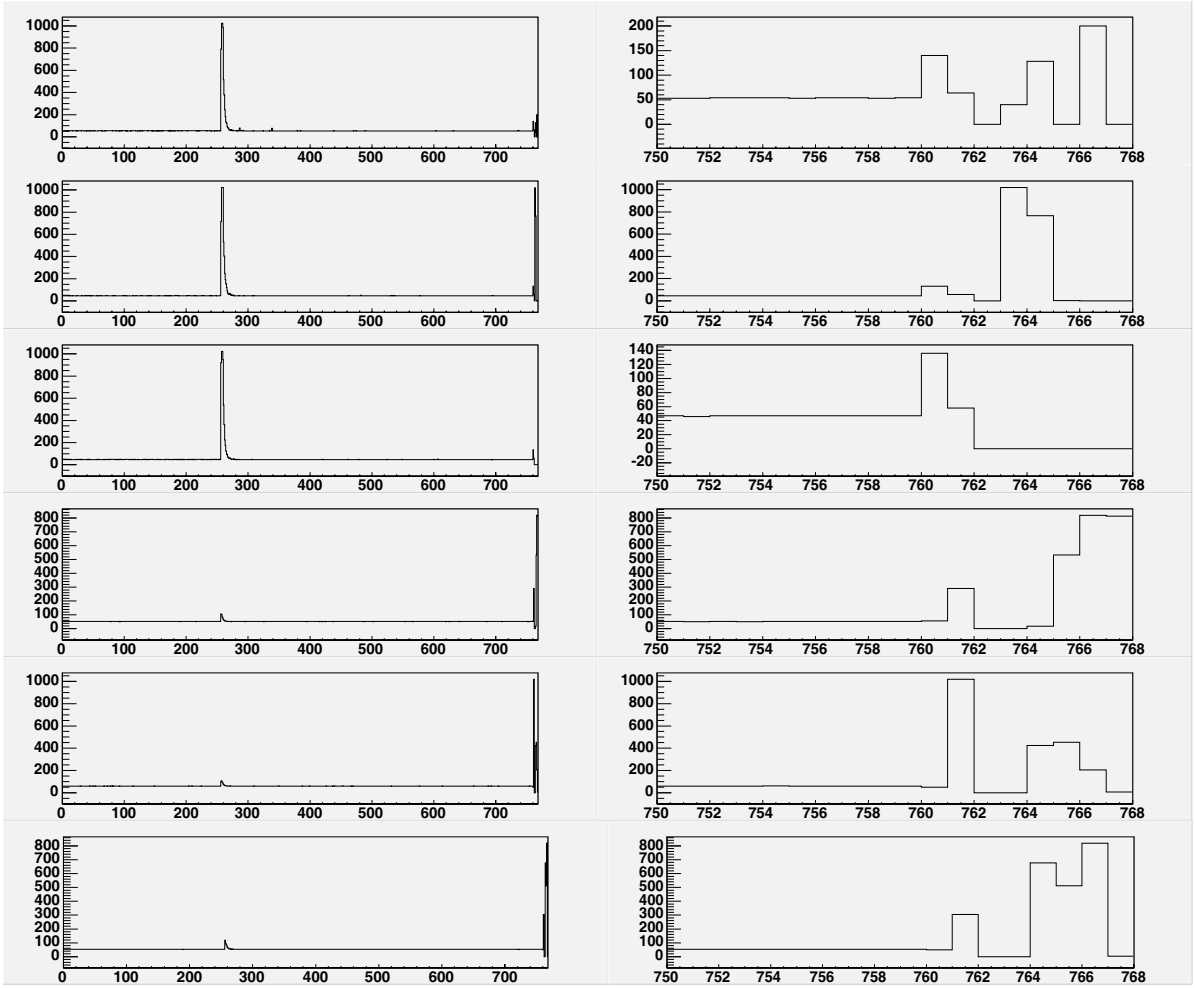

Figure 90 – The event 04744545 registered in the diagnostic mode. The left plot shows FADC traces in the full time range, the right one shows zoomed range of (750 … 767) time bins.

The tail of the trace, where the registers are inserted, follows the trigger after 504 time bins = 12.6 μs. This delay does not matter from the point of view of the monitoring (a slow control) in comparison to the sampling period of minutes in the standard CDAS approach.

The registers inserted into the 767^{th} time bin of the high-gain channel corresponds to the counter zeroed only after rebooting of the UB. It counts the system 40 MHz clock. First 22 bits are not monitored as related to the fractional seconds. The clock cycle 25 ns multiplied by $2^{22} = 4 \times 2^{20} \cong 4 \times 10^6$ gives 0.1 s interval, the resolution of monitored rebooting period.

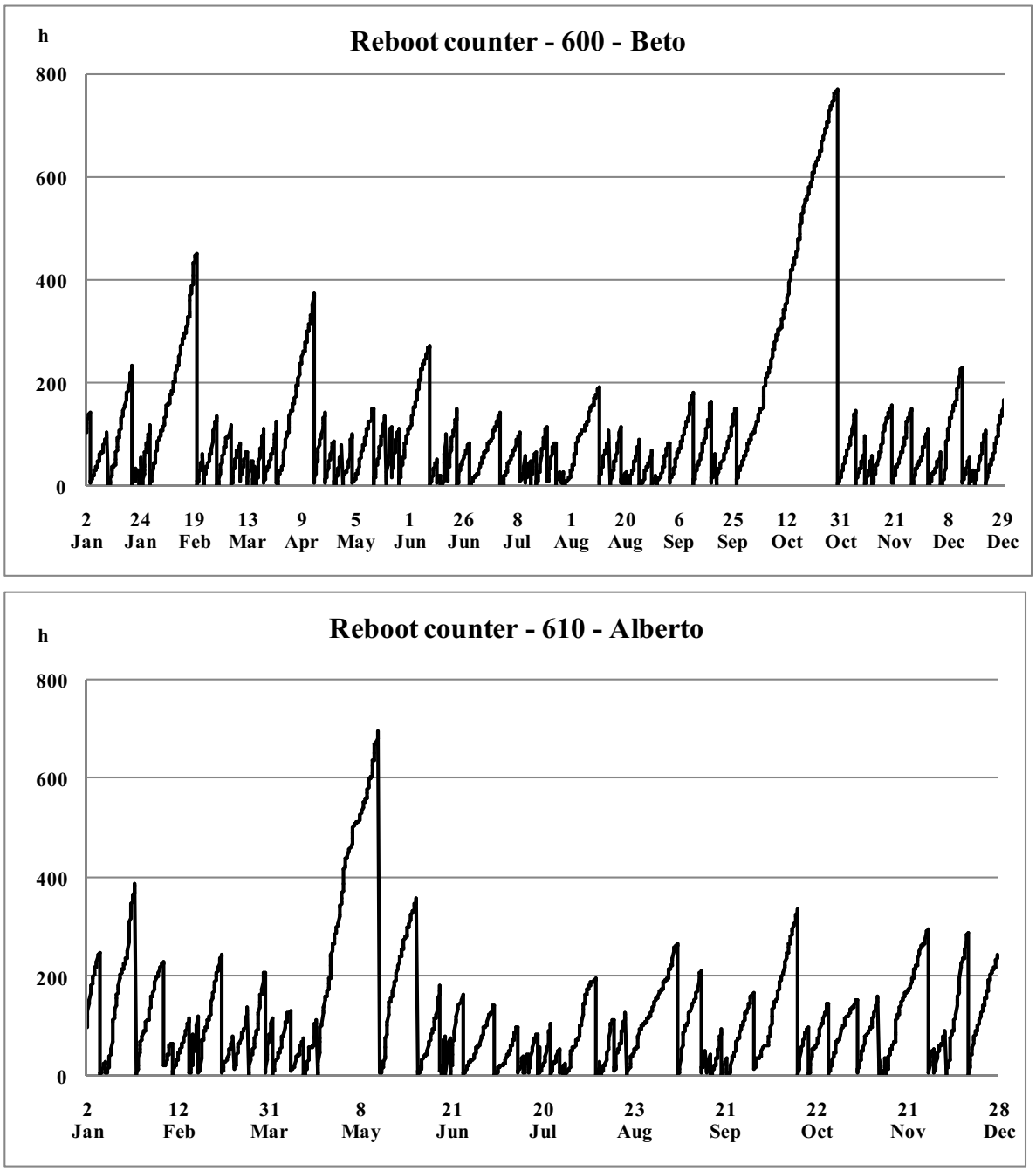

Figure 91 – Graphs showing periods of continuous works of the UB in the selected surface detectors: Beto and Alberto between successive rebooting in 2008. The maximal period between rebooting reaches ca. one month (780 hours). However, the average continuous UB work takes only ca. 100 hours.

Figure 91 shows time of continuous work extracted from 30 most significant bits of reboot counter for selected test tanks. A relatively long period of non-interrupted work between Feb. 1st and 19th for Beto, Fierita, Cacho corresponds to pretty good weather without storms.

Daily (even more than 40 ºC in the electronic box – see Figure 92) and long-term temperature variation is the reason of the pedestal drifts, which reaches even several ADC-counts (Figure 93). In order not to saturate the transmission channel (via microwave link) the T1 trigger rate has to be kept on the level roughly 100 Hz. The sigma-delta calibration procedure adjusts thresholds for all three high-gain channels trying to keep trigger rate stable in time. Variations of pedestals violate a stability of the system and force thresholds tuning in all three channels simultaneously.

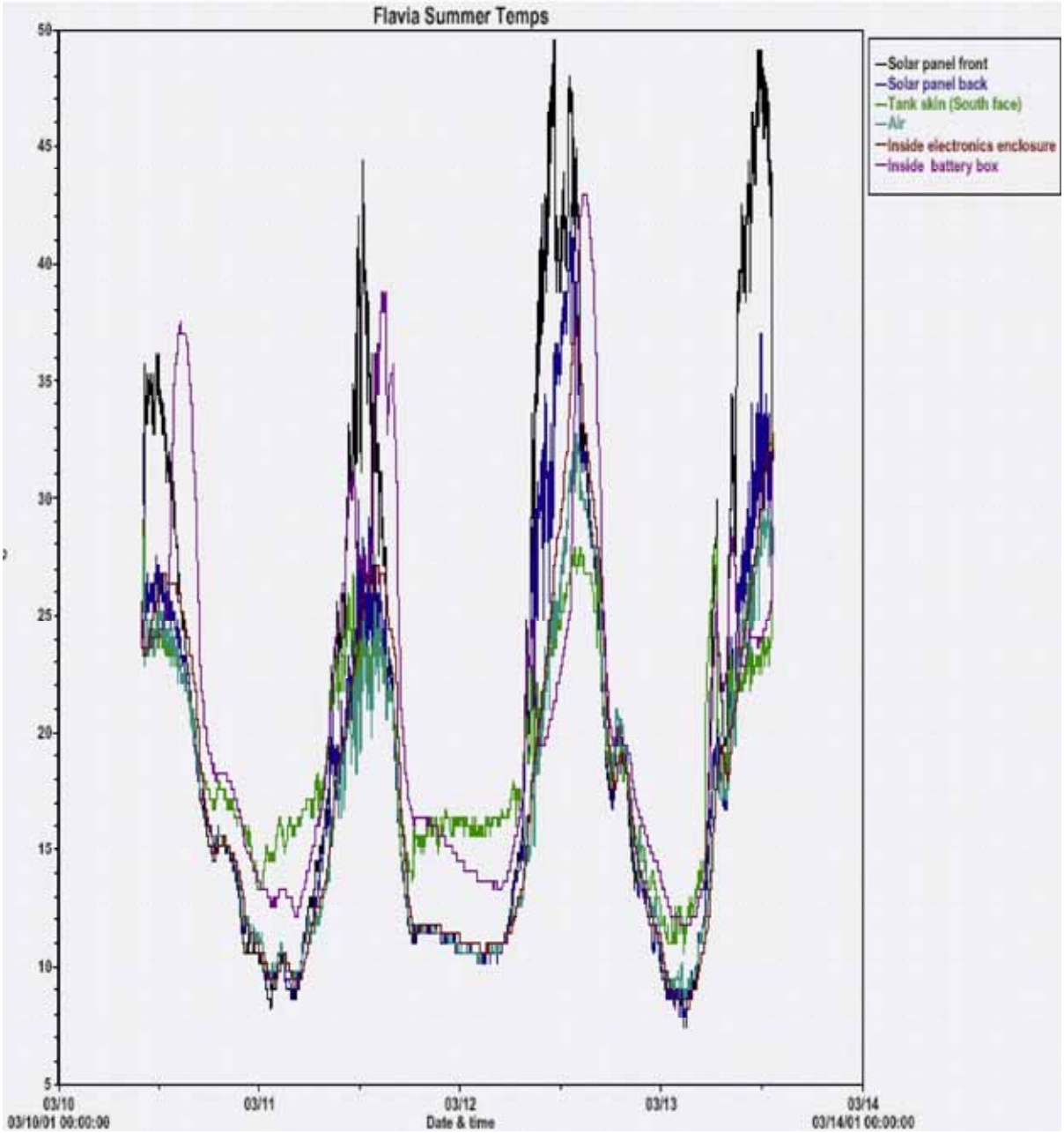

Figure 92 – Surface detector temperature profiles in summer [56].

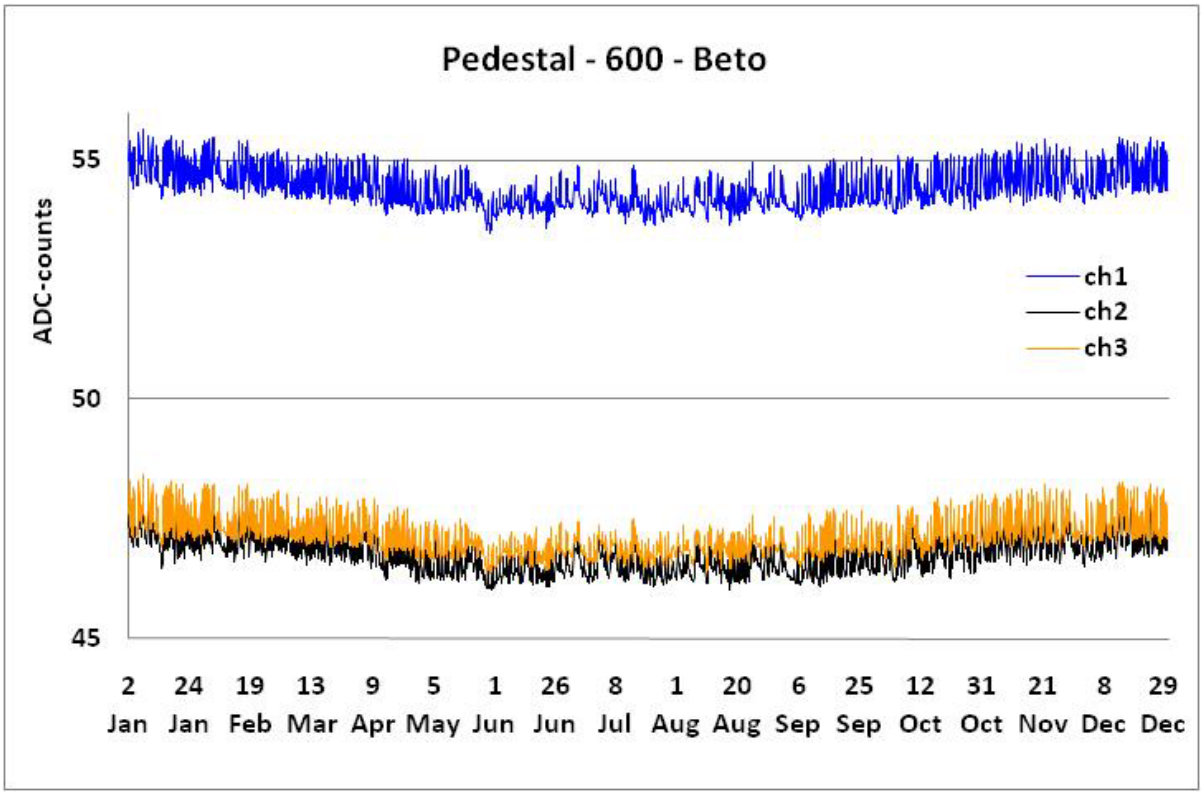

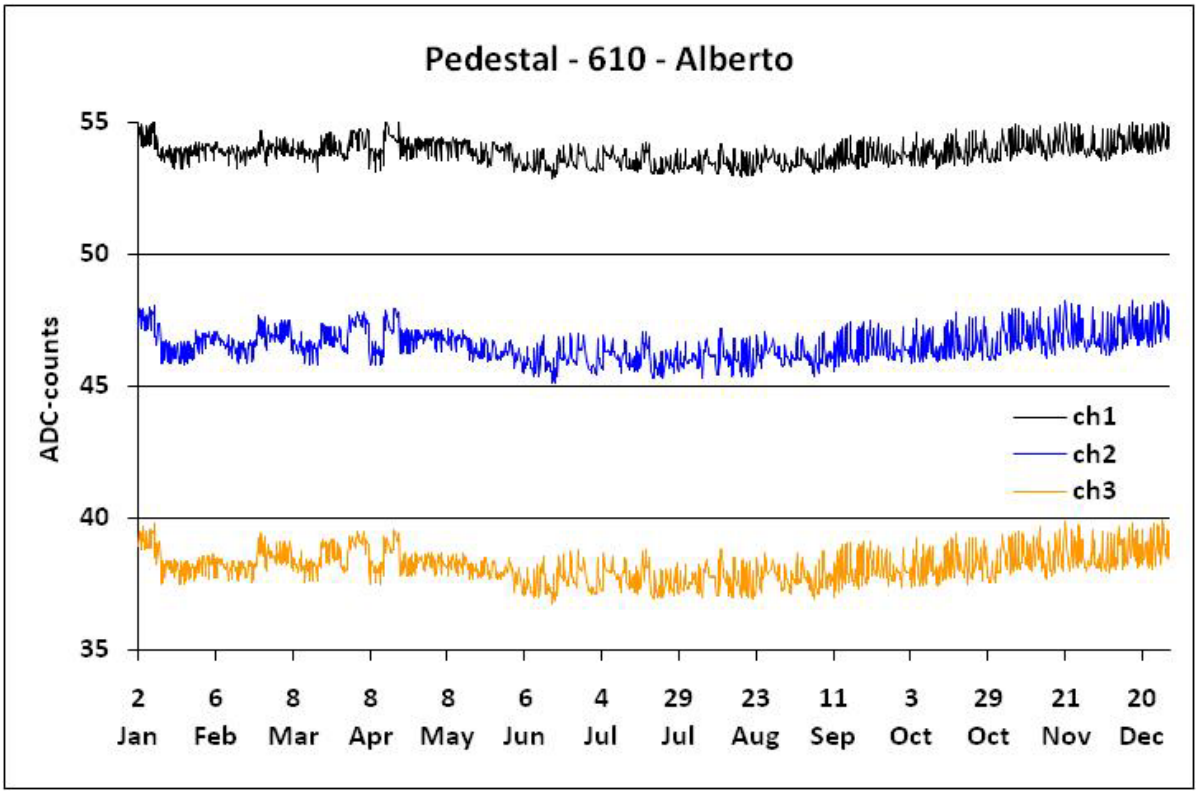

Figure 93 – Pedestals of the high-gain channels for two test tanks Beto and Alberto for the year 2008.

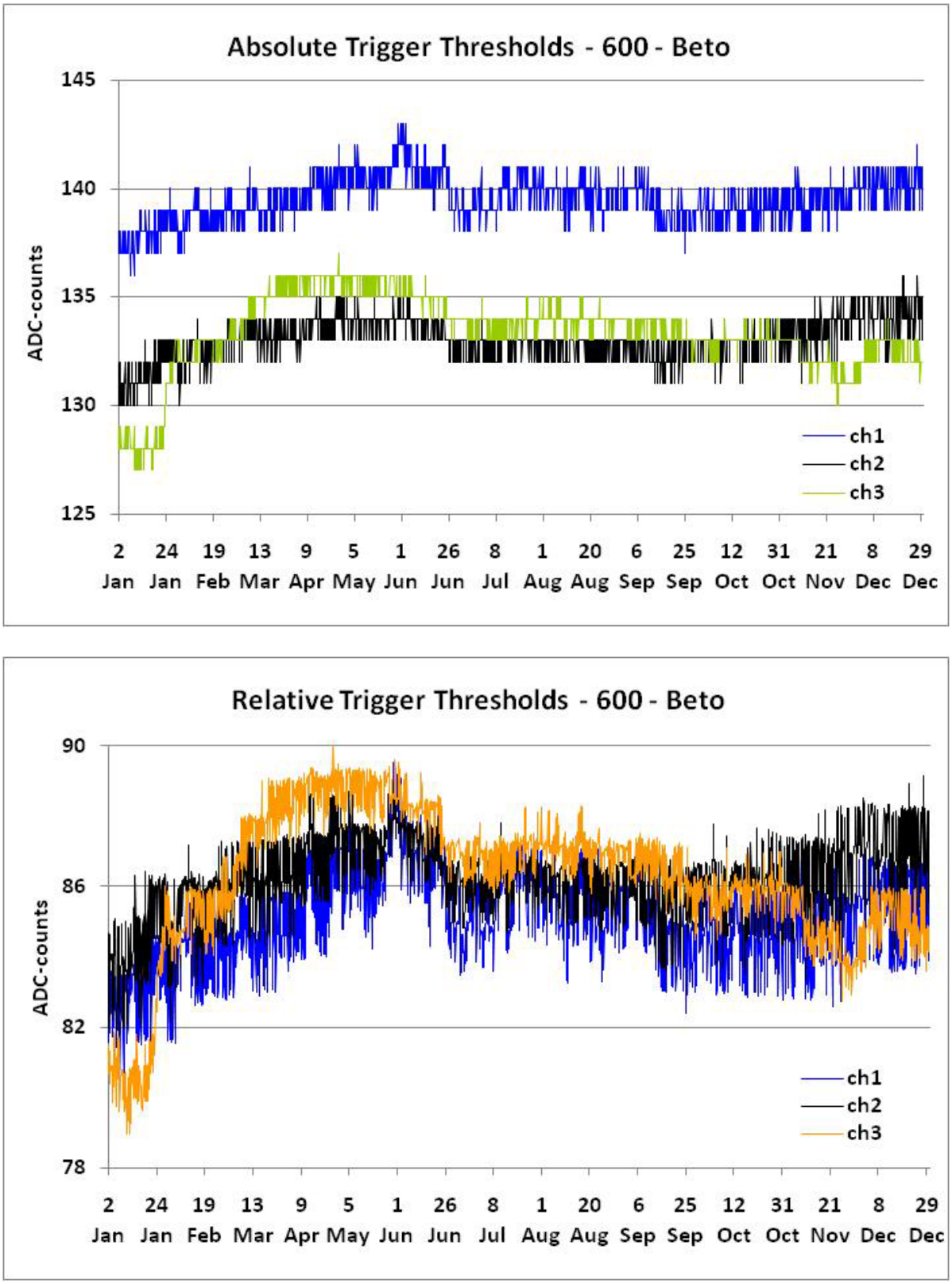

Figure 94 – Absolute and relative (a difference between the absolute threshold and the pedestal) thresholds for the high-gain channels for the test tank: Beto in the year 2008.

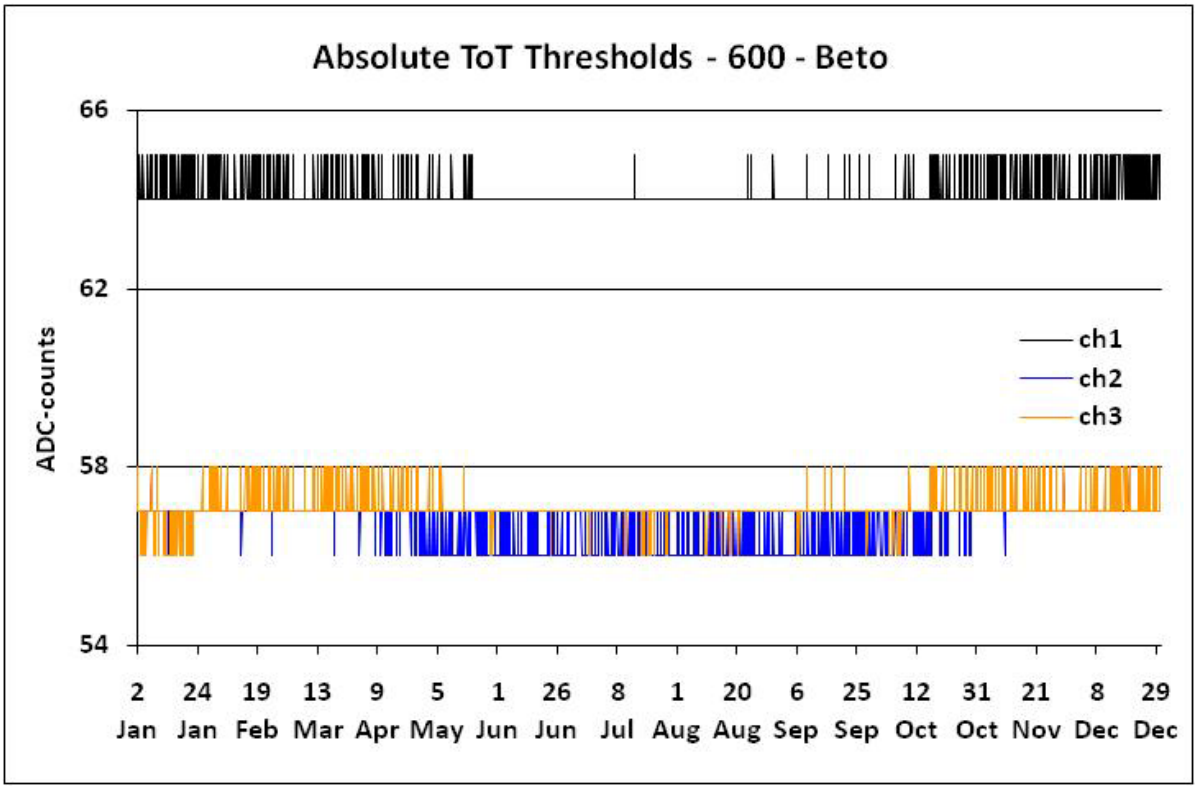

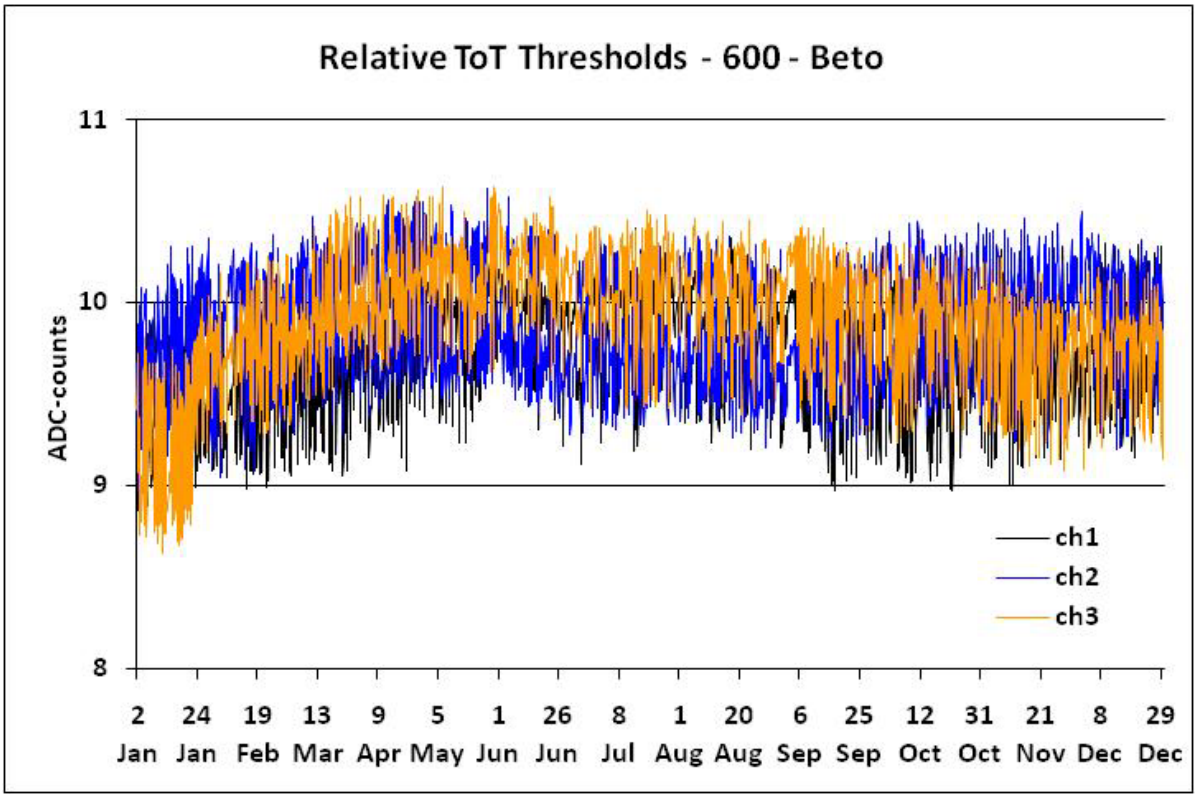

Figure 95 – Absolute and relative ToT thresholds for the high-gain channels in 2008 in the test tank Beto.

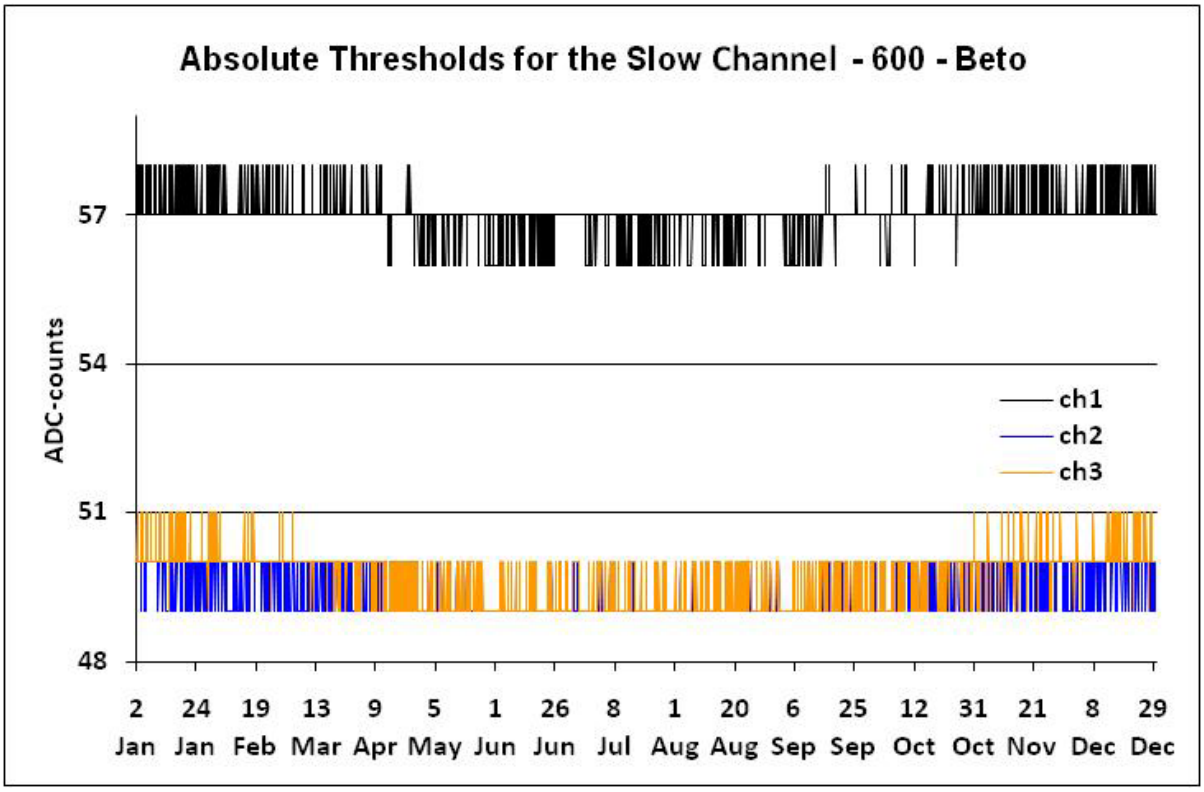

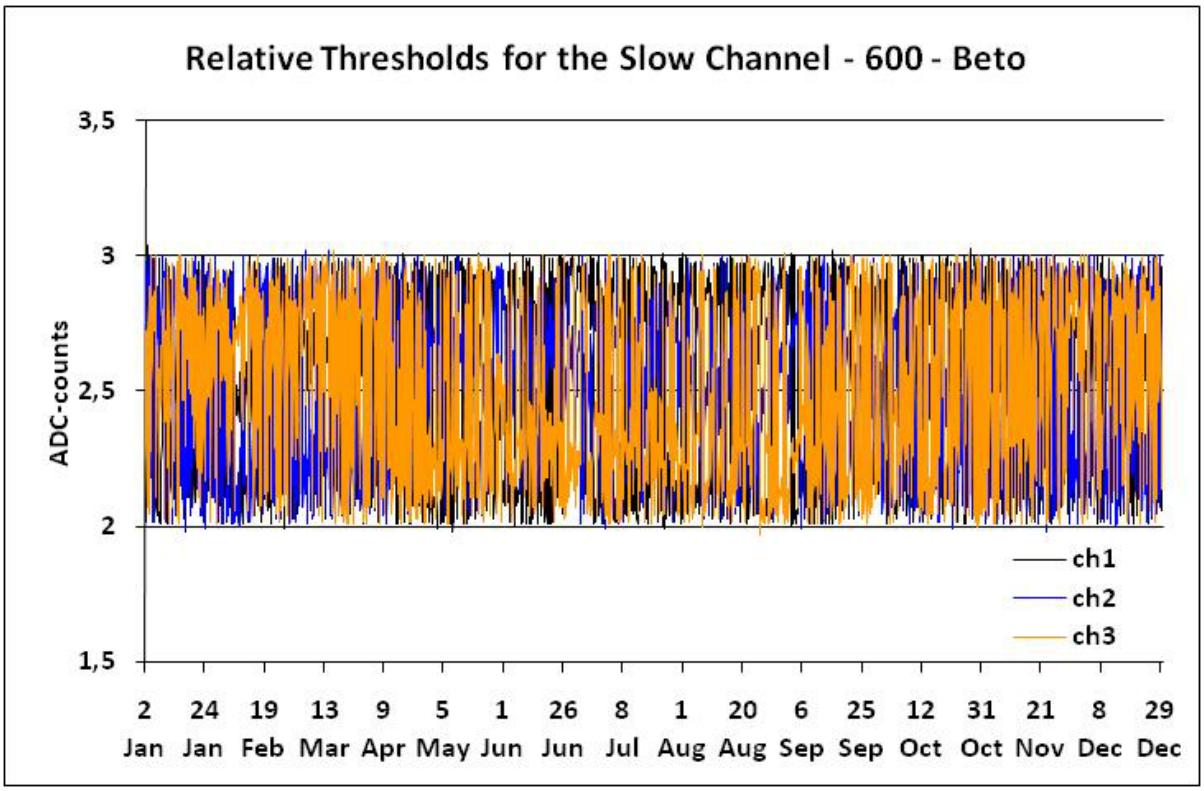

Figure 96 – Absolute and relative thresholds for the slow channel in 2008 in the test tank Beto.

3.4 Cyclone III design

In 2008 the deployment of all surface detectors has been accomplished. Roughly the 1st half of the array is equipped in the 2nd generation of the Front-End Boards based on the Altera ACEX® family, the 2nd half in the 3rd generation based on the Cyclone™ chips. Planned extension of the array – Infill Array (see Chapter 7) would require a fabrication of the new boards. Taking into account a permanent progress in electronics it is worth considering a development of the new generation of the boards using newer chips with higher performance, larger amount of resources (both logic elements and internal memories).

AMIGA project being developed on the Infill Array will be working with the additional underground scintillator muonic detectors sampled with the frequency of 80 MHz. The R&D for the 2nd part of the Auger Observatory located on the Northern hemisphere in Colorado (Auger North) anticipates new electronics with 100 MHz sampling for the surface detectors. The 4th generation of the FEB intended for the AMIGA project and as a test platform for the Auger North requires new analog part with faster FADC (sampling at least 100 MHz). Redesigning of the PCB for the analog part gives a possibility of an updating also the digital section.

Altera® offers a cost-optimized, memory-rich FPGA family the Cyclone® III. These FPGA are built on TSMC's 65-nm low-power process technology with additional silicon optimizations and software features to minimize power consumption. With this third generation in the Cyclone series, Altera broadens the number of high volume, cost-sensitive applications that can benefit from FPGA.

Table 5 – Cyclone III FPGA Device Family Features [57].

Table 1–1. Cyclone III FPGA Device Family Features

Feature	EP3C5	EP3C10	EP3C16	EP3C25	EP3C40	EP3C55	EP3C80	EP3C120
Logic Elements	5,136	10,320	15,408	24,624	39,600	55,856	81,264	119,088
Memory (Kbits)	414	414	504	594	1,134	2,340	2,745	3,888
Multipliers	23	23	56	66	126	156	244	288
PLLs	2	2	4	4	4	4	4	4
Global Clock Networks	10	10	20	20	20	20	20	20

A large internal memory suggests avoiding supports of the slow channel by the external dual-port RAM. The capacity of IDT70V3569S6DRI used in both 2nd and 3rd generations of the FEB is 16k×32-bits = 512 kbits. Two buffers in the fast channel for the 40 MHz sampling required 96 kbits (Chapter 3.1). In order to investigate the FADC traces in the same intervals for the higher sampling the size of buffers has to be extended by the factor of $f_{sampling}/f_{40MHz}$. For the 100 MHz frequency the factor is fractional. If it is approximated to the integer value = 2, the corresponding investigating time window is limited to 15.36 μs (originally 19.2 μs). The analysis of the Auger database suggests an approval of such a limitation as in the tail of traces we observe mostly the noise. So, for the factor of 2 the size of the fast buffer is 192 kbits and a total required internal memory 704 kbits. The minimal chip fulfilling the requirements is EP3C40. An additional advantage of this chip is large amount of the DSP blocks allowing an introduction of sophisticated trigger algorithms.

EP3C25 contains twice more logic elements than EP1C12 used in the 3rd generation of the FEB. Theoretically with some software tricks the slow channel also could fully be implemented into the internal memory. However, EP3C40 chip has been selected due to large amount of the DSP blocks giving higher flexibility for the future [58].

The structure of the buffers for the fast channels (Figure 41) remains the same also for the higher sampling. However the size of buffers increases twice: 512 words before the trigger and 1024 after. Bigger size of the buffers and larger amount of data would require a modification of the transmission radio channel. Due to limited bandwidth and a necessity of keeping homogenous structure of CDAS data, the structure of data transmitted to the CDAS is adjusted to the current information containing in the FADC traces. Most of traces correspond to events having significant signal level around the trigger (close to 256th time bin – for the 40 MHz sampling). For higher sampling, trigger position equals exactly to 512th time bin. An additional algorithm inside the FPGA analyses online the content of the trace. If in the time bins (0 … 255) and (1024 … 1535) the noise dominates and this information is not essential, only the samples from the time range (256 … 1023) are sent. The rest information is rejected. However, if there is significant contribution of the signal in the tails or in the beginning of the trace (i.e. corresponding to the ToT trigger), the full trace should be taken into account. The mode is selected by an arbitrarily setting of the control register. Due to limitations mentioned above data can be transmitted either

- in the interlaced mode (each 2nd sample) or
- in averaged mode (two neighboring samples are summed and divided by the factor of 2 in order not to exceed 10-bit dynamic range).

It means in both modes the package transferred from the fast channel contains 768 words of 64 bits.

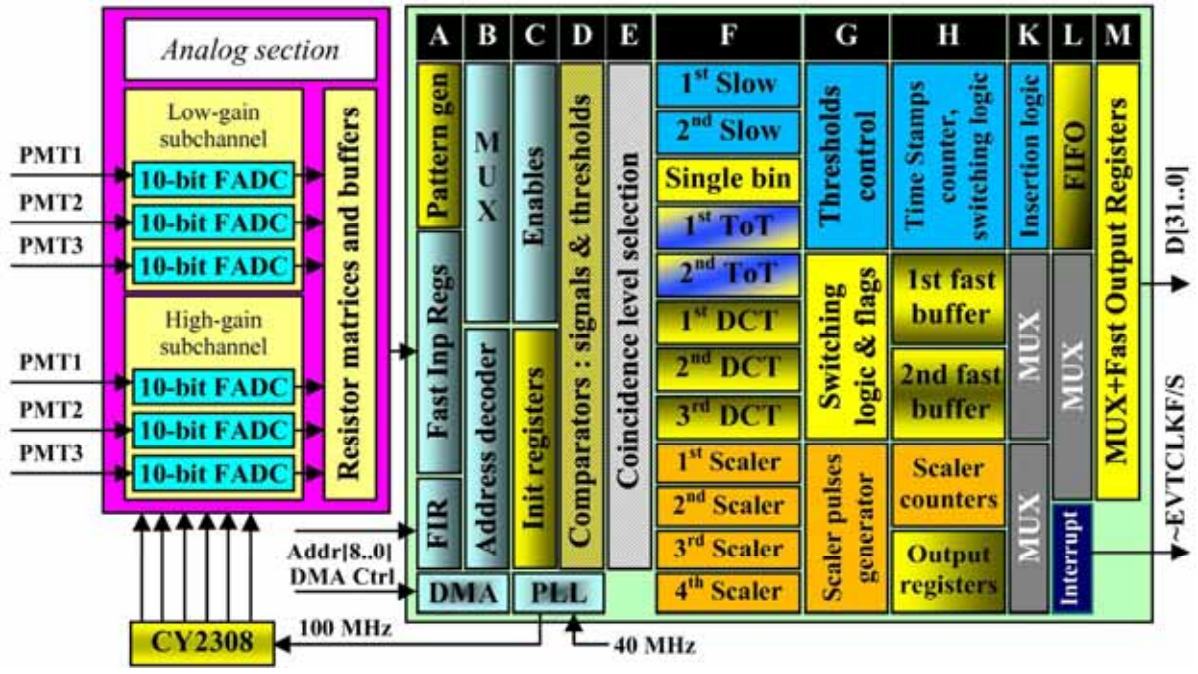

Figure 97 – The internal structure of the single chip Cyclone III.

In contrary to the previous generations of the FEB the slow channel is fully implemented into the FPGA and does not require any support from the external memory. The

internal FIFO has replaced the external dual-port RAM. The size of the slow buffer remained the same. Previously the dual-port RAM worked with two data banks. When the 1st bank has been fulfilled the FPGA sent the reading request to the UB (~EVTCLKS interrupt) while the 2nd bank could be fulfilled by next data. The FIFO simplifies the organization of the data storage, as it does not need the address management. When FIFO_A is fulfilled the Cyclone III sends the interrupt as the reading request while fulfilling of the FIFO_B is continued. The UB transfers 8192 words exactly in the same way as in previous designs. The slow channel is visible for the UB in the same way. The only small difference is for the 1st transferred word from the Fast Output Register, which comes from the previous fast data block. The last "fast" package corresponds to the low-gain data of the AF/BF buffers. 31st and 30th bits are set on "1" indicating a type of currently transferred block (Figure 39). However, these two bits set high would indicate the time stamp for the slow channel (Figure 59 - Figure 63). The "slow" data are used for some statistics and the time stamps recognize its structure. The time stamp begins each sub-package. If the 1st word in the full 8192-word package came from the fast channel it would be recognized wrong as the time stamp. In order to avoid misinterpretation and simultaneously not to change the UB software, the 1st transferred word in the "slow" DMA mode is set to zero (synchronous reset of the fast output registers for only 2 clock cycles – needed in 1WS mode). So, the 1st sub-package is not recognized and it is ignored. However, sub-packages from the slow channels are collected for a relatively long time (ca. 1 minute) to obtain sufficient statistics needed for histograms. Ignoring a single sub-package in the slow DMA transfer may only insignificantly increase a collection of data for histograms.

Figure 98 – The prototype Front End Board with the single FPGA Cyclone III [58].

4 New triggers for the Pierre Auger Surface Detector

4.1 Area over Threshold (AoT) trigger

The currently used ToT trigger is relatively sensitive to the pedestal and temperature fluctuations. ToT performs actually one bit analysis, firing time–bins above a fixed threshold. Cumulative fired bins in a sliding window generate the final ToT trigger. In assumption the threshold and the occupancy are optimized to select signals with relatively small amplitude, spread in time, which correspond to events far from the shower core. New powerful FPGA chips allow implementing much more sophisticated algorithms to improve a stability, reliability and noise suppression. It could support registering of events treated currently as the background.

For ToT trigger the threshold is relatively low (0.2 VEM) and the occupancy threshold is selected on the 13 fired time bins. It means the structure of the signal below a threshold is neglected and even if the signal is just below the threshold does not give a contribution to the fired time bins. Figure 99 shows a ToT event, which is recorded due to some contribution of a tail. A signal significantly above the threshold was not sufficient for final ToT trigger generation, until a short low spike in a tail, which fired a 13^{th} time bins. It looks like as a game. On-line analysis taking into account a full 10–bit structure of FADC traces seems to be more adequate and less sensitive on fluctuations. Especially, when at present a lot of registered ToT events do not allow reconstructing a track and energies.

The author proposes an extension of ToT idea as an area of all bins in a sliding window. The area of the time bins correspond to the charge from PMTs and to the Cherenkov flux collected in the tank.

Let us analyze an estimate rate of possible missing events with significant signals, which however were too low to be triggered by Threshold trigger or had not sufficient occupancy to be triggered by ToT. In order to simplify and make the analysis unequivocal we select the data from the tanks equipped with the 3^{rd} generation FEB with Cyclone, which were managed by the code with original buffer switching structure. For events marked as Threshold trigger, triggers appeared always exactly on the 256^{th} time bin. The code modified by MTU and managing the entire array does not provide the stable position of the trigger. It varies from 241^{st} till 246^{th} time bin and introduces additional uncertainty [59].

A tank calibration on ~110 pps T1 rate gives a sharp threshold = 1.53 VEM (Figure 100), what corresponds to the minimal registered non-calibrated signal 4.7 VEM, peak ~10 VEM and are spread over wide range more than 100 VEM (Figure 100).

If we suppress artificially the amplitude of FADC traces by some factors, however having kept the pedestal we can investigate, which events would be still registered. That procedure does not relate to signal suppression for the bigger distance from the shower core. In fact, the structure of traces change, signals are more spread in time. Nevertheless, obtained profiles of traces could correspond to the lower energy showers. We can select four classes of "events" related to the following conditions:

A) Suppressed traces still obey the 3-fold coincidence (will be triggered as normal Threshold event);

B) At least one of suppressed traces is below the threshold for 3-fold coincidence and the signal is below 4.7 VEM (that event will be rejected);

C) At least one of suppressed traces is below the threshold for 3-fold coincidence, however the signal is above 4.7 VEM;

D) As C) but the condition for ToT trigger fails (occupancy of fired bins is less than 13. This event will be also rejected)

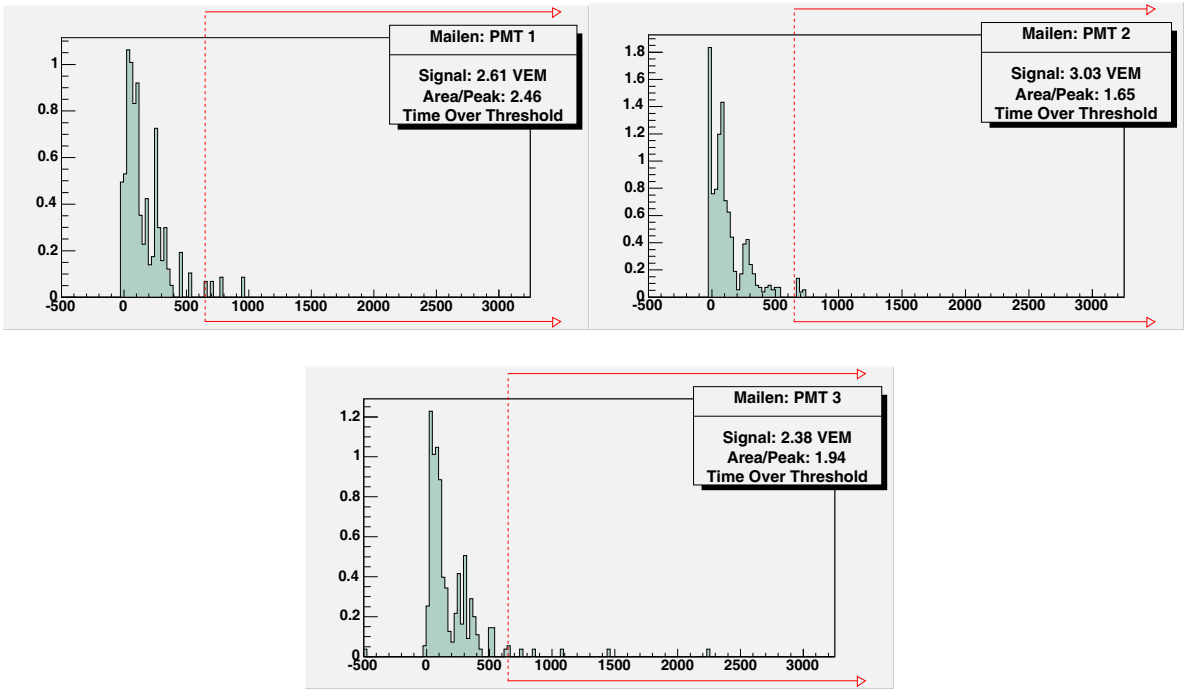

Figure 99 – An example of the event (#00804825), when the contribution of fired bins from the hump is not sufficient to generate a ToT trigger. The trigger is generated due to a contribution of some tail: 2-fold coincidence of PMT1 and PMT3 in a single time bin close to 500 ns. The vertical dashed line denotes the trigger position [27].

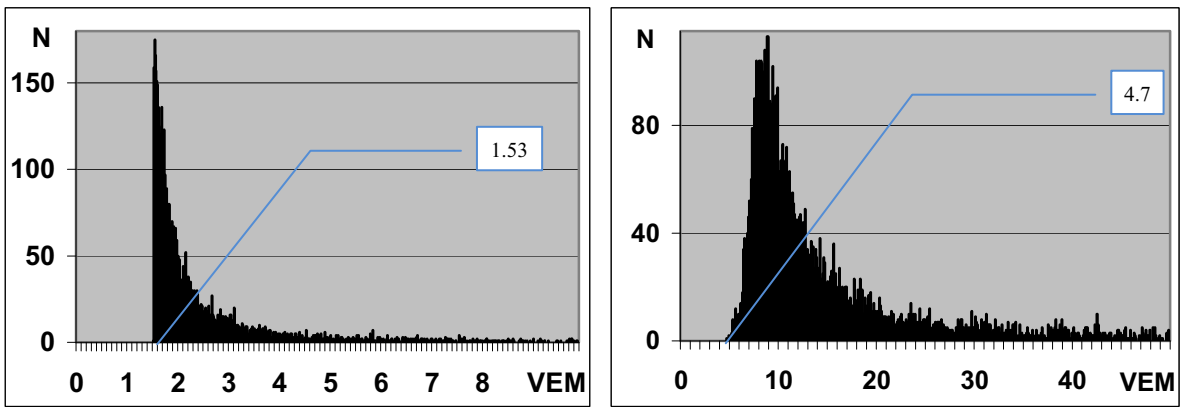

Figure 100 – Histogram of signals (minimum from all high-gain channels responsible for a trigger generation) in 256th time bin for tanks equipped with the Cyclone FEB (2005.04-09). Minimal value of signals, for which events are still registered, = 1.53 VEM (left). Histogram of signals (threshold trigger) integrated over an integration range. Minimal value of signal = 4.7 VEM. This value is treated as a reference one for the future analysis (right).

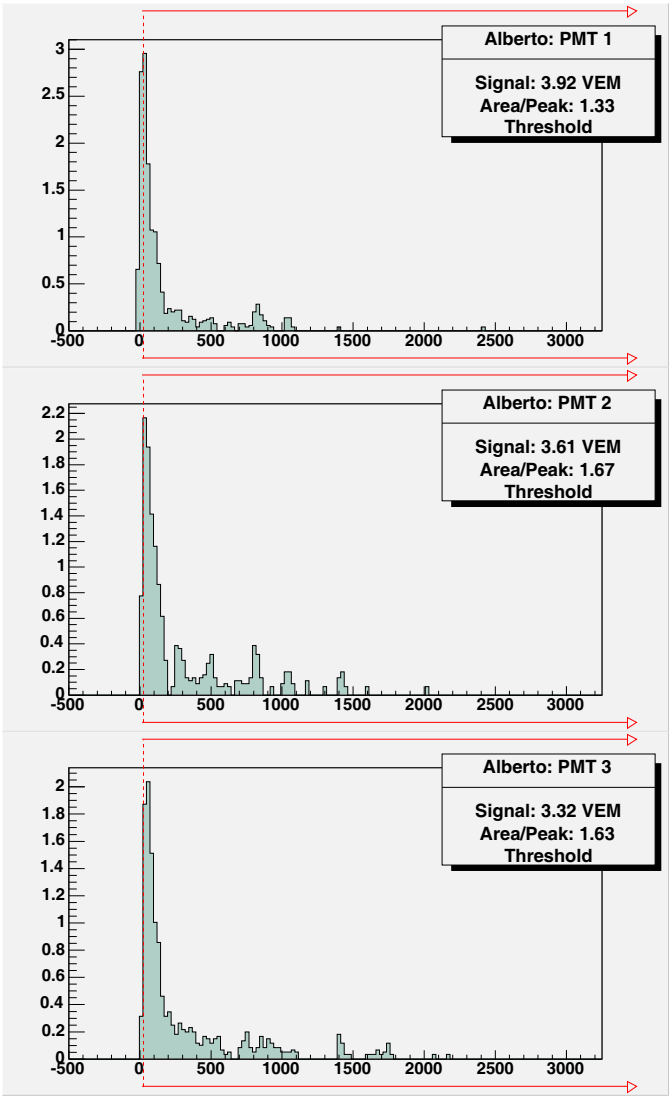

Figure 101 – An example of an event with high but narrow hump triggered by a threshold trigger. If the PMT traces were suppressed by a factor of 1.5, the condition for 3-fold coincidence would not be obeyed and additionally the occupancy for ToT would be less than 13 [27].

The D class of events seems to be crucial. The original event, triggered by Threshold trigger, may have sharp rising edge and also long tail. Total occupancy of fired bins in the standard ToT sliding window may reach relatively big value, which also obeys the ToT trigger condition. However, if the rising edge is sharp, the threshold trigger appears first, before the occupancy reaches 13. On the other hand, if the signal is suppressed and it stopped obeying 3-fold coincidences for the threshold trigger, it may be still registered by ToT condition. However, if the occupancy is not sufficient, the relatively energetic event will be lost.

Figure 101 shows a relatively energetic event triggered by the threshold trigger. The 3-fold coincidence occurred in several time bins. However, if this event were suppressed (all PMT signals simultaneously) by the factor of ~1.4, the signal from PMT2 would be below 1.53 VEM, too low for 3-fold coincidence and this energetic event would not be registered by the threshold trigger, although the signal in VEM units would be still relatively high. On the other hand, the significant hump appears only for ~250 ns, which corresponds to ~10 time bins (the global clock = 40 MHz and the clock cycle = 25 ns). The amount of time bins with

2-fold coincidences would be below the occupancy threshold and this particular event would not be registered as ToT also.

Let us suppress artificially the amplitude of FADC traces (see an example of traces shown in Figure 102) by factors: 0.8, 0.6, 0.4 (pedestals remain without a change), and investigate, which fraction of events will not be registered, although they still have not negligible signal values.

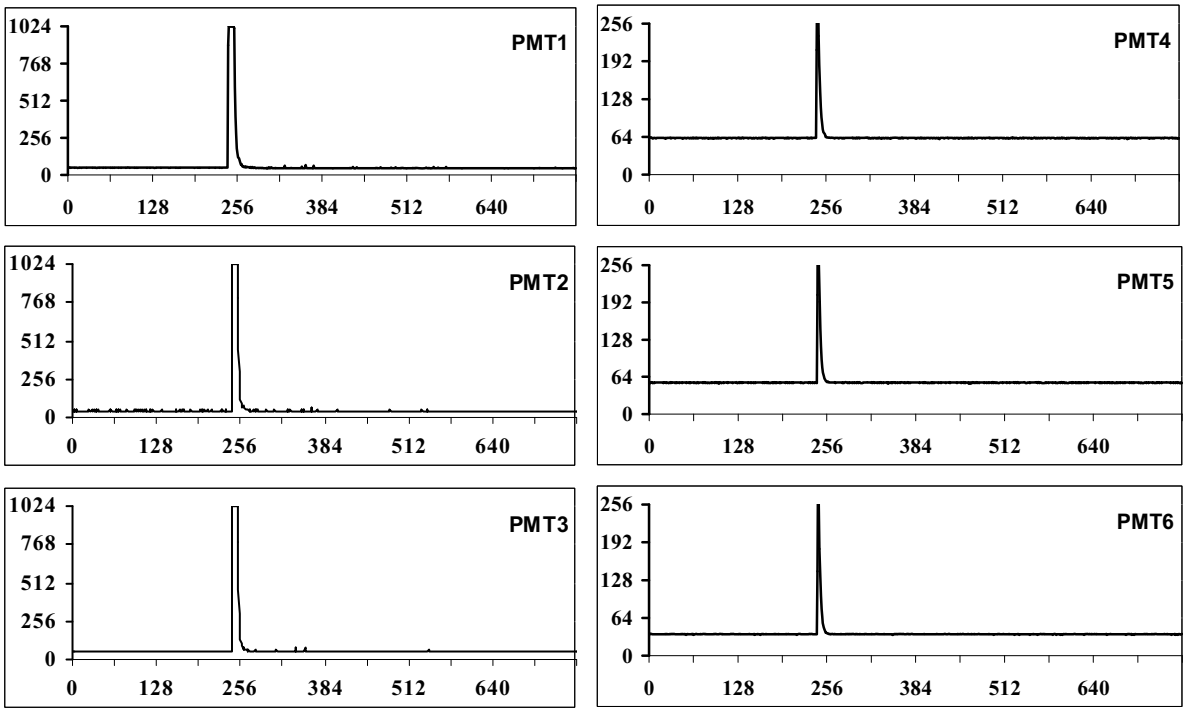

Figure 102 – FADC traces of an event (#06879576, detector - #618, 2008.12.01) with saturation in a high-gain channel (left) and still strong peak in the low-gain channel (right)

An artificial suppression reduces amplitudes of traces by an arbitrarily chosen factor without a pedestal change. From the Figure 103 and the Table 6 we can see, that significant amount of suppressed traces (originally triggered by Threshold trigger) corresponding to signals > 4.7 VEM will not obey ToT condition and will be rejected. This bias could be significantly reduced for a new signal trigger taking into account a structure of traces.

The 1st and the 2nd generation of the First Level SD Trigger based on the APEX™ 20K and ACEX® 1K Altera® chips did not have sufficient resources and an internal memory to implement more sophisticated triggers than a simple threshold – and ToT triggers.

In the Cyclone chip we can implement new types of triggers utilizing more resources. ToT trigger performing actually 1-bit trace analysis required relatively simple routine, supported by the 256-bit shift register.

A natural extension of ToT trigger is at least 10-bit on-line analysis, calculating an "area" of traces in a sliding window. Such an "Area over Threshold" trigger with a simple threshold for "area" (which corresponds to signals, currently calculated off-line) should be less sensitive to fluctuation and will accept also more energetic events, which currently may be rejected.

Data from FADC are given simultaneously on an adder and a shift register (120-clock cycles length). Data appear on the output of the shift register with 120-clock cycles delay in comparison to the input. During an initialization of the system, FADC data are summed over

120 time-bins. Afterwards, in each clock cycle, new data from FADC are added to the previous sum and simultaneously old data from the output of the shift registers are subtracted. The obtained value corresponds to the sum of a trace in the sliding window of 120 time-bins. AoT trigger is generated if this value is above a selected "AoT" threshold.

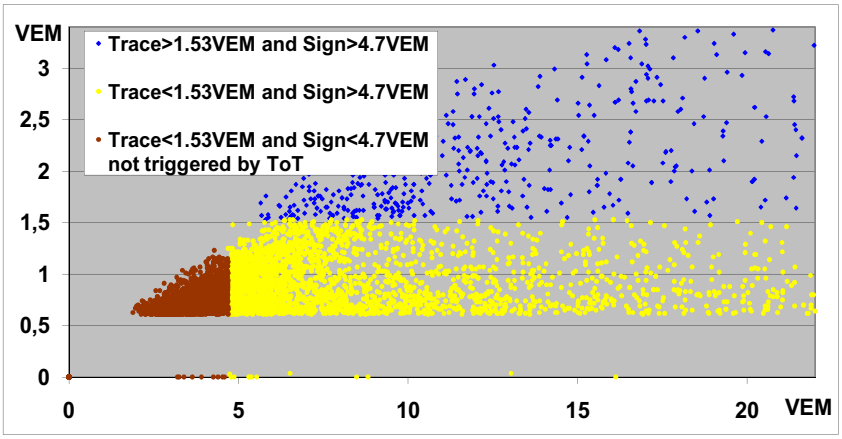

Figure 103 – Acceptance graph for the suppression factor 0.4. On vertical axis is the minimal value of trace from 256th time bin responsible for a trigger, on horizontal axis, non-calibrated signal.

Table 6 – Numbers of events for analyzed Cyclone database. Column E shows the rate of C class events, which do not survive under ToT condition.

Suppression	A	B	C	D	E
0.8	3955	55	3915	3195	81.6%
0.6	1903	964	5058	3932	77.7%
04	795	4072	3094	1867	60.3%

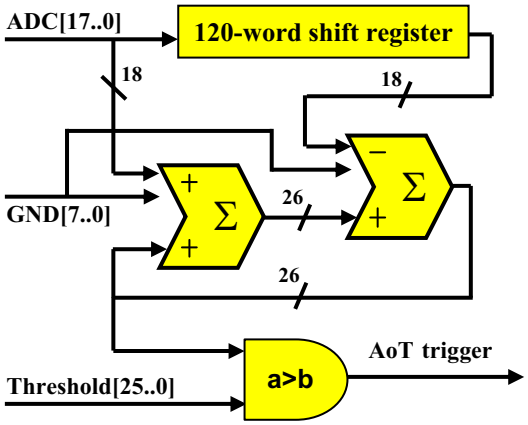

$$AoT: \left\{ \sum_{i=0}^{len} (A_i - ped_i) > Thr_A \right\}$$

Figure 104 – A structure of a full size AoT trigger routine. Pipeline stages not shown.

4.2 Spectral triggers for horizontal and very inclined showers

Extremely rare flux of UHECR requires sophisticated detection techniques. Standard methods oriented on the typical events may not be sensitive enough to capture rare events, crucial to fix a discrepancy in the current data or to confirm/reject some new hypothesis. Currently used triggers in water Cherenkov tanks in the Pierre Auger surface detector, which select events above some amplitude thresholds or investigate a "length" of traces are not optimized to the horizontal and very inclined showers, interesting as potentially generated by neutrinos [60].

The surface detector is particularly suitable for the detection of inclined showers, because the water Cherenkov tanks work actually as volume detectors. Additionally, the number of stations within a given distance to shower axis dramatically increases above the zenith angle of 60°. The surface array of the area of 3000 km^2 can detect even very inclined air showers till to exactly horizontal ones. The total depth of the atmosphere increases from 1740 g/cm^2 at 60° to 31 kg/cm^2 at 90° (Figure 105). The shape of a signal registered in PMTs in surface detector tanks for very inclined showers depends strongly on the depth in the atmosphere of the first interaction. Typical cosmic ray showers start their development at the top of the atmosphere in the first few hundreds $g \cdot cm^{-2}$. For very inclined showers, the slant depth is huge and the electromagnetic component is strongly suppressed. Muonic component starts to have a significant contribution; however the electromagnetic one is "refreshed" due to muon decays (compare the region is greater than 3000 g/cm^2 in Figure 105).

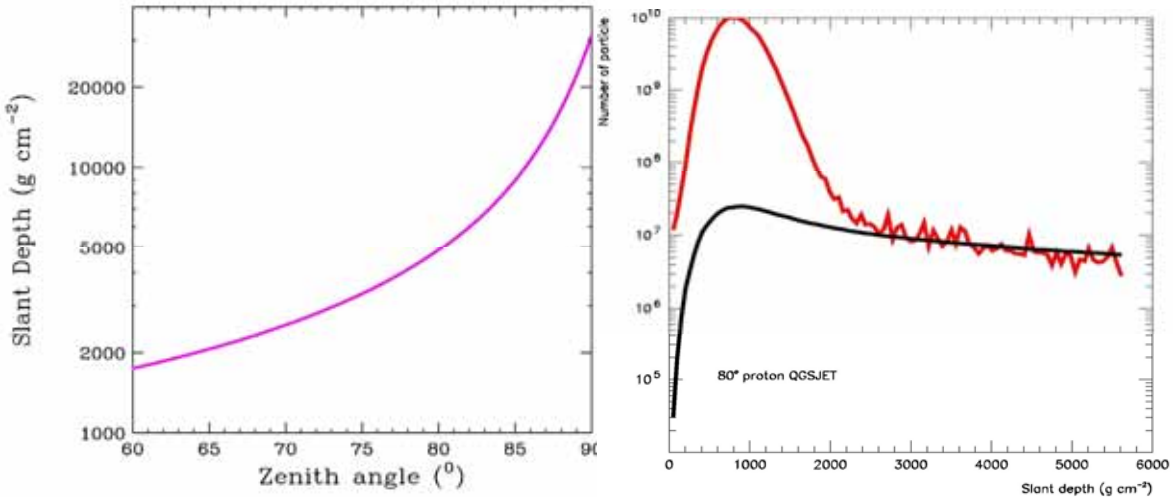

Figure 105 – Slant depth for very inclined showers [61] (left) and Longitudinal development of electromagnetic (with hump) and muonic components of a typical shower induced by a high-energy proton at zenith angle 80º [62].

Muon decays are the reason of the cut-off in the muon spectrum at lower energies. The probability of muon decays grows with the slant depth. Thicker atmosphere moves the cut-off to the higher energies. More energetic muons survive. On the other hand, for higher energies the probability of pion interaction starts to dominate over pion decays to muons. Nevertheless, for very large zenith angle the first interactions occur in the beginning of the atmosphere, it means, in not so dense media, which rather favors decays than interactions. It causes the cut-off of muon spectrum moves towards higher energies.

Neutrinos, due to their small cross section, can penetrate the atmosphere deeply and interact at all possible slant depths. Neutrino-induced showers can start their development in regions inaccessible for hadron or electromagnetic components. Very inclined showers originated from the hadron interactions and started their development early in the atmosphere will produce a narrow muonic front (Figure 106). These showers could be triggered using their signatures: i.e. a low curvature of the shower front, transformed into the rise time of signals giving a sharp peak in FADC traces and a total signal in a narrow sliding window (compare a real event in Figure 110). A sharp peak will correspond also to the bigger contribution of the higher Fourier components [63]. Neutrino-induces young showers, starting their development deeply in atmosphere with the slant depth less than 2000 g/cm^2 will give traces much more spread in time due to not suppressed electromagnetic component (compare Figure 107).

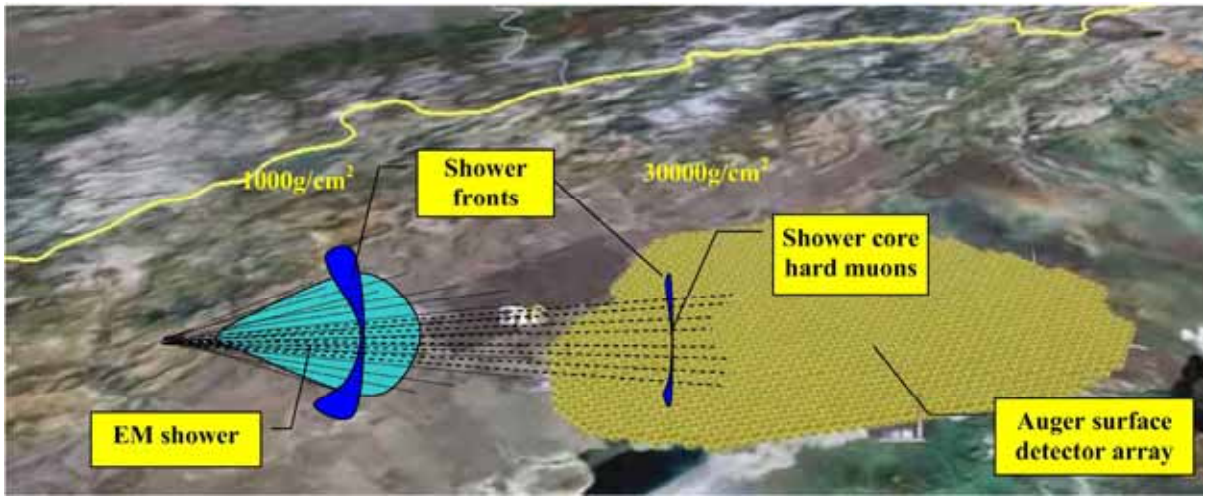

Figure 106 – Development of showers generated early and deeply in the atmosphere.

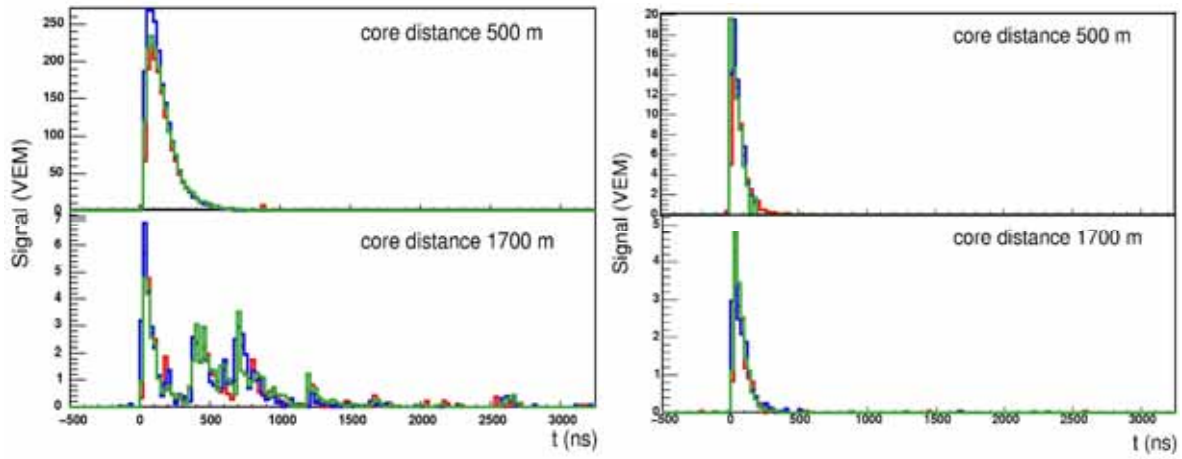

Figure 107 – Simulated traces for "young" showers. The signal gets smaller and more spread in time as the core distance increases (left) and FADC traces of old shower with short traces at all core distances (right) [61].

In the Pierre Auger surface detector, signals from PMTs are analyzed on-line in both amplitude and time domains. Strong signals in all PMT channels, corresponding to energetic showers detected near the core, are registered because of 3-fold coincidence single bin

trigger with fixed thresholds. Showers detected far from the core give much lower signals, usually spread in time. The ToT trigger investigating the structure of signal in a sliding time window detects such events.

Hadron induced showers with dominant muon component give an early peak with a typical rise time mostly from 1 to 2 time bins (by 40 MHz sampling) (Figure 109a) and decay time of the order of 80 ns [64] (see also Figure 109b). The expected shape of FADC traces (see real traces of very inclined shower in Figure 110 suggests to use a spectral trigger on-line, instead of a pure threshold analysis.

Both types of triggers do not seem to be optimized for very inclined or horizontal showers, also generated by neutrinos. The signals from that type of showers are usually too low to be detected by the single bin trigger. On the other hand, the signals could be too short to provide sufficient occupancy to be detected by ToT trigger.

Muonic front produces a bump, which can be a starting signature of horizontal showers. The bump for the "old" showers is shorter and sharper than for the "young" ones and results in a larger contribution of higher Fourier terms. For "young" showers, with relatively smooth shape of a signal profile, the lower Fourier components should dominate. The on-line spectral analysis may trigger specific events.

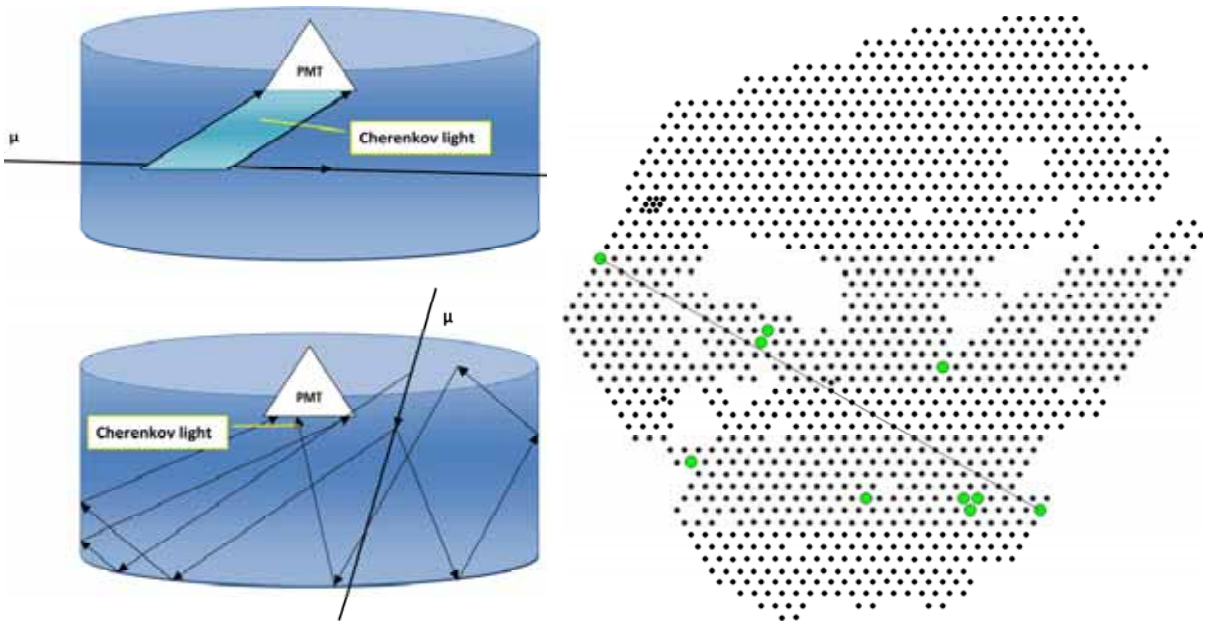

Figure 108 – (a) Geometry of Cherenkov light paths for horizontal and vertical muons crossing the Auger tank. (b) Position of triggered tanks on the Auger array of event nr 1155555. Muons triggered only few tanks although they should have crossed partially ten or more tanks. A distance between opposite tanks is greater than 54 km.

Cherenkov light generated by very inclined showers crossing the Auger tank can reach the PMT directly without reflections on Tyvec® liners (Figure 108a). Especially for "old" showers the muonic front is very flat. This together corresponds to very short direct light pulse falling on the PMT and in consequence very short rise time of the PMT response. For vertical or weakly inclined showers, where the geometry does not allow reaching the Cherenkov light directly on the PMT, the light pulse is collected from many reflections on the tank walls. Additionally, the showers developing for not so high slant depth are relatively thick. These give a signal from a PMT as spread in time and relatively slow increasing.

Figure 109a shows that for very inclined showers (a range 60°-90°) the front of edges is much sharper than for less inclined calculated from pedestal level either only to the threshold of the 1*st* trigger or to the maximal value. The estimation of the rise time for the front on the base of one or two time bins is rather rough. The rise time calculated as for two time bins may be overestimated due to a low sampling rate and an error in a quantization in time. Higher time resolution is strongly recommended.

The expected shape of FADC traces (see inclined shower in Figure 110) suggests using a spectral trigger, instead of a pure threshold analysis in order to recognize the shape of the FADC traces characteristic for the traces of very inclined showers. The monitoring of the shape would include both the analysis of the rising edge and the exponentially attenuated tail.

A very short rise time together with a relatively fast-attenuated tail could be a signature of very inclined showers. We observe numerous very inclined showers crossing the full array but which "fire" only few surface detectors (see Figure 108b). For such showers, much more tanks should have been hit. Muonic front produces PMT signals not high enough to generate 3-fold coincidences, some of signals are below of thresholds. This is a reason of "gaps" in the array of activated tanks.

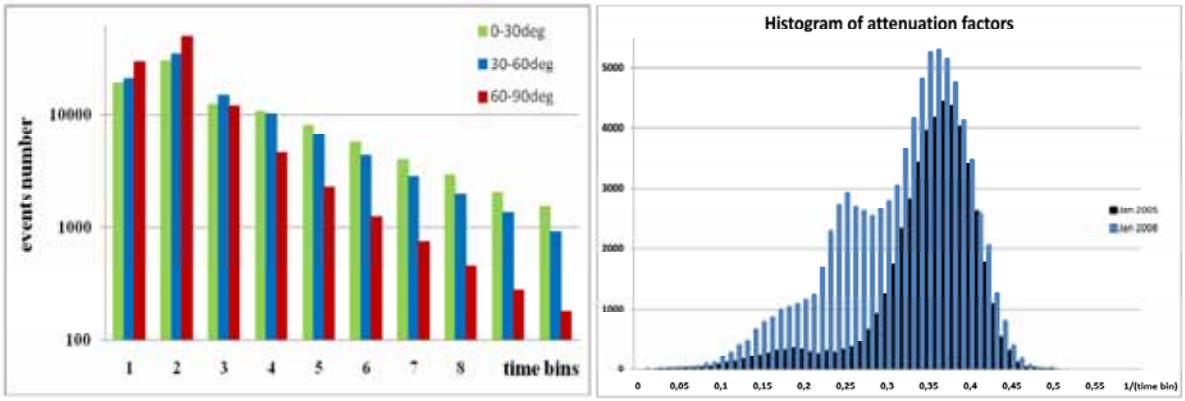

Figure 109 – (left) Distributions of rise times for all reconstruct-able showers from Oct. 2008 grouped in ranges 0°– 30°, 30°– 60° and 60°– 90° calculated from the pedestal to the peak. (right) Histogram of attenuation factors for January 2005 and 2008 respectively. $\beta_{Jan2005} \approx (-0.344 \pm 0.062)$, $\beta_{Jan2008} \approx (-0.310 \pm 0.076)$.

A next-generation Auger Observatory, "Auger North", is currently being designed. It is intended to be located in Colorado, USA, and be larger in size than the Southern Observatory in Mendoza, Argentina. In order to improve the time resolution of measured events and consequently the pointing accuracy of the surface detector, the specification of the surface electronics assumes 100 MHz sampling of the analog signals [65]. For this reason SD electronics for the Auger North requires a new Front-End.

The 100 MHz sampling chosen for the Auger North is a compromise between a requirement of improvements (better time resolution) and a hardware limitation (i.e. keeping power consumption on the level appropriate for a solar panel supply, an adjustment of a trigger rate and a size of transmitted data for the bandwidth of the microwave link).

The Auger North design assumes to use a single PMT in each surface detector. The coincidence technique for noise suppression cannot be longer used. In order to keep a reasonable trigger rate and not to saturate the communication channel, the trigger threshold has to be significantly increased. But, this yet more rejects under-threshold signals. The new spectral approach allows recognition of a shape of signals independently of their amplitudes.

However, this requires a new hardware trigger to assure registered events also for off-line analysis.

4.2.1 16-point DFT based on the Radix-2 FFT algorithm

Currently available powerful and cost-effective FPGA can provide sufficient resources to implement new triggers not available in the past. This chapter describes the implementation proposal of 16-point Discrete Fourier Transform based on the Radix-2 FFT algorithm [66] into Altera Cyclone FPGA, used in the 3rd generation of the surface detector trigger. All complex coefficients are calculated on-line in pipelined routines.

The existing software procedures, available as commercial routines, can calculate Fourier coefficients effectively utilizing a FFT algorithm. However, the commercial software is too slow to be able to trigger events in the real time [67] (see Table 7). It is optimized for flexible parametric configuration and for relatively long-point structure (from 256 up to 4096). Such an approach requires utilization of the internal memory, calculations require hundreds clock cycles for the 256-point transformation. 16-point transformation still requires tens of clock cycles and of course cannot be used as a trigger, which has to calculate n-point transform in each clock cycle (in pipeline structure). Modern powerful FPGA can do this job, however the resource requirement increases dramatically with the number of points. The analysis time interval should be a reasonable compromise between a time resolution and the resources occupancy in the FPGA.

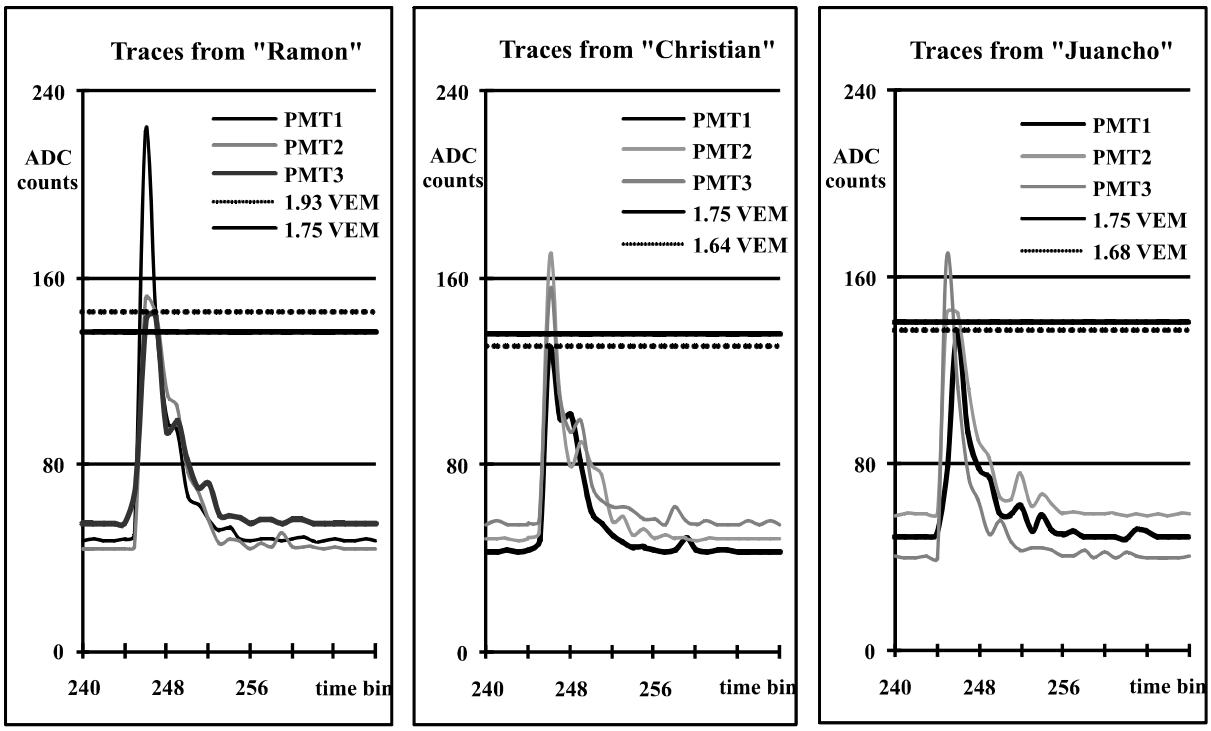

Figure 110 – FADC traces (above) and estimators of the weakest signal among three channels (below) of a horizontal shower (nr 01145055, $\theta = 83.3°$). The signal in Ramon tank only is above the standard threshold of 1.75 I_{VEM}. Signals in Cristian and Juancho tanks are below the standard thresholds and they are detected by chance.

Table 7 – Stratix II Device Performance Using the Buffered Burst Data Flow Architecture [39].

Table 2: Stratix II Device Performance Using the Buffered Burst Data Flow Architecture									
Device	Points	Width (1)	Num Engines	F_{max} MHz	Transform Calculation		Data Load & Transform		Block Throughput (Clock Cycles)
					Cycles	Time (us)	Cycles	Time (us)	
EP2S15F484C3	256	16	1	323.62	235	0.73	491	1.52	331
EP2S15F484C3	256	16	2	312.7	141	0.45	397	1.27	299
EP2S30F484C3	256	16	4	265.18	118	0.44	374	1.41	283
EP2S15F484C3	1024	16	1	319.8	1,069	3.34	2,093	6.54	1,291
EP2S15F484C3	1024	16	2	310.08	593	1.91	1,617	5.21	1,163
EP2S300F484C3	1024	16	4	275.25	340	1.24	1,364	4.96	1,099
EP2S30F484C3	4096	16	1	314.07	5,167	16.45	9,263	29.49	6,157
EP2S30F484C3	4096	16	2	306.47	2,654	8.66	6,750	22.02	4,619
EP2S90F11020C3	4096	16	4	257.8	1,378	5.35	5,474	21.23	4,363

The algorithm described here will be experimentally verified on the Auger South array. Therefore, the FPGA chip must be selected the same as in the 1st level Auger trigger [63]. Preliminary analysis of resources occupancy in the Cyclone EP1C12Q240I7 chip suggests a limitation to the DFT points N = 16. A 16-point structure clocked with 40 MHz gives the DFT in 400 ns window. This interval seems to be sufficient for the preliminary analysis of the muonic bump, especially for the "old" showers. Nevertheless, "young" showers can be treated as pre-trigger, turning on the channel investigating next the signal over longer time, corresponding to the electromagnetic component of the shower. The enlarged length of shift registers (by the factor of 16) can provide an analysis in 6.4 μs-sliding window. If the pre-trigger appears, the same hardware FFT structure is multiplexed to the integration circuit, integrating data over 16 time bins (see Figure 6 in [36]).

Let us consider a Discrete Fourier Transform $\overline{X}$ of dimension N [66]

$$\overline{X}_k = \sum_{m=0}^{N-1} x_m W^{mk} \tag{10}$$

where: k = 0, 1, ..., N – 1 and $W = e^{-j2\pi/N}$

If N is the product of two factors, with $N = N_1N_2$, we can redefine the indices m and k as follows: $m = N_1m_2 + m_1$, where $m_2 = 0,\ldots,N_2 - 1$ and $m_1 = 0,\ldots,N_1 - 1$

$$\overline{X}_k = \sum_{m_2=0}^{N_2-1}\sum_{m_1=0}^{N_1-1} x_{N_1m_2+m_1} W^{mk} \tag{11}$$

$k = N_2k_1 + k_2$, where $k_2 = 0,\ldots,N_2 - 1$ and $k_1 = 0,\ldots,N_1 - 1$

$$\overline{X}_{N_2k_1+k_2} = \sum_{m_2=0}^{N_2-1}\sum_{m_1=0}^{N_1-1} x_{N_1m_2+m_1} W^{(N_1m_2+m_1)(N_2k_1+k_2)} =$$

$$= \sum_{m_2=0}^{N_2-1}\sum_{m_1=0}^{N_1-1} x_{N_1m_2+m_1} W^{N_1m_2N_2k_1} W^{N_1m_2k_2} W^{m_1N_2k_1} W^{m_1k_2} =$$

$$= \sum_{m_2=0}^{N_2-1} W^{m_1 N_2 k_1} W^{m_1 k_2} \sum_{m_1=0}^{N_1-1} x_{N_1 m_2 + m_1} W^{N_1 m_2 N_2 k_1} W^{N_1 m_2 k_2} =$$

$$= \sum_{m_2=0}^{N_2-1} W^{m_1 N_2 k_1} W^{m_1 k_2} \sum_{m_1=0}^{N_1-1} x_{N_1 m_2 + m_1} W^{N_1 m_2 k_2} \tag{12}$$

Because of

$$W^{N_1 m_2 N_2 k_1} = W^{(N_1 N_2) k_1 m_2} = W^{N(k_1 m_2)} = 1^{k_1 m_2} = 1 \tag{13}$$

$$\overline{X}_{N_2 k_1 + k_2} = \sum_{m_1=0}^{N_1-1} W^{N_2 m_1 k_1} W^{m_1 k_2} \sum_{m_2=0}^{N_2-1} x_{N_1 m_2 + m_1} W^{N_1 m_2 k_2} \tag{14}$$

For the Radix-2 FFT algorithm: $N = 2^t$. $N_1 = 2$, $N_2 = 2^{t-1} = N/2$ $W^{N/2} = -1$

$$\overline{X}_{N_2 k_1 + k_2} = \sum_{m_1=0}^{1} W^{N_2 m_1 k_1} W^{m_1 k_2} \sum_{m_2=0}^{N/2-1} x_{2m_2 + m_1} W^{2 m_2 k_2} = \tag{15}$$

$$= \sum_{m_2=0}^{N/2-1} x_{2 m_2} W^{2 m_2 k_2} + W^{N_2 k_1 + k_2} \sum_{m_2=0}^{N/2-1} x_{2 m_2 + 1} W^{2 m_2 k_2}$$

If we replace m_2 by m, we get for indices 0,…,N – 1

$$\overline{X}_k = \sum_{m=0}^{N/2-1} (x_{2m} + W^k x_{2m+1}) W^{2mk} \tag{16}$$

If we split a sum and redefine indices, we get

$$\overline{X}_k = \sum_{m=0}^{N/4-1} x_{2m} W^{2mk} + \sum_{m=N/4}^{N/2-1} x_{2m} W^{2mk} + W^k \sum_{m=0}^{N/4-1} x_{2m+1} W^{2mk} + W^k \sum_{m=N/4}^{N/2-1} x_{2m+1} W^{2mk} =$$

$$= \sum_{m=0}^{N/4-1} (x_{2m} W^{2mk} + x_{2(m+N/4)} W^{2(m+N/4)k}) + \tag{17}$$

$$+ W^k \left(\sum_{m=0}^{N/4-1} x_{2m+1} W^{2mk} + x_{2(m+N/4)+1} W^{2(m+N/4)k} \right) =$$

$$= \sum_{m=0}^{N/4-1} (x_{2m} + (-1)^k x_{2(m+N/4)}) W^{2mk} + W^k \left(\sum_{m=0}^{N/4-1} x_{2m+1} + (-1)^k x_{2(m+N/4)+1} \right) W^{2mk}$$

We can introduce the new set of variables defined for m = 0,…,N/4 – 1 as follows:

$$A_{2m} = x_{2m} + x_{2m+N/2} \qquad A_{2m+1} = x_{2m+1} + x_{2m+1+N/2} \tag{18}$$

$$A_{2m+N/2} = x_{2m} - x_{2m+N/2} \qquad A_{2m+1+N/2} = x_{2m+1} - x_{2m+1+N/2}$$

$$\overline{X}_k = \sum_{m=0}^{\mathrm{N}/4-1}(A_{2m} + W^k A_{2m+1})W^{2mk} \tag{19}$$

$$\overline{X}_k = \sum_{m=0}^{\mathrm{N}/4-1}(A_{2m+N/2} + W^k A_{2m+1+N/2})W^{2mk} \tag{20}$$

for even and odd indices respectively.

The DFT coefficients $\overline{X}_k$ represent signals in the time domain. They can be easily available from outputs of shift registers clocked synchronously with FADC. $\overline{X}_k$ can be expressed by new set of variables A_m. Because A_m are simple linear combination of x_m, they can be calculated by typical adders and sub-tractors in a single clock cycle. The input values x_m are real and positive, since they represent the signal in the real time. Coefficients of DFT in the real domain additional simplify due to the following symmetry:

$$\mathrm{Re}(\overline{X}_k) = +\mathrm{Re}(\overline{X}_{N-k}) \qquad \mathrm{Im}(\overline{X}_k) = -\mathrm{Im}(\overline{X}_{N-k}) \tag{21}$$

The Radix-2 algorithm allows on regrouping of inputs elements in the DFT expression in order to utilize some symmetries of Fourier coefficients. In a single step of the Radix-2 algorithm, we can redefine the new set of variables by some mathematical expression of the previous ones. This step will correspond to an elementary process in the pipeline chain. The redefinition of variables in (18) corresponds to the 1st stage of the pipeline, which utilizes the feature of the following twiddle factor:

$$W_A = W^{\mathrm{N}/2} = e^{-j\pi} = -1 \tag{22}$$

So, the 1st stage can be implemented in a very simple way. The implementation of the multi-points algorithm requires multiple pipeline stages and apart from adders and sub-tractors also requires multipliers, which correspond to the W^k coefficients relating to the fractional "angle" $e^{-j\frac{2k\pi}{\mathrm{N}}}$. The Radix-2 algorithm used in the next stage reduces again the abundance of W^k coefficients due to the next twiddle factors' related to the 2nd stage of the pipeline.

$$W_B = W^{\mathrm{N}/4} = e^{-j\pi/2} = -j \tag{23}$$

The W_B suggests the similar splitting structure in the 2nd pipeline stage as in the 1st one, however the imaginary unit imposes the DFT calculation separately for their real and imaginary parts. If we split the sum in (19) and in (20) similarly as in (16), we get for k = 0,2,…,N – 2

$$\overline{X}_k = \sum_{m=0}^{\mathrm{N}/8-1}(A_{2m} + (-j)^k A_{2m+N/4})W^{2mk} + \tag{24}$$

$$+ \sum_{m=0}^{\mathrm{N}/8-1}(A_{2m+1} + (-j)^k A_{2m+1+\mathrm{N}/4})W^{(2m+1)k}$$

Let us consider separately two subset of even indices: k=4n and k=4n+2 (n = 0,…,N/4 - 1)

$$\overline{X}_{4n} = \sum_{m=0}^{\frac{\mathrm{N}}{8}-1}\left((A_{2m} + A_{2m+\mathrm{N}/4})W^{8mn} + (A_{2m+1} + A_{2m+1+\mathrm{N}/4})W^{(2m+1)4n}\right) \tag{25}$$

Notice that $\overline{X}_0$ and $\overline{X}_{N/2}$ are real.

$$\overline{X}_{4n+2} = \sum_{m=0}^{\frac{\mathrm{N}}{8}-1}\left((A_{2m} - A_{2m+\mathrm{N}/4})W^{2m(4n+2)} + (A_{2m+1} - A_{2m+1+\mathrm{N}/4})W^{(2m+1)(4n+2)}\right) \tag{26}$$

If we introduce the new variables

$$\begin{aligned} B_{2m} &= A_{2m} + A_{2m+\mathrm{N}/4} & B_{2m+1} &= A_{2m+1} + A_{2m+1+\mathrm{N}/4} \\ B_{2m+\mathrm{N}/4} &= A_{2m} - A_{2m+\mathrm{N}/4} & B_{2m+1+\mathrm{N}/4} &= A_{2m+1} - A_{2m+1+\mathrm{N}/4} \end{aligned} \tag{27}$$

$$\overline{X}_{4n} = \sum_{m=0}^{\mathrm{N}/8-1}(B_{2m} + B_{2m+1}W^{4n})W^{8mn} \tag{28}$$

$$\overline{X}_{4n+2} = \sum_{m=0}^{\mathrm{N}/8-1}(B_{2m+\mathrm{N}/4} + B_{2m+1+\mathrm{N}/4}W^{(4n+2)})W^{8mn+4m} \tag{29}$$

However, repeating the above procedure for odd indices related to (20) gives more sophisticated formulae, which cannot be simplified due to complex coefficients $W^{4(n+p)}$

$$\begin{aligned} \overline{X}_{4n+p} = &\sum_{m=0}^{\mathrm{N}/8-1}W^{2mn(4n+p)} \times \\ &\times\left(\left(A_{2m+\mathrm{N}/2} + A_{2m+1+\mathrm{N}/2}W^{4(n+p)}\right) \mp j\left(A_{2m+3\mathrm{N}/4} + A_{2m+1+3\mathrm{N}/4}W^{4(n+p)}\right)\right) \end{aligned} \tag{30}$$

where $\mp$ corresponds to p = 1,3 respectively.

Next simplification is possible due to symmetries of trigonometric functions. However, general considerations give relatively complicated formulae, which seem to be unnecessary here. Here, the 16–point algorithm will be presented because of required timing and a limitation of FPGA resources.

For N = 16 and odd indices we get

$$\begin{aligned} \overline{X}_{4n+p} = &(A_8 \mp jA_{12}) + (j)^n(A_9(-1)^nW^p - jA_{15}W^{4-p}) + \\ &+ (-j)^{(p-1)/2}(-1)^nW^2(A_{10} \mp jA_{14}) \pm (j)^n(A_{11}W^{4-p} - jA_{13}(-1)^nW^p) \end{aligned} \tag{31}$$

Since of $W^4 = -j$, all coefficients can be expressed as a linear combination of the complex base W^1, W^2, W^3.

$$W^1 = \cos(\pi/8) - j\sin(\pi/8) = \alpha - j\beta \tag{32}$$

$$W^2 = \cos(\pi/4) - j\sin(\pi/4) = \gamma(1 - j) \tag{33}$$

$$W^3 = \cos(3\pi/8) - j\sin(3\pi/8) = \beta - j\alpha \tag{34}$$

Symmetries in (32) – (34) allow the following simplifications. Notice that

$$(A_{10} \mp jA_{14})W^2 = \gamma\left((A_{10} \mp A_{14}) \mp j(A_{10} \mp A_{14})\right) \tag{35}$$

$$A_9(-1)^n W^p - jA_{15}W^{4-p} = \hat{X}\left((-1)^n A_9 - A_{15}\right) - j\hat{Y}\left((-1)^n A_9 + A_{15}\right) \tag{36}$$

$$A_{11}W^p - jA_{13}(-1)^n W^{4-p} = \hat{Y}\left(A_{11} - (-1)^n A_{13}\right) - j\hat{X}\left(A_{11} + (-1)^n A_{13}\right) \tag{37}$$

where $\hat{X} = \alpha, \beta$, $\hat{Y} = \beta, \alpha$ for p = 1,3.

We can extend the set of variables (27) also to odd indices of $\overline{X}$.

$$B_{9,15} = A_9 \pm A_{15} \qquad B_{10,14} = A_{10} \pm A_{14} \tag{38}$$

$$B_{11,13} = A_{11} \pm A_{13} \qquad B_{8,12} = A_{8,12} \tag{39}$$

Formulae (38) – (39) show that the entire 2nd pipeline stage can be built also from only adders and sub-tractors. Signals $A_{8,12}$ have to be delayed in parallel shift registers in order to assure synchronization with adjacent ones. For N = 16 the DFT coefficients can be expressed by the B_m variables as follows:

$$\mathrm{Re}(\overline{X}_{0,8}) = B_0 \pm B_1 + B_2 \pm B_3 \qquad \mathrm{Re}(\overline{X}_4) = B_0 - B_2 \tag{40}$$

$$\mathrm{Re}(\overline{X}_{2,6}) = B_4 \pm \gamma(B_5 - B_7) \qquad \mathrm{Im}(\overline{X}_{2,6}) = \mp B_6 - \gamma(B_5 + B_7)$$

$$\mathrm{Re}(\overline{X}_{1,7}) = B_8 \pm \alpha B_{15} + \gamma B_{14} \pm \beta B_{13} \qquad \mathrm{Im}(\overline{X}_{1,7}) = \mp B_{12} - \beta B_9 \mp \gamma B_{10} - \alpha B_{11}$$

$$\mathrm{Re}(\overline{X}_{3,5}) = B_8 \pm \beta B_{15} - \gamma B_{14} \mp \alpha B_{13} \qquad \mathrm{Im}(\overline{X}_{3,5}) = \pm B_{12} - \alpha B_9 \mp \gamma B_{10} + \beta B_{11}$$

The next, 3rd pipeline stage requires implementation of 10 multipliers calculating products from (40), 3 adders, 3 sub-tractors and 4 shift registers, according to the following formulae:

$$C_{0,2} = B_0 \pm B_2 \qquad C_{1,3} = B_1 \pm B_3 \qquad C_{5,7} = B_5 \pm B_7$$

$$C_{(9,11,13,15)A} = \alpha B_{9,11,13,15} \qquad C_{(9,11,13,15)B} = \beta B_{9,11,13,15} \tag{41}$$

$$C_{10,14} = \gamma B_{10,14} \qquad C_{4,6,8,12} = B_{4,6,8,12}$$

The 4th stage utilizes 2 multipliers, 5 adders, 5 sub-tractors and 4 shift registers

$$D_{0,1} = C_0 \pm C_1 \qquad D_{8,14} = C_8 \pm C_{14} \qquad D_{10,12} = C_{10} \pm C_{12}$$

$$D_{11} = C_{11A} + C_{9A} \qquad D_9 = C_{9A} - C_{11B} \qquad D_{5,7} = \gamma\ C_{5,7} \tag{42}$$

$$D_{13} = C_{13B} + C_{15A} \qquad D_{15} = C_{13A} - C_{15B} \qquad D_{2,3,4,6} = C_{2,3,4,6}$$

Finally in the 5th stage the set of DFT $\overline{X}_k$ coefficients is calculated by 6 adders and 6 sub-tractors supported by 4 shift registers.

$$\begin{aligned}
&\mathrm{Re}\,\overline{X}_{0,4,8} = D_{0,2,1} && \mathrm{Re}\,\overline{X}_{1,7} = D_8 \pm D_{15} && \mathrm{Re}\,\overline{X}_{2,6} = D_4 \pm D_7 \\
&\mathrm{Re}\,\overline{X}_{3,5} = D_{14} \mp D_{13} && \mathrm{Im}\,\overline{X}_{1,7} = \mp D_{10} - D_{11} && \mathrm{Im}\,\overline{X}_{2,6} = \mp D_6 - D_5 \\
&\mathrm{Im}\,\overline{X}_{3,5} = \mp D_{12} - D_9 && \mathrm{Im}\,\overline{X}_4 = -D_3 &&
\end{aligned} \tag{43}$$

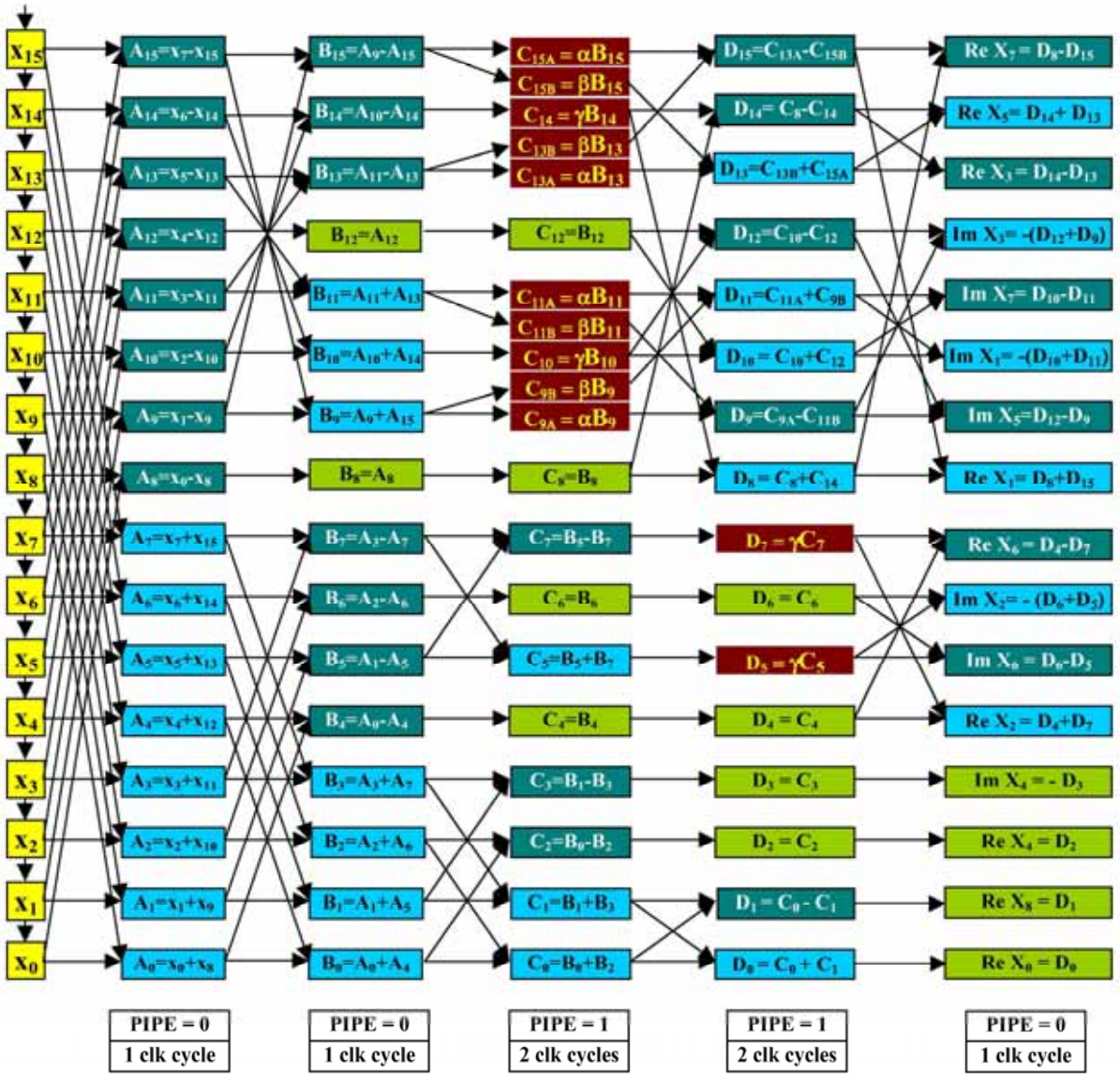

Figure 111 – A global pipeline internal structure of the FFT.

The structure of the routines implemented into FPGA is presented in Figure 111. The chain of the left side corresponds to the shift register, where signals from FADC (treated as inputs) are propagated. Fourier coefficients are next calculated in 7 clock cycles (5 stages (grouped in 5 columns): 3 stages with a single clock cycles and 2 stages with 2 clock cycles). Two first two-pipeline stages (shown in two first columns) utilize adders and differential circuits only, and can be implemented as the single bin routines; however, multipliers (appearing in 3rd and 4th stages) need at least two clock cycles to assure a sufficient registered performance (a speed of on-line calculation in a pipelined chain). Some signals (i.e. $B_8 = A_8$), which do not require any mathematical calculation, have to be delayed in appropriate

registers in order to assure the correct synchronization. Finally, Fourier coefficients are available in the last 7th clock cycle (last column on the right side). The set of all Fourier coefficients is available in each clock cycle and can be used as a trigger.

The algorithm implemented for a 10-bit FADC bus requires 12 multipliers, 28 adders, 29 differential circuits and 12 delaying routines (simple registers) for synchronization – totally ~2000 logic elements. Fixed point multiplication provides an accuracy on the level 0.05% (multiplication of two 12-bit factors gives as result 24-bit value, however, the result from multiplier is shortened to 15 bits only (in order to save resources), which provides an additional 3 bits of accuracy (in comparison with the pure cut-off of the input 12-bit signed data by the scaling factor).

In order to minimize the resource occupancy the AHDL code utilizes the Library of Parameterized Modules (LPM) with "unsigned" parameters, where possible and the fixed point multiplication structure, where the size of the fractional part is arbitrarily fixed. The intermediate results of multiplications are approximated on the next pipeline stage after next sum/difference. Re and Im coefficients are finally calculated with 10-bit resolution.

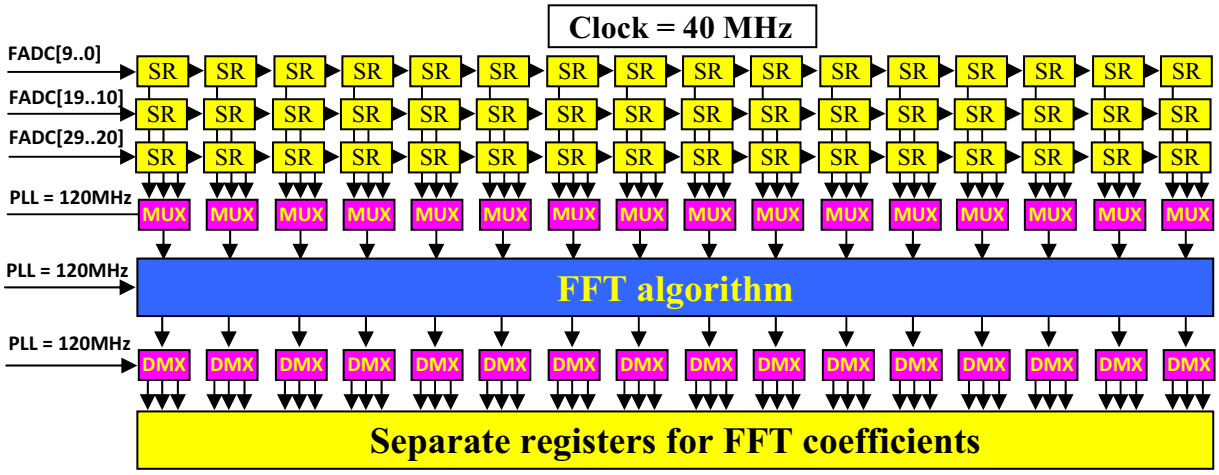

Figure 112 – The mux-demux structure allowing a calculation of FFT coefficients independently for three channels with triple PLL clock.

The very high registered performance of the FFT routine (>200 MHz) allows a utilization of the same logical structure for three 10-bit FADC channels multiplexing with three-times the frequency of the global clock (generated internally by the PLL).

The Auger input data from three shift registers (Figure 112) (corresponding to three high-gain channels) are multiplexed with 120 MHz and are fed into the FFT routine as a whole. The output FFT coefficients, calculated inside the FFT routine, are next de-multiplexed and stored in separate registers. They are then available for each channel independently and can be used for a trigger with the standard clock = 40 MHz. The initial resources occupancy increased from 54 to 78%. The final registered performance of the global code is on the level 140 MHz, which gives a sufficient safety margin [68].

High register performance and relatively low resources occupancy ~2000 logic elements/channel for 10-bit resolution provide a powerful tool to trigger the events on the traces characteristic in the frequency domain. The FFT code has been successively merged to the code of the surface detector 1st level trigger of the Pierre Auger Observatory.

4.2.2 16-point DCT algorithm

A trigger based on Discrete Fourier Transform (DFT) (Radix-2 FFT) [68] has already been implemented in the 3rd generation of the Front FEB based on Cyclone™ Altera® chip [69]. However, for real signal x_n

$$\overline{X}_{\frac{N}{2}+k} = \sum_{n=0}^{N-1} x_n e^{-j\frac{2\pi}{N}\left(\frac{N}{2}+k\right)n} = \sum_{n=0}^{N-1} x_n (-1)^n \left[e^{j\frac{2\pi}{N}kn} \right]^* = \overline{X}^*_{\frac{N}{2}-k} \tag{44}$$

The $\left(\frac{N}{2}\right)^{th}$ spectral line of $\overline{X}_k$, k = 0,1,...,N-1 is lying on a symmetry axis, the real part is symmetric, the imaginary part is asymmetric. The useful information is contained only in the 1^{st} $\left(\frac{N}{2}+1\right)$ spectral lines for k = 0,...,N/2 corresponding to frequencies $f_k = k * f_0 = \frac{k}{N\Delta t}$, changing from zero to $\frac{f_{sampl}}{2}$ with $\frac{f_{sampl}}{N}$ grid.

Discrete Cosine Transform (DCT-II) is defined as follows:

$$\overline{X}_k = \alpha_k \sum_{n=0}^{N-1} x_n \cos\left[\frac{\pi}{N}\left(n+\frac{1}{2}\right)k \right], \quad \alpha_0 = \frac{1}{\sqrt{N}}, \quad \alpha_{k>0} = \frac{2}{\sqrt{N}} \tag{45}$$

DCT for real signal x_n gives independent spectral coefficients for k = 0,1,...,N-1, changing f_k also from zero to $\frac{f_{sampl}}{2}$ but with $\frac{f_{sampl}}{2N}$ grid. DCT vs. DFT gives twice better resolution. Splitting the sum (45) and redefine the indices we get:

$$\overline{X}_k = \alpha_k \sum_{n=0}^{\frac{N}{2}-1} x_n \cos\left[\frac{\pi}{N}\left(n+\frac{1}{2}\right)k \right] + \alpha_k \sum_{n=0}^{\frac{N}{2}-1} x_n \cos\left[\frac{\pi}{N}\left(N-(n+\frac{1}{2})\right)k \right] \tag{46}$$

Due to symmetry of the cosine function

$$\overline{X}_k = \alpha_k \sum_{n=0}^{\frac{N}{2}-1} \cos\left[\frac{\pi}{N}\left(n+\frac{1}{2}\right)k \right] \times \left(x_n + (-1)^k x_{N-1-n} \right) \tag{47}$$

We can introduce the new set of variables:

$$A_n = \begin{cases} x_n + x_{N-1-n} & n=0,...,(N/2)-1 \\ x_{N-1-n} - x_n & n=(N/2),...,N-1 \end{cases} \tag{48}$$

DCT coefficients can be separated for even and odd indices respectively:

$$\overline{X}_{\begin{pmatrix} even \\ odd \end{pmatrix}} = \alpha_k \sum_{n=\begin{pmatrix} 0 \\ \mathrm{N}-1 \end{pmatrix}}^{\frac{\mathrm{N}}{2}-\begin{pmatrix} 1 \\ 0 \end{pmatrix}} A_n \cos\left[\frac{\pi}{\mathrm{N}}\left(n+\frac{1}{2}\right)k\right] \tag{49}$$

Let us notice that (49) for even indices has the same structure as (45) with only shorter range of indices. Recurrently we can introduce new sets of variables for the set of indices k = 2p, where p is integer, till k ≤ N. In order to use symmetry of trigonometric functions in a maximal way, N should be a power of 2, similarly to Radix-2 approach used in FFT algorithm. If $\mathrm{N} = 2^q$, recurrent minimization is possible till p = q. The twiddle factors for successive minimization steps m equal to $\cos\left(\frac{2\pi}{2^q}\frac{2^{p+m}}{2}\right) = -1$, because the sum of step index m and range factor p is constant and equals to q. For the rest of indices twiddle factor depends on fractional angle $\alpha = \frac{\pi 2^{q-m-1}}{\mathrm{N}}$.

After the 1st step of minimization, the terms of the sum (49) for odd indices depends on only odd multiplicity of fractional angle

$$\overline{X}_k = \alpha_k \sum_{n=\mathrm{N}-1}^{(\mathrm{N}/2)-1} A_n \cos\left(\frac{\pi}{2\mathrm{N}}(2n+1)k\right) \tag{50}$$

Using the following trigonometric identity

$$\cos\alpha = \frac{1}{2\cos\beta}\left(\cos(\alpha+\beta)+\cos(\alpha-\beta)\right) \tag{51}$$

the fractional angle can be increased by the factor of 2 for $\beta = \frac{k\pi}{2\mathrm{N}}$. Thus

$$\overline{X}_k = \frac{\alpha_k}{2\cos\left(\frac{k\pi}{2\mathrm{N}}\right)} \sum_{n=\mathrm{N}-1}^{\mathrm{N}/2} A_n \left\{\cos\left(\frac{k\pi}{2\mathrm{N}}(2n+1)k\right)+\cos\left(\frac{k\pi n}{\mathrm{N}}\right)\right\} \tag{52}$$

Let us notice that:

1). $\cos(k\pi) = (-1)^k$ for n = N-1, hence pure A_n coefficient survives,

2). $\cos(\frac{k\pi}{2}) = 0$ for $n = \frac{N}{2}$ because of odd index k,

3). the rest of indices appear in cosine terms twice in A_{n+1} and A_n coefficients, which allows introducing new set of variables

$$B_{N-1} = A_{N-1} \quad , \quad B_{N-1-n} = A_{N-n} + A_{N-1-n} \tag{53}$$

The range of B_n indices is continuous and can be split again on even and odd parts. The above procedure can be repeated in recurrence.

The 16-point DCT algorithm will be implemented in heavily pipeline structure. The 1st and the 2nd pipeline stages utilize the set of variables (48) and (53) respectively. For N = 16 the fractional angle of the twiddle factor in the 1st step of minimization equals to $\beta = \pi$.

The same fractional angle corresponds to the 2nd step of minimization for even indices corresponded to A_n

$$B_{0,1,2,3} = A_{0,1,2,3} + A_{7,6,5,4} \qquad B_{4,5,6,7} = A_{3,2,1,0} + A_{4,5,6,7} \tag{54}$$

The scaling procedure used for odd indices of $\overline{X}_k$ with the fractional angles $\beta = \frac{k\pi}{32}$ gives:

$$B_{15} = A_{15} \qquad B_{14,....8} = A_{15,...,9} + A_{14,...,8} \tag{55}$$

Coefficients $\overline{X}_k$ for even indices can be expressed by variables (54) and scaling factor

$$S_k = \cos\left(\frac{k\pi}{16}\right) \tag{56}$$

$$\begin{bmatrix} \overline{X}_0 \\ \overline{X}_8 \\ \overline{X}_4 \\ \overline{X}_{12} \end{bmatrix} = \frac{1}{2\sqrt{2}} \begin{bmatrix} S_4 & S_4 & S_4 & S_4 \\ S_4 & -S_4 & -S_4 & S_4 \\ S_2 & S_6 & -S_6 & -S_2 \\ S_6 & -S_2 & S_2 & -S_6 \end{bmatrix} \begin{bmatrix} B_0 \\ B_1 \\ B_2 \\ B_3 \end{bmatrix} \tag{57}$$

$$\begin{bmatrix} \overline{X}_2 \\ \overline{X}_{14} \\ \overline{X}_6 \\ \overline{X}_{10} \end{bmatrix} = \frac{1}{2\sqrt{2}} \begin{bmatrix} S_7 & S_5 & S_3 & S_1 \\ -S_1 & S_3 & -S_5 & S_7 \\ -S_5 & -S_1 & -S_7 & S_3 \\ S_3 & S_7 & -S_1 & S_5 \end{bmatrix} \begin{bmatrix} B_4 \\ B_5 \\ B_6 \\ B_7 \end{bmatrix} \tag{58}$$

After a scaling according to (51) we can introduce new variables for the 3rd pipeline stage:

$$4\begin{bmatrix} \overline{X}_0 \\ \overline{X}_8 \end{bmatrix} = \begin{bmatrix} 1 & 1 \\ 1 & -1 \end{bmatrix} \begin{bmatrix} C_0 \\ C_1 \end{bmatrix} \qquad 4\sqrt{2}\begin{bmatrix} S_2\overline{X}_4 \\ S_6\overline{X}_{12} \end{bmatrix} = \begin{bmatrix} 1+S_4 & S_4 \\ 1-S_4 & -S_4 \end{bmatrix} \begin{bmatrix} C_3 \\ C_2 \end{bmatrix} \tag{59}$$

$$\begin{bmatrix} S_1\overline{X}_2 \\ S_7\overline{X}_{14} \\ S_3\overline{X}_6 \\ S_5\overline{X}_{10} \end{bmatrix} = \frac{1}{4\sqrt{2}} \begin{bmatrix} 1 & S_4 & S_2 & S_6 \\ 1 & -S_4 & S_6 & -S_2 \\ 1 & -S_4 & -S_6 & S_2 \\ 1 & S_4 & -S_2 & -S_6 \end{bmatrix} \begin{bmatrix} C_7 \\ C_5 \\ C_6 \\ C_4 \end{bmatrix} \tag{60}$$

$$C_{0,1} = B_{0,1} + B_{3,2} \qquad C_{2,3} = B_{1,0} - B_{2,3} \tag{61}$$

$$C_{4,5,6} = B_{4,5,6} + B_{5,6,7} \qquad C_7 = B_7 \tag{62}$$

Scaled coefficients corresponding to odd indices

$$\overline{Z}_k = 4\sqrt{2}\,\overline{X}_k \cos\left(\frac{k\pi}{32}\right) \tag{63}$$

can be expressed by variables (54) – (55) and scaling factor (56) as follows:

$$\begin{bmatrix} \overline{Z}_{1,15} \\ \overline{Z}_{3,13} \\ \overline{Z}_{5,11} \\ \overline{Z}_{7,9} \end{bmatrix} = \begin{bmatrix} 1 & S_4 & S_2 & S_6 \\ 1 & -S_4 & S_6 & -S_2 \\ 1 & -S_4 & -S_6 & S_2 \\ 1 & S_4 & -S_2 & -S_6 \end{bmatrix} \begin{bmatrix} B_{15} \\ B_{11} \\ B_{13} \\ B_9 \end{bmatrix} \pm \begin{bmatrix} S_1 & S_3 & S_5 & S_7 \\ S_3 & -S_7 & -S_1 & -S_5 \\ S_5 & -S_1 & S_7 & S_3 \\ S_7 & -S_5 & S_3 & -S_1 \end{bmatrix} \begin{bmatrix} B_{14} \\ B_{12} \\ B_{10} \\ B_8 \end{bmatrix} \tag{64}$$

Matrix (64) can be factorized as follows:

$$\begin{bmatrix} \overline{Z}_{1,15} \\ \overline{Z}_{3,13} \\ \overline{Z}_{5,11} \\ \overline{Z}_{7,9} \end{bmatrix} = \begin{bmatrix} C_{15} + C_{11} \\ C_{15} + C_{11} \\ C_{15} - C_{11} \\ C_{15} - C_{11} \end{bmatrix} + \begin{bmatrix} C_{13}^2 + C_9^6 \\ -C_{13}^2 - C_9^6 \\ C_9^2 - C_{13}^6 \\ -C_9^2 + C_{13}^6 \end{bmatrix} \pm M \begin{bmatrix} 1 & S_4 & S_2 & S_6 \\ 1 & -S_4 & S_6 & -S_2 \\ 1 & -S_4 & -S_6 & S_2 \\ 1 & S_4 & -S_2 & -S_6 \end{bmatrix} \begin{bmatrix} C_{14} \\ C_{10} \\ C_{12} \\ C_8 \end{bmatrix} \tag{65}$$

$$C_{8,10,12} = B_{8,10,12} + B_{10,12,14} \qquad C_{14,15} = B_{14,15} \tag{66}$$

$$C_{9,13}^{2,6} = B_{2,6} S_{9,13} \qquad C_{11} = B_{11} S_4 \tag{67}$$

$$M = \begin{bmatrix} \frac{1}{2S_1} & 0 & 0 & 0 \\ 0 & \frac{1}{2S_3} & 0 & 0 \\ 0 & 0 & \frac{1}{2S_5} & 0 \\ 0 & 0 & 0 & \frac{1}{2S_7} \end{bmatrix} \tag{68}$$

Let us notice that the structures of the matrices from (60) and the 4×4 matrices from (65) are exactly the same. Thus (60) can be factorized in a following way:

$$\begin{bmatrix} S_1\overline{X}_2 \\ S_7\overline{X}_{14} \\ S_3\overline{X}_6 \\ S_5\overline{X}_{10} \end{bmatrix} = \frac{1}{4\sqrt{2}} \begin{bmatrix} 1 & 1 & 1 & 1 & 0 & 0 \\ 1 & -1 & 0 & 0 & 1 & -1 \\ 1 & -1 & 0 & 0 & -1 & 1 \\ 1 & 1 & -1 & -1 & 0 & 0 \end{bmatrix} \begin{bmatrix} C_7 \\ S_4C_5 \\ S_2C_6 \\ S_6C_4 \\ S_6C_6 \\ S_2C_4 \end{bmatrix} \tag{69}$$

A direct hardware implementation requires 5 multiplications. Well known and widely used in numerical calculations algorithm of Arai. Agui, Nakajima (AAN) [70], derived from 16-point DFT calculated for real samples, corresponds to the following factorization:

$$\begin{bmatrix} S_1\overline{X}_2 \\ S_7\overline{X}_{14} \\ S_3\overline{X}_6 \\ S_5\overline{X}_{10} \end{bmatrix} = \frac{1}{4\sqrt{2}} \begin{bmatrix} 1 & 1 & 1 & 0 & -1 \\ 1 & -1 & 0 & -1 & 1 \\ 1 & -1 & 0 & 1 & -1 \\ 1 & 1 & -1 & 0 & 1 \end{bmatrix} \begin{bmatrix} C_7 \\ S_4C_5 \\ (S_2+S_6)C_6 \\ (S_2-S_6)C_4 \\ S_6(C_6-C_4) \end{bmatrix} \tag{70}$$

and requires only 4 multiplications (compare Figure 2 in [70]). A minimization of multiplications amounts is one of a fundamental goal in long-term numerical calculations. Reduction of product terms significantly speed up sophisticated calculations, because a single multiplication requires several clock cycles of processor. Multiplications in powerful FPGA chips can be however performed in very fast dedicated DSP blocks in a single clock cycle. Signals processed in parallel threads in a hardware implementation of a pipeline design have to be synchronized to each other. Pipeline approach requires additional shift registers for synchronization also for signal currently not being processed. However, such synchronization needs additional resources.

Coefficients (60) in direct (69) factorization can be calculated in three pipeline stages. Direct implementation of the pure AAN algorithm requires two stages more, which utilize additional resources of shift registers for synchronization for operations like: X(t+1) = X(t). In a numerical calculation in processors data are simply waiting for a next performance cycle.

Additionally, the *lpm_add_sub* mega-function from the Altera® library of parameterized modules (LPM) does not support an inversion of a sum i.e. $C_4 = -(B_4 + B_5)$. This operation would have to be performed in a cascade way by an adder and a sign inversion. Cascade operations performed in the same clock cycle significantly slow down a global registered performance.

The original AAN algorithm can be optimized (oAAN) for a FPGA environment according to Figure 114. A simple implementation of a part of DCT8 algorithm for $\overline{X}_{1,3,5,7}$ shows that a reduction of a single pipeline stage at the expense of one additional multiplication performed in a dedicated DSP block significantly decreases a logic elements utilization as well as significantly improves a registered performance, because a multiplication in a DSP block is faster than a sum implemented in standard logic elements.

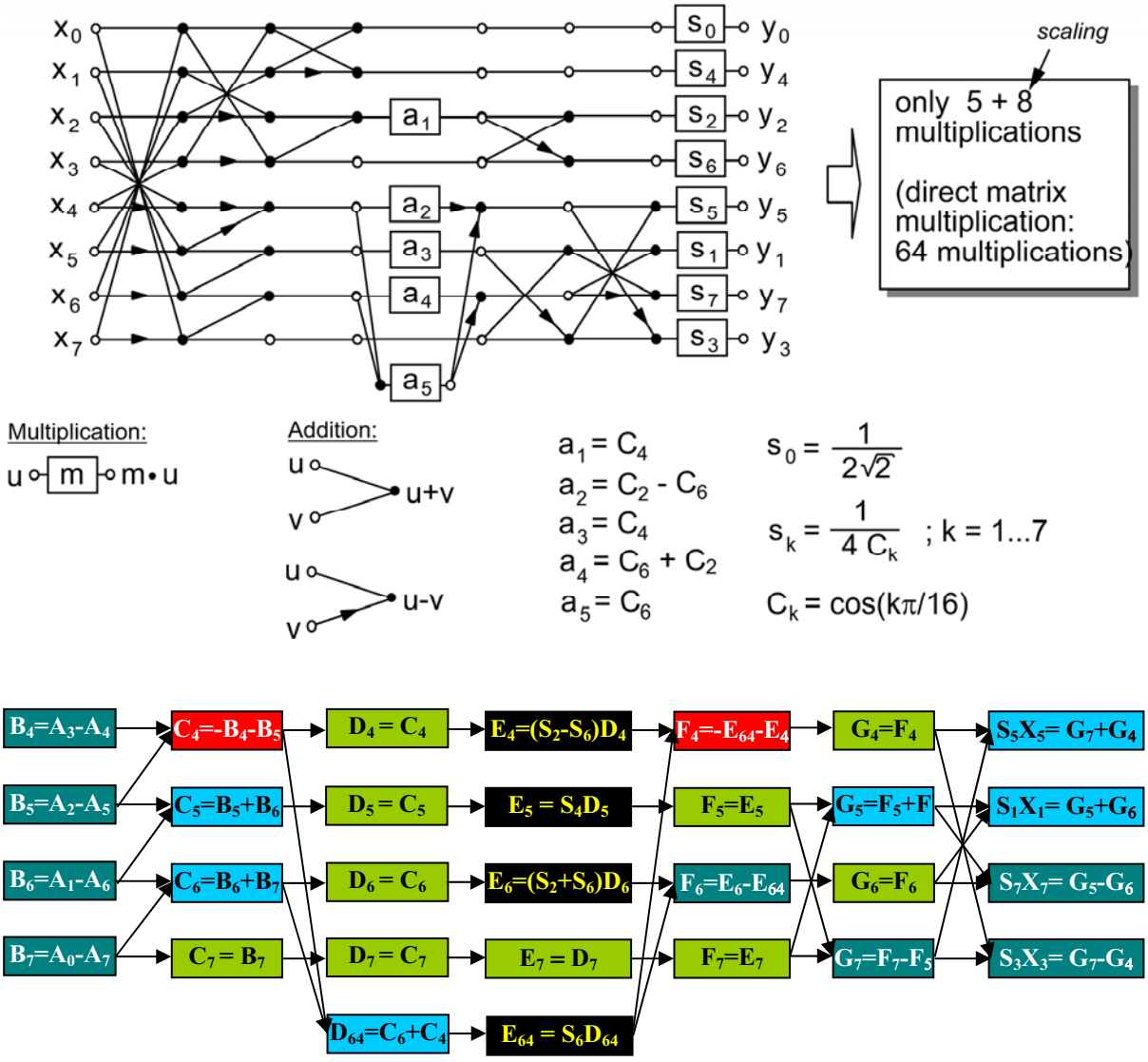

Figure 113 – Fast DCT algorithm developed by Arai, Agui and Nakajima [70] (above) and a direct, pipelined implementation of coefficients $\overline{X}_{1,3,5,7}$ into a FPGA (below).

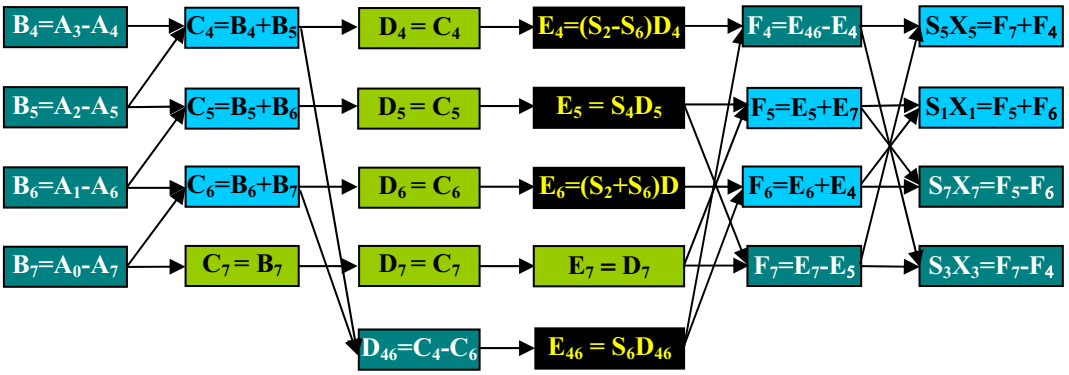

Figure 114 – Data flow in the optimized AAN algorithm. Reduced a single pipeline stage and removed difficulties with missing Altera routines.

A renaming of variables allowed avoiding problems with missing routines as well as and shorting a pipeline chain. Nevertheless, routines corresponding to D-bin are mostly shift registers for synchronization only. They could be omitted, if D_{46} and E_{46} were merged into a single routine. However, this dramatically reduces the registered performance.

The factorization (69) uses a single multiplier more in comparison to original AAN approach (70). The expense of one additional multiplication performed in a dedicated DSP block allows a significant improvement of the registered performance (from 180 MHz to 225 MHz) as well as reduction of resources utilization (from 220 to 178 logic elements) for EP3C40F324I7 Cyclone III™ chip. This factorization will be next used in a global algorithm.

In the 4th pipeline step directly from (65) we can introduce new variables:

$$D_{15,11} = C_{15} \pm C_{11} \qquad D_9 = C_{13}^6 - C_9^2 \qquad D_{13} = C_{13}^2 + C_9^6 \tag{71}$$

Rest of variables require 10 next multipliers 3 adders/sub-tractors and 3 shift registers:

$$D_{5,10} = S_4 C_{5,10} \qquad D_{4,6,8,12}^{2,6} = S_{2,6} C_{4,6,8,12} \qquad D_{3,7,14} = C_{3,7,14} \tag{72}$$

$$D_{0,1} = C_0 \pm C_1 \qquad D_2 = C_2 + C_3 \tag{73}$$

However in the 5th pipeline stage the next multiplier is needed for only E_2 variable:

$$E_2 = S_4 D_2 \qquad E_{0,1,3} = D_{0,1,3} \qquad E_4 = D_6^6 - D_4^2 \qquad E_6 = D_6^2 + D_4^6 \tag{74}$$

$$E_{\substack{7,11,15 \\ 5,9,13}} = D_{7,11,15} \pm D_{5,9,13} \qquad E_{14,10} = D_{14} \pm D_{10} \tag{75}$$

$$E_{12} = D_{12}^2 + D_8^6 \qquad E_8 = D_{12}^6 - D_8^2 \tag{76}$$

The 6th stage does not require any multiplier, only 6 shift registers for synchronization:

$$F_{0,1,9,11,13,15} = E_{0,1,9,11,13,15} \qquad F_{\substack{3,5,7,9,13 \\ 2,4,6,8,12}} = E_{3,5,7,9,13} \pm E_{2,4,6,8,12} \tag{77}$$

In the 7*th* pipeline stage 12 signals are delayed only for synchronization and 4 are scaled for the following (n,k) pairs: (14,1),(12,7),(10,3),(8,5)

$$G_n = \frac{F_n}{2S_k} \tag{78}$$

In the 8th pipeline stage pure registers for synchronization only are implemented for even indices of $\overline{X}_{0,2,4,6,8,10,12,14}$ and

$$H_{\substack{9,11,13,15 \\ 8,10,12,14}} = G_{9,11,13,15} \pm G_{8,10,12,14} \tag{79}$$

The last stage contains all scaling multipliers:

$$\overline{X}_k = \frac{H_m}{4\sqrt{2}\cos\left(\frac{k\pi}{32}\right)} \tag{80}$$

for the following (k,m) pairs: (1,15),(15,14),(7,13),(9,12),(3,11),(13,10),(5,9),(11,8),(14,7), (2,6),(6,5),(10,4),(4,3),(12,2).

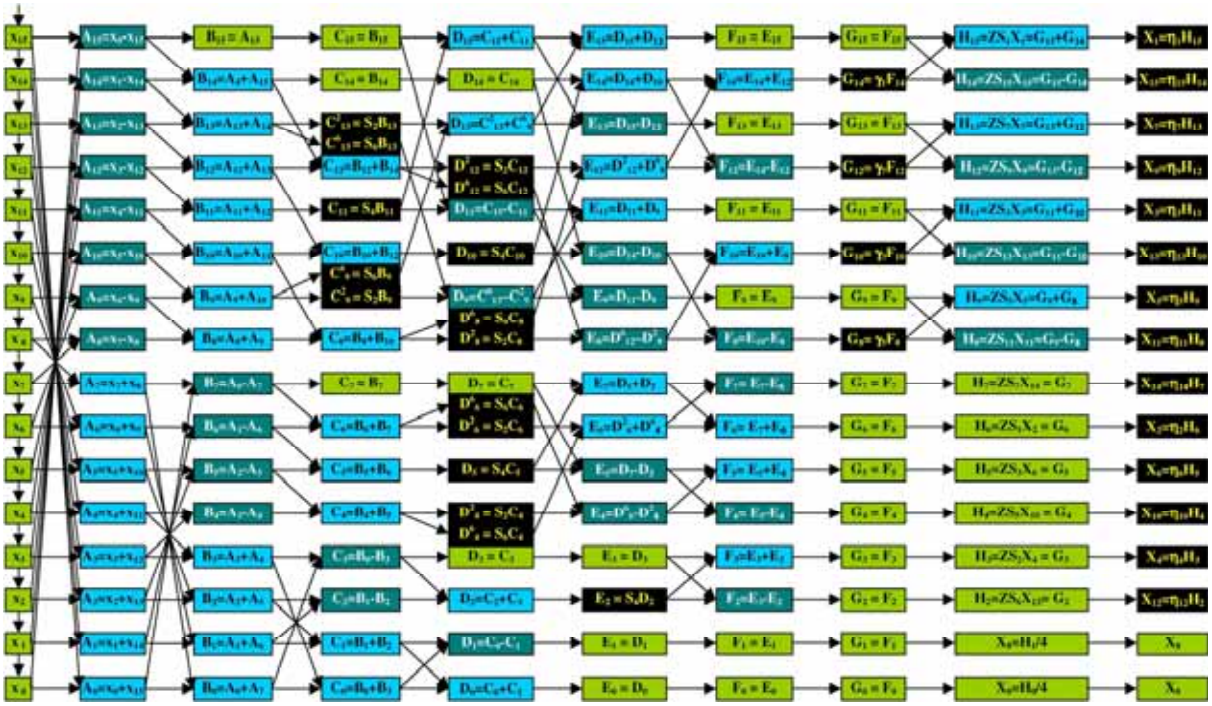

Figure 115 – Pipeline internal structure of 16-point DCT FPGA routine. Here 16-stage shift register chain is presented. However, for 100 MHz sampling modified structure according to Figure 121 is implemented.

4.2.3 DFT vs. DCT

There are several variants of the DCT with slightly modified definitions. The DCT-I is exactly equivalent (up to an overall scale factor of 2), to a DFT of 2N - 2 real numbers with even symmetry. The (45) defines the most commonly used form of the Discrete Cosine Transform (DCT-II). The DCT-III form is sometimes simply referred to as "the inverse DCT" (IDCT). A variant of the DCT-IV, where data from different transforms are overlapped, is called the Modified Discrete Cosine Transform (MDCT).

$$\overline{X}_k = \sum_{n=0}^{N-1} x_n \cos\left[\frac{\pi}{N}\left(n+\frac{1}{2}\right)\left(k+\frac{1}{2}\right)\right] \tag{81}$$

The DCT is a Fourier-related transform similar to the DFT, but using only real numbers. DCT are equivalent to DFT of roughly twice the length, operating on real data with even symmetry (since the Fourier transform of a real and even function is real and even), where in some variants the input and/or output data are shifted by half a sample. The DCT-II and DCT-IV are considered as the alternative approach to the FFT.

In fact, the FFT routine can be supplied in an interleaving mode, even samples treated as real data, odd samples as imaginary data. However, the FFT algorithm in [68] has been implemented and optimized for only real samples from the ADC.

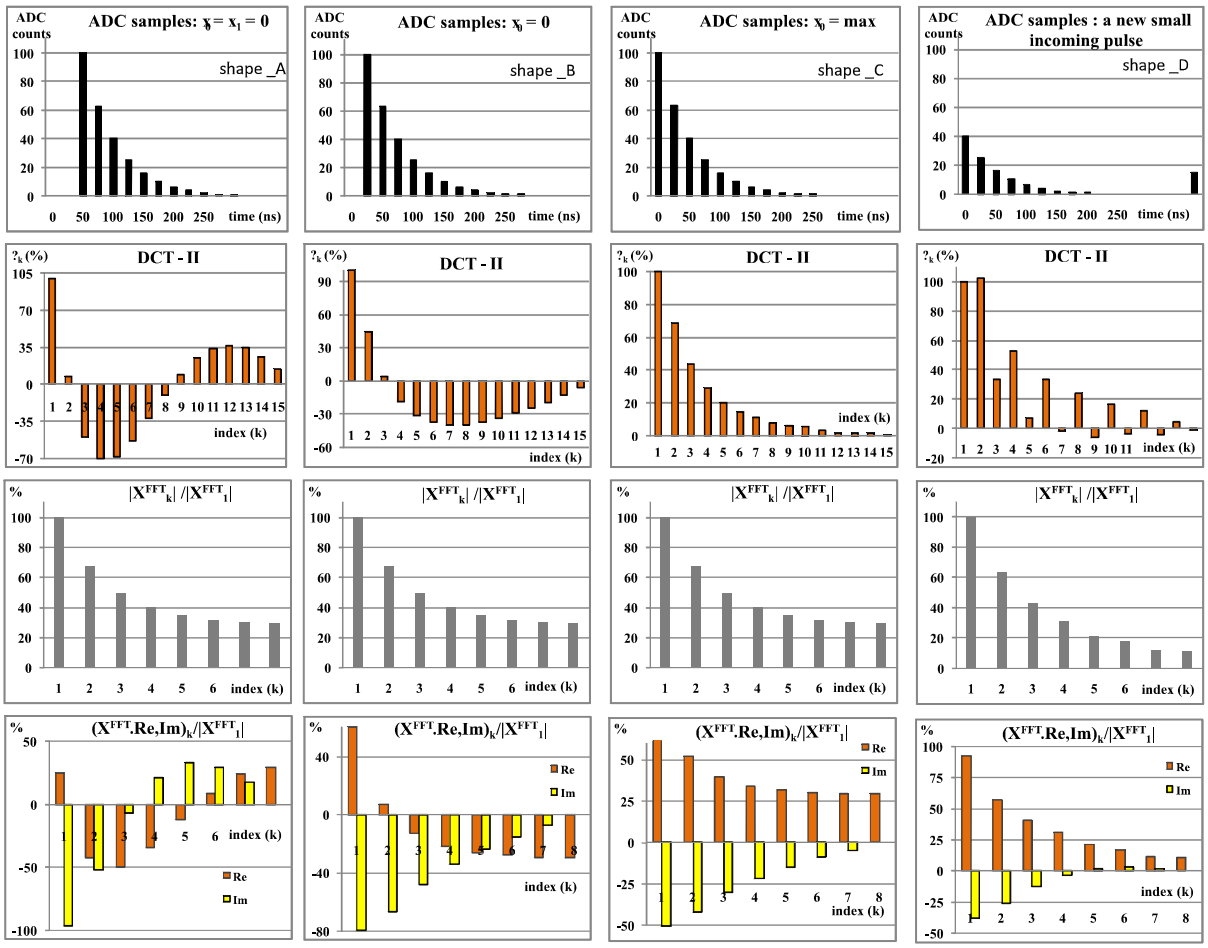

Figure 116 – A propagation of the pulse (1st row) through the shift register, DCT-II coefficients (2nd row), absolute values of the DFT (3rd row) and corresponding real (Re), imaginary parts (Im) (4th row). The 1st column shows the pulse (shape A), when two time bins are on the pedestal level, the 2nd one (shape B), when only the one time bin is still on the pedestal level, while the 3rd one (shape C) shows the pulse fully fulfilled the range of investigating shift registers. For a signal shape related to the exponential attenuation (shape C), the contribution of higher DCT coefficients is small and suitable for a trigger. When a peak appears in the declining signal (last column - shape D), the DCT coefficients immediately excesses assumed relatively narrow acceptance range for triggers. The DFT coefficients (Re and Im in 4th row) have similar structure as the DCT, however for the pure exponentially declining signal the higher real DFT harmonics have relatively high values and they are not suitable for triggering. Absolute values of DFT components (3rd row) are clearly insensitive on discussed conditions.

The upsampling, the standard procedure allowing increasing a resolution in a frequency domain, requires a data performance with multiple basic sampling frequencies. For the 100 MHz clock, even the factor of 2 for the up-sampling, needs a registered performance of 200 MHz, which is unfortunately too high for selected chip Cyclone III® The upsampling from the 40 MHz clock is not considered as the final 4th generation of the FEB will be working with 100 MHz data processing. On the other hand the upsampling for the 3rd generation of the FEB is impossible due to a lack of resources (especially DSP blocks).

The DCT algorithm has a significant advantage in comparison to the FFT one. The structure of DCT coefficients is much simpler for interpretation and for a trigger

implementation than the structure of the FFT real and imaginary coefficients (compare 4th of the FFT data vs. 2nd row for the DCT coefficients in Figure 116). For the exponentially attenuated signals from the PMTs higher DCT coefficients (scaled to the 1st harmonics) are almost negligible, while both real and imaginary parts of the FFT (scaled to the module of the 1st harmonics) give relatively significant contributions and are not relevant for triggering. When a peak appears in the pure attenuated signal (last column in Figure 116) the structure of the DCT dramatically changes and trigger condition immediately expires, while modules of FFT components almost do not change.

The structure of FFT harmonics for the last graph in Figure 116 would be more suitable for a trigger (almost negligible imaginary part for higher harmonics and also relatively low real harmonics), however it corresponds just to situation, when the pure attenuated signal is distorted by some peak on the tail and a trigger condition has been violated.

The plot in the 4th row and 3rd column on Figure 116 shows a contribution of the DFT vs. the absolute value of the 1st harmonic. For an exponential attenuated input signal (with the attenuation factor = β) the contribution of both real and imaginary coefficients decreases monotonically with a significant value for all real coefficients. From the DFT definition we get:

$$\overline{X}_k = A \cdot \sum_{n=0}^{\mathrm{N}-1} e^{\beta n} e^{-j\frac{2\pi k}{\mathrm{N}}n} = A\frac{1-e^{-\mathrm{N}\beta}}{1-e^{\beta+j\frac{2\pi}{\mathrm{N}}k}} \tag{82}$$

$$\xi = \frac{\mathrm{Re}\left(\overline{X}_k\right)}{\left\|\overline{X}_1\right\|} = \frac{1+e^{-\beta\mathrm{N}}}{\sqrt{\left(1-e^{-\beta}\cos\varphi\right)^2 + e^{-2\beta}\sin^2\phi}}, \qquad \text{where } \varphi = \frac{2\pi k}{\mathrm{N}} \tag{83}$$

Calculating (83) for boundary factors β = (0.28, 0.42) (see Figure 109 right) and for k = N/2 (as the lowest in a monotonically decreasing chain), we obtain for N = 16: ξ = 24% and 28%, respectively. These values are too large to be use for triggering. Even an extension of the DFT size does not help very much. For N = 32: we get still large values: ξ = 17% and 23%.

Almost vanishing higher DCT coefficients provide much natural trigger conditions. 32-point FFT (roughly equivalent to 16-point DCT) does not offer better stability.

The DCT algorithm presented in 4.2.2 has a significant advantage in comparison to the FFT one. For conditions discussed in 4.2.4 the structure of DCT coefficients are much simpler for interpretation and for a trigger implementation than the structure of the FFT real and imaginary coefficients (compare 4th of the FFT data vs. 2nd row for the DCT coefficients in Figure 116. For the exponentially attenuated signals from the PMTs higher DCT coefficients (scaled to the 1st harmonics) are almost negligible, while both real and imaginary parts of the FFT (scaled to the module of the 1st harmonics) have relatively complicated structure not relevant for triggering. When a peak appears in the pure attenuated signal (last column in Figure 116) the structure of the DCT dramatically changes and trigger condition immediately expires, while modules of FFT components almost do not change.

4.2.4 Preliminary assumptions for a trigger

The trigger described in [68] is based on a 16-point FFT algorithm and is clocked with 40 MHz. The "length" of the analysing sliding window equals to 400 ns, which is sufficient for an analysis of the muonic bump, especially for the "old" showers.

For the new 100 MHz sampling, 16-point samples would correspond to a 150 ns sliding window only. An analysis of the Auger database (collected for 40 MHz sampling) showed that a "length" of FADC traces corresponding to 200–250 ns is desirable.

The analysis of the attenuation part of the Auger FADC traces gives an attenuation factor roughly independent of time (Figure 109). FADC traces of almost very inclined events are characterized by a dramatic jump from the pedestal level up to maximal value due to their origin related to the geometrical configuration of PMTs in the tank (Figure 108 left).

Cherenkov light generated by very inclined showers crossing the Auger tank can reach the PMT directly without reflections on Tyvec™ liners. Especially for "old" showers the muonic front is very flat. This together corresponds to very short direct light pulse falling on the PMT and in consequence very short rise time of the PMT response.

For vertical or weakly inclined showers, where the geometry does not allow direct Cherenkov light on the PMT, the light pulse is collected from many reflections on the tank walls. Additionally the shower developed for not so high slant depth, are relatively thick. These give a signal from a PMT as relatively slow increasing. A very short rise time together with a relatively fast-attenuated tail could be a signature of very inclined showers.

The 100 MHz sampling however, should be already sensitive on a signal shape especially in the range of the rising edge of the analog signal, which corresponds to the beginning of the muonic shower. This region contains crucial information and should be sampled with full resolution. The tale of the signal, much longer than its front, contains less important information and can be sampled with a bigger grid. For 8 first samples in a 10 ns grid and next 8 samples in a 20 ns grid, the "length" of an analyzing sliding window is 230 ns and seems to be sufficient for our analysis.

The analog section of the FEB has been designed to have a pedestal of ~10 % of the full FADC range in order to investigate undershoots.

Denoting cosine factors as

$$F(k,n) = \cos\left(\frac{k\pi}{N}(n+\frac{1}{2})\right) \tag{84}$$

$$\overline{X}_k(ped) = \sum_{n=0}^{N-1}(x_n + ped)F(k,n) = \overline{X}_k + ped\sum_{n=0}^{N-1}F(k,n) = \overline{X}_k + ped \times W \tag{85}$$

Due to symmetry and parity of the cosine, we get for odd and even indices respectively:

$$W = 2\sum_{n=0}^{\frac{N}{2}-1}\left\{\cos\left(\frac{k\pi}{2}\right)\cos\left[\frac{\pi}{N}\left(n+\frac{1}{2}\right)k - \frac{k\pi}{2}\right]\right\} = \begin{cases} 0 \\ 2\sum_{n=0}^{\frac{N}{2}-1}F(k,n) \end{cases} \tag{86}$$

By a recursion repeating (86), we get finally $N/2 = 2$ and k = $0, N/2$. For k = $N/2$

$$2\sum_{n=0}^{1}\cos\left(\frac{\pi}{2}(n+\frac{1}{2})\right) = 0 \tag{87}$$

In a consequence for k ≥ 1 the DCT coefficients $\overline{X}_k$ are independent of the pedestal. The DCT coefficients normalized to the 1st harmonics

$$\xi_k = \frac{\overline{X}_k}{\overline{X}_1} \tag{88}$$

are also invariant on the scaling of a signal amplitude. It means the set of $\overline{X}_k$ (i.e 1st, 2nd and 3rd graph in the 2nd row of Figure 116 remains the same independently of the jump from the pedestal to a maximal values (if the amplitude of pulses were i.e. 500 ADC-counts or so instead of 100 ADC-counts for shapes A,B,C on the Figure 116).

As seen from Figure 109b if ADC samples propagating in the shift registers, which drive the DCT routine, match the pattern of exponential attenuation, the contribution of higher ξ_k significantly drops down. This condition we are using as a preliminary spectral trigger. If in the propagating signal a sample, significantly different from an expecting shape, appears in the input shift register, ξ_k dramatically change and stop fulfilling a trigger condition.

The trigger can be active for several time bins. The muonic front hitting a tank gives signals in three PMTs, which can be shifted between them due to a pure geometry of a shower, different characteristics of PMTs, analog channels etc. However, a shift should not exceed 25 ns, as shows the analysis of the Auger database. The interval of 25 ns corresponds to 2-3 time bins for the 100 MHz sampling. Attenuation tail has a "length" of more than 10 time bins. So, we expect overlapping trigger conditions in three channels and a final three-fold coincidence trigger for at least a single time bin.

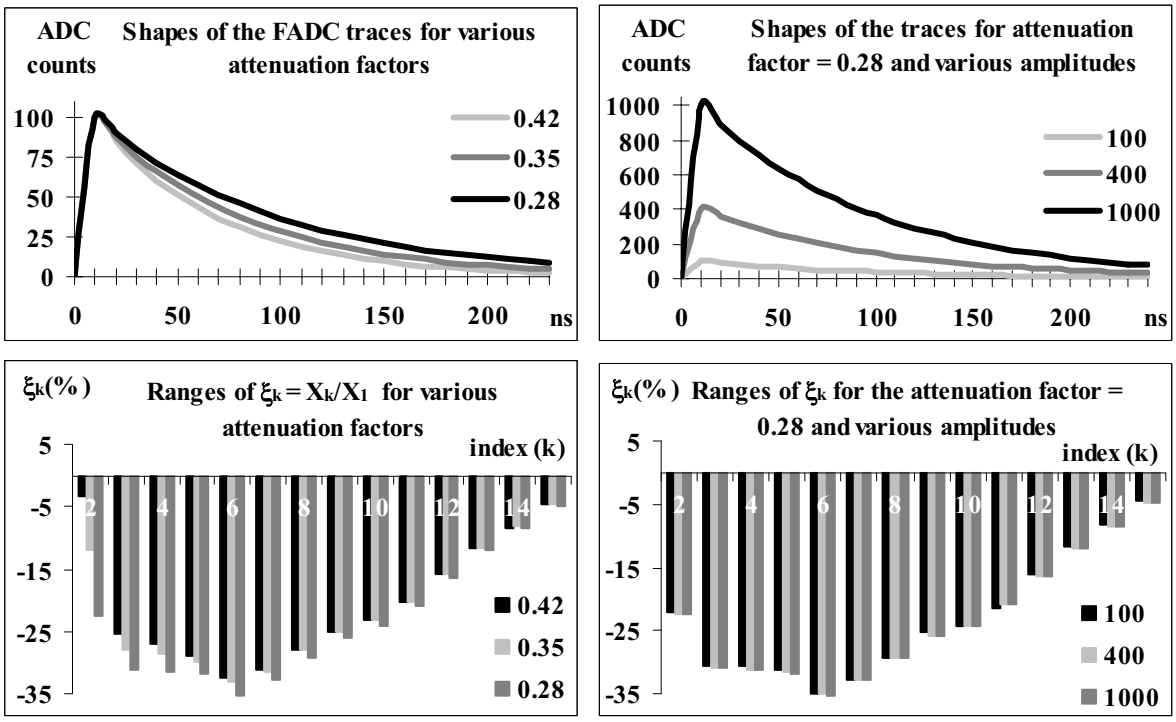

Figure 117 – Investigated shapes of Auger ADC traces with attenuation factors from Figure 109 and the corresponding set of ξ_k. ξ_1 not shown as equals to 100 %. For different attenuation factors the ξ_k almost does not change. The main variation appears for ξ_2 on the level of 20% and $\xi_{2,3,4}$ on the level less than 5%. As expected for different amplitudes, the set of ξ_k remains almost (integer representation of numbers inside the FPGA) unchanged.

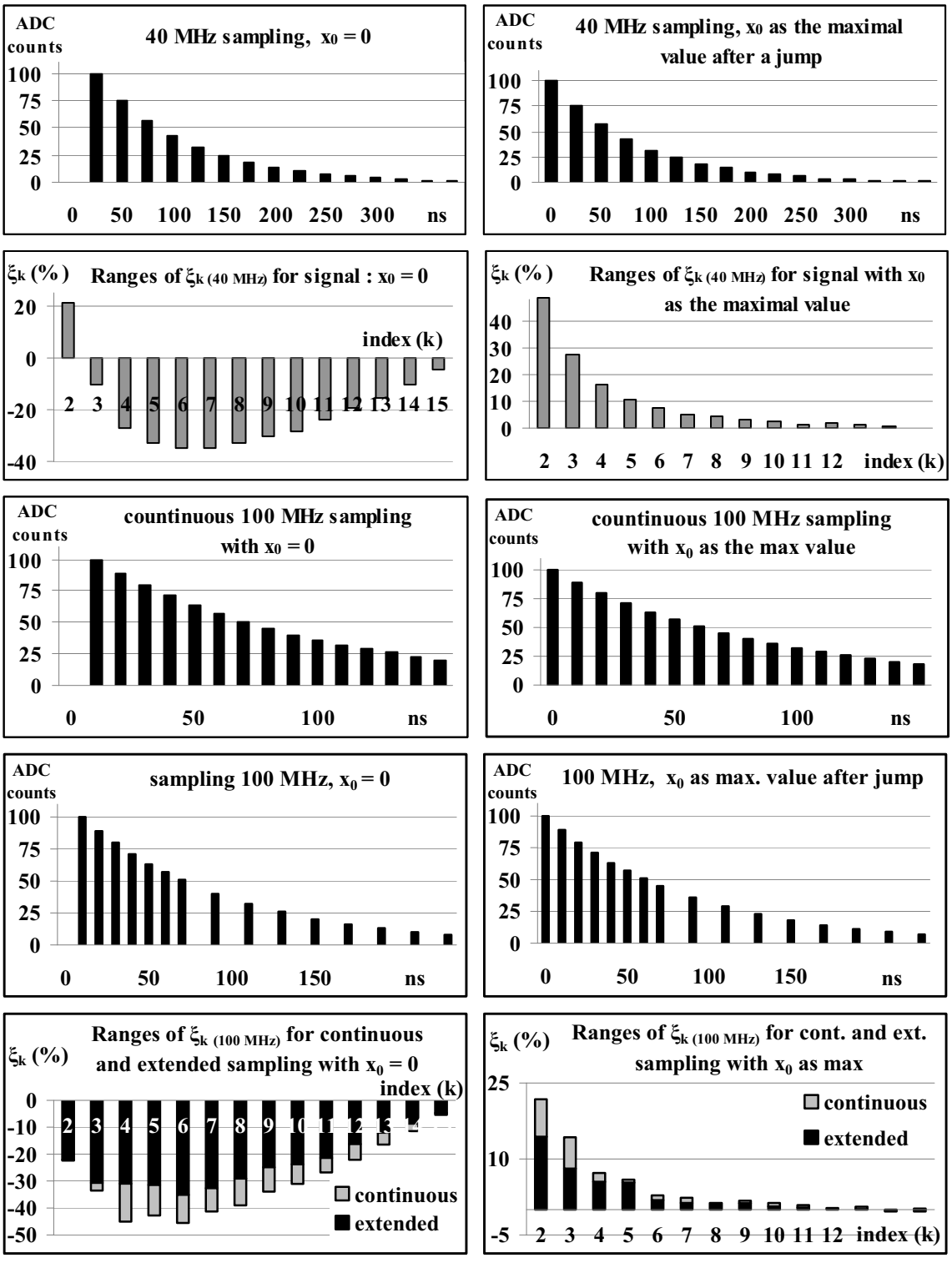

Figure 118 – Comparison of ξ_k for 40 and 100 MHz sampling respectively. Sets of ξ_k are significantly different; an analysis of the Auger data for 100MHz extrapolation requires a carefully resampling. The 100 MHz sampling with a continuous 10 ns grid gives larger ξ_k ranges in comparison to an extended grid with 1st 8 samples taken with 10 ns and the next with lower density 20 ns (2nd row). Narrower ranges of ξ_k for the extended mode as well as wider sliding window investigating the ADC trace give better trigger conditions than in a simple continuous sampling mode. The extended mode will be next the baseline for the DCT implementation.

An approach based on the exponentially declining signal (shape A) only may give too high trigger rate due to single muons. However, this trigger verifies a purity of the exponential shape of signal. Figure 121 shows the structure of FPGA procedures generating the final trigger. In this scheme three different shapes are investigated. This approach can be easily extended on numerous patterns being compared for consecutively clock cycles with respectively multiplexed thresholds in order to detect traces with more sophisticated shapes.

4.2.5 Implementation of the code into a FPGA

An internal FPGA routine, calculating coefficients of the Discrete Cosine Transform is derived from a well-known algorithm of Arai-Agui-Nakajima [70], however significantly optimized to the implementation into the FPGA [71]. Full 16-point DCT internal structure of the FPGA routine is shown on Figure 115 Figure. According to the assumptions from Chapter 4.2.4 the trigger should be generated if DCT coefficients normalized to the 1st harmonics were in an arbitrary narrow range:

$$Thr_k^L \le \xi_k = \frac{\overline{X}_k}{\overline{X}_1} = \frac{\eta_k * H_{f(k)}}{\eta_1 * H_{15}} \le Thr_k^H \tag{89}$$

where Thr_k^L and Thr_k^H are lower and upper thresholds for each spectral index k, respectively.

Altera™ Library of Parameterized Modules (LPM) contains the lpm_divide routine supporting a division of fixed-point variables. However, this routine needs huge amount of logic elements and is slow (calculation requires ca. 14 clock cycles in order to keep sufficiently high registered performance). DSP blocks also do not support this routine. A simple conversion to

$$H_{15} * \Theta_k^L = H_{15}\left(\frac{\eta_1}{\eta_k} Thr_k^L\right) \le H_{f(k)} \le H_{15}\left(\frac{\eta_1}{\eta_k} Thr_k^H\right) = H_{15} * \Theta_k^H \tag{90}$$

allows an implementation of fast multipliers from the DSP blocks and calculation of products in a single clock cycle. Θ_k^L and Θ_k^H are lower and upper scaled thresholds, respectively, which are set as external parameters.

According to (90) the calculation of a sub-trigger needs two multipliers, two comparators and an AND gate (Figure 122). The multiplier stage of an embedded multiplier block supports 9×9 or 18×18 bit multipliers. Depending on the data width or operational mode of the multiplier, a single embedded multiplier can perform one or two multiplications in parallel. Due to wide data busses embedded multiplier blocks do not use the 9×9 mode in any multiplication. Each multiplier utilizes two embedded multiplier 9-bit elements. The full DCT procedure needs the calculation of all coefficients 70 DSP blocks. However, the scaling of $\overline{X}_k$ in the last pipeline chain is no longer needed. It is moved to the thresholds according to (90). Removing last pipeline chain reduces amount of DSP blocks to 40. Sub-triggers routines (Figure 122) need 2 DSP blocks each. The chip EP3C40F324I7 selected for the 4th generation of the 1st level SD trigger contains 252 DSP 9-bit multipliers. So, for 3-fold coincidences and an implementation of 3 “engines” the single DCT “engine” can support only 11 independent DCT coefficients.

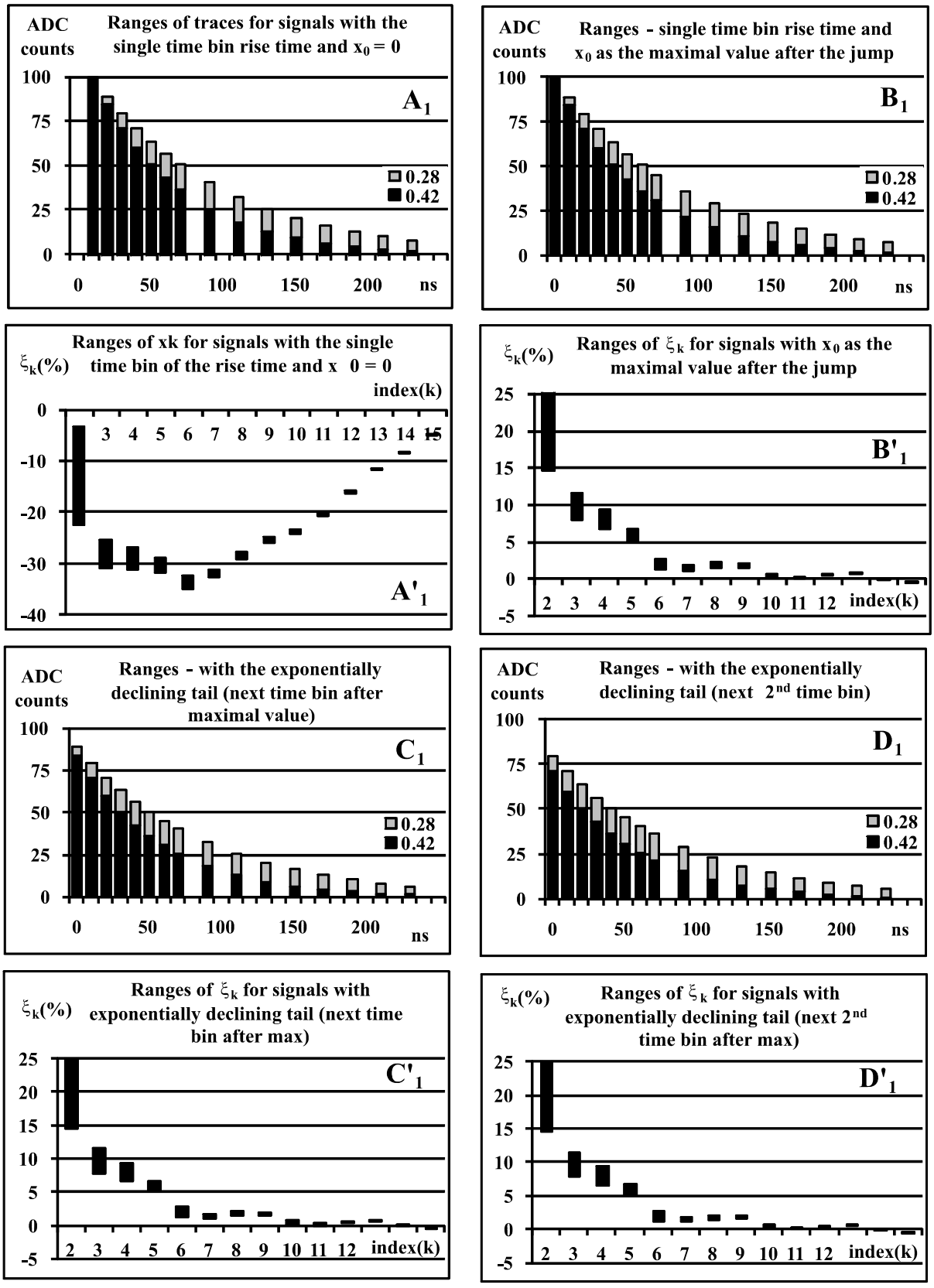

Figure 119 – Propagation of pulses with the single time bin of the rising edge and corresponding ranges of allowed ξ_k coefficients. The ξ_k set for exponentially declining tails are very similar (compare graphs: B'_1, C'_1 and D'_1).

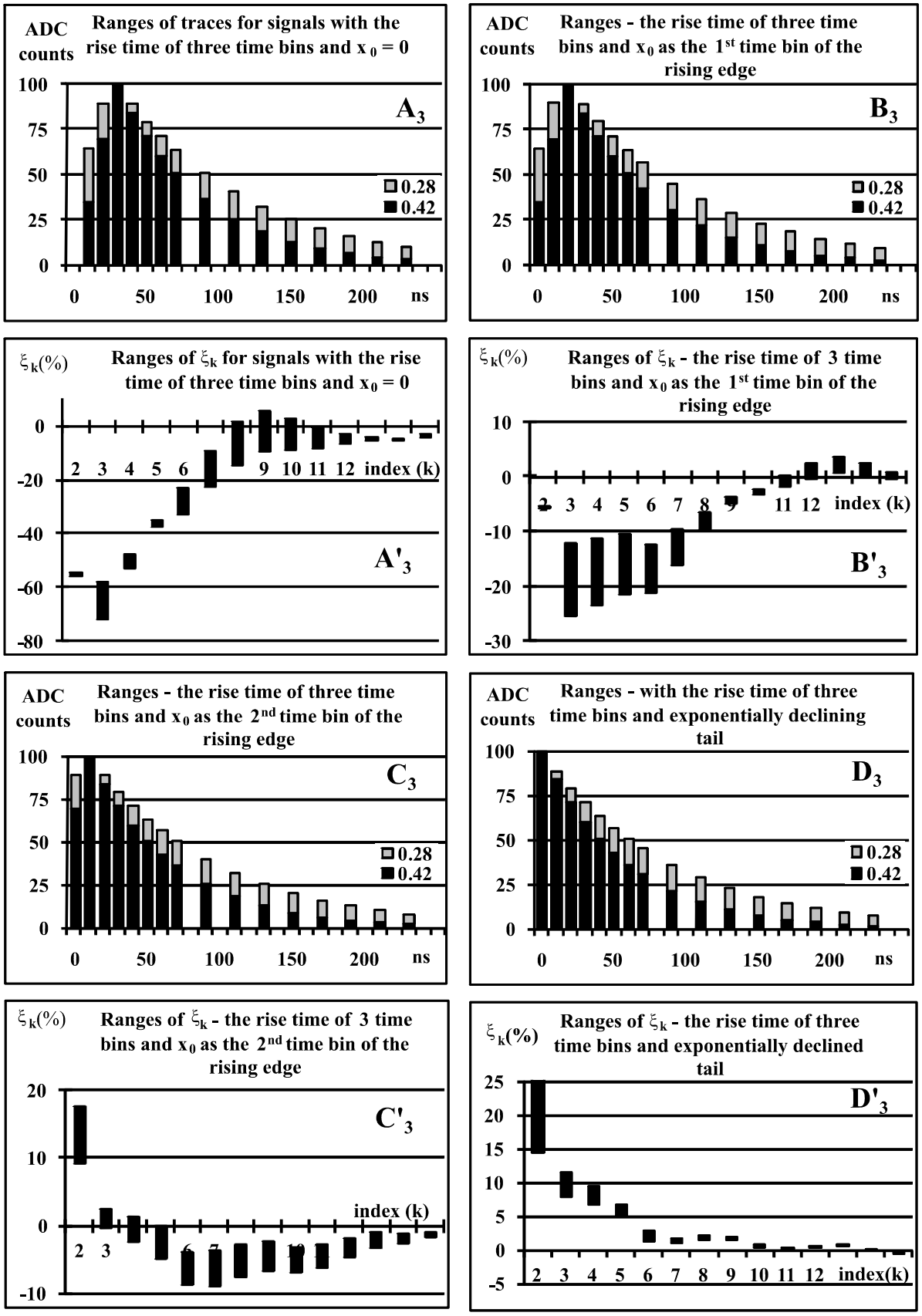

Figure 120 – Propagation of pulses with three time bins of the rising edge and corresponding ranges of allowed ξ_k coefficients. D'$_3$ is very similar to B'$_1$, C'$_1$ and D'$_1$.

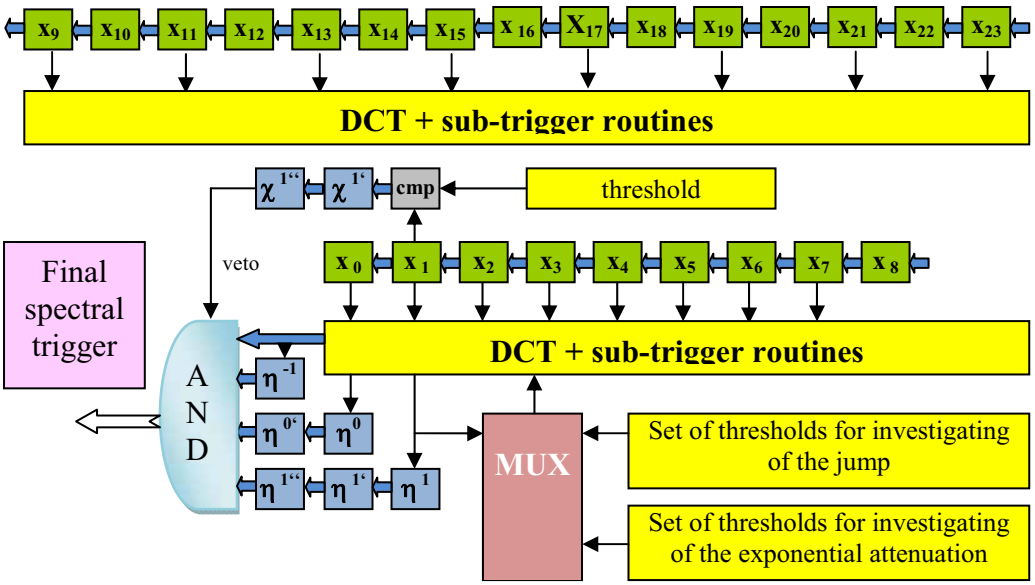

Figure 121 – A scheme of the final trigger generation. Sub-triggers $A_k^{0,1,2,3}$, $B_k^{0,1,2}$, $C_k^{0,1}$ and D_k^{0} are generated for the patterns A_k, B_k, C_k and D_k (k = 2,4,6) from Figure 119 respectively. Sub-triggers are synchronized to each other in shift registers in order to put simultaneously on an AND gate. In order to keep a trigger rate below the boundary deriving from the limited radio bandwidth, additionally the amplitude of the jump is verified. If the jump is too weak, a veto comparator disables the AND gate. Thus if spectral coefficients ξ_k match pattern ranges for each time bins selected by multiplexer totally in 4 consecutive time bins and if veto circuit is enabled the final trigger is generated. A delay time for the veto signal depends on the type of shape, which is an interest of an investigation. For the single time bin of the rising edge the veto is delayed on 3 clock cycles, for the investigated pattern corresponding to the three time bins of the rising edge the maximal ADC value appears 2 clock cycles later in comparison to the previous case, so the veto should be delayed on a single clock cycle only.

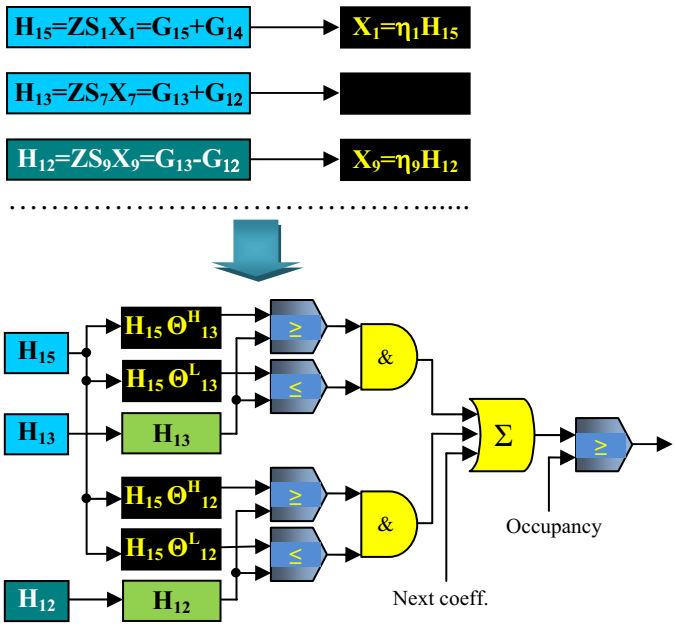

Figure 122 – The structure of sub-triggers.

Table 8 – Utilization of resources for various FPGA codes. Slack is the margin by which a timing requirement was met. The last column gives the slack for the most critical path at the given speed.

Code - chip	LE	DSP mult	Memory	Slack Clk
Auger - EP1C12	7489 (62%)	0	96 kb (41%)	17ns (40 MHz)
Merged - EP3C40	15002 (38%)	246 (98%)	0.6 Mb (54%)	0.9 ns (100 MHz)

$\overline{X}_0$ is not relevant (as the simple sum of 16 samples), $\overline{X}_1$ already implemented as the reference factor for a normalization, $\overline{X}_{15}$ is excluded from reasons given above. $\overline{X}_{13}$ and $\overline{X}_3$ have also not been implemented.

Table 8 shows that the 3 DCT trigger "engines" have been successfully merged with the Auger code working with 100 MHz sampling. The final code utilizes only 38% of logic elements, but all embedded multipliers. The large amount of free resources gives an opportunity to add new, sophisticated algorithms. The slack reported by the compiler corresponds to a maximal sampling frequency 112 MHz (ca. 12% more than required), which gives a sufficient safety margin for a stable operation of the system.

For sufficiently high amplitudes of the ADC samples the Threshold trigger will be generated at least 32 clock cycles earlier than the spectral trigger (24 clock cycles of propagation in the shift registers + 8 clock cycles of performance in the DCT chain). If the Threshold trigger has been already generated, the next triggers are inhibited for 768 time bins necessary to fulfill memory buffers (see Figure 7 in [48]). Because the Threshold trigger (sensitive to bigger signals) has a higher priority than the spectral trigger, ADC samples will not be delayed for the Threshold trigger in order to synchronize it with the spectral one.

The system uses 10-bit resolution (standard Auger one). A compilation for the 12-bit resolution for the current chip EP3C40F324I7 failed, due to a lack of the DSP blocks. 12-bit system requires bigger chip EP3C55. The slack times are on the same level as for EP3C40. All pipeline routines shown in Figure 115 are implemented in a direct mode (no pipeline mode - like i.e. in the 2nd generation of the FEB based on the ACEXR family (see Figure 2 in [48]) or for the FFT implementation in the Cyclone™ family (compare Figure 2 in [63]). So, a performance of a signal requires a single clock cycle only. All routines are fast enough to work with 100 MHz sampling without an additional pipeline stages and they do not introduce an additional latency

4.2.6 Accuracy

10-bit resolution of FADC in the high-gain channels (responsible for a trigger generation) implies the ranges of $\overline{X}_k$ coefficients given in the 2nd column of Table 9.

Multiplications of integer values N by real scaling factors sf [72] give floating-point results. In order to keep possible high speed of calculation and not to utilize resources spendthrift the fixed-point algorithm of processing has been chosen. N*sf were approximated on each pipeline stage again to the integer value. For almost all scaling factors: sf ≤ 1, N*sf has a representation of the same or less amount of bits. For sf ≥ 1, N*sf extends the representation on 1 or 2 bits. This approximation introduces errors, however mostly in the LSB, apart from $\overline{X}_{15}$. The coefficient $\overline{X}_{15}$ will not be used for a trigger.

The main advantage of the spectral trigger is the scaling feature. The set of the ξ_k coefficients (88) depends only on the shape of signals, not on their amplitudes. Triggers

sensitive on the shape of FADC traces may detect events with expected characteristics i.e. the fast attenuated, very short peaks related to the muonic, flat fronts coming from very inclined showers. Independence of the amplitude is especially promising for the Auger North, where due to a single PMT in the surface detectors the coincidence technique cannot be used. In order to keep reasonable trigger rate for the 1st level trigger (ca. 100 Hz), the threshold for the 1st trigger should be much higher than in the Auger South, where 3-fold coincidences attenuated a noise.

The spectral triggers have been implemented in 7 test tanks (a hexagon configuration) together with the currently used Threshold and ToT triggers in the 4th generation of the Front-End. Thresholds for coefficients ranges are being tuned experimentally to keep a balance between the rates of all triggers (Thr, ToT and spectral) and in order not to exceed the existing transmitted data rate due to the bandwidth limits.

Table 9 – Ranges of $\overline{X}_k$ coefficients and relative errors for least significant bits of $\overline{X}_k$. For k ≤14 the errors appear practically only in the LSB.

k	$\overline{X}_k$ range	LSB	2nd bit	3rd & more	k	$\overline{X}_k$ range	LSB	2nd bit	3rd & more
0	0…4092	0.0%	0.00%	0.00%	8	± 2041	0.00%	0.00%	0.00%
1	± 2521	13.1%	0.00%	0.00%	9	± 12224	23.8%	1.55%	0.00%
2	± 2581	8.7%	0.00%	0.00%	10	± 4557	12.8%	0.00%	0.00%
3	± 2914	13.1%	0.00%	0.00%	11	± 7519	17.7%	0.00%	0.00%
4	± 2348	4.8%	0.00%	0.00%	12	± 5671	11.5%	0.00%	0.00%
5	± 4019	15.1%	0.00%	0.00%	13	± 9605	24.3%	2.00%	0.00%
6	± 3045	8.6%	0.00%	0.00%	14	± 12978	26.9%	2.86%	0.00%
7	± 10032	23.1%	1.10%	0.00%	15	± 25597	30.9%	25.08%	6.83%

Spectral triggers are being optimized in the Auger South test tanks with the configuration of 3 “engines” and 3-fold coincidences working for the single selected shape A_k, B_k, C_k, D_k (Figure 119) for k = 1 or 3 or 5.

This configuration can be used immediately in AMIGA design. According to estimations, the configuration with 3 “engines” does not support all ξ_k sub-triggers due to limited amount of DSP blocks. However, the neglected coefficients are not especially relevant. For the Auger North for the single PMT, 3 “engines” will be implemented to investigate and to detect 3 different shapes of FADC traces corresponding to different rise time of the rising edge.

Furthermore, the implementation of the algorithm presented above may be applied in on-line video signal processing, where Discrete Cosine Transform is widely used [73].

5 Performance of the Pierre Auger Observatory

The Pierre Auger Observatory is the hybrid detector consisting of a surface detector and an atmospheric fluorescence detector. The duty cycle of the surface detector is nearly 100% whereas the fluorescence detector duty cycle may be only 10%. The hybrid data set obtained when both detectors are working together will be especially important for evaluating the systematic errors of both detectors. It will also provide an energy spectrum with small energy uncertainties. The hybrid data set will also provide the best evaluation of the primary particle composition utilizing all of the known parameters that are sensitive to the primary particle type.

The use of the two techniques allows the determination of the primary energy improved with respect to former arrays and with no basic dependence on interaction models and hypothesis on the primary composition. The technique is based on the calibration of the energy estimator of the surface detector (SD) through the fluorescence detector data (FD): the SD provides the required statistics thanks to its collecting area and its much larger duty cycle. The signal measured at a specific distance from the shower axis, S(r), is well established as an energy estimator for the surface detector. Figure 123 shows that shower-by-shower fluctuations reach minimum for r ~ 1000m, which is the main reason for choosing it as the primary energy estimator.

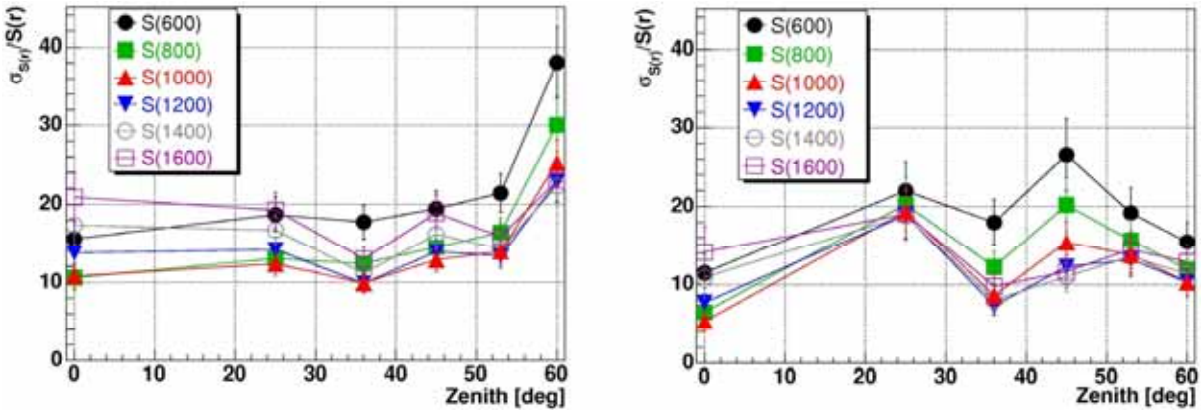

Figure 123 – Statistical uncertainty in S(r), for various values of r, vs. zenith angle, for 10 EeV primary protons (left) and for 10 EeV primary irons (right) simulated by QGSJET interaction model [87].

The accuracy in the determination of such estimator depends on the detector resolution and sampling fluctuations, and on shower fluctuations in the longitudinal development, since the measurement is performed at a single, fixed atmospheric depth. The SD energy estimator is not directly measured, but interpolated by a fit to a lateral distribution function (LDF) in precise non-linear interpolation even where no tank exists at that particular core distance [74].

5.1 Fluorescence Detector

In November 2005 three of the four fluorescence sites have been completed and are in operation. Two of them, Los Leones and Coihueco, have been collecting data since January

2004, with Los Morados beginning data taking in March 2005. The fourth site at Loma Amarilla started to be operational in the 2nd half of 2006.

The main goal of the FD is the measurement of air shower energies with an uncertainty smaller than 15%. This requires the FD calibration with a precision of about 8% as well as the regular monitoring. An absolute calibration of each telescope is performed three or four times a year, and relative calibrations are performed every night during detector operation.

Using a large homogeneous diffuse light source attached at the front of the telescope diaphragm performs the absolute calibration. The source has the shape of a drum with a diameter of 2.5 m. The light flux emitted by the drum at the diaphragm is known from laboratory measurements [75]. The ratio of the drum intensity to the observed signal for each PMT gives the required calibration. At present, the precision in the PMT calibration using the drum (at a single wavelength of 375 nm) is about 12% [75]. Drum is also used to adjust gains for uniform response of the pixels.

In the relative calibration light signals are propagated via optical fibers to three different diffuser groups for each telescope: at the center of the mirror to illuminate the camera, along the lateral edges of the camera body facing the mirror and facing two reflecting Tyvec foils glued on the inner side of the telescope shutters, respectively. The total charge per pixel is measured with respect to reference measurements made at the time of absolute drum calibrations. This procedure allows the monitoring of short and long term stability, the relative timing between pixels and the relative gain of each pixel [76]. The systematic uncertainty is ~3%, which contributes to the overall 12% systematic uncertainty in the FD calibration.

The FD calibrations are crosschecked by a reconstruction of energy of laser beams that are fired with known energy into the atmosphere from various, fixed positions in the SD array. Part of the laser light is scattered by the atmosphere (Rayleigh and aerosol scattering). The FD telescopes detect and measure this scattered light and allow on comparison the estimated laser energy with the real one. The observed difference between the reconstructed energy and the real laser energy is of the order of 10% to 15% [77], consistent with the current level of uncertainty in calibrations and knowledge of the atmosphere.

Energies of showers are estimated via sophisticated procedures, starting from a reconstruction of the shower geometry, determination of the shower axis and the shower-detector plane (SDP). The uncertainty in the reconstructed SDP depends on the size of each PMT field of view (1.5°), the observed angular track length, and on the width of the shower image. For a typical shower (23° track length) the estimated uncertainty in the normal to the reconstructed SDP is estimated to be 0.3° [78]. If the length of track visible by the FD camera is small, the uncertainty of geometry reconstruction may dramatically increase. However, a support from even a single surface detector (moves to the hybrid analysis – see Chapter 5.3) significantly improves a core location to ca. 50 m and axis orientation to 0.5° [79].

The overall uncertainty in the conversion from photons at the detector to emitted fluorescence photons is of the order of 12% [80]. The amount of light emitted at the shower track is calculated on the basis of the shower geometry, the known atmospheric conditions, the spectrum of the light and the detector's relative wavelength response. Standard Auger procedure takes also into account the direct and scattered Cherenkov light measured by the FD [81]. The calculation procedure of the fluorescence yield includes a systematic uncertainty on the absolute yield of 13% [82], and systematical uncertainty related to the pressure (4%), temperature (5%) and humidity (5%). The integral of the shower energy deposit profile provides a calorimetric measure of the cosmic ray energy. A small correction is made for unseen energy – an energy-dependent correction of 5–15% with a systematic uncertainty of about 3% [83].

5.2 Surface Detector

The Auger water Cherenkov detectors have been designed, fabricated, deployed and operated in the Engineering Array [84] and the pre–production phase. The data collected with the EA provided stringent checks of the performance of the surface detectors, which exceeded our expectations. Simulations, analysis of the EA data and additional studies, performed in several test stations, have demonstrated the performance of the surface detector electronics. The remote control and difficulty of accessing each detector impose an automatic remote calibration procedure. Cosmic muons are used to monitor and update the calibration constants. By performing this calibration for all the PMT, all surface detectors have been calibrated and monitored routinely at an overall precision of better than 5% [85]. The fluctuations in the signals recorded by the surface detectors directly affect the reconstruction of the physical parameters. Two stations located near the center of the EA array, separated by 11 m, were used to investigate fluctuations in the signal density measurements.

The environment to which an Auger Surface Detector is exposed is somewhat hostile for the electronics. At 1400 m a.s.l. and with clear skies, day-night temperature variations are of the order of 20°C, however the temperature variations in the electronics box may reach even 50°C. The terrain properties vary on the 3000 km^2 of the array, and some detectors have to face high salinity corrosive air, while others face dusty air from sandy ground. Humidity is present both in the ground (rivers, groundwater) and in the tank due to condensation.

To monitor the whole array accurately various sensors are installed in each tank. Temperature is measured on each PMT base, on the electronics board, and on each battery. PMT voltage and current are also monitored, as well as solar panel voltages, individual battery voltage, and charge current. These data are used to detect a wide range of failures, from broken solar panels to discharging batteries, and correlations like unstable PMT behavior related to temperature.

Weather stations reporting temperature, pressure, humidity, wind speed and direction are installed at each fluorescence site and in the center of the array, to complete the environmental monitoring. These data allow extra checks such as the influence of the pressure on the calibration.

Table 10 – Fraction of poorly performing detectors. Note, that the Baseline (Front End Boards) is the most reliable segment in the surface detector [86].

issue	fraction of stations
PMT connector	0.9 %
PMT unstable	2.5 %
PMT various	1.4 %
Electronics generic	4 %
Power issue	5 %
Baseline	0.3 %
VEM	5 %
Charge/Peak	0.9 %
Dynode/Anode	0.5 %

The calibration is operated on-line every minute, and sent to CDAS every 6 minutes for monitoring. A number of quantities are available to check the behavior of the tank: baseline values, single muon peak signal, single muon average charge, dynode/anode ratio, and PMT stability. In addition, high statistics histograms of the charge distribution from muons (more than 150 000 counts) and average pulse shapes are sent every time a station records an event.

This information allows detailed monitoring of the evolution of the calibration and various crosschecks. The on-line calibration takes into account most temperature fluctuations at the local trigger level as reflected in the same figure by the stability of the trigger rate over time. Over the whole array, correlation of the trigger rate with temperature are -0.04 ± 0.03% per degree for the FLT (T1), 0.08 ± 0.05% per degree for the SLT (T2), and 0.2 ± 0.5% per degree for the ToT trigger. The SD array therefore operates with stable trigger threshold even with 20 degrees daily temperature variations.

Finally, analysis of all these parameters allows detection poorly performing detectors. Table 10 shows the fraction of detector in which some monitoring parameters fall outside of the expected range or exhibit large fluctuations.

The shower direction is estimated with the ground array from the arrival times of the shower front at the different SD stations, which are determined from the PMT FADC traces, and the position of the SD stations which are known at the level of 1 m from GPS positioning. The angular fit is strongly based on the measurement of the arrival time. The large sample of data collected with the EA has allowed detailed studies of the time measurement by the SD stations and its impact on the angular reconstruction of EAS. These studies included analysis of time synchronization within a tank, relative time synchronization of the EA tanks and time offsets of each EA station.

The stable performance (despite very unfavorable environmental conditions and big daily temperature variation) of the surface array of the Pierre Auger Observatory has been confirmed since January 2004. On-time for 2004 is above 94% [86]. Only a small number of stations indicated poor performance. Most failures appeared in the first period of operation. Fraction of stable detectors is increasing and reached 97% at June 2005. Up to this time, more than 180 000 events have been recorded with an average rate of about 0.9 per station per day, also with a significant number of very inclined events. For the completed array, we expect a rate of about 1500 physics events per day. The angular resolution for the surface detector angular was found to be better than 2.2° for 3-fold events ($E < 4$ EeV), better than 1.7° for 4-folds events ($3 < E < 10$ EeV) and better than 1.4° for higher multiplicity ($E > 8$ EeV) [79] and around 10% for the SD energy estimator (signal at 1000 m from the core [87]).

Till May 25, 2009, 1661 tanks have been deployed, 1655 filled with pure water and 1627 equipped with electronics. Full South array has been completed.

5.3 Hybrid mode

The hybrid prototype enabled testing new concepts in triggering, data communications, and merging and reconstruction procedures. The times recorded by SD stations are used to help pick out the best geometry by requiring that their times agree with the expected times at their locations. The angular resolution in hybrid mode is a small fraction of a degree, exceeding our original design specification.

The Auger Observatory is the only experiment that works in hybrid mode. The Auger FD is expected to operate always in conjunction with the SD, which records the lateral distribution of particles at ground level, while the FD measures longitudinal shower

development, providing the calibration of the primary energy. For zenith angles $\theta < 60^{o}$ the primary energy can be estimated from the SD data, fitting a LDF to the observed densities, and then using the signal S(1000) as an energy estimator. Thus, the energy reconstruction requires, as a first and crucial step, estimation of S(1000) from a few measured signals at various distances and from an *a priori* unknown core position.

The measurements of angular resolution of the hybrid events are supported by artificial showers generated by laser shots from the **C**entral **L**aser **F**acility (CLF), located in the middle of the array at about 30 km from each fluorescence detector. CLF contains a remotely controlled laser, which produces vertical "showers" (within 0.01°). At the same time it sends a pulse of light to a surface station to generate an artificial hybrid event. The laser shot is reconstructed with the same algorithm used to reconstruct real events with only one surface station. From those artificial showers, the σ value obtained from the adjusted Gaussian resolution function ($\sim\exp(-\Omega^2/2\sigma^2)$), where Ω is the angle between the reconstructed shower axis and the true one) is 0.2°, corresponding to 0.15° for the shower angle inside the shower detector plane and 0.15° for the determination of the SDP itself. This σ corresponds to the angular resolution of 0.3°. We define the angular resolution as the angular radius that would contain 68% of showers coming from a point source, which is approximately 1.5 times the parameter coming from the Gaussian resolution function. Also, the core location is determined with an uncertainty of 50 m, which is independent of the shower geometry. It is determined by the spacing of 1.5 km between the surface detectors and by the SD and FD synchronization, which is better than 100 ns.

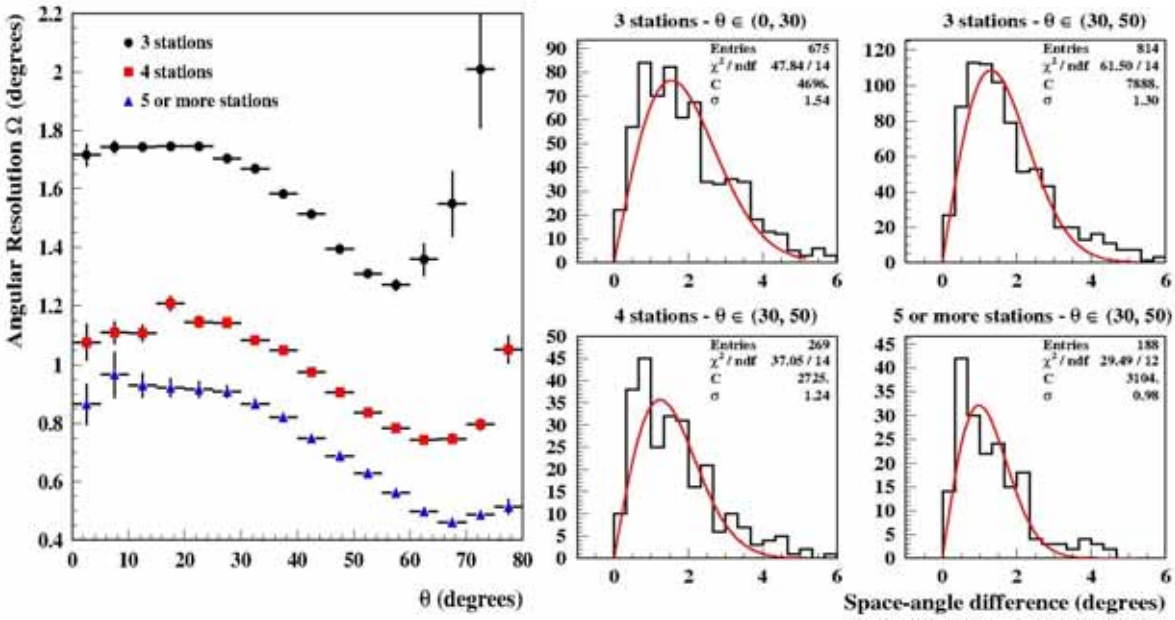

Figure 124 – Angular resolution for the surface detector as a function of the zenith angle for various stations multiplicities: circles 3 stations (E < 4 EeV), squares, 4 stations (3 < E < 10 EeV) and triangles more than 4 stations (E > 8 EeV) (left). Comparison between hybrid and SD-only space-angle differences shown for: top, for 3 stations with two zenith angle ranges 0º and 30º, bottom left, 4 stations, bottom right 5 stations or more, both with 30º [79].

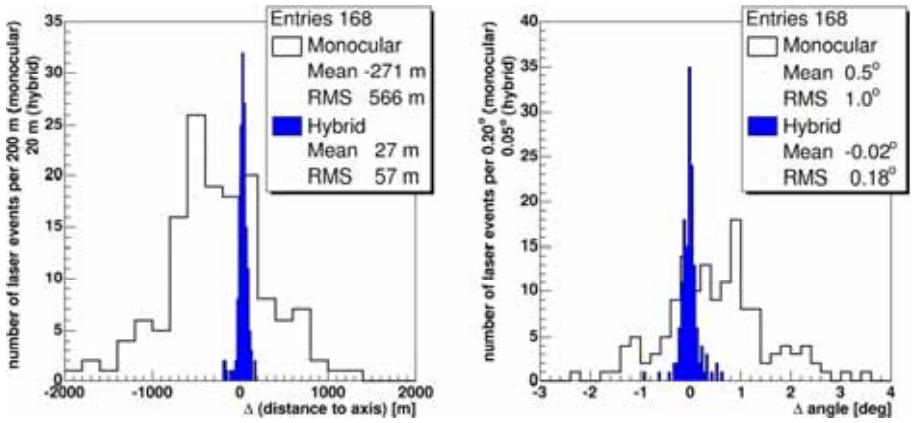

Figure 125 – Difference between the reconstructed and true distance from the eye to the vertical laser beam using the monocular and hybrid techniques. The location of the laser is known to 5 m (left). And the angular difference between reconstructed and true direction of the laser beam using the monocular and hybrid techniques. The laser beam is vertical within 0.01° (right) [88].

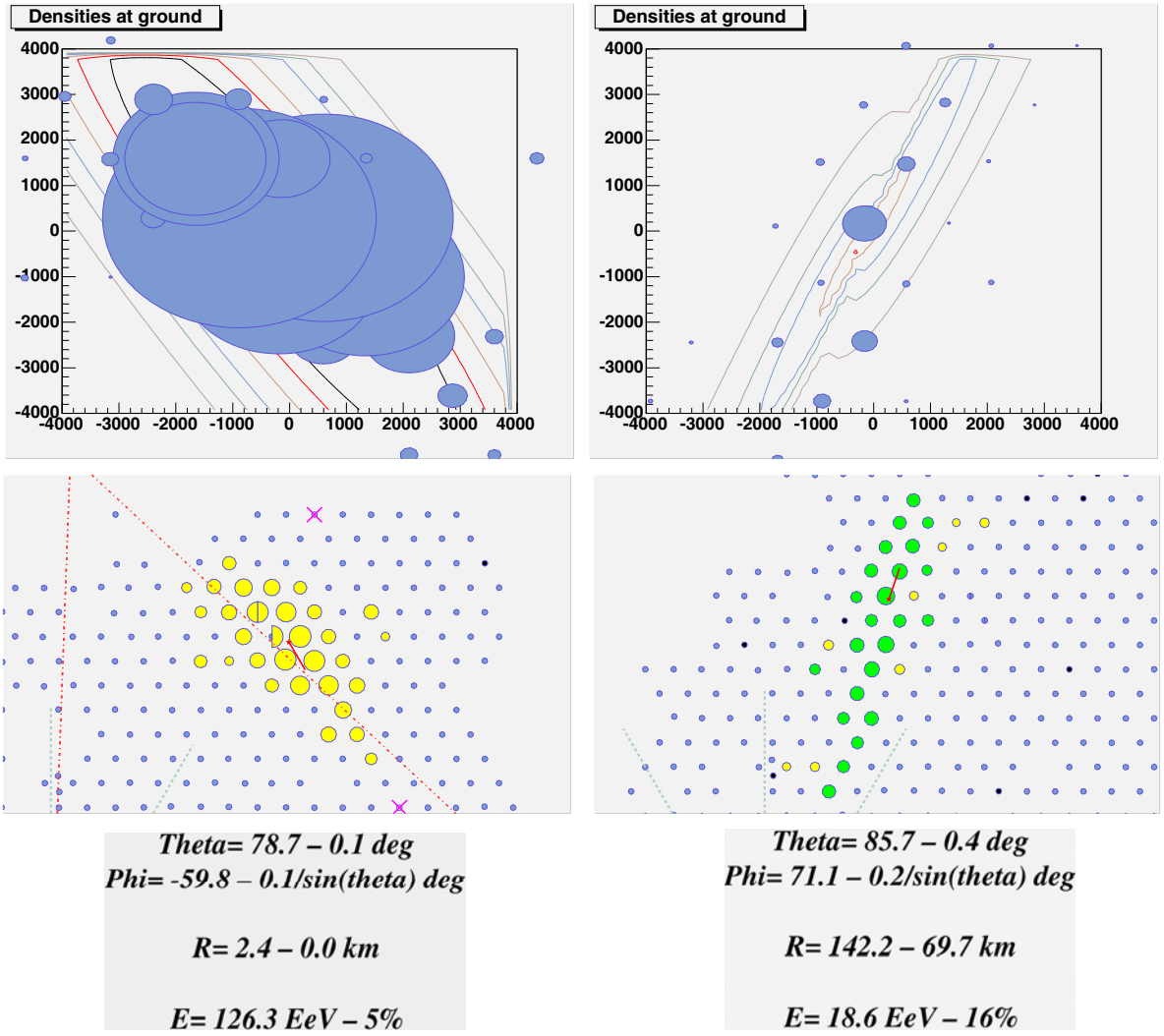

Figure 126 – An inclined Hybrid Golden Event (left - #0850019) and very inclined event (#1145171) .

Angular resolution for the surface detector is a function of the zenith angle and increases with stations multiplicities (see Figure 124). Comparison between hybrid and SD-only geometrical reconstruction shows that the hybrid reconstruction is a significant enhancement and provides much better angular accuracy than the SD mode only (Figure 125).

The Auger hybrid system was built with a "cross–triggering" capability. Data were recorded from both the SD and the FD whenever either system was triggered. In most cases the FD, having the lower energy threshold, promoted a sub–threshold SD trigger, bringing then the hybrid energy threshold well below the design of 10 EeV.

Very inclined showers with zenith angle greater than 80º were also recorded (see Figure 126) showing very energetic (denoted also as a Golden event with $\theta \sim 71º$). Understanding these showers is important because they will allow significant enhancement of the array aperture and they constitute the background to search for very inclined showers induced by ultra high–energy neutrinos. In these showers the majority of the particles reaching ground level are energetic muons nearly parallel to the incoming cosmic ray direction. Their trajectories are deflected by the magnetic field of the Earth, deforming slightly the symmetric pattern observed in vertical showers. However, the main deformation of patterns for very inclined showers is coming due to geometry. The directions of very inclined showers are obtained by fitting the particle arrival times recorded at each station to a plane or curved front. To reconstruct the energy a theoretical prediction of the muon density pattern is required.

Measurements by the Pierre Auger Observatory are planned for the next 15–20 years. The Southern Site has been completed in the end of 2008. The Southern part only will have the greatest integrated aperture in the world. Together with the Northern Site Pierre Auger Observatory provides the measurement opportunities unavailable in the other concurrent experiments (Figure 127).

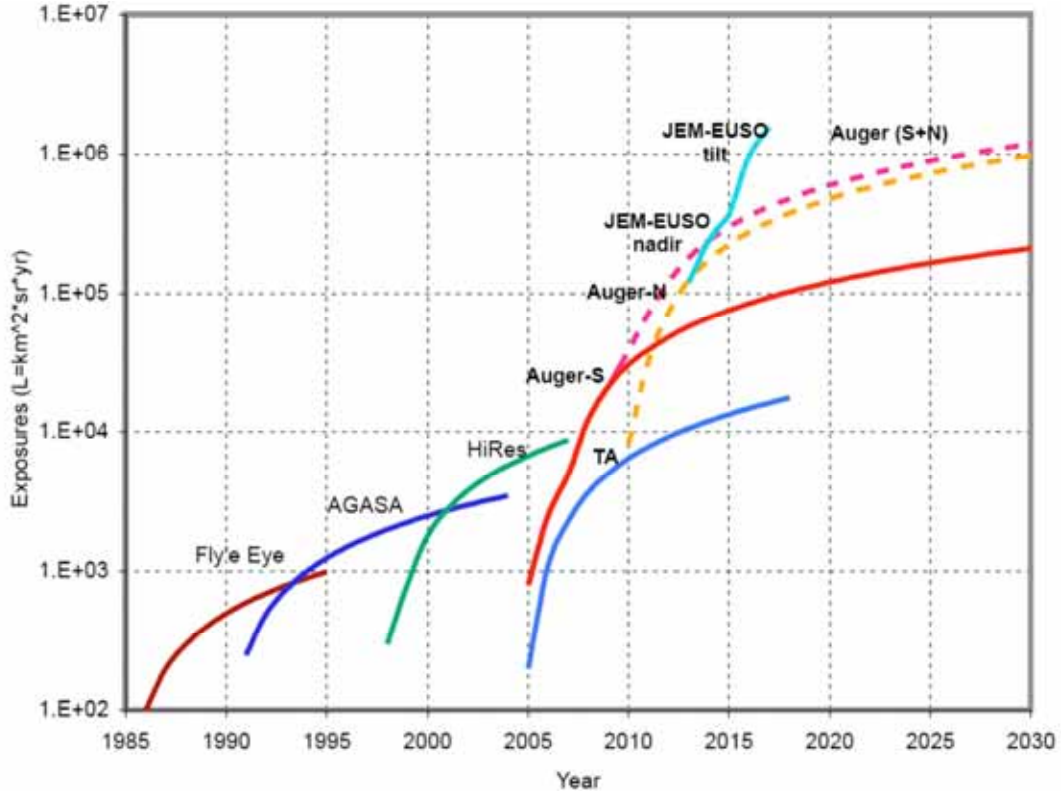

Figure 127 – Comparison of integrated aperture for the greatest cosmic rays experiments [89].

6 Preliminary results from the Pierre Auger Observatory (2007)

6.1 First Estimate of the Primary CR Energy Spectrum above 3EeV

In June 2006 almost ¾ of the South array has been completed. The cumulative exposure exceeded the value achieved in the largest currently running experiments. Already available data can give a preliminary estimation of the cosmic ray energy spectrum in the southern sky. Due to the hybrid technique of events registration, both fluorescence and surface detector data taken into calculation allow reduction of uncertainties. For the preliminary analysis only the data from the last 1.5-year (January, 2004 – June, 2005) has been selected [90]. We are still aware of possible bias due to contaminated data and problems reported earlier.

Accepted events are contained in the zenith angle range 0-60º, energy is above 3 EeV (3525 events). For the above criteria the detection efficiency of showers is close to 100%, so the simple geometric aperture can express the acceptance at any time. The cumulative exposure is estimated on ~1750 km^2 sr yr, which is 7% greater than the total exposure obtained by AGASA [91].

Energy of SD events is calculated in the following process:

1) **S(1000)** is determined (from integrated water Cherenkov signals S(r) from each station) by fitting (θ - dependent) the lateral distribution function (LDF) for each event (see Figure 128);

2) The slant depth of the surface array varies from 870 g/cm^2 for vertical showers to 1740 g/cm^2 for showers at zenith angle θ = 60º. The signal S(1000) is attenuated at large slant depths. Its dependence on zenith angle is derived empirically by exploiting the nearly isotropic intensity of cosmic rays. By fixing a specific intensity I_0 (counts per unit of $\sin^2\theta$), one finds for each zenith angle the value of S(1000) such that I(> S(1000)) = I_0. A particular constant intensity cut gives the curve CIC(θ) of Figure 129. The S(1000) values are shown relative to the value at the median zenith angle (θ ~ 38º). Given S(1000) and for any measured shower, the energy parameter S_{38} is defined by

$$S_{38} = S(1000) / CIC(\theta) \tag{91}$$

It may be regarded as the S(1000) measurement the shower would have produced if it had arrived 38º from the zenith.

3) S_{38} is well correlated with the FD energy measurements (see Chapter 5.1) in hybrid events that are reconstructed independently by the FD and SD (see Figure 130). The fitted line gives an empirical rule for assigning energies (in EeV) based on S_{38} (in VEM):

$$E = 0.16 \times S_{38}^{1.06} = 0.16 \times \left(S(1000) / CIC(\theta)\right)^{1.06} \tag{92}$$

The S_{38} formula implicitly assumes that all constant intensity curves can be rescaled from the reference curve CIC(θ) of Figure 129, which corresponds to S_{38} = 15 VEM. Higher values of also yield curves of constant intensity to the accuracy that can be checked with current statistics. With a much larger data set, it will be possible to investigate any change in shape of

the constant intensity curve with energy and thereby reduce any systematic error that might be associated with this simple formula for S_{38}.

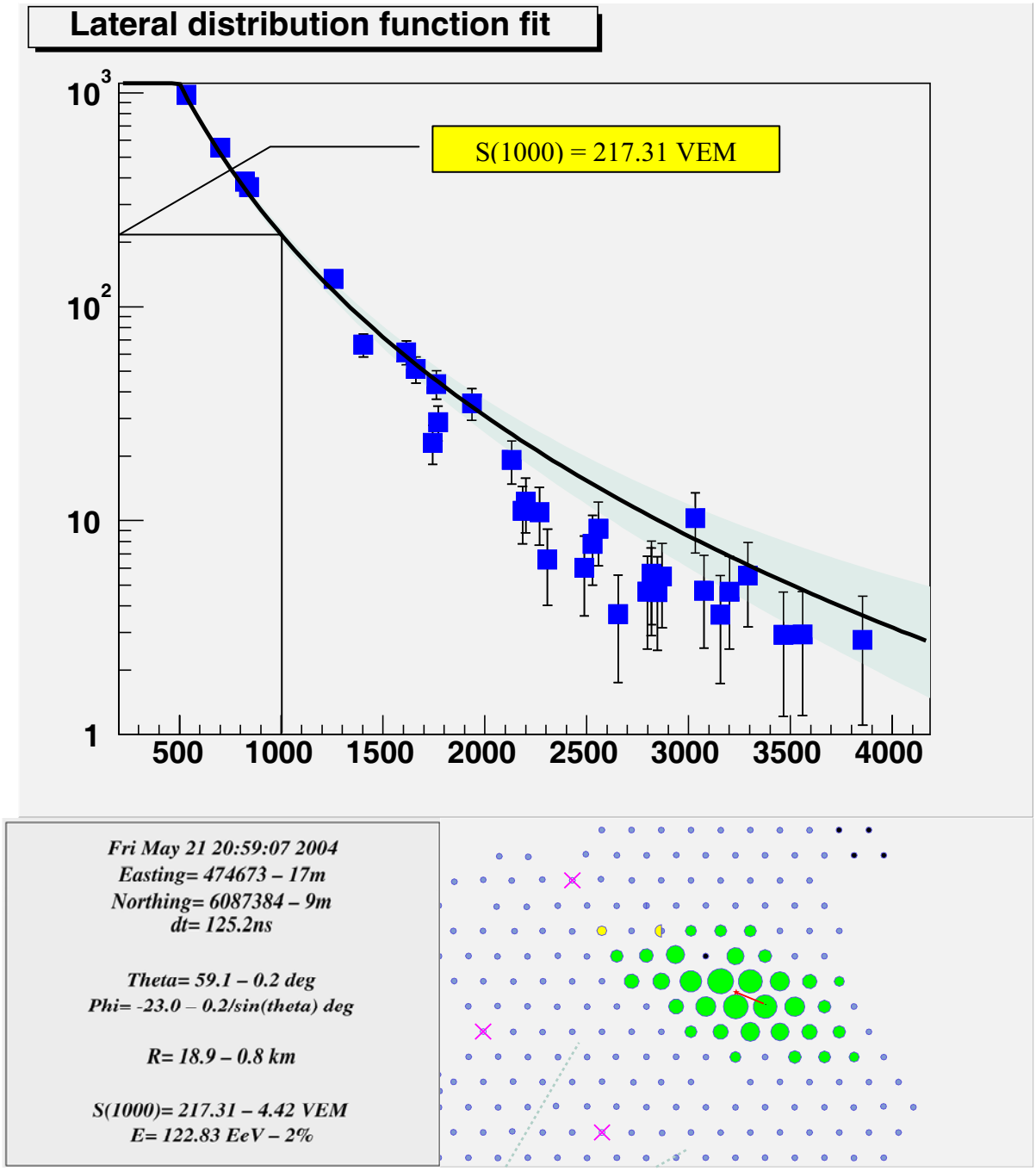

Figure 128 – Fitted LDF for the Golden events (#00787469, 122.83 EeV ± 2%, θ = 59.2º ± 0.2º) [27].

Some hybrid events in Figure 130 have energy below 1 EeV. For that energy the acceptance is 100%, however preliminary analysis shows that these events are very close to the SD trigger and quality conditions. They help increasing the statistics not introducing a significant bias.

The distribution over ln(E) produced by this procedure becomes the energy spectrum of Figure 131 and Figure 132 after dividing by the exposure 1750 km^2 sr yr.

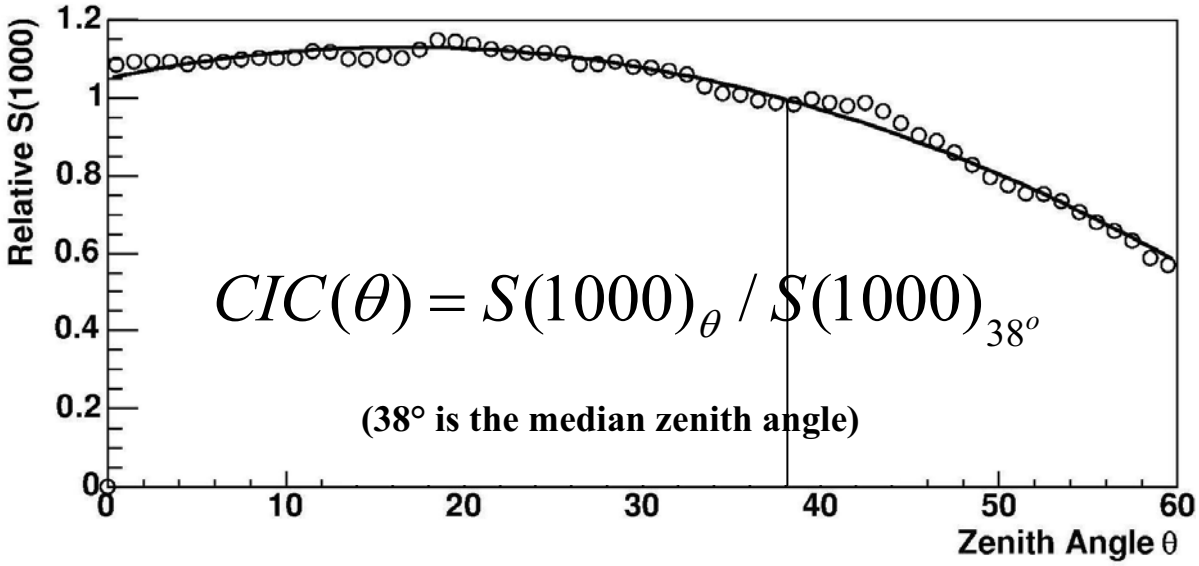

Figure 129 – The constant intensity curve is determined by having the same number of events for $\sin\theta \cos\theta \Delta\theta = 0.1$ at each θ (plotted points are not independent). Values are relative to S(1000) at the median zenith angle of 38°. The approximating quadratic curve is $CIC(\theta) = 1.049 + 0.00974\,\theta - 0.00029\,\theta^2$ [90].

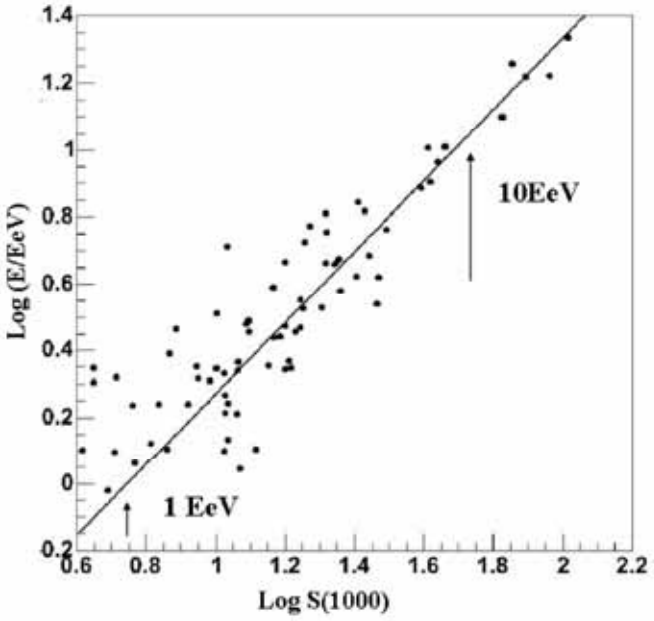

Figure 130 – The plot of log S(1000) vs. the log of the fluorescence determined energy for a set of hybrid events [92].

The Auger Observatory will measure the spectrum over the southern sky accurately in coming years. The spectrum in Figure 131 is only a first estimate. It has significant systematic and statistical uncertainties. The indicated statistical error for each point comes directly from the Poisson uncertainty in the number of measured showers in that logarithmic energy bin.

The conversion of S_{38} to energy is charged by a large systematic uncertainty. Real FD measurements estimate uncertainty as 15%, and the absolute calibration of the FD telescopes is currently limited to 12%. The total systematic uncertainty in the FD energy measurements is estimated as 25%. The uncertainty of correlation in Figure 130 gives an additional contribution to the final systematic uncertainty in energy estimation. Relatively low current statistics limits accuracy. Lower statistics in higher energies increases uncertainty with energy.

We estimate that the total systematic energy uncertainty grows from 30% at 3 EeV to 50% at 100 EeV. Horizontal arrows in Figure 131 indicate this uncertainty, and vertical arrows indicate a 10% systematic uncertainty in the exposure. The deviation from the best-fit power law is shown in Figure 132.

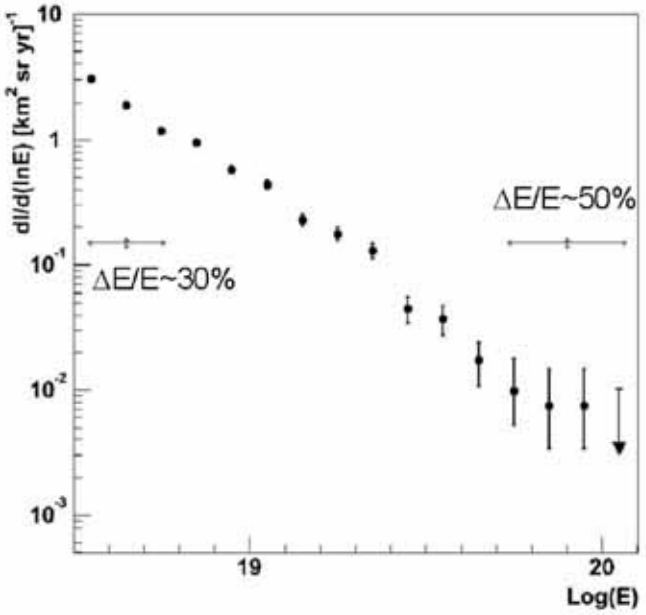

Figure 131 – The Auger energy spectrum. Plotted on the vertical axis is the differential intensity dI/d ln(E) = E dI/dE. Error bars on points indicate statistical uncertainty (or 95% CL upper limit). Double arrows at two different energies indicate systematic uncertainty [92].

Neutrinos and other weakly interacting particles do not produce fluorescence light and their energy is "invisible". Because the primary particle is unknown and also models of hadronic interactions do not take into account all possible configurations, an accuracy of estimation of "invisible" energy is limited. That fraction of uncertainty related to above interactions is estimated to 4%.

The preliminary results are biased with relatively big statistical and systematic errors due to still low statistics. The Auger Observatory is still in development stage. Currently we cannot yet ascertain, whether GZK suppression exists. However, the enlarged hybrid data set will reduce systematic uncertainty in the FD calibration of the SD energies.

Figure 133 shows the comparison of the Auger spectrum with that of AGASA [91] and HiRes1 (mono) [93]. The integrated aperture of Auger is close to that of AGASA but less than that of HiRes1. The number of events above 10^{20} eV is often used to confirm or reject the GZK suppression. Taking into account the uncertainty in energy, at least in the case of Auger preliminary results, a significant number of events about 10^{20} eV may be consistent

with a GZK feature while no events above 10^{20} eV may correspond also to the lack of GZK. However, let us notice that there are no events above 10^{20} eV in the spectrum. Recorded a hybrid event with energy of 140 EeV (assuming only a pure Rayleigh atmosphere) was unfortunately just outside that array and did not meet out criteria (quality cut – [42]) for inclusion in the spectrum [94].

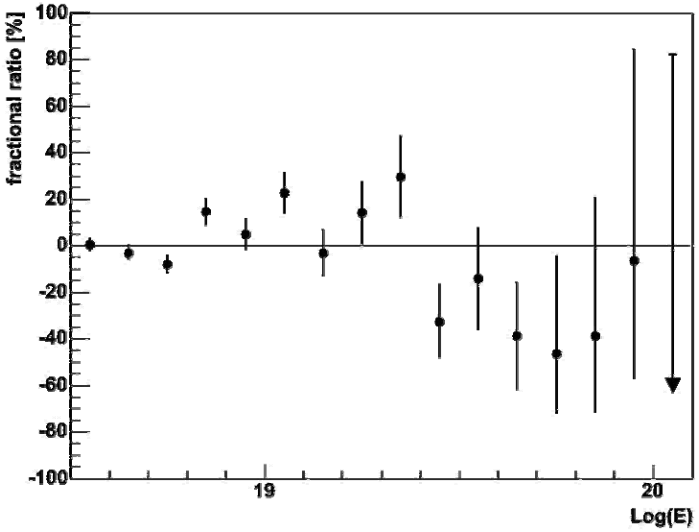

Figure 132 – Percentage deviation from the best-fit power law: $\frac{100}{F}\frac{dI}{d\ln(E)} - F$. The fitted function is $30.9 \pm 1.7 * (E/\mathrm{EeV})^{-1.84\pm0.03}$. The χ^2 per degree of freedom in the fit is 2.4 [90].

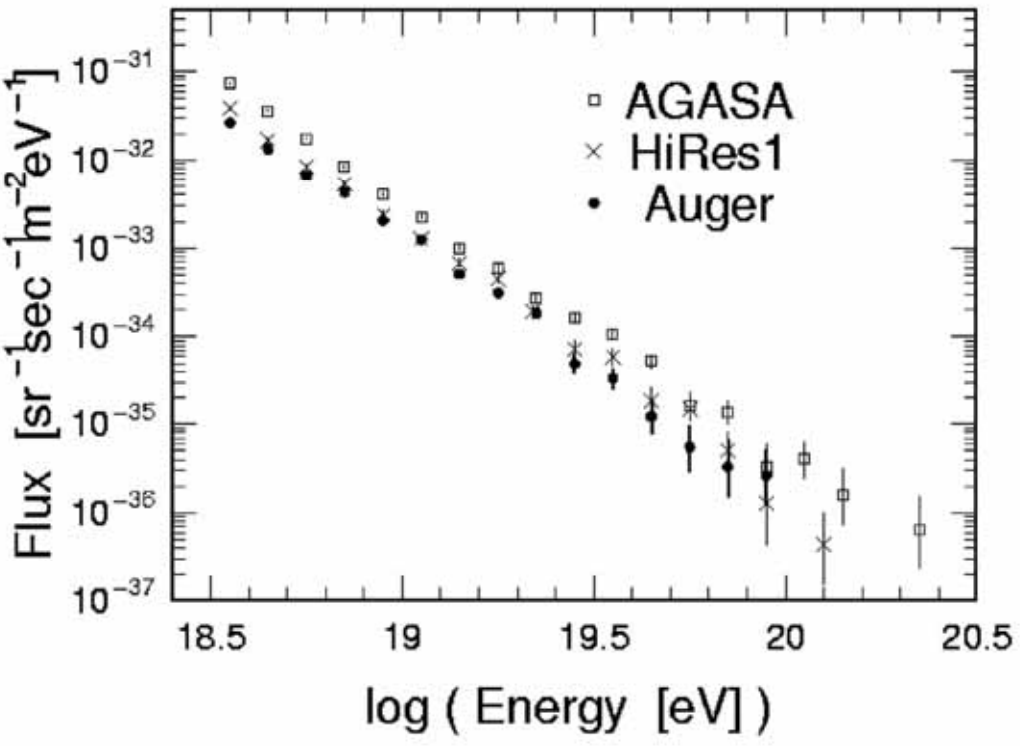

Figure 133 – Comparison of the Auger spectrum with those of AGASA and HiRes1 (mono) [92].

6.2 Upper limit on the primary photon fraction from the Pierre Auger Observatory

One of the important measured parameters allowing distinguishing between model predictions of the origin of the UHECR is the fraction of primary CR photons. In non-acceleration ("top-down") models a significant fraction of the generated particles are UHE photons [95]. They may be produced uniformly in the universe by the decay/annihilation of relic topological defects (TD) [96]. During propagation to the Earth, they interact with background radiation fields and most of them cascade down to GeV energies, where the extragalactic photon flux is constrained by the EGRET experiment [97]; the remaining UHE photons can contribute to the cosmic-ray flux above 10 EeV. In the Super Heavy Dark Matter (SHDM) model [98], the UHE photons are generated in the decay of relic meta-stable particles (such as "cryptons" [99]) which are clustered as cold dark matter in our Galaxy. Since the halo is believed to be effectively transparent to such UHE photons, they would be directly observed at Earth with little processing. In the Z-Burst (ZB) scenario [100], photons are generated from the resonant production of Z bosons by UHE cosmic neutrinos annihilating on the relic neutrino background.

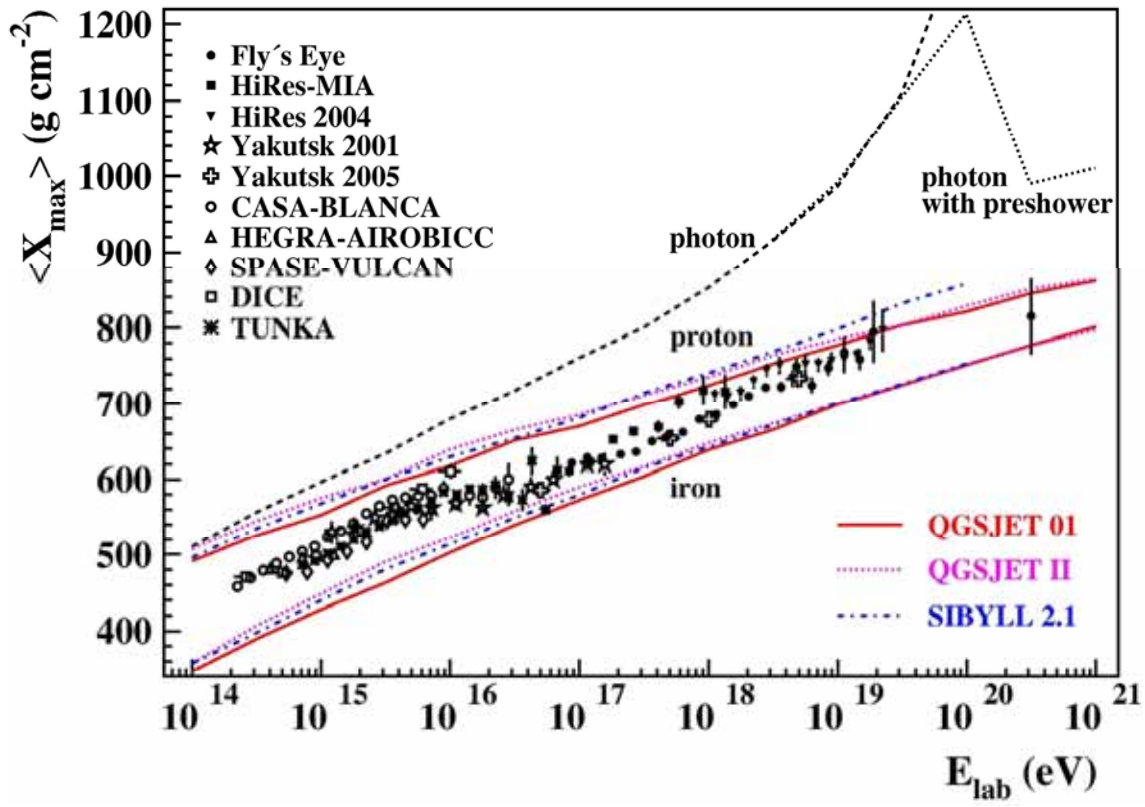

Figure 134 – Average depth of shower maximum $\langle X_{max} \rangle$ vs. energy simulated for primary photons, protons and iron nuclei. Depending on the specific particle trajectory through the geomagnetic field, photons above 5×10^{19} eV can create a pre-shower as indicated by the splitting of the photon line, the average $\langle X_{max} \rangle$ values then do not only depend on primary energy but also arrival direction. For nuclear primaries, calculations for different hadronic interaction models are displayed (QGSJET 01 [101], QGSJET II [102], SIBYLL 2.1). Experimental data are taken from references to the experiments, collected in [103]).

The determination of the photon contribution is a crucial probe of CR source models. Separating photon-induced showers from events initiated by nuclear primaries is experimentally much easier than distinguishing light and heavy nuclear primaries. Average depths of shower maximum at 10 EeV primary energy are predicted to be about 1000 g/cm^2, 800 g/cm^2, and 700 g/cm^2 for primary photons, protons, and iron nuclei, respectively. Moreover, analyses of nuclear composition are uncertain due to our insufficient knowledge of hadronic interactions at very high energies. Photon showers, being driven mostly by electromagnetic interactions, are less affected by such uncertainties and can be modeled with greater confidence. Additionally, air showers initiated by photons at energies above 10^{19} eV are in general expected to have fewer secondary muons compared to nuclear primaries.

The spectrum of Figure 131 is derived from the water Cherenkov signal S(1000). A development of showers induced by hadrons and photons significantly differ from each other. Showers generated by photons contain low muonic fraction, so the S(1000) signal would be lower. Showers generated by hadrons with the same energy will give higher S(1000) signal due to muon contribution. One estimates that a discrepancy with energy estimation between these showers may reach the factor of 2. It is important to obtain upper limit on photon flux at all energies. Currently estimated upper limit does not concern the highest energy range. The preliminary results from the Figure 131 are obtained by implicitly assuming that the primary photon component does not significantly biases the energy spectrum [104].

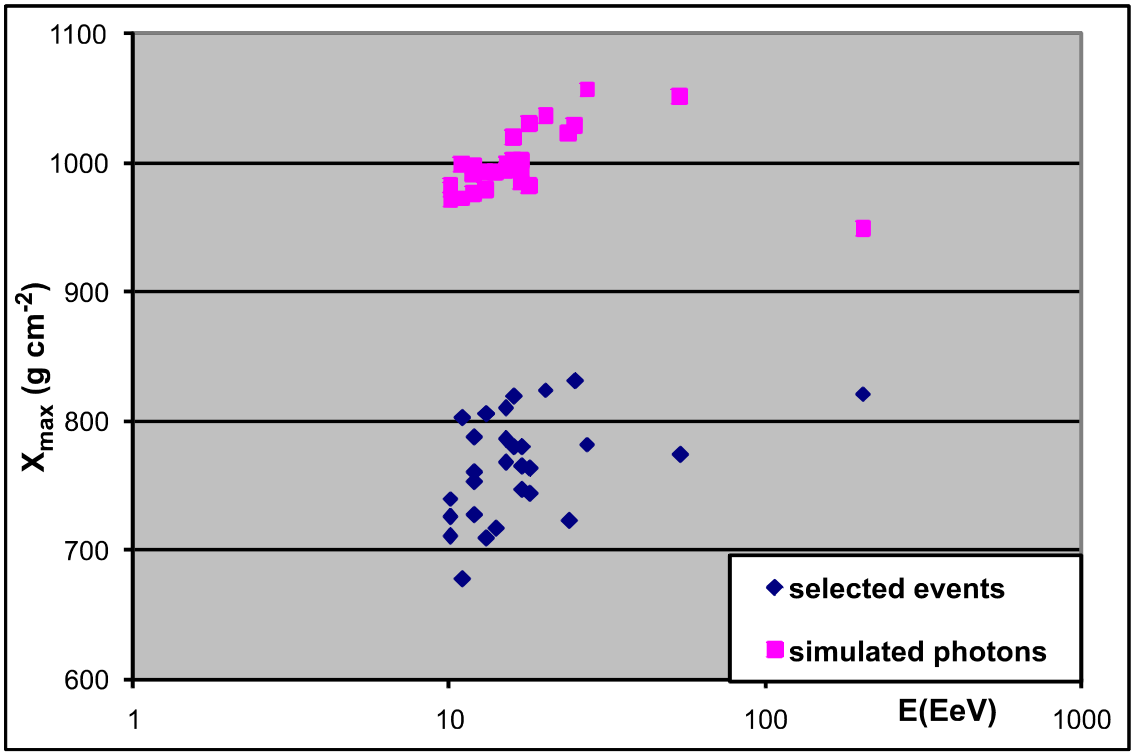

Figure 135 – Depth of shower maximum vs. primary, estimated energy for the selected events and for simulated showers induced by photons with the same energies.

Analysis of Auger data selected events with the following quality cuts (necessary to reduce as possible uncertainties):

- Quality of hybrid geometry by comparing the array tank with largest signal to the reconstructed shower plane: core distance < 1.5 km, time residual < 300 ns.
- Primary energy E > 10^{19} eV.

- X_{max} observed.
- Number of phototubes triggered by shower ≥ 6.
- Quality of Gaisser-Hillas (GH) profile fit: χ^2 (GH) per degree of freedom < 6 and χ^2 (GH)/ χ^2 (line) < 0.9, where χ^2 (line) refers to a straight line fit.
- Minimum viewing angle of shower direction towards the telescope > 15°.
- Cloud monitors confirm no disturbance of event observation by clouds.
- Zenith angle > 35° + g(E), where g(E) = 10 · (log(E/EeV) - 1.0)° for log(E/EeV) ≤ 1.7 and g(E) = 7° for log(E/EeV) ≥ 1.7.

Maximum distance of telescope to shower impact point < 24 km + 12 · (log(E/eV) – 1.0) km.

Till June 2006, only 29 events obey these criteria. Figure 135 shows that for selected Auger events there is significant discrepancy in X_{max} between real observed showers and showers simulated for the same energies and induced by photon. For each event, 100 showers were simulated as photon primaries. For all events, the observed X_{max} is well below the average value expected for photons. The differences between photon prediction and data range from +2.0 to +3.8 standard deviations. It is extremely unlikely that all 29 events were initiated by photons (probability < 10^{-10}), so an upper limit to the fraction of CR photons above 10 EeV can be reliably set.

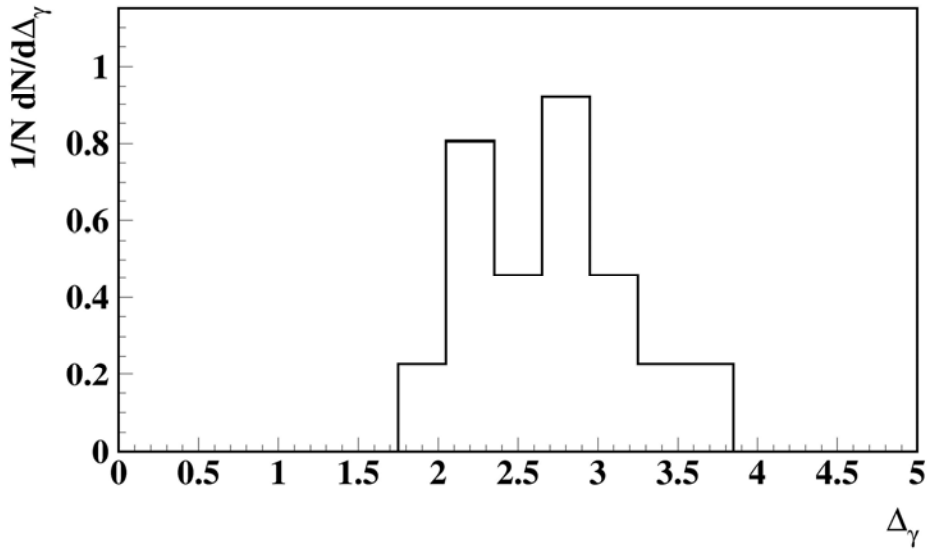

Figure 136 – Distribution of differences Δ_γ in standard deviations between primary photon and data for the 29 selected events [105].

The calculation of the upper limit is based on the statistical method introduced in [106], which is tailor-made for relatively small event samples. For the selected Auger data, an upper limit to the photon fraction of 16% at a confidence level of 95% is derived. In Figure 137, this upper limit is plotted together with previous experimental limits and some illustrative estimates for non-acceleration models. Two different expectations for SHDM decay [95, 99] are shown to illustrate the sensitivity to assumptions made about the decay mode and the fragmentation, as well as the normalization of the spectrum. The derived limit is the first one based on observing the depth of shower maximum with the fluorescence technique. The result confirms and improves previous limits above 10 EeV that came from surface arrays. It is worth mentioning that this improved limit is achieved with only 29 events above 10 EeV, as compared to about 50 events in the Haverah Park analysis and about 120 events in the AGASA analysis.

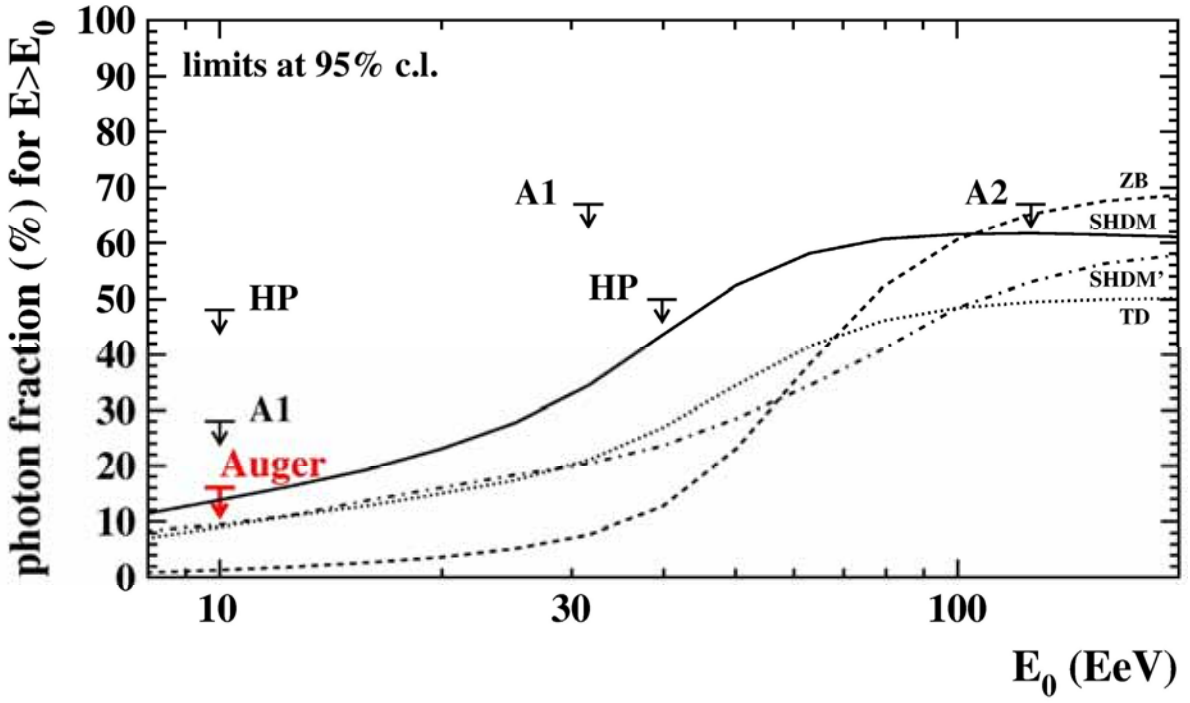

Figure 137 – Upper limits (95% c.l.) to the cosmic-ray photon fraction derived in the Auger analysis and obtained previously from AGASA (A1) [107], (A2) [106] and Haverah Park (HP) [108] data, compared to expectations for non-acceleration models (ZB, SHDM, TD from [95], SHDM' from [105])

The small number of events mainly limits the photon bound calculated in this analysis. The data statistics of hybrid events will considerably increase in the near future, and much lower primary photon fractions can be tested. Moreover, the larger statistics will allow us to increase the threshold energy of 10^{19} eV chosen in the present analysis to energy ranges where even larger photon fractions are predicted by some models.

6.3 Anisotropy around the Galactic Center at EeV energies

Previous experiments indicated excesses of events near the direction of the Galactic Center. AGASA reported a 4.5 σ excess of cosmic rays with energies in the range 1 - 2.5 EeV in a 20° radius region centered at (δ,α) ~ (-17, 280)° [109]. Later SUGAR data did not confirm fully AGASA results, however reported a 2.9 σ excess flux of cosmic rays with energies 0.8 < E < 3.2 EeV in a region of 5.5° radius centered at (δ,α) ~ (-22, 274)° [110].

The Galactic Center is an interesting region to investigate an anisotropy also for the Pierre Auger Observatory. In this region the collected Auger statistics are already larger than that of any previous experiment.

The preliminary analysis of Auger data was performed to look for excesses of events within a few degrees from the Galactic Center in the energy range from 0.8 - 3.2 EeV as well as correlations of cosmic ray arrival directions with the Galactic plane and with the super-galactic plane at energies in the range 1-5 EeV.

For the preliminary analysis data from January 2004 until June 2005 have been selected. Events from the surface detector passed the criteria described in Chapter 3.1.2. In all our

analyses a zenith angle has been cut at 60° like AGASA while SUGAR used all zenith angles.

3-fold trigger efficiency (for Auger surface detector configuration) is better than 30% for proton-induced showers and better than 50% for iron-induced shower above 0.8 EeV. The 4-fold trigger reaches the same efficiency at about 2 EeV. The efficiency ratio between Iron and proton is always below 1.6 above 0.8 EeV and this difference can be taken into account when setting upper limits on point sources.

Table 11 shows the statistics (10 times more than SUGAR) for the SD data set in the various energy ranges used in the preliminary analysis. This is the first search in the southern hemisphere since the SUGAR analysis.

For the hybrid sample, 24 epochs have been defined each of which corresponds to a given telescope configuration. The SD sample have been randomized within 5 ranges of the zenith angle, the UTC hours and Julian days of the events and drawn the azimuth from a uniform distribution. Figure 138a shows the coverage map obtained from SD samples in a region around the Galactic Center.

Table 11 – Event statistics [111].

Data Set	>0.1 EeV	0.8 - 3.2 EeV	1.0 - 5.0 EeV	> 5.0 EeV	> 10.0 EeV
SD	122636	41792	29773	1359	387

Figure 138b, c and d show the chance probability distributions (mapped to positive Gaussian significance for excesses and negative for deficits) in the same region for various filtering and energy cuts corresponding to various criteria. In these map the filtering is chosen as to maximize the appearance of eventual structures at a certain scale. 1.5° corresponds to Auger 2.2° angular resolution and therefore to point sources, 3.7° is similar to a 5° window and also corresponds to the SUGAR excess size, 13.3° is similar to a 20° window and to the size of the excess reported by AGASA. In these maps the chance probability distributions are consistent with those expected as a result of statistical fluctuations from an isotropic sky.

For the region reporting the excess by AGASA, the Auger Observatory registered 1155 events, while 1160.7 are expected (ratio 1.00 ± 0.03) for the energy range (1.0-2.5) EeV. It is almost 3 times more than the AGASA events in this region. These results do not support the excess observed by AGASA. Even if the source were protons and the background much heavier (e.g. Iron), the difference in detection efficiency of the Auger trigger at 1 EeV would reduce the sensitivity to source excess. However, using the Fe/proton efficiency ratio at 1 EeV (70%/50% = 1.44, an upper limit in the range (1-2.5) EeV) 5.2 σ event excess in the Auger data set is still expected.

Due to possible systematic differences between the energy calibrations of the two experiments, a scanning of the region maintaining the high/low energy ratio and moving the interval center by ± 40% has extended the analysis. The energy range has been also enlarged to (0.8–3.2) EeV. No significant excess in any of those cases has been found. For the SUGAR condition, for which the excess has been reported, 144 events have been observed and 150.9 expected (ratio 0.95 ± 0.08) in corresponding angular/energy window. Because of much higher Auger statistics (over an order of magnitude) the SUGAR excess cannot be also confirmed.

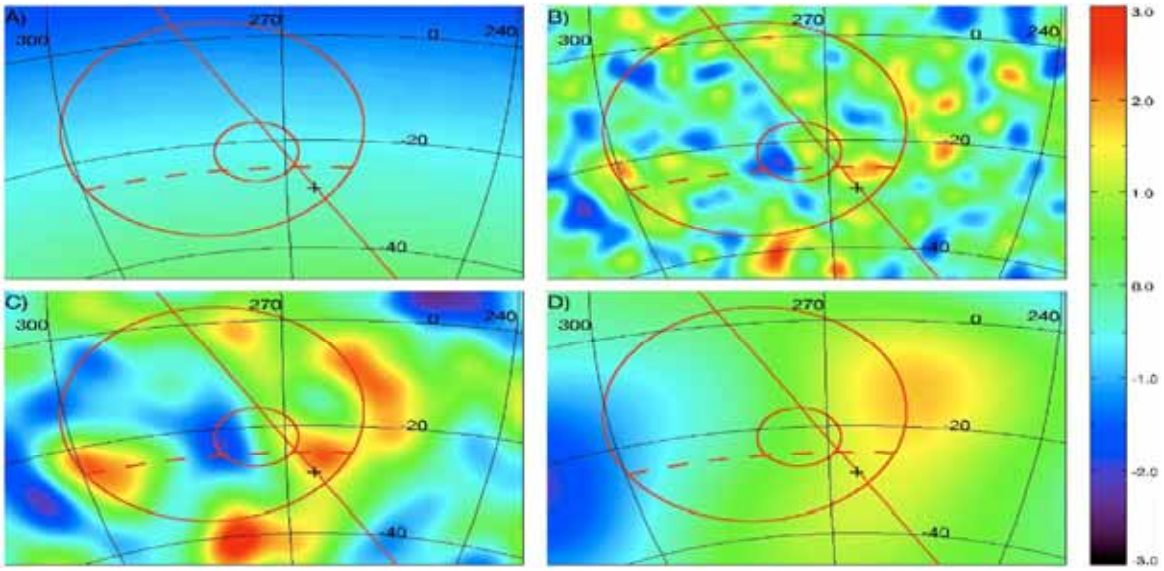

Figure 138 – Projections of the galactic center region, GC (cross), galactic plane (solid line), regions of excess of AGASA and SUGAR (circles), AGASA f.o.v. limit (dashed line). a) A coverage map (same color scale as the significance maps, but in a range (0-1.0)). b) A significance map in the range (0.8-3.2) EeV smoothed using the individual pointing resolution of the events and a 1.5° filter (Auger like excess), c) same smoothed at 3.7° (SUGAR like excess), d) in the range (1.0-2.5) EeV smoothed at 13.3° (AGASA like excess) [111].

The next step of the analysis was a searching of point-like sources in the direction of the Galactic Center with a 1.5° Gaussian filter relating to the angular resolution of the SD [79]. In the energy range (0.8–3.2) EeV, 24.3 events were observed and 23.9 were expected (ratio 1.0 ± 0.1). A 95% CL upper limit on the number of events coming from a point source in that window is $n_s(95\%) = 6.7$. From this limit we can obtain a flux upper limit assuming expected number of events for a given flux Φ_s integrated over the energy range. Because in the EeV energy range the trigger efficiency depends on energy and primary composition, the ratio (Φ_s/n_s) will be also dependent on the spectral shape and source features. By the simple assumption that the source spectrum differs significantly from the overall cosmic rays spectrum ($dN/dE \sim E^{-3}$), $\Phi_s = n_s\, \Phi_{CR}\, 4\pi\sigma^2/n_{exp}$ where σ is the size of the Gaussian filter.

For $\Phi_{CR}(E) = 1.5\, \xi(E/EeV)^{-3} \times 10^{-12}$ ($EeV^{-1}\ m^{-2}\ s^{-1}\ sr^{-1}$), where $\xi \in (1, 2.5)$ denotes the uncertainty on the CR flux ($\xi \sim 1$ for Auger and 2.5 for AGASA), and for the Iron/proton detection efficiency ratio ($1 < \varepsilon < 1.6$ for $(0.8 < E < 3.2)$ EeV) integration over that energy range gives:

$$\Phi_s < 2.6\, \varepsilon\, \xi \cdot 10^{-15}\ m^{-2}\ s^{-1} \quad \text{at} \quad 95\%\ \text{CL}. \tag{93}$$

Because the detector efficiency increases with energy, a harder source flux would lead to a stronger flux bound. In the worst way, where both ξ and ε are maximal, the bound is $\Phi_s = 10.6\times10^{-15}\ m^{-2}\ s^{-1}$ and still excludes the neutron source scenario suggested in [109, 112] to explain the AGASA excess, or in [113] in connection with the HESS measurements.

For the better angular resolution provided by the hybrid reconstruction, a point-like flux limit can be calculated inside a 1°–radius cone around the direction of the Galactic Center. Because of the limited statistics, all hybrid events with energies above 0.1 EeV (10 589) have been used in the analysis. In the analysis window only 4 events have been observed for 3.4

expected. This result does not indicate significant excess. At 95% CL an upper limit for a neutron source at the Galactic Center above 0.1 EeV is:

$$\Phi_s < 1.2\ \xi \cdot 10^{-13}\ m^{-2}\ s^{-1} \quad \text{at} \quad 95\%\ \text{CL}. \tag{94}$$

The origin of the cosmic rays probably changes from Galactic to extra- galactic in the energy region (1-10) EeV. The analysis of looking for excess of events inside ±10° angle along the Galactic Plane in the energy range from 1 to 5 EeV and along the Super Galactic Planes above 5 and 10 EeV gave 5077, 229, and 68 observed events respectively for expectations of 5083.3, 235.6, and 67.4 (ratios 1.00 ± 0.01, 0.97 ± 0.07, and 1.0 ± 0.1). This result still does not show any significant discrepancy. Figure 139 shows the corresponding probability maps smoothed on a 10° scale. Again all chance probabilities are consistent with isotropy.

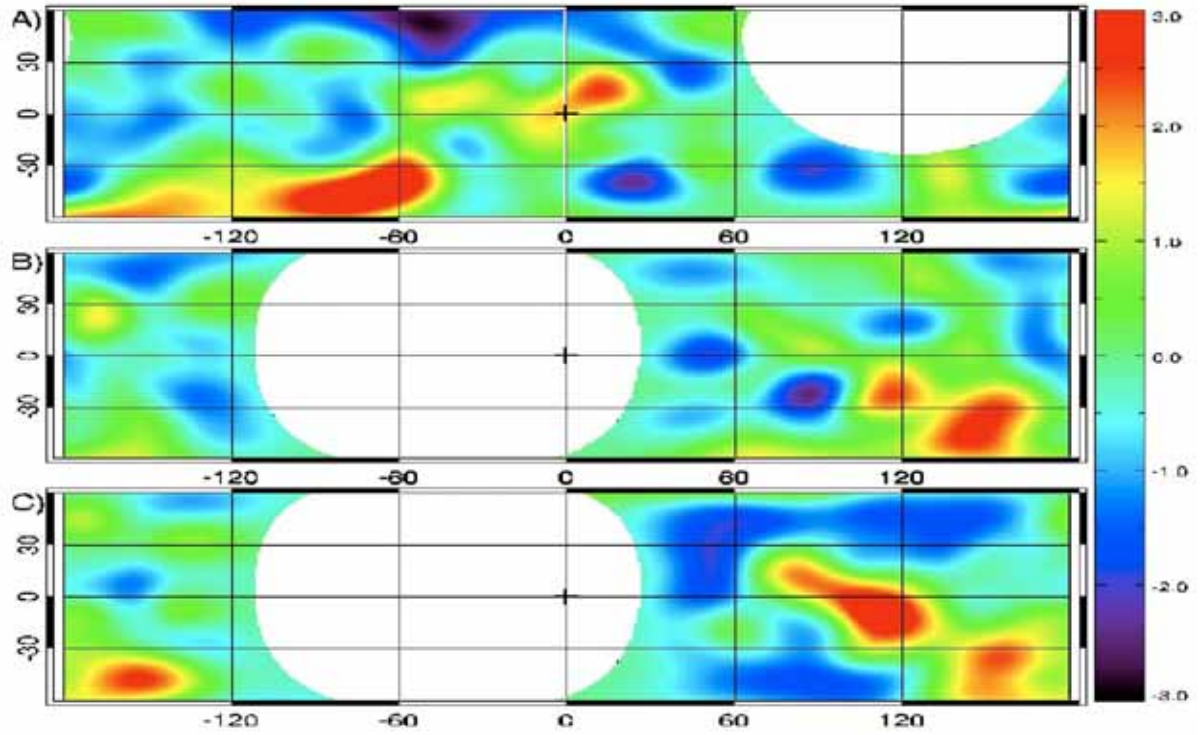

Figure 139 – Significance map from the SD data in galactic coordinates for events with 1 EeV < E < 5 EeV (top), in super-galactic coordinates for events with E > 5 EeV (middle) and the same with E > 10 EeV (bottom) [111].

7 Auger Muons and Infill for the Ground Array[1]

7.1 Introduction

The Pierre Auger Observatory has been designed to study the highest-energy cosmic rays in nature ($E > 10^{18,5}$ eV). The determination of their arrival direction, energy, and composition is performed by the analysis of the atmospheric showers they produce. The Auger surface detector (SD) array consist of 1600 water Cherenkov detectors placed in an equilateral triangular grid of 1.5 km spacing. The aim of the AMIGA project is to show that the addition of a "small" area (due to the rapidly decaying flux with energy) of SD stations with nearby buried muon counters at half or less the above mentioned spacing would allow a dramatic increase of the physical scope of this Observatory, reaching lower energies at which the transition from galactic to extragalactic sources is expected. Lowering the Auger energy threshold by more than one order of magnitude will allow a precise measurement of the cosmic ray spectrum in the very interesting regions of the second knee and the ankle.

AMIGA propose to enhance the Auger acceptance at full efficiency down to 10^{17} eV by means of an SD graded infill deployed at smaller distances over an area much smaller than Auger. Trigger simulations show that grids of 433 m and 750 m detector spacing are fully efficient down to 0.35×10^{17} eV and 10^{17} eV, respectively and therefore these geometries are being adopted. Areas of 5.9 and 23.5 km^2 will suffice to have a reasonable flux and they will require, apart from the Auger tanks at the 1.5 km spacing, an extra 24 and 42 SD's, respectively, The infill SD stations are exactly the same Cherenkov detectors as employed in the present Auger surface array, the only design parameter being changed is its spacing.

Each one of the proposed muon detectors will have an area of 30 m^2, and will be buried at the side of each SD station at a depth of approximately 2.5 m. The distance to the station will be large enough to avoid shadowing from the water tank, guaranteeing a uniform shielding, but small enough to represent the same physical point inside the shower front and to be able to share GPS time signals and telecommunications with its associated surface detector. Muon detectors will be made of the same extruded plastic scintillators already developed and used by the MINOS experiment. They will work as counters (i.e. signals above a tunable threshold are counted) having an appropriate segmentation to prevent pile-up, which greatly increases both their data taking robustness and results trustworthiness, with a reduced volume of transmitted data.

7.2 Energy

Auger is optimized for energies above $10^{18.5}$ eV, that is, from the middle of the ankle up to the highest energies. Most of the proposed enhancements, AMIGA included, have as a prime objective to lower the energy threshold of the detector down to $10^{17.0}$ eV (Figure 140). Such extension allows the complete inclusion of the ankle and the second knee inside the observation range of Auger. This offers also the additional advantage of adding an overlap with KASCADE Grande [114, 115, 116], which may be of fundamental importance in order to validate results.

[1] Chapter 7 prepared also on the basic of [142]

The second knee has been observed in the vicinity of 4×10^{17} eV by Akeno [117], Fly's Eye stereo [118, 119, 120], Yakutsk [121, 122] and HiRes [123]. The physical interpretation of this spectral feature is uncertain at present. It may be either the end of the Galactic cosmic ray component, the pile-up from pair creation processes due to proton interactions with the cosmic microwave background radiation during propagation in the intergalactic medium or both.

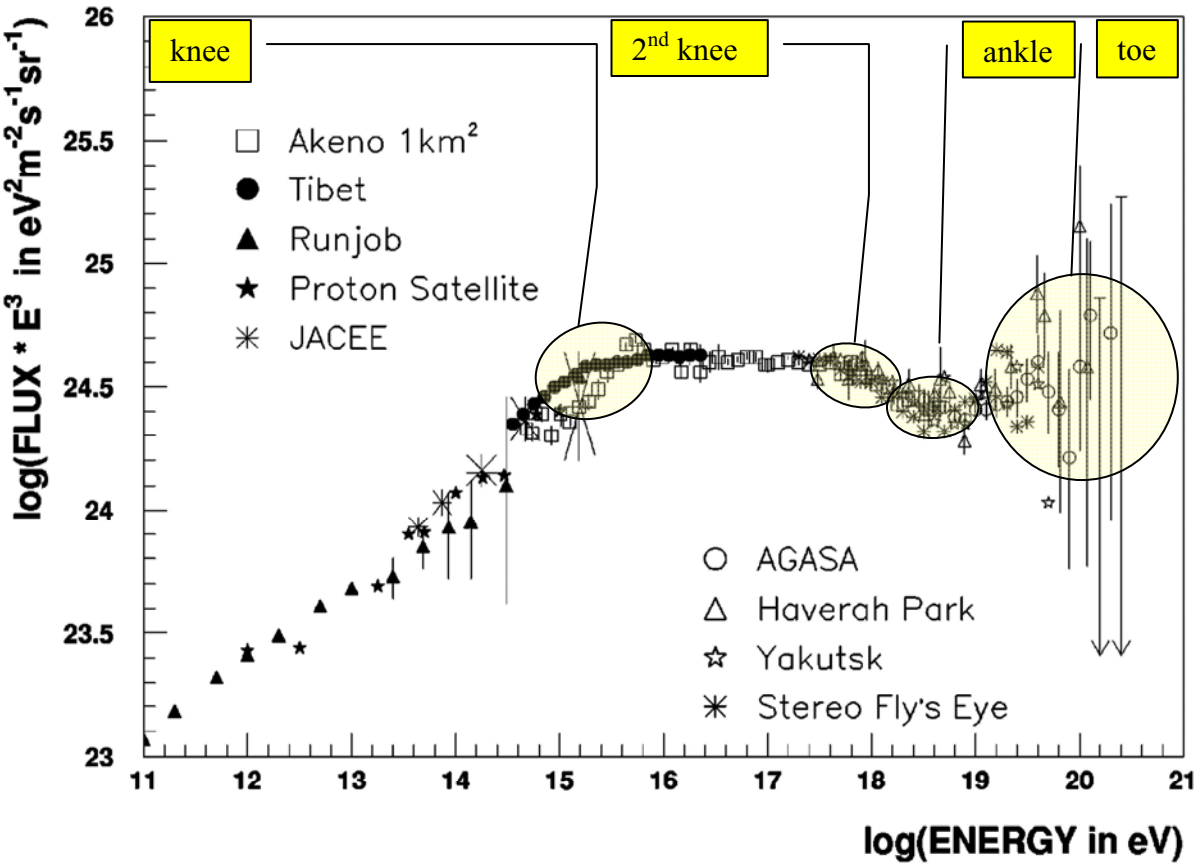

Figure 140 – Cosmic ray energy spectrum and its main features: knee (few PeV), second knee (0.5 EeV), ankle (EeV to few tens of EeV) and the still poorly known highest energy tail. The energy regions covered by Auger at present and the one that would be added by AMIGA are shown. It is important to note that some overlap with KASCADE Grande would also be added to, allowing for an independent verification of results [8].

The ankle, on the other hand, is a broader feature that has been observed by Fly's Eye around 3×10^{18} eV as well as by Haverah Park [124] at approximately the same energy. These results have been confirmed by Yakutsk [121, 122] and HiRes [123]. AGASA also observed the ankle, but they locate it at a higher energy, around 10^{19} eV [125]. Several physical interpretations are possible which are intimately related with the nature of the second knee. The ankle may be the transition point between the Galactic and extragalactic components, the result of pair creation by protons in the cosmic microwave background, or the result of diffusive propagation of extragalactic nuclei through cosmic magnetic fields.

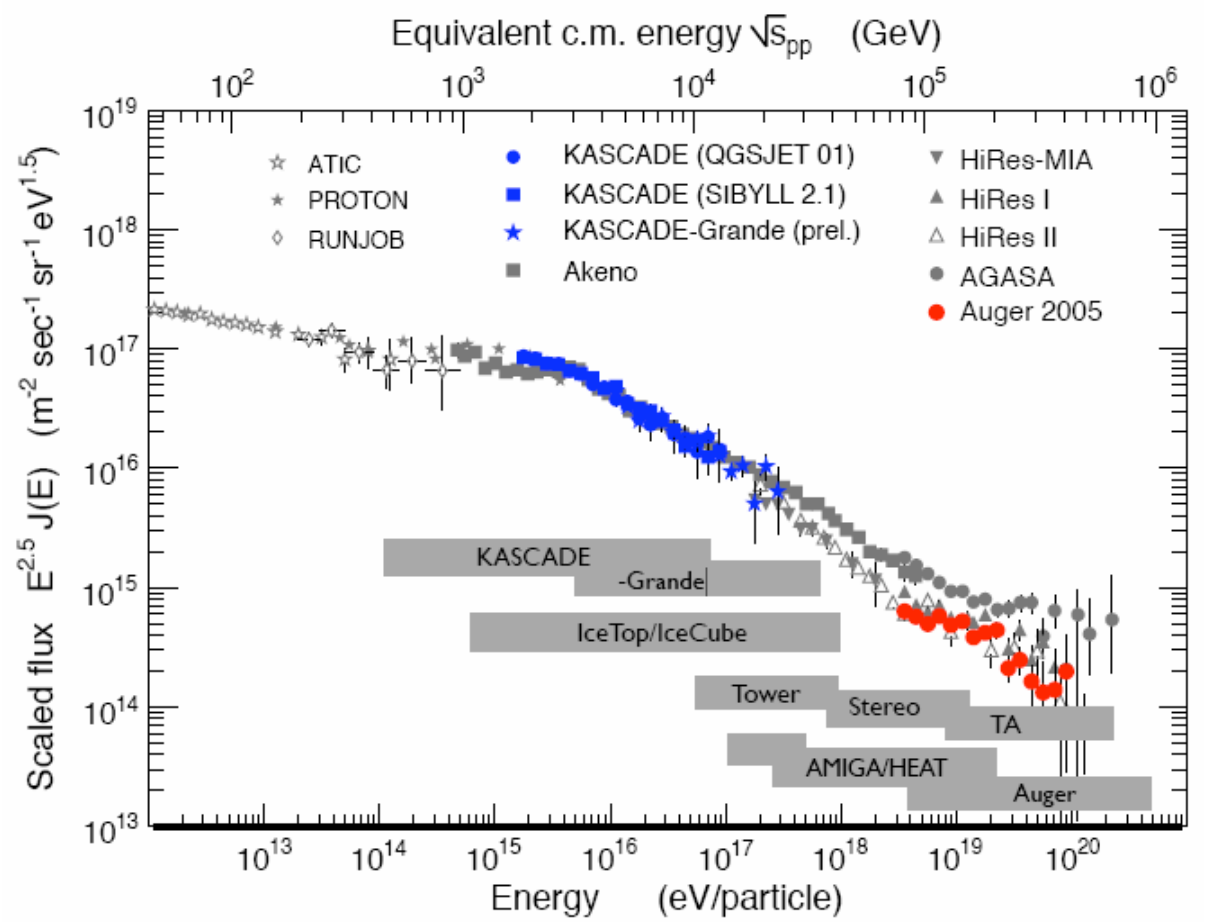

Figure 141 – Energy ranges investigated by different experiments [161].

7.3 Composition

Several techniques have been used to determine the composition of cosmic rays along the spectrum and, in particular, in the highest energy region [126]:

- depth of maximum of the longitudinal distribution,
- Xmax [127, 128];
- fluctuations of Xmax [129, 130];
- muon density [131];
- steepness of the lateral distribution function [132, 133];
- time profile of the signal, in particular rise time of the signal [134];
- curvature radius of the shower front;
- multi-parametric analyses, such as principal component analysis and neural networks [135], etc.

Unfortunately, as is frequently the case in physics, whenever several techniques are applied to measure the same physical magnitude, correspondingly, several results are obtained and, not always agreeable among themselves. As will be shown below, this is critical to the understanding of the astrophysics of ultra high-energy cosmic rays.

In order to analyze the astrophysical implications of the composition along our target energy region, it is more instructive to start from much lower energies. A significant point is

the first knee. Following KASCADE [136], a gradual change in composition is observed through the knee, from a lighter to a heavier composition. The first knee is a broad feature, which can be understood as a composition of power law energy spectra with breaks that are in agreement with a rigidity scaling of the knee position. However, the experimental situation is not clear enough at present, and even a mass scaling could still be possible.

Therefore, at energies above few times 10^{16} eV, the flux is dominated by iron nuclei. These particles are of Galactic origin. What is being detected is, very likely, the end of the efficiency of supernova remnant shock waves as accelerators, since the Larmor radii or characteristic diffusion scale lengths of the nuclei become comparable to the radius of the remnants. If there are not more powerful accelerators in the Galaxy, the Galactic cosmic ray flux should continue to be dominated by iron above 10^{17} eV and up to the highest energies produced inside the Milky Way. It must be noted that, even if the previous results are quantitatively dependent on the hadronic interaction model used in the data analysis, they are qualitatively solid and there is considerable degree of consensus on the existence of a progressive transition in composition through the knee. At higher energies, the composition has been measured by several experiments in the past, e.g., Haverah Park, Yakutsk, Fly's Eye, HiRes-MIA prototype and HiRes in stereo mode (see Figure 142).

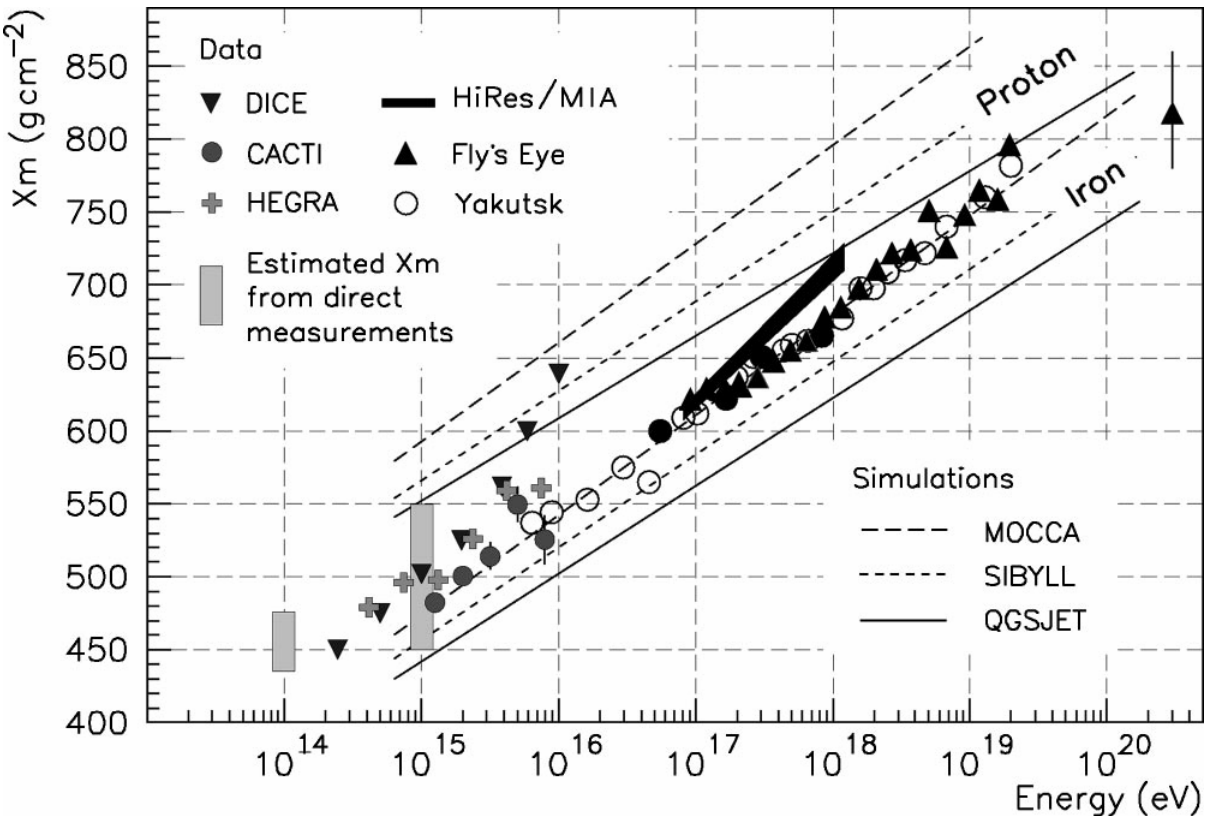

Figure 142 – Variation of Xmax with energy (elongation rate) shows an apparent change in composition from heavy to light nuclei along the target energy interval. This variation is at least possibly associated to the transition from Galactic to extragalactic cosmic rays [8]. Elongation rate measured by the HiRes-MIA prototype shows a rapid change to a light composition above 10^{18} eV.

The X_{max} data suggest that, above $10^{16.6}$ eV, the composition changes once more progressively from heavy to light. At the lower limit of the target energy interval, the composition is still heavy, i.e., iron dominated, in accordance to KASCADE results.

Nevertheless, at energies of 10^{19} eV, even if still showing signs of a contamination by heavy elements, it is more consistent with a flux dominated by lighter elements.

Despite the fact that there is a consensus among most of the experiments about the reality of this smooth transition, there is no consensus about the rate and extent to which the transition occurs. In fact, the combined data from the HiRes-MIA prototype and HiRes in stereo mode, point to a much more rapid transition from heavy to light composition starting at 10^{17} eV, but which would be over by 10^{18} eV [137] (Figure 142). Beyond that point, the composition would remain light and constant.

The later scenario, however, is not supported by the data of other experiments. Haverah Park, for example, shows a predominantly heavy composition up to 10^{18} eV, followed by an abrupt transition to lighter values compatible with HiRes stereo at around 10^{18} eV. Volcano Ranch, even though there is a single experimental point, is compatible with a heavy composition still at 10^{18} eV, some-what in accordance to Haverah Park data. AKENO, on the other hand, is consistent with a continuation of the gradual transition from the second knee all across the ankle up to at least 10^{19} eV, only reaching there the same light com-position that HiRes stereo claims from an order of magnitude below in energy. It must also be noted that, above 10^{19} eV, AGASA is only able to set upper limits for the fraction of iron, but these limits are high enough to leave room for much more complex astrophysical scenarios with a substantial admixture of extragalactic ultra-high energy heavy elements [131].

7.4 Galactic sources and propagation

The region that will be covered by AMIGA, i.e., $\sim(10^{17}\ldots10^{19})$ eV is for astrophysics highly significant from at least two points of view. At these energies, there is a change in the origin and acceleration of the primary particles, as well as in the propagation regimes in the intervening media. At lower energies, the Galaxy is undoubtedly the source of the cosmic ray particles and of their kinetic energy. There is not a consensus about the actual source of the particles in themselves, but the two main lines of thought propose either nuclei pre-accelerated at the chromospheres of normal F and G type stars or ambient electrically charged dust grains condensed in the dense winds of blue or red giant stars. Several acceleration mechanisms must be at play but it is widely expected that the dominant one is first order Fermi acceleration at the vicinity of supernova remnant shock waves. Nevertheless, theoretically the Galactic accelerators should become inefficient in the range of $\sim(10^{17}\ldots10^{18})$ eV. This upper limit could be extended to $\sim10^{19}$ eV if additional mechanisms were operating in the Galaxy, e.g., spinning inductors associated with compact objects or cataclysmic events like acceleration of iron nuclei by young strongly magnetized neutron stars through relativistic MHD winds [138].

At the target energies, particles also start to be able to travel from the nearest extragalactic sources in less than a Hubble time. Consequently, at some point above $10^{17.5}$ eV a sizable cosmic ray extragalactic component should be detectable and probably becomes dominant above 10^{19} eV. Therefore, it is expected that the cosmic ray flux detected between the second knee and the ankle of the spectrum be a mixture of a Galactic and an extragalactic flux, highlighting the astrophysical richness and complexity of the region.

From the point of view of propagation of charged particles in the interstellar medium, it is important to note that the Galaxy is a magnetized medium, where the field is structured on

scales of kpc and typical intensities of the order of some few micro Gauss. This transforms the Galaxy in an efficient confinement region for low energy charged particles. The confinement region is a flattened disk of approximately 20 kpc of radius and thickness of the order of a few kpc [33]. The cyclotron radius of a nucleus of charge Ze can be conveniently parameterized as:

$$r_{L(kpc)} \approx \frac{1}{Z} \times \left(\frac{E_{(EeV)}}{B_{(\mu G)}} \right) \tag{95}$$

Equation (95) shows that, given the typical intensity of the magnetic fields present in the interstellar medium, the type of propagation strongly depends on the charge of the corresponding nucleus. Protons, with energies > 10^{17} eV, have gyro-radii comparable or larger than the transverse dimensions of the effective confinement region and, therefore, can easily escape from the Galaxy. On the other end of the mass spectrum, just the opposite occurs for iron nuclei that, even at energies of the order of 10^{19} eV, have gyro-radii < 10^2 pc and must be effectively confined inside the magnetized interstellar medium.

The previous results are based only on the consideration of the regular component of the Galactic magnetic field. However, there exist a superimposed turbulent component whose intensity is at least comparable to that of the regular field. Its spectrum seems to be of the Kolmogorov type, extending from the smallest scales probed, ~1 pc, to L_c ~ 100 pc, the correlation length of the turbulent field.

Wave-particle interactions between cosmic rays and MHD turbulence are resonant for wavelengths of the order of the Larmor radius, $\lambda \sim r_L$. This means that, for a nucleus of charge Z, a critical energy, E_c, can be defined according to (95) as $r_{L(kpc)} \approx L_c$, what for $L_c \approx 10^2$ pc gives the energy

$$E_{c(EeV)} \approx 0.5 \times Z \tag{96}$$

below which modes resonant with the particle gyro-radius exist that are able to efficiently scatter the particle in pitch angle. Consequently, at energies below E_c the diffusion coefficient is small enough for the particle trajectory to be diffusive. At energies above E_c, on the other hand, the propagation is essentially ballistic.

Due to the interaction with the turbulent magnetic component, protons experience a propagation regime very different than iron nuclei inside AMIGA target energy region. Protons propagate ballistically in the interstellar medium above ~3×10^{17} eV, while iron nuclei propagate diffusively even at energies >10^{19} eV. Therefore, along the energy region targeted by AMIGA, extending from the second knee up to almost the end of the ankle, all nuclei from p to Fe, i.e. 1 < Z < 26, experience a transition in their propagation regime inside the interstellar medium changing gradually from diffusive to ballistic as the energy increases.

With increased statistics and good control of the acceptance across the ankle and second knee, it should be possible to measure large-scale anisotropies, with potentially crucial scientific reward. First, a change in anisotropy, both in amplitude and direction, should be associated with the galactic/extragalactic transition. Second, the evolution of the anisotropy with energy is, in principle), directly related to the energy evolution of the diffusion coefficient. Thus measuring the increase of the anisotropy amplitude with energy would help in constraining both the magnetic field structure and the CR source spectral index. Third, for reasons already mentioned above, the anisotropy of the proton and Fe components should be very different in the Galactic CR component in this energy range. Hence, correlating anisotropy patterns with heavy and light components of the flux can become an additional tool.

7.5 Extragalactic propagation and superposition of the extragalactic and Galactic fluxes

In the same way as the magnetic characteristics of the interstellar medium allow Galactic particles at the target energies to escape into the extragalactic environment, extragalactic cosmic rays are also able to penetrate inside the Galactic confinement region. But, of course, extragalactic particles must first be able to reach us from the nearest Galaxies in less than a Hubble time.

A crude approximation to this effect can be made in the following way. Faraday rotation measurements statistically impose to the extragalactic magnetic field the following restriction [139]: $B \times \sqrt{L_c} \leq 1nG \times \sqrt{Mpc}$, where L_c is the correlation length of the magnetic field that we arbitrarily assumed of the order of 1 Mpc. Assuming that the diffusion coefficient can be estimated by the Bohm approximation $K \approx \frac{r_L c}{3}$, according to (??) we get

$$K \approx \frac{0.1}{Z}\left(\frac{E_{(EeV)}}{B_{(\mu G)}}\right)\frac{Mpc^2}{Myr} \tag{97}$$

The diffusive propagation time from an extragalactic source at a distance D can be estimated as: $\tau \approx D^2/K$ or

$$\tau_{(Myr)} \approx 10 \times D^2_{(Mpc)} \times Z \times \left(\frac{B_{(nG)}}{E_{(EeV)}}\right) \tag{98}$$

Equation (98) shows that there is a rather restrictive magnetic horizon. Basically, no nucleus with energy smaller than 10^{17} eV is able to arrive from regions external to the local group (D ~ 3 Mpc) if indeed the intergalactic fields have nG strengths. Taking as a minimum characteristic distance D = 10 Mpc, which defines a very localized region completely internal to the super-galactic plane and even smaller than the distance to the nearby Virgo cluster, only protons with $E > 2\times10^{17}$ eV, or Fe nuclei with $E > 5\times10^{18}$ eV are able to reach the Galaxy in less than a Hubble time.

Therefore, it is at the energies of the second knee and the ankle that different nuclei start to arrive from the local universe. Concomitantly, at these same energies, the magnetic shielding of the Galaxy becomes permeable to these nuclei, allowing them to get into the interstellar medium and, eventually, to reach the solar system. Effectively, the energy interval from $\sim2\times10^{17}$ to 10^{19} eV is the region of mixing between the Galactic and extragalactic components of cosmic rays.

Above few times 10^{17} eV, the dominant interactions experienced by cosmic rays are due to the cosmic microwave background radiation (CMBR) and, additionally in the case of nuclei, to the infrared background (CIBR) [140]. The diffuse background in radio, despite its much lower density, must in turn become important at high enough energies.

At energies above $\sim10^{19.2}$ eV, the dominant process is the photo production of pions in interactions with the CMBR (see Figure 143a), which drastically reduces the mean free path of protons to few Mpc, making the universe optically thick to ultra-high energy cosmic rays (Figure 143b). This interaction, in the most conservative models, should produce a strong depression in the energy spectrum, with a major fall in the observed flux above 10^{20} eV, the GZK cut-off. These are the energies for which the PAO was originally designed.

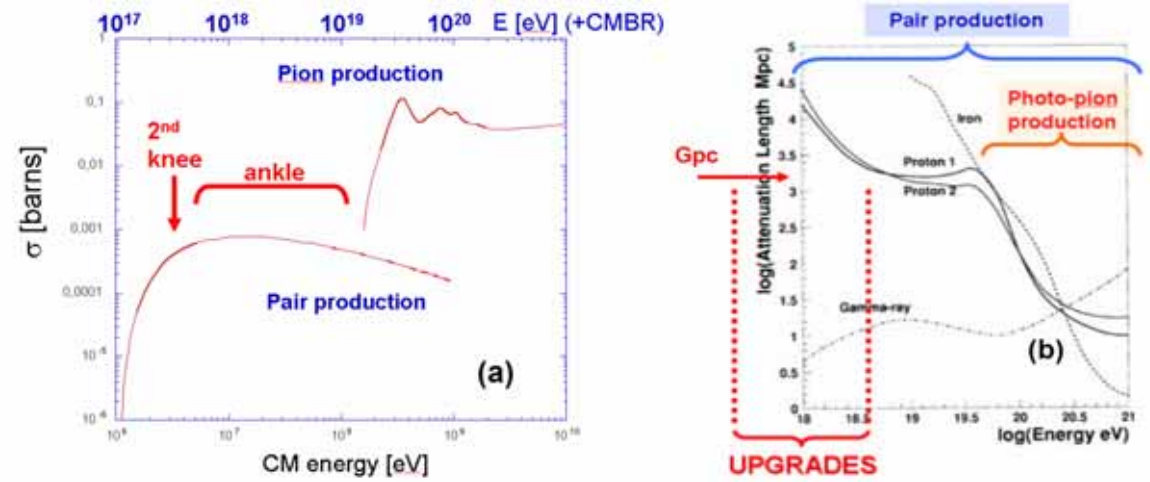

Figure 143 – (a) Cross section for pair production and pion production in interaction with the CMBR. The positions of the second knee and the ankle are also shown, demonstrating that electron positron pair production is the relevant interaction in the region of operation of AMIGA. Note the similitude between the shape of the cross section for this interaction and the shape and location of the ankle. (b) Attenuation length in Mpc as a function of energy [141], showing how the universe, which is opaque at energies above the photo-pion production threshold, becomes transparent at lower energy for baryons [142].

At energies smaller than ~$10^{19.2}$ eV, which includes the AMIGA target region, the dominant process is the photo-production of electron-positron pairs in interactions with the CMBR. At these lower energies the attenuation length attains values of the order of Gpc and, therefore, the universe is essentially optically thin to energetic baryons. AMIGA, observing at these energies, will be sampling the universe at cosmological distances, contrary to the highest energies that sample the PAO, a sphere of a few tens of Mpc in diameter, i.e., a small portion of the local universe [143, 144, 145]. Therefore, strictly from the point of view of propagation in the extragalactic medium, the immediate effect of the proposed extension is to open an energy window in which cosmic rays from an observable horizon from 10 to 10^3 Mpc can be probed, i.e., essentially the whole universe.

It can also be seen from Figure 143a, that the dependence of the cross section with energy is consistent with the shape and position of the ankle in the cosmic ray energy spectrum. In fact, the structure of the ankle can be explained exclusively as a result of pair photo-production by nucleons traveling cosmological distances between the source and the observer [146].

AMIGA is designed to operate in the energy region where the Galactic and extragalactic spectra overlap. This is a theoretically challenging region where the smooth matching of the two rapidly varying spectra has yet to be explained. It must be noted that, even if the shape of the spectrum is important, it is by far insufficient to decipher the underlying astrophysical model. The Galactic magnetic fields are intense enough to dilute any directional information, which prevents the discrimination between the Galactic and extragalactic components from the arrival direction of the incoming particles. The variation of the composition vs. energy becomes the key, which allows discrimination of both fluxes and selection a solution among a variety of theoretical options.

As in the case of the interstellar medium, it is expected, that the intergalactic media have a strong magnetic turbulent component, which can severely affect propagation [147]. The correlation length estimated from Faraday rotation measurements, L_c, is consistent with a

maximum wavelength for the MHD turbulence determined by the largest kinetic energy injection scales in the intergalactic medium, $L_{max} \sim L_c \sim 1$ Mpc. Therefore, analogous to equation (95):

$$r_{L(Mpc)} \approx \frac{1}{Z} \times \left(\frac{E_{(EeV)}}{B_{(nG)}} \right) \approx L_{\max} \approx 1 Mpc \qquad E_{c(EvV)} \approx 1.0 \times Z \tag{99}$$

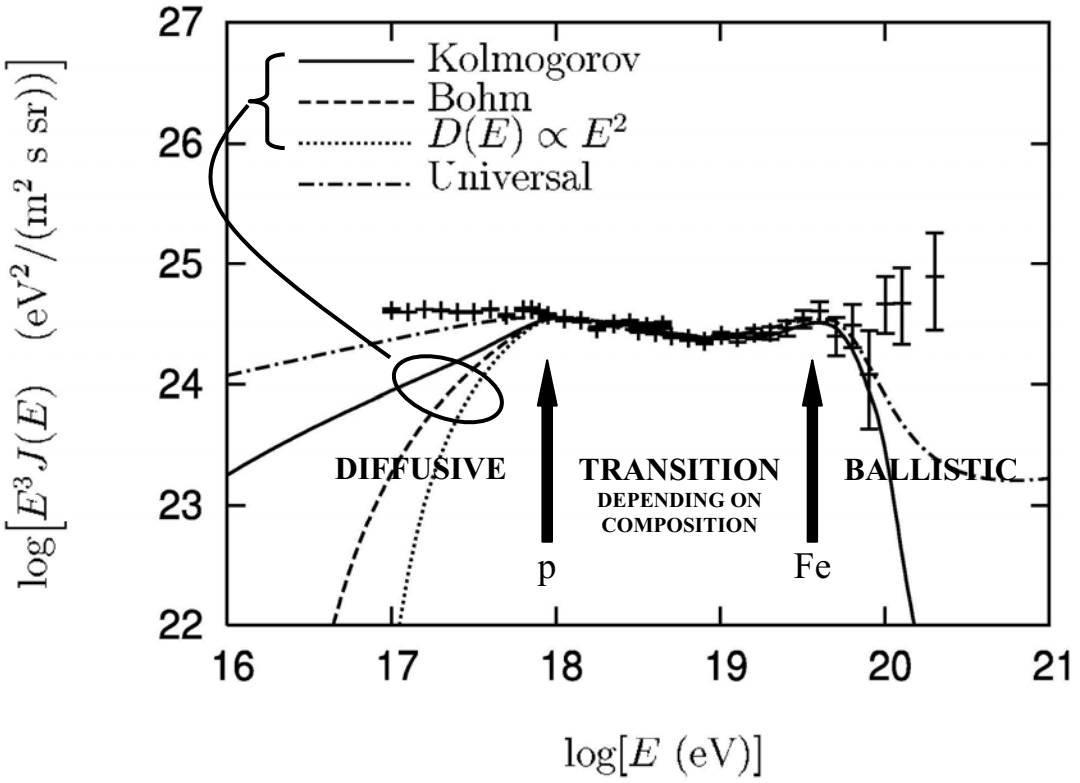

Figure 144 – Correlation between the detailed structure of the lower end of the extragalactic spectrum and the type of turbulence present in the intergalactic medium. This emphasizes the importance of the intergalactic turbulent component in the observed matching between the Galactic and extragalactic cosmic ray flux. The arrows roughly indicate the energies where the transition from diffusive to ballistic propagation takes place for p and Fe respectively [148].

For a given nucleus of charge Ze, the propagation is ballistic for $E > E_c$ being diffusive otherwise. Therefore, protons are ballistic above ~10^{18} eV, but diffusive at the energies of the second knee. Iron nuclei, on the other hand, propagate diffusively along the whole target energy interval and even at energies as high as ~5×10^{19} eV. Once more, the AMIGA target energy interval appears as a transition region in the conditions of propagation, highlighting the fundamental importance of the knowledge of the variation of composition as a function of energy of the cosmic ray flux in this particular energy interval. The boundaries for the transition between the ballistic and diffusive propagation regime for proton and Fe nuclei are shown in the Figure 144.

Furthermore, besides the total intensity and the minimum wave number, also the energy distribution among the different modes, that is the type of turbulence present in the intergalactic medium, have observational expression. In this case, the affected portion of the extragalactic spectrum is the region of lower energies, where the flux is strongly suppressed by magnetic horizon effects. Figure 144 shows clearly this effect for three different assumptions for the diffusion coefficient.

Obviously, this has profound theoretical implications not only for the structure of the extragalactic magnetized medium, but also for cosmic ray acceleration conditions inside the Galaxy. This is exemplified in Figure 145**,** where it is graphically illustrated that, by subtracting a given extragalactic spectrum from the observed total spectrum, conclusions can be drawn about relevant aspects of the Galactic component. For example, an extragalactic spectrum that has a small contribution at low energy can imply the existence of additional acceleration mechanisms in the Galaxy other than the shock waves of supernova remnants.

7.6 Degeneracy of astrophysical models

There is an additional problem at very high energies above the threshold for pion photo-production, which is not always addressed explicitly. When the statistics are low, different astrophysical scenarios, with different sources, density and luminosity red-shift evolutions, magnetic structures and turbulent spectra, can still produce energy spectra experimentally indistinguishable at very high energy [149].

This degeneracy, beyond few times 10^{19} eV, can only be broken with supplementary information coming either from higher energy neutrinos or from lower energy spectral composition. In the region of the second knee and ankle, differences in propagation conditions, intervening medium structure, interactions with diffuse radiation fields and source evolution critically modify the shape of the spectrum and the resultant cosmic ray composition, making possible to discriminate among different astrophysical models, something which would be otherwise impossible with only baryonic information above 10^{19} eV.

7.7 Composition at the sources and its observational counterpart

It is clear from composition observations around the first knee of the cosmic rays spectrum, that the acceleration mechanism by shock waves, either first order Fermi or drift, is limited by the magnitude of the radius of curvature of the shock. This results in the preferential acceleration of large charge nuclei, those with the smallest Larmor radius, to the highest energies.

Even if the mechanism responsible for the acceleration of the ultra-high energy extragalactic component is essentially unknown, the most conservative view points to bottom-up mechanisms. If the later is actually the case, then any electromagnetic acceleration mechanism would treat all nuclei in the same way, provided that they have the same rigidity and losses, e.g. by photodisintegration, in the source can be neglected. Therefore, the highest energy output should be the heaviest nuclei that are able to survive inside the source.

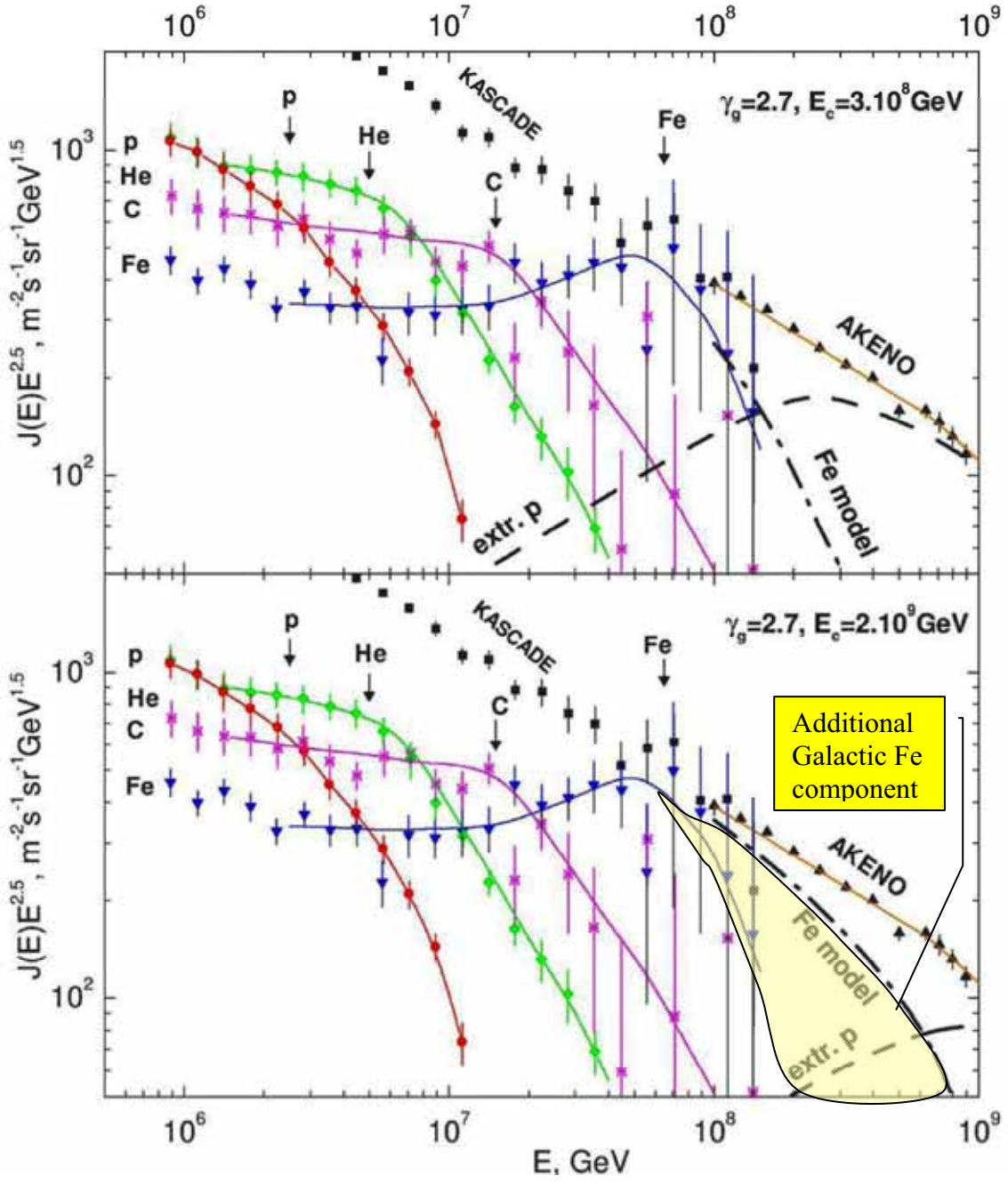

Figure 145 – Impact of the detailed characteristics of the extragalactic spectrum on our comprehension of the most powerful acceleration mechanisms in our Galaxy [150]. The calculated spectra of extragalactic protons (thick dashed curve labeled "extr. p") and of galactic iron nuclei (dash-dotted thick curve labeled "Fe model") in comparison with the Akeno and KASCADE data. The values of γ_g and E_c used in the calculations are indicated in each panel. The all-particle spectrum of Akeno is shown by filled triangles and by solid curve. The sum of the curves "extr. p" and "Fe model" is exactly equal to all-particle spectrum of Akeno, given by curve "AKENO". The data of KASCADE for different nuclei are shown as: protons (filled circles), helium (diamonds), carbon (stars), and iron (inverted triangles). The thin full curves smoothly connect the data points. The arrows labeled by p, He, C and Fe show the positions of corresponding knees, calculated as $E_Z = ZEp$, with $Ep = 2.5\times10^6$ GeV. One can notice the satisfactory agreement between calculated and observed positions of the knees.

In this minimal, but still realistic, scenario the most likely high energy out-put would be heavy nuclei, very likely Fe as in the Galactic case. At lower energies, progressively lighter nuclei should be observed due to two factors: (a) the acceleration process in itself and (b) the photo-disintegration, on flight, of the heavier nuclei due to their interaction with the CIBR. The latter process is very efficient, and can extract approximately one nucleon at each 2 Mpc of flight, depending on the CIBR level.

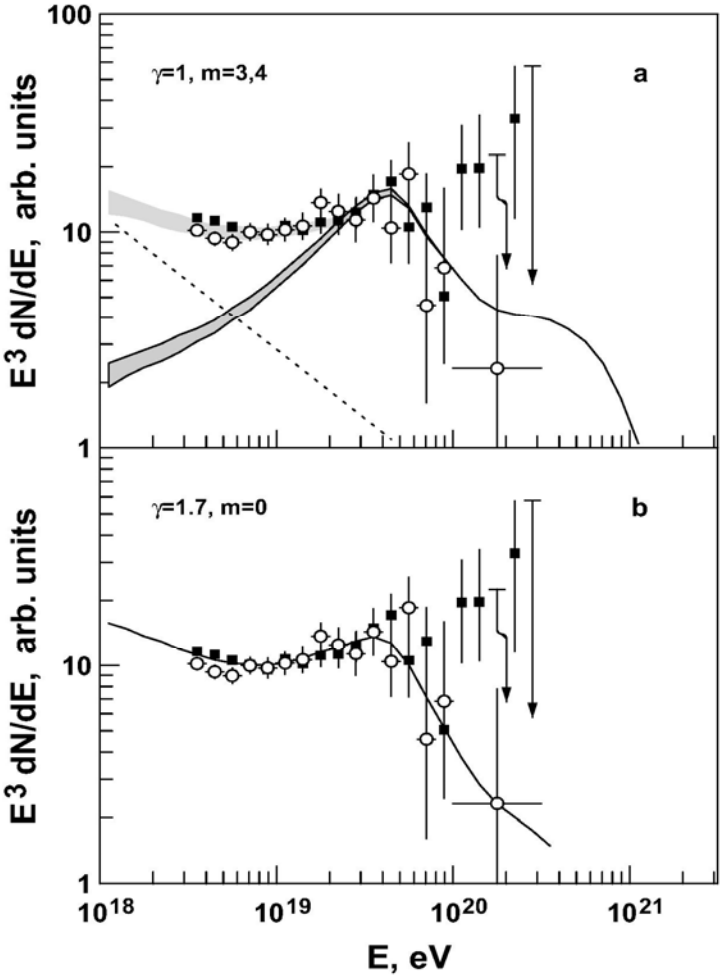

Figure 146 – Different astrophysical scenarios that are observationally degenerate from the point of view of the energy spectra, which become distinguishable in the ankle region [149]. The UHECR spectrum is fitted with flat extragalactic injection spectrum. Upper edge of shaded area is for m=4, lower for m=3. Galactic contribution is (dotted line) with γ=2.6. b) Fitting with steep injection spectrum (γ=1.7).

Figure 147 shows that power law spectra injected at cosmological sources with different compositions can produce experimentally very similar spectra at the highest energies. Nevertheless, they can always be distinguished at smaller energies in the ankle region. The pure proton model with $\beta = 2.6$ provides a good fit to the data down to $\sim 10^{18}$ eV (in a scenario with uniform source distribution and no magnetic field). In such a model, the transition from Galactic to extragalactic cosmic rays should thus occur at lower energies around the second knee [150]. However, no acceleration process is known to yield a spectrum as steep as $\beta = 2.6$. Instead, both analytical and numerical studies of particle acceleration in

relativistic shocks give injection spectra with $\beta \sim 2.2$–2.3 [151, 152, 153]. Such spectral indices can provide equally good fits to the high-energy data, assuming a realistic source model with a mixed composition $\alpha \sim \beta$. In such a scenario, the transition from GCR to EGCR occurs at the ankle, which thus keeps its "standard" interpretation.

On the other hand, for a heavier mixed composition, the extragalactic spectrum falls down steadily with decreasing energy. In this scenario, the ankle must be the result of the competition between the Galactic and extragalactic spectra. Moreover, the composition will be a strong function of energy inside this interval, giving an additional tool to assess details of the astrophysical model.

The effects of photo - disintegration are clear in Figure 148 [154], where the evolution of a pure iron injected spectrum as it propagates out from the source is shown. Blue (dark) histograms correspond to p, white to the original surviving Fe and red (gray) to intermediate mass nuclei.

As the distance to the source increases, intermediate nuclei are produced at increasingly smaller masses and less total energy (fragmentation takes place at roughly constant mass per nucleon). At distances of the order of the GZK horizon, the region with larger mixing of nuclei, i.e., with a larger composition gradient, is the ankle. Consequently, this is the ideal region for the discrimination of the primary composition from local composition measurements.

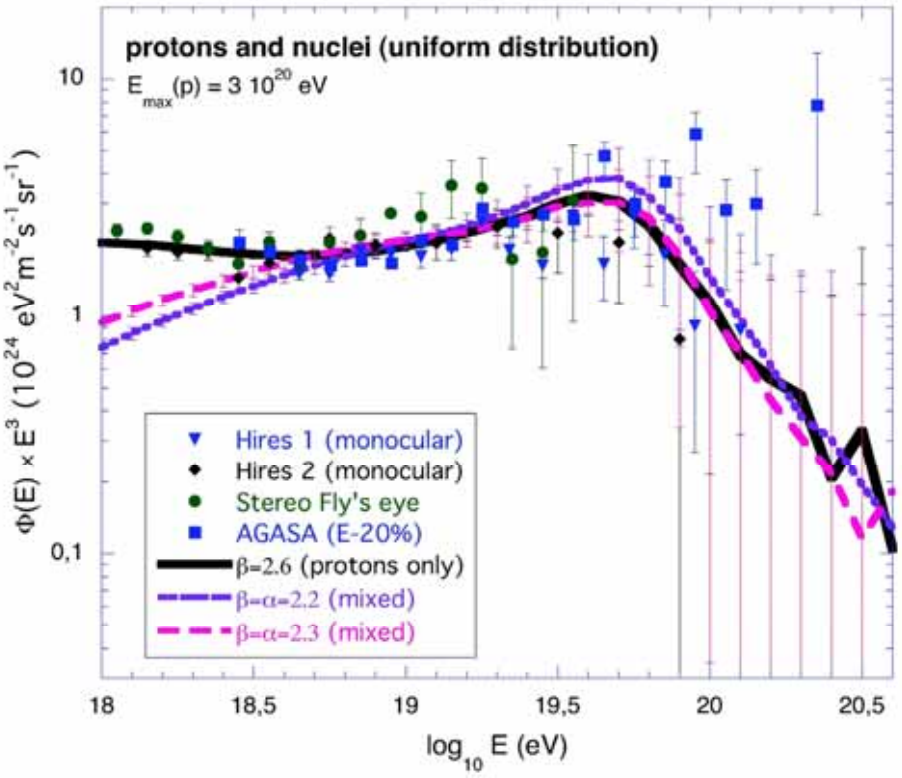

Figure 147 – Different primary compositions may produce extragalactic spectra essentially indistinguishable at the highest energies. However, as shown in (a) for protons and (b) for heavier mix, the spectra are considerably different at lower energies below the bottom of the ankle [155].

7.8 Tasks for AMIGA

Main objective of AMIGA is an extension of the PAO capabilities to measure cosmic rays down to 10^{17} eV, to determine their energy spectrum, possible large-scale anisotropies and composition. AMIGA will also be a useful tool for enhancing the capabilities of the baseline Auger Observatory at its lower energy range. Understanding the Auger surface detector at its lower energy range will in turn be useful for extrapolating these results to higher energies.

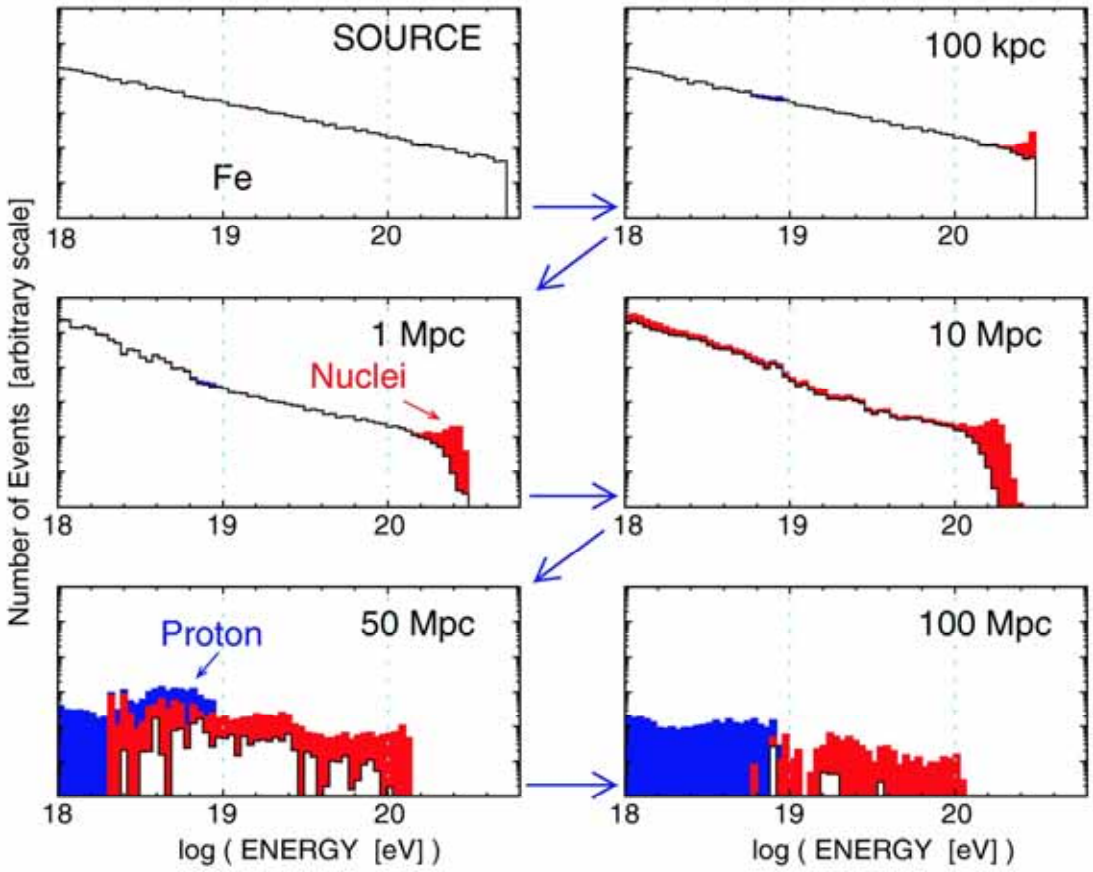

Figure 148 – Variation of the composition as a function of distance to the source for pure Fe power law injection. Blue (dark) histograms correspond to p, white to the original surviving Fe and red (grey) to intermediate mass nuclei [154]. Variation of energy distribution of particles, that began as Fe after propagation over various distances from a single source. The distances from the source are indicated in each panel. The number of particles (arbitrary scale) is shown as a function of energy. Primary nuclei (Fe), secondary lighter nuclei, and protons are indicated by white, light shade and dark shade in the histograms respectively. The differential source spectrum is assumed to be a power law, $\sim E^{-2}$, with energy cut-off at $Z \times 2 \times 10^{19}$ eV (upper left panel). At 100 Mpc from the source, most of the Fe disappears because of their low rigidity.

The energy calibration of the SD Auger detectors is presently based on cross-calibration with FD through hybrid events, since the fluorescence measurement is expected to be almost calorimetric for a fraction as large as 90% of the primary energy [156, 157]. However, with an SD calibration based solely on Monte-Carlo shower and detector response

simulations, a shift in energy of 30% is obtained. A possible explanation for this difference may come from the fact that water Cherenkov tanks are very sensitive to muons, and that the ratio between muon signal and the electromagnetic component is not well reproduced by shower simulations. An independent measure of the muon component will allow analysis whether this difference is at the root of the energy calibration divergence between FD and SD.

The best energy estimator used for the Auger Surface Detector is given by S(1000), the expected signal at 1000 meters from the shower core, as calculated by fitting a Lateral Distribution Function (LDF) to the detector signals at different distances. Although S(1000) has been chosen as the optimum parameter because it minimizes the shower-to-shower fluctuations and the composition dependence, but if the shower core falls close to one of the detectors (up to 300-400 meters), the distribution of tank distances to the core is very inconvenient: only one detector is located below 1000 meters while all others are at distances larger than 1000 meters [158]. In this way, and given that the LDF might not be well understood at low distances, the determination of S(1000) results in an extrapolation of the LDF rather than an interpolation, with the corresponding uncertainties and systematic errors. With an infill at 750 meters, all showers above 3 EeV will trigger a large number of detectors and the distance distribution will be very uniform around 1000 m, allowing to search for systematics in the baseline 1500 m grid.

Furthermore, the inclusion of Muon Detectors will allow an independent construction of LDFs for different shower components (muon vs. electromagnetic), a suitable tool for verifying the accuracy of simulations and the response of the detectors to both types of signals.

The infill array will naturally be able to trigger with full efficiency on lower energy events for which the baseline Auger SD is not fully efficient any more. This will allow measurements experimentally, without resorting to simulations, the acceptance curve of the Auger Observatory. This information will not only give a suitable tool for analyzing the detector simulations, it might also be employed to help towards a determination of chemical composition [159]. An infill array with a detector separation of 750 m is equivalent to 3 superimposed Auger-like grids with detectors spaced 1500 m. This allows a reconstruction of single events with 3 independent subsets of detectors, a powerful tool for the study of fluctuations and reconstruction errors.

7.9 Capabilities of the Infill Array

The standard Auger array with a 1.5 km grid does not guarantee the full detector efficiency for the low energy events, which corresponds to the region of the second knee and the ankle, due to a degradation of the angular and energy resolution, because of limited hit tanks.

Parameters of registered showers strongly depend on atmospheric conditions, temperature and other variables introducing large uncertainties. In order achieve the full efficiency in lower energy region; the AMIGA proposes a reduction of distances between surface detectors in two smaller spacing than that of the original Auger surface array. The area of this infill can be made much smaller than Auger because of the rapid increase in cosmic ray flux with decreasing energy. The infill is implemented using the same technology of Auger and sharing the existing infrastructure at the site (detector design, data acquisition system, analysis tools, etc.). Additional detectors are added to the existing array keeping the

same Auger triangular and equilateral configurations. AMIGA is being developed in several different directions:

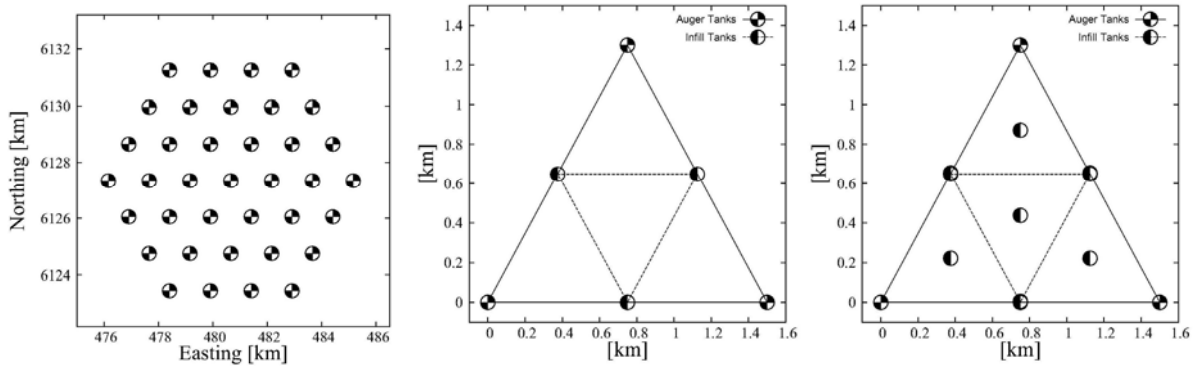

Figure 149 – Different infill configurations generated inside the original array with 1500 m spacing (left). A detector added at half distance between the original detectors *(middle*) results in a grid of 750 m. A detector placed at the center of each triangle of 750 m (*right*) produces a grid of 433 m.

- Detectors at half the distance between Auger tanks, resulting in a triangular grid of 750 m spacing (Fig.3.1: bottom, left)
- Detectors at the center of each triangle of 750 m from grid b), giving a triangular grid with a spacing of 433 m (Fig. 3.1: bottom, right)

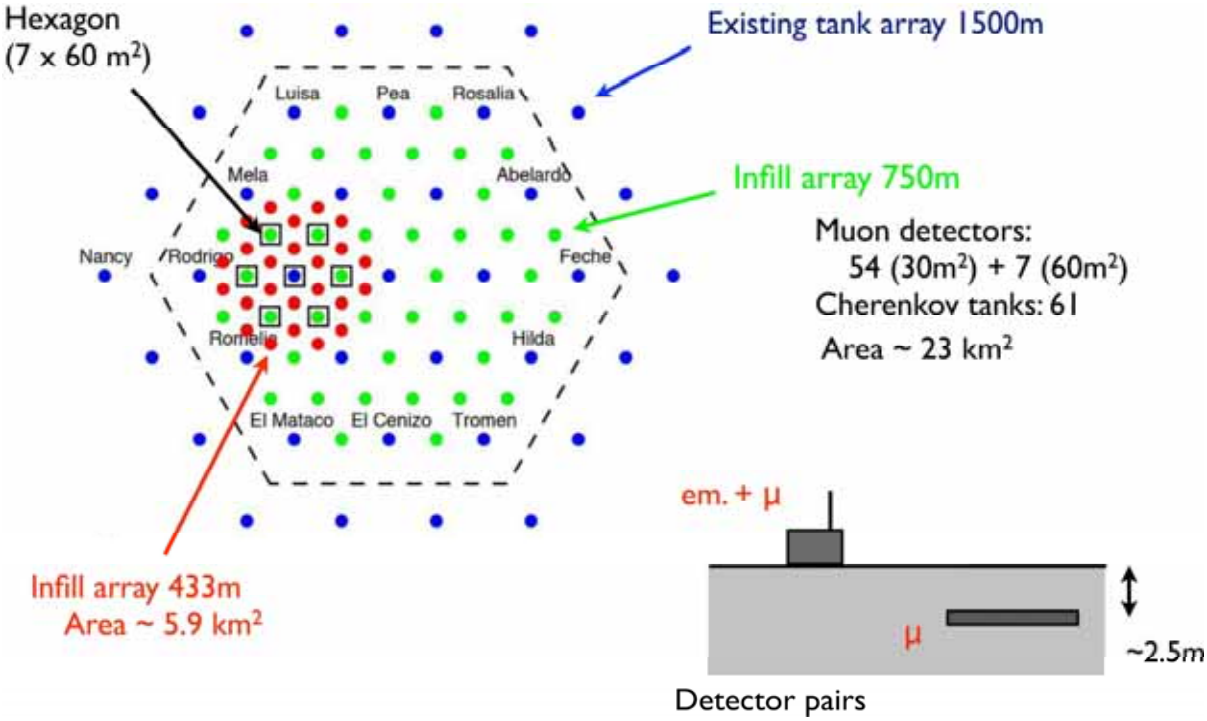

Figure 150 – AMIGA infill tanks and muon counters protons (open marks) and iron (closed marks) [161].

Relative acceptance for infill grids shown on Figure 152 confirms main AMIGA assumptions regarding an enhancement of energy measurements towards lower energy range

in comparison to the standard Auger one. A separation of 750 m between detectors guarantees a detection efficiency of 95% for proton (iron) showers with an energy of 3.6×10^{17} eV (1.8×10^{17} eV). With a detector spacing of 433 m, a similar acceptance can be obtained for showers of as low as 9×10^{16} eV and 4×10^{16} eV for proton and iron primaries, respectively. According to this calculation, at 3×10^{18} eV the Pierre Auger array achieves full acceptance independently of composition [160].

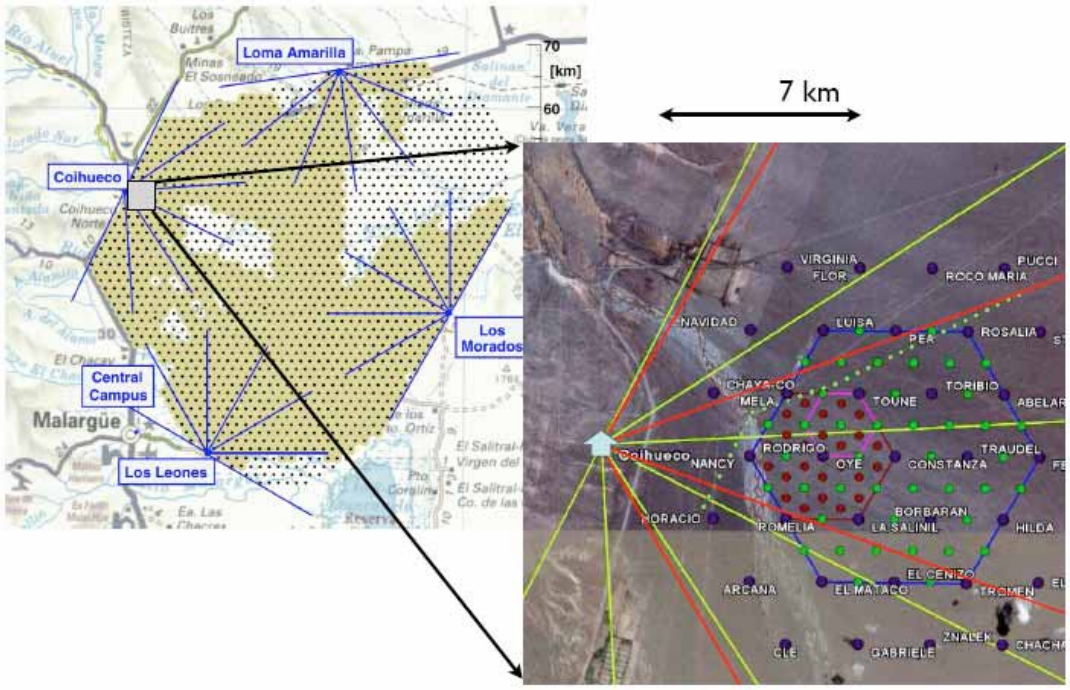

Figure 151 – Location of the Infill Array and AMIGA low-energy enhancement [161].

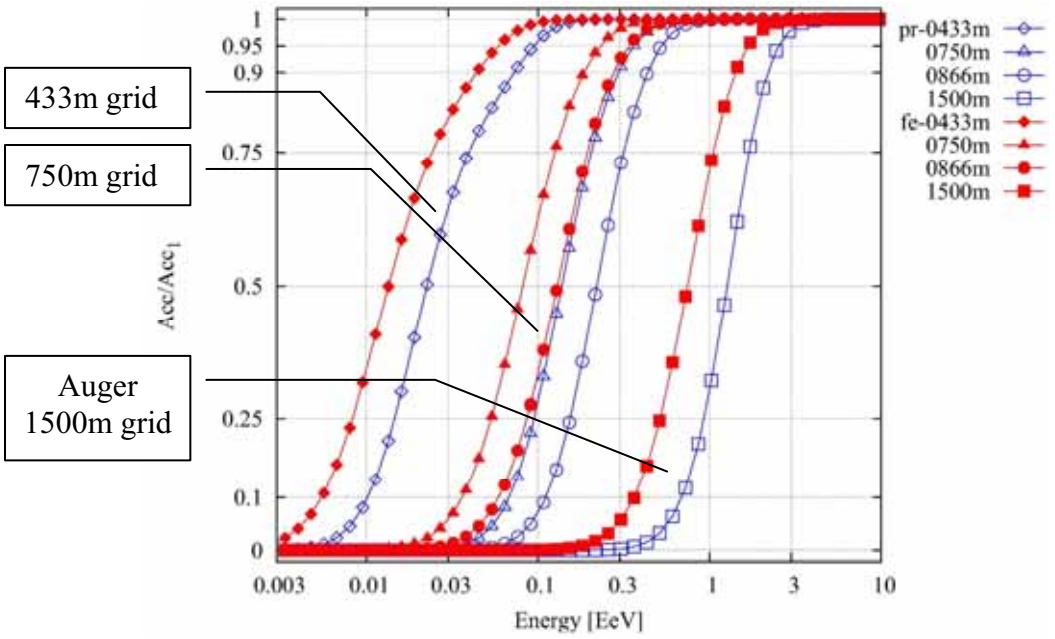

Figure 152 – Relative acceptance for different configurations of Infill Cherenkov tank array for protons (*open symbols*) and iron (*closed symbols*) [142], [161].

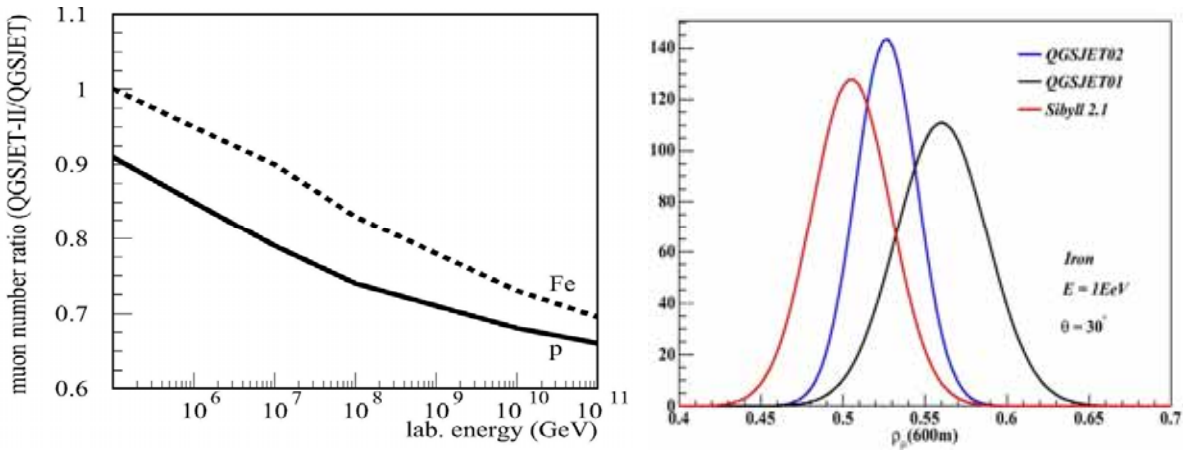

Figure 153 – Relative N_μ-difference (Eμ > 1 GeV) at sea level between QGSJET-II and QGSJET-I models for vertical proton and iron induced EAS (left) [162] and fits to muon density histograms (in number of muons/m^2 units) for Fe shower, θ = 30º, with a threshold of ≅ 1.0 GeV for Sibyll 2.1, QGSJET-II, and QGSJET-I (right) [142].

The content of muons in air showers is very sensitive to primary composition. Showers generated by heavy nuclei produce more muons than lighter ones. The muon number at a certain distance to the shower axis appears to be the best parameter to discriminate proton from iron primaries [163]. However, in order to perform reliable measurements of muon densities both: hadronic model interactions dependence and fluctuations have to be carefully taken into account.

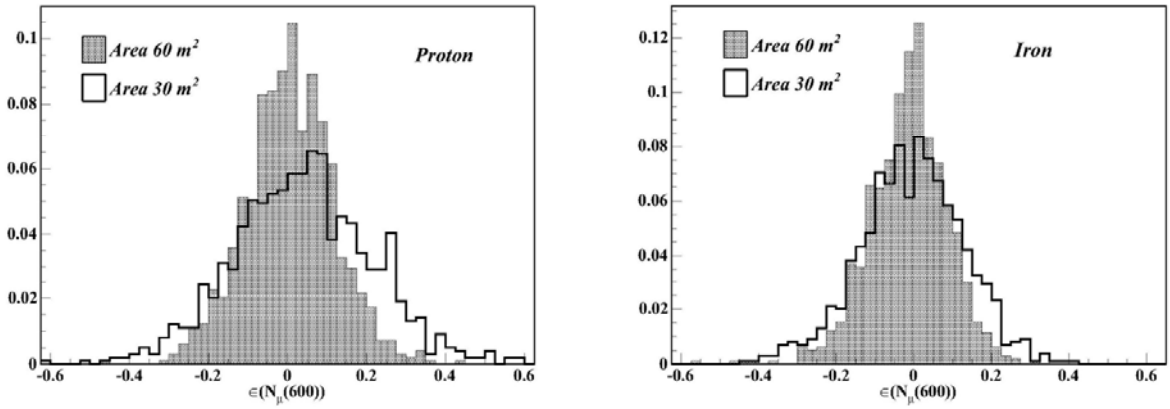

Figure 154 – Composition resolution in the determination of the number of muons at 600 m from the core for proton and iron primaries and for 30 m^2 and 60 m^2 muon detectors [142].

Commonly used models of hadronic interaction QGSJET and Sibyll showed in the past a large discrepancies in muon air shower content [164]. The new version of QGSJET-II generates less muons (-30% at 10^{18} eV) in comparison to QGSJET-I (Figure 153a). Discrepancies between models and version still exist, however a permanent progress in understanding of processes and optimization of models has a tendency to diminishing of their importance in context of 30% muon content differences between p – Fe (Figure 153b).

The other possible drawback for muon density composition studies is the fluctuations. There are two types of muon density fluctuations: shower to shower and Poisson fluctuations. The 1st is intrinsic to the physics of the air shower development, while the 2nd depends on the detector size. Detectors of two different surface areas, 30 and 60 m^2, are considered.

Simulations show (compare histograms in Figure 154) that the resolutions for 30 m^2 detector are 13% and 17% for iron and proton primaries, respectively, while for a 60 m^2 counter, 10% and 11%. These results suggest that the smaller detector is a good cost-performance compromise and to evaluate this further abundance determination is performed.

The efficiency of the detectors is assumed as 100%. Each muon counter is placed close to an Auger water Cherenkov tank and buried underground to prevent contamination from shower electrons and gammas (via pair production). The ground level of the Auger site is at 1400 m above the sea level approximately: ~840 g/cm^2 of air mass. At this depth, showers of around 10^{18} eV, if not very inclined, are mainly composed of gammas, $e^{\pm}$ and $\mu^{\pm}$.

Figure 155 shows the energy distributions for each of these particles at 200m from a proton shower core. Gammas and $e^{\pm}$ are the most abundant particles while $\mu^{\pm}$ have, by far, the highest energies. The distributions of the electromagnetic component peak below 100 MeV while the muon maximum is close to 10 GeV. Scintillators are sensitive to charged particles in general. Although gammas and $e^{\pm}$ are much less penetrating than $\mu^{\pm}$ they can, for high enough energies, produce electromagnetic showers inside the soil. The later can extend down to the scintillator and produce a detectable signal, which would be, for AMIGA scintillator, undistinguishable from true muon energy deposition (punch through). The assumed (optimized from simulations) depth of 3 m sets a lower energy threshold of ~ 0.9 GeV for a vertical coming muon: only muons with a higher energy may reach a buried counter since they will lose energy (mainly through ionization) as they propagate downwards through the earth. The energy of a muon that traveled a distance x through the shielding, assuming an energy loss independent of energy and proportional to the track length, is given by:

$$E(x) = E_0 - \alpha\rho x \tag{100}$$

where E_0 is the initial energy, $\rho = 1.8\times10^6$ g/m^3 the density of the shielding and the energy loss per unit column density $\alpha = 2.1\times10^{-7}$ GeV m^2/g [165].

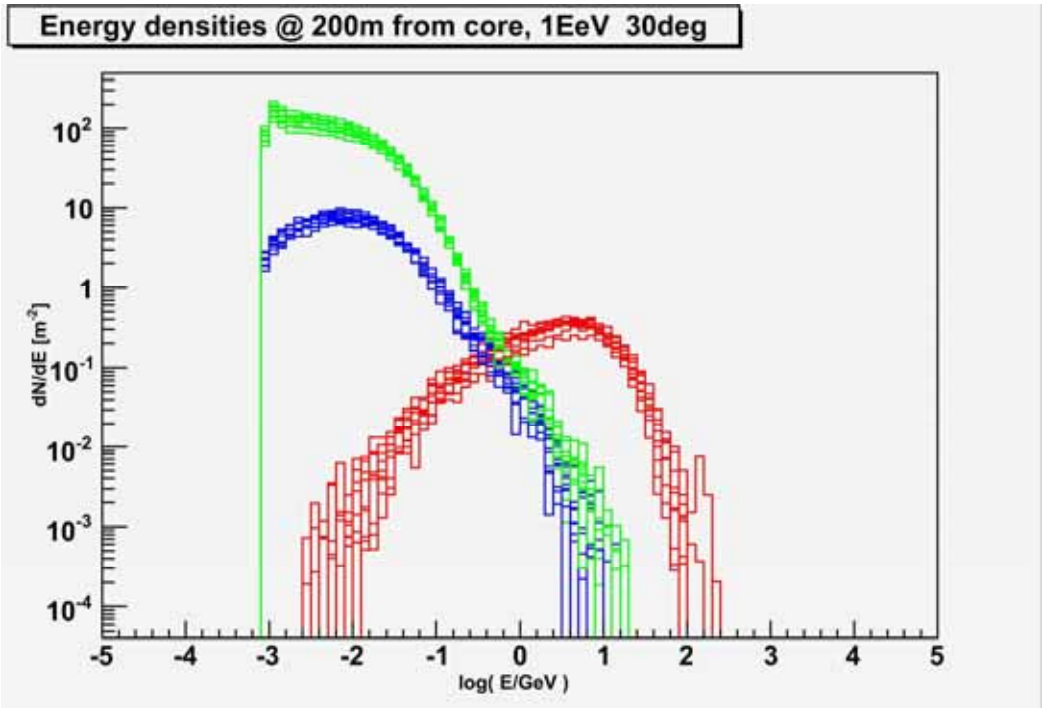

Figure 155 – gammas, $e^{\pm}$ and $\mu^{\pm}$ energy density distributions at 200m from the shower core [142].

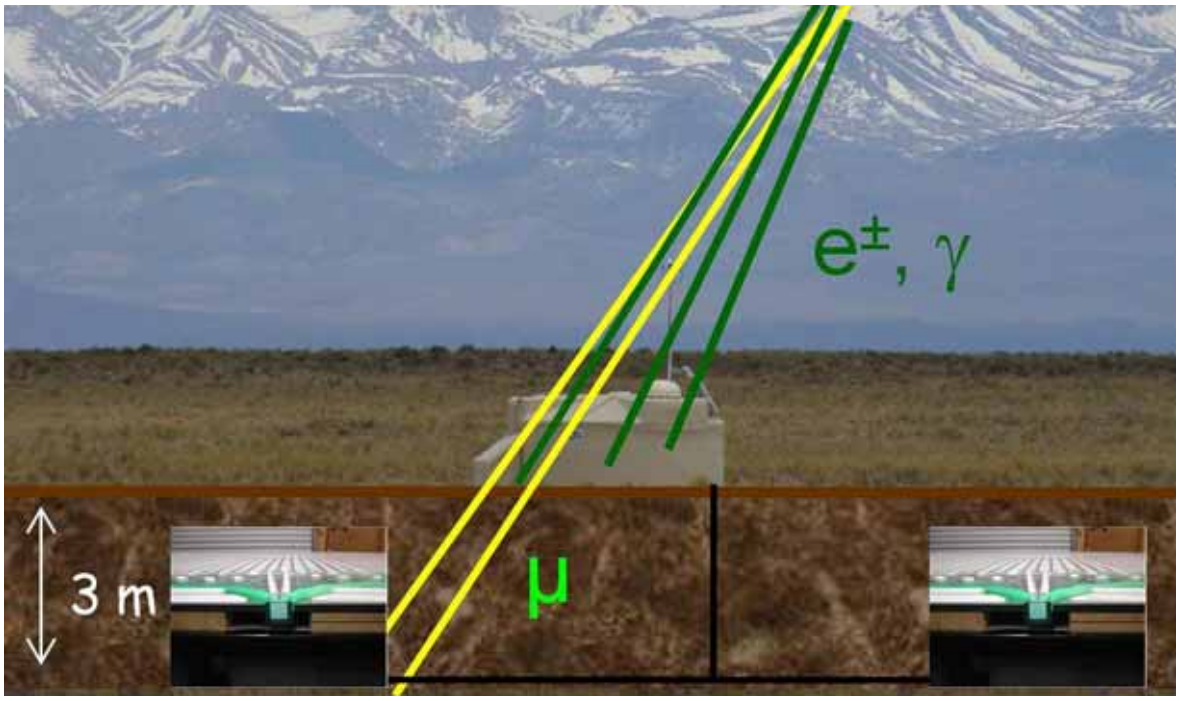

Figure 156 – Configuration of connections between the surface detector and underground scintillator.

7.10 Underground hardware

The main aim of the underground muon systems is a detection only of the presence or absence of muons in showers. In the analog electronics, because of much simplified: the threshold instead of multi-bit shape analysis, the comparators instead of FADC have been used. The threshold in each comparator corresponding to a muon channel is tunable by the individually subordinated DAC. Signals from comparators are next sampled with 80 MHz clock. Although the input electronics is much simpler in comparison to the surface detector, the physics results are trustworthy at the cost of increasing the number of electronic channels due to segmentation. Muon counters rely on the SD array for the event reconstruction, i.e., for triggering and for both geometry and energy reconstructions.

Each muon detector has an area of 30 m^2 and will be buried alongside each SD station at a depth of ~3m. The distance to the station will be large enough to avoid the water-tank shadow, guaranteeing a uniform shielding, but small enough to represent the same physical point inside the shower front and to be able to share GPS time signals and the micro-wave link with its associated surface detector. The relatively small distance allows the full synchronization of the surface and underground detectors by a triggering of the muon counters from the surface detector via dedicated fast transmission line.

The design of the muon detectors is being developed on the same plastic scintillator already used by the MINOS experiment. Scintillator strips are extruded polystyrene doped with fluors: PPO (1%) and POPOP (0.03%). They have a middle groove, which lodges a wavelength shifter (WLS) fiber: Kuraray Y-11 175 ppm double-clad 1.2 mm diameter, which is glued into the groove and covered with reflective foil. The strips are co-extruded with a TiO_2 reflective coating, which prevents the light from leaving the scintillator (Figure 157) [166].

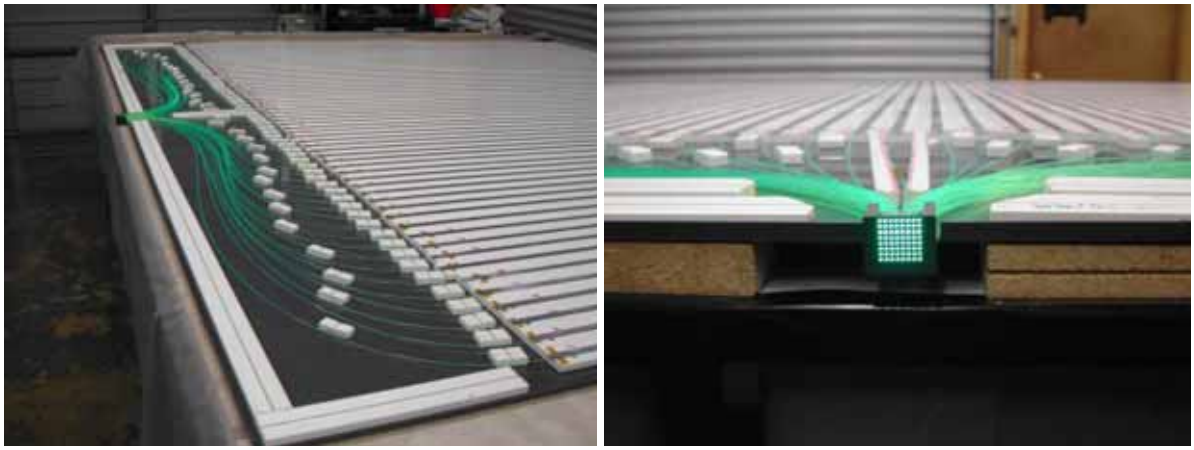

Figure 157 – Scintillator strips: *left*: general mounting in the PVC housing, *right*: detail of the 64 pixels optical connectors.

Each module will consist of 64 strips with the fibers ending on an optical connector matched to a 64 multi-anode Hamamatsu H7546B PMT of 2mm×2mm pixel size lodged in a PVC casing. Each muon counter will be composed of three of these modules buried alongside a water Cherenkov tank, i.e. 192 independent channels.

Light is produced after a charged particle traverses a scintillator strip and a fraction of it will enter the fiber, and be absorbed and reemitted at a different frequency. The WLS fibers guide this light onto a PMT equipped with an associated electronic circuit, which will amplify, discriminate, conform and digitize the signals in a synchronized way with the SD electronics. The light collected in a scintillator will be guided towards a 64 channels low cross talk, with high-speed response Hamamatsu PMT. According the PMT specification, the width at the base of a typical pulse seen by the PMT is ~2 ns. The complete system with scintillator and WLS fibers enlarges the width of the pulse to ~10 ns (Figure 158). The PMT are negatively biased and the signal is coupled from the anodes to the amplifiers directly, without coupling capacitors.

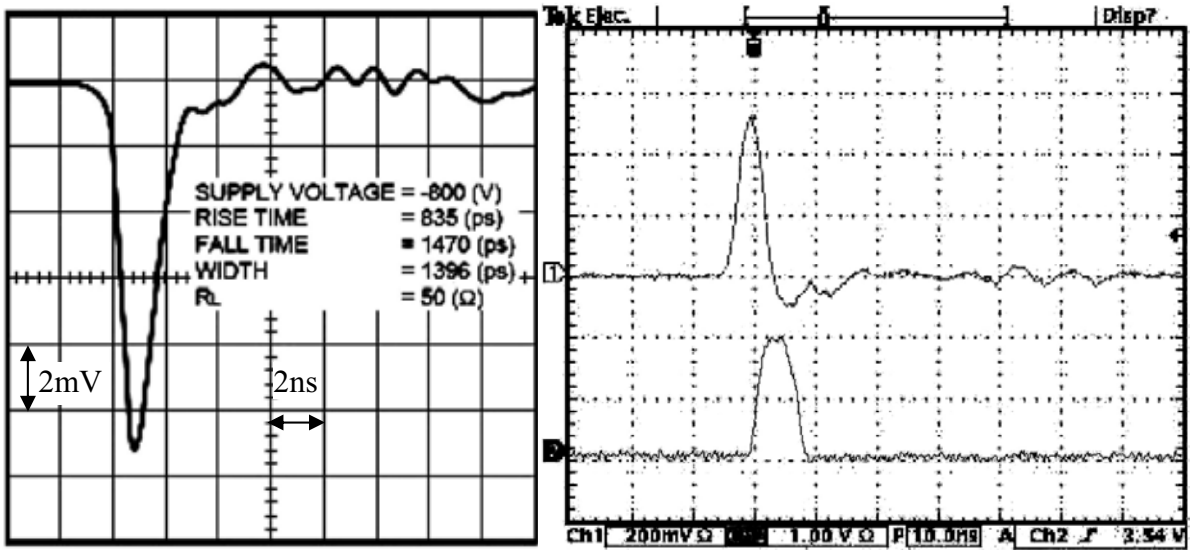

Figure 158 – A typical pulse from the multi-anode Hamamatsu PMT (left) and the AMIGA pulse after amplification (right-top) and discrimination (right-bottom).

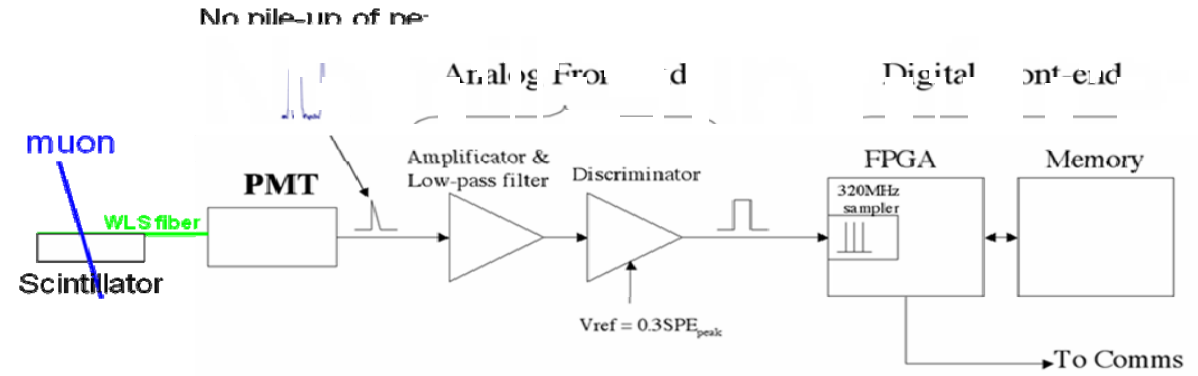

Figure 159 – The structure of the muon signal processing.

AMIGA electronics will have both an underground and a surface section powered by solar panels. Each of the three underground modules per counter will have attached a PCB with the data handling FPGA (Cyclone III™ – EP3C25F324C7) and the TMS470R1B1M 16/32-Bit RISC Flash micro-controller managing a communication and monitoring system. Each electronic channel will have an amplifier and a discriminator, set at ca. 30% of the pixel mean single photoelectron amplitude. The pulses from all strips are synchronized to the water tank clock and after discrimination each strip output will either be 0 or 1. These numbers are stored in a circular buffer and upon reception of a tank trigger signal; they are adequately channeled by the micro-controller (μC) to the surface electronics via CAN BUS. On the surface, a single-board microcomputer receives the data and which upon a request from the CDAS, transmits both tank and muon counter data by radio link. Also, and in order to test each strip, a monitoring mode is envisaged by detecting atmospheric background muons.

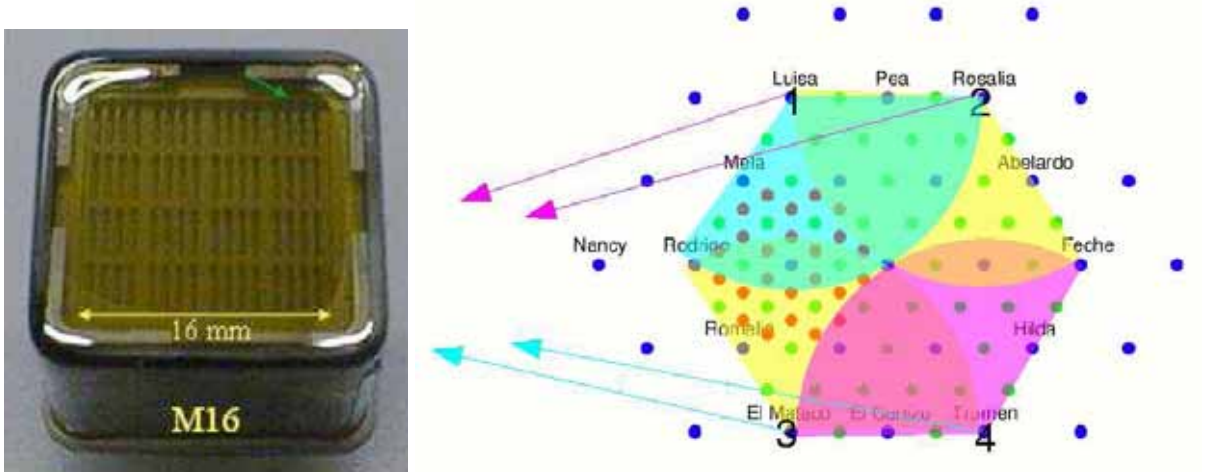

Figure 160 – Hamamatsu multi-anode 64-channel PMT (left) and AMIGA two level telecommunication star topology. Concentrators are labeled from 1 to 4. In this layout concentrator-subscriber systems 2 and 3 use the same 802.11 independent channels. Bottom and upper arrows show channeling of data to the two access points (right).

AMIGA will communicate using an 802.11 standard wireless network (WiFi), taking advantage of the low cost and wide availability of this technology. As a plus, the high communication bandwidth will allow for the recollection of high amount of data at the early stages of the experiment, in order to study better the characteristics of muon counters and

showers. This system must also carry the surface detectors data and so the wireless local area network must integrate with the existing communications. The antennas and physical network topology are chosen to cover long distances and avoid interferences. Setting concentrators relatively close to the subscriber stations chose a two level star topology. These concentrators are the center of four lower level logical stars (Figure 160b) and they have a directional 120º sector antenna, which collects the signal from the stations directional antennas. These stations use three 802.11 independent channels but since there are four concentrators, one of these channels is used twice.

7.11 Triggers, data flow and synchronization between the underground electronics and the Auger surface detector

The underground electronics can work in two different modes:

a) with the external trigger coming from the surface detector (synchronous mode) or
b) with self-trigger generated from scintillator pulses (autonomous mode).

In the synchronous mode the trigger has to be transmitted from the standard Auger tank to the underground electronics with a minimal delay, without a jitter and with correct sharpness of its rising edge. All these requirements can be accomplished only by a dedicated transmission line with a perfect adjustment of the wave impedance both: to transmitter driving the line and receiver resuming the signal. A distance between surface detector and the AMIGA scintillator does not exceed 15 m. The lines are the twisted pair wires transmitting trigger in a differential mode in order to suppress potential interferences, appearing on both wires simultaneously. The transmitter and receiver have to provide undistorted data transfer with possible minimal jitter. The additional source of the signal delay and possible jitter is the galvanic barrier, separating grounds between surface tank and underground electronics. Both grounds have to be separated in order to avoid loop currents. However, this requirement imposes an insertion an additional devices in both transmission chains: for the trigger and for the communication link between the underground micro-controller and the **S**urface **S**ingle **B**oard **C**omputer (SSBC).

Both: surface and underground electronics are clocked with 80 MHz (with independent, not synchronized clocks). In order to assure sharp as possible the rising edge of the transferred trigger signal, the barrier could not be build with even the fastest opto-couplers as still too slow. The ADuM1100 - a digital isolator based on Analog Devices Inc. *i*Coupler® technology has been used. It merges high speed CMOS and monolithic air core transformer technology and provides outstanding performance characteristics superior to alternatives, such as opto-coupler devices. The ADuM1100UR can operate up to maximum temperature 125 ºC and supports data rates up to 100 Mbps. However, in order to achieve this data rate it has to be supplied by relatively high voltage +5 V.

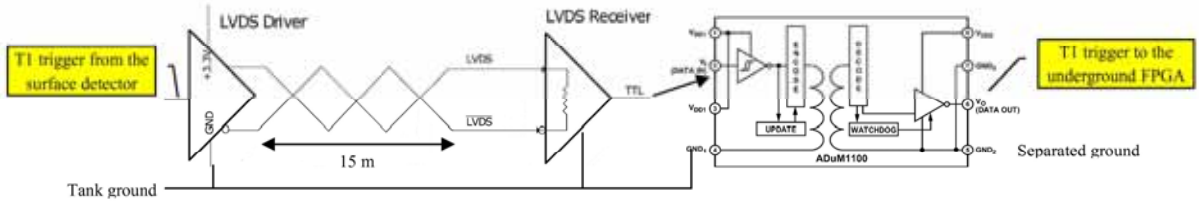

Figure 161 – The scheme of the dedicated transmission line for the trigger.

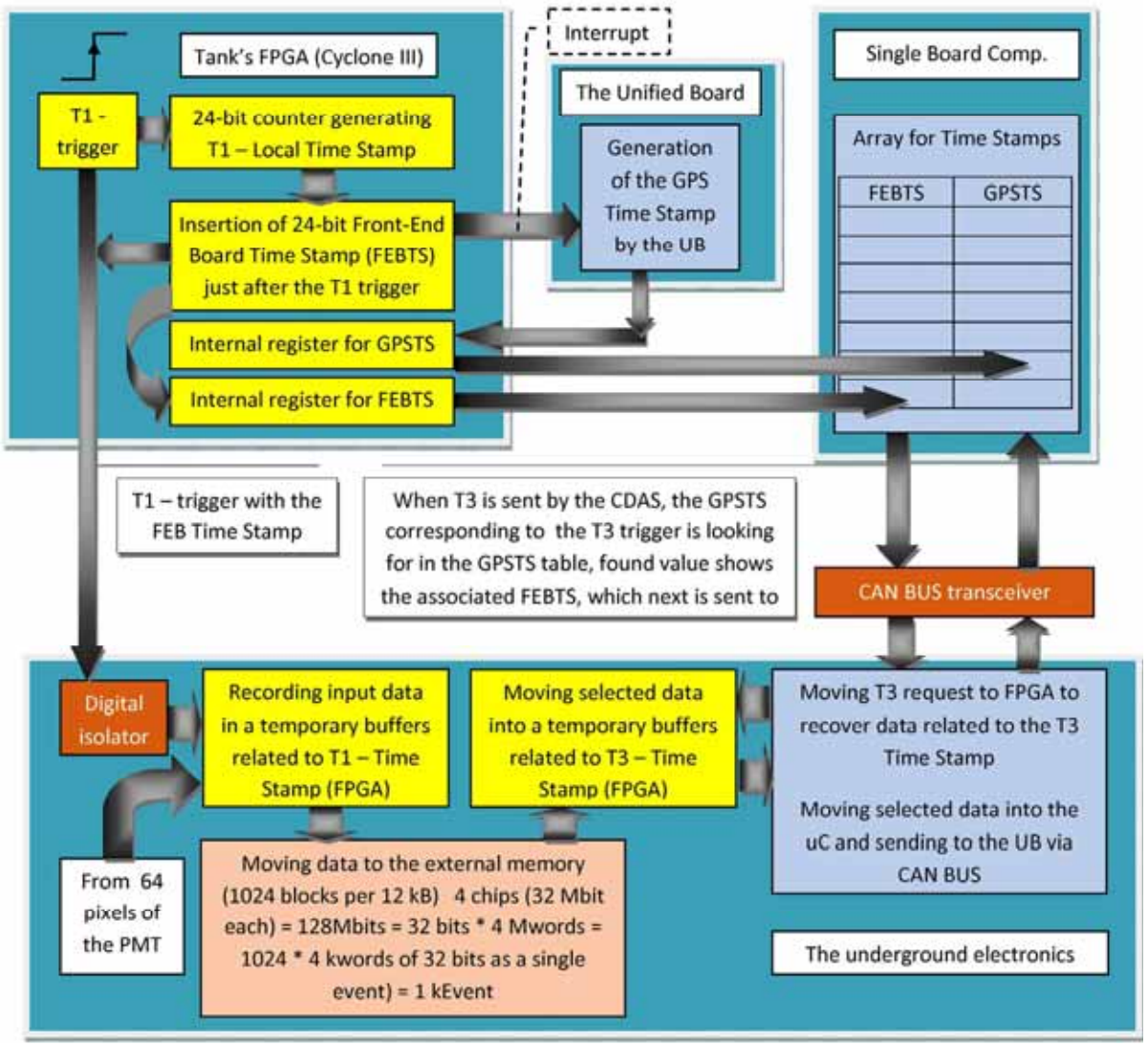

Figure 162 – The structure of the data flow and the synchronization of the underground electronics with the Auger surface detector.

In the synchronous mode data recorded in both surface and underground detectors are synchronized in that sense that they correspond roughly to the same time window. A small phase shift is due to a propagation delay on the trigger transmission path. In order to provide a data synchronization, the surface detector firmware has been equipped additionally with the time stamps counter. The T1 trigger rate (the rate of events temporarily stored in the FPGA buffers in the surface detector trigger/memory system – see Chapter 3.1.2 and Chapter 3.1.5) is tuned in the calibrating process to ca. 100 Hz. All data relating to the T1 are transferred to the UB and next investigated to look for a correlation with neighboring tanks in order to extract physics events (real showers). The searching process requires an extensively communication with the CDAS. If a real shower appears and several tanks are hit simultaneously, the CDAS generates the T3 trigger and sends a request to all hit tanks for full data transmission. However, it takes even up to several seconds. In mean time data (shower profiles) are stored in the UB cache memory. Assuming maximal time 10 s and the average T1 trigger rate 100 Hz, the cache memory has to have a capacity to store 1000 event data. In order to recognize data corresponding to the T3 trigger among stored event in the cache

memory, the time stamp counter indexes all event data. Shower profiles are registered in the time window of 19.2 μs. Assuming 20-bit time stamp counter, the full time range of counting is ca. 20 s, long enough in order to avoid any misinterpretation. The indices from the event counter are transferred to the underground electronics just after the T1 trigger via the same dedicated transmission line. The speed of transferred time stamp is lower than the T1 trigger ca. 400 ns per bit. The protocol takes into account also a parity control. Time stamps are next stored in the internal memory of the FPGA [167].

A storage of 1024 scintillator events from 64 channels for 19.2 μs by 80 MHz sampling and only 1-bit resolution requires 1024×64×19.2μs/12.5ns = 100 663 296 bits = 12 MB of memory. The selected FPGA does not contain such big internal memory. The system has to be supported by the external memory buffer. The external memory should be low-power type especially in the idle mode. Assuming full speed for writing (the same clock as for sampling), the write process of the single event would take only 19.2 μs (in 64-bit data us configuration). However, the T1 rate is only ca. 100 Hz, it means average interval between events is ca. 10 ms, 500 more than the writing process. Even if we decrease the writing clock to 10 MHz and use 32-bit bus, time needed to write a single event into the external memory is 307.5 μs, still short in comparison to T1 interval. It means the external memory works mostly in the idle mode. This condition practically eliminates **S**ynchronous **S**tatic **RAM**, because of huge power consumption, also in the idle mode. This type of memories is used mostly in very fast application, where a power budget is not an issue. Additionally these memories are really expensive and with relatively low capacity. The other option **S**ynchronous **D**ynamic **RAM** could be a good choice (only a single chip and still fully synchronous design), however Altera® provides only the DDR (**D**ouble **D**ata **R**ate) controller requiring a minimal clock 83 MHz. Practically, due to reasonable factors in the PLL circuit, 100 MHz has to be used. DDRAM working with 100 MHz loses its advantages, because of the power consumption increasing with the clock.

Finally the Asynchronous Static RAM has been chosen. The CY62177DV30 is a high-performance CMOS static RAM organized as 2M words by 16 bits. This device features advanced circuit design to provide ultra-low active current. This is ideal for providing More Battery Life™ (MoBL®) in portable applications such as cellular phones. The device also has an automatic power-down feature that significantly reduces power consumption. Due to 19.2μs/12.5ns = 1536 < 2^{12} words, we used 4 chips of ASRAM with 32-bit data bus and 4194304 depth, which corresponds to 22-bit address bus. The ASRAM – CY62177DV30 works with only 10 MHz clock. The current consumption in the idle mode is only 1 μA (in comparison to 120 mA of CMOS Standby Current for SSRAM like i.e. CY7C1486V25). An application of the SDRAM driven from the FPGA is keeping as an option, if the integrated PCB would require more space (1 SDRAM chip instead of 4 chips of ASRAM).

Triggered event from scintillator is temporarily buffered in the internal FPGA memory. 64 channels with 512+1024 time bins in investigated time window required by the AMIGA design correspond exactly to the same memory structure used in the surface detector trigger/memory system (Figure 97). Here 64 (1-bit) channels replace 6 (10-bit) FADC buses. 2 bits on 32-bit data bus for AC/AF indices denoting circular or fixed buffers for high- or low-gain channels are used now for real scintillator channels.

Data stored temporarily in the FPGA buffer internal memory, which correspond to the registered event triggered by the surface detector T1 trigger, are next transferred to the external memory with a large capacity. The time stamps are stored inside the FPGA. Two memory buffers working in the interlaced mode reduce a dead time of the system. When the 1st buffer is receiving data from the scintillator, the 2nd can independently transfer previously collected data into the external memory, working as a ring buffer. After ca. 10 s, the new one

is overwriting the old data. The old ones are irrevocably lost. The system works in infinite loop. However, when the CDAS generates the T3 trigger, the SSBC sends via CAN BUS a request to the underground micro-controller asking to extract physics data related to the T3. The SSBC attaches to the T3 request also the corresponding time stamp.

The time stamp generated in the special counter in the Front-End FPGA of the surface detector is attached as the 762nd word on the tail of the trace of the high-gain channel. The SD firmware works in the diagnostic mode. 762nd word was originally occupied by SDThr threshold in the slow channel, however it actually is not used and can be replaced by the AMIGA time stamp. Such an approach does not require a significant modification of the UB and CDAS software. When the T3 trigger appears, the UB has to extract only a single word from the stored shower profile and send to the SSBC.

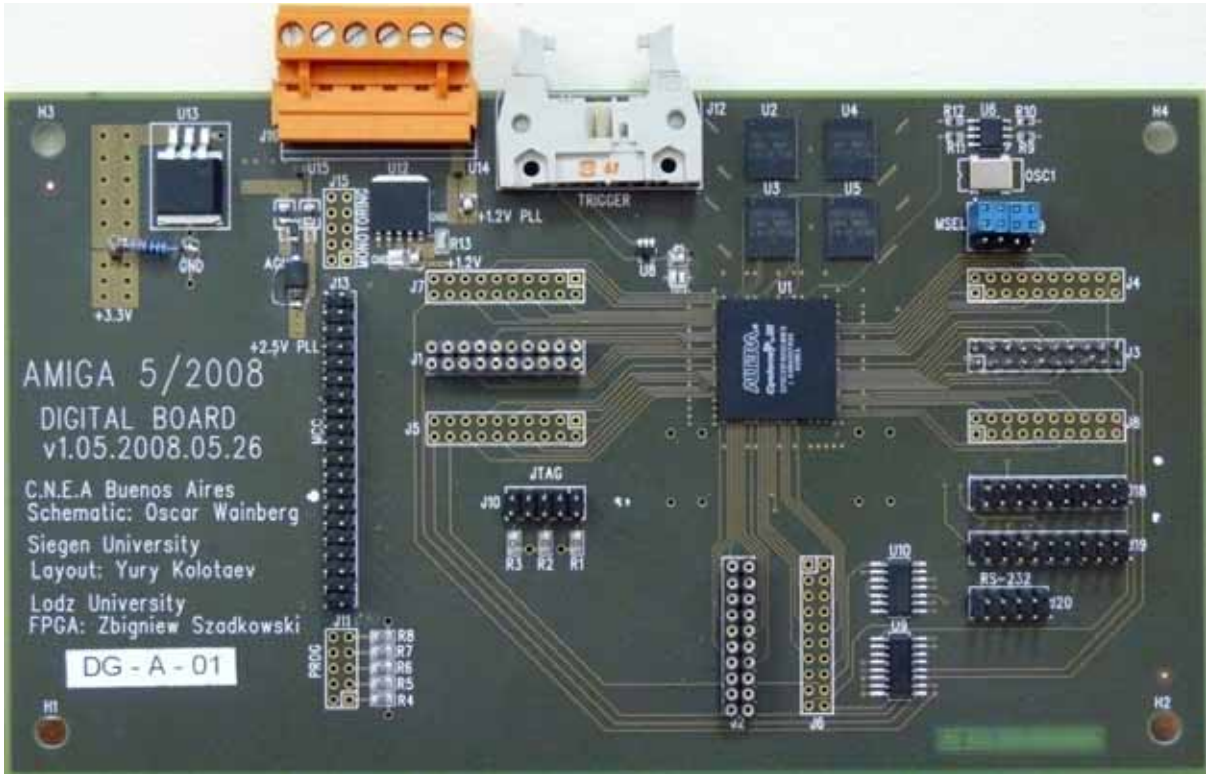

Figure 163 – The prototype of the digital AMIGA board [167].

When the time stamp achieves finally the FPGA via CAN BUS and the underground micro-controller, it is used to generate the address of the event stored in the external memory. The best tool would be the **C**ontent **A**ddressable **M**emory (CAM). The data contained in a CAM is a set of patterns that can be searched in a single-clock cycle. If the input pattern given to the CAM matches one of the patterns stored in the CAM, the address of the matching stored pattern is generated. CAM can be treated as the inverse of RAM. When read, RAM produces the data for a given address. Conversely, CAM produces an address for a given data word. When searching for data within a RAM block, the search is performed serially. Thus, finding a particular data word can take many cycles. CAM searches all addresses in parallel and produces the address storing a particular word.

Unfortunately, the family Cyclone III™ does not support the CAM mega-function. It is available only in obsolete APEX families. The routine generating the address has to use the standard comparison mechanism word by word. For the depth of the time stamp memory of

1024 words, it takes maximal 1024×12.5 ns = 12.8 μs. It is not a big pain. The T3 rate is on the level of minutes. Also 10 s storage intervals give a sufficient safety margin. A probability that data cannot be extracted from the RAM due to additional searching procedure is negligible.

The address associated to the time stamp allows extraction of data from the external memory. It appears without any synchronization with the writing process of scintillator data. In order not to interrupt the data transfer from the FPGA to the external memory, when the event address is ready, the FPGA sets a flag blocking the next data transfer. When the current transfer expired, the FPGA starts the reverse process, reading data from the external RAM and transferring their to the internal memory buffer – FIFO**.** Because of the same clock, the reading process takes exactly 307.5 μs. When the FIFO is full, the FPGA automatically changes a direction of the data transfer, from the FPGA to the ASRAM.

Data from the FIFO are available for the μC and they are next transmitted via CAN BUS to the SSBC and finally via Wi-Fi to the CDAS (Figure 162).

8 High Elevation Auger Telescopes (HEAT)

8.1 Introduction

Cosmic rays with energies in the range between 10^{17} eV and 5×10^{18} eV are of special interest for the determination of the details of the transition from galactic to extragalactic cosmic rays. The precise shape of the energy spectrum and the possible changes in primary composition should be well known to enable stringent tests of models for the acceleration and transport of both, galactic and extragalactic, cosmic rays.

The fluorescence technique for the detection of air showers encounters difficulties at energies below 10^{18} eV. The signal in fluorescence photons per unit path length is (at air shower maximum) roughly proportional to the primary energy. Therefore, the effective distance range of air shower detection gets smaller at lower energies. DAQ will be triggered only by relatively close-by showers. At these small distances the height of observation by the FD telescopes is limited. Thus, the crucial region around the shower maximum is generally not observable. In addition, lower energy air showers reach their maximum of development at higher altitudes. This height cutoff effect naturally gets even worse for air showers incident at larger zenith angles.

The maximum of shower development will thus quite often fall outside the field of view of the existing FD telescopes, which is limited to about 30º above the horizon. For an unambiguous reconstruction of the shower profiles this leads to severe cuts in the triggered data, which may be dependent on primary mass. The telescope detection efficiency for showers, which hit the ground at a certain distance from the "eye", also depends on the shower-detector geometry. Showers approaching the telescopes will have a higher trigger probability due to the angular dependence of the scattered Cherenkov light. Also, the efficiency for successful reconstruction of the shower profile and X_{max} increases. Therefore, a larger elevation range of the fluorescence telescopes gives significant advantages for reconstruction of showers for lower energies.

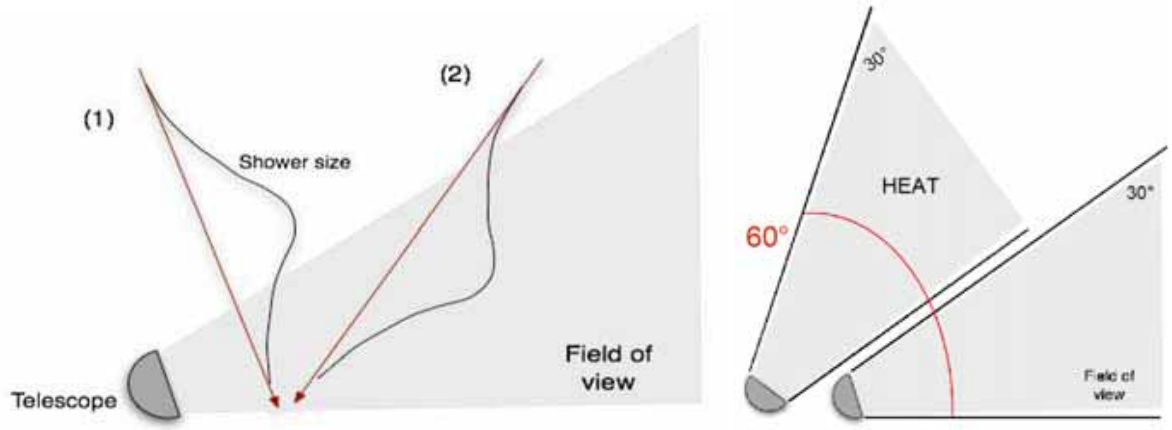

Figure 164 – Severe effects of a limited field of view of fluorescence telescopes. Showers approaching the "eye" have higher reconstruction efficiency [168-169].

8.2 Auger FD and the HEAT Telescopes

In the Pierre Auger Observatory 24 fluorescence telescopes have already been installed at the Southern site in Argentina. The telescopes are taking data in four FD buildings (45 km apart from each other at the edges of the array) overlooking the 3000 km² array of 1600 particle detector tanks.

Each telescope has a field of view of 30^{o} x 30^{o}. The Schmidt optics of the telescopes has an effective aperture of about 3 m². The signal/noise ratio is improved by the use of UV transmitting filter glass (M-UG6) for the entrance windows. The high sensitivity of the Auger telescopes enables the detection of showers with $E > 10^{19}$ eV up to distances of more than 40 km. Therefore, most of the highest energy events are detected in stereo mode by at least two telescopes simultaneously.

The strength of the Auger experiment is the operation in Hybrid mode. More than 10% of all events are detected by the surface detector system (SD) and at least one (FD) telescope. These events are especially valuable in two different ways. The FD information allows the independent energy calibration of well measured SD events at higher energies. On the other hand, the FD traces for low energy events can be reconstructed much better, if at least one of the SD detector tanks has triggered and its timing information can be used for the event reconstruction. In this "brass hybrid mode" the energy threshold of reconstruction is much lower than for the surface detector alone, where at least five tanks must trigger for good reconstruction quality of all shower parameters.

In the context of design studies for the Auger North experiment planned for a Colorado site it became obvious to the FD study group that the quality of the fluorescence telescopes operating in Argentina is very satisfying. Apparently, there is no need for major design changes.

In 2006 the Auger Collaboration decided to extend the original fluorescence detector, a system consisting of 24 telescopes located at four sites, by three High Elevation Auger Telescopes (HEAT). These telescopes are located 180 m North-East of the Coihueco FD building. The design of HEAT is very similar to the original FD system, except for the possibility to tilt the telescopes upwards by 29º. In both cases a large field of view of about 30º×30º is obtained using a Schmidt optics. Fluorescence light entering the aperture is focused by a spherical mirror onto a camera containing 440 hexagonal PMTs. An UV transmitting filter mounted at the entrance window reduces background light from stars effectively. An annular corrector ring assures a spot size of about 0.6º despite the large effective aperture of 3 m^2. The high sensitivity of the Auger FD telescopes enables the detection of high energy showers up to 40 km distance. A slow control system for remote operation from Malargue allows safe handling. Differences between the conventional FD telescopes and HEAT are caused by the tilting mechanism. While the original 24 FD telescopes are housed in four solid concrete buildings, the 3 HEAT telescopes are installed in individual, pivot-mounted enclosures (Figure 166).

Each telescope shelter is made out of lightweight insulated walls coupled to a steel structure. It rests on a strong steel frame filled with concrete. An electric motor can tilt this heavy platform though a commercial hydraulic drive by 29º within two minutes. The whole design is very rigid and can stand large wind and snow loads as required by legal regulations.

All optical components are connected to the heavy-weight ground plate to avoid wind induced vibrations and to keep the geometry fixed.

Mirror and camera are adjusted in horizontal position. However, by tilting the telescope the varying gravitational force on camera body and mirror can change their relative position. Supplemental fixing bolts and an improved support structures are foreseen to keep the alignment of the optical system stable, which is essential for telescope pointing and optical resolution. Sensors for inclination are mounted at the mirror top, camera top and bottom, and at the aperture box. Distance sensors monitor the critical distance between camera and several points at the mirror system. These sensors are readout frequently for monitoring purposes.

Figure 165 – Photo of the 3 HEAT telescopes tilted upward, end of January 2009. In the background the telecommunication tower of Coihueco [170].

HEAT uses also an improved DAQ electronics. The concept of the new electronics is the same as before, but as several electronic circuits have become obsolete, every front-end board has been redesigned. Like the conventional FD electronics, the DAQ of one HEAT telescope contains 20 Analog Boards for analog signal processing, 20 First Level Trigger (FLT) boards for signal digitizing and storage, and one Second Level Trigger (SLT) board for the recognition of fluorescence light tracks and the initiation of data readout. Along with faster FPGA logic the sampling rate was increased from 10 MHz to 20 MHz. The cut-off frequency of the anti-aliasing filters in the analog sections was adapted to about 7 MHz, but the other functions of the board remained the same. The redesigned FLT board implements all functions in FPGA of the Cyclone II FPGA family. A new custom-designed backplane provides dedicated point-to-point links between the FLT and SLT which lead to a factor 40 higher readout speed compared to the previous design. The HEAT DAQ system is also the baseline design and the prototype for the Auger North FD electronics.

The horizontal (‘down’) position is the only position in which a person can physically enter the enclosure. This configuration is used for installation, commissioning, maintenance of the hardware, as well as the absolute calibration of the telescopes. Due to an overlapping of the field of view of the existing Coihueco telescopes with HEAT in down position, air showers or laser tracks can be recorded simultaneously. A comparison of the reconstruction results from both installations determines directly the telescope resolution in energy and *X*max. Recording the same event in Coihueco and with the Auger North prototype allows a direct comparison of the trigger and reconstruction efficiencies.

Figure 166 – A single HEAT fluorescence telescope under construction in horizontal (‘down’) position (left) and tilted (‘up’) position (right) [171].

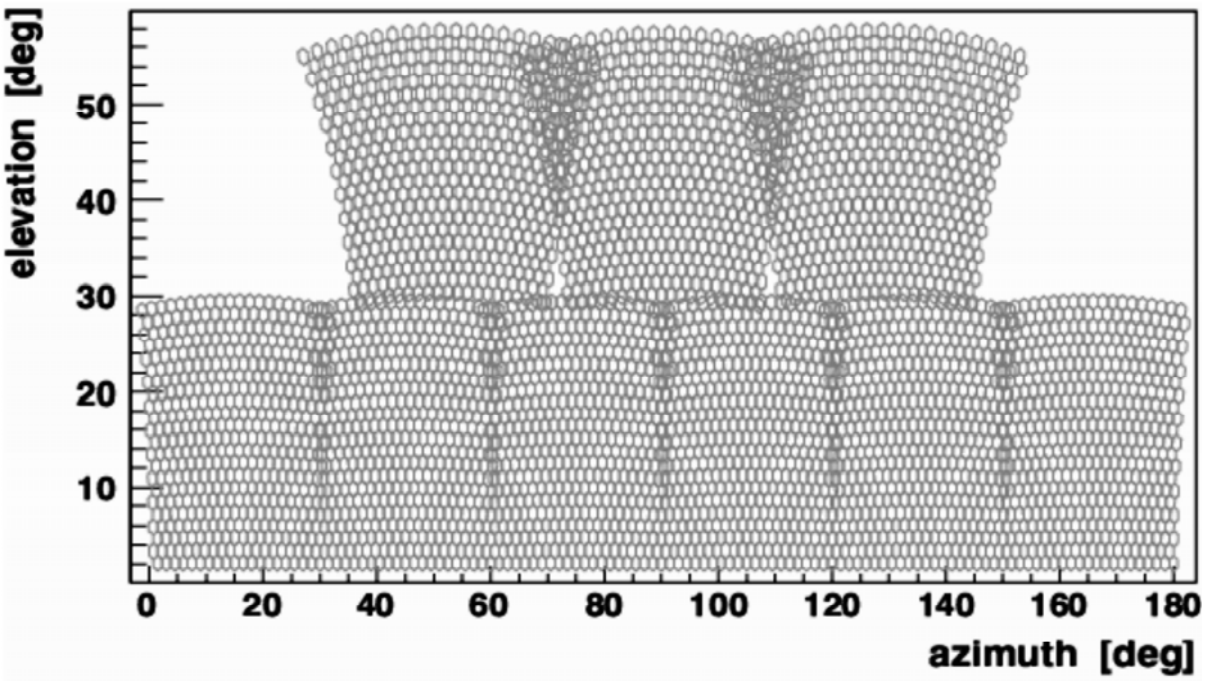

Figure 167 – A field of view observed by standard FD PMT 6 matrices (below) and HEAT 3 matrices (above) [171].

The tilted ('up') position is the default HEAT state. Telescopes are moved into this position at the beginning of a measuring run and stay that way until the end of the run. From the trigger point of view the telescopes operate like a fifth FD building. Data of the different installations (HEAT, different FD sites, infill and AMIGA, surface detector) are merged offline only, but the exchange of triggers in real time makes the recording of hybrid showers possible. The combined data will improve the accuracy of shower energy and *X*max determination at all energies, but especially at the lower end down to 10^{17} eV.

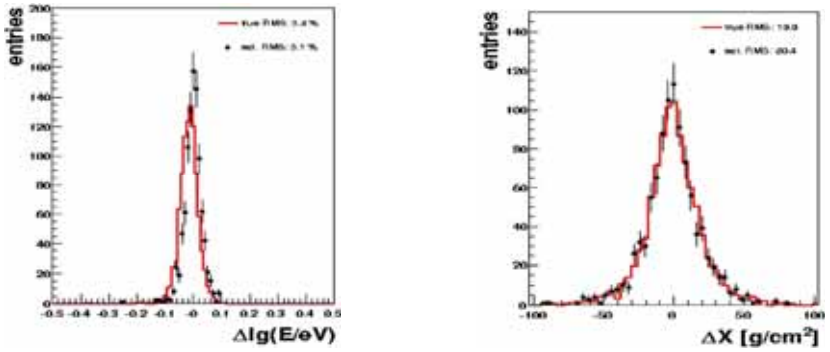

Figure 168 – Telescope resolution study simulating a "double-downward" measurement campaign for the energy range above 10^{18} eV [168].

8.3 First measurements

The operation of HEAT telescopes is very similar as for the existing ones. The absolute calibration of the telescopes has been performed only in the horizontal position of the shelters. Possible changes in telescope properties due to the tilting of the whole system are monitored by a high accuracy relative calibration system based on pulsed LEDs with measurements in both orientations and careful tracing of any gain variations due to e.g. the change of the orientation of the PMTs in the Earth magnetic field. Data taking on cosmic ray air showers or laser shots will are both in the "up" and in the "down" position. In the "down" position the telescopes cover the same field of view as standard telescopes at the Coihueco building, which is located at a distance of less than 200 m from the HEAT area.

First measurements were performed with HEAT telescope #2 at the end of January 2009. From January, 30th to February, 1st the telescope was operated for two nights in up and down position. At first, the camera was illuminated with a short light pulse from a blue LED located at the center of the mirror. The High Voltage for the PMTs and the individual electronic gains were adjusted to achieve uniform light response in every pixel. Subsequent measurements with the LED pulse generator were performed at different tilting angles, but with the same settings as found in down position. No indications were found for a gain change due to changed orientation of the PMTs in the Earth's magnetic field.

In the next step, the mechanical stability of the optical system was verified. The telescope was tilted several times from down to up position and back. The readings of the inclination and distance sensors were recorded during the movement. The analysis of the distance between camera and center of the mirror showed damped oscillations of low amplitude which stopped within seconds after the movement terminated. At rest the distance change between up and down position is less than 0.5 mm which is negligible for the telescope's optical properties.

After these cross-checks several showers were recorded with the telescope tilted in up position and in coincidence with Coihueco telescopes #4 or #5 (Figure 169). The event data of both telescopes match very well in time.

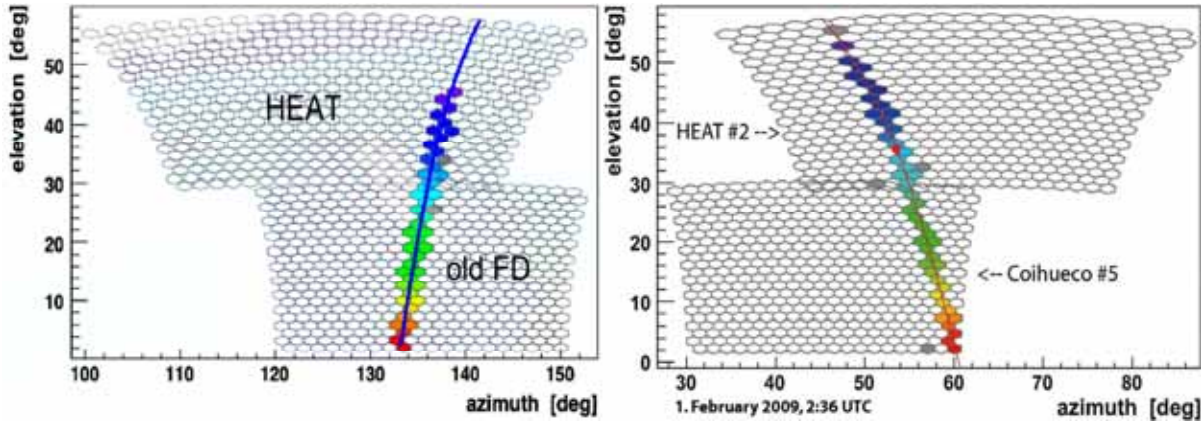

Figure 169 – A sample of real events registered simultaneously by standard FD and HEAT telescopes (left [169], right [170] - for this particular event the reconstruction yields a shower distance of 2.83±0.06 km from Coihueco and an energy of the primary particle of (2.0 ± 0.2)×10^{17} eV). The relative arrival time of the fluorescence light is coded in the color of the pixel. The solid line is a fit of the shower detector plane.

Figure 170 shows the reconstructed longitudinal shower profile together with a fit to a Gaisser-Hillas function. The fit yields a value of (657 ± 12) g cm^{-2} for *X*max. The plot also accentuates the need for HEAT telescopes for an accurate reconstruction: Using only the data point above a slant depth of 700 g cm^{-2} (Coihueco data) it would not have been possible to fit the profile and find a precise maximum.

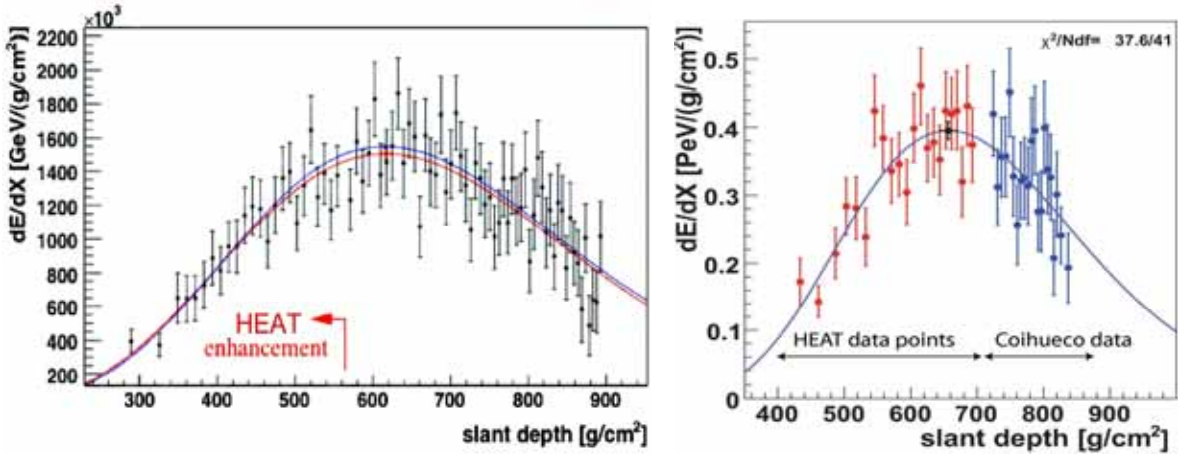

Figure 170 – Longitudinal shower profiles of events in Figure 169 together with Gaisser-Hillas-fit. Only a fit using both HEAT (left) and Coihueco (right) [170] data points results in a reasonable *X*max value.

First measurements with a single telescope have demonstrated that HEAT will improve the energy threshold of the Pierre Auger Observatory at the Southern site down to about 10^{17} eV. The HEAT design satisfies all requirements with respect to stability and ease of operation. It is expected that all three HEAT telescopes are fully operational in September 2009. They will provide interesting data in the transition region from galactic to extragalactic sources and allow important prototype tests for the design of the Auger North FD system.

9 Triggers for a detection of radio emission from cosmic ray air showers[2]

9.1 Introduction

For almost 40 years we know that cosmic ray air showers are the sources of pulsed radio emission in the frequency range from a few to a few hundred MHz. This emission is being studied by upcoming fully digital "software radio telescopes" such as LOFAR and the enhancement of particle detector arrays such as KASCADE-Grande or the Pierre Auger Observatory. However, there are still a lot of open questions regarding the strength of the emission as well as the underlying emission mechanism.

The pulsed radio emission accompanying extensive air showers has been discovered in the mid-1960ies and triggered intensive development of both the experimental and the theoretical researches. However, in the late 70ies, these activities have been almost completely ceased due to technical problems, appearing troubles with the interpretation of the experimental data. Also the great success of the alternative observing techniques caused a fall of the interest of this measurement technique. Today, we can observe a rebirth of the interest in radio emission from cosmic ray air showers as an additional observing technique for cosmic ray research.

Radio measurements of EAS allow opening an entirely new approach to the observation of cosmic rays. Similar to the currently used fluorescence technique, the radio approach provides a much more direct view into the air shower cascade than particle measurements on the ground. The fluorescence technique allows analysis of the air shower evolution during their development. The radio technique provides simplified characteristics integrated over the full evolution of the air shower, although the radio signal pretty good correlates well with the muon number measured by particle detector arrays, as almost all muons generated in the shower cascade reach ground-level.

The main advantage of the radio technique in comparison to the fluorescence technique is 100% duty cycle. FD measurements can be performed only by clear, dark, moonless nights far away from any light pollution that limits the duty cycle of optical fluorescence detectors to typically less than 10%.

In the mid-1960s, Jelley et al. [172] discovered that extensive air showers initiated by high energy cosmic rays generate strong pulsed radio emission at frequencies around 44 MHz. The effect was explained by the theoretical Askaryan's predictions [173]. The discovery triggered intensive researches over the frequency-range from a few to a few hundred MHz.

The first measurements were very rudimentary from the current point of view. E.g. in the early Haverah Park installation a receiver system of only a few MHz bandwidth was connected to oscilloscopes continuously measuring the radio signals. The Haverah Park particle detector array triggered a still photo-camera to take a photo of the pulses visible on the oscilloscope screen. At present, due to a huge crowd in the ether, the radio frequency interference would preclude such simple approach (in the 60ies, e.g., BBC stopped its TV transmissions during the nights).

Even up to now the absolute emission level was very uncertain and remains unclear, although several independent groups measured the radio pulses. While earlier Haverah Park

[2] Chapter 9 prepared also on the basic of [185]

experiments found emission strengths of order ε_v = 10 μV m^{-1} MHz^{-1} [174], next works reported values of ε_v = 1 μV m^{-1} MHz^{-1} or even lower [175]. Some of these discrepancies could be explained by systematic deviations in the primary particle energy calibration used at that time. More probably, however, the calibration of the radio receiving systems themselves is responsible for the discrepancies, especially in case of the differences between the different groups [176].

Recently we can observe a growth of interest in the measurement of radio emission from cosmic ray air showers. One of the main reasons is a huge progress in digital signal processing, both in hardware and algorithms. In particular, the development of digital radio-interferometers such as LOFAR with their capability of simultaneous monitoring of the full sky for transient radio signals promise an effective study of the radio emission even in today's environments of high radio-frequency interference. The 1st step is a development of a **LO**FAR **P**rototyp**E** **S**tation (LOPES) for the dedicated measurement of extensive air showers. Apart from the LOPES project, a few other experiments have been performed in the recent past. Green et al. (2003) posted an individual antenna near the CASA/MIA array in Utah. Their setup, however, was limited by high levels of radio-frequency interference and was not able to measure radio pulses associated with cosmic ray air showers. As an upper limit for the emission strength they found ε_v = 31–34 μV m^{-1} MHz^{-1}.

The CODALEMA experiment (**CO**smic ray **D**etection **A**rray with **L**ogarithmic **E**lectro**M**agnetic **A**ntennas) situated in Nançay, France [177] uses the radio-astronomical DecAMetric array (DAM) in the frequency range from 1–100 MHz in conjunction with high-speed digital oscilloscopes trying to detect radio pulses in coincidence between multiple antennas. The CODALEMA experiment is situated in an extremely radio-quiet environment with very little radio-frequency interference. Despite this up to now it does not have any independent information on the arrival of cosmic ray air showers. Moreover, CODALEMA measures only one circular polarization component of the emission. Rather poor statistics of the radio pulses alone cannot be used to come to robust conclusions whether the measured radio pulses really originate from air showers. The CODALEMA experiment is equipped with particle detectors based on highly sophisticated, expensive, oscilloscope technology. It would be extremely difficult to increase an amount of such detectors for application in giant air shower arrays such as the Pierre Auger Observatory.

One of the most promising approaches is the LOPES project [178]. It based on the framework of the digital radio-interferometer LOFAR, originally invented as a pure radio-astronomical instrument for the low-frequency domain of 10–200 MHz [179] and provides an ideal platform for observation of radio emission from extensive air showers [180]. It covers full sky as with a "low-gain" antenna design and its signal processing capabilities allow a very efficient noise reduction as in a "high-gain" antenna design through digital beam-forming, and additionally facilitate the digital filtering of radio-frequency interference. The fully digital processing of signals allows also a detection of transient events such as the pulses associated to air showers. The R&D of LOPES based on the LOFAR skeleton exploits many of the LOFAR designs for antennas, readout-electronics and other components. Tens of thousands of individual antennas are intended to use in LOFAR. So, one of its major aim is to reduce a cost per antenna. The LOPES experiment currently consists of 30 antennas working as a phased array in cooperation with KASCADE-Grande array. Unfortunately, the high level of radio-frequency interference (mainly from PMTs of the KASCADE detectors) introduces a significant contamination of the environment. Nevertheless, direct triggering by the particle detector array allows a perfect recognition of radio signals and air shower events. This is a fundamental necessity for the study of the radio signal properties as a function of the air shower parameters, especially in the current phase of uncertain knowledge of the radio

emission's absolute strength. LOPES has the capability to measure linearly polarized emission, which is especially useful for the verification of geomagnetic deflection of charged particles as the dominant emission mechanism. The experiment has been taking quality data since January 2004 and has so far found hundreds radio pulses that are unambiguously associated to cosmic ray air showers.

The coherent geo-synchrotron radiation is considered as the main mechanism of the radio emission from cosmic ray air showers. The emission is treated as synchrotron pulses from highly relativistic electron-positron pairs gyrating in the earth's magnetic field. Radiation at low frequency range is expected to be coherent, as the emission wavelength is larger than the extent of the air shower "pancake" (e.g., 30 m wavelength vs. a few meters pancake thickness at 10 MHz). Other mechanisms such as the Askaryan-type Cherenkov emission are rather considered as subsidiary.

9.2 Auger Engineering Radio Area (AERA)

Results from the Southern Pierre Auger Observatory as well as the baseline design of the Northern Observatory point to the need of very large aperture detection systems for ultra-high energy cosmic rays. There are a number of worldwide efforts to develop and establish new detection techniques that promise a cost-effective extension of currently available apertures to even larger dimensions. These are, for example, the observation of showers from space (EUSO – [181]) - or the use of radio antenna arrays.

With its nearly 100% duty cycle, a signal-to-noise ratio scaling with the square of the cosmic-ray energy, its high angular resolution, and its sensitivity to the longitudinal air-shower evolution, the radio technique is particularly well-suited for detection of UHECR in large-scale arrays. The present challenges are to understand the emission mechanisms and the features of the radio signal, and to develop the corresponding measurement techniques.

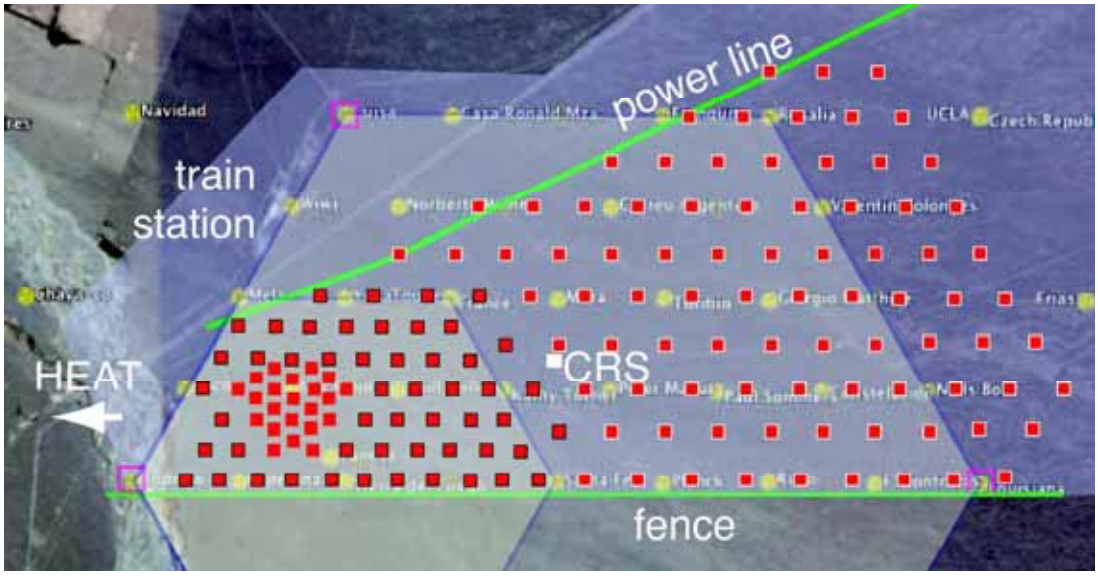

Figure 171 – Layout of the proposed antenna field [182].

AERA proposes an R&D project to study UHECR using detection of coherent radio emission from air showers in the Earth's atmosphere. The R&D will be needed for the design of a full-scale array covering the complete area of Auger South and/or North. The dimension

of this radio array will be about 20 km^2 (Figure 171). For such an area we expect an UHECR rate of about 5000 identified radio events per year, allowing a study of both scientific and technological questions. At the same time, the scale of such an array is sufficiently large to test concepts for deployment, operation, and the sustainability of critical parts for a large array. AERA will use the same radio-detection technique as developed by LOPES [183] and CODALEMA [184] collaborations.

The prime physics objectives of AERA in the next few years are precise measurements of various aspects of the radio signals from which the primary energy and composition of the cosmic rays hitting the atmosphere and their arrival direction is expected to be extracted. The radio detection technique will be complementary to the water Cherenkov detectors and allows a more precise study of the development of the electromagnetic part of air showers in the atmosphere. These complementary data sets can be used also to study hadronic interactions at high energies. In addition to a strong physics motivation, a lot of technical aspects relating to the efficiency, saturation effects and the dynamic range, the precision for timing, the stability of the hardware developed, deployed, and used, as well as the data taking and system-health monitoring processes will be studied and optimized.

9.2.1 Results of phase 1

In March 2006, the Auger Collaboration Board approved the Phase 1 for the Radio R&D project at Auger South. In the last 3 years initial measurements have been made using hardware and software developed by various groups, showing that indeed radio detection of UHECR can be performed at Auger South. Still the number of radio events in coincidence with SD is relatively few, mainly because of the relatively small footprints of the initial detector arrays used, because of problems with the sustainability of the hardware, and the difficulty to separate transient events from real cosmic ray induced events. The initial R&D projects took place at sites near the Balloon Launching Station (BLS site) and near the Central Laser Facility (CLF site) [185]. The following results have been obtained:

- Externally triggered radio-detection stations recorded several coincident events between SD and themselves [186]. In about 10 cases a coincidence with SD have in three different detector stations, separated by about 100 m each, have been recorded,. This allowed a comparison in these cases the arrival direction as determined by our radio-detection stations with that from SD. In addition, the lateral distribution function has been studied [187] at energies higher than those at LOPES and CODALEMA.
- Studies with solitary systems have been performed. These systems are powered using solar energy (solar panels, batteries), have a wireless connection to a central DAQ system, and operate in self-trigger and/or externally triggered modes. Special attention has been paid to reduce self-induced noise caused by DC-DC converters and by digital electronics. Self-triggered events have been obtained as well. However, for these events where the radio stations were self-triggered, there were no data from more than two radio stations and thus the arrival direction could not be compared with that from SD. Nevertheless, this is the first time ever that such an independent detection has been achieved using radio-detection stations [188].
- DAQ systems have been made where data from individual radio-detection stations are being combined in a central processing station.
- The externally triggered data have been used to train new systems where embedded software is being used as a self-trigger algorithm.

- Noise levels have been studied in detail [189]. We have identified the contribution caused by strong celestial radio sources, which are concentrated in the galactic plane, passing over the radio-detection stations once per (sidereal) day. These studies enabled us to study the overall detection threshold and the gain pattern of used antennas.
- Signal development of radio pulses induced by UHECR in the atmosphere has been modeled using extensive Monte-Carlo simulations, tracking electron- and positron density distributions, and using much faster macroscopic calculations. In addition, a modular detector simulation package has been written, where various important components of the signal development as it passes through the electronics chain can be simulated and compared with data [190].

9.2.2 Strategy for Phase 2

After approval by the CB and with the consent of the management, we will start to deploy stations in the northern part of the AMIGA array. The hardware and the software for AERA will be developed and used together by all groups working in the Auger Radio R&D project, allowing to make faster progress in the integration of our concepts and ideas into one system. Still we foresee that in the coming years, as more and more data is coming in, changes in the hardware and software might be required or that optimization in the hardware and software will lead to better performance and price reduction. Therefore, interfaces of the various subsystems have been defined carefully. The systems, which are still operational in the field near the BLS and near the CLF will be maintained and will be used as test benches and as sand boxes for quick R&D questions, thus not interfering with the overall aim to have an integrated system by the end of 2009.

9.3 Synchrotron radiation

Any acceleration of a charged particle causes an electromagnetic radiation. For the charged ultra-relativistic particle its radiation can be considered as a coherent superposition of contributions coming from tangential (in the direction of the instantaneous velocity vector) and centripetal (perpendicular) acceleration. Total radiation powers emitted for the tangential and centripetal accelerations are respectively:

$$P(t) = \frac{2e^2}{3c^3}\left|\dot{v}\right|^2 \gamma^4 \qquad\qquad P(t) = \frac{2e^2}{3c^3}\dot{v}^2 \gamma^6 \tag{101}$$

From (101) the radiation power for centripetal acceleration is stronger on the factor of γ^2 in comparison to the tangential acceleration. As a consequence, any arbitrary particle motion, including the helical motion of a charged particle in a homogeneous magnetic field, can be approximated as an instantaneous circular trajectory with adequate curvature radius.

For highly relativistic particles the retardation effects caused by the finite speed of light focus the radiation in a very narrow beam (with a cone of order of γ^{-1}), which sweeps over the observer in a very short time, leading to strongly pulsed emission dominated by frequency components significantly higher than the particle gyration frequency.

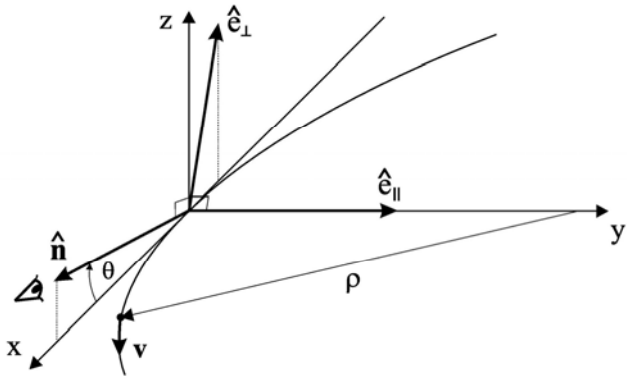

Figure 172 – Geometry of single particle synchrotron radiation for an observer with line-of sight vector $\hat{}\boldsymbol{n}$ enclosing a minimum angle θ to the instantaneous particle velocity vector $\boldsymbol{v}$. The equivalent curvature radius is given by ρ, and the emission can be conveniently divided into the components $\hat{}\boldsymbol{e}_\perp$ and $\hat{}\boldsymbol{e}_\parallel$. The particle trajectory lies in the x-y plane.

A distribution of the radiation power is given as [191][3]

$$\frac{d^2 I}{d\omega d\Omega} = \frac{e^2\omega^2}{4\pi^2 c}\left| -\varepsilon_\parallel A_\parallel(\omega) \pm \varepsilon_\perp A_\perp(\omega)\right|^2 \tag{102}$$

where the plus-sign corresponds to electrons and the minus-sign for positrons, e denoting their unit charge. The amplitudes of electric fields are

$$A_\parallel(\omega) = \frac{\rho}{c}\left(\frac{1}{\gamma^2}+\theta^2\right)\int_{-\infty}^{\infty} x e^{\left[i\frac{3}{2}\xi\left(x+\frac{x^3}{3}\right)\right]}dx \qquad A_\perp(\omega) = \frac{\rho}{c}\sqrt{\frac{1}{\gamma^2}+\theta^2}\int_{-\infty}^{\infty} e^{\left[i\frac{3}{2}\xi\left(x+\frac{x^3}{3}\right)\right]}dx \tag{103}$$

The integrals used above can be expressed by the Airy or modified Bessel functions:

$$\int_{-\infty}^{\infty} x\sin\left[\frac{3}{2}\xi\left(x+\frac{x^3}{3}\right)\right]dx = \frac{1}{\sqrt{3}}K_{2/3}(\xi) \qquad \int_{-\infty}^{\infty} \cos\left[\frac{3}{2}\xi\left(x+\frac{x^3}{3}\right)\right]dx = \frac{1}{\sqrt{3}}K_{1/3}(\xi) \tag{104}$$

$$\int_{-\infty}^{\infty} x e^{\left[i\frac{3}{2}\xi\left(x+\frac{x^3}{3}\right)\right]}dx = \int_0^{\infty} x e^{\left[i\frac{3}{2}\xi\left(x+\frac{x^3}{3}\right)\right]}dx - \int_0^{\infty} x e^{-\left[i\frac{3}{2}\xi\left(x+\frac{x^3}{3}\right)\right]}dx = 2i\int_0^{\infty} x\sin\left[\frac{3}{2}\xi\left(x+\frac{x^3}{3}\right)\right]dx = \frac{2i}{\sqrt{3}}K_{2/3}(\xi) \tag{105}$$

$$\int_{-\infty}^{\infty} e^{\left[i\frac{3}{2}\xi\left(x+\frac{x^3}{3}\right)\right]}dx = \int_0^{\infty} e^{\left[i\frac{3}{2}\xi\left(x+\frac{x^3}{3}\right)\right]}dx + \int_0^{\infty} e^{\left[-i\frac{3}{2}\xi\left(x+\frac{x^3}{3}\right)\right]}dx = 2\int_0^{\infty} \cos\left[\frac{3}{2}\xi\left(x+\frac{x^3}{3}\right)\right]dx = \frac{2}{\sqrt{3}}K_{1/3}(\xi) \tag{106}$$

$$A_\parallel(\omega) = i\frac{2\rho}{\sqrt{3}c}\left(\frac{1}{\gamma^2}+\theta^2\right)K_{2/3}(\xi) \qquad A_\perp(\omega) = \frac{2\rho}{\sqrt{3}c}\sqrt{\frac{1}{\gamma^2}+\theta^2}\,K_{1/3}(\omega) \tag{107}$$

where
$$\xi = \frac{\omega\rho}{3c}\left(\frac{1}{\gamma^2}+\theta^2\right)^{3/2} \tag{108}$$

[3] Eqs. (103) describing $A_\parallel(\omega)$ and $A_\perp(\omega)$ are swapped in the Polish edition of [191].

$$\frac{d^2I}{d\omega d\Omega} = \frac{e^2}{3\pi^2 c}\left(\frac{\omega\rho}{c}\right)^2\left(\frac{1}{\gamma^2}+\theta^2\right)^2\left[K_{2/3}^2(\xi)+\frac{\theta^2}{\gamma^{-2}+\theta^2}K_{1/3}^2(\xi)\right] \tag{109}$$

Since the energy spectrum is proportional to $|\boldsymbol{A}(\boldsymbol{R},\omega)|^2$ it grows as N^2 with particle number N if one assumes fully coherent emission. Given a specific distance to the observer R the frequency component of the E-field can be calculated as

$$E(R,\omega) = \sqrt{\frac{4\pi}{c}}\frac{A(R,\omega)}{R} \tag{110}$$

For an observer-frame distribution of gyrating particles, the corresponding $\boldsymbol{E}(\boldsymbol{R},\omega)$ can then be superposed to calculate the total emission.

9.4 Synchrotron-theory: electron-positron pairs

In the air shower, electrons and positrons are created in pairs. The symmetry arising from the opposite curvature of electron and positron trajectories can lead to a significant simplification of the calculation. For an electron-positron pair with perfect symmetry of trajectories regarding to the observer, the $A_\parallel$ contributions from the two particles add up to $2A_\parallel$, whereas the $A_\perp$ contributions completely cancel each other.

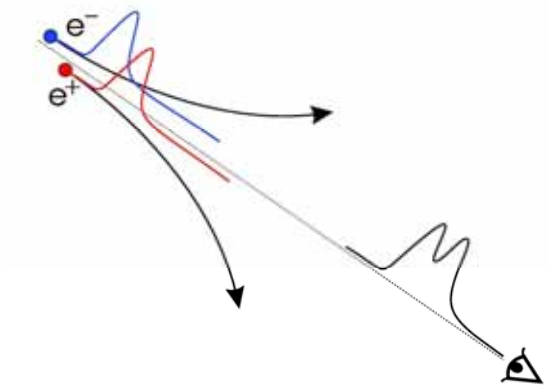

Figure 173 – Misalignment between the electron and the positron in an electron-positron pair no longer allows coherent addition of the individual emissions [192].

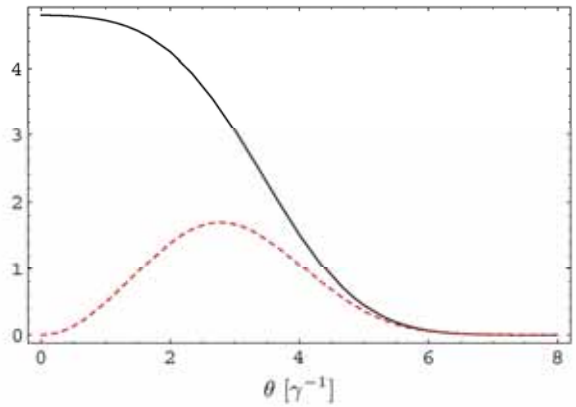

Figure 174 – Comparison of $|A_\parallel|$ (solid) and $|A_\perp|$ (short-dashed) for ν = 100 MHz, γ = 60 and B = 0. 3 G. Absolute scale is arbitrary [192].

However, this is an idealistic case, which does not describe the real situation. The cancellation of the $A_\perp$ as well as the summation of the $A_\parallel$ depends on the direction from which the observer sees the particle pair. Additionally, the pulses emitted by the relativistic particles are very short. The coherence associated to the emissions of individual particles is significantly violated, if the phase difference is too large (Figure 173).

A more detailed analysis at the numbers and characteristics of the particle distributions in the shower shows that an assumption of full summation and cancellation of $A_\parallel$ and $A_\perp$ for an “effective” electron-positron pair does not introduce too large error. This approximation

works well if electron-positron pairs are considered rather as group pairs of positrons and electrons together such that their trajectories overlap symmetrically as seen by the observer.

For coherent addition of the positron and electron emission to be possible, a significant portion of those parts of the particle trajectories from which the observer actually receives radiation must overlap. (That part has a length of ~ 110 m for $\gamma = 60$, given by the length over which the instantaneous velocity vector encloses an angle $\leq \gamma$ with the observer's line of sight.) In a typical 10^{17} eV air shower the shower "pancake", even somewhat before and after the shower's maximum development, consists of $\sim 10^8$ particles at any time. Even if the particles were distributed homogeneously in the shower pancake, this would lead to a particle density of ~ 1000 m^{-3}. For the realistic distributions, the densities in the dominating center region are a lot higher. This illustrates that each particle (except in the unimportant outskirts of the shower pancake) will a priori have a high number of particles in its direct vicinity with which it can be paired. The probability that there is a significant overlap between the paired particles' trajectories is high because the particles' mean free path length of ~ 450 m is considerably larger than the ~ 110 m of the trajectory from which the observer receives radiation [192]. In this scenario of high particle density and δ-distribution of velocity directions, the emission from an "effective" electron-positron pair can therefore be approximated as that from a pair with perfectly symmetric trajectories.

9.5 Experimental setup

Preliminary estimations show that at least 1000 events per year should be enough for better understanding of radio emission at the highest shower energies. To obtain this statistics a sufficiently large area of roughly 20 km^2 has to be equipped with about 160 radio stations. The lateral distribution of radio signals has to be detected up to the largest possible distance from the shower core. Theoretical calculations and simulations of radio emission from cosmic-ray showers indicate that low frequencies dominate at large distances. Thus a wide-band antenna is preferred. However, due to power radio emitters at 27 MHz and above 80 MHz to the band should be limited to the range between roughly 30 and 80 MHz (-3 dB). The falloff outside this measuring band should be 50 dB per 5 MHz. As the atmosphere is transparent for radio signals in the relevant frequency range from 30 to 80 MHz, AERA will measure the coherent superposition of all radio signals created in the shower. That is an essential advantage compared to the detection of secondary shower particles at ground level, where the electromagnetic part of the shower is significantly reduced. From geometry, the majority of air showers are expected to arrive at large zenith angles. But at these angles (larger than 60 °) the showers are absorbed in the atmosphere and cannot be observed with the surface or fluorescence detectors. But neutrino-induced horizontal showers might be observed, both in the surface and in the radio detectors. Nevertheless, we are aware that a large background of human-made radio signals can significantly hamper a radio-detection at all.

9.5.1 Antenna

At the current stage, 5 types of antennas have been tested: a short Fat Dipole Antenna, a V-shaped Dipole Antenna, a Butterfly Dipole Antenna, a Small Aperiodic Loaded Loop Antenna (SALLA), and a Logarithmic Periodic Dipole Antenna (LPDA). The latter was

proven the longest time to be successful under measuring conditions in Argentina and Europe. Our strategy is to take this design for the first 20 to 25 antennas as the basic design as long as another design does not outperform the quality, cost-effectiveness, robustness, sensitivity, and simplicity.

.

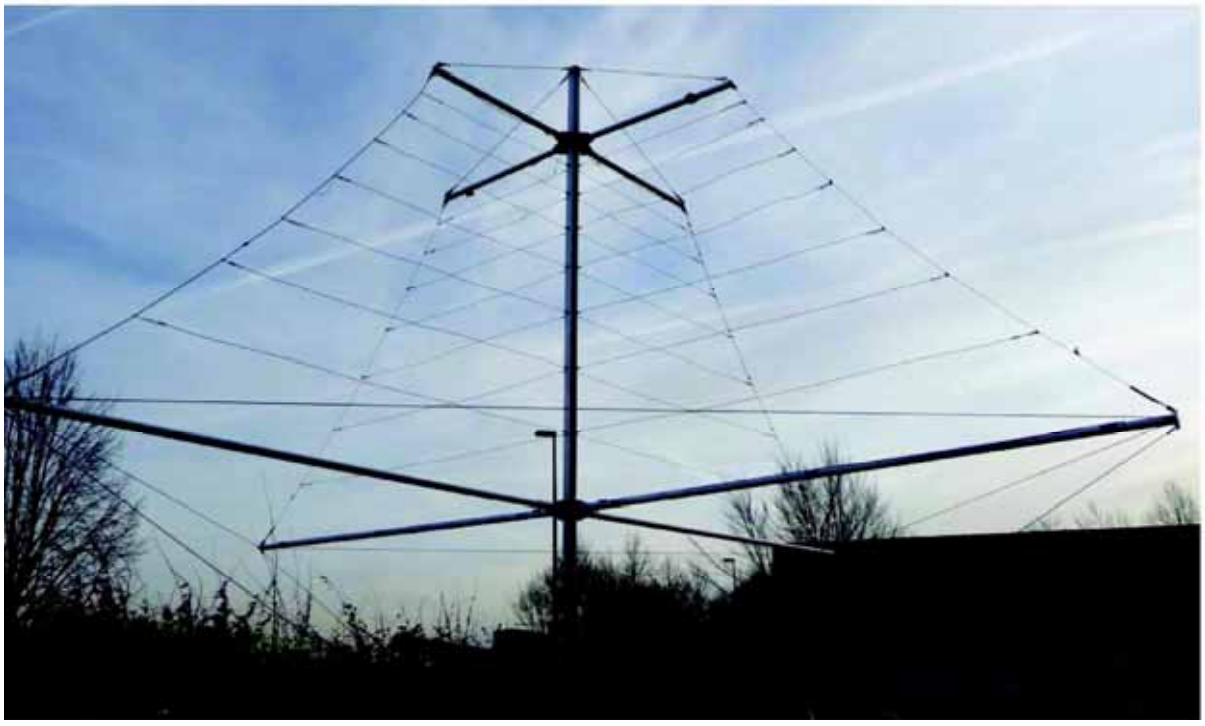

Figure 175 – The LPDA developed for AERA and used in the Pampas [193].

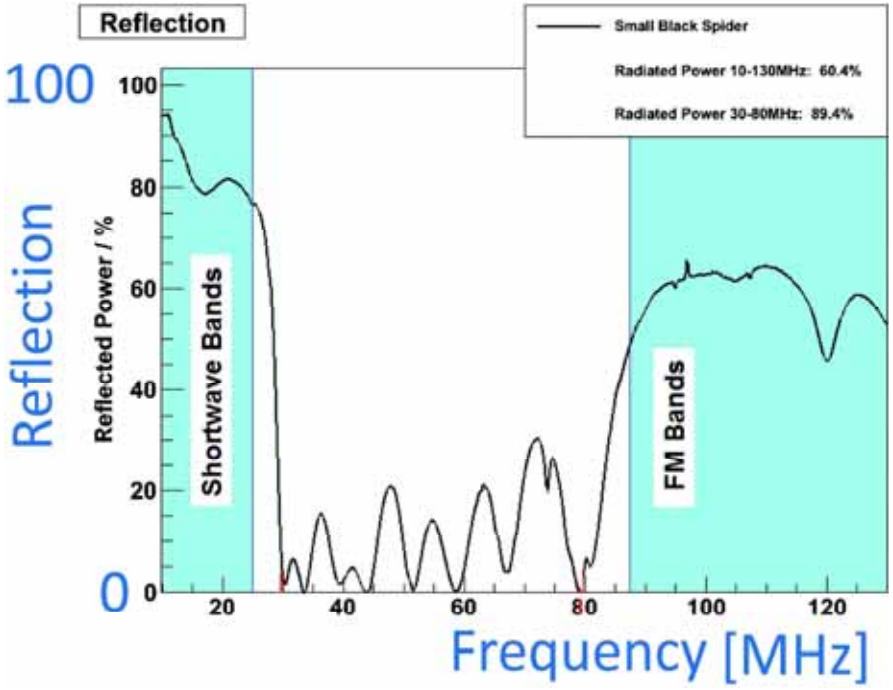

Figure 176 – The frequency characteristic of the LPDA [193].

The present accepted antenna design consists of two crossed LPDAs (Figure 175) with high sensitivity in the frequency range 35 - 80 MHz (Figure 176). The actual version with most stable conditions uses copper wires with UV safe clothing as dipoles. The wires of lengths up to 2 m have been tested over three months under a strong varying load in a laboratory setup and show no damage. Also, ten completes LPDAs installed in Aachen, Groningen, and Argentina have withstood storm conditions with wind speed up to 150 km/h and survived without damage. No UV damage has been observed in one year of operation. The wires are connected to a Lecher conductor inside a strong aluminum bar, 3.2 m long and 0.07 m in diameter. The low-noise amplifier (LNA) is integrated into the Lecher system and electrically protected against over-voltages above 6 V. The complete antenna with both LPDAs including LNA can be folded like an umbrella with length 3.2 m and diameter 0.25 m. The weight amounts to 18 kg and can be carried by a single person

9.6 Electronics

The theory of geomagnetic emission indicates the pulse height of the radio signal depends on the energy in the electromagnetic part of the shower. This theory predicts increasing pulse length with increasing distance of the antenna from the shower axis (10 ns at about 100 m). Such pulses have a continuous wideband frequency spectrum with significant contributions from some MHz up to the reciprocal pulse length, e.g., 100 MHz at 10 ns. Within the receiver bandwidth the noise in a quiet-rural environment as the Pampas is dominated by external sources like the omnipresent galactic noise with noise temperatures of 5000 K at 60 MHz.

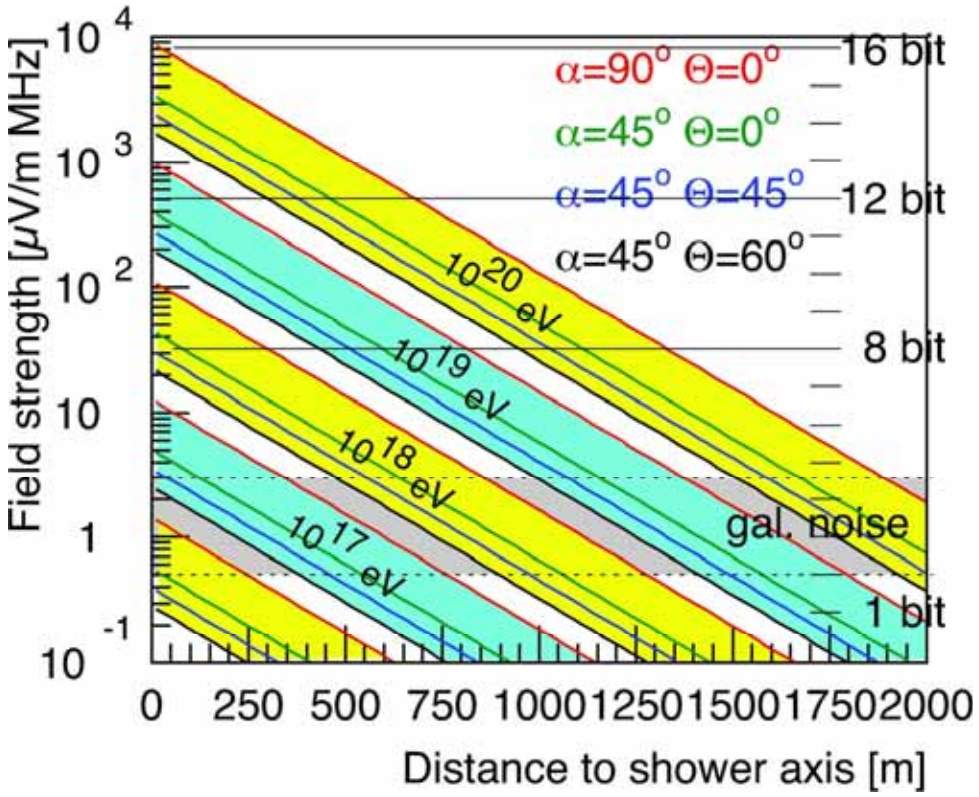

Figure 177 – Field strength of the radio emission in air showers vs. a distance to the shower core [182].

The electric field strength on ground level for air showers of different energies and different zenith angles has been calculated as a function of the distance to the shower axis on the basic of LOPES parameterization [194] (Figure 177). This plot indicates the noise level caused by radio sources in our galaxy, which can be used to calibrate the complete detection chain. It means that the noise introduced by the station electronics (directly through cables or indirectly through EMI) should be below equivalent field strength of 1 μV/(m MHz).

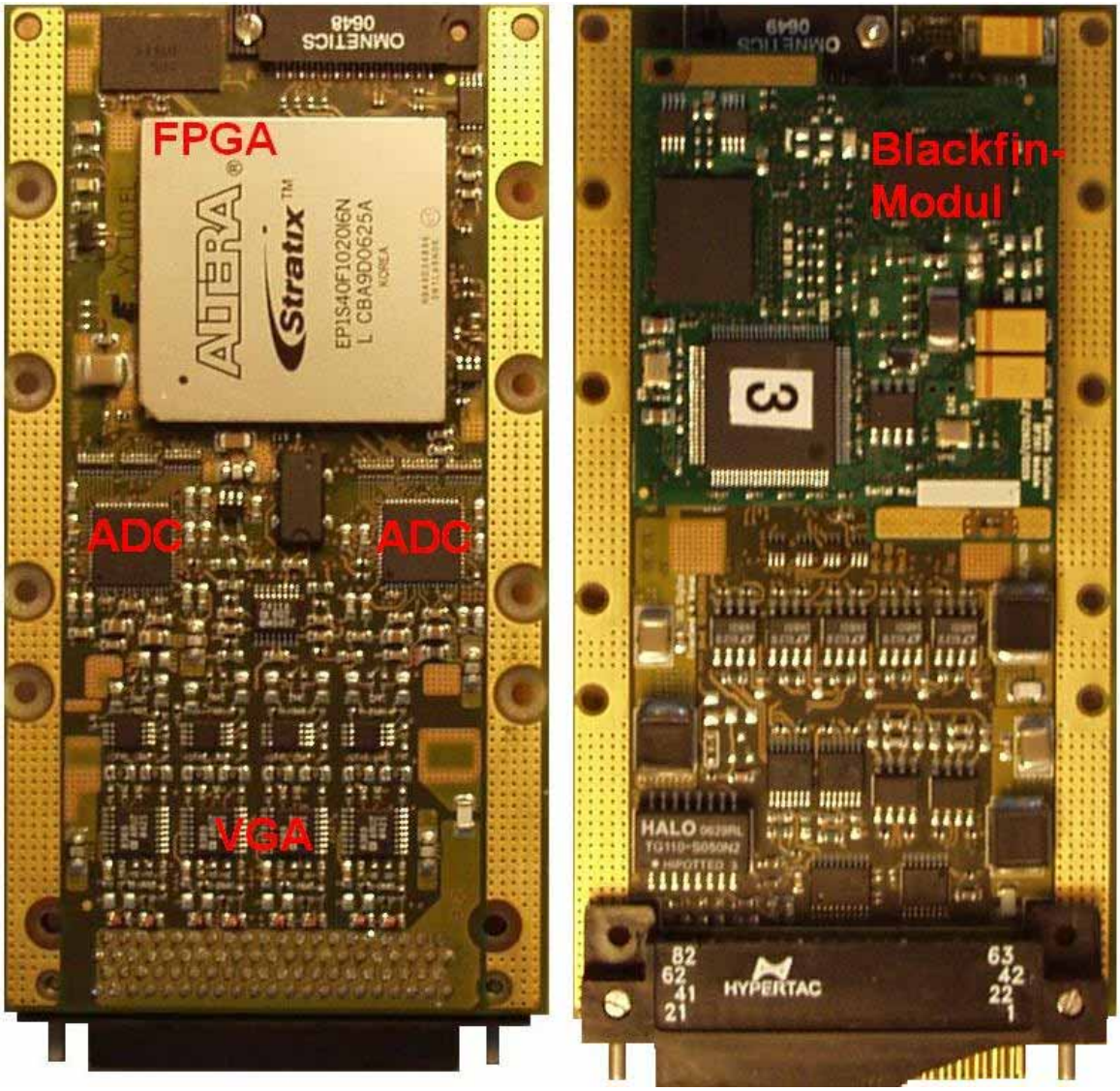

Figure 178 – The prototype based on the Altera Stratix FPGA EP1S40F1020I6 and a dual core Blackfin DSP BF 561.

The signals from the antenna will be split into two polarizations. According to Figure 177, for showers with a core distance less than 200 m, our readout will thus have a detection threshold at energy of $10^{17.2}$ eV. Because of the coherent emission of the radio signals at these energies and because of the dependency of the signal height as a function of the distance to the shower core, a dynamic range of 16 bits is necessary.

The sampling frequency should be high enough to provide a sufficient accuracy of digitized representation of the analog signal. According to the Nyquist theorem, for 80 MHz cut-off the sampling frequency should be at least 160 MHz. However, the algorithm was

implemented on an Altera Stratix EP1S40 device, taking data at 80 MHz sub-sampled in the second Nyquist domain.

During November and December 2008 the first stages of the trigger concept were tested on site using prototype hardware in a wired 3 antennas setup. Each antenna was connected to a trigger box, containing a complete trigger chains for each of the two polarizations. The test hardware for the described conception was a board containing two 10-bit ADCs working with 80 MHz sampling, the Altera Stratix FPGA EP1S40F1020I6 with 40k logic elements and 112 internal 9 bit multiply & add elements, 3.4 Mbit internal SRAM and a dual core Blackfin DSP BF 561 working at 2*600 MHz.

The test was quite successful, especially the RFI suppression turned out to be an efficient and reliable method to improve the signal to noise ratio by a factor of 3. Applying a low threshold 6 times above the RMS (corresponding to 110 μV/m at the antenna) results in a trigger rate of 4 kHz. As the noise is not uniform but contains relatively high pulses, increasing the threshold does not reduce the trigger rate as strong as expected. Subsequent cuts on the pulse shape and filter are necessary to reduce the rate to a value which wireless communications is capable to handle.

Due to a significant contamination of the radio environment, the trigger circuit will contain also digital pulse-shape filter. The online pulse-shape analysis together with the main self-trigger circuit will be implemented in a FPGA. Additionally, the system can be externally triggered to force a coincidence with the other detectors. This external trigger can be derived from auxiliary detectors, requiring a logic trigger pulse, or from other detection stations (AMIGA or radio-detection stations) enabled by a request for buffered data at a given time in the radio-detection station.

9.6.1 Digital front-end electronics

Besides galactic background, there are two types of human made background, which could be discriminated against the signal by a complex trigger system. The two types are continuous background as by radio and TV stations and transients produced by machines. Without an effective trigger a stable and low-level energy threshold is not guaranteed. Furthermore, the data rate for communication of the triggered data to the central DAQ would exceed the available power budget.

For self-triggered measurements, the data in real time by will be digitized and processed by the powerful FPGA chip. The radio frequency interference (RFI) has to be strongly suppressed before a trigger. Very narrow peaks in the frequency domain corresponding to the mono-frequent carriers characterize the radio noise. A removal of these peaks is the main goal of the RFI filter. The filter transforms the signals from the time domain to the frequency one by the Fast Fourier Transform (FFT) routine provided by Altera. The median filter eliminates next, mono-frequent carriers, but broadband radio pulses from cosmic showers are not affected. After a second inverse FFT routine signals are converted back to the time domain. This chain of digital signal processing strongly enhanced signal to noise ratio, and thus improves the radio pulse detection sensitivity.

To apply these algorithms including the Fast Fourier Transform as FPGA code on the steady stream of incoming data at a rate of 80 MHz, the data stream in blocks of 512 time slices was divided. The finite block length produces a leakage effect, which has been diminished by overlapping segments of 64 samples at the beginning and the end of the block. A linear rising/falling window function instead of a Hann window is a good compromise between expenditure of FPGA resources, as logic elements and multipliers, and minimization

of leakage effects. This method of the RFI suppression the narrow bandwidth radio emitters uses a 4.5 MHz wide median-filter applied to the Fourier spectrum of the data. This method is more efficient and less complicated to implement in the FPGA than a cut-off method used in software analysis. The cut-off method cuts the resonance at a moving average threshold. The large width of the median filter is necessary to suppress also TV-video signals.

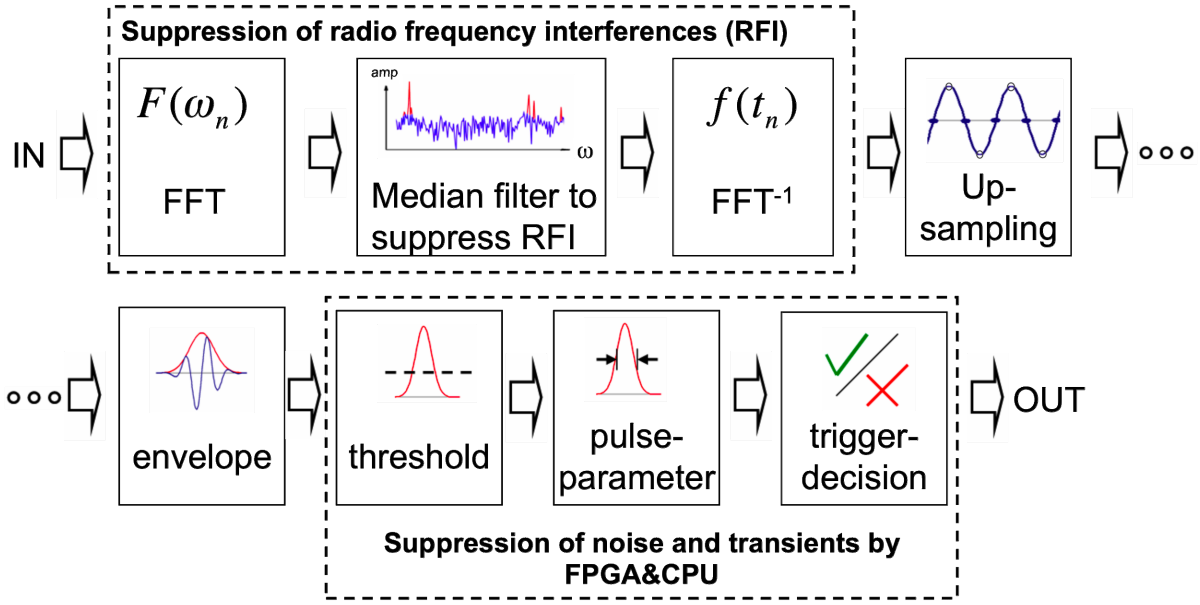

Figure 179 – Schematic of the trigger in the FPGA [195].

Furthermore, up-sampling by a factor of 2 and envelope pulse forming by a simple maximum finder for each pair of two adjacent time slices was applied to reconstruct the input pulse in shape and height. The input data and result are compared in Figure 180. The increased quality after digital processing is impressive: the signal-to-noise ratio is improved by a factor more than five. For the suppression of transients, pulse shape parameters of the envelope pulse were extracted, if the pulses exceed the signal-to-noise level by an adjustable value of about 10. Useful parameters for the suppression of transients are the width of the trigger pulses at half height, and integrated intensities over fixed time windows at pre and past-trigger time. These parameters are evaluated before the coincidence of antennas in a second trigger stage is tested. As coincidence time a window corresponding to elevation angles of the incoming shower larger than 30 degree were selected. Finally, the background noise of a typical signal pattern at Forschungszentrum Karlsruhe was reduced by a factor of 2 to 10 and stable trigger operations were possible, due to the higher threshold to noise level.

After a dynamic threshold trigger the pulse shape is parameterized and atypical formed pulses are rejected by cuts on these parameters in order to lower the trigger rate further. The resulting single channel triggers of at least three neighboring antennas within a fixed coincidence window create a joint trigger signal that initiates the readout of the raw ADC trace. The coincidence window is chosen small enough to discriminate horizontally incoming pulses, which are mainly human made noise.

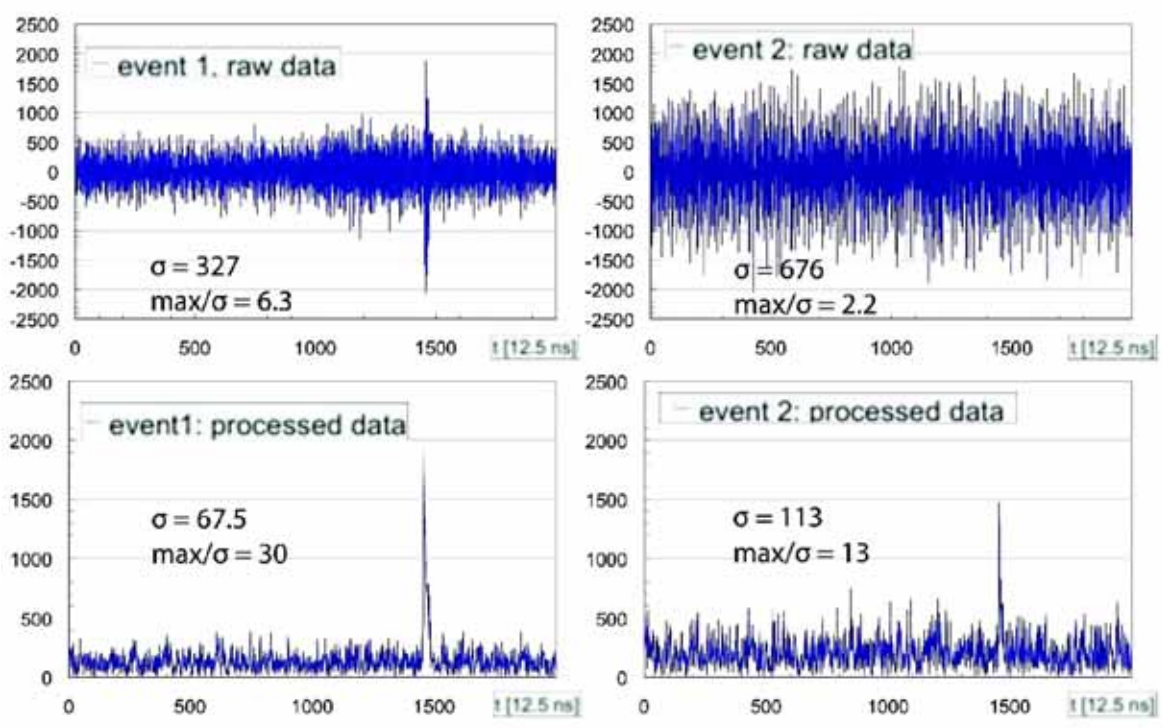

Figure 180 – Improvement of the raw data (ADC counts) in its time representation (12.5 ns per channel) by application of a 4.5 MHz wide Median filter. The raw data input is from the Lopes^{STAR} experiment (upper two examples) and the median filtered result is shown as envelope pulse in the lower row. The signal-to-noise ratio max/σ was improved by a factor greater 5. The second event was measured at an antenna with a factor 2 larger background and shows the strength of the method [195].

9.6.2 1st prototype based on Stratix EP1S40F1020I6

The FPGA code for the 1st prototype based on the EP1S40F1020I6 Stratix chip has been developed to implement two parallel, independent "engines" related to two polarizations. Altera provides the FFT routines, which can be configured in various architectures, widely parameterized and optimized for a specific application. The selected EP1S40F1020I6 chip contains a lot of memory, but relatively few DSP blocks. The FFT routines utilize intensively DSP blocks to provide maximal efficiency of the transformations. Final selection of the architecture and performance accuracy was the compromise allowing an implementation of two engines in a single chip.

The FFT routine provides 4 types of architectures:

- Streaming,
- Variable streaming,
- Buffered burst,
- Burst

The streaming architecture utilizes relatively few logic elements, but relatively much memory. Selected EP1S40F1020I6 chip with 3 423 744 memory bits can "sacrifice" significant part of the memory without a detriment for other processes. The variable

streaming architecture utilizes more logic elements but economizes the memory. This architecture can be implemented either with fixed point or floating-point algorithm. The 2nd one provides better accuracy, but needs almost half of logic elements and 86% of DSP blocks. This disqualifies this algorithm, because the selected chip has to accommodate 2 FFT + 2 FFT^{-1} routines.

Table 12 – Stratix Device Overview [196].

Feature	Device						
	EP1S10	EP1S20	EP1S25	EP1S30	EP1S40	EP1S60	EP1S80
Logic Elements (LEs)	10,570	18,460	25,660	32,470	41,250	57,120	79,040
M512 RAM Blocks (512 Bits + Parity)	94	194	224	295	384	574	767
M4K RAM Blocks (4 Kbits + Parity)	60	82	138	171	183	292	364
M-RAM Blocks (512 Kbits + Parity)	1	2	2	4	4	6	9
Total RAM bits	920,448	1,669,248	1,944,576	3,317,184	3,423,744	5,215,104	7,427,520
DSP Blocks	6	10	10	12	14	18	22
Embedded Multipliers (1)	48	80	80	96	112	144	176
PLLs	6	6	6	10	12	12	12
Maximum User I/O Pins	426	586	706	726	822	1,022	1,203
Production Device Availability	Buy Now	Buy Now	Buy Now	Buy Now	Buy Now	Buy Now	Buy Now

The blocks of 256 samples have to be processed online. It means the processing time should be maximal 256 clock cycles. However, both buffered burst and burst architectures require longer processing interval.

The variable streaming architecture transforms the samples into the frequency domain either in natural sequence or bit-reverse order. The 2nd option allows saving some memory, but it is completely useless for a filtering in the frequency domain. The median filter has to analyze data in a natural order.

The FFT Mega-Core® function uses block-floating-point (BFP) arithmetic internally to perform calculations. BFP architecture is a trade-off between fixed-point and full floating-point architecture. Unlike an FFT block that uses floating-point arithmetic, a block-floating-point FFT block does not provide an input for exponents. Internally, a complex value integer pair is represented with a single scale factor that is typically shared among other complex value integer pairs. After each stage of the FFT, the largest output value is detected and the intermediate result is scaled to improve the precision. The exponent records the number of left or right shifts used to perform the scaling. As a result, the output magnitude relative to the input level is: output*$2^{-exponent}$. For example, if exponent = –9, the input samples are shifted right by three bits, and hence the magnitude of the output is output*2^{9}= 512.

The streaming architecture uses the same number of bits for input and output. Output data are scaled by 6-bit exponent factor (signed representation). However, the scaling factor corresponds to a full frame. The frame is the block of data corresponding to the length (N) of the FFT. The 0^{th} component of the FFT: $X_0 = \Sigma\, x_i$ strongly depends on pedestal. So, if data are coming from a n-bit ADC setting for bipolar symmetric voltage, zero of signals would correspond to the pedestal of $(n-1)^{th}$ bit. Thus, X_0 will be very large in comparison to the rest

of components. If all components are scaled by the same factor within the frame, for n>0 the resolution of X_n will be significantly reduced (Figure 182).

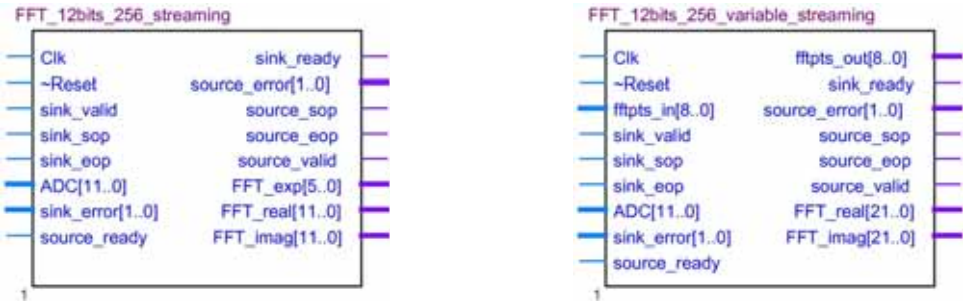

Figure 181 – I/O pins for two architectures of the FFT routine driven from 12-bit ADC and processing a packet of 256 samples.

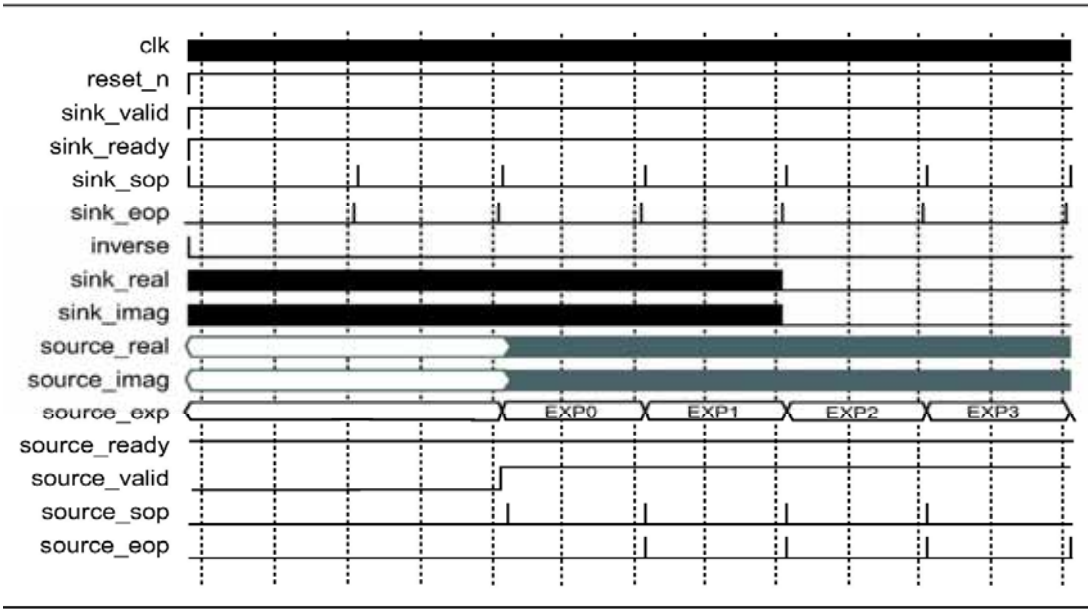

Figure 182 – FFT Streaming Data Flow Architecture Simulation Waveform.

Only two architectures can be selected for the RFI filtering: streaming or variable streaming with fixed-point algorithm providing output data in the natural order. The FFT routine with the variable streaming architecture transforms N-bit data from the time domain into N+10 data bus in the frequency domain. Additional 10 bits correspond to the fractional part. Taking into account in the FFT^{-1} routine wider than 12-bit bus requires more DSP blocks, which also are needed for other procedures.

Finally, only FFT routines with the streaming architecture could be implemented in the 1st prototype with EP1S40F1020I6 Stratix chip. Although the driving ADC have 10-bit resolution, for the processing 12-bit option has been chosen. This is due to some internal limitation of the Altera FFT routine.

For an analysis the following artificial data were generated:

$$X_k = Pedestal + Amp \times \cos\left(\frac{k \times freq \times \pi}{128}\right) + random \times Noise \qquad (111)$$

where: *random* corresponds to the rectangular random generator from the range (0,1), *freq* is the multiplication factor of the basic frequency, *Amp* is the amplitude of the periodic signal and *Noise* is the amplitude of the noise. Two sets of data (*Freq, Pedestal, Amp, Noise*) were analyzed: (*4, 1024, 400, 512*) and (*32, 750, 350, 1024*).

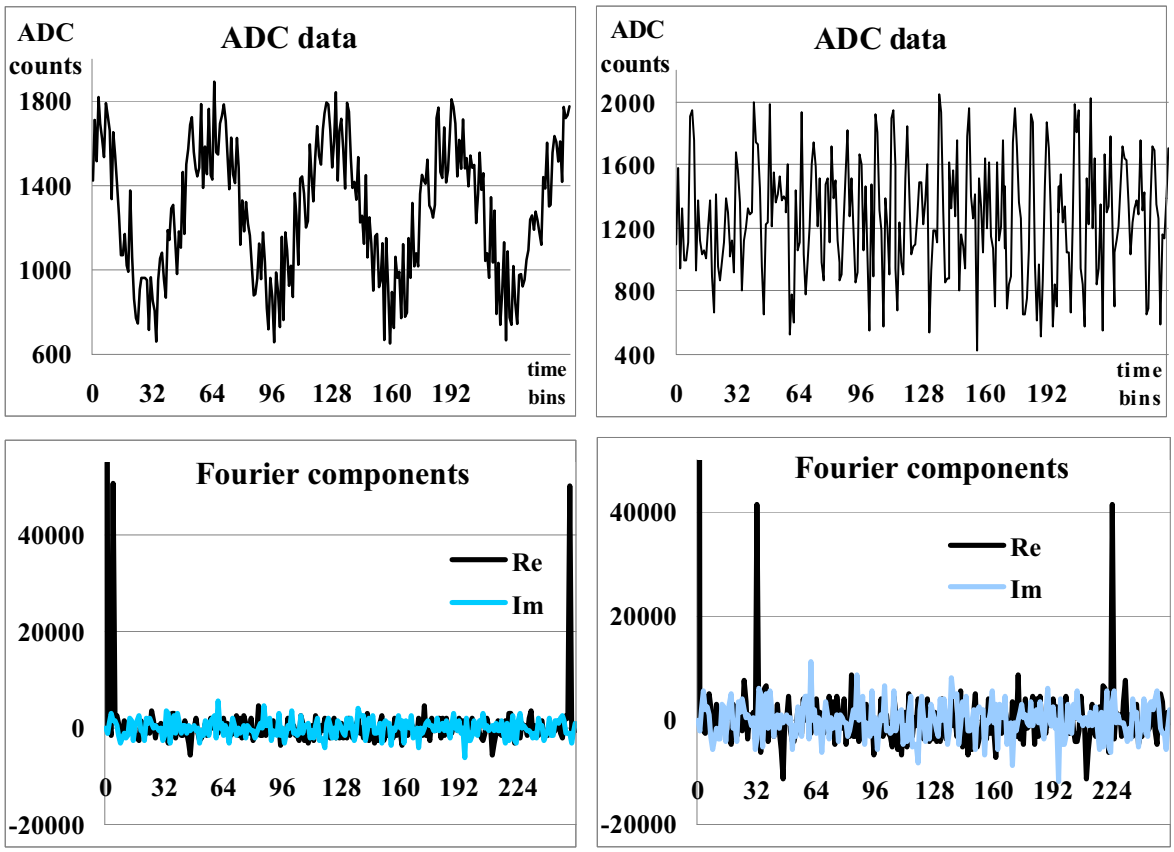

Figure 183 – Simulated data in the time domain (above) and their expected Fourier components (below). X_0 is cropped as irrelevant.

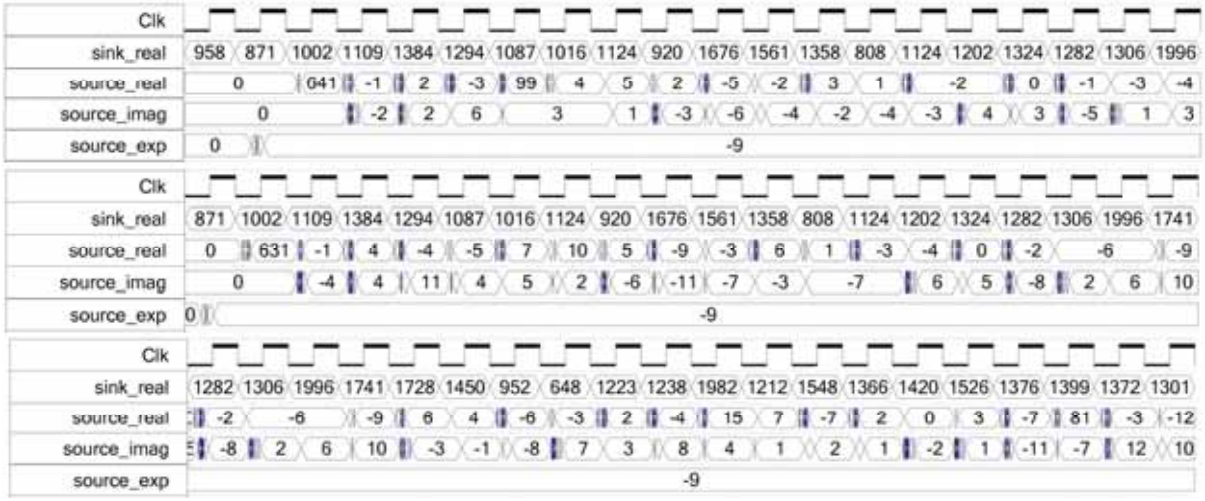

Figure 184 – Simulations in QuartusII for selected test vectors (from Figure 183). The 1st plot corresponds to the variant of (*4, 1024, 400, 512*), the 2nd and 3rd to the variant of (*32, 750, 350, 1024*). The 3rd plot is a continuation of the 2nd one.

X_0 is much larger than the rest of components. If the output data has N-bit resolution but with the *exponent* factor, shifting these data to right, it means, effective resolution for lower Fourier components id reduced to (N-exponent) bits. This causes a huge approximation error.

Data approximated to integer values during the internal processes in the FFT routine are next the source of significant errors for the next calculations. Although huge errors shown in Figure 185 are generated for artificial data, but for real data with smaller amplitudes this algorithm introduces also relatively large errors, unacceptable for final precise measurements. So, the 1st prototype with this type of the architecture has been treated as the test platform for a development of the final, precise FPGA code, processing the data with a sufficient precision and accuracy.

Figure 184 shows the FFT coefficients obtained in simulations. For the 1st variant of (*4, 1024, 400, 512*), $Re(X_0) = 641$, while $Re(X_3) = 99$. The ratio of 99/641 roughly corresponds to the expected ratio from Figure 183. For the 2nd variant of (*32, 750, 350, 1024*), the agreement for the 31st harmonics ($Re(X_{31}) = 81$) is on the same level. However, due to the constant scaling for the full 256-point package, the rest of harmonics is approximated to the resolution of ca. 3-4 bits. This is a source of significant relative errors (Figure 185).

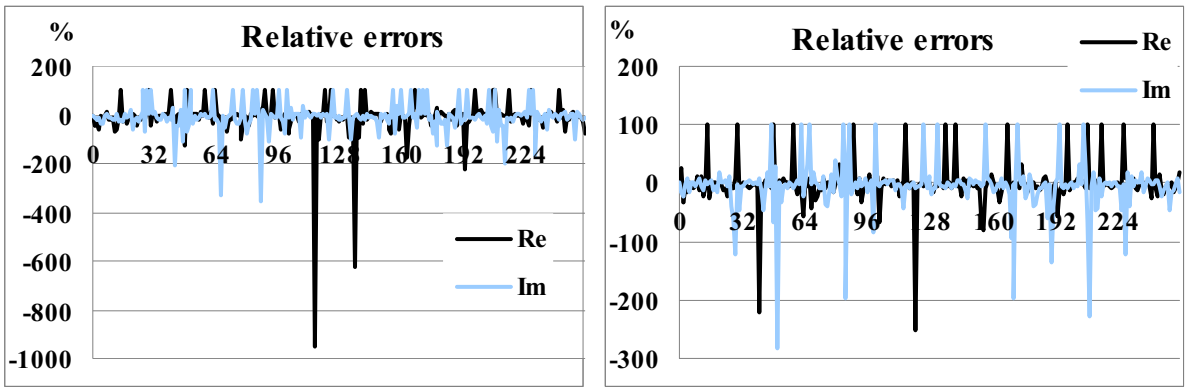

Figure 185 – Relative errors for the streaming architecture in comparison to expected exactly calculated values.

The variable streaming architecture has been also tested for the signals from Figure 183. As seen on Figure 186 relative errors for the 1st variant are reasonable, but for the 2nd one are absolutely unacceptable. Let see carefully the structure of input data: only in a single time bin the input data value exceedes 2047, MSB = 1, let's consider artificially cut-off in order to keep MSB = 0. From Figure 187 we see that if MSB = 0 for the full transforming package, the relative errors drop down to acceptable level.

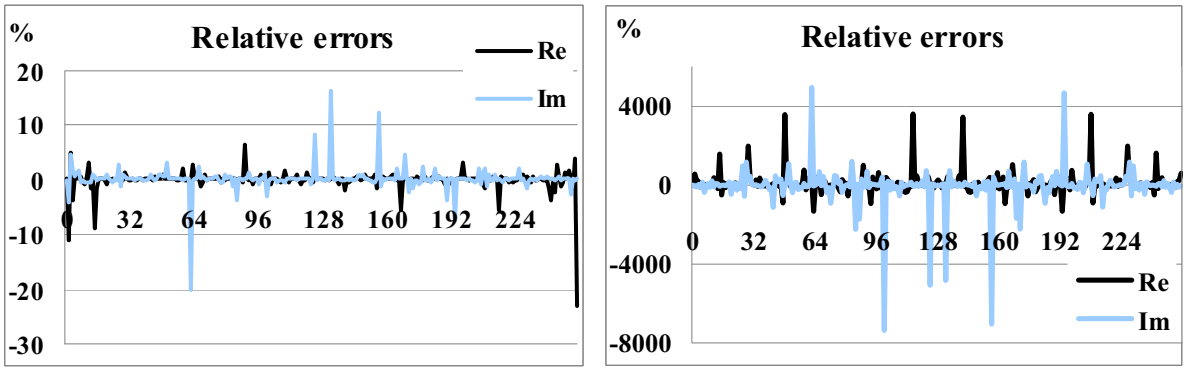

Figure 186 – Relative errors for variants from Figure 183 for the variable streaming architecture.

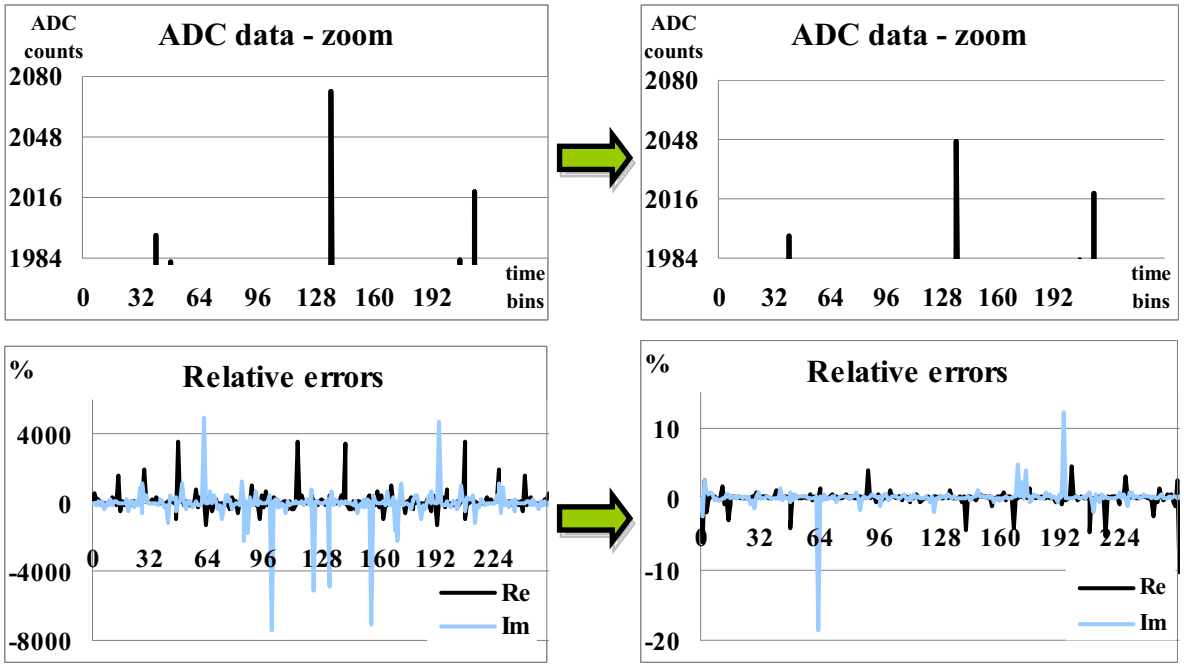

Figure 187 – Huge reduction of the errors by artificial data cut-off by forcing MSB = 0.

This strange undocumented feature of the Altera FFT routine raised vigilance and enforced to time-consuming verification of IP-routines delivered by world-known company.

The variable streaming architecture is recommended due to much better accuracy vs. the streaming architecture. The wider output bus requires more resources for the next stage: FFT^{-1}, however a dramatic reduction of the accuracy at the 1st stage rather disqualify the streaming architecture for the final design.

In the variable streaming architecture the Most Significant Bit has to be kept grounded in order to avoid an internal overflow. For 10-bit ADC, 12-bit inputs worked well, however for a full 12-bit ADC the input of the variable streaming engine has to be extended to 14 bits.

9.6.2.1 Median filter

Arranging all the observations from lowest value to highest value and picking the middle one can find the median of a finite list of numbers. If there is an even number of observations, the median is not unique, so one often takes the mean of the two middle values.

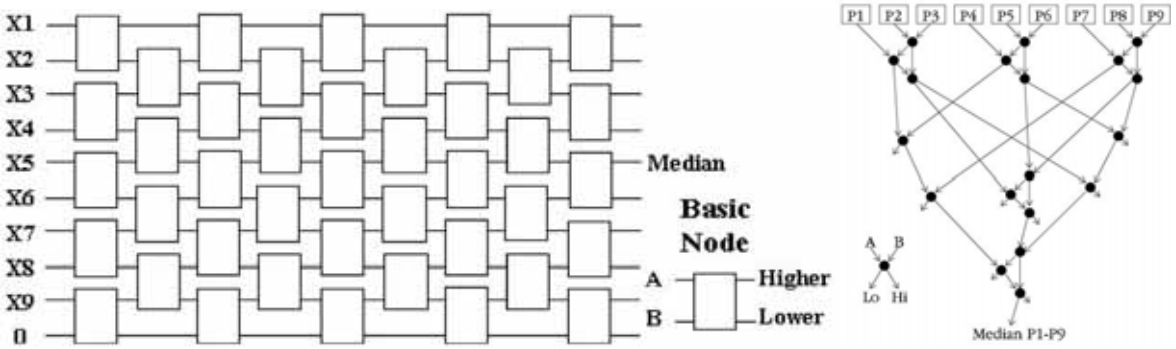

Figure 188 – Classic systolic array for sorting 9 pixels (left) and optimized algorithm [197] (right).

A classical approach for the median calculation is spendthrift in resources utilization. There are a lot of optimized applications, however they focus rather on 3 × 3 pixel matrix as a part of a picture, from which the noise is being removed. For nine inputs the classical algorithm requires 41 basic nodes allowing swapping data from two inputs, however a simple optimization reduces the amount of nodes to 19 only (Figure 188). This algorithm has been adapted to the FPGA pipeline structure as follows (Figure 189).

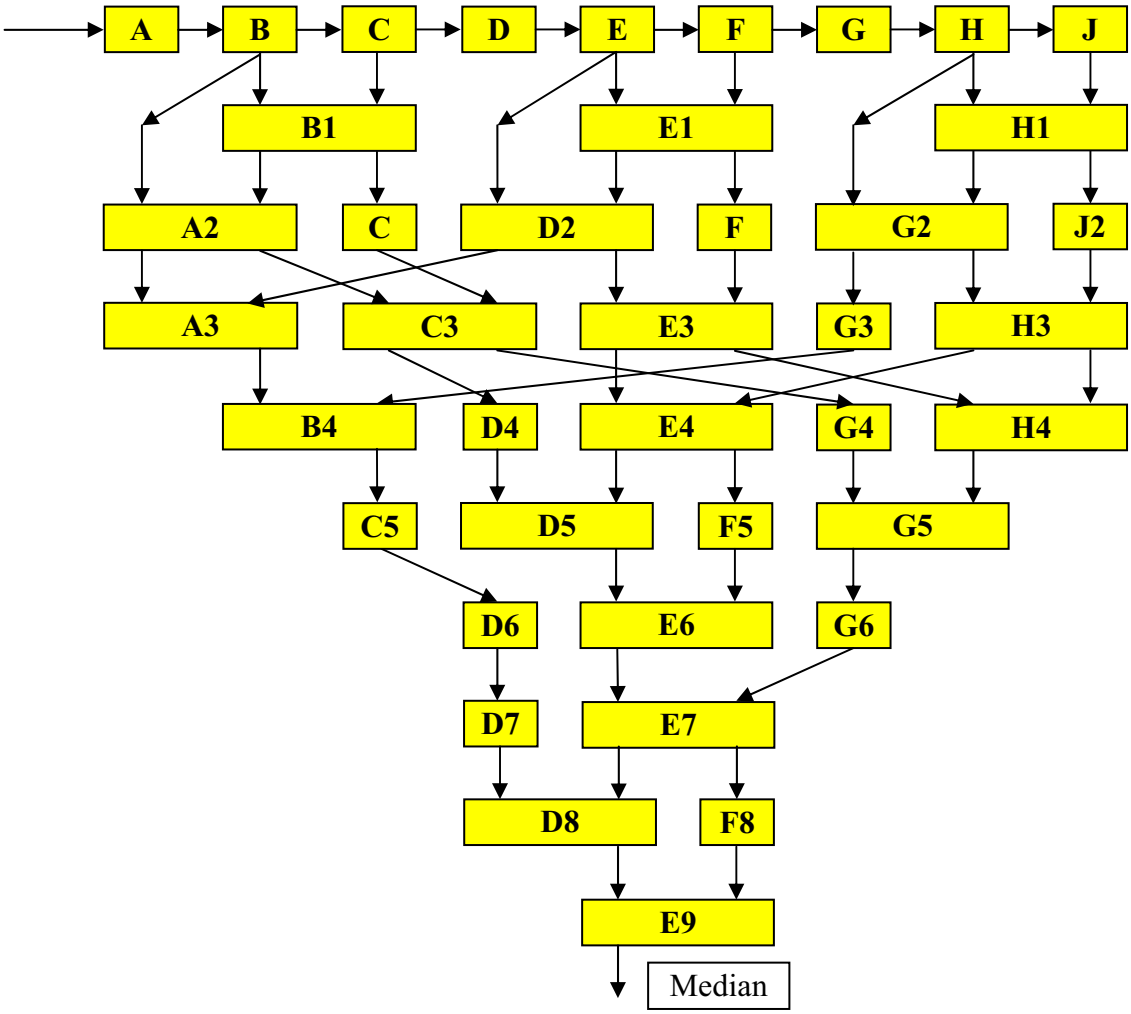

Figure 189 – The median filter implemented into the FPGA.

Filtering data in the frequency domain by the 9-input median filter (Figure 190) allows a removal narrow-band RFI. The efficiency of filtering slightly improves for 15-input filter (Figure 190).

For the investigated band range of roughly 40 MHz and 256-point FFT, the frequency grid is 156.25 kHz. Median_9 filter allows rejecting 4 frequency bins, which would correspond to maximal RTV carrier width of 625 kHz. Median_15 removes wider RFI of ca. 1 MHz. However, for the packages length of 1024 or 2048, when the frequency grid will decrease to 39 or 19 kHz, respectively, efficient filtering requires 63, 127 or 255-point median filter, which a FPGA implementation will become a serious challenge. In the 1st prototype finally 31-point median filter has been used, with only approximated accuracy. Roughly for 50% of cases, a single frequency grid in comparison to the expected has shifted the real median obtained from normal calculations.

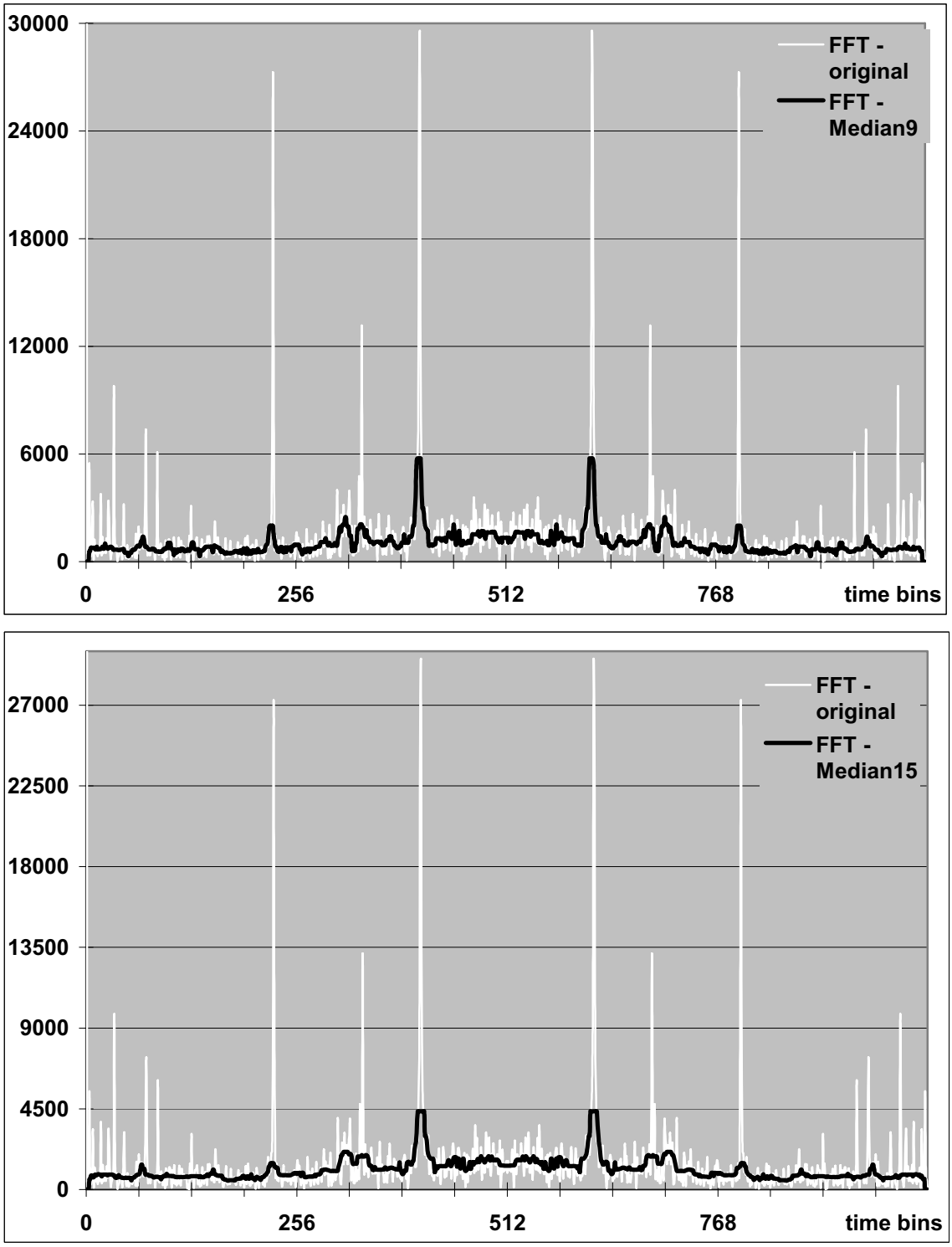

Figure 190 – Filtering of the noise data by the Median_9 (above) and Median_15 (below) filter. Unfiltered absolute values of Fourier components contain huge peaks corresponding to RFI (thin white lines). Median filters (thick black lines) suppresses strongly RFI. Suppression factors depend on the width of the peaks. For this particular event, they are ca. 5 and 7 (for highest peaks) and even 13.7 and 16.7 (for narrow 2nd high peaks), respectively.

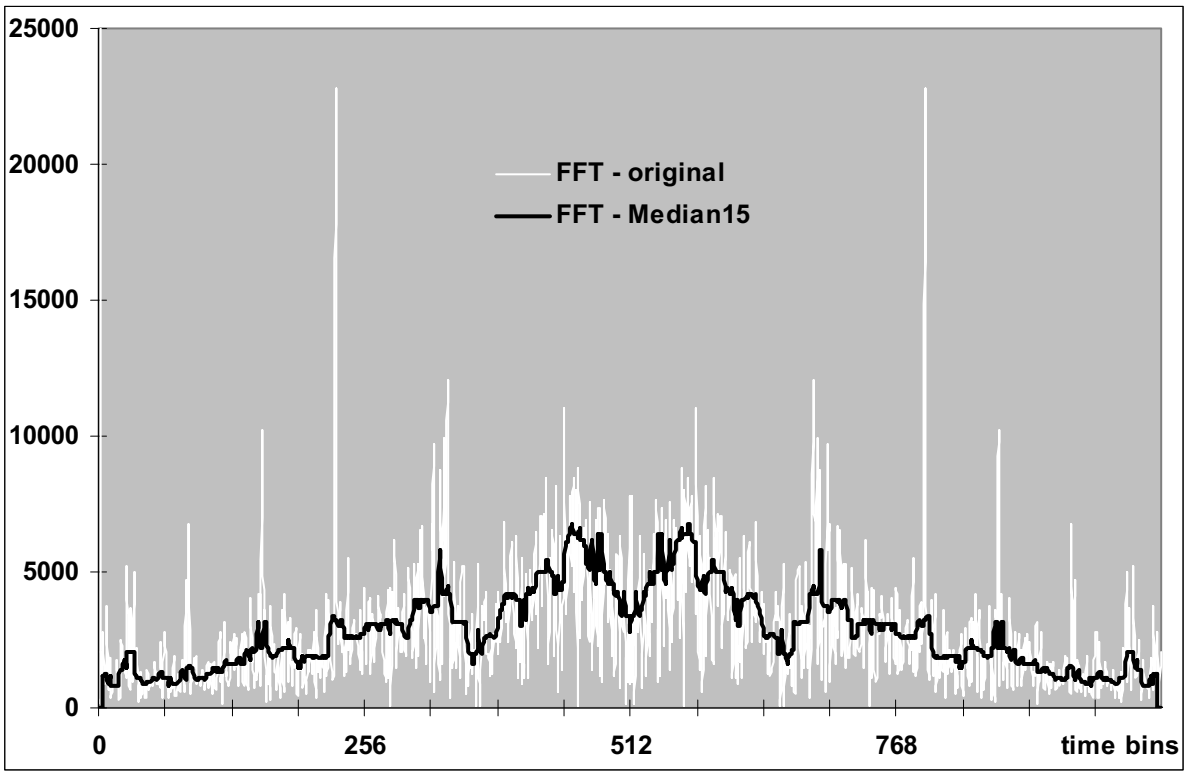

Figure 191 – Absolute values of Fourier components for a real radio event (see FADC in Figure 192). Median filter significantly cleans frequency domain from the RFI.

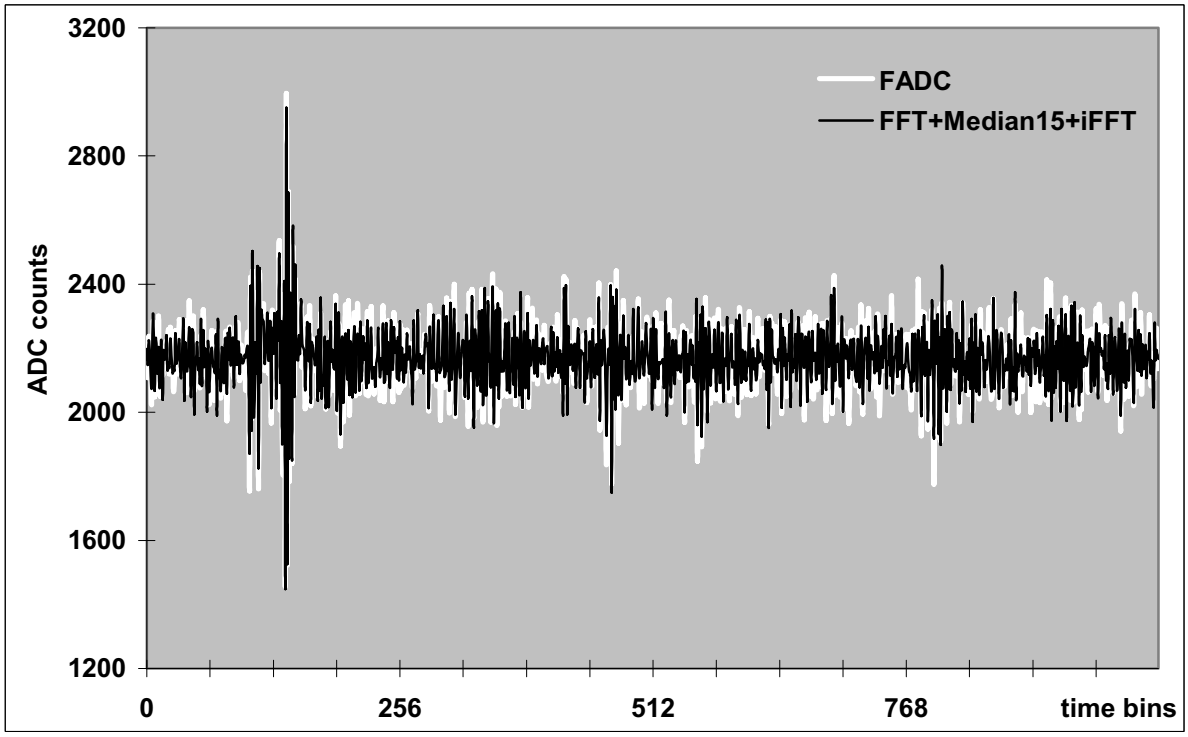

Figure 192 – Results of the RFI removing in the frequency domain. The structure of the filtered data did not significantly change in comparison to the original FADC data.

The median filter processes only the real data. However, output data from the FFT routines are complex. So, the absolute values of complex samples in the frequency domain are used as the input data for the median filter. Next, simultaneously both real and imaginary parts are scaled by the real output of the median filter (Figure 193). These scaled data are next inputs to the iFFT routine converting data from the frequency domain again into the time one.

An additional routine, calculating online the signal to noise ratio, has been also implemented as a support for the trigger decision (Figure 194).

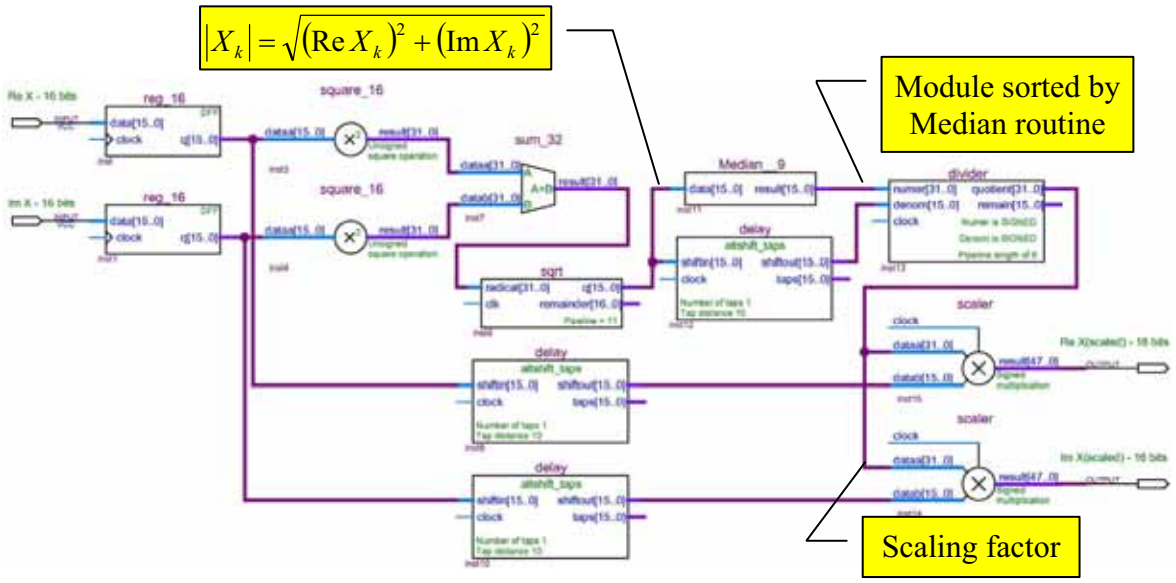

Figure 193 – Schematics of the scaling routine.

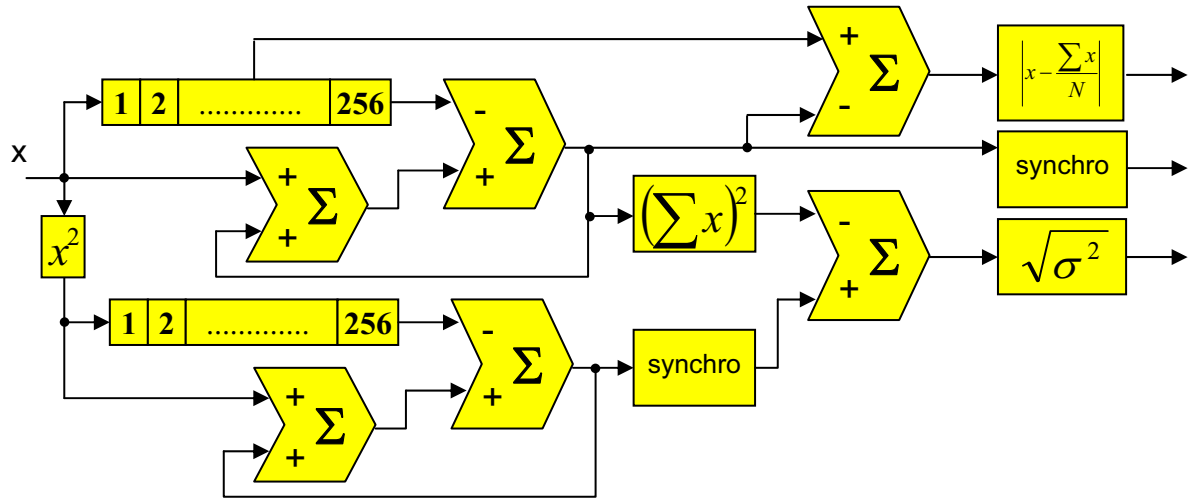

Figure 194 – Schematics of the routine calculating online the signal to noise ratio.

9.6.2.2 FIR filter

Data processed in the FFT + Median + FFT^{-1} chain may be a little bit contaminated by an internal approximation processes inside the FPGA. Thus, the additional band-pass filter implemented as a FIR (Finite Impulse Response) helps to polish output data for the final triggering. The FIR routine is available as the MegaCore® function, which can be flexibly tailored for a particular application. The implemented FIR function has been configured as 71-point Blackman windowed band-pass filter with cut-off frequencies 3.8 and 3.62 MHz, respectively. The frequency characteristic even for the fixed coefficient response suppresses undesirable bands in sufficient way, more than –60 dB (Figure 195).

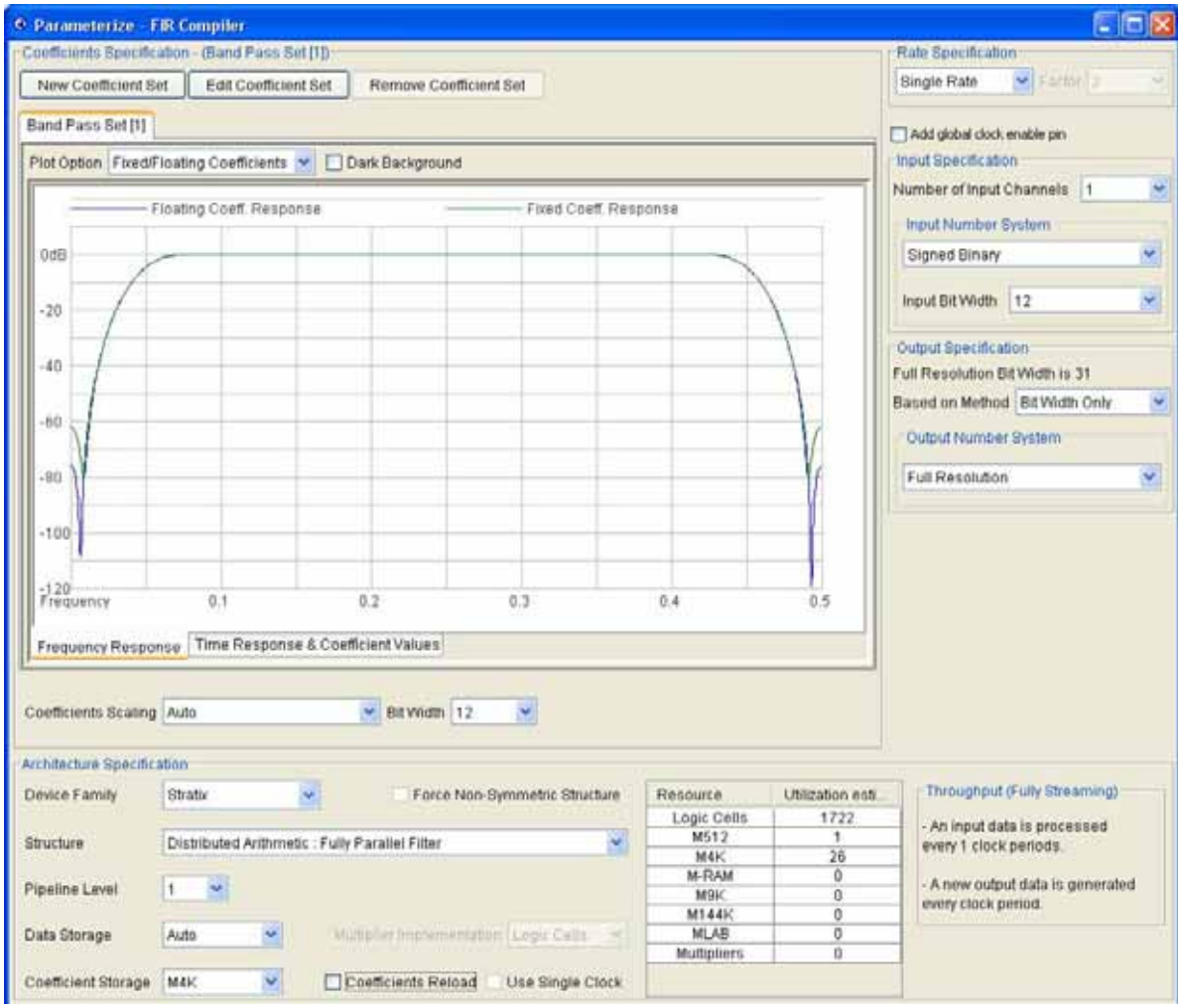

Figure 195 – Finite Impulse Response filter as MegaCore function provided by Altera.

Very fast oscillating signal is not suitable for triggering. The envelope from filtered signal is created and the trigger is generated according to the conditions from Figure 196. For 250 ns before and 750 ns after, respectively, the time positions corresponding to the level, where the width of the hump corresponds to ca. 20% of the peak, the signal is integrated. The final threshold is generated on the basic on the integral/max ratio.

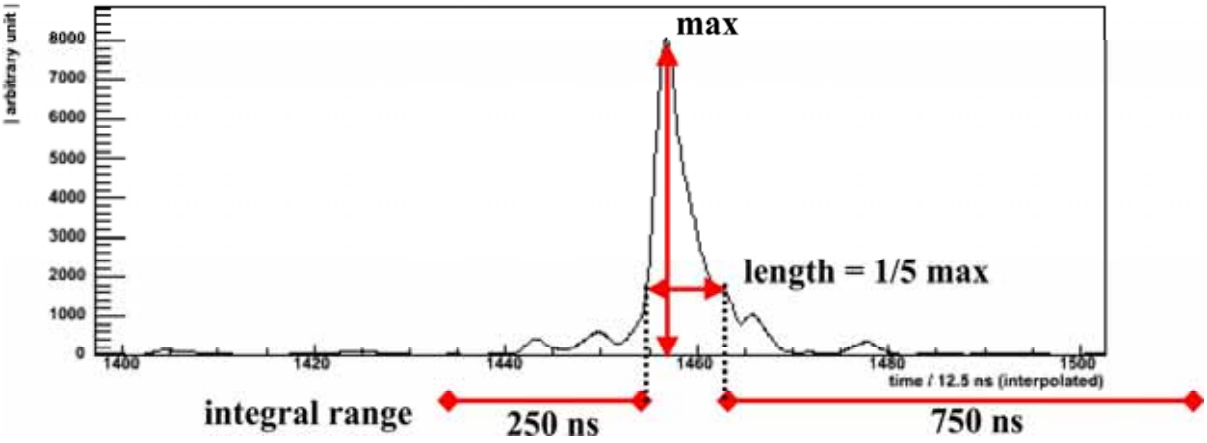

Figure 196 – Conditions for final trigger [198].

Finally, two engines (Figure 197) for two polarizations have been implemented successfully into Stratix EP1S40F1020I6 chip. By more than 71% resources occupancy of logic elements, 86% of DSP blocks and only 8% of the internal memory, the registered performance was only 122 MHz [199]. The chip used in the 1st prototype became obsolete, when the next version started to be developed. The new families StratixII, StratixII and CycloneIII offered modern internal architecture, much more internal resources, and much faster registered performance. However, higher speed requires much higher power consumption. Even if the financial aspect is not taken into account, the power budget became a crucial parameter significantly reducing a flexibility of the design [200].

9.6.3 Next generation based on Cyclone III EP3C80F780C6

For the radio engineering-array several changes in the newly designed hardware will be necessary. Currently, no any ADC with 16-bit resolution and at least 160 MHz sampling is currently available (the 1st Nyquist is selected). In order to achieve the required 16-bit dynamic range, signals for each polarization are split into two high-gain and low-gain channels and next digitized with 12-bit resolution in 12-bit ADCs (Figure 198). The overlapping of the dynamic ranges is 6 bits, so the final dynamic range is 18 bits.

The recorded frequency band is still from ~30 MHz to ~80 MHz as in previous prototype. Because of the 1st Nyquist, data acquisition requires a sampling rate of at least 160 MHz. The AD9626 chip is a good ADC candidate, capable of maximal 250 MS/s with only ~300 mW power consumption per channel and a parallel output, which simplifies the connection to the FPGA.

The fast Fourier transform into the frequency domain is executed in blocks of 1024 or 2048 entries. This block length was found to be a good compromise between frequency resolution and hardware consumption. To avoid leakage effects due to the prompt signal change at the edges of each block, a window function must be used. A good solution is a simple trapezoid window, linearly fading in for 1/8 of the block length, staying constant for 3/4 and then fading out again for the last 1/8 of the block. A 31-entry median filter flattens the resulting spectrum and inverse Fourier transformed back to the time domain. When the resulting filtered 1024 (2048)-entry blocks are pieced back together to a continuous trace, the first and the last 1/8 of each block has to be thrown away, as affected by the window

function. Therefore the blocks from the beginning need an accordant overlap, and both FFT and the median-filter have to run with 4/3 of the base clock.

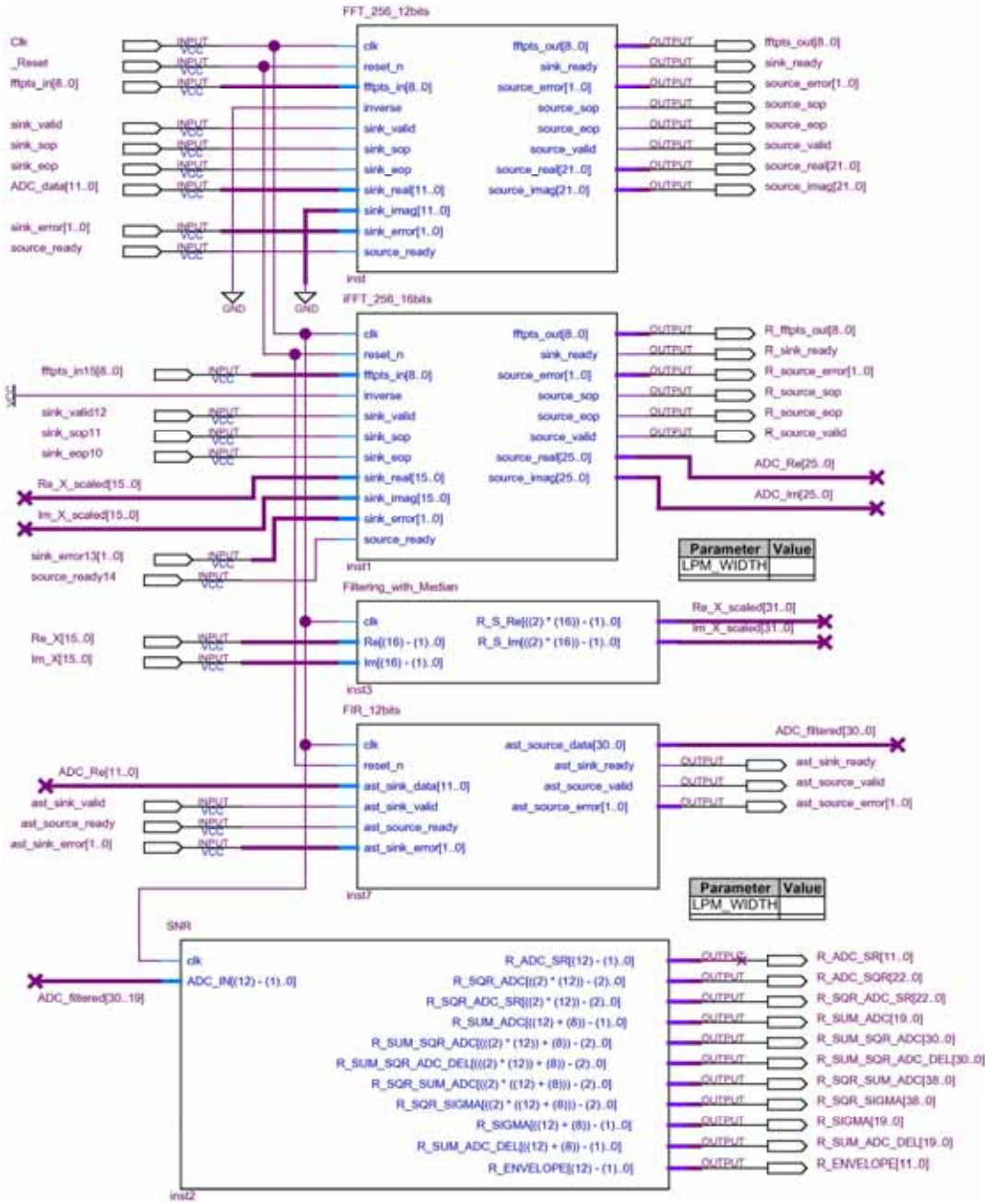

Figure 197 – Block scheme of the single “engine”. Pins denoted as I/O are connected to the master routine (higher in the hierarchy of the FPGA code), but unnecessarily to the physical chip pins.

The high clock frequencies disqualify low cost FPGA of the Cyclone III series, as simulations resulted in a critical frequency of 180 MHz for our algorithm on the fastest available speed grade 6. The high end Stratix III EP3SE50, which not only allows frequencies up to 300 MHz (speed grade 2), was considered. It also offers enough spare resources for a third channel or an extended trigger algorithm. However, the power consumption according

to simulations at 200 MHz will be around 5 W. The price of the Stratix III chips, on the level of 4k$, is an additional argument to look for an alternative solution.

Finally, if the sampling remains on the required level of 180 MHz, but the trigger will be generated with twice less frequency 90 MHz, the registered performance of one of the largest chip EP3C80F780C6 from the cost-effective family Cyclone III is high enough to process all algorithms with a sufficient safety margin. The largest chip EP3C120F780 is not available in the speed grade 6. Simulations showed that it could not fast enough by higher utilization of resources.

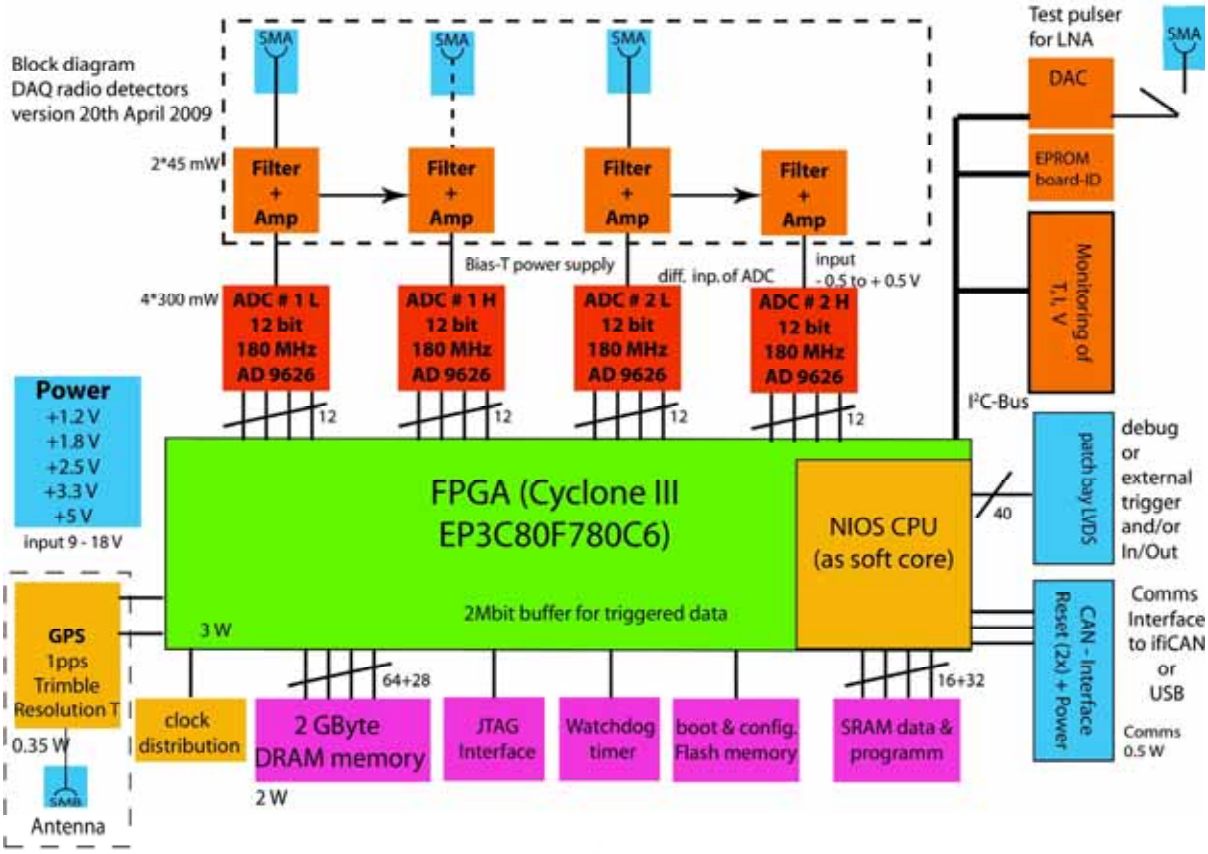

Figure 198 – Block diagram of the electronics under development [201].

As interface to the wireless communication but also for configuring and monitoring purposes an additional processor is needed. A soft core NIOS II implemented on the FPGA has been chosen. However, the processor will consume about 1W of power.

The wireless communication for the generation of a coincidence trigger will need some time, for which the radio traces have to be buffered. In order to learn as much as possible about the radio emission of cosmic rays, we also want to be able to read out antennas at the edge of the radio events, which might not have triggered. Therefore we must not only store first level triggered events, but also have to store the raw radio stream in a ring-buffer for about 2-3 seconds, until a coincidence trigger decision is received. This results in memory requirements of 2 GB for a continuous ring-buffer. For this purpose DDR2 SODIM modules are best suited, as their wide interface bus simplifies the high-speed data access. One module has a power consumption of 1–2 W. But without a reduction of the trigger rates per antenna to 100 Hz (or lower) the communication problem is not solvable with conventional methods [202].

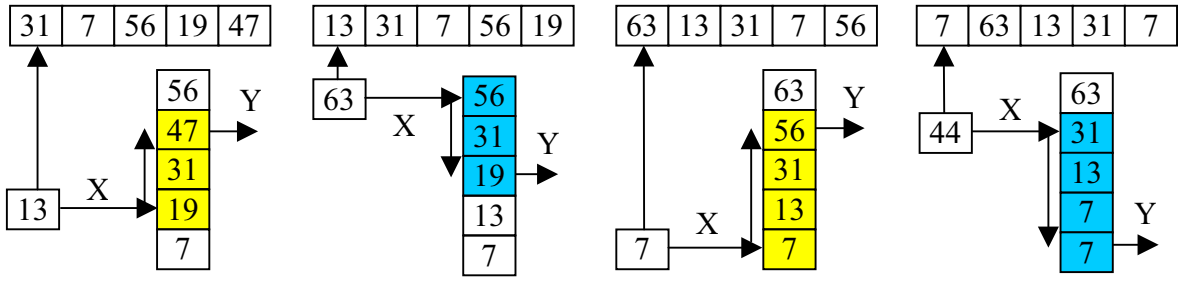

Figure 199 – Schematics of data flow in the arranged vector (vertical) and the shift registers (horizontal) working as a delay line.

Much wider blocks of 1024 or 2048 samples converting by the FFT requires also wider median filter. Classical systolic array for sorting (Figure 188) is extremely ineffective for the wide window. $N\frac{N-1}{2}$ nodes are required for N (odd) inputs. The new approach is being developed for the next generation of the radio trigger. The new, incoming sample is inserted on the correct position in the arranged vector. Its position is determined by a set of comparators. Simultaneously a part of samples is shifted in a proper direction. The direction corresponds to the relation between the new, incoming sample (X) and the oldest, outgoing one (Y) from the FIFO. If X<Y, the new value X is inserted closer the bottom of the vector, all bigger samples are shifted towards the top till the sample, which should be removed as the oldest one. If X>Y, the X is inserted closer the top of the vector, all smaller samples are shifted towards the bottom till the sample corresponding to the outgoing from the delay line as the oldest one (Figure 199). The set of comparators and state machines prepare the direction of the shift, enables for registers, addresses for multiplexers etc., the new order of samples in the (vertical) vector (and simultaneously the median as the output of the middle register) is available in a single clock cycle [203].

10 Results from the Pierre Auger Observatory on basis of data till June 2009 [4]

10.1 Measurement of the CR energy spectrum above 10^{18} eV using the Pierre Auger Observatory

The Pierre Auger Observatory uses two independent techniques to study extensive air showers created by ultra-high energy cosmic rays in the atmosphere, a ground array of more than 1600 water-Cherenkov detectors (see Chapter 1.5.1) and a set of 24 fluorescence telescopes (see Chapter 1.6.1). Construction of the baseline design was completed in June 2008. With stable data taking starting in January 2004, the world's largest dataset of cosmic ray observations has been collected over the last 4 years during the construction phase of the observatory. An update significantly increased relative to the accumulated exposure of the energy spectrum measurements previously reported in [204] and [205].

Due to its high duty cycle, the data of the surface detector are sensitive to spectral features at the highest energies. Its energy scale is derived from coincident measurements with the fluorescence detector. A flux suppression around $10^{19.5}$ eV has been established based on these measurements [204] in agreement with the HiRes measurement [206].

An extension to energies below the threshold of $10^{18.5}$ eV is possible with the use of hybrid observations, i.e. measurements with the fluorescence detectors in coincidence with at least one surface detector. Although statistically limited due to the duty-cycle of the fluorescence detectors of about 13%, these measurements make it possible to extend the energy range down to 10^{18} eV and can therefore be used to determine the position and shape of the ankle at which the power law index of the flux changes [207], [208], [209], [210]. A precise measurement of this feature is crucial for an understanding of the underlying phenomena. Several phenomenological models with different predictions and explanations of the shape of the energy spectrum and the cosmic ray mass composition have been proposed [211], [212].

The surface detector array of the Pierre Auger Observatory covers ~3000 km^2 of the Pampa Amarilla. Since its completion in June 2008 the exposure is increasing each month by about 350 $km^2 \cdot sr \cdot yr$ and amounts to 12790 $km^2 \cdot sr \cdot yr$ for the time period January 2004 – December 2008 considered for the analysis. The exposure is calculated by integrating the number of active detector stations of the surface array over time. Detailed monitoring information of the status of each surface detector station is stored every second and the exposure is determined with an uncertainty of 3 % [204]. The energy of each shower is calibrated with a subset of high quality events observed by both the surface and the fluorescence detectors after removing attenuation effects by means of a constant-intensity method. The systematic uncertainty of the energy cross-calibration is 7% at 10^{19} eV and increases to 15% above 10^{20} eV [213].

The derived energy spectrum of the surface detector is shown in Figure 200a together with the event numbers of the underlying raw distribution. Combining the systematic uncertainties of the exposure (3%) and of the forward folding assumptions (5%), the systematic uncertainties of the derived flux is 5.8%.

[4] The chapter has been prepared on basis of official Pierre Auger papers published in 31st ICRC2009 in Łódź

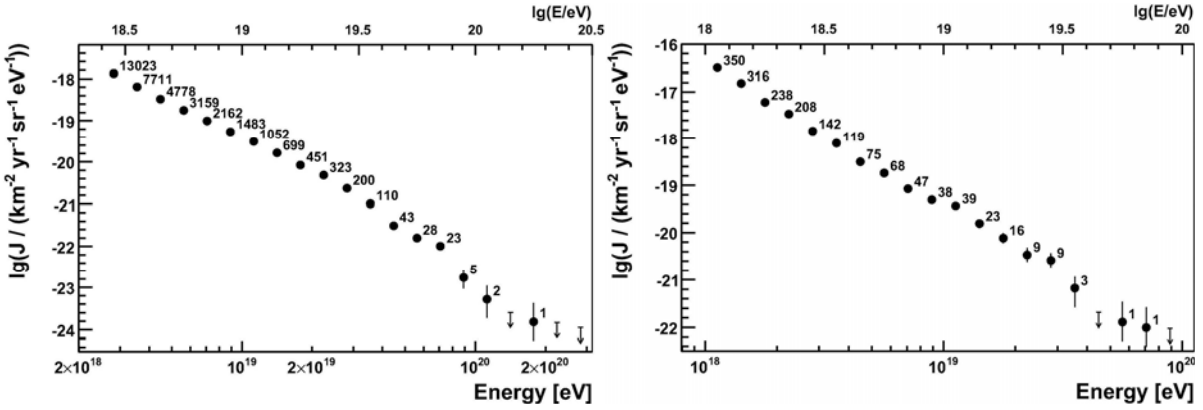

Figure 200 – Energy spectrum derived from surface detector data calibrated with fluorescence measurements (left). Energy spectrum derived from hybrid data (right). Only statistical uncertainties are shown [214].

Two complementary air shower detection techniques offers the chance to validate the full MC simulation chain and the derived hybrid exposure using air shower observations themselves. Based on this end-to-end verification, the calculated exposure has been corrected by 4%. The total systematic uncertainty of the derived hybrid spectrum is 10% at 10^{18} eV and decreases to about 6% above 10^{19} eV. Figure 200b shows the energy spectrum derived from hybrid measurements recorded during the time period December 2005 – May 2008.

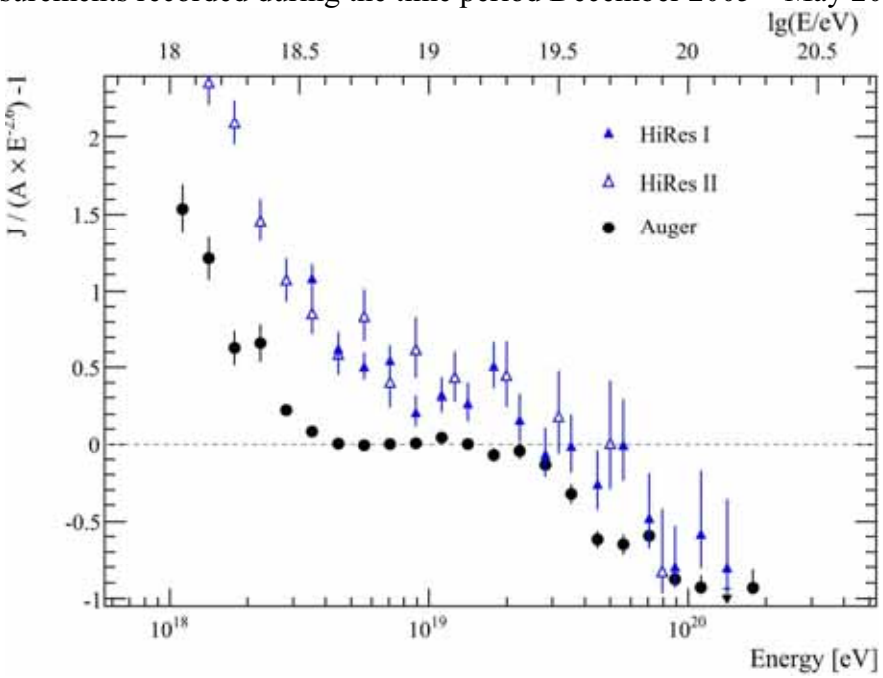

Figure 201 – The fractional difference between the combined energy spectrum of the Pierre Auger Observatory and a spectrum with an index of 2.6. Data from the HiRes instrument [206], [215] are shown for comparison.

The Auger energy spectrum covering the full range from 10^{18} eV to above 10^{20} eV is derived by combining the two measurements discussed above. The combination procedure utilizes a maximum likelihood method, which takes into consideration the systematic and statistical uncertainties of two spectra. The procedure derives flux scale parameters to be applied to the individual spectra. These are $k_{SD} = 1.01$ and $k_{FD} = 0.99$ for the surface detector

data and hybrid data, respectively, showing the good agreement between the independent measurements. The systematic uncertainty of the combined flux is less than 4%.

We should be aware that both spectra share the same systematic uncertainty for the energy assignment, because the surface detector data are calibrated with hybrid events. The main contributions to this uncertainty are the absolute fluorescence yield (14%) and the absolute calibration of the fluorescence photo-detectors (9.5%). Including a reconstruction uncertainty of about 10% and uncertainties of the atmospheric parameters, a total systematic uncertainty of the energy scale has been estimated on 22% [213].

The fractional difference of the combined energy spectrum with respect to an assumed flux $\sim E^{-2.6}$ is shown in Figure 201. Two spectral features are evident: an abrupt change in the spectral index near 4 EeV (the "ankle") and a more gradual suppression of the flux beyond about 30 EeV.

A modest systematic energy shift applied to one or both experiments could account for most of the difference between the two. The spectral change at the ankle appears more sharp in our data. The energy spectrum is fitted with two functions. Both are based on power-laws with the ankle being characterized by a break in the spectral index γ at E_{ankle}. The first function is a pure power-law description of the spectrum, i.e. the flux suppression is fitted with a spectral break at E_{break}. The second function uses a smooth transition given by

$$J(E; E > E_{ankle}) \approx E^{-\gamma_2} \frac{1}{1+\exp\left(\frac{\lg E - \lg E_{1/2}}{\lg W_c}\right)} \tag{112}$$

in addition to the broken power-law to describe the ankle. This fit is shown as black solid line in Figure 202.

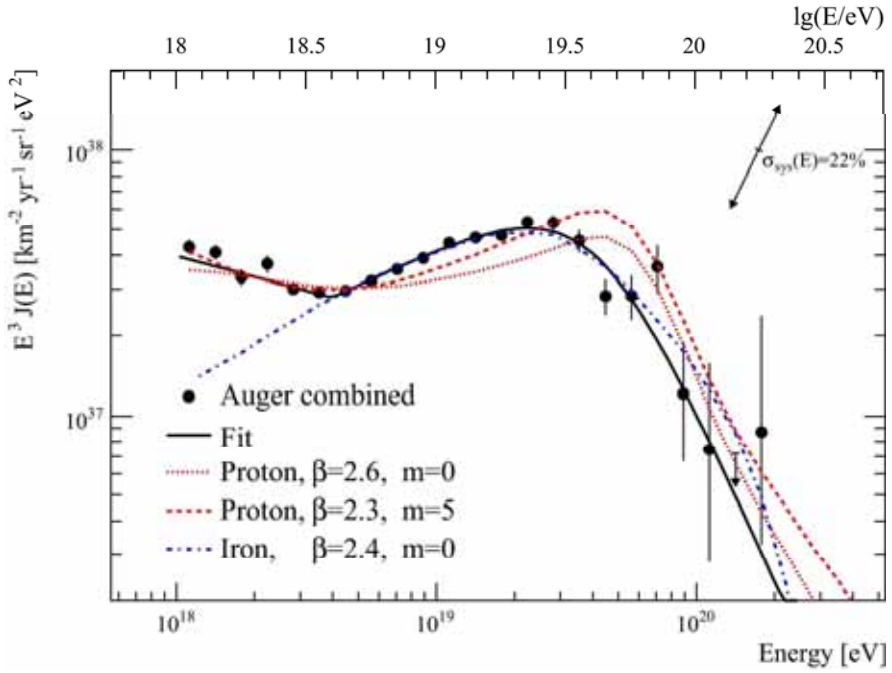

Figure 202 – The combined energy spectrum compared with several astrophysical models assuming a pure composition of protons (red lines) or iron (blue line), a power-law injection spectrum following $E^{-\beta}$ and a maximum energy of $E_{max} = 10^{20.5}$ eV. The cosmological evolution of the source luminosity is given by $(z+1)^m$. The black line shows the fit used to determine the spectral features [214

].

Figure 202 shows a comparison of the combined energy spectrum with spectral shapes expected from different astrophysical scenarios. Assuming for example a uniform distribution of sources, no cosmological evolution of the source luminosity ($(z + 1)^m$, i.e. m = 0) and a source flux following $\sim E^{-2.6}$ a spectrum that is at variance with our data is obtained. Better agreement is obtained for a scenario including a strong cosmological evolution of the source luminosity (m = 5) in combination with a harder injection spectrum ($\gamma \sim E^{-2.3}$). A hypothetical model of a pure iron composition injected with a spectrum following $\gamma \sim E^{-2.4}$ and uniformly distributed sources with m = 0 is able to describe the measured spectrum above the ankle, below which an additional component is required.

The flux of cosmic rays above 10^{18} eV has been measured with unprecedented precision. Two analysis techniques have been used to extend the spectrum downwards from 3×10^{18} eV, with the lower energies being explored using a novel technique that exploits the hybrid strengths of the instrument. The systematic uncertainties, and in particular the influence of the energy resolution on the spectral shape, are addressed. The spectrum can be described by a broken power-law of index 3.3 below the ankle which is measured at $\lg(E_{ankle}/eV) = 18.6$. Above the ankle the spectrum is described by a power-law $\sim E^{-2.6}$ and a flux suppression with $\lg(E_{1/2}/eV) = 19.6$.

10.2 Correlation of the Highest Energy Cosmic Rays with Nearby Extragalactic Objects in Pierre Auger Observatory Data

In 2007 the Pierre Auger Observatory has reported [216], [217] evidence of anisotropy in the CR arrival directions with energies exceeding ~60 EeV, on basis of data collected between January 1st, 2004 and August 31st, 2007. The arrival directions were correlated with the positions of nearby objects from the 12th edition of the catalog of quasars and **A**ctive **G**alactic **N**uclei (AGN) by Véron-Cetty and Véron [218] (VCV catalog). This catalog is not an unbiased statistical sample, since it is neither homogeneous nor statistically complete. This is not an obstacle to demonstrating the existence of anisotropy if CR arrive preferentially close to the positions of nearby objects in this sample. However, the nature of the catalog limits the ability of the correlation method to identify the actual sources of CR. The observed correlation identifies neither individual sources, nor a specific class of astrophysical sites of origin. It provides clues to the CR extragalactic origin with the highest energies and suggests that the suppression of the flux (see [204] and [206]) is due to interaction with the cosmic background radiation.

The analysis of correlation with AGN in the VCV catalog by including data collected through March 31st, 2009 has been repeated. The distribution of arrival directions with respect to the location of the Centaurus cluster and the radio source Cen A has been also analyzed.

The data set analyzed in 2009 is consistent with events observed by the Pierre Auger Observatory prior to March 31st, 2009. Only events with zenith angles smaller than 60º have been taken for analysis. The event selection implemented required at least five active nearest neighbors surrounding the station with the highest signal, when the event has been recorded, and the reconstructed shower core was inside an active equilateral triangle of detectors. The integrated exposure for this event selection amounts to 17040 $km^2 \cdot sr \cdot yr$ (±3%), nearly twice the exposure used in 2007 [216], when the list of only 27 events with $E > 57$ EeV has been

published. Since then, the reconstruction algorithms and calibration procedures of the Pierre Auger Observatory have been updated. The lowest energy among these same 27 events is 55 EeV according to the latest reconstruction. Reconstructed values for the arrival directions of these events differ by less than 0.1º from their previous determination. There are now 31 additional events above the energy threshold of 55 EeV. The systematic uncertainty of the observed energy for events used here is ~ 22% and the energy resolution is ~ 17% [214], [219]. The angular resolution of the arrival directions for events with energy above this threshold is better than 0.9º [220].

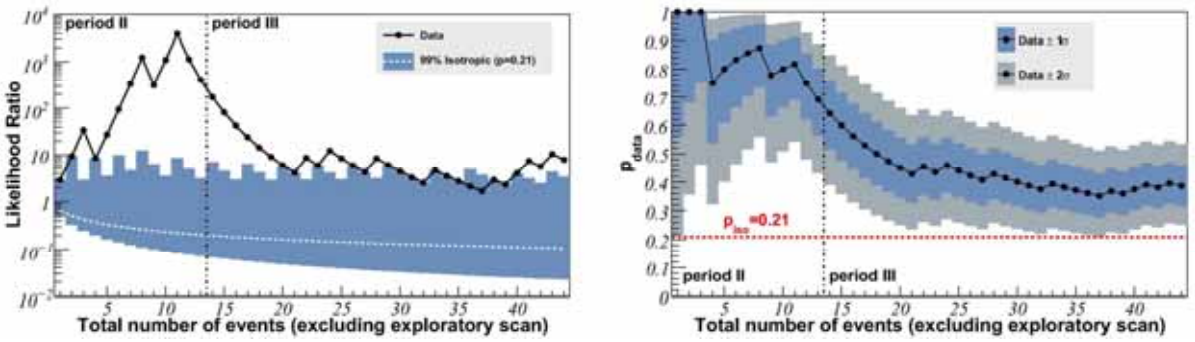

Figure 203 – Monitoring the correlation signal [221]. *Left:* The sequential analysis of cosmic rays with energy greater than 55 EeV arriving after May 27th, 2006. The likelihood ratio log10 R (see Eqn (113)) for the data is plotted in black circles. Events that arrive within $\tilde{A}$max = 3.1± of an AGN with maximum red-shift z_{max} = 0.018 result in an up-tick of this line. Values above the area shaded in blue have less than 1% chance probability to arise from an isotropic distribution (p_{iso} = 0.21). *Right:* The most likely value of the binomial parameter $p_{data} = k/N$ is plotted with black circles as a function of time. The 1¾ and 2¾ uncertainties in the observed value are shaded. The horizontal dashed line shows the isotropic value p_{iso} = 0.21. The current estimate of the signal is 0.38 ± 0.07. In both plots events to the left of the dashed vertical line correspond to period II of Table I and those to the right, collected after [216], correspond to period III.

To avoid the negative impact of trial factors in *a posteriori* analyses, the statistical significance of the anisotropy reported in [216] was established through a test with independent data. The parameters of the test were chosen by an exploratory scan using events observed prior to May 27th, 2006. The scan searched for a correlation of CR with objects in the VCV catalog with red-shift less than z_{max} at an angular scale ψ_{max} and energy threshold E_{th}. The scan was implemented to find a minimum of the probability P that k or more out of a total of N events from an isotropic flux are correlated by chance with the selected objects at the chosen angular scale, given by

$$P = \sum_{j=k}^{N} \binom{N}{j} p_{iso}^{j} (1 - p_{iso})^{N-j} \qquad (113)$$

p_{iso} has been taken to be the exposure-weighted fraction of the sky accessible to the PAO that is within ψ_{max} degrees of the selected potential sources. The minimum value of P has been found for the parameters ψ_{max} = 3.1±, z_{max} = 0.018 and E_{th} = 55 EeV (in the present energy calibration). The probability that an individual event from an isotropic flux arrives within the fraction of the sky prescribed by these parameters by chance is p_{iso} = 0.21.

Of the 27 events observed prior to August 31st, 2007, 13 were observed after the exploratory phase. Nine of these arrival directions were within the prescribed area of the sky,

where 2.7 are expected on average if the flux were isotropic. This degree of correlation provided a 99% significance level for rejecting the hypothesis that the distribution of arrival directions is isotropic.

Figure 203a displays the likelihood ratio of correlation as a function of the total number of time-ordered events observed since May 27th, 2006, i.e. excluding the data used in the exploratory scan that lead to the choice of parameters. The likelihood ratio R is defined as (see [222] and [223])

$$R = \frac{\int_{p_{iso}}^{1} p^k (1-p)^{N-k}\, dp}{p_{iso}^k (1-p_{iso})^{N-k+1}} \tag{114}$$

This quantity is the ratio between the binomial probability of correlation – marginalized over its range of possible values and assuming a flat prior – and the binomial probability in the isotropic case ($p_{\rm iso} = 0.21$). A sequential test rejects the isotropic hypothesis at the 99% significance level (and with less than 5% chance of incorrectly accepting the null hypothesis) if $R > 95$. The likelihood ratio test indicated a 99% significance level for the anisotropy of the arrival directions using the independent data reported in [216]. Subsequent data neither strengthen the case for anisotropy, nor do they contradict the earlier result. The departure from isotropy remains at the 1% level as measured by the cumulative binomial probability ($P = 0.006$), with 17 out of 44 events in correlation.

Table 13 – A numerical summary of results for events with E ≥ 55 EeV [221].

Period	Exposure	GP	N	k	k_{iso}	P
I	4390	unmasked	14	9	2.9	
		masked	10	8	2.5	
II	4500	unmasked	13	9	2.7	2×10^{-4}
		masked	11	9	2.8	1×10^{-4}
III	8150	unmasked	31	8	6.5	0.33
		masked	24	8	6.0	0.22
II+III	12650	unmasked	44	17	9.2	6×10^{-3}
		masked	35	17	8.8	2×10^{-3}
I+II	8890	unmasked	27	18	5.7	
		masked	21	17	5.3	
I+II+III	17040	unmasked	58	26	12.2	
		masked	45	25	11.3	

Figure 203b shows the degree of correlation ($p_{\rm data}$) with objects in the VCV catalog as a function of the total number of time-ordered events observed since May 27th, 2006. For each new event the best estimate of $p_{\rm data}$ is k/N. The 1σ and 2σ uncertainties in this value are determined such that the area under the posterior distribution function is equal to 68% and 95%, respectively. The current estimate, with 17 out of 44 events that correlate in the independent data, is $p_{\rm data} = 0.38$, or more than two standard deviations from the value expected from a purely isotropic distribution of events. More data are needed to accurately constrain this parameter.

The correlations between events with E ≥ 55 EeV and AGN in the VCV catalog during the pre- and post- exploratory periods of data collection are summarized in Table I. The left most column shows the period in which the data was collected. Period I is the exploratory period from January 1st, 2004 through May 26th, 2006. The data collected during this period was scanned to establish the parameters which maximize the correlation. Period II is from

May 27th, 2006 through August 31st, 2007 and period III includes data collected after [216], from September 1st, 2007 through March 31st, 2009. The numbers in bold correspond to period II+III and give the results for the post-exploratory data (see Figure 203). The exposure for each period is listed in units of km^2·sr·yr and has an uncertainty of 3%. If the region of the sky within 12º of the galactic plane (GP) is included in the analysis then the third column is marked "unmasked" (and $p_{iso} = 0.21$), if not then it is marked "masked" (and $p_{iso} = 0.25$). The average number of events from an isotropic flux expected to correlate is listed as $k_{iso} = N\, p_{iso}$, where N is the total number of events observed during each period. k is the number of events that arrive within 3.1º of an AGN with a red-shift of 0.018. The cumulative binomial probability (see Eqn (113)) is shown in the right most column. This value is not included for any row containing period I because this period was used to determine the correlation parameters for the rest of the table and cannot, therefore, be interpreted as a statistical significance.

Note that during period I+II (reported in [216]), 18 out of 27 events arrive within 3.1º of an AGN in the VCV catalog with red-shift less than 0.018. 1 There are 31 additional events (during period III) above the specified energy threshold, 8 of which have arrival directions within the prescribed area of the sky, not significantly more than the 6.5 events that are expected to arrive on average if the flux were isotropic.

While the degree of correlation with objects in the VCV catalog has decreased with the accumulation of new data, a re-scan of the complete data set shows that the values of ψ_{max}, z_{max} and E_{th} that characterize the correlation have not changed appreciably from the values reported in [216].

Next, the complete set of 58 events with energy larger than 55 EeV collected before 31 March, 2009 is analyzed. To complement the information given in Table I over different angular scales, the distribution of angular separations between the arrival directions of the 58 events with $E > 55$ EeV and the position of the closest object in the VCV catalog within red-shift $z_{max} \leq 0.018$ is plotted in Figure 204. In Figure 203b the 13 events with galactic latitudes $|b| < 12$º have been shaded. Note that only 1 of these 13 events is within 3º of a selected AGN. Incompleteness of the VCV catalog due to obscuration by the Milky Way or larger magnetic bending of CR trajectories along the galactic disk are potential causes for smaller correlation of arrival directions at small galactic latitudes.

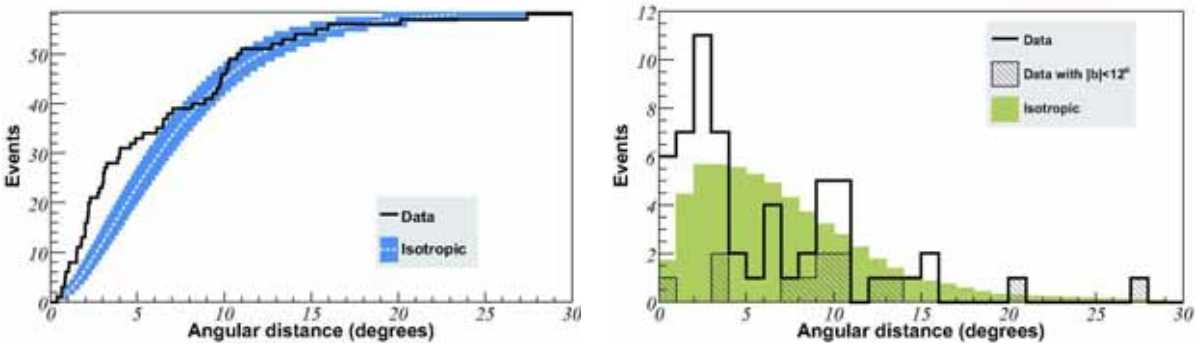

Figure 204 – The distribution of angular separations between the 58 events with $E > 55$ EeV and the closest AGN in the VCV catalog within 75 Mpc [221]. *Left:* The cumulative number of events as a function of angular distance. The 68% the confidence intervals for the isotropic expectation is shaded blue. *Right:* The histogram of events as a function of angular distance. The 13 events with galactic latitudes $|b| < 12$º are shown with hatching. The average isotropic expectation is shaded brown.

An excess of events as compared to isotropic expectations is observed from a region of the sky close to the location of the radio source Cen A ((l, b) = (−50.5º, 19.4º) [224]). Figure 205 shows the distribution of events as a function of angular distance from Cen A. In a Kolmogorov-Smirnov [225] test 2% of isotropic realizations have maximum departure from the isotropic expectation greater than or equal to the maximum departure for the observed events. The excess of events in circular windows around Cen A with the smallest isotropic chance probability corresponds to a radius of 18º, which contains 12 events where 2.7 are expected on average if the flux were isotropic. The (differential) histogram of angular distances from Cen A is in the right panel of Figure 205.

By contrast, the region around the Virgo cluster is densely populated with galaxies but does not have an excess of events above isotropic expectations. In particular, a circle of radius 20º centered at the location of M87 ((l, b) = (76.2º, 74.5º) [224]) does not contain any of the 58 events with energy E > 55 EeV. This is a region of relatively low exposure for the Pierre Auger Observatory and only 1.2 event is expected on average with the current statistics if the flux were isotropic.

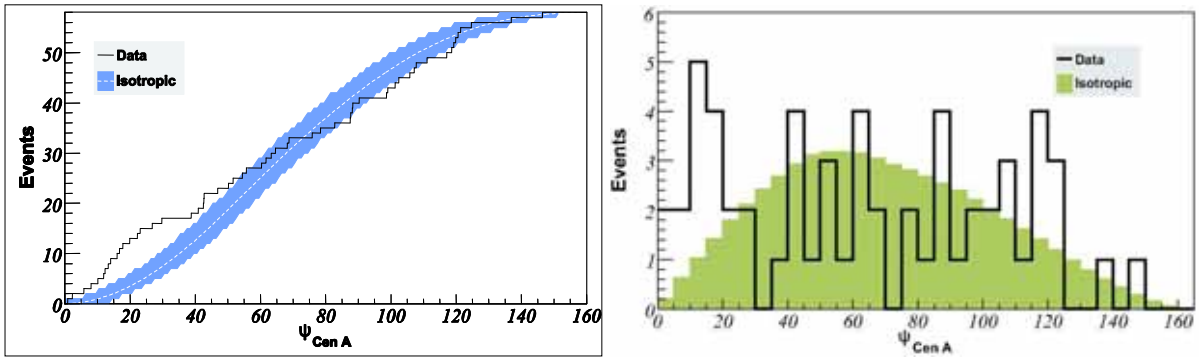

Figure 205 – Left: The cumulative number of events with $E \geq 55$ EeV as a function of angular distance from Cen A [221]. The average isotropic expectation with approximate 68% confidence intervals is shaded blue. Right: The histogram of events as a function of angular distance from Cen A. The average isotropic expectation is shaded brown.

With data collected by the Pierre Auger Observatory between January 1st, 2004 and March 31st, 2009, the analysis from [216] of correlation between the arrival directions of the highest energy cosmic rays and the positions of nearby objects has been updated from the 12th edition of the VCV catalog of quasars and active galactic nuclei. The total number of events above 55 EeV is 58. A subset of 44 events are independent of those used to determine the parameters (ψ_{max} = 3.1º, z_{max} = 0.018 and E_{th} = 55 EeV) with which we monitor the correlation signal (see Table I for more details). 17 of these 44 events correlate under these parameters. This correlation has a less than 1% probability to occur by chance if the arrival directions are isotropically distributed. The evidence for anisotropy has not strengthened since the analysis reported in [216]. The degree of correlation with objects in the VCV catalog appears to be weaker than suggested by the earliest data.

An excess of events in the present data set close to the direction of the radio source Cen A, a region dense in potential sources is observed. This excess is based on *a posteriori* data but suggests that the region of the sky near Cen A warrants further study.

10.3 Limits on the diffuse flux of ultra high energy neutrinos set using the Pierre Auger Observatory

The array of water-Cherenkov detectors of the Pierre Auger Observatory is sensitive to neutrinos of > 1 EeV of all flavors. These interact through charged and neutral currents in the atmosphere (down-going) and, for tau neutrinos, through the ”Earth skimming” mechanism (up-going). Both types of neutrinos can be identified by the presence of a broad time structure of signals in the water-Cherenkov detectors in the inclined showers that they induce when interacting close to ground. Using data collected from January 1st, 2004 to February 28th, 2009, we present for the first time an analysis based on down-going neutrinos and place a competitive limit on the all-flavor diffuse neutrino flux. We also update the previous limit for up-going tau neutrinos. Sources of possible backgrounds and systematic uncertainties are discussed.

All models of Ultra High Energy Cosmic Ray (UHECR) production predict neutrinos as the result of the decay of charged pions, produced in interactions of the CR within the sources themselves or in their propagation through background radiation fields [226], [227]. Neutrinos are also copiously produced in top-down models proposed as alternatives to explain the production of UHECRs [226].

The surface detector of the Pierre Auger Observatory allows a detection and identification of UHE neutrinos (UHE_s) in the EeV range and above. Earth-skimming tau neutrinos [228], [229] are expected to be observed through the detection of showers induced by the decay products of an emerging τ lepton, after the propagation and interaction of a flux of υ_τ inside the Earth. A limit on the diffuse flux of UHE υ_τ was already placed using this technique with data collected from January 1st, 2004 to August 31st, 2007 [229].

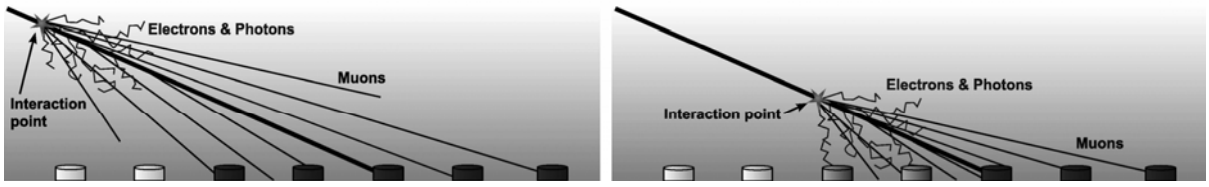

Figure 206 – Left: sketch of an inclined shower induced by a hadron interacting high in the atmosphere [230]. The EM component is absorbed and only the muons reach the detector. Right: deep inclined shower. Its early region has a significant EM component at the detector level.

The SD of the Pierre Auger Observatory is also sensitive to “down-going” neutrinos of all flavors interacting in the atmosphere, and inducing a shower close to the ground [231]. For the first time down going neutrinos and place a competitive limit on the all flavor diffuse neutrino flux have been analyzed using data from January 1st, 2004 up to February 28th, 2009. The limit on the up-going tau neutrinos has been also updated.

Identifying neutrino-induced showers in the much larger background of the ones initiated by nucleonic cosmic rays is based on a simple idea: neutrinos can penetrate large amounts of matter and generate “young” inclined showers developing close to the SD exhibiting shower fronts extended in time (Figure 206 right). In contrast, UHE particles such as protons or heavier nuclei interact within a few tens of $g \times cm^{-2}$ after entering the atmosphere, producing “old” showers with shower fronts narrower in time (Figure 106 and Figure 206 left).

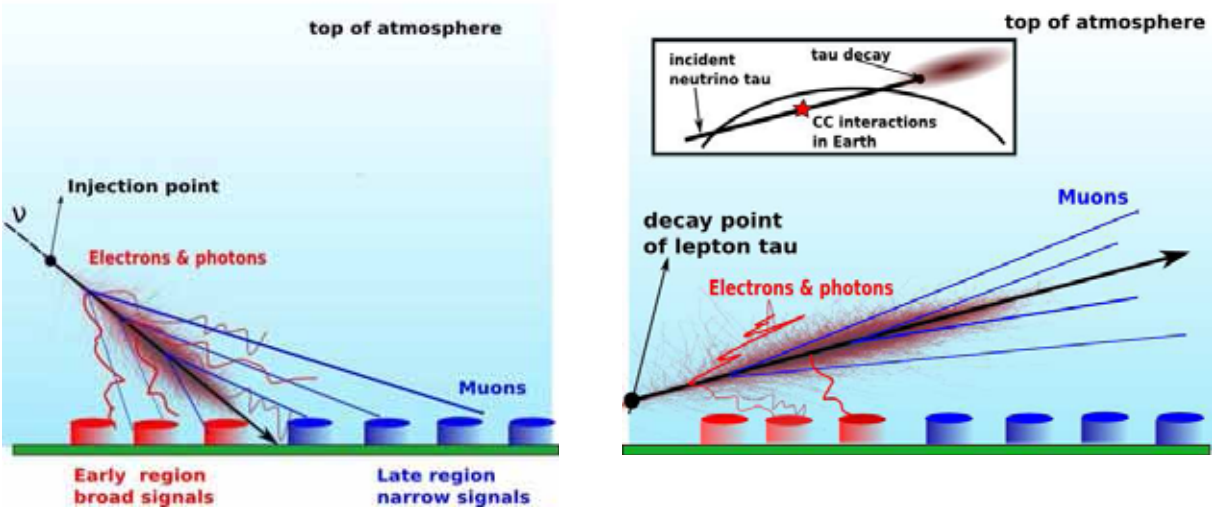

Figure 207 – Sketch of a down-going shower initiated in the interaction of a υ in the atmosphere close to the ground; In the "early" ("late") region of the shower before (after) the shower axis hits the ground we expect broad (narrow) signals in time due to electromagnetic (muonic) component of the shower (left) and The sketch of a shower induced by the decay of a τ lepton emerging from the Earth after originating from an Earth skimming υ_τ. The earliest stations are mostly triggered by electrons and γ [232].

Although the SD is not directly sensitive to the nature of the arriving particles, the 25 ns time resolution of the FADC traces in which the signal is digitized in the SD stations, allows a discrimination of narrow signals in time, expected from a shower initiated high in the atmosphere, from the broad signals expected from a young shower [232].

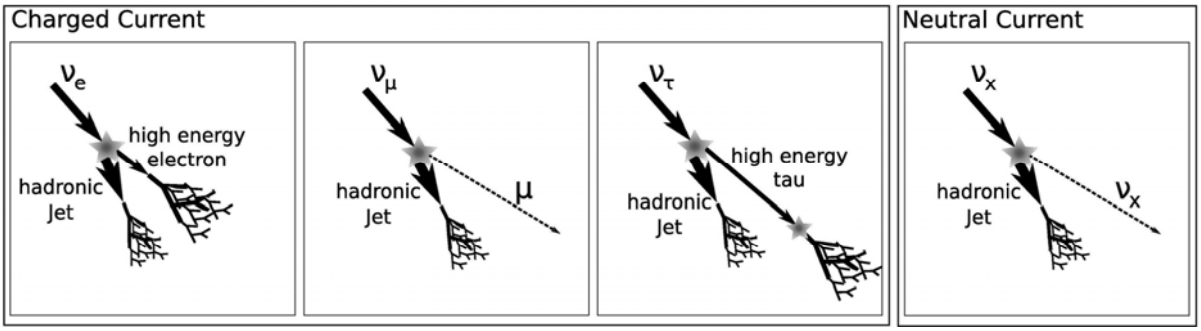

Figure 208 – Neutrinos can initiate atmospheric showers through charged (CC) or neutral (NC) current interactions [230]. On υ_e CC interactions all the energy of the primary neutrino is transferred to the shower. This is not the case of the NC channel where the primary neutrino energy is only partially transferred to the shower while a significant fraction is carried away by the scattered neutrino. Similar behavior is seen on the υ_μ CC induced showers where the emerging high energy muon usually decays under the ground and doesn't produce a shower. Note that υ_τ CC initiated showers may have a "double bang" structure due to the fact that the out-coming high energy τ may travel a long distance before decay producing a second displaced shower vertex.

Down-going neutrinos of any flavor interacting through charged (CC) or neutral (NC) current, may induce showers in the atmosphere that can be detected using the SD of the Pierre Auger Observatory (Figure 208). Detailed simulations of UHE neutrinos forced to interact deep in the atmosphere were produced. "Double bang" showers produced by tau

neutrinos (CC interaction followed by the decay in flight of the tau lepton) has been also taken into account, to simulate the tau decay products.

The simulations indicate that only the signals in the first few triggered tanks are expected to be broader in time than those induced by a shower initiated high in the atmosphere [232]. This asymmetry is due to the larger grammage of atmosphere that the later portion of the shower front crosses before reaching ground [233], (Figure 206 right).

A set of conditions has been designed to select inclined showers initiated by down-going neutrinos. As they are expected to be identified over a wide range of zenith angles, an identification criterion different from the one applied to search for up-going neutrinos (Figure 207) [229], [232] has been developed. For this purpose data collected with the SD between January 1st, 2004 and October 31st, 2007 – corresponding to ~ 1.2 years of the full SD array - was used as "training" data. From the showers that trigger the SD array, those arriving during periods in which instabilities in data acquisition occur are excluded. After that the FADC traces are cleaned to remove segments that are due to accidental muons not belonging to the shower but arriving close in time with the shower front. Moreover, if 2 or more segments of comparable area appear in a trace the station is classified as ambiguous and it's not used. Then a selection of the stations actually belonging to the event is done based on space-time compatibility among them. Events with less than 4 tanks passing the level 2 trigger algorithm are rejected. This sample is then searched for inclined events requiring that the triggered tanks have elongated patterns on the ground along the azimuth arrival direction. A length L and a width W are assigned to the pattern [232], and a cut on their ratio is applied ($L/W > 3$). Then the apparent speed of the signal in the event moving across the ground along L, using the arrival times of the signals at ground and the distances between tanks projected onto L [234] has been calculated. The average speed $\langle V \rangle$ is measured between pairs of triggered stations, and is required to be compatible with that expected in a simple planar model of the shower front in an inclined event with $\theta \geq 75^{o}$, allowing for some spread due to fluctuations ($\langle V \rangle \leq 0.313$ m·ns^{-1}). Furthermore, since in inclined events the speed measured between pairs of tanks is concentrated around $\langle V \rangle$ [229] the r.m.s. scatter of V in an event to be smaller than $0.08 \langle V \rangle$ is required. The zenith angle θ of the shower is also reconstructed, and those events with $\theta \geq 75^{o}$ are selected.

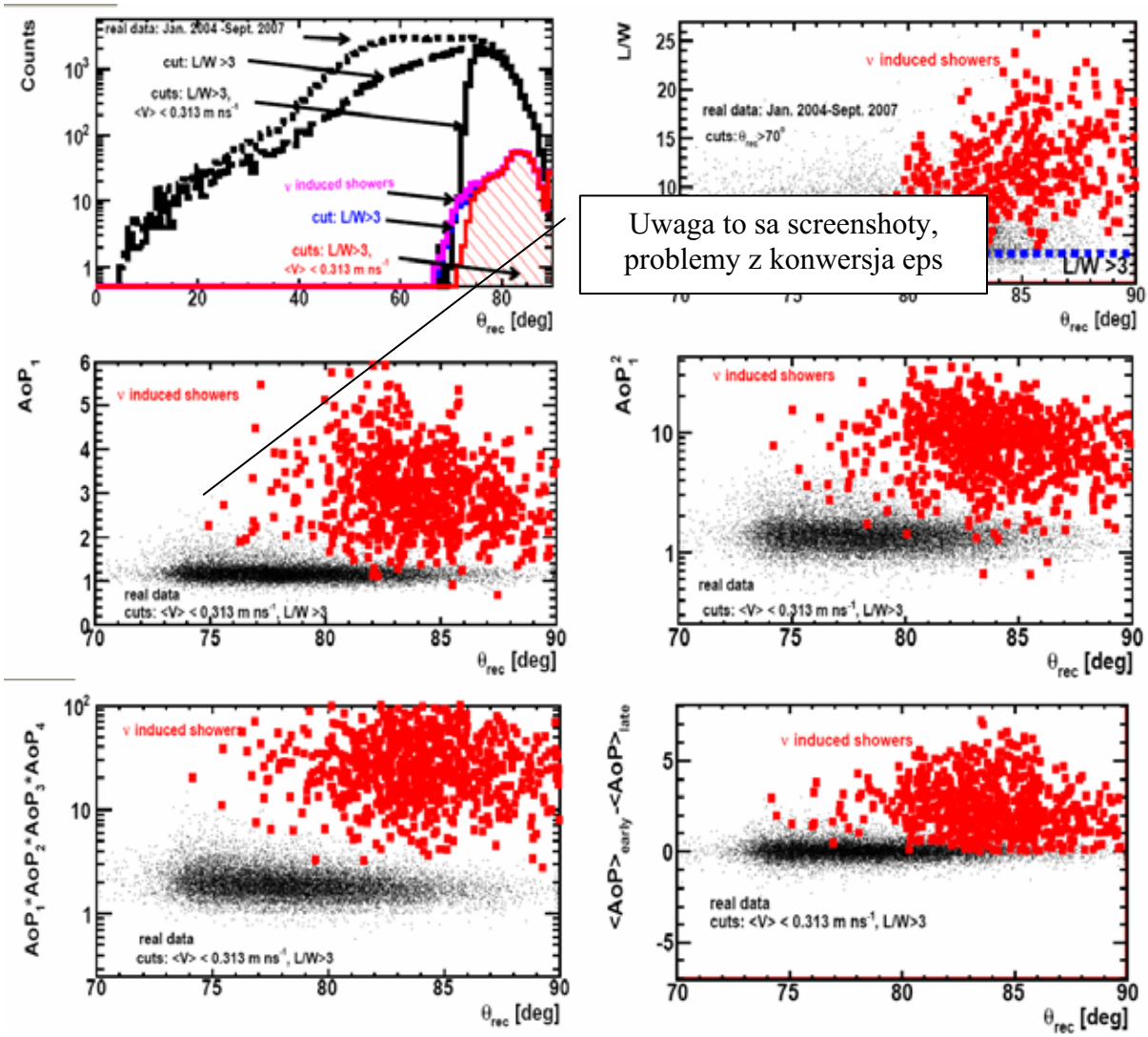

Figure 209 – (Left upper panel) The zenith angle distribution of neutrinos with E^{-2} flux and real events; (right upper panel) the ratio L/W as the function of the reconstructed zenith angle. Neutrino induced showers have larger ratio L/W than real data at high zenith angles. The area over peak for first triggering station (AoP_1) (left middle panel) the square of the area over peak for first triggering station (AoP^2_1) (right middle panel), the product of AoP of four first triggering stations (left bottom panel) and a global early-late asymmetry parameter ($<AoP>_{early} - <AoP>_{late}$) as the function of zenith angle [232].

The sample of inclined events is searched for "young" showers using observables characterizing the time duration of the FADC traces in the early region of the event. To optimize their discrimination power the Fisher discriminant method [235] to the training data – overwhelmingly has been applied, if not totally constituted of nucleonic showers – and to the Monte Carlo (MC) simulations – exclusively composed of neutrino-induced showers. Given two populations of events – nucleonic inclined showers and υ-induced showers in our case – characterized by a set of observables, the Fisher method produces a linear combination of the various observables – *f* the Fisher discriminant – so that the separation between the means of *f* in the two samples is maximized, while the quadratic sum of the r.m.s. of *f* in each of them is minimized.

Since events with a large number of tanks N (large multiplicity) are different from events with small multiplicity the sample of training data is divided into 3 sub-samples corresponding to events with number of tanks $4 \leq N \leq 6$, $7 \leq N \leq 11$ and $N \geq 12$, and a Fisher discriminant is obtained using each of the sub-samples as training data. We use the Area-over-Peak (AoP) [232] and its square of the first 4 tanks in each event, their product, and a global early-late asymmetry parameter of the event as the discriminant variables of the Fisher estimator. Distributions of these observables for real data and MC simulated neutrinos are shown in Figure 209.

Figure 210 shows the distribution of the Fisher discriminant for data collected between January 1st, 04 - October 31st, 07 and for the neutrino simulations. A clear separation between the two samples is achieved. The expected number of background events can be computed by extrapolating the exponential tail of the distribution of the data. By this means three cut values f_{cut} – corresponding to each of the sub-samples are chosen, so less than one background event every 20 years above its value is expected. Events with $f > f_{cut}$ are considered to be neutrino candidates. These cuts reject all real events in the training data samples while keeping a significant fraction of the neutrino simulations.

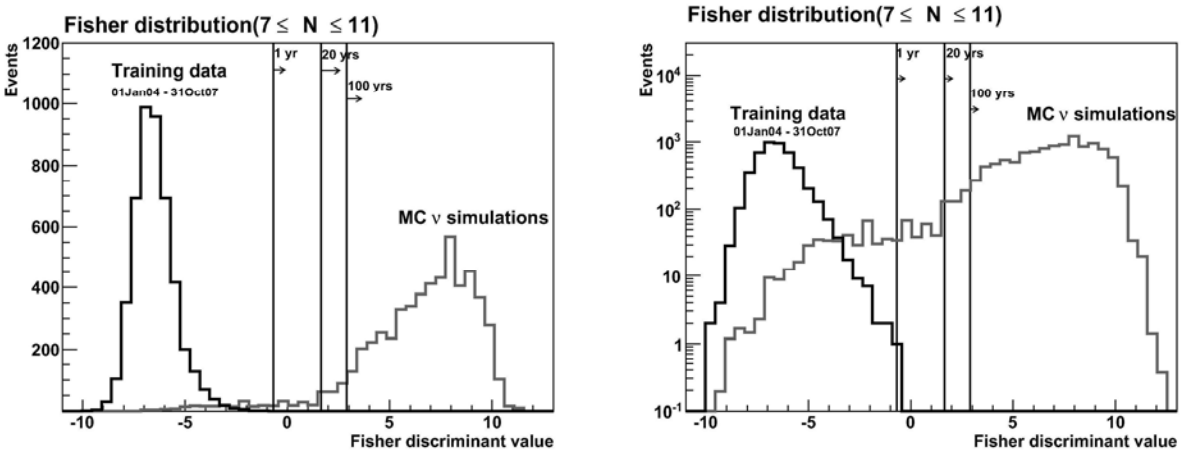

Figure 210 – Distribution of the Fisher discriminant in linear (left) and logarithmic (right) scale for real data in the training period (January 1st, 04 - October 31st, 07) and Monte Carlo simulated down-going neutrinos for events with multiplicity $7 \leq N \leq 11$ [230].

Exactly the same selection procedure and cuts in f are applied "blindly" to data collected between November 1st, 2007 and February 28th, 2009 – corresponding to ~0.8 yr of the full SD array. These data were not used for training of the Fisher method. No neutrino candidates were found and an upper limit on the UHE diffuse flux of ultra-high energy neutrinos can be placed.

For this purpose the exposure of the SD array to UHE neutrinos is calculated. For down-going neutrinos this involves folding the SD array aperture with the interaction probability and the identification efficiency, and integrating in time taking into account changes in the array configuration due to the installation of new stations and instabilities in data taking. The identification efficiency ε, for the set of cuts defined above, depends on the neutrino energy E_υ, the depth along the atmosphere at which the neutrino interacts D, the zenith angle θ, the position of the shower in the surface S covered by the array, and the time t through the instantaneous configuration of the array. Moreover it depends on the neutrino flavor (υ_e, υ_μ or υ_τ), and the type of interaction – charged (CC) or neutral current (NC) – since the different combinations of flavor and interaction induce different type of showers. The

efficiencies ε were obtained through MC simulations of the development of the shower in the atmosphere and the simulation of the surface detector array.

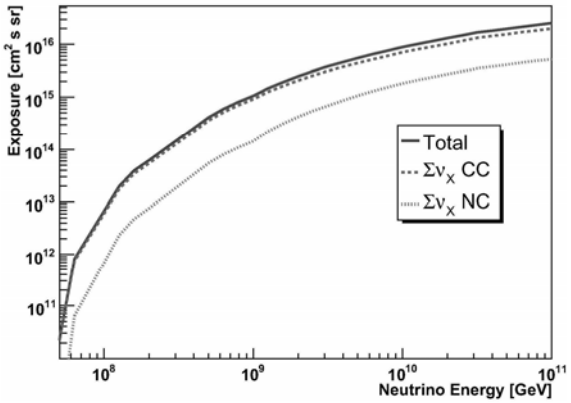

Figure 211 – Exposure of the SD array to down-going neutrinos in the search period (November 1st, 2007 up to February 28th, 2009) [230].

The exposure was calculated using purely MC techniques and also integrating the neutrino identification efficiencies ″ over the whole parameter space [232]. All the neutrino flavors and interactions are accounted for in the simulations. In particular for υ_τ the possibility that it produces a double shower in the atmosphere triggering the array – one in the υ_τ CC interaction itself and another in the decay of the τ lepton, has been taken into account. The exposure for the period November 1st, 2007 up to February 28th, 2009 is shown in Figure 211 for CC and NC channels.

Several sources of systematic uncertainties have been taken into account and their effect on the evaluated exposure. A ~ 20% systematic uncertainty due to the neutrino-induced shower simulations and the hadronic model (SIBYLL 2.1 vs QGSJETII.03) has been tentatively assigned. Another source of uncertainty comes from the neutrino cross section. Using [236] we estimate a systematic uncertainty of ~ 10%. The topography around the Southern Site of the Pierre Auger Observatory enhances the flux of secondary τ leptons. However, this effect has been neglected. Simulations indicated that including it will improve the limit by roughly ~ 15 – 20%.

Finally assuming a $f(E_\upsilon) = k\, E_\upsilon^{-2}$ differential neutrino flux we have obtained a 90% C.L. limit on the all-flavor neutrino flux using down-going showers:

$$k < 3.2 \times 10^{-7}\, Gev \cdot cm^{-2} \cdot s^{-1} \cdot sr^{-1} \tag{115}$$

shown in Figure 212. The updated limit based on Earth-skimming up-going neutrinos:

$$k < 4.7^{-2.5}_{+2.2} \times 10^{-7}\, Gev \cdot cm^{-2} \cdot s^{-1} \cdot sr^{-1} \tag{116}$$

where the upper/lower values correspond to best/worse scenario of systematics [234]. The limit in differential format to show the range in energies at which the sensitivity of the Pierre Auger Observatory to down-going and Earth-skimming υ peaks has also been included.

A preliminary limit on the flux of UHE neutrinos from the position of Centaurus A (Galactic coordinates – δ ~ -43º , l ~ -35.2º) – assuming a point source at that position – was also obtained. For that purpose we have integrated the identification efficiency ″ over the fraction of the time (~15.6%) the source is seen in the SD array with θ between 75º and 90º. The preliminary limit is ~ 3×10^{-6} neutrinos per GeV cm^{-2} s^{-1}.

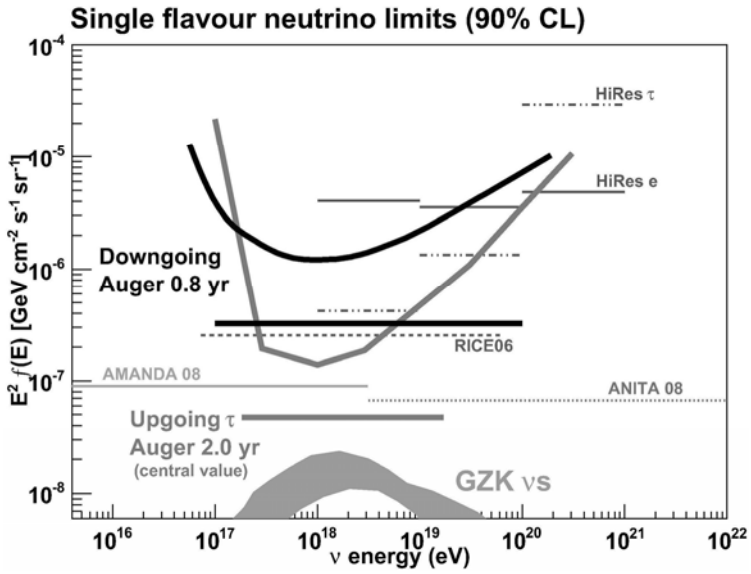

Figure 212 – Differential and integrated upper limits (90% C.L.) from the Pierre Auger Observatory for a diffuse flux of down-going υ in the period November 1st, 2007 up to February 28th, 2009 and up-going υ (January 1st, 04 - February 28th, 2009) [230]. Limits from other experiments [237] and a theoretical flux for GZK neutrinos [227] are shown.

11 Summary

The history of the Pierre Auger Observatory has started in 1992, when Jim Cronin (Nobel prize winner) and Alan Watson decided to realize their dreams on huge cosmic ray detector allowing explaining mysteries of the Universe. Although from the beginning such giant project seemed to be rather unrealistic, however heroic Jim and Alan's efforts crystallized and materialized at present in the world largest experiment investigating the UHECR. The way from the idea to the practical realization was long and rugged. The idea is magnificent; nevertheless to build the giant detector, a lot of scientists and technicians had to solve a lot of minor and major technical and practical problems. Only thanks to a brilliant cooperation of more than 400 people from 18 countries, Pierre Auger Observatory has become the powerful tool challenging the current physics.

In the author's humble opinion, the ideas presented above made the significant progress in the Pierre Auger Observatory development and allowed building the detector in the highest technological level available in that time.

12 Abbreviations

ACEX - family of Altera® cost-effective PLD chips,
AGASA - **A**keno **G**iant **A**ir **S**hower **A**rray,
AGN - **A**ctive **G**alactic **N**uclei,
AHDL - **A**ltera **H**ardware **D**escription **L**anguage,
AMIGA - **A**uger **M**uons and **I**nfill for the **G**round **A**rray,
AoT - **A**rea **o**ver **T**hreshold,
APEX - family of Altera® PLD chips,
ASIC - **A**pplication **S**pecified **I**ntegrated **C**ircuit,
CAM - **C**ontent-**A**ddressable **M**emory,
~CAS3 - **C**olumn **A**ddress **S**trobe signal (active low state),
CDAS - **C**entral **D**ata **A**cquisition **S**ystem,
CERN - **C**onseil **E**uropéen pour la **R**echerche **N**ucléaire,
CLF - **C**entral **L**aser **F**acility,
CMB - **C**osmic **M**icrowave **B**ackground,
CR - **C**osmic **R**ays,
CVS - **C**oncurrent **V**ersioning **S**ystem,
DFF - **D** **F**lip-**F**lop,
DMA - **D**irect **M**emory **A**ccess,
DPRAM - **D**ual-**P**ort **R**andom **A**ccess **M**emory,
DSP - **D**igital **S**ignal **P**rocessing,
EA - **E**ngineering **A**rray,
EAB - **E**mbedded **A**rray **B**lock,
EAS - **E**xtensive **A**ir **S**hower,
EGRET - **E**nergetic **G**amma-**R**ay **E**xperiment **T**elescope,
ESB - **E**mbedded **S**ystem **B**lock,
FADC - **F**lash **A**nalog to **D**igital **C**onverter,
FD - **F**luorescence **D**etector,
FE - **F**ront **E**nd,
FEB - **F**ront **E**nd **B**oard,
FFT - **F**ast **F**ourier **T**ransform,
FIFO - **F**irst **I**n **F**irst **O**ut (type of memory),
FLEX - family of Altera® PLD chips,
FLT - **F**irst **L**evel **T**rigger,
FPGA - **F**ield **P**rogrammable **G**ate **A**rray,
GCR - **G**alactic **C**osmic **R**ays,
GPS - **G**lobal **P**ositioning **S**ystem,
GRB - **G**amma **R**ay **B**ursts,
GUT - **G**rand **U**nified **T**heories,
GZK - effect of **G**reisen, **Z**atsepin, and **K**uzmin,
I/O - **I**nput **O**utput system,
KASCADE - **KA**rlsruhe **S**hower **C**ore and **A**rray **De**tector,
kpps - **k**ilo **p**ulse **p**er **s**econd,
LAN - **L**ocal-**A**rea **N**etwork,
LE - **L**ogic **E**lement,

LPM - **L**ibrary of **P**arameterized **M**odules
LUT - **L**ook **U**p **T**able**,**
μC - micro-controller**,**
Msps - **M**ega **s**ample **p**er **s**econd,
MSI - **M**iddle **S**cale of **I**ntegration,
MTU - **M**ichigan **T**echnological **U**niversity,
MUX - multiplexer,
PAO - **P**ierre **A**uger **O**bservatory,
PLD - **P**rogrammable **L**ogic **D**evices,
PLL - **P**hase **L**ocked **L**oop,
PMT - **P**hoto-**M**ultiplier **T**ube,
PoT - **P**ower **o**ver **T**hreshold,
pps - **p**ulse **p**er **s**econd,
RAM - **R**andom **A**ccess **M**emory,
ROM - **R**ead **O**nly **M**emory,
SD - **S**urface **D**etector,
SDE - **S**urface **D**etector **E**lectronics,
SDP - **S**hower **D**etector **P**lane,
SLT - **S**econd **L**evel **T**rigger,
SUGAR - **S**ydney **U**niversity **G**iant **A**ir Shower **R**ecorder,
ToT - **T**ime **o**ver **T**hreshold (type of trigger),
UB - **U**nified **B**oard (board with μC and controlling the SDE),
UHECR - **U**ltra–**H**igh **E**nergy **C**osmic **R**ays,
UV - **U**ltra-**V**iolet radiation,
VEM - **V**ertical **E**quivalent **M**uon unit,
VHDL - **V**ery High Speed **H**ardware **D**escription **L**anguage,
VLSI - **V**ery **L**arge **S**cale of **I**ntegration,
WS - **W**ait **S**tate.

13 References

[1] P. Auger *et al*., Comptes Rendus **206**, 1721 (1938),
P. Auger, Rev. Mod. Phys. **11**, 288 (1939),

[2] J. Linsley, *Evidence for a Primary Cosmic-Ray Particle with Energy 10^{20} eV*, Phys. Rev. Lett. **10**, 146 (1963),

[3] A. A. Penzias and R. W. Wilson, Ap.J. **142**, 419 (1965),

[4] G. T. Zatsepin and V. A. Kuźmin, JETP Letters **4**, 78 (1966),
K. Greisen, *End to the Cosmic-Ray Spectrum?* Phys. Rev. Lett. **16**, 748 (1966),

[5] M. Takeda *et al*., *Small-Scale Anisotropy of Cosmic Rays above 10^{19} eV Observed with the Akeno Giant Air Shower Array*, Ap.J. **522**, 225 (1999),
Y. Uchihori *et al*., *Cluster analysis of extremely high energy cosmic rays in the northern sky,* Astropart. Phys. **13,** 151 (2000),

[6] J.W. Belz for the HiRes Collaboration, *Anisotropy Studies of Ultra-High Energy Cosmic Rays Using Monocular Data Collected by the High-Resolution Fly's Eye (HiRes),* Proc. 28th ICRC, Tsukuba, Japan, **HE 1.3**, 425 (2003),

[7] C.B. Finley, S. Westerhoff, *On the Evidence for Clustering in the Arrival Directions of AGASA's Ultrahigh Energy Cosmic Rays,* astro-ph/**0309159**,

[8] M. Nagano, A. A. Watson, *Observations and implications of the ultrahigh-energy cosmic rays,* Rev. Mod. Phys. **72,** 689 (2000),

[9] Yu. A. Fomin *et al*., Proc. 20th ICRC, Moscow, USSR, **6**, 110 (1987),

[10] J. W. Cronin, Nucl. Phys**. 28B** (Proc. Supp.), **213**, 2130 (1992),

[11] E. Fermi, Phys. Rev., **75**, 1169 (1949),

[12] G. F. Krymsky, Dok. Acad. Nauk. USSR, **234**, 1306 (1977),
R. D. Blandford, J. P. Ostriker, Astrophys. J., **221**, L29 (1978),

[13] A. M. Hillas, Ann. Rev. Astronomy. & Astrophysics. **22**, 425 (1984),

[14] P. Meszaros, *Theories of Gamma-Ray Bursts*, astro-ph/**0111170**,

[15] G. Sigl, *Particle and Astrophysics Aspects of UHECR*, astro-ph/**0008364**,

[16] M. Takeda *et al., Energy Determination in the Akeno Giant Air Shower Array Experiment,* Proc. 28th ICRC, Tsukuba, Japan, 381 (2003),

[17] N. Hayashida *et al*., *Updated AGASA event list above 4×10^{19}eV*, astro-ph/**0008102**,

[18] T. Abu-Zayyad et al., *Measurement of the CR Energy Spectrum and Composition from 10^{17} to $10^{18.3}$ eV using a Hybrid Fluorescence Technique*, astro-ph/**0010652**,

[19] D. De Marco *et al*., *The GZK Feature in the Spectrum of UHECRs: What is it Telling Us?* Proc. 28th ICRC, Tsukuba, Japan, 655 (2003),

[20] D. R. Bergman for the HiRes Collaboration, *Measurement of the Flux of UHE Cosmic Rays by the HiRes Detectors Observing in Monocular Mode*, Proc. 28th ICRC, Tsukuba, Japan, 397 (2003),

[21] A. Cordero, E. Cantoral, A. Fernandez, R. Pastrana, *Proposal for the Optical System of the Fluorescence Detectors of the Pierre Auger Project*, GAP-1996-039 (1996),
Pierre Auger Collaboration, *The Fluorescence Detector of the Pierre Auger Observatory*, submitted to NIMA (2009),

[22] Pierre Auger Design Report, http://www.auger.org/admin/DesignReport/index.html

[23] P. Sommers, *Capabilities of a giant hybrid air shower detector*, Astropart. Phys., **3,** 349 (1995),
M. Giller, G. Wieczorek, A. Kacperczyk, H. Stojek, W. Tkaczyk, *Energy spectra of electrons in the extensive air showers of ultra-high energy*, J. Phys. G: Nucl. Part. Phys. **30,** 97 (2004),
M. Giller, A. Kacperczyk, J. Malinowski, W.Tkaczyk and G. Wieczorek, *Similarity of extensive air showers with respect to the shower age*, J. Phys. G: Nucl. Part. Phys. **31,** 947 (2005),

[24] I. Lhenry-Yvon, T. Suomijärvi, B. Genolini, T.Nguyen Trung, E. Parizot, J. Pouthas, IPNO DR-01-009, 2001,
[25] http://lb.auger.org.ar/Deployment/,
[26] H.Salazar, L.Nellen, L.Villasenor, for the Pierre Auger Collaboration, *Statistical and systematic uncertainties in the event reconstruction and S(1000) determination by the Pierre Auger surface detector*, Proc. 27th ICRC, Hamburg, Germany (2001),
[27] Pierre Auger Database, ccali.in2p3.fr/sps/pauger/Malargue/Raid/data,
[28] S.Argiro *et al*., *The Analog Signal Processing System for the Auger Fluorescence Detector Prototype*, GAP-2000-048 (2000),
[29] Z. Szadkowski, *FPGA based triggers in the Pierre Auger Observatory***,** Proc. SPIE Vol. **6937,** 69370V (2007),
[30] T. Kutter, C. Pryke, *Self Calibration of the Water Cerenkov Tanks: Experimental Results*, GAP-1997-025 (1997),
[31] M. Aglietta *et al.* for the Pierre Auger Collaboration, *Calibration of the surface array of the Pierre Auger Observatory*, Proc. 29th ICRC, Pune, India (2005),
[32] A. Tripathi, T. Ohnuki, K. Arisaka, M. Healy, D. Barnhill, W. Slater, *A Systematic Calibration of Surface Detectors using Muon Data from the EA*, GAP-2002-046 (2002), http://www.auger.org/admin/GAP_Notes/,
[33] Z. Szadkowski, *An Analysis of Propagation Times for the Altera Largest and Fastest FLEX10k Chip to the Fast First Level Trigger in Auger Fluorescence Detector*, GAP-1998-023 (1998),
[34] Z. Szadkowski, *An Implementation of the Altera FLEX10k Family to the Fast First Level Trigger in Auger Fluorescence Detector*, GAP-1998-029 (1998),
[35] Z. Szadkowski, *Second-level Trigger in the Pierre Auger Fluorescence Detector*, Nucl. Instr. Meth. **A465,** 540 (2001),
[36] H. Gemmeke, A. Grindler, H. Keim, M. Kleifges, N. Kunka, Z. Szadkowski, D. Tcherniakhovski*, Design of the Trigger System for the Auger Fluorescence Detector,* IEEE Transaction on Nuclear Science, **47**, 2 (2000),
[37] R. Ball, D. Nitz, *Auger Front End Planning Schematics*, Rev. C2, GAP-1998-067 (1998),
[38] Z. Szadkowski, *A PLD200 First Level Fast Trigger in the Pierre Auger Observatory Surface Detector*, GAP-2002-050 (2002).
[39] http://www.altera.com
[40] D. Allard,…, Z. Szadkowski,. *et al*. for the Pierre Auger Collaboration, *The trigger system of the Pierre Auger Surface Detector: operation, efficiency and stability*, Proc. 29th ICRC, Pune, India (2005),
[41] C.Bonifazi for the Pierre Auger Collaboration, *Angular Resolution of the Pierre Auger Observatory*, Proc. 29th ICRC, Pune, India (2005),
[42] D. Allard,…, Z. Szadkowski,. *et al*. for the Pierre Auger Collaboration, *The trigger system of the Pierre Auger Surface Detector: operation, efficiency and stability*, Proc. 29th ICRC, Pune, India (2005),
[43] Z. Szadkowski, *A PLD200 First Level Slow Trigger in the Pierre Auger Observatory Surface Detector*, GAP-2002-058 (2002),
[44] Z. Szadkowski, D. Nitz, *A PLD Implementation of the Pierre Auger Observatory First Level Trigger*, Proc 27th ICRC, Hamburg, Germany (2001),
[45] Z. Szadkowski *et al*., *The Surface Detector Trigger for the Pierre Auger Observatory*, 805, 28th ICRC, Tsukuba, Japan (2003),
[46] Z. Szadkowski, D. Nitz, *Implementation of the first level surface detector trigger for the Auger Observatory Engineering Array*, Nucl. Instr. Meth. **A545,** 624 (2005),
[47] Z. Szadkowski, *A PLD100 First Level Trigger in the Pierre Auger Observatory Surface Detector,* GAP-2002-069 (2002),
[48] Z. Szadkowski, *The concept of an ACEX cost-effective first level surface detector trigger in the Pierre Auger Observatory*, Nucl. Instr. Meth. **A551,** 477 (2005),

[49] Z. Szadkowski, Pierre Auger Collaboration Meeting, Malargüe, April 21-25, 2002,
[50] Z. Szadkowski, *Preliminary Temperature and High Frequency Tests for PLD100 (ACEX) Surface Detector Trigger*, GAP-2002-070 (2002).
[51] Z. Szadkowski, *A Proposal of a Single Chip or 80 MHz sampling Surface Detector Trigger based on Altera Cyclone™ Family*, GAP-2002-071 (2002),
[52] Z. Szadkowski, *A Proposal of a Single Chip Surface Detector Trigger Based On Altera® Cyclone™ Family*, Proc. 28th ICRC, Tsukuba, Japan, 809 (2003),
[53] Z. Szadkowski, K-H. Kampert, *Deutsche Physikalische Gesellschaft*, Mainz (29.03–01.04.2004),
[54] Intratec GmbH, Beim Haferhof 5, D-25479 Ellerau; www.intratec.de,
[55] Z. Szadkowski *et al*., *The 3rd Generation Front-End Cards of the Pierre Auger Surface Detectors: Test Results and Performance in the Field*, Nucl. Instr. Meth, **A606,** 439 (2009),
[56] M.A DuVernois, *Surface Detector Temperature Profiles in Summer*, GAP-2001-014 (2001),
[57] http://www.altera.com/products/devices/cyclone3/overview/cy3-overview.html
[58] Z. Szadkowski, *A prototype of 100 MHz sampling 1st level surface detector trigger in the Pierre Auger Observatory based on a single CycloneIII™ FPGA*, Proc. 31st ICRC, Łódź, Poland (2009),
[59] Z. Szadkowski, K-H. Kampert, *Analysis of the SD-PLD firmware and implications to physics data*, GAP-2006-27,
[60] V. S. Berezinski, G. T. Zatsepin, *Cosmic Rays at ultra high energies (neutrinos?)*, Phys. Lett. **B28,** 423 (1969),
[61] L. Nellen for Pierre Auger Collaboration, *Detection of Very Inclined Showers with the Auger Observatory*, Proc. 29th ICRC, Pune, India (2005),
[62] E. Zas, *Neutrino Detection with Inclined Air Showers*, astro- ph/**0504610**,
[63] Z. Szadkowski, *16-point Discrete Fourier Transform based on the Radix-2 FFT algorithm implemented into Cyclone FPGA as the UHECR trigger for horizontal air showers*, Proc. 29th ICRC, Pune, India (2005),
[64] M. Aglietta *et. al*, Response of the Pierre Auger Observatory Water Cherenkov Detectors to Muons, Proc. 29th ICRC, Pune, India (2005),
[65] Z. Szadkowski, 4*th* generation of the 1*st* level surface detector trigger in the Pierre Auger Observatory, Proc. 30th ICRC, Merida, Mexico (2007),
[66] H.J. Nussbauer, *Fast Fourier Transform and Convolution Algorithms*, Springer-Verlag, Berlin, 1981,
[67] http://www.altera.com/products/ip/dsp/transforms/m-ham-fft.html
[68] Z. Szadkowski, *16-point Discrete Fourier Transform based on the Radix-2 FFT algorithm implemented into Cyclone FPGA as the UHECR trigger for horizontal air showers*, Nucl. Instr. Meth. **A560/2**, 309 (2005),
[69] Z. Szadkowski, K-H. Becker, K-H. Kampert, "*Development of a New First Level Trigger for the Surface Array in the Pierre Auger Observatory based on the Cyclone™ Altera® FPGA*", *Nucl. Instr. Meth.*, **A545,** 793 (2005),
[70] Y. Arai, T. Agui, M. Nakajima, *A fast DCT-SQ scheme for images*, Trans. IEICE, E-71, **11** 1095 (1988),
[71] Z. Szadkowski, *16-point DCT as the spectral 1st level SD trigger in the Pierre Auger Observatory*, Proc. 30th ICRC, Merida, Mexico (2007),
[72] Z. Szadkowski, *An optimization of 16-point Discrete Cosine Transform implemented into a FPGA as a spectral 1st level surface detector trigger in the Pierre Auger Observatory*, NSS & MIC, IEEE, Dresden 2008,
[73] Z. Szadkowski, *A spectral 1st level FPGA trigger for detection of very inclined showers based on a 16-point Discrete Cosine Transform for the Pierre Auger Observatory*, Nucl. Instr. Meth. **A606,** 330 (2009),

[74] D. Barnhill *et. al.* for the Pierre Auger Observatory, *Measurement of the lateral distribution function of UHECR air showers,* Proc. 29th ICRC, Pune, India (2005),
[75] J. Brack *et al*., for the Auger Collaboration, *Absolute Calibration of the Auger Fluorescence Detectors*, 29th ICRC, Pune, India (2005),
[76] C. Aramo *et al*., for the Auger Collaboration, *Optical Relative Calibration and Stability Monitoring for the Auger Fluorescence Detector*, Proc. 29th ICRC, Pune, India (2005),
[77] F. Arqueros *et al*., for the Auger Collaboration, *A Technique for the Optical Characterization of Imaging Air-Cherenkov Telescopes*, Proc. 29th ICRC, Pune, India (2005),
[78] The Pierre Auger Collaboration, *Performance of the Fluorescence Detectors of the Pierre Auger Observatory*, Proc. 29th ICRC, Pune, India (2005),
[79] C. Bonifazi *et. al*., for Pierre Auger Collaboration, *Angular Resolution of the Pierre Auger Observatory*, Proc. 29th ICRC, Pune, India (2005),
[80] P. Bauleo *et. al*., for the Pierre Auger Collaboration, *Absolute Calibration of the Auger Fluorescence Detectors*, Proc. 29th ICRC, Pune, India (2005),
[81] F. Nerling *et al*., *Parameterisation of Cherenkov light production in high-energy showers*, Proc. 29th ICRC, Pune, India (2005),
[82] M. Nagano *et. al*., *New measurements on photon yields from air and the application to the energy estimation of primary cosmic rays*, Astropart. Phys., **22**, 235 (2004),
[83] H. Barbosa, *et. al*., *Determination of the calorimetric energy in extensive air showers*, Astropart. Phys., **22**, 159 (2004),
[84] Pierre Auger Collaboration (J. Abraham,…,Z. Szadkowski,…*et. al*.), *Properties and Performance of the Prototype Instrument for the Pierre Auger Observatory*, Nucl. Instr. Meth. **A523**, 50 (2004),
[85] X. Bertou , for the Pierre Auger Collaboration*, Calibration and Monitoring of the Pierre Auger Surface Detectors*, Proc. 28th ICRC, Tsukuba, Japan, 813 (2003),
[86] X. Bertou for the Pierre Auger Collaboration, *Performance of the Pierre Auger Observatory Surface Array*, Proc. 29th ICRC, Pune, India (2005),
[87] Pierre Auger Collaboration, *Statistical and systematic uncertainties in the event reconstruction and S(1000) determination by the Pierre Auger surface detector*, Proc. 29th ICRC, Pune, India (2005),
[88] Pierre Auger Collaboration, *The Hybrid Performance of the Pierre Auger Observatory*, Proc. Proc. 29th ICRC, Pune, India (2005),
[89] G. Medina-Tanco, *JEM-EUSO Science Objectives*, Proc. 31st ICRC, Łódź, Poland (2009),
[90] P. Sommers for the Pierre Auger Collaboration, *First Estimate of the Primary Cosmic Ray Energy Spectrum above 3 EeV from the Pierre Auger Observatory*, Proc. 29th ICRC, Pune, India (2005),
[91] M. Takeda *et al*., *Energy determination in the Akeno Giant Air Shower Array experiment*, Astropart. Phys. **19**, 447 (2003),
[92] P. Mantsch, Pierre Auger Observatory, *Progress and First Results*, Proc. 29th ICRC, Pune, India (2005),
[93] High Resolution Fly's Eye Collaboration, *Observation of the ankle and evidence for a high-energy break in the cosmic ray spectrum*, Phys. Lett. **B619**, 271 (2005),
[94] J. Matthews for the Pierre Auger Collaboration, *A description of some ultra high energy cosmic rays observed with the Pierre Auger Observatory*, Proc. 29th ICRC, Pune, India (2005),
[95] G. Gelmini, O.E. Kalashev, and D.V. Semikoz, *GZK Photons as Ultra High Energy Cosmic Rays,* astro-ph/**0506128** and references therein,
[96] C.T. Hill, *Monopolonium*, Nucl. Phys. **B224**, 469 (1983),
M.B. Hindmarsh, T.W.B. Kibble, Rep. Prog. Phys. **58**, 477 (1995),
[97] http://cossc.gsfc.nasa.gov/docs/cgro/egret/
[98] V. Berezinsky, M. Kachelrieß, A. Vilenkin, *Ultrahigh Energy Cosmic Rays without Greisen-Zatsepin-Kuzmin Cutoff,* Phys. Rev. Lett. **79**, 4302 (1997),

M. Birkel, S. Sarkar, *Extremely high energy cosmic rays from relic particle decays,* Astropart. Phys. **9**, 297 (1998),
[99] J. Ellis, V. Mayes, D.V. Nanopoulos, *UHECR Particle Spectra from Crypton Decays* , astro-ph/**0512303**,
[100] T.J. Weiler, Phys. Rev. Lett. **49**, 234 (1982),
T.J. Weiler, *Cosmic-ray neutrino annihilation on relic neutrinos revisited: a mechanism for generating air showers above the Greisen-Zatsepin-Kuzmin cutoff,* Astropart. Phys. **11**, 303 (1999),
D. Fargion, B. Mele, A. Salis, *Ultra-High-Energy Neutrino Scattering onto Relic Light Neutrinos in the Galactic Halo as a Possible Source of the Highest Energy Extragalactic Cosmic Rays***,** Astrophys. J. **517**, 725 (1999),
[101] N. Kalmykov, S. Ostapchenko, A. Pavlov, *Quark-gluon-string model and EAS simulation problems at ultra-high energies,* Nucl. Phys. B (Proc. Suppl.) **52B**, 17 (1997),
[102] S. Ostapchenko, *QGSJET-II: towards reliable description of very high energy hadronic interactions*, Nucl. Phys. B (Proc. Suppl.) **151** , 143 (2006),
[103] J. Knapp et al., *Extensive air shower simulations at the highest energies*, Astropart. Phys. **19**, 77 (2003),
[104] The Pierre Auger Collaboration, *Upper limit on the primary photon fraction from the Pierre Auger Observatory*, Proc. 29th ICRC, Pune, India (2005),
[105] The Pierre Auger Collaboration, An *upper limit on the photon fraction in cosmic rays above 10^{19} eV from the Pierre Auger Observatory*, Astropart. Phys. **27**, 155 (2007),
[106] M. Risse *et al*., *Upper Limit on the Photon Fraction in Highest-Energy Cosmic Rays from AGASA Data***,** Phys. Rev. Lett. **95**, 171102 (2005),
[107] K. Shinozaki *et al*., *Upper Limit on Gamma-Ray Flux above 10^{19} eV Estimated by the Akeno Giant Air Shower Array Experiment*, Astrophys. J. **571**, L117 (2002),
[108] M. Ave *et al*., *New Constraints from Haverah Park Data on the Photon and Iron Fluxes of Ultrahigh-Energy Cosmic Rays***,** Phys. Rev. Lett. **85**, 2244 (2000); Phys. Rev. **D65**, 063007 (2002),
[109] N. Hayashida *et al*., (AGASA Collaboration), *The Anisotropy of Cosmic Ray Arrival Direction around 10^{18} eV*, astro-ph/**9906056**,
[110] J.A. Bellido *et al*., *Southern Hemisphere Observations of a 10^{18}eV Cosmic Ray Source Near the Direction of the Galactic Center*, astro-ph/**0009039**,
[111] The Pierre Auger Collaboration, *Anisotropy Studies Around the Galactic Centre at EeV Energies with Auger Data, Proc.* 29th ICRC, Pune, India (2005),
[112] M. Bossa *et al*., *Decaying neutron propagation in the galaxy and the cosmic ray anisotropy at 1 EeV*, J. Phys G **29**, 1409 (2003),
[113] F. Aharonian, A. Neronov, *High energy gamma rays from the massive black hole in the galactic center*, astro-ph/**0408303**,
[114] T. Antoni *et al*, *The cosmic-ray experiment KASCADE*, Nucl. Instr. Meth **A513**, 490 (2003),
[115] A. F. Badea *et al*., *The KASCADE-Grande Experiment and the LOPES Project*, Nucl. Phys. B (Proc. Suppl.) **136**, 384 (2004),
[116] G. Navarra *et al*, *KASCADE-Grande: a large acceptance, high-resolution cosmic-ray detector up to 10^{18} eV*, Nucl. Inst. Meth. **A518**, 207 (2004),
[117] M. Nagano *et al*., J. Phys. **G10**, 1295 (1984),
[118] D. J. Bird *et al*., Phys. Rev. Lett. **71**, 3401 (1993),
[119] D. J. Bird *et al*., Astrophys. J. **441**, 144 (1995),
[120] T. Abu-Zayyad *et al*., Astrophys. J., *Measurement of the Cosmic-Ray Energy Spectrum and Composition from 10^{17} to $10^{18.3}$ eV Using a Hybrid Technique,* **557**, 686 (2001),
[121] M. Pravdin *et al*., **3**, 292, Proc. 26th ICRC, Salt Lake City, USA (1999),
[122] M. Pravdin *et al*., *Energy Spectrum of Primary Cosmic Rays in the Energy Region of 10^{17} – 10^{20} eV by Yakutsk Array Data*, 389, Proc 28th ICRC, Tsukuba, Japan (2003),
[123] HiRes Collaboration, Phys. Rev. Lett. **92**, 151101 (2004).

[124] M. Ave *et al*., *The Energy Spectrum of Cosmic Rays Above 3×10^{17} eV as measured with the Haverah Park Array*, **1**, 381, Proc. 27th ICRC, Hamburg, Germany (2001), astro-ph/**0112253**,
[125] M. Takeda *et al*., *Energy determination in the Akeno Giant Air Shower Array experiment*, Astropart. Phys. **19**, 447 (2003),
[126] A. A. Watson, *The mass composition of cosmic rays above 10^{17} eV*, Nucl. Phys. B (Proc. Suppl.) **136**, 290 (2004),
[127] J. Linsley, Proc 15th ICRC, Plovdiv, Bulgaria, **12**, 89 (1977),
[128] M. Zha, J. Knapp, S. Ostapchenko, *Systematic Uncertainties in High-Energy Hadronic Interaction Models*, Proc 28th ICRC, Tsukuba, Japan, **2**, 515 (2003),
[129] T. K. Gaisser *et al*., Phys. Rev. **D47**, 1919 (1993),
[130] G. Archbold *et al*., Proc. 28th ICRC, Tsukuba, Japan, **1**, 405 (2003),
[131] K. Shinozaki, M. Teshima and AGASA Collaboration, *AGASA Results,* Nucl. Phys. B (Proc. Suppl.) **136**, 18 (2004),
[132] M. Ave, *et al*., *Mass Composition of Cosmic Rays in the Range 2×10^{17}- 3×10^{18} Measured with Haverah Park Array*, Astropart. Phys. **19**, 61 (2003), astro-ph/**0203150**,
[133] M. T. Dova *et al*., *The mass composition of cosmic rays near 1018 eV as deduced from measurements made at Volcano Ranch*, Astropart. Phys. **21**, 597 (2004),
[134] M. Ave *et al*., *Time structure of the shower front as measured at Haverah Park above 10^{19} eV*, **1**, 349, Proc 28th ICRC, Tsukuba, Japan (2003),
[135] A. Tiba, G. Medina Tanco, S. Sciutto, *Neural Networks as a Composition Diagnostic for Ultra-high Energy Cosmic Rays,* astro-ph/**0502255**,
[136] K-H. Kampert *et al*., *Cosmic Ray Energy Spectra and Mass Composition at the Knee – Recent Results from KASCADE*, Nuclear Physics B (Proc. Suppl.) **136**, 273 (2004),
[137] T. Abu-Zayyad *et al*., *Measurement of the Cosmic-Ray Energy Spectrum and Composition from 10^{17} to $10^{18.3}$ eV Using a Hybrid Technique*, ApJ. **557**, 686 (2001),
[138] P. Blasi, R. Epstein, A. Olinto, *Ultra-High Energy Cosmic Rays from Young Neutron Star Winds*, astro-ph/**9912240**,
[139] P. P. Kronberg, Rep. Prog. Phys. **57**, 325 (1994),
[140] V. S. Berezinsky, S. Bulanov, V. Dogiel, V. Ginzburg, V. Ptuskin, Astrophysics of Cosmic Rays 1990, North-Holland Publishing Company, Amsterdam (ISBN:0444886419),
[141] V. S. Berezinsky, S. I. Grigoreva, A & A **199**, 1 (1988),
[142] AMIGA Design Report,
[143] T. Stanev, *On the Luminosity of the Ultra High Energy Cosmic Rays Sources*, astro-ph/**0303123**,
[144] T. Stanev, D. Seckel, R. Engel, *Propagation of ultrahigh energy protons in regular extragalactic magnetic fields*, Phys. Rev. **D68**, 103004 (2003),
[145] T. Stanev *et al*., *Propagation of ultrahigh energy protons in the nearby universe*, Phys. Rev. **D62**, 093005 (2000),
[146] V. S. Berezinsky, A. Z. Gazizov, S. I. Grigorieva, *Dip in UHECR spectrum as signature of proton interaction with CMB*, astro-ph/**0502550**,
[147] G. Medina Tanco *et al*, *Non-diffusive propagation of ultra high energy cosmic rays*, Astropart. Phys., **6**, 337 (1997),
[148] R. Aloisio, V. S. Berezinsky, *Anti-GZK Effect in Ultra-High-Energy Cosmic Ray Diffusive Propagation,* Astrophys. J., **625**, 249 (2005),
[149] D. Seckel, T. Stanev, *Neutrinos: the Key to UHE Cosmic Rays*, Phys. Rev. Lett. **95**, 141101 (2005), astro-ph/0502244,
[150] V. S. Berezinsky, S. I. Grigorieva, B. I. Hnatyk, *Extragalactic UHE proton spectrum and prediction for iron-nuclei flux at 10^{8}–10^{9} GeV*, Astropart. Phys., **21**, 617 (2004),
[151] J. Bednarz, M. Ostrowski, *Energy Spectra of Cosmic Rays Accelerated at Ultrarelativistic Shock Waves,* Phys. Rev. Lett., **80**, 3911 (1998),

[152] J. G. Kirk, A. W. Guthmann, Y. A. Gallant, A. Achterberg, ApJ., *Particle Acceleration at Ultrarelativistic Shocks: An Eigenfunction Method*, **542**, 235 (2000),
[153] M. Lemoine, G. Pelletier, ApJ., *Particle Transport in Tangled Magnetic Fields and Fermi Acceleration at Relativistic Shocks*, **589**, L73 (2003),
[154] T. Yamamoto *et al*., *Signatures of ultra-high energy cosmic ray composition from propagation of nuclei in intergalactic photon fields*, Astropart. Phys. **20**, 405 (2004),
[155] D. Allard *et al*., *UHE nuclei propagation and the interpretation of the ankle in the cosmic-ray spectrum,* astro-ph/**0505566**,
[156] J. Linsley, Proc 18th ICRC, Bangalore, **12**, 144 (1983),
[157] C. Song *et al., Energy estimation of UHE cosmic rays using the atmospheric fluorescence technique,* Astropart. Phys. **14**, 7 (2000),
[158] G. Medina Tanco, I. Allekotte, M. Gomez Berisso, 29th ICRC, Pune, India (2005),
[159] D. Allard *et al*., *Aperture Calculation of the Pierre Auger Observatory Surface Detector*, 29th ICRC, Pune, India (2005),
[160] D. Allard *et al*., *The Trigger System of the Pierre Auger Surface Detector: Operation, Efficiency and Stability*, 29th ICRC, Pune, India (2005),
[161] R. Engel, *Auger Enhancement Projects: AMIGA & HEAT,* Aspen Workshop on Cosmic Ray Physics (2007),
[162] S. Ostapchenko, *Non-linear effects in high-energy hadronic interactions*, astro-ph/**0412591** V1 (2004).
[163] Pierre Auger Collaboration, 29th ICRC, Pune, India (2005),
[164] J. Alvarez-Muñiz *et al*., *Hybrid simulations of extensive air showers*, Phys. Rev. **D66**, 033011, 3 (2002),
[165] D. Groom et al., Atomic Data and Nuclear Data Tables 78.
[166] A. Etchegoyen for the Pierre Auger Collaboration, *AMIGA – Auger Muons and Infill for the Ground Array*, 30th ICRC, Merida, Mexico (2007),
[167] Z. Szadkowski, *Triggers, data flow and the synchronization between the Auger surface detector and the AMIGA underground muon counters*, Proc. 31st ICRC, Łódź, Poland (2009),
[168] H. Klages, *HEAT – Enhancement Telescopes for the Pierre Auger Southern Observatory,* Proc. 30th ICRC, Merida, Mexico (2007),
[169] D. Kruppke, *The HEAT Extension of the Pierre Auger Observatory* , 5. Schule für Astroteilchenphysik, Obertrubach-Bärnfels (2008),
[170] M. Kleifges, *Extension of the Pierre Auger Observatory using high-elevation fluorescence telescopes (HEAT),* Proc. 31st ICRC, Łódź, Poland (2009),
[171] J. Harton, *Prospects for the Auger Observatory: Increasing acceptance at Higher and Lower Energies, North and South,* 25JTIPN (2009),
[172] J. V. Jelley, J. H. Fruin, N. A. Porter *et al*., Nature, **205**, 327 (1965),
[173] G. A. Askaryan, Soviet Phys. JETP, **14**, 441 (1962),
G. A. Askaryan, Soviet Phys. JETP, **21**, 658 (1965),
[174] H. R. Allan, Prog. in Element. part. and Cos. Ray Phys., **10**, 171 (1971),
[175] H. R. Allan, P. F. Shutie, M. P. Sun, J. K. Jones, 1973, Proc. 13th ICRC, Denver, USA, **4**, 2407 (1973),
H. R. Allan, M. P. Sun, J. K. Jones, Proc. 14th ICRC, München, Germany, **8**, 3082 (1975),
[176] V. B. Atrashkevich, O. V. Vedeneev, H. R. Allan *et al*., Sov. J. Nucl. Phys., **28**, 366 (1978),
[177] A. Belletoile, D. Ardouin, D. Charrier *et al*., *Radio Detection of Cosmic Ray Extensive Air Showers: present status of the CODALEMA experiment*, Proc. of the SF2A 2004, astro-ph/**0409039**,
[178] A. Horneffer, T. Antoni, W. D. Apel *et al*., Astronomical Telescopes and Instrumentation 2004, Gravitational Wave and Particle Astrophysics Detectors, Proc. of the SPIE, **5500**, 129 (2004),

[179] H. Röttgering, A. G. de Bruyn, R. P. Fender *et al.*, XXI Symposium on Relativistic Astrophysics, Tuscany, Texas, USA, 69 (2003),
[180] H. Falcke, P.W. Gorham, *Detecting radio emission from cosmic ray air showers and neutrinos with a digital radio telescope*, Astropart. Physics, **19**, 477 (2003),
[181] http://euso.riken.jp/,
[182] J. R. Hörandel, Pierre Auger Collaboration Meeting, Malargue, April, 2009,
[183] A. Horneffer *et al.*, for the LOPES Collaboration, Int. Journ. Mod. Phys. A21 Suppl., 168 (2006),
[184] D. Ardouin *et al.*, *Radioelectric field features of extensive air showers observed with CODALEMA*, Astropart. Phys. **26**, 341 (2006),
[185] *AERA - proposal for the construction of the 20 km^2 Auger Engineering Radio Array at the Southern Auger Observatory*, March 17, 2009,
[186] A.M. van den Berg *et al.*, *First detection of radio signals from cosmic rays at the Pierre Auger Observatory*, GAP-note 2007-065,
[187] J. Coppens for the Pierre Auger collaboration, Proc. of the ARENA Conf., Rome, Italy, 2008,
[188] S. Acounis *et al.*, *First detection of radio signals from cosmic ray air showers with a self-triggered, fully autonomous system*, GAP-note 2007-130,
B. Revenu *et al.*, *Geomagnetic feature of the events observed by the self triggered, fully autonomous radio-detectors system installed at the CLF*, GAP-note 2009-005,
B. Revenu for the Pierre Auger collaboration, Proc. of the ARENA Conf., Rome, Italy, 2008,
[189] M. Erdmann *et al.*, *A Measurement of the Continuous Radio Background at the Pierre Auger Observatory*, GAP-note 2007-120,
J. Coppens *et al.*, *Analysis of Galactic Radio Background Noise*, GAP-note 2007-123.
J. Coppens, J. Hörandel, C. Timmermans, A.M van den Berg, *A radio survey at the AMIGA site*, GAP-note 2009-003,
[190] S. Fliescher for the Pierre Auger collaboration, Proc. of the ARENA Conf., Rome, Italy (2008),
[191] J. D. Jackson, *Classical electrodynamics*, J. Wiley & Sons Inc., (1975),
[192] T. Huege, H. Falcke, *Radio emission from cosmic ray air showers,* Astronomy & Astrophysics, **412**, 19 (2003),
[193] M. Erdmann, Pierre Auger Collaboration Meeting, Malargue, April, 2009,
[194] A. Horneffer for the LOPES collaboration, *Primary Particle Energy Calibration of the EAS Radio Pulse Height*, Proc. 30th ICRC, Merida, Mexico, **4**, 83 (2007),
[195] H. Gemmeke, T. Asch, D. Bormann, O. Krömer, M. Manewald, L. Petzold, A. Schmidt, *Techniques for Radio Detection of Ultra-High Energy Cosmic Rays,* **SORMA** WEST 2008, Berkeley, USA (2008),
[196] http://www.altera.com/products/devices/stratix-fpgas/stratix/stratix/overview/stx-overview.html
[197] J.L. Smith, *Implementing Median Filters in XC4000E FPGAs, Xcell*, **23(4)**, 16, (1996),
[198] T. Asch, *Digital Self-Trigger for Radio Detection*, Radio R&D Meeting, Amsterdam (2007),
[199] Z. Szadkowski, *Prototype for a real time digital self trigger for radio detection*, Forschungszentrum Karlsruhe meeting (2007),
[200] Z. Szadkowski, Radio R&D Meeting, Nijmengen (2009),
[201] H. Gemmeke, Pierre Auger Collaboration Meeting, Malargue (2009),
[202] H. Gemmeke, *Radio_frontend_electronics_proposal_v3*,
[203] Z. Szadkowski, *A single clock cycle median filter*, in preparation.
[204] The Pierre Auger Collaboration, *Observation of the Suppression of the Flux of Cosmic Rays above 4×10^{19} eV,* Phys. Rev. Lett. **101**, 061101 (2008),
[205] L. Perrone for the Pierre Auger Collaboration, *Measurement of the cosmic ray spectrum above 10^{18} eV using data recorded with the fluorescence detectors and at least one detector of the surface array of the Auger Observatory*, Proc. 30th ICRC, Merida, Mexico (2007),

[206] R. U. Abbasi et al., *First Observation of the Greisen-Zatsepin-Kuzmin Suppression*, Phys. Rev. Lett. **100,** 101101 (2008),
[207] J. Linsley. *Proc of 8th Int. Cosmic Ray Conf., Jaipur*, **4**, 77 (1963),
[208] M. A. Lawrence, R. J. O. Reid, and A. A. Watson. *J. Phys.*, **G17**, 733 (1991),
[209] M. Nagano et al. *J. Phys.*, **G18**, 423 (1992),
[210] D. J. Bird et al. *Phys. Rev. Lett.*, **71**, 3401 (1993),
[211] V. Berezinsky, A. Z. Gazizov, and S. I. Grigorieva. *Phys. Lett.*, **B612**, 147 (2005),
[212] A. M. Hillas. *J. Phys.*, **G31**, R95 (2005),
[213] C. Di Giulio for the Pierre Auger Collaboration, *Energy calibration of data recorded with the surface detectors of the Pierre Auger Observatory*, Proc. 31st ICRC, Łódź, Poland (2009),
[214] F. Schüssler for the Pierre Auger Collaboration, *Measurement of the cosmic ray energy spectrum above 1018 eV with the Pierre Auger Observatory*, Proc. 31st ICRC, Łódź, Poland (2009),
[215] High Resolution Fly's Eye Collaboration*, Observation of the ankle and evidence for a high-energy break in the cosmic ray spectrum***,** Phys. Lett **B619**, 271 (2005),
[216] The Pierre Auger Collaboration, *Correlation of the Highest-Energy Cosmic Rays with Nearby Extragalactic Objects,* Science, **318**, 938 (2007),
[217] The Pierre Auger Collaboration, *Correlation of the highest-energy cosmic rays with the positions of nearby active galactic nuclei*, Astropart. Phys., **29**, 188 (2008),
[218] M.-P. Véron-Cetty and P. Véron, Astron. Astrophys., **455**, 773 (2006),
[219] C. Di Giulio for the Pierre Auger Collaboration, *Energy calibration of data recorded with the surface detectors of the Pierre Auger Observatory*, Proc. 31st ICRC, Łódź, Poland (2009),
[220] C. Bonifazi for the Pierre Auger Collaboration, *The angular resolution of the Pierre Auger Observatory*, Nucl. Phys, **B190** (Proc. Suppl.) 20 (2009),
[221] J. D. Hague for the Pierre Auger Collaboration, *Correlation of the Highest Energy Cosmic Rays with Nearby Extragalactic Objects in Pierre Auger Observatory Data*, Proc. 31st ICRC, Łódź, Poland (2009),
[222] A. Wald, *Sequential Analysis*, John Wiley and Sons, New York,1947,
[223] S. Y. BenZvi *et al.* , *Sequential Analysis Techniques for Correlation Studies in Particle Astronomy*, Astrophys. J, **687**, 1035 (2008),
[224] NASA/IPAC Extragalactic Database. http://nedwww.ipac.caltech.edu/.
[225] W. T. Eadie *et al. Statistical Methods in Experimental Physics*. North-Holland, Amsterdam, 1971. pp 269–271.
[226] F. Halzen et al. Rep. Prog. Phys. **65**, 1025 (2002),
P. Bhattacharjee et al. Phys. Rep. **327**, 109 (2000),
[227] R. Engel, D. Seckel, T. Stanev*, Neutrinos from propagation of ultrahigh energy protons,* Phys. Rev. **D64,** 093010 (2001),
D. Allard *et al.*, JCAP 9, 5 (2006),
L. Anchordoqui *et al.*, *Predictions for the cosmogenic neutrino flux in light of new data from the Pierre Auger Observatory*, Phys. Rev. **D76**, 123008 (2007),
[228] X. Bertou *et al.*, Astropart. Phys **17,** 183 (2002),
[229] Pierre Auger Collaboration, *Upper Limit on the Diffuse Flux of Ultrahigh Energy Tau Neutrinos from the Pierre Auger Observatory*, Phys. Rev. Lett. **100**, 211101 (2008),
[230] Javier Tiffenberg for the Pierre Auger Collaboration, *Limits on the diffuse flux of ultra high energy neutrinos set using the Pierre Auger Observatory*, Proc. 31st ICRC, Łódź, Poland (2009),
[231] K. S. Capelle et al.; Astropart. Phys. **8**, 321 (1998),
P. Billoir *et al.* Procs. of NOW 2006, Lecce, Italy,

[232] D. Gora for the Pierre Auger Collaboration, *UHE neutrino signatures in the surface detector of the Pierre Auger Observatory,* Proc. 31st ICRC, Łódź, Poland (2009),

[233] J. Alvarez-Muñiz for the Pierre Auger Collaboration, *The sensitivity of the surface detector of the Pierre Auger Observatory to UHE neutrinos*, Proc. 30th ICRC, Merida, Mexico (2007),

[234] Pierre Auger Collaboration, *Limit on the diffuse flux of ultrahigh energy tau neutrinos with the surface detector of the Pierre Auger Observatory*, Phys. Rev. **D79**, 102001, 267 (2009),

[235] R. Fisher, Ann of Eugenics **7**, 179 (1936),

[236] A. Cooper-Sarkar and S. Sarkar, JHEP **0801**, 075 (2008),

[237] Ackermann *et al.*, *Search for Ultra-High-Energy Neutrinos with AMANDA-II,* Astrophys. J. **675**, 1014 (2008),
I. Kravchenko *et al.*, *RICE limits on the diffuse ultrahigh energy neutrino flux*, Phys. Rev. **D73**, 082002 (2006),
P.W. Gorham *et al.*, arXiv:0812.2715v1,
R.U. Abbasi *et al.*, *An Upper Limit on the Electron-Neutrino Flux from the HiRes Detector,* Astrophys. J. **684**, 790 (2008),
K. Martens [HiRes], arXiv:0707.4417.